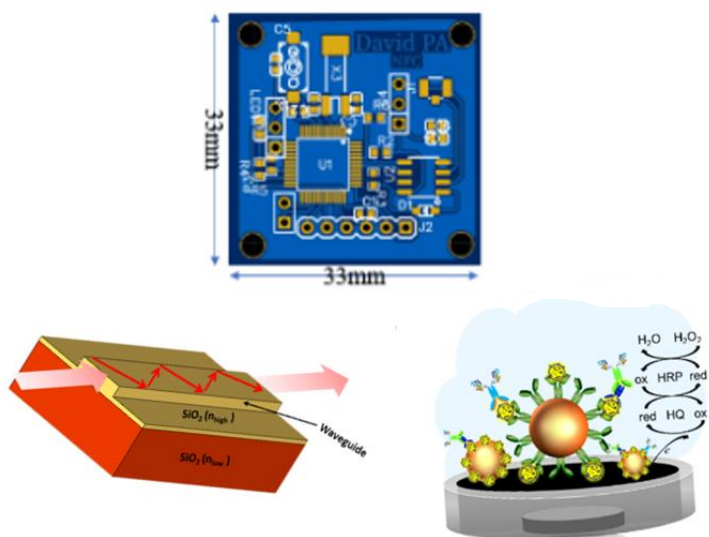


UM OLHAR SOBRE OS SENSORES NA PENÍNSULA IBÉRICA E AMÉRICA LATINA: ANO 2022

UNA MIRADA A LOS SENSORES EN LA PENÍNSULA IBÉRICA Y
AMÉRICA LATINA: AÑO 2022

A LOOK AT SENSORS IN THE IBERIAN PENINSULA AND LATIN
AMERICA: YEAR 2022



Coordenadoras
M. Teresa S. R. Gomes
Marta I. S. Veríssimo



universidade de aveiro
theoria potesis praxis

**UM OLHAR SOBRE OS SENSORES NA PENÍNSULA IBÉRICA E
AMÉRICA LATINA: ANO 2022**

UNA MIRADA A LOS SENSORES EN LA PENÍNSULA IBÉRICA Y AMÉRICA LATINA: AÑO 2022

A LOOK AT SENSORS IN THE IBERIAN PENINSULA AND LATIN AMERICA: YEAR 2022

12º Congresso Ibero-Americano de Sensores

Aveiro – PORTUGAL

M. Teresa S. R. Gomes e Marta I. S. Veríssimo

(coordenadoras)

FICHA TÉCNICA

Título:

Um olhar sobre os sensores na Península Ibérica e América Latina: Ano 2022

Coordenadoras:

M. Teresa S. R. Gomes, Marta I. S. Veríssimo

Revisores:

Carlos Domínguez-Horna | Carlos Silva Cárdenas | Cecilia Jiménez-Jorquera | Cyro Ketzer Saul | Enrique Ernesto Valdés Zaldívar | Fredy Segura-Quijano | Hesner Coto Fuentes | Idalia Ramos | Jahir Orozco Holguín | João A. B. P. Oliveira | José Antonio Plaza | José Antonio Rodríguez | Julián Alonso-Chamarro | Manel del Valle | Manuela Vieira | Marcelo Bariatto | María Gabriela Calle | M. Teresa S. R. Gomes | Mariano Aceves | Mário Ricardo Gongora-Rubio | Marta I. S. Veríssimo | Olimpia Arias de Fuentes | Salvador Alegret

Design e paginação:

Marta I. S. Veríssimo

Editora:

UA Editora

Universidade de Aveiro

Serviços de Documentação, Informação Documental e Museologia

1ª edição – Julho 2022

e-ISBN:

978-972-789-792-6

DOI:

<https://doi.org/10.48528/h76t-t092>

Os conteúdos apresentados são da exclusiva responsabilidade dos respetivos autores. © Autores. Esta obra encontra-se sob a Licença Internacional Creative Commons Atribuição 4.0.

Agradecemos o apoio financeiro ao CESAM através da FCT/MCTES (UIDP/50017/2020 + UIDB/50017/2020 + LA/P/0094/2020UIDP), através de fundos nacionais.

ÍNDICE | ÍNDICE | INDEX

Prefácio	9
Prefacio	11
Preface	13
CONVIDADOS INVITADOS INVITED	15
<i>Implantable neural probes</i>	17
<i>Recent developments in nanostructured electrochemical sensors and biosensor platforms and applications</i>	21
<i>Chemical sensors and “real” analytical chemistry</i>	25
SENSORES ELECTROQUÍMICOS SENSORES ELECTROQUÍMICOS ELECTROCHEMICAL SENSORS	29
<i>Electrochemical nano-immunosensor based on cerium oxide-doped PEDOT nanocomposite for the detection of anti-p53 autoantibodies</i>	31
<i>Sensing ferrocene derivatives using a modified glassy carbon electrode with a PEDOT/carbon microspheres thin-film</i>	34
<i>Modified ISFETs with silk fibroin membrane for pH measurements in biological matrices</i> ...	38
<i>Lignosulfonate-based polyurethanes doped with carbon nanotubes towards sensor applications</i>	43
<i>Microelectrode sensors for corrosion studies</i>	48
<i>Optimization of an electrochemical phagomagnetic assay based on signal amplification of β-GLU-Cu₃(PO₄)₂ hybrid nanoflowers for selective quantification of live <i>Listeria monocytogenes</i></i>	53
<i>Two potentiometric microsensors for Cu²⁺ determination in corrosion processes</i>	58
<i>Dissolved oxygen biosensing using electrochemical electrodes and solid electrolyte polymer</i>	65
<i>Inkjet-printed electrode modified with magnetite particles and carbon nanotubes for the non-enzymatic amperometric determination of hydrogen peroxide</i>	70
<i>Novel ISE’s membranes formulation solvent and polymeric matrix free</i>	74

SENSORES ÓTICOS E FOTOACÚSTICOS | SENSORES ÓPTICOS Y FOTOACÚSTICOS
| OPTICAL AND PHOTOACOUSTIC SENSORS 81

Biosensor based on polymer optical fiber and gold nanoparticle for rapid detection of Escherichia coli..... 82

Colorimetric based test-strips with virus-like particles as a recognition layer for SARS-CoV-2 virus..... 86

Single and cascaded long period fiber grating coated with a polydimethylsiloxane sensing film for acetone detection..... 91

Fe₃O₄-coated plastic optical fiber for H₂S sensing 96

Proposition of a photoacoustic based sensor for microplastic identification in marine environment..... 102

Oxygen sensor for oceanographic applications 107

Towards a NO_x microanalyser: miniaturized nitric oxide (NO) chemiluminescence analyzer prototype, for automotive industry applications..... 112

BIOSENSORES E APLICAÇÃO À ANÁLISE DE ALIMENTOS | BIODIAGNÓSTICOS Y APLICACIONES AL ANÁLISIS DE ALIMENTOS | BIODIAGNOSTICS AND APPLICATION TO FOOD ANALYSIS 117

Colorimetric pyranoflavylum-containing sensor films for food spoilage monitoring 118

Determinação cinética de histamina usando uma sonda ratiométrica fotoluminescente combinando pontos quânticos de carbono e pontos quânticos ternários..... 122

Development of an electrochemical aptasensor for the detection of a banned antimicrobial in milk..... 127

Disposable molecularly imprinted electrochemical sensor containing reduced graphene oxide and nickel nanoparticles for determination of p-coumaric acid in fruit peels 132

NOVOS MATERIAIS | NUEVOS MATERIALES | NEW MATERIALS 137

Laser-induced graphene on polyimide and paper substrates for low-cost and flexible electrochemical biosensors 138

UV photodetector based on reduced graphene oxide and n-type Si heterojunction..... 142

Host-guest sensing system based on sulfonatocalixarene and pyranoflavylum dye for biogenic amine sensing during food spoilage..... 148

Photosensitive nanopolymersomes as electroactive species carriers: towards the development of biosensors..... 151

Natural nanostructured materials as tuneable photonic sensing platforms..... 155

<i>Colorimetric assays for cardiovascular biomarkers detection using gold nanoparticles.....</i>	<i>159</i>
<i>A flow injection setup to determine oxytetracycline with a piezoelectric quartz crystal.....</i>	<i>164</i>
<i>Simultaneous voltammetric determination of acetaminophen, ascorbic acid and uric acid by use of integrated array of sensors modified with mesoporous carbon and metallic nanoparticles and electronic tongue principles</i>	<i>169</i>
<i>Modification of natural photonic crystals by tailoring of the refractive index contrast</i>	<i>174</i>
<i>Synthesis of microparticles of Cu₂ZnSnS₄ by hydrothermal method and its application as Congo Red photocatalyst</i>	<i>178</i>
<i>Characterization of Al₂O₃ and SiO₂ ultra-thin films deposited by ALD for microfabricated rubidium vapor cells</i>	<i>181</i>
<i>Structural and optical properties of sprayed undoped ZnO thin films suitable for resistive gas sensors</i>	<i>185</i>
<i>SRO/nitride-based electrophotonics for sensing applications</i>	<i>190</i>
DESENHO E TECNOLOGIA DE SENSORES E MEMS DISEÑO Y TECNOLOGÍA DE SENSORES Y MEMS DESIGN AND TECHNOLOGY OF SENSORS AND MEMS	195
<i>CoNi and Ni-based barcodes toxicity for tagging and magnetic manipulation of HeLa cells</i>	<i>196</i>
<i>Photonic planar taper waveguide</i>	<i>201</i>
<i>Sistema electrónico para medición de calidad de sustancias: diseño e implementación</i>	<i>209</i>
<i>Projeto de encapsulamento de sensores inerciais usando tecnologia LTCC.....</i>	<i>214</i>
<i>MEMS-based fabrication of an atomic vapor cell for brain magnetic field measurement</i>	<i>218</i>
<i>MEMS rubidium vapor cell for optically pumped magnetometers</i>	<i>223</i>
<i>MEMS-based waveguide SiO₂ fabricated by RIE process for optical sensing.....</i>	<i>227</i>
<i>Rubidium vapor cells fabricated by additive manufacturing</i>	<i>231</i>
CONDICIONAMENTO DE SINAL E INSTRUMENTAÇÃO ACONDICIONAMIENTO DE SEÑAL Y INSTRUMENTACIÓN SIGNAL CONDITIONING AND INSTRUMENTATION	237
<i>Inexpensive corn starch based supercapacitor for signal conditioning and detection</i>	<i>238</i>
<i>Feature extraction acceleration by the prediction of the steady state response for solid state gas sensors.....</i>	<i>242</i>
<i>Integración de redes neuronales con sistemas analíticos integrados para la cuantificación de metales pesados en solución acuosa.....</i>	<i>247</i>

<i>Multi-photon microscopy setup for integration in colonoscopes: an overview</i>	252
<i>Simulación de la instrumentación electrónica asociada al isfet mediante el circuito integrado CD-4007</i>	257
MICROSSISTEMAS ANALÍTICOS INTEGRADOS E LAB-ON-A-CHIP MICROSISTEMAS ANALÍTICOS INTEGRADOS Y LAB-ON-A-CHIP ANALYTICAL INTEGRATED MICROSYSTEMS AND LAB-ON-A-CHIP	263
<i>Microreactors in protein pegylation: towards higher yields and specificity</i>	264
<i>Functionalization of a fully integrated electrophotonic silicon circuit for sensing biomolecules</i>	270
<i>Microanalizadores automáticos modulares para la monitorización de metales pesados en procesos hidrometalúrgicos</i>	274
<i>Optimización del sistema analítico integrado para el monitoreo de ión cobre en efluentes de una mina</i>	279
<i>Development of a microswitch made in LTCC-PDMS technology applicable to micro total analysis systems</i>	284
<i>Integração e automatização do funcionamento e do processo de aquisição de dados leitura de um sistema de sensores numa bancada de calibração de medidores de vazão de líquidos ..</i>	289
SENSORES INTELIGENTES E REDES SEM FIOS SENSORES INTELIGENTES Y REDES INALÁMBRICAS SMART SENSORS AND WIRELESS NETWORKS 	295
<i>Architecture of a bi-directional VLC system for navigation and message transmission</i>	296
<i>Intelligent split intersections using cooperative vehicle visibility communication</i>	301
<i>A visible light communication system to support indoor guidance</i>	307
<i>Wireless sensor network system for landslide monitoring</i>	313
SENSORES DE ONDAS ACÚSTICAS SENSORES DE ONDAS ACÚSTICAS ACOUSTIC WAVE SENSORS	319
<i>Automation of the drop-casting deposition method for polymeric sensing films over a quartz crystal microbalance</i>	320
<i>Development of a relative humidity pid control for the characterization of gas sensors based on quartz resonators</i>	325
<i>Response measurement acceleration of QCM-based gas sensors using the transient response</i>	329

APLICAÇÕES AO MEIO AMBIENTE E AGRICULTURA. POUPANÇA DE ENERGIA | APLICACIONES AL MEDIO AMBIENTE Y A LA AGRICULTURA. AHORRO DE ENERGÍA | APPLICATIONS TO THE ENVIRONMENT AND AGRICULTURE. ENERGY SAVING333

Plastic-optical-fiber-based solar tracker development applied for ambiences illumination .334

Aveiro steam city project: a good practice with urban air quality sensors network.....339

Intercomparison between air quality microsensors and conventional monitoring data344

Sistema para el monitoreo de la calidad del aire en la zona metropolitana de la laguna.....348

Evaluation of in-soil nutrient probes in different types of soils353

Inductive salinity sensor.....358

APLICAÇÕES À BIOMEDICINA E À SAÚDE | APLICACIONES A LA BIOMEDICINA Y A LA SALUD | APPLICATIONS TO BIOMEDICINE AND HEALTH363

Biosensing strategies for exosomes.....364

Simultaneous quantitative analysis of several electrolytes in sweat samples using a flow system and potentiometric devices369

Impedimetric and capacitive biosensing of β -1,4-galactosyltransferase-v colon cancer biomarker.....374

Disposable biomedical devices for at-home monitoring of different metabolic diseases.....379

Surface modification of gallium nanoparticles and their interaction with human serum albumin383

Detection of defects on displays based on microscopic and optical coherence tomography examination.....388

Cu₂O/CuO composite synthesis by thermal treatment of Cu₂O thin films and its application as a non-enzymatic glucose sensor.....392

Gallium nanoparticles interaction with IAPP: can GaNPs inhibits oligomerization?396

ÍNDICE DE AUTORES | ÍNDICE DE AUTORES | |AUTHORS' INDEX |401

PREFÁCIO

O campo dos sensores continua a crescer e a evoluir, mas está longe de responder às necessidades atuais. Fruto das ligações históricas, partilha linguística do português e do espanhol e intercâmbios atuais, nasceu a comunidade IBERSENSOR, que organizou o seu primeiro congresso sobre a referida temática há 24 anos. Havana em Cuba foi o primeiro local de reunião, em 1998, a que se seguiram Buenos Aires (Argentina) em 2000, Lima (Peru) em 2002, Puebla (México) em 2004, Montevideo (Uruguai) em 2006, São Paulo (Brasil) em 2008, Lisboa (Portugal) em 2010, San Juan (Porto Rico) em 2012, Bogotá (Colômbia) em 2014, Viña del Mar (Chile) em 2016, Barcelona (Espanha) em 2018, e depois de uma interrupção ditada pela pandemia, Aveiro (Portugal) em 2022. A longevidade, regularidade dos congressos, diversidade geográfica e número de participantes mostram que a comunidade está viva.

Este livro reúne 77 trabalhos, selecionados após revisão por pares. Os resumos reunidos são tão diversos como as línguas em que estão escritos e, principalmente, em que serão apresentados. O inglês surge como língua franca para a comunicação científica e foi usado na maioria dos textos escritos e em todos os diapositivos, mas, fruto da coesão entre os participantes e na proximidade, quantas vezes enganadora, entre o português e o espanhol, assistir-se-á a apresentações nas três as línguas oficiais, entendíveis pela esmagadora maioria da audiência. A liberdade linguística traduz-se numa comunicação vívida e sem complexos, que ganha em espontaneidade, riqueza de imagens e justeza nos termos. O IBERSENSOR ganha mais uma dimensão: a de divulgação do vocabulário tecnológico nas línguas maternas.

As comunicações são uma mostra daquilo que se faz na comunidade, onde os sensores eletroquímicos dominam. O estado da arte em termos de plataformas para sensores eletroquímicos, aplicações e perspectivas futuras é tema da comunicação convidada do Professor Christopher Brett. Não faltam, contudo, sensores baseados noutra tipo de transdutores, como os piezoelétricos e os óticos. Há ainda um número significativo de trabalhos dedicados a novos materiais, necessários para modificar a superfície do sensor, a fim de a tornar seletiva, melhorar o sinal, ou permitir a imobilização de enzimas e outras biomoléculas. Desenvolvimentos ao nível da conceção e tecnologia, instrumentação, condicionamento do sinal e comunicação sem fios estão na ordem do dia. A miniaturização das operações laboratoriais até à escala do circuito integrado “*lab-on-a-chip*” está contemplada.

Transpor a porta do laboratório e trazer os sensores para o mundo real é um dos maiores desafios. Esta temática é discutida pelo Professor Tony Edmonds, que traz exemplos concretos. O Professor Edmonds fala-nos ainda da relação entre os sensores químicos e a química analítica, e como a mesma, nas vertentes de purificação, síntese e comparação, tem que integrar a estrutura e protocolo dos mesmos.

Há um número significativo de aplicações, algumas das quais com dispositivos interessantes, outras que valem pela discussão dos resultados de medições no campo do ambiente, agricultura, alimentos e biomedicina. Um dos campos onde há uma grande apetência por sensores é a saúde. Dispositivos simples que permitam detetar precocemente algumas patologias, entre as quais o cancro, ou obter parâmetros analíticos para avaliação clínica estão entre os mais procurados. O Professor Higinio Correia tem neste livro um resumo dedicado a dispositivos neuronais, cuja função será restaurar funções sensoriais e motoras.

Para esta coleção de trabalhos reunidos neste livro, trabalhou um número considerável de investigadores, mais de duas centenas, a quem manifesto o meu agradecimento. O agradecimento estende-se à comissão científica, que teve a tarefa de rever todos os trabalhos, de seleccionar aqueles que aparecem nesta publicação, e ainda de sugerir alterações, sempre que as julgou necessárias. Agradeço também ao comité permanente, que me honrou com a sua confiança ao delegar em mim a realização deste 12º Congresso IBERSENSOR e ao comité organizador local, pelo apoio na concretização desta tarefa.

Faço votos para que esta seja uma conferência frutífera para cada um dos participantes, e que disfrutem da cidade de Aveiro.

julho de 2022



M. Teresa S. R. Gomes

Presidente da conferencia

PREFACIO

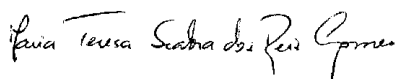
El campo de los sensores sigue creciendo y evolucionando, pero está lejos de responder a las necesidades actuales. Fruto de las conexiones históricas, del compartir lingüístico del portugués y del español, y de los intercambios actuales nació la comunidad IBERSENSOR, que organizó, hace 24 años, su primer congreso sobre el tema mencionado. El primer lugar de encuentro fue en La Habana, Cuba, en 1998, seguido de Buenos Aires (Argentina) en 2000, Lima (Perú) en 2002, Puebla (México) en 2004, Montevideo (Uruguay) en 2006, São Paulo (Brasil) en 2008, Lisboa (Portugal) en 2010, San Juan (Puerto Rico) en 2012, Bogotá (Colombia) en 2014, Viña del Mar (Chile) en 2016, Barcelona (España) en 2018, y tras una interrupción dictada por la pandemia, Aveiro (Portugal) en 2022. La longevidad, la regularidad de los congresos, la diversidad geográfica y el número de participantes muestran que la comunidad está viva. Este libro reúne 77 trabajos, seleccionados después de la revisión por pares. Los resúmenes son tan diversos como los idiomas en que están escritos y en que se presentarán. El inglés es la lengua franca para la comunicación científica, y se utilizó en la mayoría de los textos escritos y además en todas las diapositivas, pero, en resultado de la cohesión entre los participantes y en la proximidad, muchas veces engañosa por la similitud, entre portugués y español, uno asistirá a presentaciones en los tres idiomas oficiales, comprensibles para la mayoría de la audiencia. La libertad lingüística se traduce en una comunicación con vivacidad y sin complejos, que gana en la espontaneidad, riqueza de imágenes y precisión en los términos. El IBERSENSOR gana otra dimensión: la de difusión del vocabulario tecnológico en los idiomas maternos.

Las comunicaciones son un ejemplo de lo que se está haciendo en la comunidad. Los sensores electroquímicos constituyen la mayoría de los trabajos. El estado del arte, en términos de plataformas para sensores electroquímicos, aplicaciones y perspectivas futuras, es tema de la comunicación del profesor invitado Christopher Brett. Sin embargo, no faltan sensores basados en otro tipo de transductores, como los piezoeléctricos y los ópticos. Todavía hay un número importante de trabajos dedicados a nuevos materiales, necesarios para modificar la superficie del sensor para hacerla selectiva, mejorar la señal o permitir la inmovilización de enzimas y otras biomoléculas. Los desarrollos en diseño y tecnología, instrumentación, acondicionamiento de señal y comunicación inalámbrica están a la orden del día. También se encuentra el tema de la miniaturización de las operaciones de laboratorio hasta la escala del circuito integrado "*lab-on-a-chip*".

Cruzar la puerta del laboratorio y traer sensores al mundo real es uno de los mayores desafíos. Este tema es discutido por el profesor Tony Edmonds, quien aporta ejemplos concretos. El profesor Edmonds también nos habla de la relación entre los sensores químicos y la química analítica, y cómo la misma, en términos de purificación, síntesis y comparación, debe integrar su estructura y protocolo.

Hay un número importante de aplicaciones, algunas de las cuales, con dispositivos interesantes, otras dignas de ser discutidas por los resultados de las mediciones en el campo del medio ambiente, la agricultura, la alimentación y la biomedicina. Uno de los campos donde hay un gran interés por la utilización de sensores es el de la salud. Entre los más demandados se encuentran dispositivos sencillos que permiten la detección precoz de algunas patologías, incluido el cáncer, u obtener parámetros analíticos para la evaluación clínica. El profesor Higinio Correia tiene en este libro un resumen dedicado a los dispositivos neuronales, cuya función será restaurar las funciones sensoriales y motoras. Para esta colección de trabajos reunidos en este libro han trabajado un número considerable de investigadores, más de doscientos, a los que expreso mi agradecimiento. El reconocimiento se hace extensivo al comité científico, que tuvo la tarea de revisar todos los trabajos, seleccionar los que aparecen en esta publicación, así como sugerir cambios, cuando lo consideró necesario. También agradezco al comité permanente, que me honró con su confianza delegando en mí la celebración de este XII Congreso de IBERSENSOR, y al comité organizador local, por su apoyo en la realización de esta tarea. Espero que esta sea una conferencia fructífera para cada uno de los participantes y que disfruten de la ciudad de Aveiro.

Julio, 2022



M. Teresa S. R. Gomes

Presidente de la conferencia

PREFACE

The field of sensors continues to grow, and to evolve, but it is far from responding to current needs. As a result of historical connections, linguistic sharing of Portuguese and Spanish languages, and current exchanges, the IBERSENSOR community was formed. The first IBERSENSOR congress on the aforementioned topic took place 24 years ago. Havana in Cuba was the first meeting place, in 1998, followed by Buenos Aires (Argentina) in 2000, Lima (Peru) in 2002, Puebla (Mexico) in 2004, Montevideo (Uruguay) in 2006, São Paulo (Brazil) in 2008, Lisbon (Portugal) in 2010, San Juan (Puerto Rico) in 2012, Bogotá (Colombia) in 2014, Viña del Mar (Chile) in 2016, Barcelona (Spain) in 2018, and, after an interruption dictated by the pandemic, Aveiro (Portugal) in 2022. The longevity, regularity of congresses, along with geographic diversity and number of participants show that the community is alive.

This book brings together 77 works, selected after peer review. The gathered abstracts are as diverse as the languages in which they are written and, above all, in which the works will be presented. English emerges as the dominant language for scientific communication and was used in most of the written texts and on all the slides. However, as a result of the cohesion between the participants and the proximity, often misleading, between Portuguese and Spanish, one can witness presentations in the three official languages, ordinarily understandable by the majority of the audience. Linguistic freedom translates into vivid and relaxed communication, which gains in spontaneity, richness of images and correctness of terms. IBERSENSOR gains another dimension, that of disseminating technological vocabulary in mother tongues.

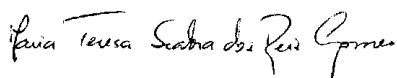
The extended abstracts are an example of what is being done in the community. The electrochemical sensors dominate. The state of the art, in terms of platforms for electrochemical sensors, applications and future perspectives is the theme of the invited communication by Professor Christopher Brett. However, there is no lack of sensors based on other types of transducers, such as piezoelectric and optical ones. There is still a significant number of works dedicated to new materials, needed to modify the sensor surface in order to make it selective, improve the signal, or allow the immobilization of enzymes and other biomolecules. Developments in terms of design and technology, instrumentation, signal conditioning and wireless communication are on the agenda. Miniaturization of laboratory operations “lab-on-a-chip” down to the scale of the integrated circuit is contemplated.

Crossing the laboratory door and bringing sensors into the real world is one of the biggest challenges. This theme is discussed by Professor Tony Edmonds, who brings real examples. Professor Edmonds also tells us about the relationship between chemical sensors and analytical chemistry, and how the that three-fold approach (purification, synthesis and comparison) has been, can be and should be encoded into the structure and protocol of the chemical sensors.

There are a significant number of applications, some with interesting devices, others with results that deserve to be discussed, dedicated to measurements in the fields of environment, agriculture, food and biomedicine. One of the fields where there is a great appetite for sensors is health. Simple devices that allow the early detection of some pathologies, including cancer, or obtain analytical parameters for clinical evaluation are among the most sought after. Professor Higinio Correia has, in this book, a summary dedicated to neural probes, whose aim will be to restore sensory and motor functions.

A considerable number of researchers worked for the extended abstracts gathered in this book. They were more than two hundred, to whom I express my gratitude. The acknowledgment is extended to the scientific committee, which had the task of reviewing all the works, selecting those that appear in this publication, and also suggesting changes, whenever deemed necessary. I also thank the permanent committee, which honoured me with its trust and have delegated to me the organization of this 12th IBERSENSOR Congress. I am grateful to the local organizing committee, which was essential to carrying out this task. I hope that this will be a fruitful conference for each of the participants, and that they will enjoy the city of Aveiro.

July 2022



M. Teresa S. R. Gomes

Conference chair

CONVIDADOS | INVITADOS | INVITED

IMPLANTABLE NEURAL PROBES

José Higinio Correia

CMEMS – UMinho, University of Minho, Campus Azurem – 4800-058, Guimarães – Portugal

LABELS – Associate Laboratory, Braga/Guimarães, Portugal

e-mail: higinio.correia@dei.uminho.pt

Introduction

Devices capable of interfacing with neural circuits, either by recording or modulating their activity, have been a reality for a few decades. Neuroscientists are taking advantage of these interfaces to map brain networks, and gather knowledge of their working mechanisms and interrelations. The ultimate goal of these devices, also known as neural probes, is to restore sensory and motor functions, and to treat neurological disorders. Conventionally, neural probes consist of electrical conductors that are in contact with the aqueous ionic solutions of brain tissue. Early electrodes consisted of insulated wires capable of acquiring bioelectric signals, by transducing ionic currents into electric currents [1].

Recording neural activity was quickly followed by electrical stimulation capable of brain network neuromodulation. Probing and perturbing neural activity has matured to various clinical applications. Implantable neural interfaces are emergent therapeutics in nervous system diseases. Deep brain stimulation (DBS) has shown beneficial effects in a variety of neurological conditions, such as depression, obsessive compulsive disorder (OCD), chronic pain, Parkinson's disease, epilepsy, essential tremor, dystonia and Tourette syndrome. Cochlear and retinal implants are also widely used in the therapy of deafness and blindness, respectively. Indeed, cochlear neuroprostheses are a successful therapeutic method. Neuroprosthetics are also applied to peripheral neural system disabilities, by trying to achieve control of artificial limbs in individuals with tetraplegia. Despite having represented a major breakthrough in the field of neuroscience, electrical interfaces still hold clinical restrictions such as an inability to target specific cell types within a neural circuit [2-4].

Overcoming this limitation in 2005, a new field of research in neuroscience emerged: optogenetics. The first published study described how a microbial opsin, a natural light-sensitive ion-transporting membrane protein, could be expressed in neurons to make their electrical activity influenced by light.

Over the last decade, optogenetics has seen a rapid rise in the number of publications, therefore becoming a widespread research subject in neuroscience.

An optrode architecture includes optical, electrical, structural and hardware components: (i) a light source is required to activate photosensitive proteins in neurons; (ii) electrical recording sites are used for simultaneous electrophysiology studies; (iii) optical and electrical parts are assembled on a rigid or flexible platform for fixation purposes; and, finally, (iv) data acquisition, transmission and processing electronics can be external or monolithically coupled to the structural part of the device. Optrodes delivering light in combination with any other recording technique (optical, chemical or magnetic) have been referred as optoprobes.

Methods

Medical devices have a great impact but rigorous production and quality norms to meet, which pushes manufacturing technology to its limits in several fields, such as electronics, optics, communications, among others. This paper briefly explores how the medical industry is absorbing many of the technological developments from other industries, and making an effort to translate them into the healthcare requirements. An example is discussed in depth: implantable neural microsystems used for brain circuits mapping and modulation. Conventionally, light sources and electrical recording points are placed on silicon neural probes for optogenetic applications. The active sites of the probe must provide enough light power to modulate connectivity between neural networks, and simultaneously ensure reliable recordings of action potentials and local field activity. These devices aim at being a flexible and scalable technology capable of acquiring knowledge about neural mechanisms. In addition, PDMS micro-lenses on LEDs top surface are presented for focusing and increasing light intensity on target structures [5-7].

Results

Figure 1 shows a potential 3D optrode design comprising micro-LED arrays enabling multiple wavelengths. Integration of micro-LEDs with multiple wavelengths at this point will only be possible by LED transfer techniques. For the collimation of the divergent light emitted from the top surface of μ -LEDs, polymer-based lenses could be fabricated over their surface, ultimately enhancing the light density at each optical site. Planar surface micro-LEDs showing a Lambertian pattern can benefit from a dome-shaped lens encapsulation combined with a rear side reflector structure that demonstrated to improve the emitted light intensity using exclusively a transparent polydimethylsiloxane (PDMS) lenses, fabricated over flat commercial LEDs, has shown to substantially reduce the divergence of the emitted light.

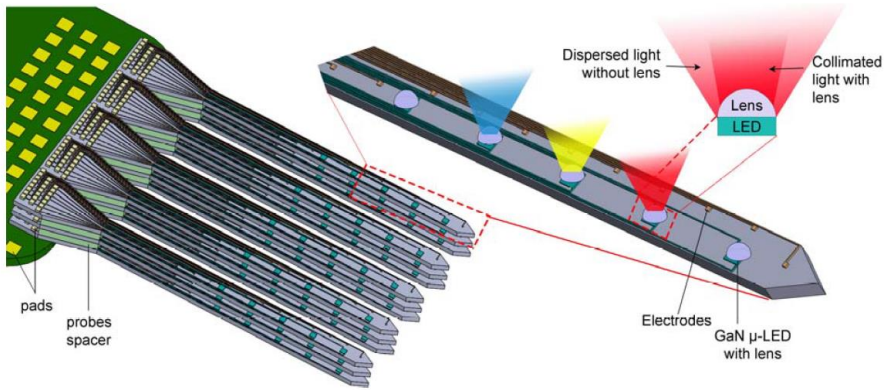


Figure 1: 3D optrode array schematic resulting from the assembly of several planar optrode units. Each optrode is expected to promote simultaneous electrical recording and optical stimulation through micro-LEDs. The individually addressable micro-LED arrays enable multiple wavelengths and collimated light by employing micro-lenses.

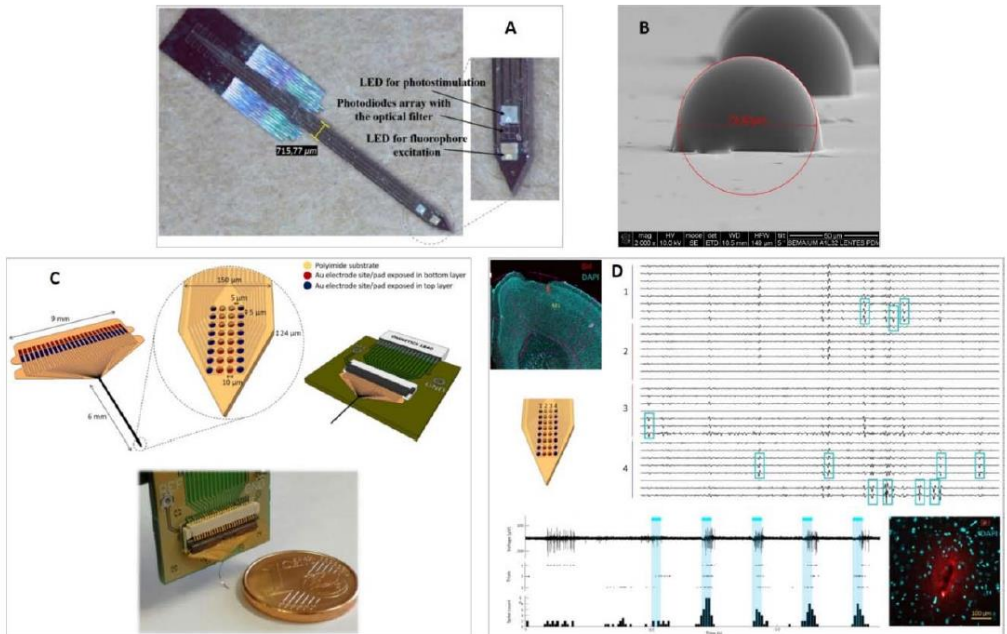


Figure 2: A - shows the neural probe with all the optical components (microLEDs and optical filter on the top of the CMOS photodiodes array). B - shows a SEM image of a PDMS microlens. C – shows a flexible fabricated neural probe. D - the in-vivo recordings in the mouse cortex.

Figure 2 shows in Figure 2A the neural probe with all the optical components (microLEDs and optical filter on the top of the CMOS photodiodes array). Figure 2B shows a SEM image of a PDMS microlens. Figure 2C shows a flexible fabricated neural probe and Figure 2D the in-vivo recordings in the mouse cortex.

Conclusions

The design and manufacturing approaches available are reviewed, and the current challenges to accomplish appropriate multimodality and optical devices are discussed. Finally, an optrode and a flexible neuronal probe, with electrophysiological recording sites are presented.

References

- [1] S.B. Goncalves, J.F. Ribeiro, A.F. Silva, R.M. Costa, J.H. Correia, Design and Manufacturing Challenges of Optogenetic Neural Interfaces: A Review, *J Neural Eng.*, Vol. 14, pp 041001, 2017.
- [2] S Pimenta, JP Pereira, NM Gomes, JF Ribeiro, MF Silva, SB Goncalves, G Minas, JH Correia, Highselectivity neural probe based on a Fabry Perot optical filter and a CMOS silicon photodiodes array at visible wavelengths, *J Biomed Opt, SPIE*, vol. 23, pp. 105004, October 2018.
- [3] SB Goncalves, JM Palha, HC Fernandes, MR Souto, S Pimenta, T. Dong, Z Yang, JF Ribeiro, JH Correia, μ LED optrode with integrated temperature sensing for optogenetics, *Micromachines*, MDPI, vol. 9, No. 473, September 2018.
- [4] SB Goncalves, AM Loureiro, HC Fernandes, S Pimenta, JF Ribeiro, JH Correia, High-aspect ratio Si neural shafts: fabrication and brain implantation, *J. Microelectromech. Syst, IEEE*, vol. 27, No. 6, December 2018.
- [5] J. A. Rodrigues, S. Pimenta, J.P. Pereira, Low-cost silicon neural probe: fabrication, electrochemical characterization and in vivo validation, *Journal Microsystem Technologies*, Springer, May 2020.
- [6] J. R. Freitas, S. Pimenta, J. F. Ribeiro, Tao Dong, Z. Yang, J. H. Correia, Simulation, fabrication and morphological characterization of a PDMS microlens for light collimation on optrodes, *Journal Optik*, Vol. 227, article 166098, 1-8 pages, February 2021.
- [7] S. Pimenta, J. A. Rodrigues, F. Machado, J. F. Ribeiro, M. J. Maciel, O. Bondarchuk, P. Monteiro, J. Gaspar, J. H. Correia, L. Jacinto, Double-layer flexible neuronal probe with closely spaced electrodes for highdensity in-vivo brain recordings, *Frontiers in Neuroscience*, 15, 663174, 2021.

Acknowledgments

This work was supported by: project MME, FCT, project OpticalBrain reference PTDC/CTMREF/28406/2017, operation code POCI-01-0145-FEDER-028406, through the COMPETE 2020; CMEMS-UMinho Strategic Project UIDB/04436/2020; project Infrastructures Micro&NanoFabs@PT, operation code NORTE 01-0145-FEDER-022090, POR Norte, Portugal 2020 and project Brain-Lighting funded by ANI, FEDER with the reference POCI-01-0247-FEDER-003416.

RECENT DEVELOPMENTS IN NANOSTRUCTURED ELECTROCHEMICAL SENSORS AND BIOSENSOR PLATFORMS AND APPLICATIONS

Christopher M. A. Brett

*Department of Chemistry, CEMMPRE, Faculty of Sciences and Technology, University of
Coimbra, 3004-535 Coimbra, Portugal
e-mail: cbrett@ci.uc.pt*

In this lecture, some recent developments and trends in electrochemical sensor and biosensor platforms are surveyed and illustrative applications from our research are given together with future perspectives.

In choosing a sensor or biosensor, the first question to be asked is what are the advantages of sensors and biosensors being electrochemical. The answer at a fundamental level is due to the possibility of externally controlling the energy of the transferrable electrons in oxidation or reduction processes, that confers and can enhance selectivity. Other advantages are easy adaptation to different media in which measurements are made, portability and miniaturization, possibility of automation, low detection limits and high sensitivity [1]. Consideration of such factors enables the development strategies to be focused on the sensing needs, particularly in complex matrices. Further aspects concern the materials for sensor construction and their cost and ease of use, calibration, response time, accuracy, repeatability and reproducibility, amount of sample available. Electrochemical sensors and biosensor platforms are versatile and applicable to different types of analysis that include environmental, food and clinical/pharmaceutical. Nowadays, software permits relatively sophisticated analysis of the sensor response as well as remote measurements through wireless connections. Some of these aspects will be addressed in the context of fixed potential amperometric, voltammetric and impedimetric sensors.

The general modification strategy followed by us in recent research is based on deposition of nanomaterials that may be followed by deposition of polymer films formed by potential cycling. Such nanomaterials can be carbon (principally nanotubes or graphene), metal or metal oxide nanoparticles [2]. The rationale behind this is to exploit possible electrocatalytic effects as well as increase sensitivity via an increase in active electrode area. For example, the electrochemical characterization of cefadroxil antibiotic can be performed at glassy carbon electrodes modified with different loadings of multiwalled carbon nanotubes (MWCNT) dispersed in chitosan and gold nanoparticles (AuNP) with

enhancement of the oxidation response and evidencing synergistic effects [3]. Similar conclusions were reached with estradiol in environmental samples at a sensor platform with the same architecture [4]. Benefits of modification by carbon nanomaterials together with gold nanoparticles lead to synergistic effects, as shown in voltammetric and impedimetric sensors for bisphenol A [5].

Electrode surface modification by nanomaterials has been combined with electrodeposition of films of electroactive redox polymers prepared from phenazine or triarylmethane dyes, as redox mediators, to give further enhancement of sensor and biosensor performance. Some of the ways in which such composite modification can be achieved are shown in Fig.1. The electropolymerisation of phenazines and triarylmethanes on carbon electrodes or carbon electrodes modified with carbon nanomaterials leads to microenvironments that are suitable for the posterior immobilization of enzymes and other biomolecules. This has been explored in aqueous electrolytes, room temperature ionic liquids and, more recently, in deep eutectic solvents (DES) [6]. In DES, the eutectic effect is due to strong hydrogen bonding interactions between a hydrogen bond acceptor HBA (commonly choline chloride) and a hydrogen bond donor (HBD) (examples being ethylene glycol, urea and glycerol) to give sufficient conductivity, especially if acid-doped, and are normally of low toxicity. Applications have been in many fields, including electrochemical sensors. The high viscosity influences the rate of polymer nucleation and of polymer growth, normally leading to improved polymer deposition compared to aqueous electrolytes.

Polymerisation in different DES has been investigated, particularly in ethaline (choline chloride: ethylene glycol in a 1:2 ratio). The polymerization of phenazine dyes in acid-doped ethaline on nanomaterial-modified electrodes increases the polymer surface uniformity and leads to improved sensing capabilities, better electrocatalytic effects and film stability than in films formed in aqueous electrolyte. Composites of these nanostructured redox polymer films plus MWCNT, iron oxide (Fe_2O_3), CuO or Prussian blue nanoparticles are successful combinations e.g. [7-10]. These examples will be used to demonstrate the strategy followed for the construction, characterisation and application to key environmental, food and pharmaceutical analytes, of such sensors, enzyme biosensors and enzyme inhibition biosensors.

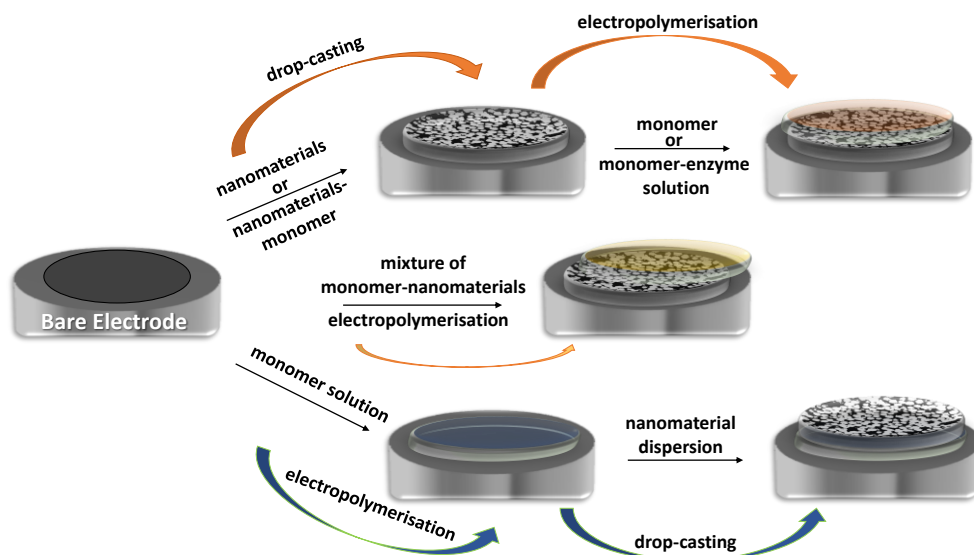


Fig. 1. Schematic preparation of redox polymer/nanomaterial-based electrochemical sensors and biosensors, see [2] for more details.

An on-going trend towards self-assembled monolayer sensors that use less reagents and are more stable will be presented [11]. New self-assembled layer-by-layer (LbL) strategies for constructing thin, multilayer electrochemical sensors and biosensors have the potential to improve analyte access to the reaction sites and reduce the diffusion time of the analytes and reaction products, whilst also increasing sensor robustness. At the same time, self-assembly by electrostatic attraction as deposition methodology enables organised and stable architectures to be formed.

Future perspectives will be discussed.

References

- [1] C.M.A. Brett, A.M. Oliveira Brett, Future tasks of electrochemical research, *J. Solid State Electrochem.*, 24 (2020) 2051-2052.
- [2] B. Dalkiran, C.M.A. Brett, Polyphenazine and polytriphenylmethane redox polymer/nanomaterial-based electrochemical sensors and biosensors: A review, *Microchim. Acta*, 188 (2021) 178.
- [3] C.G. Sanz, S.H.P. Serrano, C.M.A. Brett, Electroanalysis of cefadroxil antibiotic at carbon nanotube / gold nanoparticle modified glassy carbon electrodes, *ChemElectroChem*, 7 (2020) 2151-2158.

- [4] M. Masikini, M.E. Ghica, P.G.L. Baker, E.I. Iwuoha, C.M.A. Brett, Electrochemical sensor based on multi-walled carbon nanotube / gold nanoparticle modified glassy carbon electrode for detection of estradiol in environmental samples, *Electroanalysis*, 31 (2019) 1925-1933.
- [5] N. Ben Messaoud, M.E. Ghica, C. Dridi, M. Ben Ali, C.M.A. Brett, Electrochemical sensor based on multiwalled carbon nanotube and gold nanoparticle modified electrode for the sensitive detection of bisphenol A, *Sens. Actuat. B*, 253 (2017) 513-522.
- [6] C.M.A. Brett, Deep eutectic solvents and applications in electrochemical sensing, *Curr. Opin. Electrochem.*, 10 (2018) 143-148.
- [7] W. da Silva, M.E. Ghica, C.M.A. Brett, Choline oxidase inhibition biosensor based on poly(brilliant cresyl blue) – deep eutectic solvent / carbon nanotube modified electrode for dichlorvos organophosphorus pesticide, *Sens. Actuat. B*, 298 (2020) 126862.
- [8] W. da Silva, A.C. Queiroz, C.M.A. Brett, Poly(methylene green) – ethaline deep eutectic solvent / Fe₂O₃ nanoparticle modified electrode electrochemical sensor for the antibiotic dapsone, *Sens. Actuat. B*, 325 (2020) 128747.
- [9] B. Dalkiran, C.M.A. Brett, A novel nanostructured poly(thionine)-deep eutectic solvent/CuO nanoparticle film modified disposable pencil graphite electrode for determination of acetaminophen in the presence of ascorbic acid, *Anal. Bioanal. Chem.*, 413 (2021) 1149-1157.
- [10] W. da Silva, C.M.A. Brett, Electrosynthesis and characterisation of novel poly(Nile blue)-deep eutectic solvent/Prussian blue nanoparticle modified electrodes and their biosensing application, *J. Electroanal. Chem.*, 896 (2021) 115188.
- [11] C.M.A. Brett, Perspectives and challenges for self-assembled layer-by-layer biosensor and biomaterial architectures, *Curr. Opin. Electrochem.*, 12 (2018) 21-26.

Acknowledgments

Financial support from Fundação para a Ciência e a Tecnologia (FCT), Portugal, of CEMMPRE, project UIDB/00285/2020 by FEDER funds through the program COMPETE – Programa Operacional Factores de Competitividade, and by national funds through FCT is gratefully acknowledged.

CHEMICAL SENSORS AND “REAL” ANALYTICAL CHEMISTRY

Tony Edmonds

Varhn, Agglestone Road, Studland Dorset United Kingdom

e-mail: t.e.edmonds@btconnect.com

On the 10th April 1912, the biggest and most luxurious passenger ship of its time set sail from Southampton in England with around 2224 passengers and crew aboard. The ship was described as unsinkable. At a 11:40am on the 15th April the ship struck an iceberg in the North Atlantic Ocean. At 2:40pm the vessel broke apart and sank with the loss of over 1500 lives. It remains to this day the deadliest peacetime sinking of a superliner or cruise ship.

In 1988, a young research scientist and Analytical chemist wrote in the introduction to the first British book on Chemical Sensors: “It is not an up-to-the-minute-review of every piece of chemical sensor research. Well-trodden paths have been deliberately avoided, as has the tendency to dwell on Friday afternoon laboratory curiosities that work well at the end of the week but fail on Monday” and “the research chemist engaged in sensor development should be mindful of the fact that the ultimate target for these devices is the real world, and that a successful laboratory device operating under well-defined conditions and careful calibration does not constitute a chemical sensor.”

In 2014, Theranos, a company that claimed to be able to perform over 240 individual diagnostic tests on a single pinprick of blood was valued at around \$9 billion. The company was set to revolutionise diagnostic medicine and to change the world. Its founder and CEO, Elizabeth Holmes was hailed as the next Steve Jobs. But four years later Holmes relinquished her post as CEO and was, along with others charged with fraud and making misleading claims about her company and its product. In January of this year Holmes was found guilty on four charges of defrauding investors, and now faces up to 20 years in prison. The technology simply did not and could not work.

What links these first three paragraphs? In each case it is the interface, the conjunction, the nexus of the theoretical and controlled with the harsh reality of the world as it is, not the world as imagined by the engineer, the research scientist or the medical diagnostic entrepreneur. Or to put it more colloquially, it is where the rubber hits the road.

In this lecture I want to underline how important it is to keep the reality of the world always in mind when undertaking sensor research and to look at ways in which this issue is being addressed in current research and hopefully to look to the future.

First, I shall consider the nature of Analytical Chemistry itself, that branch of chemistry most intimately concerned with making accurate and reliable chemical measurements in the reality of the world, in blood, in soil, in the atmosphere, in chemical process streams, human beings and so on. I shall show that the essential work of Analytical Chemistry is not primarily analysis, but a process of purification, synthesis and then comparison. It is this threefold action that yields reliable results. Having established the Analytical Chemical process I shall examine the relationship between chemical sensors and Analytical Chemistry to demonstrate that in some way that three-fold approach has been, can be and should be encoded into the structure and protocols of chemical sensors. To some extent sensor protocols are as important as the actual structure and mechanism of sensing. The sensor developer/researcher needs to consider such questions as: where is the sensor to be used; is there an argument for contextual selectivity; what is the nature of the desired chemical information (i.e. is a truly quantitative answer required, or will a yes/no answer be sufficient)?

Second, I shall look at current applications of chemical sensors in the analysis and monitoring of soil. In this case I want to examine the way in which pre-or post-calibration, contextual selectivity and sample modification are used. Soil is a remarkably complex system in which to make measurements. It is, surprisingly, more complex than blood, being a heterogeneous three phase system (solid, gas and liquid). Temperature, pH and the physical environment can be quite variable and quite large-scale organisms frequent this zone. Those working in chemical sensing in this area adopt a number of strategies to deal with these problems including some limited sample modification and the use of membranes or pre-conditioning chemistries. For example, the assessment of carbon content of soil via the carbonate carbon has been estimated using a purely physical method, a ZnO-based micro-cantilever, to determine the gas pressure produced by the selective secretion of CO₂ in a closed system. However, to determine the total soil organic matter (SOM) a more chemical approach has been used in which ten identical polymer-MOx composite material gas sensors were operated at different temperatures to provide a “fingerprint” of the SOM. This was related to the actual SOM using a back-propagated neural network. Significantly the efficacy of this method was checked against standard SOM determination using oxidation of the soil sample with potassium dichromate. Finally in-situ measurement of nitrate

fertilization has been attempted using a thick-film sensor probe. The probe incorporates three sensors, each at a different depth and featuring a copper plate as the reference electrode. Calibration is performed in-situ by adding standard solutions. Full analysis of the soils using the Kjeldahl method validated the device and demonstrated that coupled with suitable data processing and telemetry the device could be used to monitor fertilisation.

Third, I shall examine current methods of gas analysis using sensors and machine learning. But before we get to that, it is worth noting that in this area of sensing as in soil sensing some kind of sample purification may be undertaken. For example, “holey” graphene oxide (GO) filter membrane has been placed over sensing material (PdO–WO₃ nanosheets) to act as a molecular sieving layer, selectivity passing target analyte according to the pore size distribution on its surface. A pore size-tuned GO porous layer showed superior cross-selectivity to acetone (0.46 nm), ethanol (0.45 nm), cycloheptatriene (0.59 nm), and hydrogen sulphide (0.36 nm). However, in general, the two most significant problems that affect gas sensing are selectivity and drift. Machine learning has been shown to be an effective way of delivering improved selectivity and stability. For example, the use of electronic nose devices (e-noses) in the measurement of volatile organic compounds (VOC) in human breath for both diagnostic and forensic reasons calls for excellent selectivity. There are many VOC in human breath, ensuring the detection and determination on the correct VOC is beyond the capability of a single sensor, but multiple sensor arrays coupled with data processing can achieve the desired selectivity. Such an approach frequently employs learning sets of standard compounds that in effect “teach” the algorithm how to detect the target compounds. It is this kind of approach that I shall examine and hopefully demonstrate that from a philosophical point of view the three step Analytical Chemical approach (purification, synthesis and comparison) is present to some extent in these procedures.

SENSORES ELECTROQUÍMICOS | SENSORES ELECTROQUÍMICOS |
ELECTROCHEMICAL SENSORS

O1 |

ELECTROCHEMICAL NANO-IMMUNOSENSOR BASED ON CERIUM OXIDE-DOPED PEDOT NANOCOMPOSITE FOR THE DETECTION OF ANTI-P53 AUTOANTIBODIES

A. F. Cruz-Pacheco¹, J. Quinchia¹ and J. Orozco¹

¹ *Max Planck Tandem Group in Nanobioengineering, Institute of Chemistry, Faculty of Natural and Exact Sciences, University of Antioquia, Complejo Ruta N, Calle 67 No. 52-20, Medellín 050010, Colombia*

**e-mail: grupotandem.nanobioe@udea.edu.co*

Introduction

Electrochemical immunosensors detect the specific antigen-antibody interaction by changes in the electrical signals generated in the formation of the immune complex [1]. Likewise, nanomaterial-based electrochemical immunosensors have improved analytical performance, especially in sensitivity and detection limits, due to nanostructured materials' high surface/volume ratio increasing bioreceptor loading; and amplifying the electrochemical signals. In addition, nanomaterials also facilitate the miniaturization of the sensing platform to develop portable devices. Thus, nano-immunosensors have the potential for the rapid, sensitive, and specific early diagnosis of diseases such as cancer by detecting emerging biomarkers such as anti-p53 autoantibodies (Aabs) [2]. These autoantibodies are produced by the individual's immune system against tumor-associated antigens (TAA) several months or years before the onset of clinical symptoms of the disease [3]. In this context, integrating nanocomposites based on metal oxide nanoparticles (NPs) and semiconductor polymers on screen-printed electrodes (SPE) offers opportunities to develop robust nano-immunosensors for ultrasensitive on-site screening anti-p53 autoantibodies.

Methods

The synergy of a nanobiocomposite material based on the extraordinary conductivity, stability, and antifouling capacity of poly(3,4-ethylenedioxythiophene) (PEDOT) was integrated for the first time with the high surface area, and direct biofunctionality of cerium oxide (CeO₂) NPs linked to p53 antigen for label-free electrochemical immunosensing of Aabs. Furthermore, individual NPs and each stage of the nanobiocomposite-based immunosensor architecture were characterized extensively in chemical, physical, and electrochemical features. As a result, this nano-immunosensor specifically and selectively detected anti-p53 Aabs by differential pulse voltammetry (DPV) in

clinically relevant concentrations with a quantitative response in human serum samples [4].

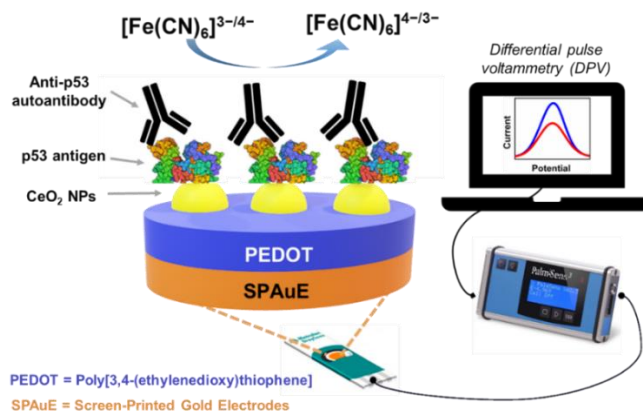


Figure 1. Schematic illustration of the modification of SPAuE with the p53/Ce/PEDOT nanobiocomposite to detect anti-p53 autoantibodies by DPV in a PBS 1X pH 7.4 solution containing 5 mM [Fe(CN)₆]^{3-/4-} as a redox mediator.

Results

A label-free nano-immunosensor based on p53/CeO₂/PEDOT nanobiocomposite-modified screen-printed gold electrodes (SPAuE) was developed for the electrochemical detection of anti-p53 autoantibodies. CeO₂ NPs were synthesized by a soft chemistry method and functionalized with cyanopropyltriethoxysilane (CPTES). The nano-immunosensor architecture was formed by in-situ electrochemical polymerization of 3,4-ethylenedioxythiophene (EDOT) on SPAuE in the presence of CeO₂ NPs. Cross-linking-free covalent bonding allowed the p53 protein to immobilize on the CeO₂/PEDOT-modified SPAuE.

The NPs and the modified electrodes were characterized by transmission electron microscopy (TEM), X-ray diffraction (XRD), Fourier-transform infrared spectroscopy (FTIR) and scanning electron microscopy (SEM). DPV was used to follow each step of the nano-immunosensor assembly and detect anti-p53 autoantibodies in a linear range from 10 to 1000 pg mL⁻¹ ($r^2 = 0.992$). The sensitivity was 0.152 $\mu\text{A pg}^{-1} \text{mL cm}^{-2}$, and the limit of detection (LOD) and the limit of quantification (LOQ) calculated with the linear arrangement were 3.2 pg mL⁻¹ and 10.6 pg mL⁻¹, respectively. Tests with various interferences spiked in synthetic serum samples confirmed the device's high specificity, selectivity, and relevant performance for detecting anti-p53 Aabs.

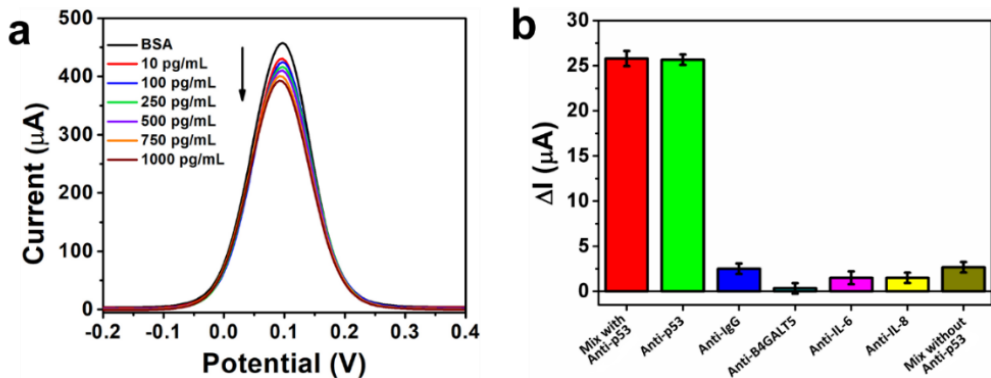


Figure 2. (a) DPV signals of the label-free electrochemical nano-immunosensor in different concentrations of anti-p53 Aabs. (b) Change in DPV response of the nano-immunosensor in 1000 ng mL⁻¹ interfering antibodies, 0.1 ng mL⁻¹ anti-p53 Aabs, and a mixture of all antibodies, respectively, in a 5 mM of [Fe(CN₆)]^{3-/4-} solution as a redox probe.

Conclusion

Incorporating functional nanoparticles in polymeric matrices on SPAuEs can provide a simple-to-assemble, quick, ultra-sensitive technology for on-site screening of anti-p53 autoantibodies and other disease biomarkers with low sample consumption.

References

- [1] F. Mollarasouli, S. Kurbanoglu, S.A. Ozkan, The role of electrochemical immunosensors in clinical analysis, *Biosensors*. 9 (2019) 1–19.
- [2] J. Quinchia, D. Echeverri, A.F. Cruz-Pacheco, M.E. Maldonado, J.A. Orozco, Electrochemical biosensors for determination of colorectal tumor biomarkers, *Micromachines*. 11 (2020) 1–46.
- [3] S. Campuzano, M. Pedrero, A. González-Cortés, P. Yáñez-Sedeño, J.M. Pingarrón, Electrochemical biosensors for autoantibodies in autoimmune and cancer diseases, *Anal. Methods*. 11 (2019) 871–887.
- [4] A.F. Cruz-Pacheco, J. Quinchia, J. Orozco, Cerium oxide-doped PEDOT nanocomposite for label-free electrochemical immunosensing of anti-p53 autoantibodies, *Microchim. Acta.* (2022).

Acknowledgments

The work has been funded by MINCIENCIAS, MINEDUCACIÓN, MINCIT and ICETEX through the Program Ecosistema Científico Cod. FP44842-211-2018, project number 58536. J.O thanks support from The University of Antioquia and the Max Planck Society through the cooperation agreement 566-1, 2014. We thank The Ruta N complex and EPM for hosting the Max Planck Tandem Groups.

O2 |

SENSING FERROCENE DERIVATIVES USING A MODIFIED GLASSY CARBON ELECTRODE WITH A PEDOT/CARBON MICROSPHERES THIN-FILM

Vergara del Toro, N.¹, Meléndez, A.², Ramos, I.², Rivera-Claudio, M.¹, Castillo, J.¹, and Oyola, R.¹

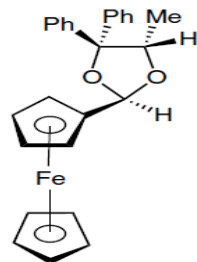
¹Department of Chemistry, University of Puerto Rico-Humacao, Call Box 860, Humacao PR 00792

²Department of Physics & Electronics, University of Puerto Rico-Humacao, Call Box 860, Humacao PR 00792

*e-mail: rolando.oyola@upr.edu

Introduction

Electrochemical technique is a powerful analytical tool that has several advantages including facile operation, sensitivity and time saving. Conducting polymers (CPs) have many superior properties such as good mechanical stability, simple preparation method, possibility of miniaturization, and interesting electrical and electrochemical properties. CPs have attracted extensive interest for the fabrication of efficient chemo/biosensors.[1] The conducting polymers, poly(3,4-ethylenedioxythiophene) (PEDOT), has received attention and is broadly studied because of its important properties. In comparison with other conducting polymers, it has good electrical conductivity, low band gap, superior



SCHEME 1:
FERROCENE ACETAL

environment stability and good biocompatibility [2-5]. Owing to these properties, PEDOT has rapidly become the subject of considerable interest for the preparation of efficient chemo/biosensors. In this work, we explore the use of thin-film deposition of PEDOT:PSS and PEDOT:PSS with carbon microspheres (CS) over glassy carbon electrode (GCE) with the aim of increasing analytical sensitivity. We proof the system using chiral acetal (2R,5R)-2-ferrocenyl-5-methyl-4,4-diphenyl-1,3-dioxalene (Scheme 1) or ferrocene. The chiral acetal shows positive response against mammalian cancer cell lines.[6] Ferrocene derivatives have been proposed for in a wide range of applications.[7]

Methods

Tetrabutylammonium perchlorate (TBAP), ferrocene, and acetonitrile were purchased from Sigma-Aldrich (USA). PEDOT:PSS was from Ossila Company (USA). Carbon microspheres were synthesized as reported previously.[8] The

cyclic voltammograms were recorded in acetonitrile solution in 0.1 M TBAP as the supporting electrolyte using a SP-150 model (Biologic, USA) electrochemical analyzer instrument controlled by EC-LAB Software Ver. 11.33. A three-electrode cell consisting of a GCE, a platinum wire auxiliary electrode and Ag/AgCl electrode as the reference electrode was used for all the experiments. Cyclic voltammograms were recorded at scan rate range of 20 to 100 mV/s. Before thin-film deposition, GCE was polished by chamois leather containing 0.05 μm alumina slurry until a mirror surface was achieved. Subsequently, the GCE was ultrasonically cleaned in nanopure water, absolute ethanol, and nanopure water each for 5 min, respectively. The electrochemical cell was saturated with nitrogen for five minutes before measurements and kept constant on the solution surface during measurements. The thin-film was prepared by placing a drop over the GCE and drying it for 24 hours. For PEDOT:PSS/CS, a vial was weighed and the required PEDOT:PSS was added with a syringe. Carbon spheres were added to the vial to the desired weight percent. Afterwards, the mixture was stirred for 30 minutes and then placed in an ultrasonic bath for one hour. A drop was placed over the GCE and dried for 24 hours. The PEDOT:PSS/CS film thickness ranged from 10 to 40 μm across the top of the GCE electrode. An irregular surface of the PEDOT:PSS/CS can be appreciated in the SEM image shown in Figure 1. For PEDOT:PSS film, the surface morphology was more uniform along the electrode, showing a thickness range of 0.4 to 2.3 μm .

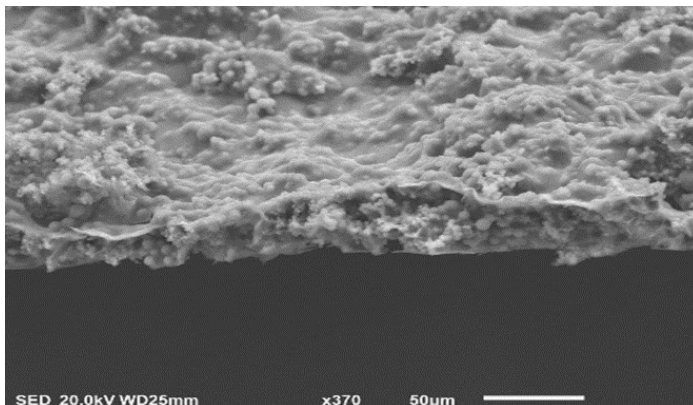


Figure 1: SEM image of PEDOT:PSS/CS film

RESULTS

The background corrected CV of ferrocene acetal using bare GCE and PEDOT:PSS/CS electrode against Ag/AgCl electrode are shown in Figure 2. Oxidation and reduction peaks are observed at 0.38 and 0.46 mV, respectively ($E_{1/2} = 0.42$ mV).

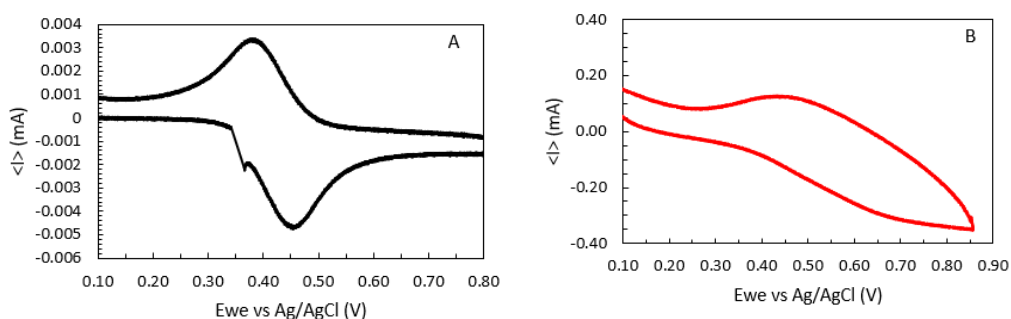


Figure 2: Cyclic voltammogram of 2-diphenyl ferrocene (0.50mM) in CH₃CN/TBAP/N₂ saturated solution at 20mV/s: A) bare GCE electrode and B) GCE/PEDOT electrode.

On the other hand, the thin-film deposition of PEDOT:PSS shifts the oxidation and reduction peaks to 0.45 and 0.66 mV, respectively. This shift can be explained in terms of slower electron transfer reaction. Interestingly, the current amplitude is higher for PEDOT:PSS electrode than for bare GCE. Therefore, we explore this observation for quantitative analyses. Oxidation peak integration at different concentrations of ferrocene acetal and ferrocene were used to build the linear calibration curves shown in Figure 3. It is observed that the calibration sensitivity increases from GCE (1.10 ± 0.01 A/(V*M)) < PEDOT (1.66 ± 0.07 A/(V*M)) < PEDOT/CS(5% w/w) (8.3 ± 0.3 A/(V*M)) all with correlation coefficients (R^2) better than 0.99.

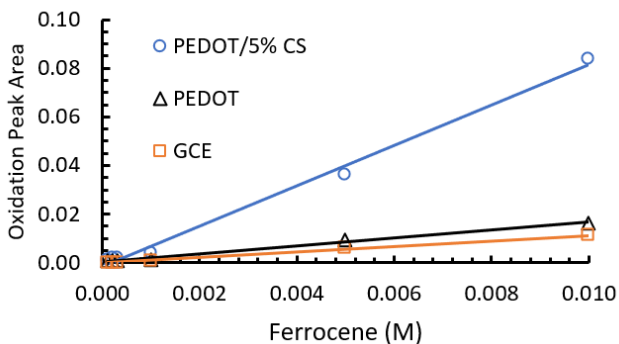


Figure 3: Calibration curves for ferrocene in CH₃CN/TBAP/N₂ saturated solution at 40 mV/s. Solid lines correspond to linear regression analysis.

Conclusions

In summary, GCE modified with thin-film of PEDOT:PSS or PEDOT:PSS with carbon microspheres increases cyclic voltammogram current amplitude of ferrocene and ferrocene acetal. The calibration curve sensitivity increases by a factor of 7.5 times for PEDOT:PSS/CS relative to GCE.

References

- [1] Zhanga, Z., Xua, J., Wenb, Y., Zhanga, J., Dinga, W., The electro-synthesized imprinted PEDOT film as a simple voltametric sensor for highly sensitive and selective detection of vitamin K3 in poultry drug samples. *Synthetic Metals*, 2017, 230, 79-88.]
- [2] L. Groenendaal, F. Jonas, D. Freitag, H. Pielartzik, J.R. Reynolds, Poly (3, 4-ethylenedioxythiophene) and its derivatives: past, present, and future, *Adv. Mater.* 12 (2000) 481–494.
- [3] L. Groenendaal, G. Zotti, P.H. Aubert, S.M. Waybright, J.R. Reynolds, Electrochemistry of poly (3, 4-alkylenedioxythiophene) derivatives, *Adv. Mater.* 15 (2003) 855–879.
- [4] S. Kirchmeyer, K. Reuter, Scientific importance properties and growing applications of poly (3, 4-ethylenedioxythiophene), *J. Mater. Chem.* 2005 (2005) 2077–2088.
- [5] A. Elschner, S. Kirchmeyer, W. Lovenich, U. Merker, K. Reuter, *PEDOT: Principles and Applications of an Intrinsically Conductive Polymer*, CRC Press, 2010.
- [6] Castillo, J., Echevarría, I., Santiago, J., Pérez-Torres, M., and Rivera-Claudio, M., Synthesis and characterization of ferrocene acetals and evaluation of their antineoplastic properties by using breast cancer cell lines in vitro, *Synthesis*, 2013, 45, 1853-1856. DOI: 10.1055/s-0033-1338878
- [7] Beitollahi, H., Khalilzadeh, M.A., Tajik, S., Safaei, M., Zhang, K., Jang, H.W., and Shokouhimehr, M., Recent Advances in Applications of Voltammetric Sensors Modified with Ferrocene and Its Derivatives, *ACS Omega* 2020, 5, 2049–2059. <https://dx.doi.org/10.1021/acsomega.9b03788>.
- [8] Nieves, C.A., Meléndez, A., Pinto, N.J., and Ramos, I., Facile fabrication of carbon spheres/n-Si junction diodes based on sucrose, *J Mater Sci: Mater Electron*, 2016, DOI 10.1007/s10854-016-5445-x

Acknowledgments

This work was funded by NSF-DMR-2122102 program.

O3 |

MODIFIED ISFETS WITH SILK FIBROIN MEMBRANE FOR PH MEASUREMENTS IN BIOLOGICAL MATRICES

Alexandre Moreno Diaz^{1*}, Pablo Giménez-Gómez¹, Meritxell Rovira¹, Alfredo Cadarso¹, Cecilia Jimenez-Jorquera¹, Carlos Domínguez-Horna.¹,
Xavier Muñoz-Berbel¹

¹ *Instituto de Microelectrónica de Barcelona (IMB-CNM, CSIC), Bellaterra, Barcelona, 08193, Spain*

**e-mail: alexandre.moreno@imb-cnm.csic.es*

Introduction

pH changes are associated to the healthy/unhealthy states of organisms, tissues and cells. For this reason, pH is commonly monitored and used to identify metabolic alkalosis and acidosis in patients, as well as the metabolic condition and healthiness of cell cultures, e.g. in drug discovery. Although some technologies are currently available enabling the determination of pH in biological samples (e.g. the gasometer based on ion selective electrodes¹ (ISEs), currently the golden standard in pH detection in blood samples, or the thromboelastography²), they still present important drawbacks in terms of miniaturization, robustness and precision of the measurement.

Ion sensitive field effect transistors (ISFETs) are a good alternative to conventional glass pH electrodes or ISEs, since are highly miniaturized transducers, very sensitive and precise in the determination of pH³. However, as most of electrical/electrochemical transducers, ISFETs are prone to poisoning due to biofouling. That is, during the analysis of biological samples, components of the sample matrix, e.g. proteins, adhere to the transducer surface, resulting in a change on the sensor response that is not directly associated to the target analyte. Therefore, the adhesion of these molecules at the active sites of the dielectric gate reduces the precision of the measurement, which is very critical in clinical diagnosis where the expected changes in pH magnitude are very small.

Biofouling is generally minimized by surface modification (i.e. functionalization) of the sensor surface with a protecting membrane, e.g. a Nafion layer⁴. These membranes reduce molecular attachment, but since they are highly hydrophobic, they can impact on the general analytical performance of the sensor, e.g. increasing the response time and reducing its sensitivity and limit of detection.

Alternatively, we propose the use of ISFET functionalized with silk fibroin films as a filter. This filter presents important advantages in the pH determination, such

as good sensitivity or the possibility to implement this layer at wafer level by lithography⁵. Additionally, this natural material is very versatile, and can be processed into multiple shapes and properties⁶. In the present study, silicon nitride ISFETs were functionalized with silk fibroin protein to perform pH measurement, which is demonstrated in two different biological samples: neurobasal media and blood. To achieve this goal, the silk fibroin solution was deposited on ISFET gates, then dried and recrystallized. After this procedure, silk films were stably attached to the ISFET surface. These silk ISFETs were optically and electrochemically characterized and compared to bare ISFETs without membrane. With ATR-IR characterization, the recrystallization of silk fibroin films was confirmed. In addition, calibrations and measurements were carried out in buffer solutions, neurobasal medium and diluted pig blood samples.

Methods

The functionalization with silk fibroin films was performed by carefully casting 2.5 μl of 6% fibroin solution by drop casting into the 1 mm ISFET wells and allowed to dry overnight (18 h). ISFETs were then placed in a polycarbonate desiccator for 24 h at 900 mbar in a humid environment to recrystallize the fibroin film. Electrochemical measurements of neurobasal medium were performed. First, the conditioning of ISFETs was conducted in pH = 7 buffer (10 min). Calibrations were performed under batch conditions with pH buffer solutions of 5, 6, 7, 8, 9 and 10. The pH measurement with the desktop pH-meter is considered the real pH. The pH was adjusted to the range of interest with small volumes of concentrated solutions of HCl or NaOH while the ISFETs and desktop pH-meter measurements were recorded. The diluted blood measurement process consisted of a measurement in a pH 7 buffer solution, used to recalibrate the device, following of the cleaning of the sensor by immersion in water and agitation to eliminate residues and finally make the blood pH measurement. This process was repeated for 25 cycles to assess the possibility of making repeated measurements, as well as their quality.

Results

In Figure 1 is shown an ISFET gate without and with a silk film. These films were transparent and did not absorb light in the optical range. To confirm the crystallization of the silk films, an IR analysis of crystallized and non-crystallized fibroin was performed at the ISFET gate.

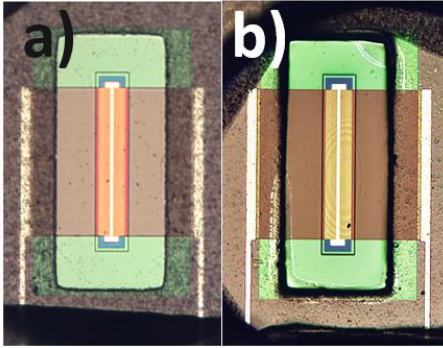


Figure 1: Optical images of (a) ISFET (b) Silk ISFET.

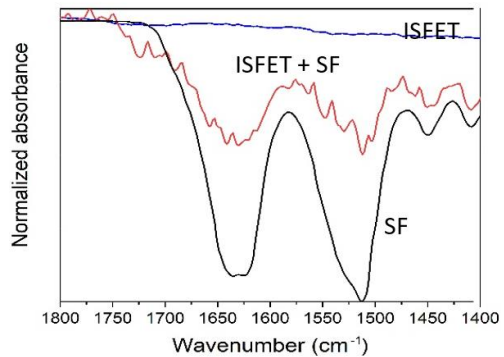


Figure 2: IR spectrum of ISFET gate, and crystallized fibroin film and a crystallized fibroin ISFET.

Crystallized silk fibroin films have a peak of 1620 cm^{-1} (Figure 2), corresponding to the amide groups of the β sheets of silk II. Silk fibroin films at the ISFETs showed the peak of crystallization (1620 cm^{-1}) after annealing with water vapour, thus confirming its crystallization. In addition, the deposited fibroin films show a peak at 1513 cm^{-1} , corresponding to the amide II groups.

Measurements in neurobasal medium

To study the hysteresis of silk ISFETs, functionalized and non-functionalized sensors were soaked in a neurobasal medium while the pH was modified by adding small volumes of HCl or KOH, performing measurements with the ISFETs and a desktop pH-meter. Figure 3a shows the recording of the sensor response, which illustrates the reversibility of response. ISFET signals are plotted against the measured pH by the pH-meter in Figure 3b. A slight variation of slope was observed from 47.1 to 48.3 mV/pH for silk ISFETs and from 51.3 to 52.5 mV/pH for non-functionalized ISFETs, and a slight change of intercept value was observed due to the drift effect.

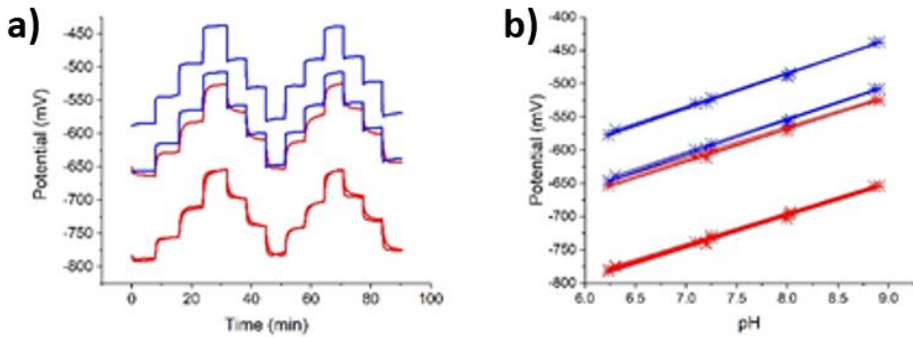


Figure 3: (a) Measurements of potential of ISFETs in different pH of culture medium with silk ISFETs (red) and bare ones (blue). (b) Potential obtained for each pH of neurobasal medium for silk (red) and bare (blue) ISFETs.

Measurements in diluted blood

ISFETs with and without silk fibroin have been used to measure the pH of diluted pig blood and compared with the pH-meter value. As seen in Table 1, ISFETs without membrane present slightly higher values than the commercial pH-meter, but within the measurement range considering the standard deviation. The ISFETs with silk membrane present similar values to those provided by the pH-meter, and less dispersion (0.03 units of SD, compared to the 0.06 units of the ISFETs without membrane). Only device ISFET4 presented significantly discordant results, which a visual inspection of the same showed a large particle in the door, which could alter the sensing capacity of the device.

Table 1: Mean and standard deviation of pH measurements in the blood sample.

	commercial pH-meter	ISFET 1	ISFE T2	ISFET3	ISFET4 (with fibroin)	ISFET5 (with fibroin)	ISFET6 (with fibroin)
Average	7.32	7.37	7.37	7.37	7.39	7.31	7.33
Standard Deviation (SD)	-	0.06	0.06	0.03	0.03	0.02	0.03

Conclusions

The fibroin films were deposited and successfully attached to the ISFET gates, demonstrating a good fixation. Moreover, these films were recrystallized, forming β sheets and making the films more hydrophobic. The performance of silk ISFETs in neurobasal medium presents a more stable signal, giving a slower time response than bare ISFETs. Moreover, as the calibration slope increases more for bare ISFETs, these are expected to have a larger drift for long-term measurements, which would cause to make periodical calibrations. pH measurements in diluted blood using ISFETs modified with silk films showed a higher correlation with the pH-meter records than bare ISFETs without membrane. Besides, silk-modified ISFETs also presented lower standard deviation. Therefore, silk ISFETs are a suitable option to measure pH in biological samples.

References

- [1] J.P. Robles Ruiz, A. Calvo Elipe, M.V. Martínez Díaz, J.L. Rodríguez Calderón. Interpretación de la gasometría arterial en enfermedades respiratorias agudas y en las agudizaciones de procesos crónicas. *Medicine*. 2011;10(88):5965-8
- [2] Ramaker, A.J.D.W.R., Meyer, P., Van Der Meer, J., Struys, M.M.R.F., Lisman, T., Van Oeveren, W., Hendriks, H.G.D. Effects of acidosis, alkalosis, hyperthermia and hypothermia on haemostasis: Results of point of care testing with the thromboelastography analyser (2009) *Blood Coagulation and Fibrinolysis*, 20 (6), pp. 436-439.
- [3] C. Jimenez, A. Baldi, N. Abramova and A. Batrov, in *Encyclopedia of Sensors*, ed. C.A. Grimes, E. C. Dickey and M. V. Pishko, American Scientific Publishers, New York, 2005, ch. 106.
- [4] Lopez-Haro, M., Guétaz, L., Printemps, T., Morin, A., Escribano, S., Jouneau, P.-H., Bayle-Guillemaud, P., Chanderzon, F., Gebel, G. Three-dimensional analysis of Nafion layers in fuel cell electrodes (Open Access) (2014) *Nature Communications*, 5, art. no. 5229.
- [5] Lawrence, B.D., Omenetto, F., Chui, K., Kaplan, D.L. Processing methods to control silk fibroin film biomaterial features (2008) *Journal of Materials Science*, 43 (21), pp. 6967-6985
- [6] Wang, Y., Kim, B.J., Peng, B., Li, W., Wang, Y., Li, M., Omenetto, F.G. Controlling silk fibroin conformation for dynamic, responsive, multifunctional, micropatterned surfaces (Open Access) (2019) *Proceedings of the National Academy of Sciences of the United States of America*, 116 (43), pp. 21361-21368.

Acknowledgments

A. Moreno is grateful to MICINN for the grant of a PhD studentship from the FPI program (PRE2019-088338). The Comité Ético del Hospital de Terrassa has evaluated the ethical issue.

O4 |

LIGNOSULFONATE-BASED POLYURETHANES DOPED WITH CARBON NANOTUBES TOWARDS SENSOR APPLICATIONS

Sandra Magina^{1*}, A. Rudnitskaya², S. Soreto³, L. Cadillon Costa³, A. Barros-Timmons¹,
D. V. Evtuguin¹

¹ CICECO and Department of Chemistry, University of Aveiro, Aveiro, 3810-193, Portugal

² CESAM and Department of Chemistry, University of Aveiro, Aveiro, 3810-193, Portugal

³ I3N and Department of Physics, University of Aveiro, Aveiro, 3810-193, Portugal

*e-mail: smagina@ua.pt

Introduction

Due to an increase in industrial and human activities, the presence of heavy metal salts such as lead (Pb), mercury (Hg), cadmium (Cd), chromium (Cr), zinc (Zn), and copper (Cu), among others, in wastewater has led to an increasing accumulation of these chemicals in the environment. Considering environmental and health concerns, their removal from wastewaters is imperative [1]. Therefore, their detection in aqueous systems is crucial and can be performed using electrochemical sensors., such as all-solid-state potentiometric sensors [2]. This type of sensors have been employed in numerous studies for the determination of metal ions in water and biological samples [3–5].

Among the different technical lignins, lignosulfonate (LS) is the only abundant source of lignin on the market that can be considered potentially interesting for the production of conductive composites. Being soluble in water and containing ionogenic (sulfonic) groups, LS is an attractive candidate for use in conductive polymer matrices for sensor applications. The production of lignin-based polymeric membranes by co-polymerization of different technical lignins, such as kraft lignin, LS, and organosolv lignin, with toluene diisocyanate-terminated poly(propylene glycol) has been reported [6–8]. However, the ensuing lignin-based sensors displayed very low or no sensitivity to most transition metal cations ions. Furthermore, the sensor properties were strongly dependent on the lignin origin.

In this work, we prepared LS-based polyurethane (PU) composite membranes sensors doped with MWCNTs [9]. The main goal was to assess the viability of using LS from the spent liquor of the acidic sulfite pulping of eucalypt wood for potentiometric sensor applications. The conductive and sensory properties of the LS-based conductive composites were compared with those based on different technical lignins [6,8].

Materials and Methods

Materials. Lignosulfonates (LS) from the industrial magnesium-based acidic sulfite pulping of *Eucalyptus globulus* wood were supplied by Caima company (Constância, Portugal) and were purified by dialysis against distilled water for 24 h. Purified LS contained 17.1% wt.% of HSO₃ groups and 2.4 wt.% of phenolic hydroxyl groups [10]. Poly(propylene glycol)-toluene diisocyanate copolymer (PPGDI) and dibutyltin dilaurate (DBTDL) were purchased from Sigma-Aldrich. Multiwall carbon nanotubes (MWCNTs) Nanocyl-3150 were supplied from Nanocyl. All solvents and other reagents were of analytical grade and were purchased from either Acros or Sigma-Aldrich. Polyaniline (PANI)-modified screen-printed electrodes (SPE) with carbon working and auxiliary electrodes and silver reference electrode were supplied by Metrohm DropSens. All solutions for the potentiometric measurements were prepared using ultrapure water (18 mΩ.cm⁻¹).

Synthesis of LS-based PU. The polycondensation reaction of purified LS with isocyanate was carried out according to the procedure described elsewhere [9]. LS powder (500 mg), or a mixture of LS powder with a certain proportion of MWCNT (0.1, 0.2, 0.5, 0.8, 1.0 and 1.4 % w/w in relation to the total mass of the mixture LS and PPGDI) was placed in a 25 mL jacketed glass reactor equipped with an overhead mechanical stirrer and a heating circulating water bath. Then, PPGDI (4 mL) was added and the mixture was stirred for 45-60 minutes at 60 °C under nitrogen atmosphere to obtain a homogeneous viscous mixture. Finally, DBTDL (ca. 2% w/w in relation to the PPGDI) was added. The homogeneous mixture was stirred for further 5-10 minutes until it started to thicken. At this point, the mixture was removed from the reactor and poured into a flat PTFE mold. The films were cured during 4 hours at 60 °C. LS-based PU membranes (undoped and doped with 1% w/w MWCNT) were characterized by FTIR, DMA, TGA and DC electrical conductivity measurements.

Potentiometric measurements. Potentiometric chemical sensors were prepared by depositing a thin layer of LS-based PU doped with 1% w/w MWCNTs (before curing) on the surface of PANI-SPE. Then the polymer was cured at room temperature in a desiccator for 4 days before using. Electrochemical measurements were carried out in the following galvanic cell: Ag|AgCl, KCl sat |sample| polymer membrane| PANI | carbon. Electromotive force values, Emf, were measured vs. a Ag/AgCl reference electrode according to the procedure described elsewhere [9].

Results

LS-based PU copolymers were obtained by the reaction of LS as a macromonomer bearing hydroxyl groups with PPDGI as a co-macromonomer comprising isocyanate groups and also acting as the solvent for LS and maintaining a NCO/OH ratio of 1.5. The reaction of LS and PPDGI with the formation of PU was confirmed by FTIR spectroscopy (data not shown). The glass transition temperature (T_g) of LS-based PUs was assessed by DMA. Both LS-based PUs, undoped and doped with 1% w/w MWCNTs, exhibited similar low T_g values of -33 ± 1 °C and -32 ± 1 °C, respectively, confirming that the addition of MWCNTs (1% w/w) did not affect the viscoelastic properties of the polymer. The negative values of T_g indicate that these materials can be used for the fabrication of self-plasticizing membranes for potentiometric chemical sensors.

The DC electrical conductivity of undoped LS-based PU polymer and the various LS-based PU polymer composites doped with variable amounts of MWCNTs was measured at room temperature (Figure 1). The incorporation of MWCNTs resulted in an increase in the electrical conductivity of PU-based LS composites from 7.2×10^{-12} in undoped polymer to 7.1×10^{-6} S·m⁻¹ in polymer doped with 1.4% w/w MWCNTs. However, the observed conductivity curve as a function of MWCNT content in the composite did not fit the percolation theory model probably due to the inhomogeneous distribution of LS in the PPDGI copolymer along with the intensive bubble formation during the synthesis leading to a porous structure.

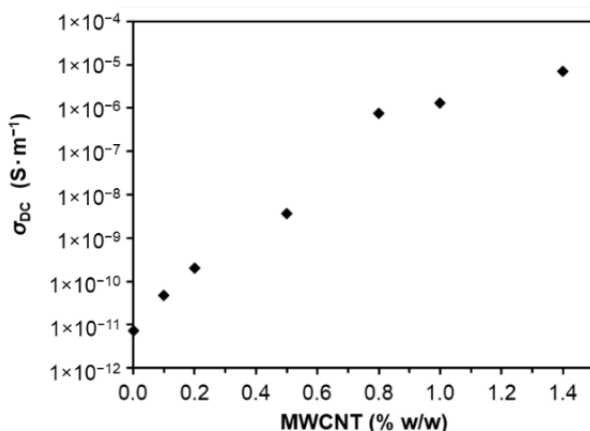


Figure 1. DC electrical conductivity, σ_{DC} , at room temperature as a function of MWCNT concentration (0%, 0.1%, 0.2%, 0.5%, 0.8%, 1%, 1.2%, and 1.4% w/w) in LS-based PU.

LS-based PUs doped with 1.0% w/w MWCNTs exhibited relevant electrical conductivity suitable for sensor applications. Therefore, potentiometric measurements for a sensitivity assessment of an LS-based PU composite membrane sensor doped with 1% w/w MWCNTs were carried out using 1 mM Tris buffer solution at pH 7. The measurements revealed that the LS-based potentiometric sensor displayed no response to Na(I) and Pb(II) but exhibited a near-Nernstian or super-Nernstian response to a wide range of transition metals, including Cu(II), Zn(II), Cd(II), Cr(III), Cr(VI), Hg(II), and Ag(I) at pH 7 (Figure 2a) and Cr(VI) at pH 2 (Figure 2b).

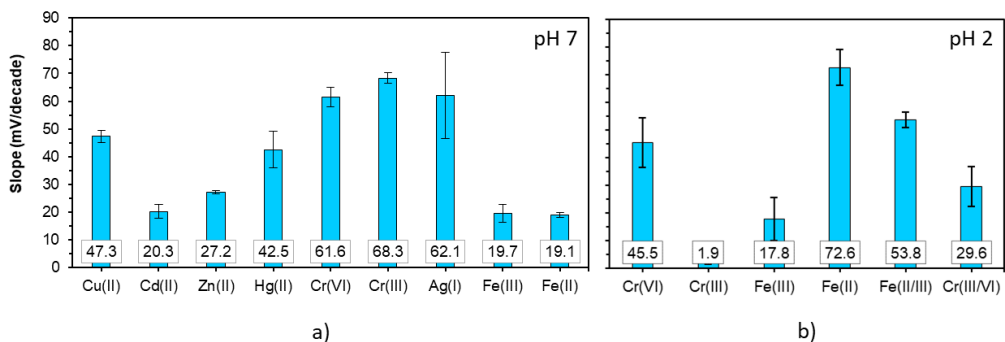


Figure 2. Slopes of the electrode function of the LS-based PU sensor doped with 1% w/w MWCNTs at pH 7 (a) and pH 2 (b) (each slope corresponds to a mean value of at least three calibrations with their respective standard deviations).

Sensors also exhibited a redox response to the Fe(II)/(III) redox pair at pH 2 (Figure 2b). Unlike other lignin-based potentiometric sensors in similar composite materials [6,8], this LS-based flexible polymeric membrane did not show irreversible complexation with Hg(II). The sensitivity of lignin-based sensors is pH-dependent, and, in the case of previously studied lignin-based sensors, it was observed only at pH 2 [6,8], while the LS-based sensor responded at both pH 7 and pH 2. It was considered that the response mechanism of lignin-based electrodes comprises the combination of ion exchange and charge transfer phenomena.

Conclusions

The results of this study showed that LS-based PU doped with MWCNTs, applied as a potentiometric sensor, showed sensitivity to Cu(II), Zn(II), Cd(II), Cr(III), Cr(VI), Hg(II) and Ag(I) at pH 7 and exhibited response to Cr(VI) and redox potential at pH 2. It was suggested that LS obtained even from the same wood and by the same process, but under different cooking conditions, exhibits distinct sensing performance.

References

- [1] N. A. A. Qasem, R. H. Mohammed and D. U. Lawal, *npj Clean Water*, 2021, **4**, 36.
- [2] M. Cuartero and G. A. Crespo, *Curr. Opin. Electrochem.*, 2018, **10**, 98–106.
- [3] Ö. Isildak and O. Özbek, *Crit. Rev. Anal. Chem.*, 2021, **51**, 218–231.
- [4] C. Jin Mei and S. A. A. Ahmad, *Arab. J. Chem.*, 2021, **14**, 103303.
- [5] M. Parrilla, M. Cuartero and G. A. Crespo, *TrAC - Trends Anal. Chem.*, 2019, **110**, 303–320.
- [6] S. S. L. Gonçalves, A. Rudnitskaya, A. J. M. Sales, L. M. C. Costa and D. V. Evtuguin, *Materials (Basel)*, 2020, **13**, 1637.
- [7] F. A. C. Faria, D. V. Evtuguin, A. Rudnitskaya, M. T. S. R. Gomes, J. A. B. P. Oliveira, M. P. F. Graça and L. C. Costa, *Polym. Int.*, 2012, **61**, 788–794.
- [8] A. Rudnitskaya, D. V. Evtuguin, L. C. Costa, M. P. F. Graça, A. J. S. Fernandes, M. R. P. Correia, M. T. S. R. Gomes and J. A. B. P. Oliveira, *Analyst*, 2013, **138**, 501–508.
- [9] S. Magina, A. Rudnitskaya, S. Soreto, L. C. Costa, A. Barros-timmons and D. V. Evtuguin, *Materials (Basel)*, 2021, **14**, 5331.
- [10] S. Magina, A. Barros-Timmons and D. V. Evtuguin, in *15th European Workshop on Lignocellulosics and Pulp (EWLP2018) - Posters Presentations*, Aveiro, Portugal, 2018, pp. 303–306.

Acknowledgments

This work was developed within the scope of the project CICECO-Aveiro Institute of Materials, UIDB/50011/2020, UIDP/50011/2020 & LA/P/0006/2020, CESAM, UIDP/50017/2020 & UIDB/50017/2020, and i3N, UIDB/50025/2020 & UIDP/50025/2020, financed by national funds through the FCT/MEC (PIDDAC) and FCT/ESF (PhD grant SFRH/BD/121275/2016).

MICROELECTRODE SENSORS FOR CORROSION STUDIES

A.C. Bastos^{1*}, O.V. Karavai¹, M. C. Reyes^{1,2}, M.G.S. Ferreira¹

¹DEMaC – Department of Materials and Ceramic Engineering, and

CICECO – Aveiro Institute of Materials, Universidade de Aveiro, 3810-193 Aveiro, Portugal

²Present address: Fusion Fuel Green Inc., Rua da Fábrica, Sabugo, 2715-376 Almargem do Bispo

*e-mail: acbastos@ua.pt

Introduction

Corrosion has a huge impact in our technological society, and a great effort is being made to understand and control it. Being corrosion an electrochemical process, electrochemical methods are well suited for its investigation. However, the traditional techniques provide the average response of the sample and miss localised features. Most of these features can be resolved with the help of microelectrodes. Three localised electrochemical techniques used for characterising the corroding surface are described in this work [1-3]. One is a small vibrating probe that senses the electrical field in solution and maps the ionic currents flowing therein. The others are micropotentiometric and microamperometric sensors, which, long before the ascension of the scanning electrochemical microscopy [4], were already being used to sense the chemical species involved in electrophysiological processes [5,6]. In corrosion, these techniques provide information about the position of anodes and cathodes in the active surface, their reaction rates, the local concentration of important species like dissolved O₂, pH, metal cations from the corroding surface, and electrolyte ions from the testing medium. Here, examples are given regarding the use of these sensors to analyse the action of a corrosion inhibitor to heal the defects on a coating applied over an aluminium alloy.

Methods**Samples**

Aluminium alloy 2024-T3 sheet was coated with 2 µm thick hybrid organic-inorganic film. Samples of 1x1 cm² were cut and glued to epoxy holders and the edges protected with beeswax+colophony (3:1 wt. ratio). Two defects on the film were produced with an approximate diameter of 150 µm and separated by 300 µm. The corrosive environment was 0.05 M NaCl made with distilled water and p.a. grade reagent. Cerium nitrate (Aldrich, p.a.) was used as corrosion inhibitor ([Ce³⁺] = 0.01 M).

Scanning Vibrating Electrode Technique

The SVET equipment was manufactured by Applicable Electronics Inc. (USA) and controlled by the ASET 2.0 program from Sciencewares (USA). The microelectrode was prepared from polymer insulated Pt-Ir microelectrodes produced by Microprobes Inc. (USA). A 10 μm diameter platinum black sphere was electrodeposited on the tip – Figure 1. The microelectrode vibrated in the normal direction to the surface (z axis) with a frequency of 162 Hz. Recordings were obtained at a plane 100 μm above the sample surface. More details can be found in references [1-3].

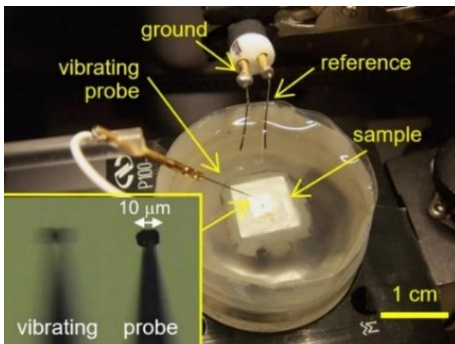


Figure 1 – SVET set-up (electrode and cell).

Micropotentiometry

Borosilicate glass capillaries with an outer diameter of 1.5 mm (WPI, USA) were thinned to a tip of 2 μm in one end. The micropipettes were silanised, back-filled with internal solution of 0.1 M KCl + 0.01 M KH₂PO₄ and front-filled with a 25 μm column of hydrogen I cocktail B ionophore (Fluka, Ref. 95293) – Figure 2.

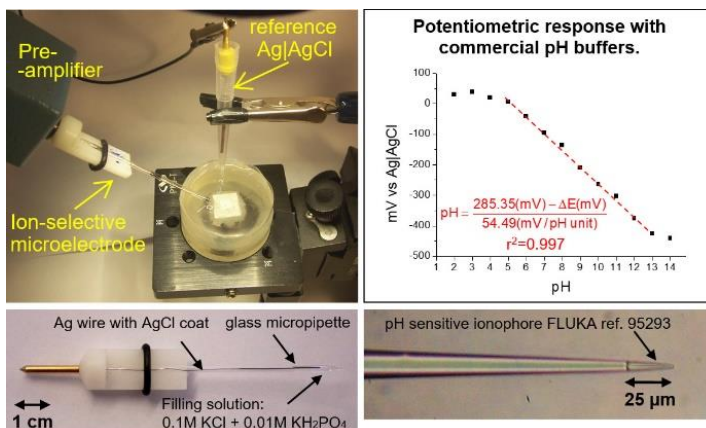
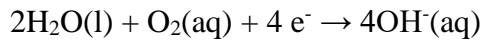


Figure 2 – Set-up for micropotentiometry.

A chloridised silver wire served as internal reference electrode and a homemade $\text{Ag}|\text{AgCl}|0.05\text{M NaCl}$ electrode was the external reference. A IPA2 amplifier (impedance $> 10^{15} \Omega$) manufactured by Applicable Electronics Inc. was controlled by the ASET program to measure and record the data. More details can be found in references [1,2].

Microamperometry

The measurement was performed using the IPA2 amplifier in the amperometric mode with a two-electrode arrangement, consisting of a $10 \mu\text{m}$ diameter platinum microdisk (CHI Instruments, USA) as working electrode (sensor) and a $\text{Ag}|\text{AgCl}$ electrode as counter and reference electrode. The sensor potential was fixed at $-0.7 \text{ V vs. Ag}|\text{AgCl}$, where the reaction



is controlled by diffusion (Figure 3). More details can be found in references [2,4,7].

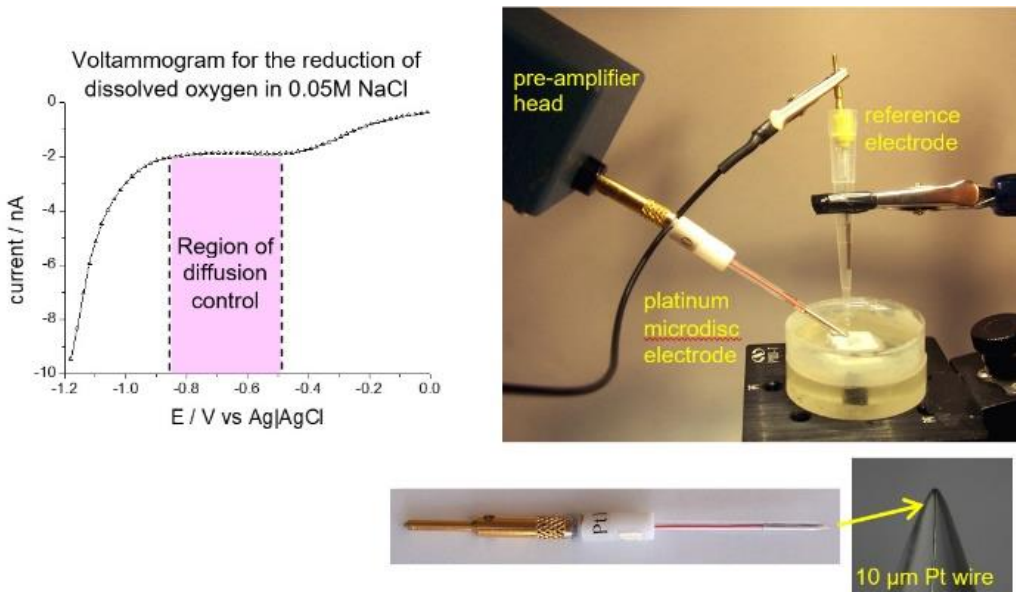


Figure 3 – Set-up for microamperometry

Results

Figure 4 shows the ionic currents, pH, and the reduction current of dissolved oxygen in lines at a constant height above the defects, before (blue lines) and 20 hours after (red lines) the addition of the corrosion inhibitor to solution. Before inhibition, the SVET line showed negative currents on the left defect and positive currents on the right defect. The negative currents were due to the reduction reactions of dissolved O_2 and water, both producing OH^- . The upward flux of negative charges was measured by SVET as a negative current. The positive current measured on the right defect was attributed to the flux of cations produced in the oxidation of the metal substrate. One defect was predominantly cathodic and the other was mainly anodic. The pH in solution showed a significant increase close to the cathode and no variation was detected above the anode. The current due to oxygen reduction (negative by definition) was constant except at the positions near the defects where it was smaller. This is because dissolved O_2 was being consumed at the metal surface exposed by the defects.

In the medium with inhibitor the three quantities – ionic currents, local pH and O_2 reduction current – presented the same values in the bulk of the solution and close to the defects (red lines). The absence of local chemical changes in solution denotes the suppression of the corrosion process that was generating them and consequently confirms the successful action of the corrosion inhibitor. The corrosion inhibition by cerium nitrate has been attributed to the blocking of the cathodic process by precipitation of cerium hydroxide/oxide in the cathodic sites [8].

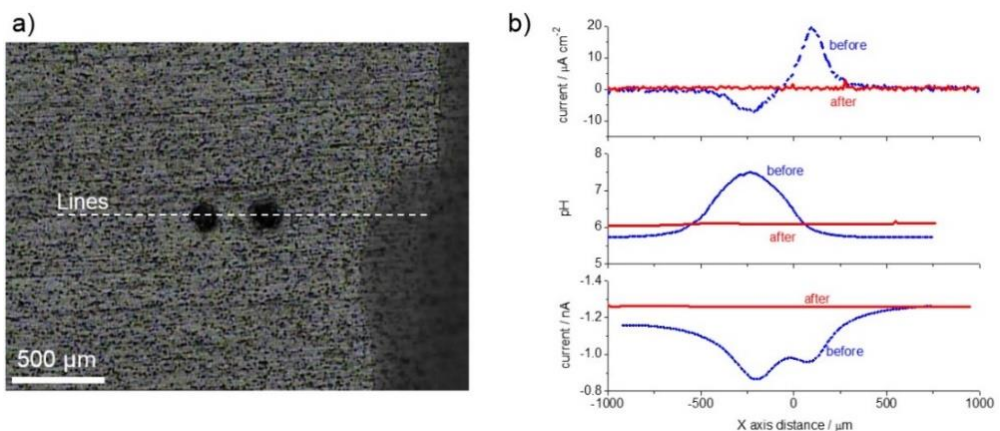


Figure 4 – a) Two defects in the transparent sol-gel film applied on aluminium alloy 2024-T3 and position of the line scans; b) line scans of ionic currents (SVET), local pH and dissolved oxygen reduction current measured at 50 μm (100 μm for SVET) above the surface, before and 20 hours after the addition of cerium nitrate [2].

Conclusions

The corrosion inhibition at defects of coated aluminium alloy 2024-T3 was investigated from the side of the solution using three microelectrode techniques. The SVET measured the ionic currents related to the anodic and cathodic processes and was complemented with localized micropotentiometric measurement of pH and microamperometric measurement of dissolved O₂. It was found cathodic activity in a defect that was thought to be only anodic according to SVET, demonstrating the importance of complementing its information with other techniques.

References

- [1] Alexandre Bastos, Application of SVET/SIET Techniques to Study Healing Processes in Coated Metal Substrates, *in Handbook of Sol-Gel Science and Technology* 2nd Ed, Springer, 2018.
- [2] A.C. Bastos, O.V. Karavai, M.L. Zheludkevich, K.A. Yasakau, M.G.S. Ferreira, Localised Measurements of pH and Dissolved Oxygen as Complements to SVET in the Investigation of Corrosion at Defects in Coated Aluminum Alloy, *Electroanalysis* 22 (2010) 2009.
- [3] A.C. Bastos, M.C. Quevedo, O.V. Karavai, M.G.S. Ferreira, On the Application of the Scanning Vibrating Electrode Technique (SVET) of Corrosion Research, *J. Electrochem. Soc.* 164 (2017) C397.
- [4] A.J. Bard, V. Mirkin (Eds), *Scanning electrochemical microscopy* 2nd Ed. Boca Raton, CRC Press/Florida Taylor & Francis Group, 2012.
- [5] D.C. Ogden (Ed.), *Microelectrode techniques, The Plymouth workshop handbook* 2nd Ed, Edited by Company of Biologists, Cambridge, UK, 1994.
- [6] Alexander G. Volkov (Ed.), *Plant Electrophysiology, Theory and Methods*, Springer-Verlag, Berlin Heidelberg, 2006.
- [7] I. Fatt, *Polarographic Oxygen Sensors. Its Application in Biology, Medicine, and Technology*, CRC Press, Boca Raton, Florida 1976.
- [8] A. J. Aldykewicz Jr., H. S. Isaacs, A. J. Davenport, The Investigation of Cerium as a Cathodic Inhibitor for Aluminum-Copper Alloys, *J. Electrochem. Soc.* 142 (1995) 3342.

Acknowledgements

This work was developed within the scope of the project CICECO-Aveiro Institute of Materials, UIDB/50011/2020, UIDP/50011/2020 & LA/P/0006/2020, financed by national funds through the FCT/MEC (PIDDAC). ACB acknowledges FCT – Fundação para a Ciência e a Tecnologia, I.P., in the scope of the framework contract foreseen in the numbers 4, 5 and 6 of the article 23, of the Decree-Law 57/2016, of August 29, changed by Law 57/2017, of July 19.

P1 |

OPTIMIZATION OF AN ELECTROCHEMICAL PHAGOMAGNETIC ASSAY BASED ON SIGNAL AMPLIFICATION OF β -GLU-Cu₃(PO₄)₂ HYBRID NANOFLOWERS FOR SELECTIVE QUANTIFICATION OF LIVE *LISTERIA MONOCYTOGENES*

Nádia F. D. Silva^{1*}, Cláudia Maciel¹, Paula Teixeira², Júlia M. C. S. Magalhães¹

¹ REQUIMTE/LAQV, Departamento de Engenharia Química, Faculdade de Engenharia, Universidade Do Porto, Rua Dr. Roberto Frias, 4200-465, Porto, Portugal

²Universidade Católica Portuguesa, CBQF - Centro de Biotecnologia e Química Fina – Laboratório Associado, Escola Superior de Biotecnologia, Rua Diogo Botelho 1327, 4169-005 Porto, Portugal

*e-mail: ndfs@fe.up.pt

Introduction

Listeria monocytogenes (LM) is a Gram-positive rod-shaped bacillus responsible for causing listeriosis in humans [1]. Listeriosis, despite its low incidence, is considered a serious medical condition associated with a high rate of hospitalization and mortality (20-30%) [2]. According to Regulation (EC) 2073/2005 of the European Commission levels of LM in foods must be below 100 CFU/g during the shelf life of ready-to-eat (RTE) products or absent in 25 g of RTE foods able to support the growth of the bacterium [3]. Thus, it is of great practical interest to implement fast, reliable, and simple methodologies to detect LM in food products.

In recent years, biosensors and electrochemical bioassays have established themselves as excellent methods in microbiological analysis, allowing, in some cases, to detect microorganisms much faster than standard colony plate counting methods [4]. However, many electrochemical biosensors fail to discriminate viable from non-viable cells and generally present selectivity problems when used directly in food matrices, requiring time-consuming or expensive pre-treatment techniques [2]. In this work, we propose the use of p100 bacteriophage, specific for *Listeria* spp., as a bioreceptor in a magnetic separation protocol to overcome recurrent food matrix effects, with the extra advantage of discriminating between viable and non-viable cells [4].

The enzymatic hybrid nanoflowers are attractive for enzymatic amplification in biosensors because they present higher levels of activity when compared to free enzymatic forms [6]. To increase the sensitivity of the method and obtain greater specificity, we also propose the use of hybrid copper phosphate nanoflowers with

the β -glucosidase enzyme, functionalized with the phage p100 (p100- β -GLU-Cu₃(PO₄)₂-NF).

Methods

Preparation of p100 functionalized magnetic beads by physical immobilization

Commercial magnetic particles, with \varnothing 2 μ m, a magnetite core and surface terminal amino groups, mediated by polyethylene glycol on its surface (PEG-MBs) were used as a magnetic platform for p100 bacteriophage loading. P100 was physically immobilized under favourable electrostatic conditions in a likely head-tail orientation resorting to a three-step optimized protocol [5] comprised of: i) PEG-MBs sterilization (in ethanol 97%, 30 min); ii) bacteriophage physical immobilization (1×10^9 PFU of p100 in 0.1 M citrate buffer pH 5, “overnight” at 350 rpm, 4 °C) and; iii) nanoparticle active binding sites blockage (BSA 1% in 0.1 M PBS pH 7.4, 8 h, at 350 rpm, 4 °C); all interspersed by two washing steps. In the end, the separated bacteriophage-functionalized magnetic particles (BSA/P100/PEG-MBs) were re-suspended in 500 μ L of SM buffer (TRIS 1 M, 8 mM MgSO₄ and 100 mM NaCl, pH 7.5). All samples were stored at 4 °C until been used.

One-pot synthesis of p100- β -GLU-Cu₃(PO₄)₂ nanoflowers

For the preparation of p100- β -GLU-Cu₃(PO₄)₂ nanoflowers, 40 μ L CuSO₄ solution (120 mM) was added to 1445 μ L PBS (100 mM, pH 7.4) containing β -glucosidase (β -GLU, 0.5 mg mL⁻¹) and 15 μ L p100 solution (Listex®, 1.8×10^{10} PFU). The mixture was incubated at 4 °C for 18h to form p100- β -GLU-Cu₃(PO₄)₂ nanoflowers. Next, the p100- β -GLU-Cu₃(PO₄)₂ nanoflowers were collected through centrifugation (5500 rpm, 10min), washed with deionized water twice and TRIS 100 mM pH 7.2 once to remove the excess phage and enzyme and were resuspended in 1500 μ L and stored at 4 °C. For blocking nonspecific adsorption sites, some samples were previously incubated with 1500 μ L 1% BSA, at different periods. The morphology, size, and composition of pre-formed p100- β -GLU-Cu₃(PO₄)₂-NF and BSA/p100- β -GLU-Cu₃(PO₄)₂ nanoflowers were accessed by scanning electron microscopy (SEM) and EDS.

Phagomagnetic assay protocol

160 μ L of p100 BSA/P100/PEG-MBs was washed twice with TRIS (100 mM, pH 7.2) and incubated with TRIS (blank assays) or LM solutions of various concentrations (500 μ L, 10/15/30 min, 350 rpm). Then, the LM cells captured on MBs (*Listeria*-BSA/P100/PEG-MBs), were magnetically attracted and washed twice to remove non-attached cells. Afterwards, different amounts of BSA/ p100- β -GLU-Cu₃(PO₄)₂ nanoflowers were added (100 μ L, 10 min, 350 rpm). After

incubation, the nanoflower-*Listeria*-BSA/P100/PEG-MBs complex was magnetically separated and washed twice. Subsequently, 100 μL of 4-nitrophenyl β -D-glucopyranoside (20 min, 37 $^{\circ}\text{C}$) was added. In the end, a NaOH (0.5M) solution was used to stop the enzymatic reaction and an electrochemical measurement was performed at a carbon screen-printed electrode. Square-wave voltammograms were obtained between 0.6–1.2V, with a 30 Hz frequency and a scan rate of 5 mV/s^{-1} .

Results

Optimization of magnetic separation protocol

Magnetic phage-probe specific immobilization and capture efficiency was evaluated by microbiologic counting number of PFU or colonies on agar plates using supernatants collected after p100 immobilization step described in 2.1 and *Listeria* incubation in 2.3. Moreover, samples of *Listeria*-BSA/P100/PEG-MBs were prepared to be visualized through SEM.

Microbiologic studies confirmed the successful PEG-MBs biofunctionalization with p100 and the preservation of their capture efficiency and lytic activity. SEM images also visually confirmed the ability of BSA/P100/PEG-MBs to selectively capture *Listeria* cells. These results suggest that the phages on phage-MBs probes were mostly deposited under a head down configuration (from capsid), also preserving the tail fiber recognition sites for bacteria anchorage.

Afterwards, the optimization of magnetic separation protocol was accessed using molybdate assay protocol. Briefly, this method is based in the reaction between phosphate groups of bacterial DNA backbone with sodium molybdate to form redox molybdophosphate precipitate, which can electrochemically quantified and indirectly related with the CFUs of initial inoculum to calculate the specific capture rates (CR%) [6]. A volume between 80-160 μL of magnetic probes, 7 as incubation solution pH and 25 $^{\circ}\text{C}$ of incubation temperature resulted in best specific capture rates in the conditions tested (e.g., CR=60.56%, 30 min capture time, 1000 CFU mL^{-1}).

Electrochemical phagomagnetic assay: β -GLU- $\text{Cu}_3(\text{PO}_4)_2$ nanoflowers as enzymatic labels

Figure 1 displays SEM images of a p100- β -GLU- $\text{Cu}_3(\text{PO}_4)_2$ hybrid nanoflowers prepared by one-pot biomineralization synthesis. Most of the nanoflowers present a uniform sphere-like shape, with an average \varnothing of $6 \pm 1 \mu\text{m}$. Moreover, a hierarchical porous surface area peony/daisy pompon-like flower morphology of β -GLU- $\text{Cu}_3(\text{PO}_4)_2$, is expected to increase the p100 load, enhancing the final

electrochemical signal and method sensitivity. As routine, enzymatic activity of all formed hybrid nanoflowers were electrochemically measured using 4-nitrophenyl β -D-glucopyranoside as enzymatic substrate, confirming a high activity after synthesis.

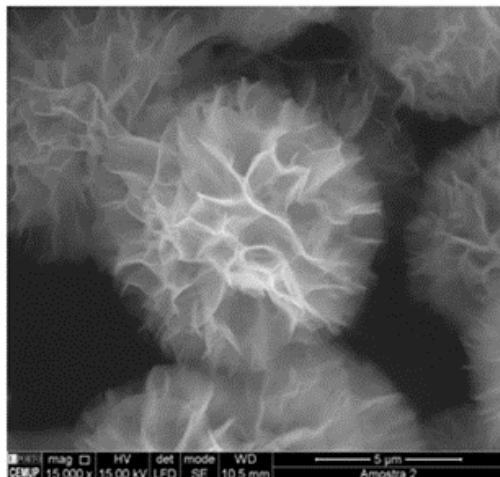


Figure 1 - SEM picture of a p100- β -GLU- $\text{Cu}_3(\text{PO}_4)_2$ hybrid nanoflower, magnitude 15.000x.

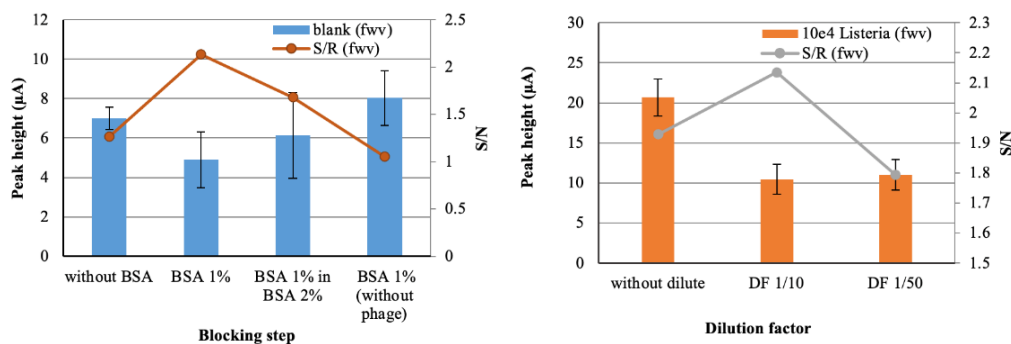


Figure 2 - Graphical representation of the study of p100- β -GLU- $\text{Cu}_3(\text{PO}_4)_2$ active surface blocking step (A) and concentration (B) effects in non-specific adsorption and phagomagnetic assay sensitivity showing blank and control assays (10^4 CFU mL^{-1} cells) and respective signal-to-noise ratio (S/N) under different assay variables.

Electrochemical phagomagnetic assay optimization followed the study of the effect of several assay variables (blockage nanoflower surface active spots, nanoflower concentration, incubation times) on assay sensitivity. At this point, the use of BSA 1% blocking step after nanoflowers synthesis and a dilution factor

of 1:10 of the enzymatic label evidenced to have a positive effect in non-specific adsorption of enzymatic probes and subsequently in assay sensitivity (see figure 2). Moreover, using the conditions just optimized it was possible to discriminate and quantify different levels of viable LM cells (10^3 – 10^6 CF mL⁻¹). However more experiments will be necessary to conduct to achieve a lower limit of detection.

Conclusions

In this work it was developed an optimized magnetic separation protocol and established a simple electrochemical methodology to evaluate the capture efficiency of p100 functionalized magnetic probes. SEM observations validate the electrochemical findings and the effectiveness of the proposed method. Favorable specific capture rates (approx. 60%) were achieved using an optimized separation protocol when compared to other magnetic separation methods [5, 7]. Additionally, it has the added value of being able to discriminate between viable and non-viable cells. In future, further optimization experiments will be taken, namely in assay format, incubation time steps, aiming to achieve a detection limit as low as possible in different food matrices.

References

- [1] Hunt, K., M.Vacelet, and K.Jordan,. Irish Journal of Agricultural and Food Research, 2017. **56**(1):p.25-30.
- [2] Silva, N.F.D., et al., Trends in Food Science & Technology, 2020. **99**: p. 621-633.
- [3] European Commission (EC), European Commission regulation on microbiological criteria for foodstuffs. 2005, Official Journal of the European Union. p. 1-26.
- [4] Rohde, A., et al., Trends in Food Science & Technology, 2017. **62**: p. 113-118.
- [5] Zhou, Y. and R.P. Ramasamy. Colloids and Surfaces B: Biointerfaces, 2019. **175**: p. 421-427.
- [6] Jiang, X., et al. Sensors and Actuators B: Chemical, 2019. **299**: p. 126944.
- [7] Liana, A. E., et al., Colloids and Surfaces B: Biointerfaces, 2017. **151**:p. 47-57.

Acknowledgments

This work received financial support from PT national funds (FCT/MCTES, Fundação para a Ciência e Tecnologia and Ministério da Ciência, Tecnologia e Ensino Superior) through the project UIDB/50006/2020 | UIDP/50006/2020 and from the European Union (FEDER funds through the NORTE2020 - Programa Operacional Regional do Norte, ref. NORTE-01-0145-FEDER-31968).

P2 |

TWO POTENTIOMETRIC MICROSENSORS FOR Cu^{2+} DETERMINATION IN CORROSION PROCESSES

O.V. Karavai^{1*}, A.C. Bastos¹, M.L. Zheludkevich^{2,3}, M.G.S. Ferreira¹

¹ CICECO – Aveiro Institute of Materials, DEMaC, University of Aveiro, 3810-193 Aveiro, Portugal

² Institute of Surface Science, Helmholtz-Zentrum Hereon, 21502 Geesthacht, Germany

³ Faculty of Engineering, Kiel University, 24143, Kiel, Germany

*e-mail:olga.karavai@ua.pt

Introduction

Copper is a metal and an important element to our everyday life. It is also a major industrial metal because of its high ductility, malleability, thermal and electrical conductivity and resistance to corrosion. Main applications of copper are in electrical industry, construction, transportation, industrial machinery, telecommunications, and also in metallurgy as alloying element (ex: brasses, bronzes, some aluminium alloys). In aluminium alloys, copper is partially in the form of intermetallic particles which often become sites of localized corrosion [1, 2]. The determination of copper dissolution from such sites is beneficial for understanding the corrosion mechanism and for choosing proper protection measures.

The electrochemical approach to chalcogenide glass preparation offered exceptional possibilities for producing Cu^{2+} -selective electrodes [3-5]. These materials in form of thin films are very suitable for all solid-state potentiometric sensors or for ISFET (ion-sensitive field-effect transistor) technology [6]. Several examples of Cu^{2+} -sensitive microsensors based on chalcogenide glasses were found [6-8]. They are now well-established sensors, but unfortunately Fe^{3+} , Ag^+ and other ions are serious interferences. A number of various carrier types has been investigated as potential ionophores for Cu^{2+} -selective electrode [9]. Among them attractive selectivity toward Cu^{2+} revealed macrocyclic and noncyclic carriers containing S atoms [9]. Following this concept, Marques de Oliveira *et al.* synthesized a dithiomacrocyclic neutral carrier, (4-phenyl-11-decanoyl-1,7-dithia-11-azacyclotetradecane-4-sulfide), which they used in all-solid-state PVC (polyvinyl chloride)-membrane for ISFET [10]. The fabricated microsensor exhibited good linear response, low detection limit and high selectivity toward variety of other cations [10]. Several others ISFETs with carrier-based PVC membranes were described too [11,12]. A chelating agent, tetra-*n*-butylthiuram disulfide (TBTDS), used as ionophore for PVC-membrane of Zn^{2+} -SE [13],

together with its derivatives were initially tested as neutral carriers for Cu (II) ions [14]. It has been demonstrated that these neutral carriers have almost ideal C-shaped cavities to fit the Cu²⁺ ion, and form a 1:1 cation-ionophore coordination sphere, and hence provide a highly selective sensor [9, 14]. The higher selectivity toward Cu²⁺, compared to Zn²⁺ ions is confirmed by $\log K_{Zn^{2+}, Cu^{2+}}^{pot} = 0.96$ (for Zn²⁺-SE based on TBTDS, potassium tetrakis(4-chlorophenyl) borate, 2-nitrophenyloctyl ether, PVC) [13]. It became obvious, the possibility to use the same composition for fabrication of both Zn²⁺ and Cu²⁺-SMEs from glass micropipettes provided both ions do not coexist in the analysing system.

In this work development and application of the two ion-selective micro electrodes for Cu²⁺ detection for localized measurements are described: one is based on a liquid membrane cocktail and another based on a metal/metal salt electrode.

Methods

The first Cu²⁺-SME was a glass capillary silanized pipette (Ø 1-2 µm), back-filled with an inner reference solution (0.1M KCl + 0.01M KH₂PO₄ + 10⁻⁵M CuCl₂). Then it was front-filled with a liquid membrane cocktail using an optical light microscope (1113AMH Binocular Microscope, VanGuard, USA) with 3D micromanipulators. The cocktail consists of 7.0 wt. % of TBTDS, 22.8 wt. % of sodium tetrakis[3,5-bis(trifluoromethyl)phenyl] borate, 1.4 wt. % of ETH500 and 68.8 wt. % of 2-nitrophenyloctyl ether. The second Cu²⁺-SME was made of Pt-Ir wire (MicroProbes Inc., USA, Ø 10 µm). Firstly, a Pt deposit was plated at the tip from a solution (0.02M H₂PtCl₆ + 2·10⁻⁴M Pb(CH₃COO)₂) at a current of -200 nA for 5 minutes followed by a current of -500 nA for 10 minutes. Secondly, copper was deposited with a solution of 0.2M CuCN + 0.6M NaCN + 0.1M Na₂CO₃ and pH 11-12 [15] at -100 nA for 60 minutes. Finally, to make the electrode sensitive to Cu²⁺ a layer of copper selenide {CuSe} was obtained on the copper surface by cathodic deposition (current of -100 nA for 30 minutes) from 0.1M Na₂SeO₃ solution adjusted to pH 6 with sulphuric acid, as described in reference [8]. All substances used were purchased from Sigma-Aldrich and were of *puriss* or *purum* grade. The solutions were prepared with deionized water (≈18MΩ).

Cu²⁺-SMEs were calibrated in Cu²⁺ solutions with NaCl background and applied for studying corrosion and inhibition by benzotriazole (C₆H₅N₃, BTAH) of a Cu wire connected to a Pt wire and immersed in NaCl. Measurements were performed using Scanning Ion-Selective Electrode Technique based on equipment from Applicable Electronics Inc. (USA) controlled by the ASET 2.0

software (ScienceWares Inc., USA). The IPA2 two channels amplifier with input resistance $>10^{12}\Omega$ was used to measure potential. An additional pre-amplifier head (gain 1 or 10 and input resistance $>10^{15}\Omega$) was used for measuring small changes in signal values of potentiometric microsensors. A homemade Ag/AgCl, 0.05M NaCl mini-electrode with the inner solution stabilized by 3% agar-agar was used as external reference electrode. The size of its orifice was around 2 mm.

Results

The TBTDS-Cu²⁺-SME response was linear in the range 1.3-5.5 pCu in pure Cu²⁺ solutions and 1.3-4.0 pCu at 5mM NaCl background having slopes of 34.9 and 34.6 mV/pCu correspondingly (Fig.1.a). The microelectrode linearity at 0.05M NaCl background was from 1.5 to 3.0 pCu, what clearly indicates limited selectivity of the TBTDS based microsensor against Na⁺ ions.

The produced Cu{CuSe} microsensor shows near Nernstian slopes in calibration graphs (Fig.1.b). The Cu²⁺ selective microsensor was linear in the concentration range from $3 \cdot 10^{-2}$ M to $3 \cdot 10^{-6}$ M in pure copper (II) solutions and from $3 \cdot 10^{-2}$ M to 10^{-5} M at 0.05M NaCl background with slopes of 34.1 and 33.1 mV / pCu correspondingly. The influence of Na⁺ on response of the Cu{CuSe} microsensor is almost negligible. It has lower detection limit around $3 \cdot 10^{-6}$ M.

Measurements of Cu²⁺ activity were performed on a Cu disk embedder in epoxy holder (Fig.2 a) dissolving in NaCl solution and coupled to a Pt to provide an extra area where O₂ can react forcing the oxidation of copper. The Cu dissolution corresponds to the anodic process; the cathodic is oxygen reduction at the Pt wire. The Cu²⁺ activity was monitored along a 5 mm line, which is shown on Fig.2 a, and at 10 μm distance from the sample surface.

Figure 2 (b) presents obtained profiles (consisted of at least 100 points) of Cu²⁺ activity obtained by TBTDS-Cu²⁺-SME. Copper activity up to $4.1 \cdot 10^{-3}$ M was detected close to the centre of the Cu wire almost immediately, i.e. 5 min after the couple had been immersed in 5mM NaCl (black line, Fig.2 b). After 2.5 h of immersion, Cu²⁺ activity in the order of $3 \cdot 10^{-5}$ M was detected (red line); it was almost the same as above the epoxy matrix, likely due to formation of corrosion products. Then the crystals of BTAH were added into solution in order to get 1 mM concentration of the inhibitor. After 30 min of immersion in 5mM NaCl + 1mM BATH solution $a_{Cu^{2+}}$ was $4.8 \cdot 10^{-5}$ M along the whole scanned line (Fig.2 b, emerald green line). No active spots were found at the metal surface. After 30 min of immersion, an artificial scratch on the copper surface was made by a sharp knife (Fig.2 a), and immediately a peak of Cu²⁺ activity was detected above the

scribe (Fig.2 b, pink line). The shiny scratch exposed pure copper to the solution, which started to dissolve instantly. Later the measured values of $a_{Cu^{2+}}$ become smaller (blue line), ca. $3.7 \cdot 10^{-4}M$ comparing to $5.7 \cdot 10^{-4}M$ (pink line), and after further 30 min the copper activity become low (ca. $4.8 \cdot 10^{-5}M$) and almost constant along the whole measured profile (orange line). The BTAH inhibitive effect could be clearly observed.

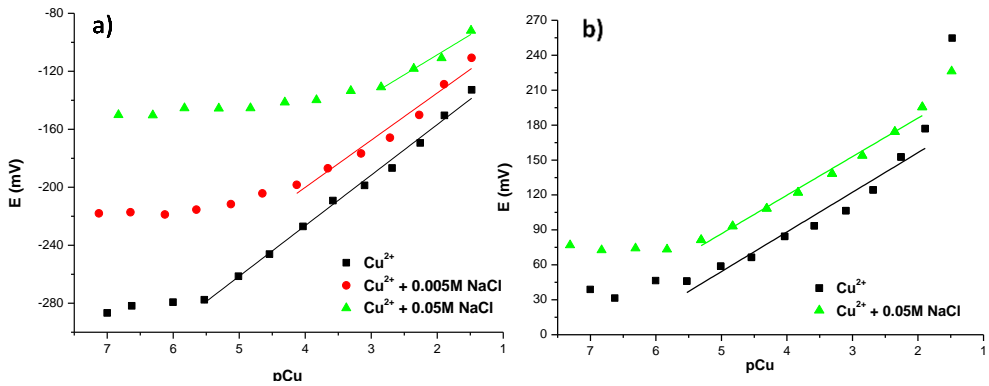


Figure 1. Calibration plots TBTDS-Cu²⁺-SME (a) and Cu{CuSe} microsensor (b) in different media.

Figure 2 (b) presents obtained profiles (consisted of at least 100 points) of Cu²⁺ activity obtained by TBTDS-Cu²⁺-SME. Copper activity up to $4.1 \cdot 10^{-3} M$ was detected close to the centre of the Cu wire almost immediately, i.e. 5 min after the couple had been immersed in 5mM NaCl (black line, Fig.2 b). After 2.5 h of immersion, Cu²⁺ activity in the order of $3 \cdot 10^{-5}M$ was detected (red line); it was almost the same as above the epoxy matrix, likely due to formation of corrosion products. Then the crystals of BTAH were added into solution in order to get 1 mM concentration of the inhibitor. After 30 min of immersion in 5mM NaCl + 1mM BATH solution $a_{Cu^{2+}}$ was $4.8 \cdot 10^{-5}M$ along the whole scanned line (Fig.2 b, emerald green line). No active spots were found at the metal surface. After 30 min of immersion, an artificial scratch on the copper surface was made by a sharp knife (Fig.2 a), and immediately a peak of Cu²⁺ activity was detected above the scribe (Fig.2 b, pink line). The shiny scratch exposed pure copper to the solution, which started to dissolve instantly. Later the measured values of $a_{Cu^{2+}}$ become smaller (blue line), ca. $3.7 \cdot 10^{-4}M$ comparing to $5.7 \cdot 10^{-4}M$ (pink line), and after further 30 min the copper activity become low (ca. $4.8 \cdot 10^{-5}M$) and almost constant along the whole measured profile (orange line). The BTAH inhibitive effect could be clearly observed.

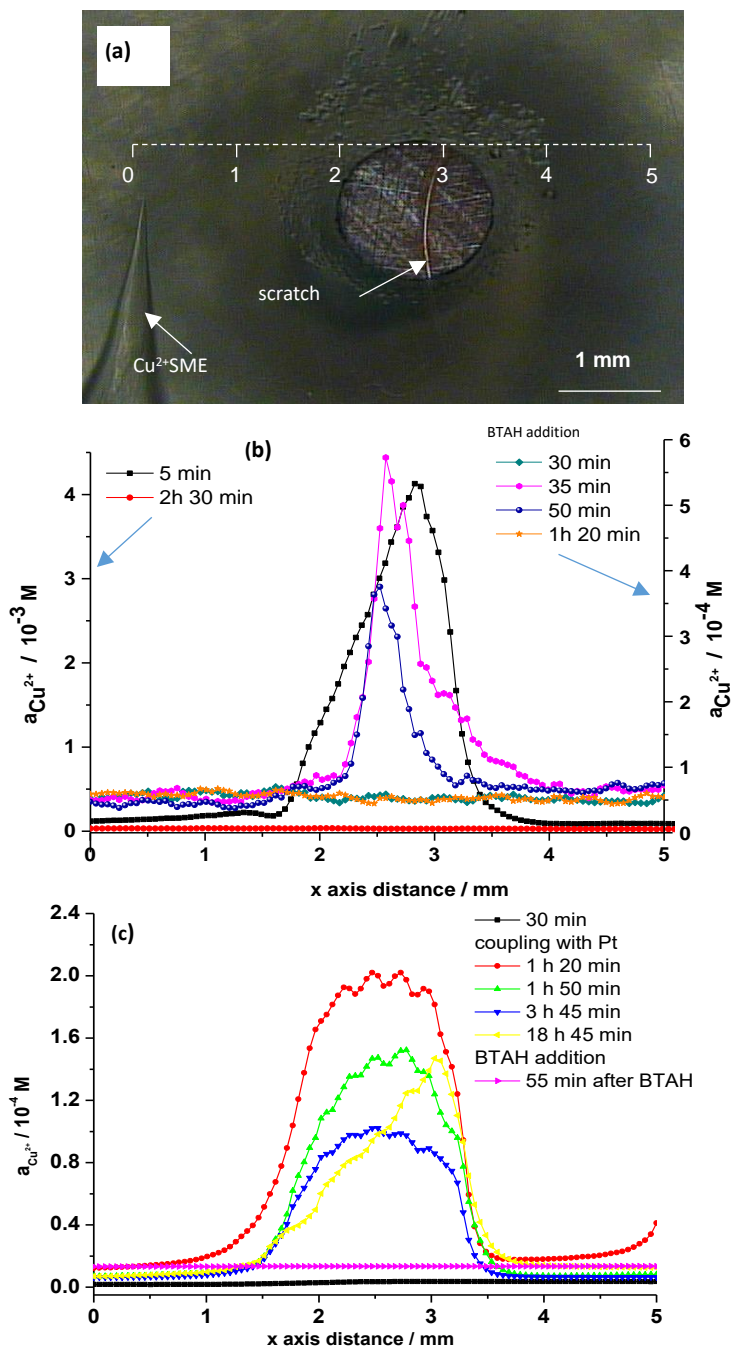


Figure 2. Optical photograph of Cu wire with a scratch (a); activity of Cu²⁺ measured by TBTDS-Cu²⁺-SME at different times of immersion in 5mM NaCl (b); activity of Cu²⁺ measured by Cu{CuSe} microsensor at different immersion times in 0.05M NaCl (c).

Figure 2 (c) shows profiles obtained by Cu{CuSe} microsensor 100 μm above the surface. No $a_{\text{Cu}^{2+}}$ changes were detected after 30 min of immersion above the not coupled copper wire (black line, Fig. 2 c). But in a galvanic couple with Pt, corrosion started very fast and after 1 h 20 min of immersion the copper began to dissolve rather intensively (red line, Fig. 2 c). Some decrease in the copper activity was observed after 3 h 45 min of immersion (blue line in Fig. 2 c), which could be explained by formation of corrosion products. After almost 19 hours of immersion the $a_{\text{Cu}^{2+}}$ profile revealed at least one active side of the copper wire (yellow line, Fig 2 c). Then BTAH crystals were added into solution in order to obtain 1 mM concentration. The sample was left during 45 min in contact with the inhibitor. Then the solution was replaced by new 0.05M NaCl solution and the activity profile was measured after 55 min of immersion. The observed values of $a_{\text{Cu}^{2+}}$ were very low and were the same above the wire and in the solution bulk, i.e. $1.3 \cdot 10^{-5}\text{M}$ (magenta line, Fig. 2 c), because a protective layer containing BTAH was formed at the copper surface, which blocked the metal dissolution.

Conclusions

Two Cu^{2+} selective microelectrodes, a glass TBTDS based Cu^{2+} -SME and a 2nd kind metal/metal salt Cu{CuSe} microsensor, were developed. Their main characteristics were determined. Both microsensors showed good sensitivity for Cu^{2+} ions giving linear response in the range of 10^{-2} - 10^{-6}M for TBTDS- Cu^{2+} -SME and $3 \cdot 10^{-2}$ - 10^{-6}M for Cu{CuSe} microsensor in pure Cu (II) solutions. The Cu{CuSe} microsensor possessed better selectivity against Na^{+} ions as was shown on calibration graphs. Both microelectrodes were applied for investigation of corrosion processes of a copper wire connected to Pt and immersed in NaCl solution with and without BTAH. Obviously, the solid state Cu{CuSe} microelectrode is mechanically more robust, but its spatial resolution is lower than for the other ME, as its tip diameter is likely to be more than 10 μm comparing to 1.5-2 μm for the TBTDS- Cu^{2+} -SME.

References

- [1] J. Electrochem. Soc. 144 (1997) 2621
- [2] J. Electrochem. Soc. 152 (2005) B140. 16.
- [3] J. Electrochem. Soc. 118 (1971) 571.
- [4] J. Electrochem. Soc. 121 (1974) 363.
- [5] Analyst 119 (1994) 1361.
- [6] Sensors Actuators B Chem. 59 (1999) 123.
- [7] Sensors Actuators B Chem. 24–25 (1995) 733.
- [8] J. Solid State Electrochem. 4 (2000) 325.
- [9] Chem. Rev. 98 (1998) 1593.
- [10] Electrochim. Acta 51 (2006) 5070.

- [11] Sensors Actuators B. Chem. 62 (2000) 8.
- [12] Sensors Actuators B Chem. 130 (2008) 187.
- [13] Anal. Sci. 10 (1994) 409.
- [14] Anal. Chem. 60 (1988) 2464.
- [15] J. Electroanal.Chem. 474 (1999)16.

Acknowledgments

The authors acknowledge funding from the project Siset - FP7-PEOPLE-IRSES-GA-2010-269282, and FCT (Portugal) for PTDC/CTM/108446/2008 and SFRH/BD/44475/2008 grants.

P3 |

DISSOLVED OXYGEN BIOSENSING USING ELECTROCHEMICAL ELECTRODES AND SOLID ELECTROLYTE POLYMER

D. R. Santos¹, P. P. Freitas¹

¹ INL – International Iberian Nanotechnology Laboratory, Av. Mestre José Veiga 4715-330, Braga, Portugal

*e-mail: denis.santos@inl.int

Introduction

Oxygen is vital for human life as adequate tissue oxygen content is fundamental to supply cellular metabolic energetic demands. The measurement of dissolved oxygen in tissue is of great importance in several biomedical fields. In oncology, tumor hypoxia is increasingly recognized as an unfavorable factor in cancer therapies. In the chronic illness diabetes, people without treatment show a simultaneous increase in tissue oxygen consumption and a decrease in the ability of the circulating blood to release oxygen. [1].

The oxygen sensors that are currently used are costly time intensive bulky devices, eliminating the possibility for real-time monitoring. Electrochemical detection is the most widely used method for real-time continuous measurements of dissolved oxygen (DO). These sensors operate by electrochemically reducing the dissolved oxygen and measuring the resulting current. The Clark type sensor is based on membrane-covered oxygen electrodes and is the most widely used oxygen sensor due to its simplicity and reliability. It consists of a working (WE), reference (RE) and counter (CE) electrodes, a liquid electrolyte, and an oxygen-permeable membrane that separates the sample from the electrolyte. The oxygen permeates through the membrane to the inner electrolyte and the reduction current of oxygen is measured at the WE (cathode).

Microfabrication technology has driven the development of several forms of Clark-type sensors. It is however challenging to incorporate the internal electrolyte solution in the microelectrode fabrication resulting in issues of robustness, and need for rehydration. Microfabricated sensors using solid-state proton exchange membranes (PEM) as solid electrolytes are potentially smaller, have increased lifetime and eliminate the need for re-hydration [2]. These are important factors when targeting biomedical implantation for disease diagnosis, treatment, and monitoring. As size is decreased, the electrodes' planar geometry becomes more relevant to the amplitude of the signal measured and consequently to the sensitivity of the devices.

In this work, several planar Clark-type DO sensors, with a biocompatible solid electrolyte layer and no oxygen-permeable membrane, have been produced by means of thin-film technology to verify the effect of geometry on the sensors' sensitivity as an early stage development targeting implantable DO biosensors.

Methods

The microelectrodes were developed in sets of one WE, RE, and CE per sensor and in two different configurations, namely interdigitated electrodes (IDE) and microdisc (MD). Each configuration was fabricated having either 100 or 200 μm^2 of total active area. Moreover, for each configuration and size, the area of the CE was either equal to the WE (1:1) or twice as big (1:2) thus resulting in 8 distinct sensors geometries. As can be seen in Figure 1-a), the microelectrodes, were fabricated on a 200 mm single side polished silicon wafer with a SiO_2 dielectric layer. The metal layers are 100 nm-thick planar structures made of sputtered platinum (10 nm TiW adhesion layer), patterned using direct writing photolithography and etched by reactive ion etching (RIE). A 200 nm-thick SiO_2 passivation layer was deposited by plasma enhanced chemical vapor deposition (PECVD) and vias were opened by RIE on top of the electrodes and contact pads. The solid electrolyte proton exchange membrane (PEM) Nafion[®] 117 was then spin-coated, after the surface of the device was treated with Silane A174 adhesion promoter, and then baked for a final thickness of 375 nm.

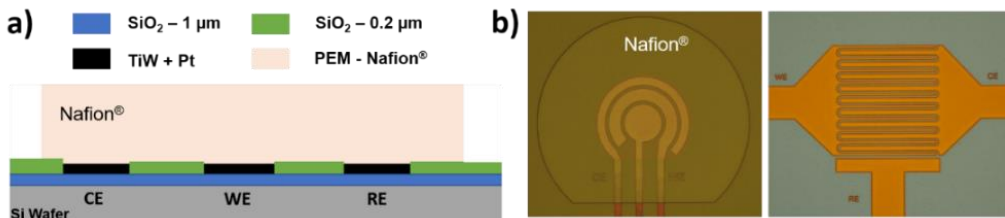


Figure 1 - a) Electrodes schematic cross-section (not to scale); b) Top-view microphotographs of: left - a MD with 100 μm external diameter and right - an IDE 200 μm square without PEM.

The fabricated sensors showed in Figure 1-b) were measured using a PGSTAT302N potentiostat. Before measurements, the oxygen concentration in the deionized water samples was measured using a commercial DO sensor (Hanna HI-98194). Two DO concentrations were used – DO 0% (nullified by addition of

an oxygen scavenger), and approx. 55% (around 4.46 mg/L). The sensors' characterization was carried out, at room temperature, in a custom made acrylic flow-through electrochemical cell. Cyclic voltammetry (CV) measurements (-1 V to 1 V at 50 mV/s) were first used to determine the bias point for activation voltage and reduction current of the device. Based on the specific sensor geometry and literature, the range of reduction voltages from -0.4V to -0.8V was of interest.

Chronoamperometry (CA) measurements were made to determine the sensitivity of the devices. The measurements were made by applying a step voltage change to the working electrode and measuring the current response at a sample rate of 20 samples/s for 20 seconds, followed by a period of 20 seconds at 0V (no oxygen reduction). This was repeated for a total of 3 steps (Figure 2-b). This protocol was performed, in succession, for three different reduction voltages. For each CA recording, the working electrode current was averaged over 2 seconds at 15 and 20 seconds to derive the mean current.

Results

The CV measurements (Figure 2-a) indicated that the activation voltage was in accordance with the literature. A set of three different voltages were tested for CA measurements for all sensors, -0.5 V, -0.575 V and -0.65 V and higher current signals were obtained with the latest for the vast majority of the sensors. It can be seen, from Figure 2-b, that the diffusion limited O₂ transport output have an expected initial transient current, followed by an approach to steady state. The default acquisition time was the averaging of the last 2 seconds of the 20 seconds measurement. The current signals could also be calculated at 15 s of acquisition without significantly affecting the sensitivity and stability of the results (Figure 2-c). The sensitivity of the sensors, shown in Figure 2-d, are in accordance with other DO electrochemical sensors found in the literature [1, 2]. Due to the interleaved proximity of WE and CE electrodes, that promote redox cycling of the electroactive species to be measured, the IDEs showed higher currents than the MDs, which resulted in higher sensitivities. The tissue volume probed for DO is related to the electrode size. The larger 200 μm wide electrodes resulted, as expected, in higher currents and are thus more sensitive. It is also important that the half-reaction at the CE (oxidation of O₂) is not limiting the speed of the reduction reaction at the WE. This was also visible since larger CE led to higher sensitivities than when the area of WE is the same as CE.

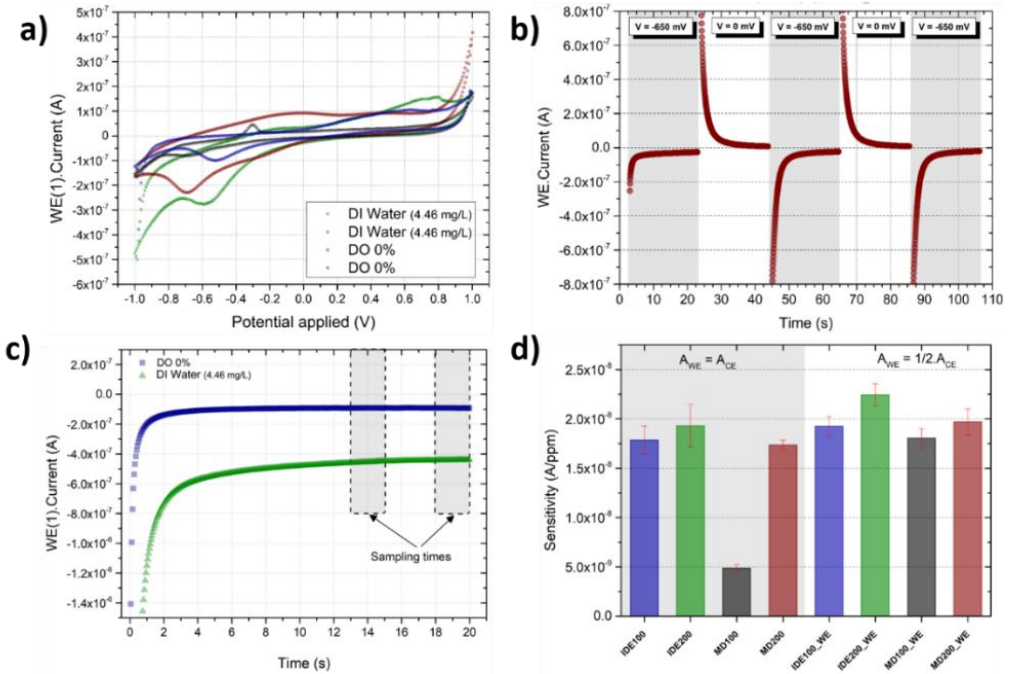


Figure 2 – a) CV plots obtained for 2 IDE sensors at 2 different oxygen concentrations (0 mg/L and 4.46 mg/L); b) Chronoamperometry cycles obtained for one sensor alternating voltage steps between 0 V and -0.65 V; c) CA current measured with an applied voltage of -0.65 V for 2 different oxygen concentrations; d) Comparison of sensitivity of all microfabricated geometries (in the left shade, the areas of WE and CE are identical, in the right, the area of WE is half of CE) (N = 5).

Conclusions

Planar miniaturized all-solid-state Clark-type oxygen sensors were constructed by means of standard microfabrication processes, at wafer level, and were coated with a Nafion[®] solid polymer electrolyte membrane to ensure robustness, biocompatibility and selectivity. The sensor was tested in DI water with or without DO, with results comparable to the ones found in the literature. The Nafion[®] film showed to be oxygen permeable and support the electrochemical reduction of oxygen at an electrode surface indicating that it would be suitable for use in a miniaturized solid-state implantable oxygen sensor in biomedical applications as well as, for instance, *in-vitro* cell cultures and microfluidic lab-on-a-chip systems.

The development of a miniaturized implantable device for the real-time, and continuous monitoring of oxygen levels in tissue is always dependent on its

biocompatibility. Future work includes the microfabrication on biocompatible flexible substrates, to minimize the inflammatory response at the material-tissue interface, and on the integration of multiple sensors to provide DO readings from a larger volume.

References

- [1] M.E. Gray, et al., *Am. J. Physiol. Liver Physiol.* 317, G242 (2019).
- [2] G.W. McLaughlin, et al., *Sensors Actuators B Chem.* 83, 138 (2002).

Acknowledgments

The authors would like to thank NORTE Regional Operational Program for funding through the research project N2020 FROnTHERA - Frontiers of technology for theranostics of cancer, metabolic and neurodegenerative diseases.

P4 |

INKJET-PRINTED ELECTRODE MODIFIED WITH MAGNETITE PARTICLES AND CARBON NANOTUBES FOR THE NON-ENZYMATIC AMPEROMETRIC DETERMINATION OF HYDROGEN PEROXIDE

M.I. Mass¹, L.S. Veiga¹, O.F. Garate¹, G.O. Ybarra^{1,*}, E. Ramón², G. Gabriel²

¹*INTI-Micro y Nanotecnologías, Instituto Nacional de Tecnología Industrial (INTI), San Martín, Buenos Aires, Argentina.*

²*Institut de Microelectrònica de Barcelona, IMB-CNM (CSIC), Campus Universitat Autònoma de Barcelona, 08193 Cerdanyola del Vallès, Barcelona, Spain.*

**e-mail: gabriel@inti.gov.ar*

Introduction

Inkjet printing is a widely used printing technology for sensor manufacture because it allows low costs and high mass-production of reproducible devices [1-3], while it has the additional advantages of versatility and high resolution for the development of prototypes. However, when it comes to enzymatic biosensors, inkjet printing of enzymes presents some challenges, especially regarding molecular stability [4]. For that reason, there is a great interest in replacing enzymes by catalytic nanoparticles. In the particular case of the reduction of hydrogen peroxide, different nanomaterials have been proved to catalyze this reaction in a similar fashion as peroxidases, such as horseradish peroxidase. Either metal or metal oxides nanoparticles have been used in combination with carbon nanotubes (CNT) for the preparation of non-enzymatic electrodes. The incorporation of catalytic nanoparticles allows a sensitive quantification of H₂O₂, while CNT provide a conductive matrix and allow efficient electron transfer with the redox catalyst. Several electrochemical sensors of this sort have been reported, including Au/CNT, Ag/CNT, and Cu₂O/CNT composites, presenting moderate to high catalytic performance towards H₂O₂ without the need of both an enzyme and a redox mediator [5-7].

In this work, we present the results obtained for a non-enzymatic electrode printed with a single-walled carbon nanotubes (SWCNT) ink containing magnetite nanoparticles for the amperometric determination of hydrogen peroxide, which presented remarkable figures of merit.

Methods

Anhydrous ferric chloride (FeCl₃), trisodium citrate, anhydrous sodium acetate, ethylene glycol (EG), were of analytical grade and used as received. Fe₃O₄

particles were synthesized via a modified solvothermal method as previously reported by Deng et al. [8]. Firstly, 1 mmol of FeCl_3 and 0.4 mmol of trisodium citrate were placed in 20 ml of EG in a closed flask under magnetic stirring. After complete dissolution of the reactants, 20 mmol of sodium acetate and 200 μL of miliQ water were added, turning the solution from an intense yellow to pale red brown after 1 hour. Then, the solution was loaded into a 25 ml Teflon-lined stainless-steel autoclave reactor, sealed, and placed in an oven at 200 °C for 12 hours. After letting the reactor cool to room temperature, the black product was washed several times with miliQ water with the assistance of a neodymium magnet. Finally, the particles were resuspended in 5 ml of miliQ water. Scanning electron microscopy (SEM) images were taken with a FEI Quanta 250 after solvent evaporation of drop casted dispersions. X-ray diffraction (XRD) patterns were obtained with a standard Rigaku diffractometer with $\text{CuK}\alpha$ radiation.

A waterborne ink was prepared containing 0.9 mg/ml SWCNT and 0.9 mg/ml Fe_3O_4 particles. A three-electrode electrochemical cell was fabricated on a 125 μm thick polyethylene terephthalate substrate, without any extra surface treatment, using a DoD Dimatix Materials Printer. For the development of the conductive path of the working electrodes (WE) with a geometric surface area (GSA) of 0.78 mm^2 and counter electrode (CE) with a GSA 5.25 mm^2 , a commercially low curing Au nanoparticle ink was used. For the reference electrode (RE), a $\text{Ag}|\text{AgCl}$ printed electrode was used. The passivation and protective layer of the electrodes was done using a dielectric PriElex® SU-8 ink. Finally, a circular area with diameter of 1 mm was printed onto the WE with the carbon nanotubes water-based ink. Electrochemical measurements were carried out using an 8-channel potentiostat 1030A Electrochemical Analyzer (CH Instruments, USA) in 0.1M phosphate buffer of pH 7.4 at an applied potential of -0.2 V at room temperature in quiescent solutions.

Results

Fig. 1a shows SEM images of magnetite nanoparticles synthesized by the solvothermal method. These citrate-stabilized nanoparticles, 80 nm in average diameter, are in fact formed by clusters of smaller nanoparticles, as demonstrated by the crystal size obtained from de XRD pattern (Fig. 1b). The NPs were mixed with a SDS-stabilized SWCNT dispersion to obtain a waterborne ink which was used to print a sensitive layer toward hydrogen peroxide onto printed gold electrodes (Fig. 2).

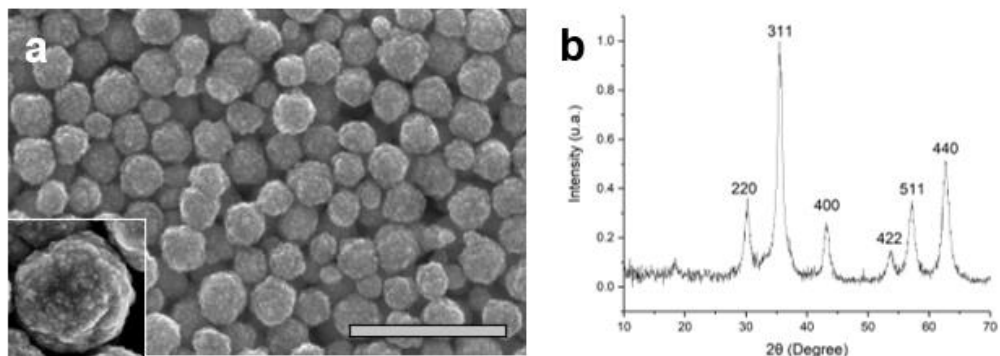


Fig. 1. SEM images (a) and X-ray diffraction pattern (b) of Fe_3O_4 particles. Bar scale = 400 μm .

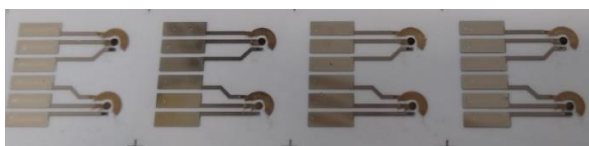


Fig. 2. Optical image of inkjet-printed non-enzymatic electrodes.

Fig. 3a shows the calibration curve obtained at low hydrogen peroxide concentration. A linear relationship was found with a sensitivity of $680 \mu\text{A M}^{-1}$. The limit of detection and the limit of quantification, calculated from the standard deviation of a blank solution, were $30 \mu\text{M}$ and $100 \mu\text{M}$, respectively. It is worth noting that the non-enzymatic electrode presented a quasi-linear response (current approx. proportional to concentration) over several orders of magnitude, up to almost 1 M.

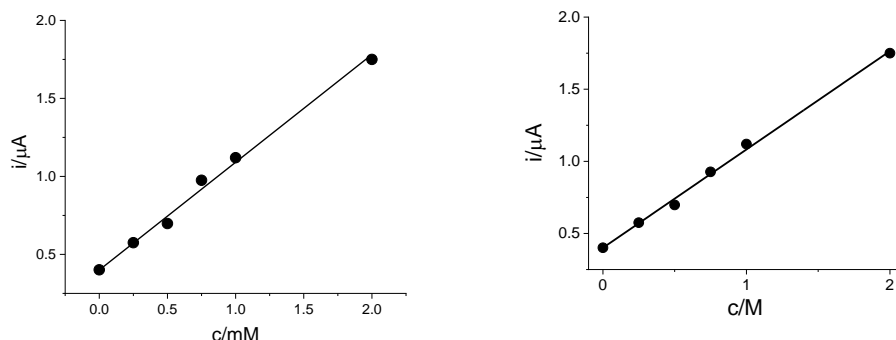


Fig. 3. Dependence of measured current with hydrogen peroxide concentration for millimolar and sub-millimolar concentration range (a) and from sub-millimolar to molar range (b, log-log plot).

A log-log plot (Fig. 3b) revealed that the experimental points could be fitted to a power function of the type $i = m c^n$, where i is the current, c is the concentration, m is a parameter related to the sensor's sensitivity, and n is an exponent or power parameter. A value of $m = 0.86$ was found for the exponent, whereas $m = 1$ would be expected for a true linear response.

Conclusions

In this work, we presented the preparation of an inkjet-printed non-enzymatic electrode for the amperometric determination of hydrogen peroxide, employing an ink containing SWCNT and magnetite particles. The sensor presented remarkable figures of merit, with a quasi-linear range of more than three orders of magnitude, from sub-millimolar concentration to almost 1 M, and a limit of detection of 30 μM .

References

1. Gao et al. Inkjet printing wearable electronic devices. *J.Mater.Chem.C.* **5** (2017) 2971-2993.
2. Andò et al. A Low-Cost Inkjet Printing Technology for the Rapid Prototyping of Transducers. *Sensors* **17** (2017) 748.
3. Cinti et al. Electroanalysis moves towards paper-based printed electronics: carbon black nanomodified inkjet-printed sensor for ascorbic acid detection as a case study. *Sens. Actuators B Chem.* **265** (2018) 155-160.
4. Mass et al. Fully Inkjet-Printed Biosensors Fabricated with a Highly Stable Ink Based on Carbon Nanotubes and Enzyme-Functionalized Nanoparticles, *Nanomaterials* **11** (2021) 1645.
5. Niamlaem et al. Highly defective carbon nanotubes for sensitive, low-cost and environmentally friendly electrochemical H_2O_2 sensors: Insight into carbon supports. *Carbon.* **170** (2020) 154-164.
6. Ensafi et al. Silver nanoparticles decorated carboxylate functionalized SiO_2 , new nanocomposites for non-enzymatic detection of glucose and hydrogen peroxide. *Electrochimica Acta* **214** (2016) 208-216.
7. Veiga et al. Performance of cuprous oxide mesoparticles with different morphologies as catalysts in a carbon nanotube ink for printing electrochemical sensors. *Journal of Alloys and Compounds* **847** (2020) 156449.
8. Deng et al. Solvothermal Monodisperse Magnetic Single-Crystal Ferrite Microspheres. *Angewandte Chemie* **44** (2005) 2782–2785.

Acknowledgments

This research acknowledges funding by “Enhancing Mobility in Health and Environment” (EMHE) and i-COOP2019 programs financed by CSIC.

P5 |
**NOVEL ISE'S MEMBRANES FORMULATION SOLVENT AND
POLYMERIC MATRIX FREE**

E. Arasa-Puig¹ and J. Alonso-Chamarro^{1,*}

¹ *Group of Sensors and Biosensors, Universitat Autònoma de Barcelona, 08193, Bellaterra, Spain*

**e-mail: julian.alonso@uab.es*

Introduction

Ion-selective electrodes (ISE's) are a widely used analytical instruments for advantages such as its fast and selective response, the low sample pre-treatment required, the high sampling frequency provided, its simplicity of functioning and its low instrumental and operational cost. They have already demonstrated their applicability for the *in situ* continuous monitoring of environmental and industrial processes. Recently, many efforts are also being made to implement them in both automated instrumentation (Point-of-Care (POC) like) or low-cost disposable devices for the fast detection of several biomarkers in capillary blood at a hospital or domiciliary environment. The aim is to obtain rapidly the information of interest without the need for sophisticated instrumentation operated by qualified personnel.

The key element of ISE's is the membrane, which provide the required selectivity to measure the analyte of interest. The membrane composition includes the ionophore, the plasticizer, the additive, and the polymer. The most common polymer used is polyvinyl chloride (PVC) due to its low cost and high mechanical and chemical stability. The plasticizer is the majority component of the membrane and should be capable of solubilize all the components of the cocktail sensor. Its dielectric strength affects the selectivity pattern. The ionophore is the key element for the recognition of the target ion and it is designed and synthesized so that they are as selective as possible towards it. All components should be lipophilic to minimize their leaching towards aqueous sample. This improves the reproducibility of the sensor's response while increasing its lifetime (lifespan).

When samples with complex matrix should be analysed in dynamic (flow) conditions or disposable devices improved membrane formulations are needed to reduce leaching of components, membrane poisoning and to minimize fabrication variability among sensors allowing to maintain membrane lifetime, robustness, and response reproducibility. Hence, research for new membrane formulations, which improve these features, is advisable. In this work, the results obtained in

the evaluation of an alternative plasticizer (AP), with higher molecular weight and lower volatility than the commonly used, will be presented. Its use has permitted to design new sensor membranes with innovative formulations and compositions.

Experimental

Sensor membranes with the conventional formulation but differentiated by the plasticizer used (the new or the standard one), were prepared. Both membrane types were evaluated with and without prior conditioning. The different components were weighed and dissolved with a volatile organic solvent, usually tetrahydrofuran (THF). This kind of membrane cocktail is then deposited drop-by-drop on the conductive transducer of the sensor, which was fabricated with FR-4 substrate (see fig. 1). The diameter of the conductive windows opened in the FR-4 surface was 20mm^2 . After that, the ISE's membrane is left to dry. Finally, if required, it must be conditioned. The time consumed in overall fabrication process was higher than 48 hours. New membrane compositions which included only ionophore and AP, neither polymeric matrix nor THF was also evaluated. For its preparation, the corresponding amount of AP were weight out. Then, it was heated until it became fluid and the ionophore was added. The mixture was thoroughly homogenized and applied on the transducer surface using a squeegee. Finally, the membrane obtained was cooled for 5 minutes at room temperature. With this novel membrane formulation, the fabrication time can be drastically reduced and, additionally, enhanced fabrication reproducibility would be achieved.

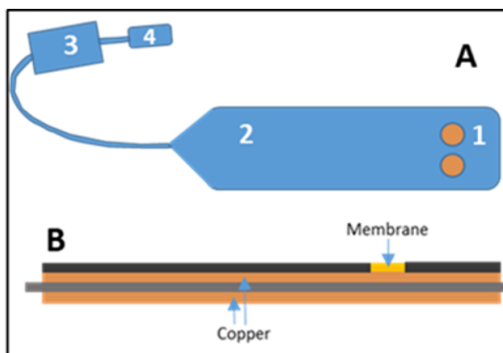


Figure 1. A) Ion Selective electrode. 1. Ion selective membranes; 2. FR-4 Substrate; 3. Data acquisition electronics; 4. Connector.

The reagents used for membrane preparations were: tridodecylmethylammonium nitrate (T-12), potassium ionophore I (valinomycin), tris-2-(ethylhexyl)phosphate (TEHP), bis-(2-ethylhexyl)sebacate (DOS), potassium tetrakis(4-chlorophenyl) Borate (KtpClPB), PVC HMW, THF. All were provided Fluka (Switzerland). AP

plasticizer was donated by the producer. The membrane compositions are detailed in table 1. Their analytical features were compared with those obtained with widely known ion selective membrane formulations, in this case, for nitrate and potassium [1,2].

Table 1. Membrane formulations and compositions evaluated

Membrane	Potassium			Nitrate		
Ionophore (%)	Valinomycin			T-12		
	2	2	2	6	6	6
Plasticizer (%)	DOS	AP	AP	TEHP	AP	AP
	65	65	97.7	65	65	94
Aditive (%)	0.3	0.3	0.3	-	-	-
PVC (%)	32.7	32.7	-	29	29	-

Results and discussion

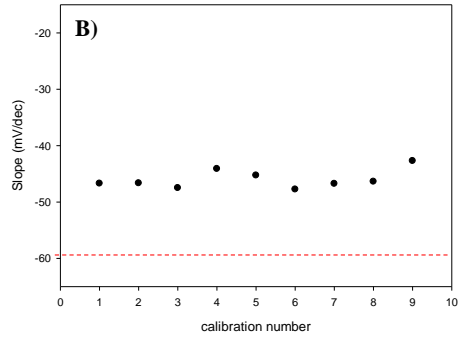
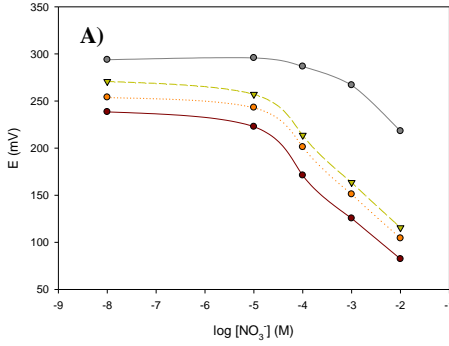
The analytical features were evaluated by successive calibrations to estimate the sensibility and the reproducibility in the response of the fabricated ISE's. In addition, the influence of the most common interfering ion was also tested. In the case of nitrate membrane, chloride 0.014M was used in the background solution while the same concentration of sodium was used in the case of potassium ones.

All the membranes were initially calibrated three times without any conditioning process in order to evaluate the analytical features of the membranes in these conditions. Results obtained can be shown in figure 2. With the conventional formulation of nitrate membranes, a constant drift in the response was observed (fig 2.1.A). Despite this, the obtained calibration slopes were quite reproducible with time although 20% lower than theoretical ones. (fig 2.1.B). Potassium membranes with conventional formulation (fig 2.1 A and B), a significant reduction of the signal after consecutive calibrations was observed. When the membrane was let to dry, the response recovered until the expected slope was achieved.

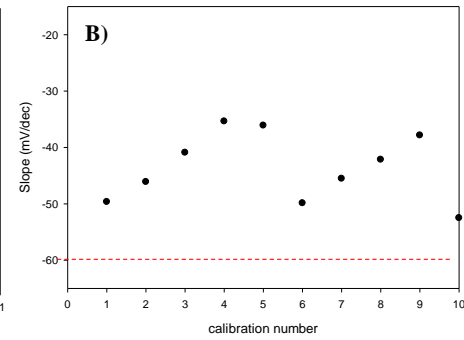
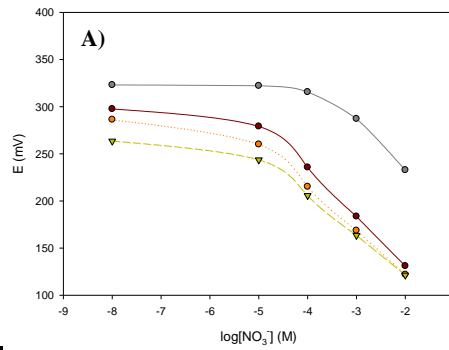
Regarding the nitrate membranes with conventional formulation using AP as plasticizer (fig 2.2 A and B), a significant reduction of the signal after consecutive calibrations was observed which is recovered when the membrane was let to dry. Conventional potassium membranes using AP as a plasticizer showed a great stability achieving the expected slope along the successive calibrations. Nevertheless, the initial slope was 7% lower than it was expected.

NO₃⁻ membranes

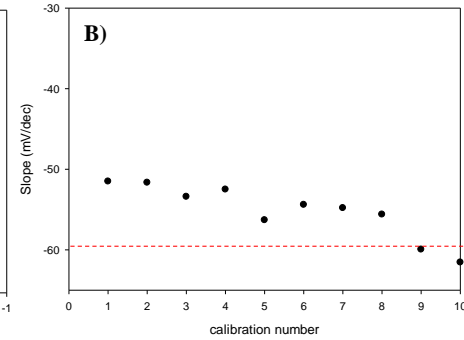
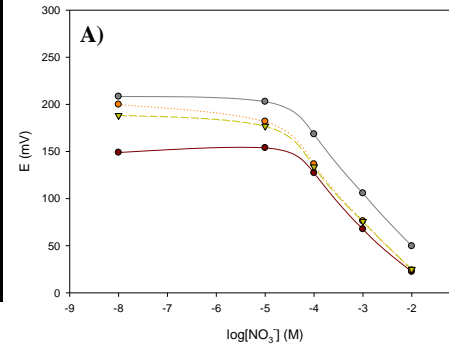
Conventional formulation (1)



Conventional formulation with AP (2)



Novel formulation (3)



K⁺ membranes

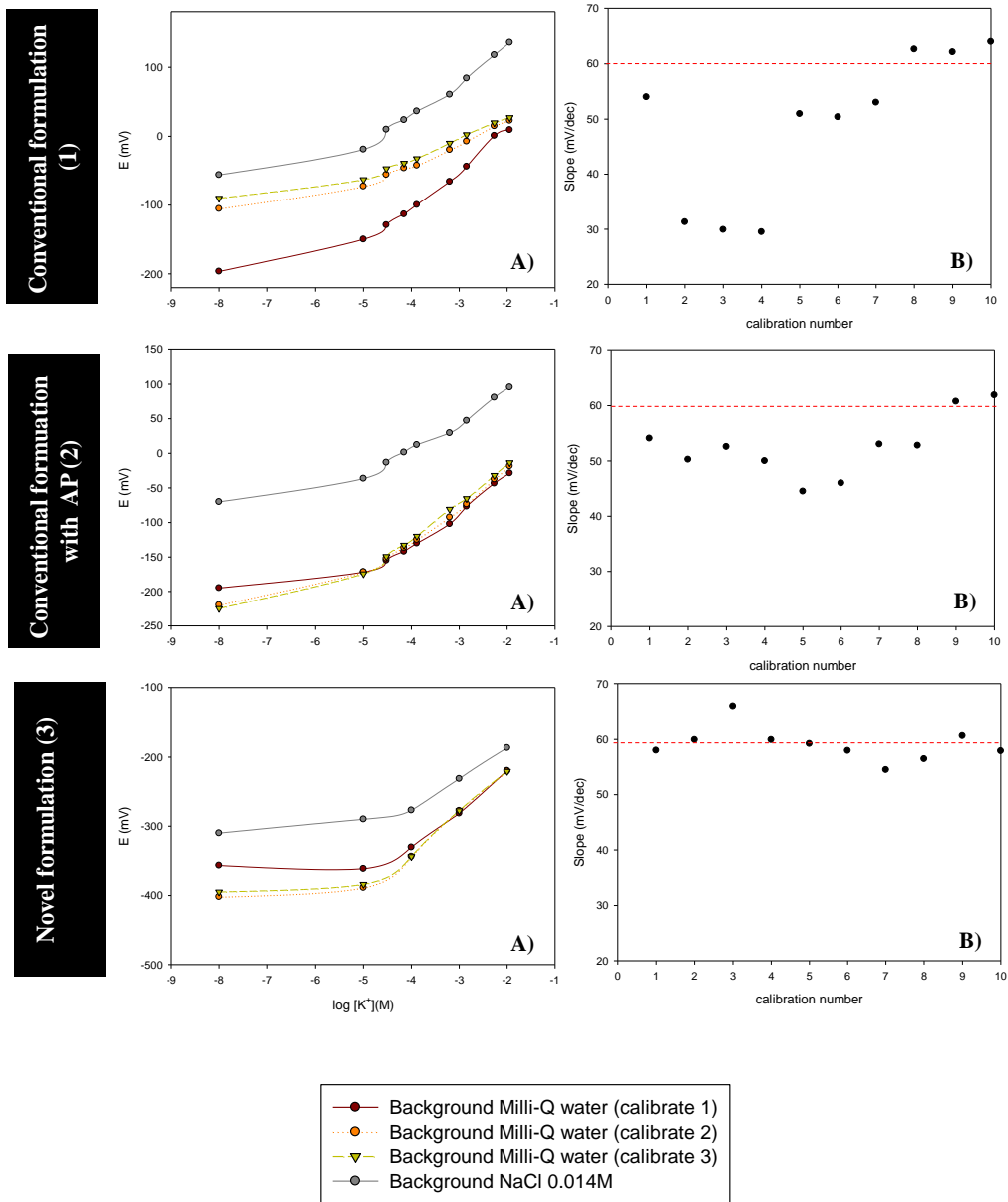


Figure 2. Three former calibration plots (A) without previous conditioning process and the slope before successive calibration (B) for nitrate and potassium membranes using conventional formulation (1), conventional formulation with AP as plasticizer (2) and novel formulation (3). Red dotted lines indicate the expected slope.

Finally, the nitrate selective electrodes prepared using novel membrane formulation (fig 2.3 A and B) presented analytical feature that were comparable with those obtained using conventional formulation. In addition, they showed better reproducibility and stability in their response. The same results were observed with the potassium selective membranes. In both cases, the novel formulations had shown a better response reproducibility and calibration slopes closer to the theoretical (expected) ones when compared with the conventional formulation. The degree of interference cause by chloride or sodium were comparable in all membrane compositions evaluated, except in the case of later nitrate 7membrane formulation where a significant interference reduction was observed.

After six months continuously submerged in water (aggressive conditions to force leaching components of membranes), nitrate conventional membrane formulation lost 30% of its sensitivity and potassium one 68%. Regarding conventional formulations with AP, nitrate membrane sensitivity lost was 53% and 47% in the case of potassium. These results indicate that in case of nitrate, the conventional membrane formulation shows better lifespan expectancy. Instead, conventional potassium electrodes incorporating AP provide better lifetime characteristics.

Conclusions and future work

The conventional membrane formulation using AP as a plasticizer had shown similar analytical characteristics to the ones using conventional plasticizers. As a remarkable feature observed, conventional potassium electrodes with AP can be used without the initial membrane conditioning process.

Novel membrane formulations has shown adequate analytical features being possible in both ions to use them without the need for initial conditioning. This novel procedure requires fewer reagents, no need for drop-by-drop deposition or solvent evaporation. It allows to obtain ready-to-use ISEs in 5 minutes instead of 48h required in the conventional procedure. Additionally, the reproducibility of the response in sequential calibration was very high, which simplifies the application of these types of ISE's as disposable ones.

References

- [1] Alegret, S.; Alonso, J.; Bartroli, J.; Lima, J.L.F.C.; Machado, A.A.S.C.; Paulis, J.M. *Anal. Lett.*, **1985**, 18, 2291.
- [2] Band, D.M.; Kratochvil, J.; Poole Wilson, P.A.; Treasure, T. *Analyst*, **1978**, 103, 246.

SENSORES ÓTICOS E FOTOACÚSTICOS | SENSORES ÓPTICOS Y
FOTOACÚSTICOS | OPTICAL AND PHOTOACOUSTIC SENSORS

06 |

BIOSENSOR BASED ON POLYMER OPTICAL FIBER AND GOLD NANOPARTICLE FOR RAPID DETECTION OF *ESCHERICHIA COLI*

Regina C. S. B. Allil^{1*}, Andressa Rebecca Brito¹, Alexandre S. Allil¹, Juan D. Lopez¹,
 Maria Eduarda A. Esteves², Alessandra S. Silva², Manuela L. da Silva²,
 Marcelo M. Werneck¹

¹Photonics and Instrumentation Laboratory, Universidade Federal do Rio de Janeiro,
 COPPE/UFRJ, Brazil

²Research Group in Computational Biology, Universidade Federal do Rio de Janeiro - UFRJ,
 Instituto Oswaldo Cruz - IOC/Fiocruz and Instituto Nacional de Metrologia, Qualidade e
 Tecnologia - INMETRO, Rio de Janeiro, Brazil

*reginaceliaallil@gmail.com

Introduction

Plastic Optical Fiber (POF) sensors have gained considerable interest in the scientific community in recent decades due to advantages such as relatively simple instrumentation, low cost and easy handling due to their small size. The development of biosensors for the detection of biological and chemical analytes is a great help for characterizations of this type in laboratory and clinical environments [1].

Therefore, we used *Escherichia coli* (*E. coli*) as a study model in this project. *E. coli* are gram-negative bacilli with great diversity among strains, often found in the intestinal tract of animals, including humans [2]. On the surface of these bacteria is found the K antigen, a T-independent antigenic polysaccharide [3], selected as a target of study for this research.

The project proposes a low-cost biosensor sensitive to the detection of K antigens with possibility of national manufacture, transferring the technology to national companies. A technology based on fiber optic functionalized with AuNPs in POF will be used and interaction evaluation of these immunological biomarkers by computational methodologies.

Methods

The development of the optical biosensor can be described in the following steps:

Manufacturing of the POF sensor

The sensor is a U-shaped curved POF (Mitsubishi Rayon Company, ESKA) with a curve of 25 mm in length and 9 mm in diameter.

Synthesis of gold nanoparticles [4]

For the protocol of synthesis and amination of AuNPs, the following reagents were used: hydrochloric acid (HAuCl₄); Cetyltrimethylammonium bromide (CTAB - C₁₉H₄₂BrN); sodium borohydride (NaBH₄); Silver nitrate (AgNO₃); Ascorbic acid (C₆H₈O₆); and Cystamine (C₄H₁₂N₂S₂).

Sensor surface functionalization [4]

For the sensor surface functionalization protocol for AuNPs fixation, the following reagents were used: Sulfuric Acid (H₂SO₄); MES Buffer Solution (C₆H₁₃NO₄S); EDAC (C₈H₁₇N₃.HCl); and NHS (C₄H₅NO₃).

Immobilization process: Process of adhesion of anti-E. coli to AuNPs [4]

For the anti-*E.coli* immobilization protocol, were used: *E. coli* antibody (anti-*Escherichia coli* polyclonal IgG, Bio-RAD); 2-Mercaptoethanol (C₂H₆OS); Sulfo-NHS (C₄H₄NNaO₆S); EDAC; and PBS Buffer Solution (Phosphate Buffer Saline, 1x).

Fixation of the bacteria on the antibody

The biosensors with the fixed antibodies were submerged in a suspension of *E. coli* concentration of 10⁸ CFU/mL (CFU-colony forming unit), prepared in 0.85% sodium chloride solution.

Data acquisition

After the development of the bacteria sensor, they were characterized in the setup shown in Figure 1.

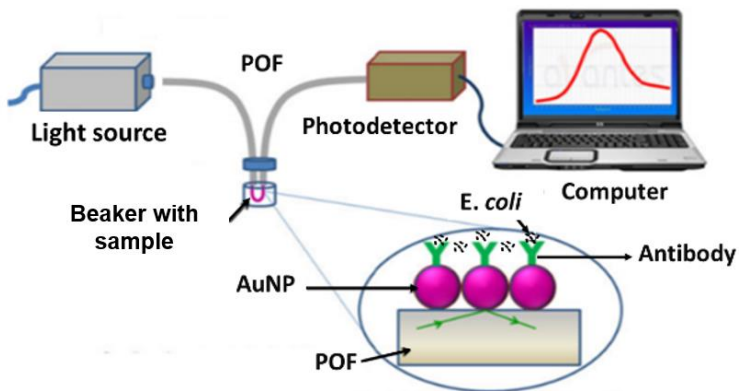


Figure 1- Experimental setup used.

One extremity of the optical fiber was connected to a white light source (SLS201, ThorLabs) and the other end to the spectrometer photodetector (HR-4000, Ocean Optics). The U-bent sensing part of the functionalized optical fiber is immersed in the beaker with the sample (10⁸ CFU of *E. coli*).

Validation of the diagnostic potential of selected applications and antigens using computational tools:

Finally, the antigen/antibody evaluation study is being carried out in order to qualitatively validate the interaction of the complex, confirming its compatibility. The K antigen lead epitopes will be evaluated for interactions with the antibody CDR receptor, using the SwissDock server (<http://www.swissdock.ch>) for this purpose. The interactions will be evaluated for electrostatic surface, contact interface and hydrophobicity, using programs such as Pymol and Maestro to select the best complex.

Results

Characterization of biosensors in contact with *E. coli* O55 bacteria

The sensors were submerged in a beaker with a solution of *E. coli* O55 bacteria with a concentration of 10^8 CFU/mL for 5 and 10 minutes. The result of the *E. coli* biosensor spectrometry is shown in Figure 2.

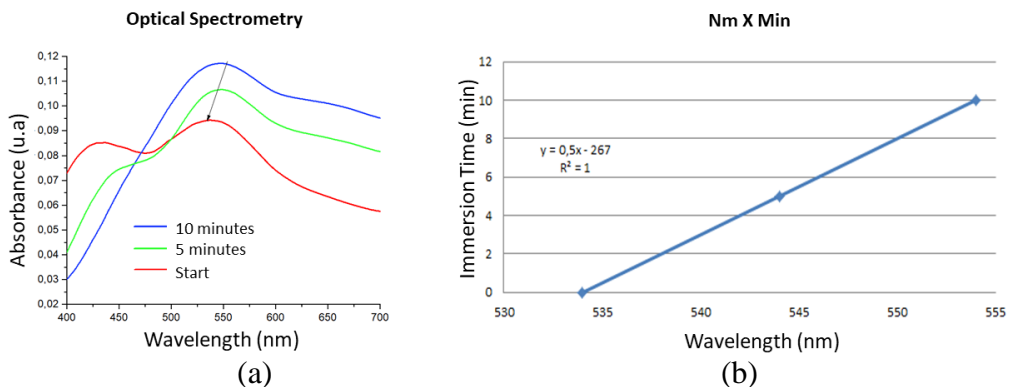


Figure 2 – (a) Optical spectrometry of the *E. coli* biosensor with bacteria suspension of 10^8 CFU/mL, showing a shift of 20 nm. Start = 534 nm, 5 min = 544 nm, 10 min = 554 nm. (b) Linear pattern of LSPR (nm) X Exposure time (min).

Once the bonding between the antibodies and the *E. coli* bacteria was made, we observed that there was a variation in the maximum wavelength of the spectrum ($\lambda = 20$ nm). When the sensor is exposed to bacterial suspension, the amount of bacteria bound to the sensor increases as the exposure time increases. This increase in bacteria causes the variation of the refractive index and results in the change of the maximum wavelength of LSPR, proving the existence of the phenomenon.

Conclusion

Preliminary results of the biosensors with *Escherichia coli* demonstrated the viability of detecting a concentration of 10^8 CFU/mL of *E. coli* immersed in a period of 10 minutes with an LSPR shift of 20 nm.

The biochemical protocols adopted in all fixation procedures (of the AuNPs on the surface of the optical fiber, as well as the fixation of anti-*E. coli* in the AuNPs and, finally, the fixation of *E. coli* bacteria in the antibodies) were adequate, considering the purpose of this paper.

The characterization by SEM microscopy was performed for analysis and study regarding the size and shape of the nanoparticles obtained. And the Confocal microscopy for analysis of the optical fiber surface regarding the immunocapture of the *Escherichia coli* bacterium in the antibody.

The promising results proved the application of the technology based on optical fiber and AuNP, which encourage us to carry out tests with other pathogens.

References

- [1] SERGEY M B, WOLFBEIS O S. “Optical Biosensors”. *Chemical Reviews*; V. 108, p.423-461, 2008.
- [2] MURRAY, P. R.; AMERICAN SOCIETY FOR MICROBIOLOGY. *Manual of clinical microbiology*. 7th ed. ed. Washington D.C.: ASM Press, 1999.
- [3] REIS, N. M. et al. Point-of-need detection with smartphone. *Smartphone-Based Detection Devices*, p. 311–362, 1 jan. 2021.
- [4] JIN Y, WONG K H, et al. “Developing localized surface plasmon resonance biosensor chips and fiber optics via direct surface modification of PMMA optical waveguides”. *Colloids and Surfaces A: Physicochem. Eng. Aspects*, V.492, p. 100–109, 2016.

Acknowledgments

This work was supported by the Fundação Carlos Chagas Filho de Amparo à Pesquisa do Estado do Rio de Janeiro (FAPERJ), RJ, Brasil.

07 |

COLORIMETRIC BASED TEST-STRIPS WITH VIRUS-LIKE PARTICLES AS A RECOGNITION LAYER FOR SARS-CoV-2 VIRUS

Mariana P. Sousa^{1,3}, Ana Cláudia Pereira^{1,3}, Bárbara P. Correia^{1,3}, Maria Teresa Cruz⁴,
M. Goreti Sales^{1,3*}, Felismina T.C. Moreira^{1,3*}

¹BioMark@ISEP, School of Engineering, Polytechnic of Porto, Porto, Portugal

²BioMark@UC, Faculty of Sciences and Technology, University of Coimbra

³CEB - Centre of Biological Engineering, University of Minho, Braga, Portugal

⁴Faculty of Medicine, Center for Neuroscience and Cell Biology, University of Coimbra, Rua
Larga, Polo I, 1st Floor, Coimbra 3004-504, Portugal

*e-mail: ftm@isep.ipp.pt

Abstract

The outbreak of coronavirus disease (COVID -19) required rapid, sensitive, and inexpensive methods to track its spread and evaluate the immunologic response to it. We developed two paper-based colorimetric biosensors as serological tools, using glutaraldehyde as a protein dye for the first time. This technology is based on the ability of glutaraldehyde to react with amino groups and produce a brown colour.

Thus, the filter paper was functionalized with (3-aminopropyl)triethoxysilane to further attach the biological recognition element. Virus-like particles (VLP) and the nucleocapsid protein were selected as biological recognition elements to detect antibodies against the spike protein and the nucleocapsid protein (protein N), respectively.

Then, the sample containing antibodies against SARS-CoV-2 was incubated on the surface of the test strip, and then the glutaraldehyde solution was added. Colour analysis was performed using the RGB coordinates of Image J software. Both test strip devices showed a linear correlation between the concentration of antibodies and the RGB coordinates of the colour produced, both in buffer and serum. The VLP device showed a linear response from 2 ng/mL to 40 ng/mL in 500-fold diluted serum using the green RGB coordinate. The protein N device showed a linear response from 4 ng/mL to 160 ng/mL in 250-fold diluted serum analysed using the blue RGB coordinate. Using real human serum samples, the sensor platform was able to detect 12.78 ng/mL of anti-S, which allowed colour discrimination of samples with the naked eye. For the selectivity studies, each sensor was incubated with glucose (0.7 mg/mL), urea (0.2 mg/mL), and BSA (1 mg/mL). Overall, both sensors were selective for their target and achieved a maximum interference of 18% for glucose.

These biosensors demonstrate a sensitive, simple, and affordable way to perform a semi-quantitative serological assay, although this technology can be adapted for detection of other molecules.

Introduction

With the spread of SARS-CoV-2, the search for effective means to monitor acquired immunity became critical, especially after vaccination became widely available. Currently, this is done using enzyme-linked immunosorbent assays (ELISA), chemiluminescent immunoassays (CLIA), immunofluorescence assays (IFA), and colloidal gold immunochromatography assays (GICA), which are commonly known as rapid tests [1,2]. Despite their high sensitivity and specificity, most of these tests still require the use of professional laboratory personnel, resulting in significant costs to healthcare systems and the general public [1]. Therefore, a growing number of biosensors for COVID -19 immunity testing are currently being developed to provide cost-effective screening. Among the various alternatives, paper-based biosensors provide cheap, renewable, and versatile platforms for tracking sensitive molecules [3]. In this article, we describe two paper-based colorimetric platforms for monitoring the concentration of antibodies to SARS-CoV-2 using glutaraldehyde as the protein dye. In doing so, we take advantage of the ability of glutaraldehyde to react with amino groups and produce a brown colour [4]. A device for targeting antibodies to spike protein has been developed using synthetic particles known as virus-like particles (VLP). By using synthetic particles, they can be modified to detect multiple molecules at once and are cheaper to produce [5]. The other device involves the nucleocapsid protein to detect antibodies against it.

Methods

The developed dipstick consists of three main steps - Figure 1. First, (i) the surface of the paper was chemically modified with an 8% solution of (3-aminopropyl)trimethoxysilane, resulting in free amine groups on the paper surface. Then (ii) a 5 µg/mL solution of a biorecognition element was dropped onto the paper by electrostatic binding and allowed to dry. Finally, (iii) samples with antibodies were added after a 5% glutaraldehyde solution. The resulting colours were analysed based on the RGB coordinates by taking an image of the papers with a smartphone and analysing it with Image J software. The VLP device was analysed using the green coordinate, while the blue coordinate gave better results for the N-protein device.

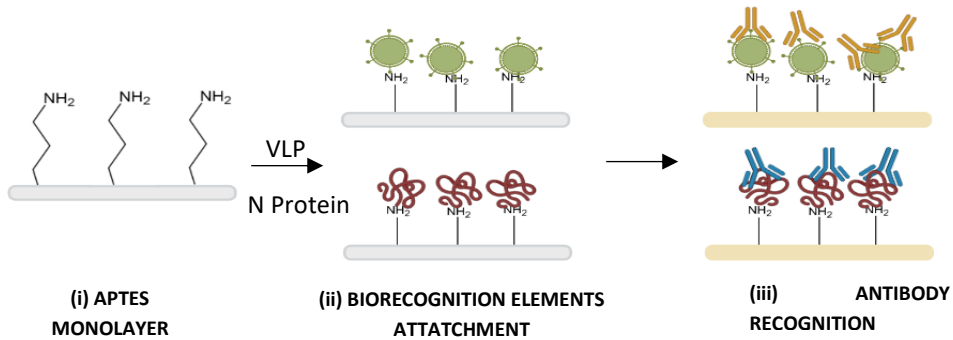


Figure 1 – Schematic representation of the main steps for the biosensor's assembly.

The cellulose paper modifications were characterized by Fourier transform infrared spectroscopy (FTIR), thermogravimetry (TG), and contact angle measurement. Calibrations of the instruments were performed in spiked phosphate buffer and spiked commercial human serum. Serum was diluted 500-fold in PBS pH 7.4 for the VLP biosensor and 250-fold for the N-protein biosensor. Selectivity studies allowed evaluation of serum species that might interfere with the biosensor response. Glucose (0.7 mg/mL), urea (0.2 mg/mL), and BSA (1 mg/mL) were selected for this study and diluted as in the serum assays. The VLP device was tested with real human serum samples previously characterized by enzymatic fluorescence assay. All assays were performed in triplicates.

Results

The analytical performance of the test strips was evaluated by calibration curves in buffer and in real serum samples and by selectivity studies. The detection and quantification of target antibodies bound to the cellulose test strip was determined by a conventional staining method. The colorimetric response of the biosensors was monitored after incubation for 20 minutes at room temperature with different polyclonal antibody S and N standard solutions prepared in buffer at pH=7. For colour development, the papers were briefly reacted with glutaraldehyde solution after washing.

Overall, as the amount of antibody in the samples increases, the concentration of free amines reacting with glutaraldehyde also increases, resulting in the formation of a darker brown colour.

In serum tests, the VLP detector performs better if you use 500-fold diluted serum, while protein N gives better results with less diluted commercial serum (250-fold). When using RGB coordinates, the VLP biosensor performed better, achieving a detection limit of 2 ng/mL compared to a LOD of 4 ng/mL for the Protein N instrument - Figure 2. However, lower concentrations are easier to detect by the naked eye for the Protein N instrument. In general, both sensors showed a linear response and distinguished up to 1 µg/mL of antibody in serum.

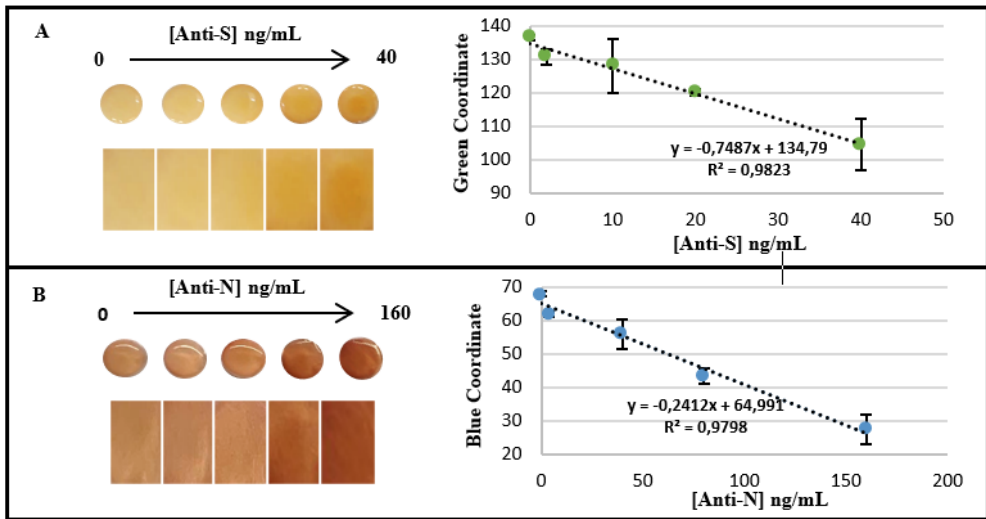


Figure 2 - Calibration curves of the colours obtained for the VLP biosensor (A) and the N protein (B) using commercial human serum. [Anti-S]: 0 ng/mL; 2 ng/mL; 10 ng/mL; 20 ng/mL; 40 ng/mL. [Anti-N]: 0 ng/mL; 4 ng/mL; 40 ng/mL; 80 ng/mL; 160 ng/mL.

For real human serum, three different samples were selected to test the colour response to low (6.39 µg/mL), medium (81.64 µg/mL) and high (176.53 µg/mL) concentration. The sensor achieved a detection efficiency of 12.78 ng/mL and was capable of colour discrimination by the naked eye. Selectivity studies showed lower interference for the VLP device, with maximum deviations of 4%. The N-protein showed more significant deviations, especially for glucose (18%).

Conclusions

The described biosensors showed good response in complex matrices and gave useful results with real human serum samples. The use of synthetic biorecognition elements does not compromise the sensitivity of the instrument and allows for a more cost-effective strategy. Thus, this work provides a simple and cost-effective way to perform a semi-quantitative serological assay. With this novel technology, these strips can also be used for the determination of other molecules of interest in a portable manner and directly at the point of care.

References

- [1] Vengesai, A., Midzi, H., Kasambala, M., Mutandadzi, H., Mdluza-Jokonya, T. L., Rusakaniko, S., Mutapi, F., Naicker, T., & Mdluza, T. (2021). A systematic and meta-analysis review on the diagnostic accuracy of antibodies in the serological diagnosis of COVID-19. *Systematic Reviews*, *10*(1), 155.
- [2] Zhou, Y., Zhang, L., Xie, Y.-H., & Wu, J. (2022). Advancements in detection of SARS-CoV-2 infection for confronting COVID-19 pandemics. *Laboratory Investigation; a Journal of Technical Methods and Pathology*, *102*(1), 4–13.
- [3] Mahadeva, S. K., Walus, K., & Stoeber, B. (2015). Paper as a platform for sensing applications and other devices: a review. *ACS Applied Materials & Interfaces*, *7*(16), 8345–8362.
- [4] Okuda, K., Urabe, I., Yamada, Y., & Okada, H. (1991). Reaction of glutaraldehyde with amino and thiol compounds. *Journal of Fermentation and Bioengineering*, *71*(2), 100–105.
- [5] Deng, F. (2018). Advances and challenges in enveloped virus-like particle (VLP)-based vaccines. *Journal of Immunological Sciences*, *2*(2), 36–41

08 |

SINGLE AND CASCADED LONG PERIOD FIBER GRATING COATED WITH A POLYDIMETHYLSILOXANE SENSING FILM FOR ACETONE DETECTION

G. Beltrán-Pérez*, J. L. Rodríguez-Garciapiña, J. Castillo-Mixcóatl, S. Muñoz-Aguirre
*Benemérita Universidad Autónoma de Puebla, Facultad de Ciencia Físico Matemáticas
Av. San Claudio y 18 Sur, Col. San Manuel, CU, C.P. 72570 Puebla, Puebla, México*
**email-gbeltran@fcfm.buap.mx*

Abstract

Two kinds of acetone sensors one based upon single long period fiber gratings (LPFG) and another based upon Mach-Zehnder fiber interferometers (MZI), formed with a pair of cascaded LPFGs were developed. Both kinds of sensors were coated with polydimethylsiloxane (PDMS). The transmission spectrum variations of the devices output were measured with an optical spectrum analyzer, stored in a computer, and analyzed by the principal components analysis method. A comparison between the performance of both kinds of sensors was carried out and it was found that the sensitivity increased up to 13 times (from $0.7 \times 10^{-4} \text{ ppm}^{-1}$ to $9.4 \times 10^{-4} \text{ ppm}^{-1}$) for the MZI sensors compared with that of single LPFG ones, which means, at best, a limit of detection (LOD) of 170 ppm.

Introduction

Diabetes can cause many complications in the human body. The disease is commonly invasively diagnosed using blood glucose test. Fortunately, the high correlation between blood glucose and acetone concentration present in the exhale breathe has opened a way for non-invasive diagnosis [1]. However, the conventional method of detecting exhale breathe acetone (e.g. GC-MS) is bulky, requires technical knowhow, do not offer real time measurements and only a few of advanced and well-founded institutions can afford the required equipment. For this reason, it is important to find a simpler mechanism for acetone vapor detection. One of them are sensors based on long period fiber gratings (LPFG). These devices have the property of changing their transmission spectrum, when they interact with some external parameters, such as temperature [2], refractive index [3], and pressure. Moreover, by coating the surface of the LPFG with some material able to modify its refractive index when interacts with some gas, several authors have fabricated gas sensors based upon LPFGs. Moreover, it is possible to increase the sensitivity of the sensor by cascading two LPFGs to create a Mach-Zehnder interferometer (MZI). In this work, we implemented four sensors for

acetone gas detection. Two of them were fabricated using a single LPFG and the other two were MZI, formed with a pair of identical cascaded LPFGs. All of them were coated with polydimethylsiloxane (PDMS). The sensor responses were analyzed by measuring the transmission spectrum amplitude variations at a fixed wavelength and using the entire spectrum by using principal components analysis (PCA). The results showed that the sensor based on MZI presented higher sensitivity (up to 13 times) for acetone gas measurements, and an LOD of 170 ppm was found.

Methods

For the sensor fabrication, the LPFG or MZI surface was coated with PDMS (DMPS12M, Purchased from Sigma Aldrich, viscosity of 12,500 cSt, density 0.96 mg/ml and refractive index of 1.36 for the range of 1520-1560 nm). It has been proven that vapor molecules such as VOCs can modify the refractive index of PDMS. This is important since the effective refractive index of the sensors depends on that of the surrounding medium. Moreover, by coating the surface of the LPFG or MZI with PDMS, we obtained a sensor that measured variations of the PDMS refractive index originated by its interaction with acetone. The deposition of the PDMS sensing film onto the LPFG/MZI surface was performed by the dip coating technique. After coating, a thermal treatment was applied to the sensors using a lab oven (OMS60, Thermo Scientific) at a temperature of 100°C for 30 min to homogenize the PDMS film on the fiber surface. After that, the sensors were stabilized at room temperature for 1 h before response measurement.

Results and Discussion

In **Figs. 1a** and **1b** the normalized spectra of one of the four sensors and their variations under the effects of acetone concentration changes in the region 1250 nm –1650 nm are presented. The response of the sensors to acetone was a deformation of the transmission spectrum (attenuation, increment or wavelength shift of the peaks) due to changes in the refractive index of PDMS when it interacts with acetone molecules, these results are similar to those presented in a previous work [4]. In **Fig. 2**, we present the first principal component (PC1) plotted in function of acetone concentration, a linear fitting was performed and the sensitivities (the slopes of the fittings) are summarized in **Table 1**.

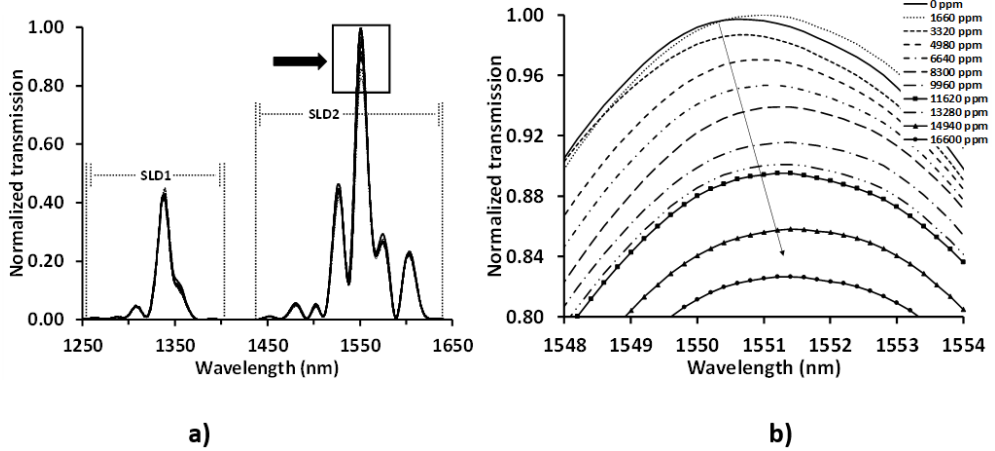


Fig. 1. Response of sensor 1 to different concentrations of acetone a) spectrum from 1250 nm to 1650 nm, SLD1 and SLD2 are the regions of the source emissions, b) zoom of the squared region in a), the arrow indicates the direction of the transmission and wavelength variations.

From **Fig. 2** and **Table 1**, it can be observed that MZI sensors are more sensitive than the single LPFG ones. The relationship between the sensitivities of MZI sensors with the single LPFG ones is around one order of magnitude. Sensor 3 is approximately 7 times more sensitive than sensor 2 and 10 times more sensitive than sensor 1; while sensor 4 is 9 times more sensitive than sensor 2 and 13 times more sensitive than sensor 1. Therefore, we can say that MZI sensors are more adequate for acetone detection. The limit of detection (LOD) was calculated (assuming a SNR=1) for all the sensors (See **Table 1**) and the best case was for Sensor 4 with a value of 170 ppm. Although Sensor 3 was the most sensitive, the best LOD was for Sensor 4 because the standard deviation for this sensor was smaller. The LOD value of 170 ppm is important since this concentration is in the range of the sensors implemented to measure acetone present in breath, furthermore, this result demonstrates that by cascading two identical LPFGs, we can increase the sensitivity up to one order of magnitude.

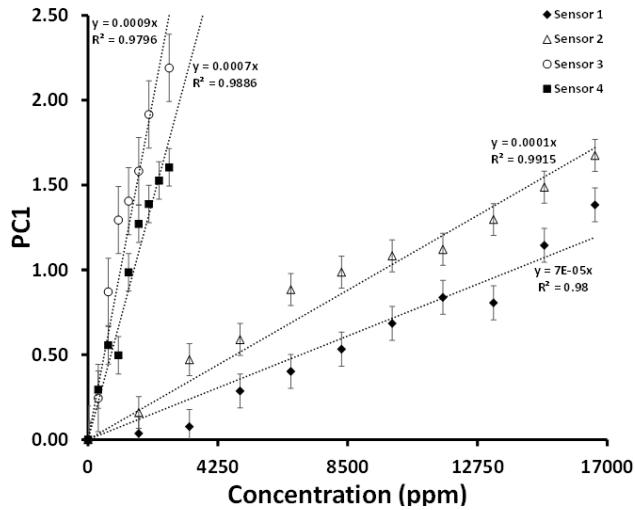


Fig. 2. Principal component analysis results for the four sensors.

Table 1. Sensitivity of the sensors

Sensor	Sensitivity (ppm^{-1})	LOD (ppm)
Sensor 1	0.7×10^{-4}	1400
Sensor 2	1.0×10^{-4}	910
Sensor 3	9.4×10^{-4}	210
Sensor 4	6.7×10^{-4}	170

Conclusions

In this work, we presented a comparison of the performance of acetone sensors fabricated with LPFG and MZI coated with PDMS. MZI sensors were fabricated with two cascaded LPFG. We have shown that the sensors allowed us to measure acetone concentration variations by using principal components analysis (PCA) applied to the measured transmission spectrum from 1250 nm to 1650 nm conformed by two SLD. It was found that the response curves in function of concentration had a linear behavior with high correlation coefficient. The use of MZI results in an increment of the sensor sensitivity, since we could attain up to 13 times of sensitivity increment and we could measure concentrations with an LOD of 170 ppm. This is important because such concentration is quite near to the concentration range to measure acetone for breath analysis as an auxiliary in the diabetes diagnosis.

5. References

- [1] D. Smith, P. Španěl, A.A. Fryer, F. Hanna, G.A.A. Ferns, Can volatile compounds in exhaled breath be used to monitor control in diabetes mellitus?, *J. Breath Res.* 5 (2011).
- [2] Rego, G., P. V. S. Marques, J. L. Santos, H. M. Salgado, Simultaneous measurement of temperature and strain based on arc-induced long-period fibre gratings. *Electron. Lett.* (2005) 41(2):60.
- [3] H.J. Patrick, A.D. Kersey, F. Bucholtz, Analysis of the response of long period fiber gratings to external index of refraction, *J. Light. Technol.* 16 (1998) 1606–1612.
- [4] C. Martínez-Hipatl, S. Muñoz-Aguirre, G. Beltrán-Pérez, J. Castillo-Mixcóatl, J. Rivera-De la Rosa, Detection of volatile organic compounds by an interferometric sensor, *Sensors Actuators, B Chem.* 147 (2010) 37–42.
- [5] G. Beltrán-Pérez, S. Muñoz-Aguirre, J. Castillo-Mixcóatl and V. Epitacio-Reyes, "Detection of volatile organic compounds with a polymeric sensing film deposited on a long period fiber grating," 2019 IEEE International Symposium on Olfaction and Electronic Nose (ISOEN), Fukuoka, Japan, 2019, pp. 1-4.
- [6] Rodríguez-Torres, M.; Altuzar, V.; Mendoza-Barrera, C.; Beltrán-Pérez, G.; Castillo-Mixcóatl, J.; Muñoz-Aguirre, S. Discrimination Improvement of a Gas Sensors' Array Using High-Frequency Quartz Crystal Microbalance Coated with Polymeric Films. *Sensors* 2020, 20, 6972.

Acknowledgments

This research was partially supported by project SEP-CONACYT, CIENCIA BÁSICA-2016, grant number 286647 and Scholarship CONACYT 2019-000002-01NACF-05032.

09 |

Fe₃O₄-COATED PLASTIC OPTICAL FIBER FOR H₂S SENSING

Juan D. Lopez^{1,2,*}, Alex Dante^{3,4}, Paulo H. Silva³, Regina C.S.B. Allil³,
 Marcelo M. Werneck^{1,3}

¹*Nanotechnology Engineering Research Program, Photonics and Instrumentation Laboratory, COPPE/UFRJ, Brazil*

²*Plasma, Laser and Applications Group, Basic Science Department, Technological University of Pereira, Colombia*

³*Electrical Engineering Research Program, Photonics and Instrumentation Laboratory, COPPE/UFRJ, Brazil*

⁴*Integrated Micro and Nanotechnologies Group, International Iberian Nanotechnology Laboratory, Braga, Portugal*

*e-mail: juandlopezv94@gmail.com

Abstract: In this paper, we report the manufacture of an H₂S sensor based on Fe₃O₄-coated plastic optical fiber (POF). The manufacture of the sensor was divided into two stages, in the first stage, the synthesis of iron oxide nanoparticles was carried out with the Pulsed Laser Ablation in Liquid (PLAL) technique. After synthesis, the nanoparticles were characterized to determine the chemical structure, morphology, and size. The characterization results allowed us to determine that the average size of the nanoparticles was 115 nm, with a spherical shape. The results of the structural analysis showed that the nanoparticles synthesized by PLAL present characteristics similar to Fe₃O₄. In the second stage, an H₂S sensor was manufactured, coating the POF with the Fe₃O₄ nanoparticles. The results showed that the sensor was capable of detecting a gaseous mixture containing 200 ppm of H₂S at room temperature (25 °C). Also, the sensor showed a quick recovery time of less than 5 min and a rise time of around 6 min.

Introduction

Hydrogen Sulfide (H₂S) is an undesirable gas commonly found in the wastewater treatment, oil and in the gas industries [1]. H₂S causes several problems in the industry because it is a toxic, corrosive, poisonous, and flammable gas. As for human health, H₂S concentrations starting in 10 ppm must be avoided, because can cause severe irritations of the eyes. Higher concentrations up to 750 ppm can cause death within moments to minutes due to respiratory paralysis. Above this limit, any concentration between 4.5% and 45% can cause an explosion [2]. In all stages of the oil and gas industry (from extraction to transport), H₂S is associated with corrosion in metals, which leads to massive economic losses [3]. In the well drilling stage, H₂S comes out mixed with oil and other gases, and, since it is highly

flammable, sensors for this gas must have an electronic system isolated from the measurement site in order to avoid any potential explosion.

In order to sense the presence and concentration of H_2S , several sensing systems have been proposed in the literature, such as electrolyte solutions, catalytic-based sensors, electrochemical sensors, optical sensors, among others [4-5]. The optical sensors based on fiber optics present several advantages over conventional sensors, the most important one is that they employ a waveguide that can be monitored kilometers away from the sensing point, while its sensitive region is on the site for H_2S sensing. Furthermore, fiber optic-based sensors can operate at room temperature (RT), which is another advantage when compared to electrochemical sensors [6].

Among the most recent studies involving fiber optic sensors, in 2021 Keley *et al.* [6] reported the manufacture of a sensor based on a CuO-coated plastic optical fiber (POF) applied to H_2S sensing. The sensor proposed by the authors presented a response time of around 5 min and a recovery time of around 10 min, during exposure to 200 ppm of H_2S . Other authors have also reported H_2S sensors using optical fibers coated with Cu-ZnO, ITO, SnO_2 , and ZnO thin films [7-9]. It is important to highlight that the sensitivity and selectivity of each sensor strongly depend on the affinity, structure, and morphology of the used nanostructure.

The present work aims to manufacture and characterize highly sensitive, selective, and fast-response optical H_2S sensors based on POF coated with Fe_3O_4 nanoparticles. To fulfill our objective, the work was divided into two stages. In the first stage, the nanoparticles were synthesized by pulsed laser ablation in liquid (PLAL) technique and after the synthesis, they were characterized by different techniques. In the second stage, an U-shaped POF was coated with nanoparticles to form a sensing prob and then exposed to 200 ppm of H_2S .

Materials and Experimental Setup

In the setup, Fe metal target (99.95 % purity) was immersed in glass beakers containing pure water and placed on a rotating surface. To perform the synthesis, a Nd:YAG pulsed laser (QUANTEL® Brilliant-b) with wavelength of 1064 nm, repetition rate of 10 Hz, pulse duration of 9 ns, and energy per pulse of 300 mJ was used. The beam laser was focused on the target using a 20-cm focal length spherical glass lens with of and a mirror to deflect the laser beam towards the target. The target was irradiated for 40 min.

After the synthesis, the average size of nanoparticles was measured using the Dynamic light scattering (DLS) characterization and, the morphology nanoparticles were characterized by Field Emission Scanning Electronic Microscope (FESEM). To characterize the structure of the nanoparticles, two techniques were used, Fourier transform infrared spectroscopy (FTIR) and selected area electron diffraction patterns (SAED). For the coating process, a U-Shape POF was immersed in a beaker containing a stable solution of nanoparticles dissolved in ultra-pure water, according to the following steps: (1) the U-Shape POF is heated to 60 °C for 5 min, then it is submerged in the liquid containing nanoparticles (2), and finally, (3) the U-Shape POF coated with nanoparticles is left at 60 °C for 5 min, so that the nanoparticles get fixed on the POF.

Results

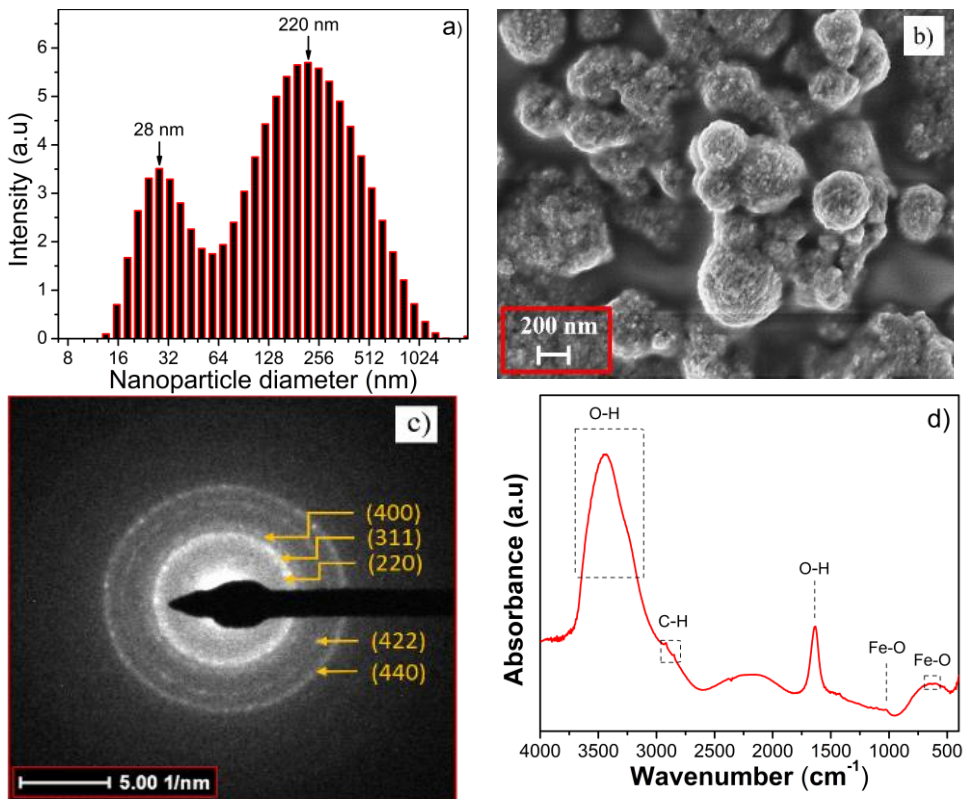


Figure 1. Results of characterizations performed to nanoparticles synthesized by PLAL; a) Average size of nanoparticles obtained from DLS, b) morphological analysis of nanoparticles using FESEM, c) crystal structure detected by SAED, and d) chemical structure analyzed by FTIR.

The results of the characterizations carried out in nanoparticles allowed us to determine the size, morphology, and structure of nanoparticles, shown in Figure 1. The nanoparticles' size was determined by DLS, giving an average particle size of 115 nm (Fig. 1a). Likewise, FESEM corroborated the results obtained by the DLS where it was possible to observe that the average particle size was approximately the same as that reported by the DLS. In addition, FESEM images (Fig. 1b) showed that some particles are spherical, but others are morphology-irregular due to the agglomeration of smaller particles.

In order to determine the crystallographic structure of nanoparticles, SAED was used. The results showed that the nanoparticles presented similar structures to Fe_3O_4 , and the results from FTIR showed that the nanoparticles synthesized by PLAL corresponded to oxidized metals and these results corroborate the results obtained from SAED. SAED and FTIR results are shown in Fig. 1(c-d).

After manufacturing the sensor (Fe_3O_4 -coated POF), it was tested with H_2S . To evaluate the performance of the sensor, the experimental configuration shown in Fig. 2a was used. In this configuration, the sensor's active region was left inside a chamber to be exposed to the test gas. Two flow controllers connected to two gas containers were used, one containing the test gas (H_2S), the other containing air, which was used to clean the test chamber. In order to acquire the sensor's signal, the U-Shape POF was connected to an infrared LED (wavelength 880 nm) at one end, and a photodiode at the other end. The LED and the photodiode were connected to an electronic system (Arduino Uno R3® + current driver + transimpedance amplifier), which was responsible for processing and sending useful data to a PC.

The sensor was subjected to a dynamic characterization that consisted of H_2S sensing for five subsequent cycles and the results can be seen in Fig. 2b. To perform a comparative analysis, the results were normalized and the comparison showed that there was a small difference of $\pm 3\%$ in the output signals, a result that demonstrates the reversibility and stability of the Fe_3O_4 -coated POF sensor. The rise and recovery times, which are important parameters, were also evaluated for the sensor. According to the results shown in Fig. 2c, the rise time for that sensor was approximately 6.3 min, while its total recovery time was measured to be 5 min. It can also be observed that, in less than 1 min, the sensor had already recovered by more than 65% of its initial signal. Comparing these results with those reported in the literature on optical sensors operating at RT, we can conclude that the sensor proposed in this work presented competitive characteristics.

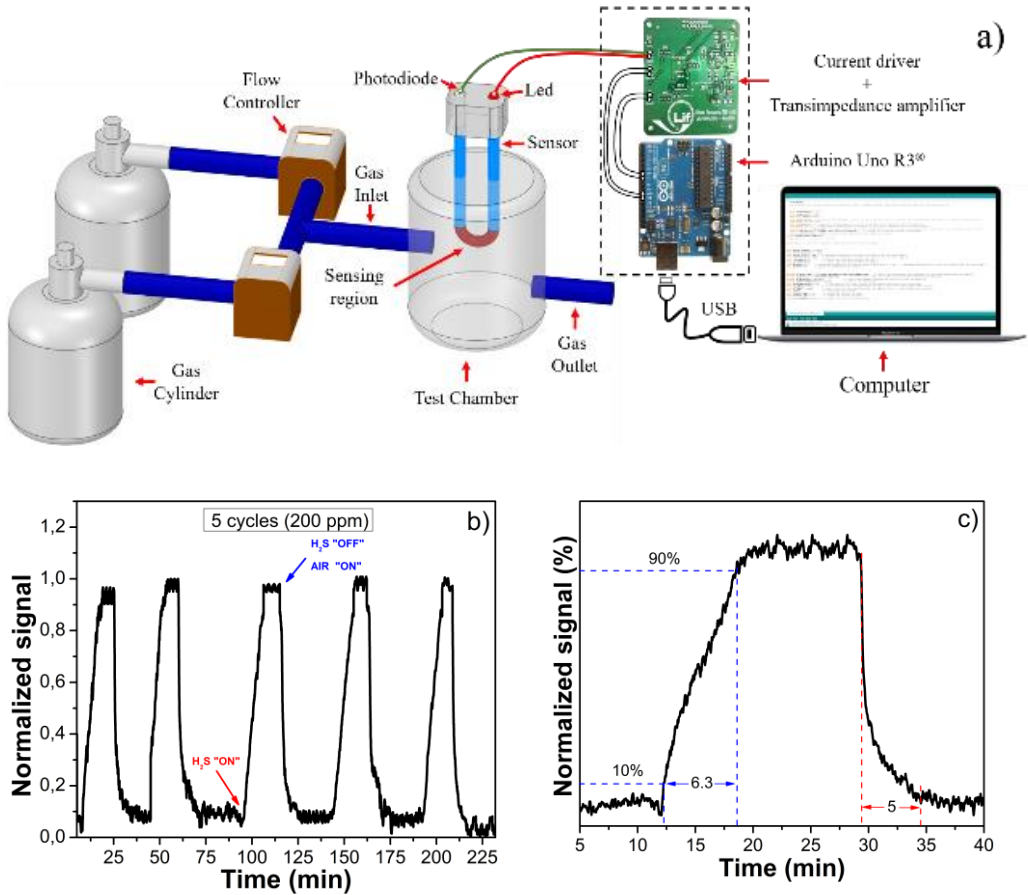


Figure 2. a) Experimental setup for sensor performance tests subjected to H₂S; b) sensor response tested with 200 ppm of H₂S at RT (25°C); and c) response time and recovery time analysis.

Conclusions

In this work, iron oxide nanoparticles were synthesized by PLAL technique aiming the development of a selective, reversible optical fiber-based sensor for H₂S sensing. The characterization results indicated that the nanoparticles structures obtained were similar to Fe₃O₄ and that the average size of the obtained spherical nanoparticles was 115 nm. The proposed sensor (Fe₃O₄-coated POF) showed reversibility, with a response time of 6.3 min and a recovery time of 5 min, which are competitive compared with the works reported in the literature. To obtain a complete characterization, additional tests must be performed in the future to evaluate the selectivity, detection limit, and detection range of the sensor.

References

- [1] A. K. Torghabeh, A. Kalantariasl, M. Kamali, and M. G. Akbarifard, "Reservoir gas isotope fingerprinting and mechanism for increased H₂S: An example from Middle East Shanul gas field," *J. Pet. Sci. Eng.*, vol. 199, no. November 2020, p. 108325, 2021.
- [2] Hydrogen Sulfide - Occupational Safety and Health Administration, OSHA, available at <https://www.osha.gov/hydrogen-sulfide/hazards>.
- [3] P. Han, C. Chen, H. Yu, Y. Xu, and Y. Zheng, "Study of pitting corrosion of L245 steel in H₂S environments induced by imidazoline quaternary ammonium salts," *Eval. Program Plann.*, vol. 112, pp. 128–137, 2016.
- [4] C. Duc, M. L. Boukhenane, J. L. Wojkiewicz, and N. Redon, "Hydrogen Sulfide Detection by Sensors Based on Conductive Polymers: A Review," *Front. Mater.*, vol. 7, no. September, 2020, doi:10.3389/fmats.2020.00215.
- [5] H. Liu, L. Weng, and C. Yang, "A review on nanomaterial-based electrochemical sensors for H₂O₂, H₂S and NO inside cells or released by cells," *Microchim. Acta*, vol. 184, no. 5, pp. 1267–1283, 2017.
- [6] M. M. Keley, F. F. Borghi, R. C. Allil, A. Mello, and M. M. Werneck, "Cu₂-xO-functionalized plastic optical fiber for H₂S sensing," *Opt. Fiber Technol.*, vol. 62, no. January, p. 102469, 2021, doi: 10.1016/j.yofte.2021.102469.
- [7] S. P. Usha, S. K. Mishra, and B. D. Gupta, "Fiber optic hydrogen sulfide gas sensors utilizing ZnO thin film/ZnO nanoparticles: A comparison of surface plasmon resonance and lossy mode resonance," *Sensors Actuators, B Chem.*, vol. 218, pp. 196–204, 2015, doi: 10.1016/j.snb.2015.04.108.
- [8] R. Tabassum, S. K. Mishra, and B. D. Gupta, "Surface plasmon resonance-based fiber optic hydrogen sulphide gas sensor utilizing Cu-ZnO thin films," *Phys. Chem. Chem. Phys.*, vol. 15, no. 28, pp. 11868–11874, 2013.
- [9] S. K. Mishra, S. Rani, and B. D. Gupta, "Surface plasmon resonance based fiber optic hydrogen sulphide gas sensor utilizing nickel oxide doped ITO thin film," *Sensors Actuators, B Chem.*, vol. 195, pp. 215–222, 2014.

Acknowledgments

This work was supported in part by the Fundação Carlos Chagas Filho de Amparo à Pesquisa do Estado do Rio de Janeiro (FAPERJ). The authors acknowledge the Human Resources Program of the Brazilian Agency of Petroleum, Natural Gas, and Biofuels – PRH-ANP (PRH-16.1).

P6 |

PROPOSITION OF A PHOTOACOUSTIC BASED SENSOR FOR MICROPLASTIC IDENTIFICATION IN MARINE ENVIRONMENT

C.M. Penso^{1*}, C.R. Ribeiro¹, L.M. Gonçalves^{1,3}, C.M. Paiva²

¹ CMEMS, Department of Industrial Electronics, University of Minho, 4800-058 Guimarães, Portugal

² Department of Polymer Engineering, Institute for Polymers and Composites, University of Minho, 4800-058 Guimarães, Portugal

³ LABBELS –Associate Laboratory, Braga/Guimarães, Portugal
*a78906@alunos.uminho.pt

Both first and second authors contributed equally for this work

Introduction

Excessive consumption of plastics, particularly single-use plastic, over the last decades has caused a critical accumulation of polymeric debris at global level, especially in the ocean.[1],[2] Microplastics (<5mm) are the result of larger plastics degradation through processes such as temperature variations, mechanical forces such as wave impact, and UV radiation.[3] The increasing dispersion of microplastics has been the subject of concern for the consequences of their inclusion in ecosystems and public health. One of the consequences of contaminating micro polymers in the oceans is their ingestion by animals, which means that humans end up consuming these particles indirectly. [4]The most common methods for laboratory identification of microplastics are Raman and FTIR technologies. [5], [6] However, none of them can perform in-situ analysis, as they are large, expensive, and time consuming methods. In addition to these techniques requiring the removal of samples from the site, which can allow contamination in the extraction, transport and reading processes, the samples will also have to be prepared for the process and reading, which usually requires them to be dried.[7]When the sample presents organic matter (such as a marine sample) the Raman technology uses IR excitation sources to avoid fluorescence. The literature proves that both microplastics and water have very high absorption in the IR range, which presents several problems for Raman and FTIR, since they can both uses IR excitation sources . [8], [9]

The proposed sensor aims to revolutionize the microplastic analysis paradigm by proposing a sensor for in-situ analysis that combines photoacoustic and infrared techniques in a single sensor. Each sensor should be accurate, portable, autonomous, low cost, and easy to operate.

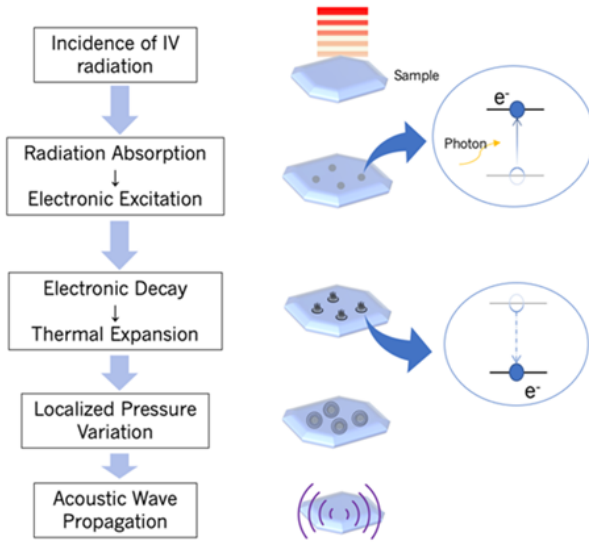


Figure 1: Photoacoustic signal generation scheme

Methods

Like chemical analysis, photoacoustic technology detects a unique fingerprint characteristic of a material. As illustrated in Figure 1, the modulated light beam that strikes and penetrates the sample is selectively absorbed, depending on the value of the optical absorption coefficient of the sample.[10]The energy that is absorbed is lost in heat through non-radiative processes. As the incident radiation is modulated, the temperature rise is periodic in the modulation frequency. The periodic rise in temperature at the sample surface induces a pressure change in the sample.

This pressure modulation can be perceived as an acoustic signal that is detected and then electronically converted into a voltage. [9]

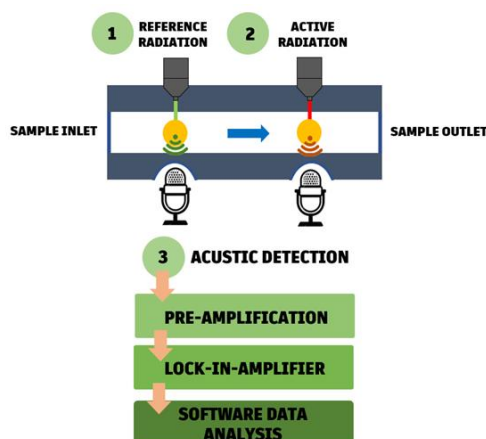
Results

According to [11] the three main types of microplastics found in the marine environment are polyethylene (PE), polypropylene (PP) and polystyrene (PS). For this reason, the carried work out was primary focused on these 3 resins.[8] The excitation source has an emission peak as close as possible to the absorption wavelength of interest. For this purpose, we selected a reference wavelength and two active wavelengths. The reference excitation was selected based on lowest absorption spectra of plastic, and the two active radiation wavelengths based on two absorption peaks (Table 1).

Table 1: Characteristic absorption peaks of the most common plastics in the marine environment.

Plastic	Absorption Peaks (nm)			Reference
PE	1680	2190, 2200	2680	[5]
PP	1709, 1729, 1772	2279, 2313, 2357		[4]
PS	1682	2145, 2169, 2188	2450	[10]

Figure 2 represents a diagram of the proposed sensor. The sensor consists of a microchannel where one microplastic passes at a time. Along the channel, the infrared absorption analysis system will be positioned. The reference wavelength selected was 750 nm and the active ones at 1020 nm and 1700 nm. IR radiation passes through the microchannel to the plastic. The plastic absorbs radiation in the form of heat, generating a wave in the surrounding medium. The control system modulates the radiation, amplifies, and demodulates the acoustic signal, allowing data analysis of the absorption bands. The acoustic detection is made using quartz-fork resonators. The thermal wave that arises due to IR absorption can be translated into a pressure wave that travels in water thanks to the good acoustic transmission of this medium. The distance between the detector and the absorption point can be calculated considering the velocity of the acoustic beads, making it possible to distinguish between the water absorption of microplastics. Use of frequency domain detection using sinusoidally modulated radiation and a lock-in system, allows to reduce costs using LEDs (generated wave has the same frequency as the excitation light).

**Figure 2** – Schematic of the Microfluidic Photoacoustic.

Conclusions

Stability represents a problem for both technologies (Raman and FTIR) as they analyze radiation resulting from plastic interaction. This problem is overcome with the photoacoustic methodology. IR excitation light generates a thermal expansion of the plastic due to light absorption.

Thermal expansion can be seen as an acoustic wave and detected independently of the IR water absorption, resulting in higher accuracy.[8] This allows sample determination without pre-treatment, regardless of whether the sample is liquid, solid or gaseous.

Sensitivity increases as the light intensity increases. This allows the construction of a multisensor platform for massive placement in an underwater environment. Massive monitoring for a large quantity of data analysis will allow a significant advance in the control of pollution of marine ecosystems.

References

- [1] N. P. Ivleva, A. C. Wiesheu, and R. Niessner, "Microplastic in Aquatic Ecosystems," *Angew. Chemie Int. Ed.*, vol. 56, no. 7, pp. 1720–1739, 2017.
- [2] Y. Picó and D. Barceló, "Analysis and Prevention of Microplastics Pollution in Water: Current Perspectives and Future Directions," 2019.
- [3] K. Zhang *et al.*, "Understanding plastic degradation and microplastic formation in the environment: A review," *Environmental Pollution*, vol. 274. Elsevier Ltd, p. 116554, 2021.
- [4] M. F. M. Santana, F. T. Moreira, and A. Turra, "Trophic transference of microplastics under a low exposure scenario: Insights on the likelihood of particle cascading along marine food-webs," *Mar. Pollut. Bull.*, vol. 121, no. 1–2, pp. 154–159, 2017.
- [5] M. R. Jung *et al.*, "Validation of ATR FT-IR to identify polymers of plastic marine debris, including those ingested by marine organisms," *Mar. Pollut. Bull.*, vol. 127, pp. 704–716, 2018.
- [6] J. L. Xu, K. V. Thomas, Z. Luo, and A. A. Gowen, "FTIR and Raman imaging for microplastics analysis: State of the art, challenges and prospects," *TrAC - Trends in Analytical Chemistry*, vol. 119. Elsevier B.V., p. 115629, 2019.
- [7] W. J. Shim, S. H. Hong, and S. E. Eo, "Identification methods in microplastic analysis: A review," *Analytical Methods*, vol. 9, no. 9. Royal Society of Chemistry, pp. 1384–1391, 2017.
- [8] M. Caniato, L. Cozzarini, C. Schmid, and A. Gasparella, "Acoustic and thermal characterization of a novel sustainable material incorporating recycled microplastic waste," *Sustain. Mater. Technol.*, vol. 28, p. e00274, 2021.
- [9] K. B. Beć and C. W. Huck, "Breakthrough potential in near-infrared spectroscopy: Spectra simulation. A review of recent developments," *Frontiers in Chemistry*, vol. 7, no. FEB. Frontiers Media S.A., 2019.
- [10] D. W. Vidrine, "Photoacoustic Fourier Transform Infrared Spectroscopy of Solid Samples," *Appl. Spectrosc. Vol. 34, Issue 3, pp. 314-319*, vol. 34, no. 3, pp. 314–319, May 1980, Accessed: Apr. 24, 2022. [Online]. Available: <https://opg.optica.org/abstract.cfm?uri=as-34-3-314>.
- [11] A. E. Schwarz, T. N. Lighthart, E. Boukris, and T. van Harmelen, "Sources, transport, and accumulation of different types of plastic litter in aquatic environments: A review study," *Mar.*

Pollut. Bull., vol. 143, pp. 92–100, 2019.

[12] “Transmission Curves of Optics Materials - GS Plastic Optics.”
<https://www.gsoptics.com/transmission-curves/> (accessed Apr. 22, 2022).

Acknowledgments

This work was funded by Project by FCT national funds, project PTDC/EAM-OCE/6797/202.

P7 |

OXYGEN SENSOR FOR OCEANOGRAPHIC APPLICATIONS

C. F. Carneiro¹, C. M. Penso¹, L. M. Gonçalves^{1,2}

¹ CMEMS-UMinho, University of Minho, Campus de Azurém, Guimarães, Portugal

² LABBELS –Associate Laboratory, Braga/Guimarães, Portugal

*e-mail: a85970@alunos.uminho.pt

Introduction

The environmental balance of marine ecosystems is essential for the organisms that inhabit them to survive and develop. Over the last few decades, there has been an exponential growth in world pollution, generating excessive exploitation of available natural resources, making it necessary to correct the over-exploitation of this environment to minimize the impact of the current environmental crisis. It is important to point out that the aquatic environment is valuable for the economy, especially in Portugal, which has a large coastal area and benefits greatly from it.

Instruments for measuring O₂ are important in several areas, namely in the food industry, water treatment plants, and healthcare[1], [2].

Dissolved oxygen (DO) comes from aquatic biotic photosynthesis or the diffusion of gas, which is present in the air, with the water surface. The concentration of dissolved oxygen (COD) is directly related to the amount of molecular oxygen that is present in each volume of liquid or solvent.

Methods

Optical sensors are based on relatively recent and innovative principles. The most widely used measurement technology is the electrochemical measurement, although the optical measurement overcomes some of the problems this measurement has. These methodologies are particularly distinguished in response time, sample interference and contamination, maintenance frequency, electrical consumption, installation direction, temperature influence, noise sensitivity, electromagnetic field, and acquisition value.[3],[4]

These sensors operate on the physical phenomenon of luminescence. The methodology used alongside this sensor was ratiometric, which is based on the comparison of two values, namely a sample reading variable and a reference variable. Sensors that are based on the intensity methodology use an indicator that does not react with oxygen and mix it in the same matrix as the sensitive indicator. When the membrane is illuminated by the excitation LED, two fluorescence

signals with different wavelengths are obtained, one of which provides the reading value, and the other simulates the maximum intensity value. [4],[5]

In the existing prototype, figure 1, the optical sensor consists of a membrane with an indicator, an optical filter, a lens, a photodiode (Hamamatsu S1336-8BK), and a UV LED (Bivar UV5TZ-385). The membrane is illuminated with UV light at 385 nm, and emits luminescence at 645 nm on red wavelength. Luminescence value is related to oxygen content, as predicted by Stern-Volmer equation. [6]

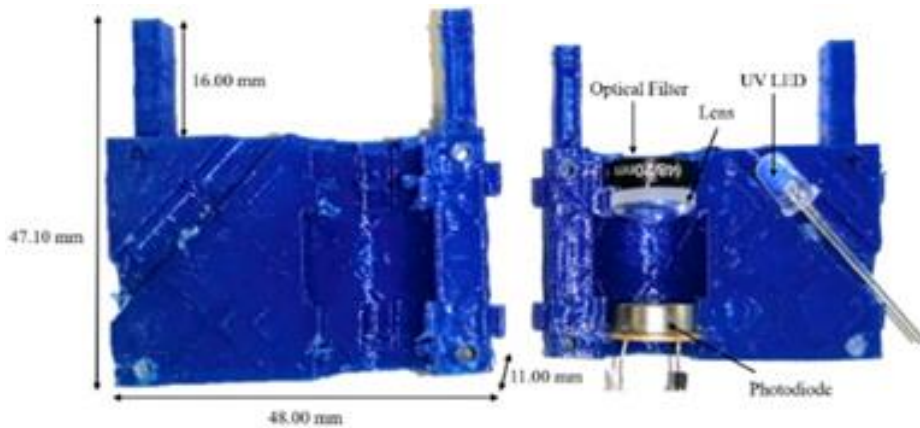


Figure 1- Oxygen sensor prototype.

The photodiode uses an optical filter to eliminate all wavelengths other than the wavelength of analysis. A plane convex lens was used to center the light on the photodiode, avoiding light dispersion. The photodiode was chosen for its quick response to variations in intensity and high signal-to-noise ratio (SNR). The photodiode electrical response should be proportional to the optical signal received, it must also have a small dark current, so this value must be selected to be as low as possible. For the excitation source, a LED was chosen since it has a very long lifespan at very low price.

The oxygen sensitive membrane is based on PDMS(Polydimethylsiloxane)/PtOEP(Platinum Octamethyl Porphyrin) mixture. PtOEP is used because of its strong phosphorescence at water temperature with a quantum yield (ϕ) close to 50%, a good separation between excitation and luminescence wavelengths, as well as a lifetime (75 μ s). The membranes were manufactured using a previously predefined method. [4]

At the level of electronics development, an electronic circuit is required to read the optical signal, as presented in figure 2. The LED excitation will be controlled with the STM32 microcontroller. The microcontroller will keep the LED supply voltage constant and thus guarantee that the LED brightness will remain constant.

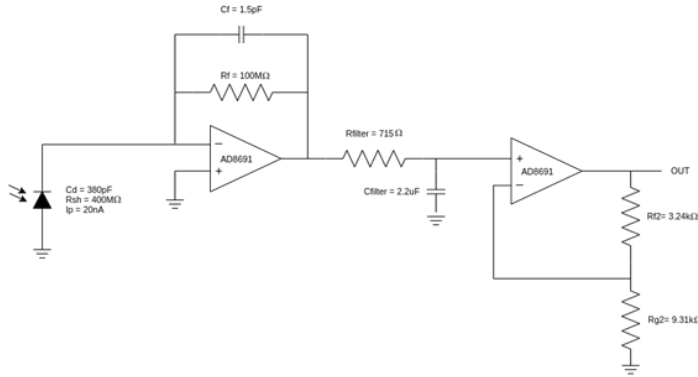


Figure 2 - The signal conditioning circuit, composed of the transimpedance amplifier, a first-order low-pass filter and a second amplifier stage.

For the optical receiver, the photodiode is connected to a transimpedance amplifier (TIA) circuit followed by a low-pass filter and a second amplifier stage.

The photodiode selected was the Hamamatsu S1336-8BK, used in photovoltaic mode, without polarization (0 V), to minimize the current in the dark. This photodiode has a large sensitive area (5.8 mm × 5.8 mm), low dark current (100 pA), good commercial availability, and excellent value for money. It directly converts the light incident on the sensitive area into current.

The transimpedance amplifier circuit (TIA) consists of two amplifier stages, based on the AD8691 precision amp (the second stage is required to avoid larger values of Rf resistor).

Results

The sensor was firstly validated in the laboratory. Absorption as a function of wavelength is presented in figure 3, comparing different solvents in the membrane fabrication (THF (tetrahydrofuran) and toluene), for equal membrane thickness (0.65 mm in the case of figure 3 – a) and 0.50 mm in the case of figure 3- b) and equal concentration of PtOEP (platinum octamethyl porphyrin) indicator (727 ppm (parts per million) of concentration). Membranes made with THF show

higher absorption compared to those made with toluene, for both thicknesses, and across the entire spectrum.

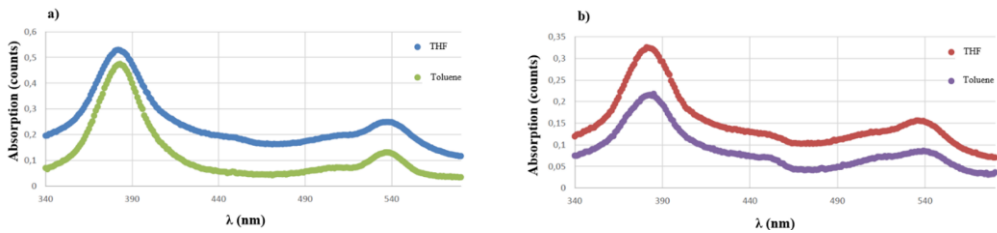


Figure 3- a) Absorption spectrum of the membranes with a concentration of 727 ppm, equal thickness (0.65 mm) when using different solvents (THF and toluene); b) Absorption spectrum of the membranes with a concentration of 727 ppm, equal thickness (0.5 mm) when using different solvents (THF and toluene).[4]

Tests were also carried out in a liquid environment since the purpose of the sensor is to be placed in the sea. As can be seen in figure 4, the inverse of luminescence intensity follows an approximately linear trend with oxygen concentration. These values allow us to conclude that the dispersion of the indicator/solvent/polymer in these membranes was more homogeneous when compared to the data observed in the toluene membranes. It is also possible to confirm the functioning of the membranes in the liquid medium, for a range of dissolved oxygen values between 0.7 – 5.5 mg/L. The luminescence intensity is equivalent for both toluene and THF membranes.

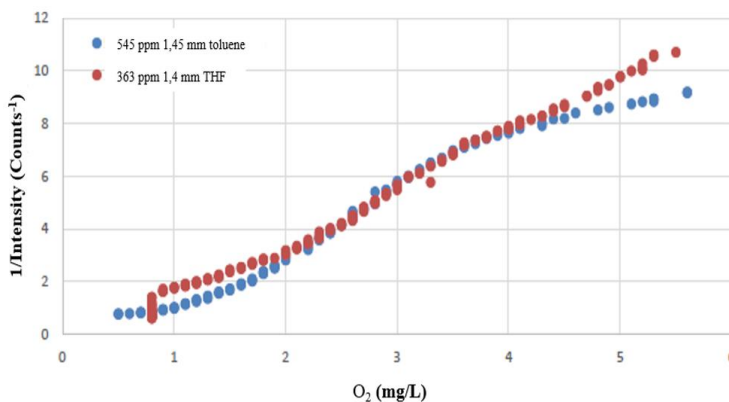


Figure 4 - Inverse of the luminous intensity of the luminescence on the membrane with 363 ppm indicator with a thickness of 1.4 mm made of THF and on the membrane with 545 ppm of indicator with a thickness of 1.45 mm. [5]

Conclusion

Fabricated PtOEP membranes present luminescence at 645 nm, inversely proportional to dissolved oxygen level (0 - 5.5 mg/L), when excited with UV (385 nm) light. An electronic circuit converts received light (by a photodiode) to a digital DO value. At this moment, the sensor is fully functional in the laboratory and the steps towards its sea adaptation have begun. The sensor design has already been prepared as can be seen in figure 1. Currently, there's work being done to optimize the electronic circuit, for later manufacture of the PCB. Following, we intend to develop the software. For this, a microcontroller will be used that will control when the sensor is active to collect measurement values from a certain location and how often it will do so, it will also be responsible for turning off the sensor whenever it does not measure. After that, the first phase of sensor testing will be carried out in the laboratory. In the final testing phase, a validation of the sensor is intended, now in a real environment. The main goal is for the sensor to be able to collect data at sea, with energy autonomy above 1 month.

References

- [1] D. A. P. de Abreu, J. M. Cruz, and P. P. Losada, "Active and Intelligent Packaging for the Food Industry," *Food Rev. Int.*, vol. 28, no. 2, pp. 146–187, 2012.
- [2] P. Raj Kannel *et al.*, "Application of Water Quality Indices and Dissolved Oxygen as Indicators for River Water Classification and Urban Impact Assessment," *Env. Monit Assess*, vol. 132, pp. 93–110, 2007.
- [3] I. Helm, G. Karina, L. Jalukse, T. Pagano, and I. Leito, "Comparative validation of amperometric and optical analyzers of dissolved oxygen: a case study".
- [4] C. M. Penso, "Dissertation: Development of a Dissolved Oxygen Sensor for Aquatic Environment," p. 186, 2021.
- [5] C. S. Chu and C. Y. Chuang, "Ratiometric optical fiber dissolved oxygen sensor based on metalloporphyrin and CdSe quantum dots embedded in sol-gel matrix," *J. Lumin.*, vol. 167, pp. 114–119, 2015.
- [6] A. V. Popov, V. S. Gladkikh, and A. I. Burshtein, "Stern-Volmer law in competing theories and approximations," *J. Phys. Chem. A*, vol. 107, no. 40, pp. 8177–8183, 2003.

Acknowledgments

This work was funded by Programa Operacional Regional do Norte (NORTE2020), Project Atlantida, NORTE-01-0145-FEDER-000040 and by FCT national funds, project PTDC/EAM-OCE/6797/2020

P8 |

TOWARDS A NO_x MICROANALISER: MINIATURIZED NITRIC OXIDE (NO) CHEMIOLUMINESCENCE ANALYZER PROTOTYPE, FOR AUTOMOTIVE INDUSTRY APPLICATIONS

Pedro Couceiro¹, David Izquierdo², Johanna Naranjo³, Ignacio Garces⁴, Mar Puyol¹,
Cynthia Martinez-Cisneros³, Julian Alonso-Chamarro*¹

¹ GSB. Department of Chemistry, Autonomous University of Barcelona, 08193 Bellaterra, Spain.

² Centro Universitario de la Defensa. Carretera de Huesca, 50090 Zaragoza Spain.

³ University Carlos III of Madrid. Av. Universidad 30. 28911-Leganés, Spain.

⁴ I3A. University of Zaragoza. C/ Mariano Esquillor s/n 50018 Zaragoza, Spain.

*e-mail: Julian.Alonso@uab.es

Introduction

NO_x is the generic term used to describe the mixture of nitrogen monoxide (NO) and nitrogen dioxide (NO₂). These gases are generated mainly by anthropogenic activity (90%), such as the automotive industry (50%), thermal power stations (20%) and energy-intensive industries (30%), contributing to the formation of smog and acid rain. Since human exposure to such gases has been correlated with pulmonary and cardiovascular diseases [1], NO_x became a standard parameter for air quality monitoring with World Health Organization recommending a maximum exposure of 25 ug/m³ (ppt) per hour.

The standard method for NO_x determination is the chemiluminescence reaction between NO and O₃ [2], which emits light in 500–3000 nm range, with a maximum emission peak at 1200 nm. This reaction is NO specific and the chemiluminescence signal is proportional to NO concentration in the 0-20 ppm range. In such analysis NO₂ is catalytically converted, at 350 °C, to NO using Molybdenum.

In chemiluminescence reactions, the obtained signal is proportional to the number of molecules that emit radiation. Therefore, the analytical signal increases with increased flow rate. Another method to amplify the chemiluminescence signal is to increase the sample injection time and integrate the obtained signal.

Commercial available NO_x analysers are very expensive rack mount units that allow 25 ug/m³ (ppt) of NO_x to be detected using 5 min. sample injection time. In order to achieve such low detection limits, bulky vacuum pumps, which allow high flow rates (8000 mL/min), are required. As a result of the high flow rates required, bulky high power on-line O₃ generators are used, therefore, limiting the possibility of miniaturization.

For applications such as car exhaust emission inspection, where NO_x concentration vary in the 1 - 100 mg/L (ppm) range, decreasing the flow rate used in the analysis allows mini-vacuum pump and, consequently, mini-ozone generator, to be used, therefore decreasing the energy required and overall analyser dimensions. The consequent decrease in obtained chemiluminescence signal can be compensated, if necessary, by increasing the sample injection time.

As part of the ongoing development of a miniaturized NO_x analyser, in this work a modular miniaturized NO analyser (MicroNO) integrating all the necessary elements for NO chemiluminescence determination is presented. The MicroNO is constituted by four modules each responsible for a unitary operation.

Methods

In order to characterize the operation of the MicroNO analyser, the experimental setup, schematically described in Fig.1, was used.

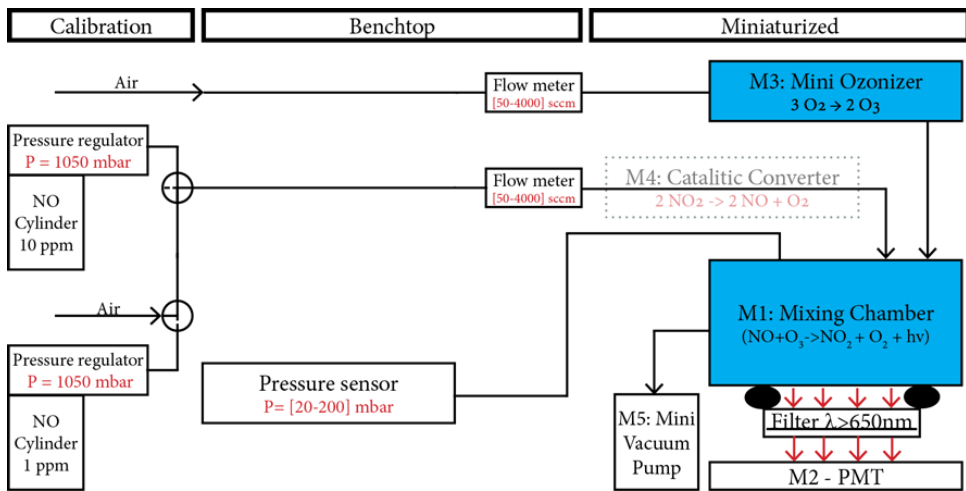


Fig 1. Schematic representation of the experimental setup used to characterize the presented NO analyser.

NO standard gas cylinders (Linde), fitted with low pressure regulators (Hy-Lok concoa series 213) where connected to 3-way solenoid valves (SMC VDW250-5G-2-01F-Q) using pneumatic tubing (Legris 1025U04 01). Manual flow meters (Key Instruments MR3A12B) allowed gas flow control into the MicroNO analyser, while a vacuum gauge (Rs Pro 188-986) used to read the pressure inside the analyser. The MicroNO analyser is composed of four modules, each

responsible for a unitary operation. A commercial mini-Ozonizer (Murata MHM501-00), a commercial mini-vacuum pump (KNF N89), a photomultiplier tube (Hamamatsu H10722-20) and a ceramic mixing chamber. The ceramic mixing chamber is constituted by a circular, 20 mm diameter, open mixing chamber, fabricated using Low Temperature Co-Fired Ceramic technology and was sealed, under vacuum operation, using an O-ring and 665 nm long pass filter optical window (Thorlabs FGL665). Solenoid valves, the mini-Ozonizer, as well the photomultiplier tube electrical signal were processed using a DAQ (NI USB-62211) and control using a homemade program developed in LabVIEW.

Results

The MicroNO analyser response to NO concentration, in 1 to 100 ppm range, was characterized using the experimental setup described in Fig 1, and the results are summarized in Table 1. The results were obtained under working conditions which ensure O₃, produced on-line by de mini-Ozonizer, to be in excess (O₃>20 mg/L (ppm)) when compare to NO concentration.

Chemiluminescence signal is proportional to the number of molecules emitting radiation and to the signal integration time, and therefore, it is proportional to flow rate and sample injection time. Commercial available NO_x analysers use long sample injection time and vacuum pumps that allow high flow rates (8000 mL/min) in order to maximize chemiluminescence signal. Using mini-vacuum pumps limit the flow rate to a maximum of 1000 mL/min, therefore decreasing the chemiluminescence signal per unit of time, which consequently increases the detection limited of the analyser.

Nonetheless, as seen in Table 1, a detection limit of 1 mg/L (ppm), was obtained using the MicroNO for an integration time of only 1 s. The fast response time (1s) opens the possibility of using the MicroNO analyser in automotive industry application, where high sample rate is necessary, such as online real-time engine regime optimization for low gas emissions or in periodic car exhaust emission inspection.

As seen in table 1, a 5-fold increase in integration time, originated a 1-fold decrease in detection limit. This strategy opens the possibility of using the MicroNO analyser in applications demanding lower detection limits and lower sample rates, such as thermal power stations and energy-intensive industries gas emission monitoring.

Table 1: Summary results obtained for the detection of NO using MicroNO analyser in the following working conditions: NO flow rate = 400 mL/min; O₃ flow rate = 400 mL/min; mini-ozoniser Duty Cycle = 30% ([O₃] = 20 ppm); Mixing chamber pressure =120 mbar; Sample injection time = 60s; Photomultiplier gain = 0.7 V; DAQ Sample size = 125000; DAQ Sampling frequency =125 KhZ).

Sample injection time	Integration time (1s)	Integration time (50s)	Linear regression	Sensitivity	Detection Limit (ug/L) (ppb)
60 s		X		6.3	1003
60s				248.6	120

Conclusions

The presented modular MicroNO analyser is composed of miniaturized elements (M1, M2, M3, M5) and non-miniaturized commercial elements (flow controllers and vacuum gauge), as seen in Fig.1. Miniaturization of flow controllers is straightforward, can be done either by incorporating passive fluidic elements in the connections between modules or by integrating fluidic restrictions in the ceramic modules, while miniaturized vacuum sensors are commercially available.

The obtained detection limit of 1 mg/L (ppm), for 1 s analysis time, meets the criteria for the MicroNO analyser in automotive industry applications, such as an external portable analyser for car exhaust emission inspection or as an online analyser for real-time engine regime optimization. Increasing the sample injection time would allow the MicroNO analyser to be used in applications that require slower analysis time and lower detection limits, such as industrial gas emission monitoring. In addition, the proposed analyser could be easily modified to measure NO₂ and NH₃ through the addition of a catalytic converter of these gases to NO.

References

- [1] doi: 10.1097/EDE.0000000000000847
- [2] doi: 10.1021/es60073a001

Acknowledgments

This work was supported by Project PID2020-117216RB-100 and Project RTC-2017-5858-4 both from the Ministerio de Ciencia y Innovación (Spain) and co-funded by FEDER

BIOSENSORES E APLICAÇÃO À ANÁLISE DE ALIMENTOS |
BIOSENSORES Y APLICACIONE AL ANÁLISIS DE ALIMENTOS | BIOSENSORS
AND APPLICATION TO FOOD ANALYSIS

O10 |

COLORIMETRIC PYRANOFLAVYLIUM-CONTAINING SENSOR FILMS FOR FOOD SPOILAGE MONITORING

Vânia Gomes, Ana Sofia Pires, Nuno Mateus, Victor Freitas, Luís Cruz*

REQUIMTE/LAQV, Department of Chemistry and Biochemistry, Faculty of Sciences, University of Porto, Rua do Campo Alegre, 687, 4169-007, Porto, Portugal.

*e-mail: luis.cruz@fc.up.pt

Introduction

Polymeric-based formulations enriched with anthocyanins as pH-sensitive natural dyes have been widely studied to produce films for food spoilage monitoring. However, anthocyanins are not promising because of their instability issues namely color fading with time, chemical and thermal degradation, and prone to oxidation reactions. On the other hand, some anthocyanin derivatives such as pyranoanthocyanin-like compounds are much more stable pigments because of their simplest chemistry and are poorly reported for those applications. Bearing this, for the first time a suitable and bio-inspired pyrano-3,7-deoxyanthocyanidin (PyF) dye was designed and further immobilized into cellulose acetate (CA)-based films to build up a colorimetric pH-freshness indicator for food packaging applications.^{1,2}

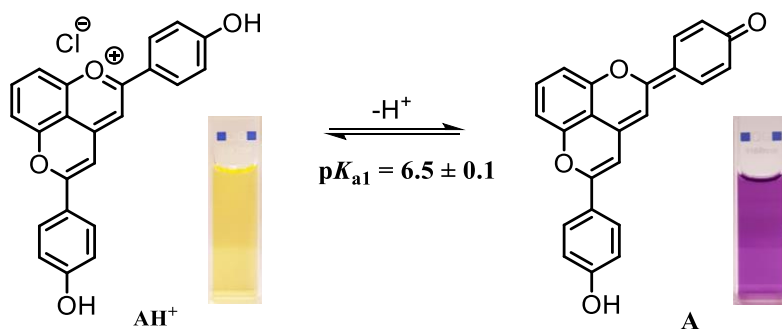


Figure 1. Chemical equilibrium of PyF dye and characteristic color in solution (EtOH 25%) of the different species: pyranoflavylium cation (AH^+) and neutral quinoidal base (A).¹

Methods

The pigment (0.1 % (w/w)) was immobilized in the cellulose acetate matrix in the absence and presence of different percentages of glycerol (Gly) (10 – 40% (w/w)). The films were obtained by the casting method and characterized by the thickness, morphology and barrier properties, thermogravimetric analysis, and color, among

others. The pH-responsive properties of the films were tested in buffer solutions at different pH values (pH 4 to 8) and in amine-rich simulated environments.

Results

The results showed that the addition of the Gly as a plasticizer to the cellulose acetate films led to the increased thickness, moisture content, swelling index, water solubility, and water vapor permeability (WVP). This behavior is due to the role of plasticizers in disrupting and restructuring intermolecular polymer chain networks, creating free volumes in its interstitial spaces. SEM images (Fig. 2) confirm the presence of these free volumes through of the porosity observed at the surface as well as in the interior of the films. Regarding the pH-responsive properties, the film without Gly showed no color-responsive to different pH environments (Fig. 3). On the other hand, the incorporation of Gly 30 % (w/w) demonstrated effective pH responsiveness after 20 min of exposure (Fig. 3). The porosity and, consequently, the higher water permeability of the film with Gly promotes the penetration of H^+ and OH^- ions, resulting in higher effectiveness and sensitivity of the film. In addition, the porosity also promoted by Gly increases the superficial area of the film which increases the contact area between the dye immobilized on the film and the water molecules in the surrounding environment, rising a faster pH response.

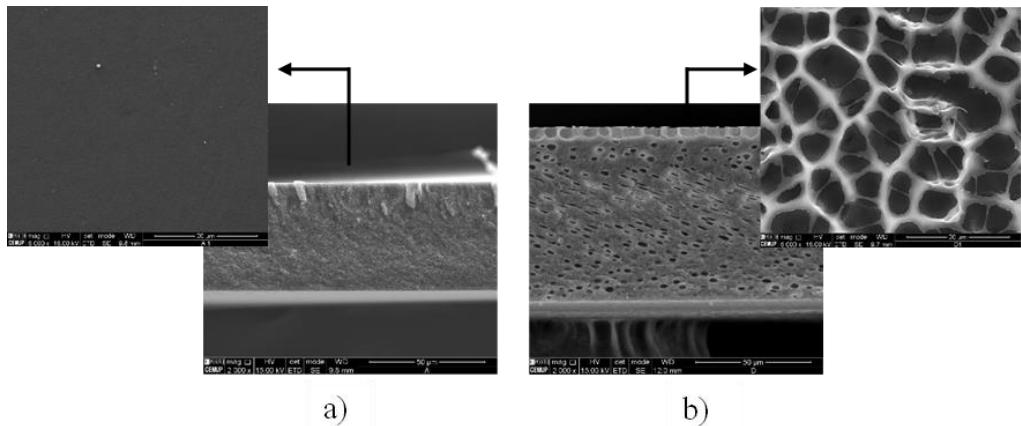


Figure 2. SEM images of cross-section and surface of the CA films with PyF and, a) Gly 0 %; b) Gly 30 %. Adapted from (2).

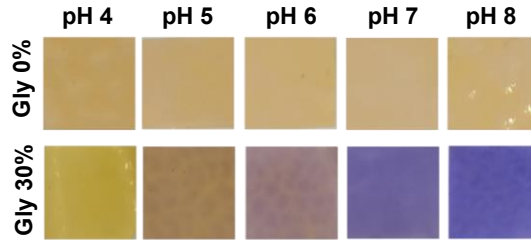


Figure 3. Color variation (photographs) of the CA films with PyF and Gly 0 and 30% after 20 min of immersion in different buffer solutions (pH 4 to 8). Adapted from (2).

For food packaging applications is important that the film give a color response to pH variation of the headspace of the packaging, without touching the food product. In general, this pH variation is the result of the production and release of the volatile basic nitrogen compounds (TVB-N), such as ammonia and biogenic amines, as a consequence of the biological degradation and microbial growth during the spoilage of many perishable food products. In order to evaluate the efficacy of the color response of the sensor to volatile basic nitrogen compounds, the CA_PyF_Gly30 film was exposed to the headspace of different solutions of BA (0.5–4 g/L) and ammonium hydroxide (0.35 and 3.5 g/L) overnight (Fig 4). In this preliminary experiment, it was possible to observe a noticeable change of the film color with increasing concentrations of BA and ammonia-containing solutions.

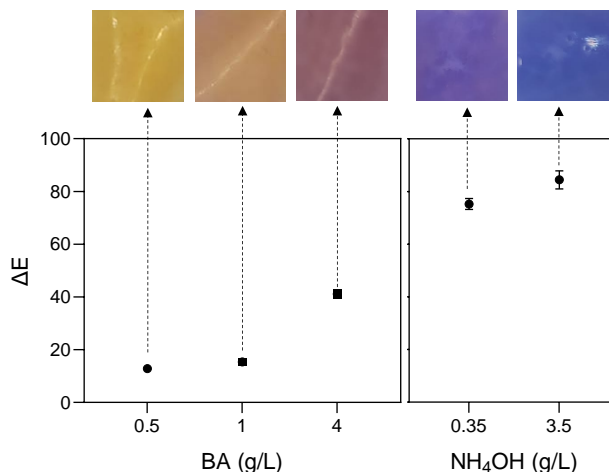


Figure 4. Color variation (ΔE) for CA_PyF_Gly30 film, after overnight headspace exposition to different BA (g/L) and ammonia solutions (g/L), and photographs of the final color of the films. Adapted from (2).

Conclusions

The glycerol-containing films showed relevant and remarkable color change at the pH range of food spoilage indicating a great potential for application as a food freshness sensor. Releasing studies of film components to food model solutions (EtOH 10% and 50%) as well as their photostability have been carried out. Validation of the pH-colorimetric response of the films on real samples is now in progress.

References

- (1) Gomes, V.; Pires, A. S.; Fernandes, I.; Mateus, N.; de Freitas, V.; Cruz, L. Synthesis of novel pyrano-3,7-deoxyanthocyanin derivatives and study of their thermodynamic, photophysical and cytotoxicity properties. *J. Photochem. Photobiol. A Chem.* **2021**, *415*, 113313.
- (2) Gomes, V.; Pires, A. S.; Mateus, N.; de Freitas, V.; Cruz, L. Pyranoflavylum-cellulose acetate films and the glycerol effect towards the development of pH-freshness smart label for food packaging. *Food Hydrocoll.* **2022**, *127*, 107501.

Acknowledgments

This work was supported by the project PTDC/OCE-ETA/31250/2017 funded by FCT and FEDER; and by the Associate Laboratory for Sustainable Chemistry, Clean Processes, and Technologies LAQV, financed by national funds from UIDB/50006/2020. Luís Cruz acknowledges the FCT research contract (DL 57/2016/CP1334/CT0008) and Vânia Gomes acknowledges the Ph.D. grant from FCT (SFRH/BD/136556/2018). This work was supported by the Associate Laboratory for Sustainable Chemistry, Clean Processes, and Technologies LAQV. The latter is financed by national funds from UIDB/50006/2020.

O11 |

DETERMINAÇÃO CINÉTICA DE HISTAMINA USANDO UMA Sonda RACIOMÉTRICA FOTOLUMINESCENTE COMBINANDO PONTOS QUÂNTICOS DE CARBONO E PONTOS QUÂNTICOS TERNÁRIOS

Rafael C. Castro*¹, Ricardo N. M. J. Páscoa¹, M. Lúcia M. F. S. Saraiva¹,
João L.M. Santos¹, David S.M. Ribeiro¹

¹ LAQV, REQUIMTE, Department of Chemical Sciences, Laboratory of Applied Chemistry,
Faculty of Pharmacy, University of Porto, Rua de Jorge Viterbo Ferreira n° 228,
4050-313 Porto, Portugal

*e-mail: rafael.castro.cl@hotmail.com

A histamina é uma amina biogénica e é um importante mediador de inúmeras reações biológicas, tais como a resposta imunológica, regulação de ácido gástrico, função intestinal e contração muscular, atuando também como um neurotransmissor. A histamina está também envolvida na resposta anti-inflamatória e é um dos intermediários mais importantes nas reações alérgicas. Para além disso, a histamina pode surgir em alguns alimentos fruto da descarboxilação da histidina desencadeada por descarboxilases exógenas libertadas por microrganismos. Por exemplo, a histamina é raramente encontrada em peixes frescos, embora possa surgir em peixe mal conservado, uma vez que o nível de histamina aumenta acentuadamente em consequência do processo de decomposição. Por outro lado, a histamina pode surgir em concentrações elevadas em alimentos, principalmente os que são produzidos por processos fermentativos, como seja o queijo curado, chucrute, vinho e carne processada. O uso de alimentos ricos em histamina pode produzir toxicidade, que se manifesta por náuseas, dores de cabeça, diarreia e taquicardia ou erupção cutânea [1,2]. Desta forma, o desenvolvimento de metodologias expeditas, sensíveis e de fácil utilização para determinação de histamina em alimentos poderá ter um importante impacto tanto em termos de saúde pública como no controle de qualidade na indústria alimentar. Os pontos quânticos (QDs) são nanomateriais semicondutores fluorescentes que apresentam propriedades óticas e químicas muito interessantes do ponto de vista da aplicação em análise química, nomeadamente no desenvolvimento de metodologias analíticas para análise alimentar, clínica, farmacêutica e ambiental. Entre estas propriedades destaca-se a facilidade e versatilidade da sua síntese, a qual permite ajustar o seu espectro de absorção e emissão em função do tamanho dos nanocristais, assim como a sua reatividade e capacidade de reconhecimento molecular, ajustáveis em função da sua química de superfície. São também de salientar a sua foto-estabilidade e elevado rendimento quântico [3,4]. Por outro lado, sendo materiais altamente fluorescentes podem ser aplicados em distintas

estratégias analíticas que envolvem não só a modulação da respetiva fluorescência por interação com o analito (aumento ou diminuição) como também a implementação de processos de transferência de energia por ressonância (FRET) [4,5].

Neste trabalho foi estudada a interação, numa perspetiva cinética, entre pontos quânticos ternários de AgInS₂ passivados na sua superfície com ácido 3-mercaptopropiónico (MPA), pontos quânticos de carbono e a histamina, com vista à determinação desta última. Para isso, foi desenvolvida uma sonda ratiométrica combinando pontos quânticos de carbono (CDs, com emissão azul, fluoróforo de referência) e pontos quânticos ternários (com emissão vermelha, fluoróforo modulado pela histamina). O uso de sondas ratiométricas permite minimizar fatores prejudiciais associados às medições fluorométricas que dependem das alterações da fotoluminescência da sonda num único comprimento de onda de emissão, tais como: flutuações na fonte de excitação, variações na concentração do fluoróforo, efeitos de matriz e fluorescência de fundo [6,7]. Na sonda ratiométrica desenvolvida, à medida que a intensidade de fluorescência dos AgInS₂ QDs é inibida, a dos CDs permanece praticamente inalterada devido à sua inércia química em relação ao alergénio.

A quimiometria foi um termo usado pela primeira vez em 1972 por Svante Wold para definir a capacidade de extrair a informação química valiosa de sistemas experimentais complexos, convertendo os dados obtidos em informação útil [8,9]. Quando usamos métodos univariados, apenas uma variável é analisada independentemente das outras, não sendo capazes de considerar a correlação entre as múltiplas variáveis. Alternativamente, estratégias multivariadas têm em consideração diferentes variáveis, permitindo uma interpretação mais detalhada dos conjuntos de dados obtidos [9].

Na literatura é possível encontrar diferentes ferramentas quimiométricas, que são métodos matemáticos e estatísticos que descrevem a relação entre os parâmetros analíticos e os dados de fluorescência. Dependendo da natureza da relação (linear ou não linear) entre as concentrações dos analitos, a intensidade de fluorescência e a finalidade da análise (identificação e/ou quantificação), a seleção do modelo quimiométrico adequado é essencial para uma análise multiparamétrica com exatidão e precisão [10].

Assim sendo, para fins analíticos, existem diversas ferramentas quimiométricas que podem ser usadas, tais como a *artificial neural network*- ANN; *partial least squares*- PLS; *multivariate curve resolution* – MCR ou *principal component regression*- PCR.

A obtenção de dados de primeira ordem (um espectro de fluorescência) permite obter a vantagem de primeira ordem, o que possibilita a quantificação precisa e seletiva de analitos na presença de substâncias interferentes, desde que esses

interferentes estejam incluídos nas amostras de calibração. Por outro lado, dados de segunda ou maior ordem tornam possível determinar com precisão o analito, mesmo na presença de interferências que não foram incluídas no conjunto de calibração, contornando a presença de componentes inesperados em matrizes complexas, tais como amostras alimentares.

A evolução ao longo do tempo dos espectros de emissão de pontos quânticos quando na presença de analitos pode ser usado como dados instrumentais de segunda ordem, o que permite obter a vantagem de segunda ordem. Assim sendo, de forma a resolver problemas relacionados com os possíveis interferentes presentes na matriz, foi realizado um ensaio cinético para obter dados instrumentais de segunda ordem. O processamento dos dados adquiridos por ferramentas quimiométricas permite superar os inconvenientes relacionados com a ocorrência de espécies interferentes na matriz da amostra, mesmo que não sejam calibradas, melhorando assim a precisão do método desenvolvido. Para além disto, a abordagem cinética permitirá reduzir o LOD e melhorar a sensibilidade e seletividade [3].

Neste trabalho, foi estudada a interação individual dos pontos quânticos (CDs e QDs) com a histamina e foi também avaliada a interação, ao longo do tempo (15 min), entre sondas ratiométricas combinadas e concentrações crescentes de histamina, de forma a ser possível obter dados de segunda ordem e assim contornar a presença de possíveis interferentes.

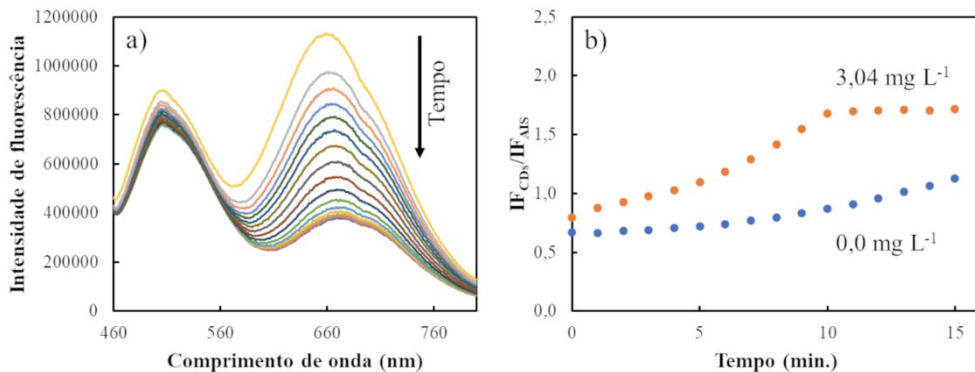


Figura 1. A) Evolução da intensidade de fluorescência da sonda ratiométrica ao longo de 15 min na presença de 3,04 mg L⁻¹ de histamina. **B)** Evolução da razão entre a intensidade de fluorescência dos CDs e dos pontos quânticos ternários na ausência e na presença de 3,04 mg L⁻¹ de histamina (na ausência de histamina: $\lambda_{max}CDs=509$; nm, $\lambda_{max}AIS=653$).

Foram testadas diferentes proporções entre os CDs e os QDs ternários, de forma a perceber qual a sonda que melhor permitiria uma determinação mais sensível da

histamina. Por outro lado, os dados obtidos ao longo de 15 minutos da interação entre a sonda racionométrica e diferentes concentrações de histamina foram processados por diferentes ferramentas quimiométricas de forma a otimizar o modelo que melhor se adequava aos dados obtidos.

Como referido anteriormente, a abordagem proposta foi avaliada por diferentes ferramentas quimiométricas, nomeadamente U-PLS (*unfolded-PLS*) e ANN, com o objetivo de verificar qual a relação entre os dados obtidos (linear ou não-linear). Os resultados indicam uma relação não linear entre a concentração de histamina e a intensidade de fluorescência da sonda racionométrica. No que diz respeito à otimização da sonda racionométrica, verificou-se que quando era utilizada uma diluição dos AIS QDs e CDs de forma a obter intensidades de fluorescência similares de ambas as bandas de emissão, foi possível obter um erro de previsão relativo (REP), limite de deteção (LOD) e de quantificação (LOQ) menores.

Para a obtenção destes resultados, foi monitorizada a interação entre a sonda racionométrica e 16 concentrações de histamina (0,38 – 10,26 mg L⁻¹), sendo utilizadas 4 destas para validação do modelo obtido. A ferramenta quimiométrica que apresentou os melhores resultados foi o ANN, baseado na função “*Radial basis function*” (RBF), com um coeficiente de determinação das amostras de previsão (R²_p) e REP de 0,98 e 4,4%, respetivamente. Além disto, o LOD e LOQ obtidos são, respetivamente, de 1,2 e 3,6 mg L⁻¹. Estes parâmetros refletem que a abordagem analítica desenvolvida tem um bom desempenho.

Concluindo, neste trabalho ficou demonstrado que o uso da interação entre o alergénio e a sonda racionométrica ao longo do tempo (cinética) é uma abordagem simples e interessante para quantificar histamina em amostras complexas, nomeadamente amostras alimentares.

References

- [1] Visciano, P., Schirone, M., Tofalo, R., & Suzzi, G. (2014). Histamine poisoning and control measures in fish and fishery products. *Frontiers in microbiology*, 5, 500.
- [2] Adivi, F. G., & Hashemi, P. (2021). Removal of histamine from biological samples by functionalized Fe₃O₄@ Agarose@ Silica nanoparticles and its fast determination by ion mobility spectrometry. *Colloids and Surfaces B: Biointerfaces*, 203, 111717.
- [3] Castro, R. C., Páscoa, R. N., Saraiva, M. L. M., Santos, J. L., & Ribeiro, D. S. (2021). Chemometric-assisted kinetic determination of oxytetracycline using AgInS₂ quantum dots as PL sensing platforms. *Analytica Chimica Acta*, 1188, 339174.
- [4] Castro, R. C., Ribeiro, D. S., & Santos, J. L. (2021). Visual detection using quantum dots sensing platforms. *Coordination Chemistry Reviews*, 429, 213637.
- [5] Castro, R. C., Lopes, A. F., Soares, J. X., Ribeiro, D. S., & Santos, J. L. (2021). Determination of atenolol based on the reversion of the fluorescence resonance energy transfer between AgInS₂ quantum dots and Au nanoparticles. *Analyst*, 146(3), 1004-1015.

- [6] Castro, R. C., Soares, J. X., Ribeiro, D. S., & Santos, J. L. (2019). Dual-emission ratiometric probe combining carbon dots and CdTe quantum dots for fluorometric and visual determination of H₂O₂. *Sensors and Actuators B: Chemical*, 296, 126665.
- [7] Castro, R. C., Páscoa, R. N., Saraiva, M. L. M., Santos, J. L., & Ribeiro, D. S. (2022). Photoluminescent and visual determination of ibandronic acid using a carbon dots/AgInS₂ quantum dots ratiometric sensing platform. *Spectrochimica Acta Part A: Molecular and Biomolecular Spectroscopy*, 267, 120592.
- [8] Wold, S. (1974). Spline functions in data analysis. *Technometrics*, 16(1), 1-11.
- [9] Picó, Y. (Ed.). (2012). Chemical analysis of food: Techniques and applications. *Academic Press*.
- [10] Castro, R. C., Saraiva, M. L. M., Santos, J. L., & Ribeiro, D. S. (2021). Multiplexed detection using quantum dots as photoluminescent sensing elements or optical labels. *Coordination Chemistry Reviews*, 448, 214181.

Acknowledgments

Rafael C. Castro thanks FCT (Fundação para a Ciência e Tecnologia) for his PhD grant ref. 2020.08465.BD. This work received financial support from PT national funds (FCT/MCTES, Fundação para a Ciência e Tecnologia and Ministério da Ciência, Tecnologia e Ensino Superior) through Grant UIDB/QUI/50006/2020. Financing from Programa INTERREG V A Espanha Portugal (POCTEP) under the project FOODSENS was also greatly appreciated.

O12 |

DEVELOPMENT OF AN ELECTROCHEMICAL APTASENSOR FOR THE DETECTION OF A BANNED ANTIMICROBIAL IN MILK

Valérie Gaudin^{1*}, Fatima Zohra Hassad¹, Céline Hédou¹, Christophe Soumet¹, Eric Verdon¹

¹ Anses, Laboratory of Fougères, European Union Reference Laboratory (EU-RL) for Antimicrobial and Dye Residue Control in Food-Producing Animals, La Haute Marche-Javené, 35302 Fougères, France

**e-mail: valerie.gaudin@anses.fr*

Introduction

Veterinary drugs can be used to treat farm animals. The persistence of veterinary drug residues and in particular antimicrobial residues in foodstuffs of animal origin can lead to risks for human health (e.g. allergies, toxicity, antimicrobial resistance). To protect public health, maximum residue limits (MRLs) are set for authorised substances [1]. For prohibited or unauthorised substances, reference point for action (RPA) takes into account the toxicological potential and pharmacological activity of the substance concerned and the dose of residues absorbed via foodstuffs [2].

Screening methods are applied for the monitoring of antimicrobial residues within the framework of national control plans, but also at the level of industry. They are the first step of the control. If a sample is declared suspect, then a confirmatory method (ie. LC-MS/MS) is performed to identify and quantify the analyte(s) present in the sample. Screening methods shall towards address the REASSURED principles (ie. real-time measurements, ease of sample collection, affordable, sensitive, specific, user-friendly, rapid and robust, equipment-free and deliverable to end users) (World Health Organization [3]). Conventional screening methods for the detection of antimicrobial residues in foodstuffs of animal origin are microbiological (based on the sensitivity of bacterial strains to the action of antimicrobials), immunological (eg. competitive immunoassay (ELISA), receptor assays), and physico-chemical methods (eg. Liquid chromatography coupled to mass spectrometry in tandem (LC-MS/MS)). Microbiological methods often lack of sensitivity, especially for non authorized substances. Immunological methods (ie. ELISA) could be applied for the screening of banned substances but they are very specific for one analyte. For non-authorised substances, most of the screening methods used for control purposes are based on LC-MS/MS techniques which are time consuming, needing expensive equipment and high skilled people.

Therefore, there is a need to develop innovative methods. Amongst biosensors, immunosensors have been widely developed for the screening of antimicrobial residues in foodstuffs [4, 5]. More recently, the interest of developing aptasensors for the detection of antimicrobial residues was demonstrated [6-8], especially for the non authorized antimicrobial chloramphenicol (CAP) [9]. Aptamers have molecular recognition properties similar to those of antibodies. They also have many advantages over antibodies, such as high thermal stability, standardised and reproducible production, tolerance to extreme pH and salt concentration, low cost (when the oligonucleotide sequence is already known) and simplicity of synthesis and labelling. Their small size allows efficient immobilisation and formation of high density monolayers. Their production and selection *in vitro* by the SELEX technique allows to obtain molecules with a very high affinity for the target.

Due to their small size, high affinity and specificity, aptasensors are considered to be a good choice for the detection of small molecules, especially antimicrobial residues. However, most of the articles are only proof of concept, usually developed for detection in aqueous solutions or buffers. Sometimes, the applicability of the system to one or two sample matrices was tested. Very few are validated as it is regulatory required for the detection of veterinary drugs in foodstuffs [10]. Therefore, aptasensors for the detection of CAP must be developed, able to detect residues below the target RPA and fully validated in the related matrices of interest.

Methods

Our objective is to develop an electrochemical aptasensor for the screening of CAP in milk, able to detect CAP below its RPA (0.3 µg/kg) which is a very low concentration.

A comprehensive bibliographical study was performed to identify the aptamers of interest for CAP [6, 9, 11]. Furthermore, regarding the different approaches for the development of aptasensors, different strategies were identified [12, 13]: Target-Induced Structure Switching mode (TISS), Target-induced dissociation mode (TID) (ie. Target induced strand release (TISR)), Target-Induced Rearrangement of aptamer fragments (TIR), competitive assay, and sandwich assay. The sandwich mode is not applicable to small molecules like antimicrobials.

We have selected four different approaches from the simplest to the more sophisticated, based on:

- TISS mode [14]: The aptamers are immobilized onto a gold electrode. In the presence of CAP, the aptamer changes to a hairpin structure, bringing CAP close to the surface and producing the electrochemical signal;
- TISR mode [15]: Magnetic nanoparticles immobilized with the aptamer (MNPs-Apt) are hybridized with a complementary DNA strand (cDNA) which is immobilized onto a gold electrode. In the presence of CAP, MNPs-Apt are released and the electrochemical signal decreases;
- TISS mode [16]: In the presence of CAP, the aptamer structure is modified and Ag⁺ ions are released; then Ag-DNAzyme is formed and cleaved its nucleic acid substrate immobilized onto the gold electrode. Therefore, the electrochemical signal increases;
- TISR mode [17]: The aptamer immobilized onto the electrode surface hybridises with a biotinylated cDNA. After addition, a streptavidine-alkaline phosphatase enzyme bound to its cDNA. The activity of the enzyme is electrochemically detected. In the presence of CAP, less enzyme could bind to the electrode and therefore the electrochemical signal decreases.

Aptasensors based on these four different approaches will be developed. They will be evaluated based on technical (ie. Detection capability, specificity, matrix effect) and non-technical criteria (ie. Quick and simple assay, cost of reagents).

Electrochemical detection (eg. Amperometric, voltametric) was selected because it is a cheap and simple technique, which allows the development of sensitive and specific methods with portable devices. Screen Printed Electrodes (SPE) are cheap, disposable devices, allowing to work with microvolumes. They were chosen because of the miniaturization and portability of the potentiostat, the easiness of use. We previously developed an amperometric method for the detection of CAP in milk based on SPE and magnetic beads immobilized with antibodies [18]. This method was inspired by the development of several methods for antibiotic residues detection performed by a Spanish team [19]. However, this method was not enough sensitive to reach a detection capability below the RPA of CAP in milk. Matrix effects are very high due to the complexity of milk samples (ie. High protein and fat contents). The extraction of CAP from the milk matrix is a critical step because it could interfere with the electrochemical detection. The ideal sample preparation should be a single dilution in buffer, but it would be possible only if the developed aptasensor is very sensitive. If not an extraction step to pre-concentrate CAP and remove matrix effects will be necessary.

Results

The project is currently in progress. The results will be presented during the symposium. Different kinds of SPE will be compared during this project (eg. Screen Printed Carbon Electrodes (SPCE), Screening Gold electrodes (SPGE). Furthermore, different electrochemical techniques will be tested and the performance characteristics compared: amperometry, cyclic voltammetry (CV), Differential Pulse Voltammetry (DPV) and Square Wave Voltammetry (SWV). The developed aptasensor(s) will be validated according to the EU regulation [10, 20]. The performance characteristics will be compared with those of the previously developed immunosensors [18].

Conclusions

The final objective is to develop a multiplex aptasensor for the detection of different banned antimicrobials: CAP, nitrofurans metabolites and dyes (eg. Malachite green) in different food matrices (eg. Milk, honey, aquaculture products). Therefore, this project is the first step that would be followed by the development of aptasensors for other banned antimicrobials. The challenge will be to gather the different aptasensors into a multiplex one. It will potentially be a useful tool for the screening of banned substances in industry or in third countries not always equipped with expensive equipment. Indeed most of multi-class methods are developed only with expensive LC-MS/MS systems [21]. These techniques are not applicable to field analyses.

References

1. Commission Regulation (EC) N° 470/2009 laying down Community procedures for the establishment of residue limits of pharmacologically active substances in foodstuffs of animal origin 2009, The European parliament and the Council: Official Journal of the European Union p. 11-22.
2. Commission Regulation (EU) 2019/1871 of 7 November 2019 on reference points for action for non-allowed pharmacologically active substances present in food of animal origin and repealing Decision 2005/34/EC (Text with EEA relevance). 2019: OJ. p. p. 41–46
3. Smith, S., et al., The potential of paper-based diagnostics to meet the ASSURED criteria. *RSC Advances*, 2018. **8**(59): p. 34012-34034.
4. Gaudin, V., Receptor-based electrochemical biosensors for the detection of contaminants in food products, in *Electrochemical Biosensors*. 2019, Elsevier. p. 307-365.
5. Felix, F.S. and L. Angnes, Electrochemical immunosensors – A powerful tool for analytical applications. *Biosensors and Bioelectronics*, 2018. **102**: p. 470-478.
6. Mehlhorn, A., P. Rahimi, and Y. Joseph, Aptamer-Based Biosensors for Antibiotic Detection: A Review. *Biosensors (Basel)*, 2018. **8**(2).
7. Gaudin, V., Contribution of Nanomaterials to the Development of Electrochemical Aptasensors for the Detection of Antimicrobial Residues in Food Products. *Chemosensors*, 2021. **9**(4): p. 69.

8. Gaudin, V., The Growing Interest in Development of Innovative Optical Aptasensors for the Detection of Antimicrobial Residues in Food Products. *Biosensors*, 2020. **10**(3): p. 21.
9. Mehta, J., et al., In vitro selection and characterization of DNA aptamers recognizing chloramphenicol. *Journal of Biotechnology*, 2011. **155**(4): p. 361-369.
10. Commission Implementing Regulation (EU) 2021/808 of 22 March 2021 on the performance of analytical methods for residues of pharmacologically active substances used in food-producing animals and on the interpretation of results as well as on the methods to be used for sampling and repealing Decisions 2002/657/EC and 98/179/EC (Text with EEA relevance). *Official Journal of the European Union*, 2021. **L 180**: p. 84–109
11. Khoshbin, Z., et al., Aptasensors as the Future of Antibiotics Test Kits-A Case Study of the Aptamer Application in the Chloramphenicol Detection. *Biosensors and Bioelectronics*, 2018.
12. Walter, J., et al., Aptasensors for Small Molecule Detection. *Zeitschrift fur Naturforschung B*, 2012. **67b**: p. 976-986.
13. Dong, X., et al., Ultrasensitive detection of chloramphenicol using electrochemical aptamer sensor: A mini review. *Electrochemistry Communications*, 2020. **120**: p. 106835.
14. Pilehvar, S., et al., Aptasensing of Chloramphenicol in the Presence of Its Analogues: Reaching the Maximum Residue Limit. *Analytical Chemistry*, 2012. **84**(15): p. 6753-6758.
15. Cao, L., et al., Separation/Concentration-signal-amplification in-One Method Based on Electrochemical Conversion of Magnetic Nanoparticles for Electrochemical Biosensing. *Electroanalysis*, 2018. **30**(3): p. 517-524.
16. Huang, Y., et al., Sensitive Detection of Chloramphenicol Based on Ag-DNAzyme-Mediated Signal Amplification Modulated by DNA/Metal Ion Interaction. *Biosensors and Bioelectronics*, 2019: p. 45-49.
17. Yan, L., et al., A simple and sensitive electrochemical aptasensor for determination of Chloramphenicol in honey based on target-induced strand release. *Journal of Electroanalytical Chemistry*, 2012. **687**(0): p. 89-94.
18. Gaudin, V., et al., Development and Optimization of an Amperometric Immunosensor for the Detection of Banned Antibiotic Residues in Honey. *Proceedings*, 2020. **60**(1): p. 48.
19. Conzuelo, F., et al., Rapid screening of multiple antibiotic residues in milk using disposable amperometric magnetosensors. *Analytica Chimica Acta*, 2014. **820**(0): p. 32-38.
20. Gaudin, V., State of the art in the validation of screening methods for the control of antibiotic residues: is there a need for further development? *Food Additives & Contaminants: Part A*, 2017. **34**(9): p. 1528-1552.
21. Chen, D., et al., Development of a multi-class method to determine nitroimidazoles, nitrofurans, pharmacologically active dyes and chloramphenicol in aquaculture products by liquid chromatography-tandem mass spectrometry. *Food Chemistry*, 2020. **311**: p. 125924.

Acknowledgments

This work was financially supported by the European Union Reference Laboratory for Antibiotic Veterinary Medicinal Product and Dye Residues in Food at the French Agency for Food, Environmental and Occupational Health & Safety (ANSES).

P9 |

DISPOSABLE MOLECULARLY IMPRINTED ELECTROCHEMICAL SENSOR CONTAINING REDUCED GRAPHENE OXIDE AND NICKEL NANOPARTICLES FOR DETERMINATION OF P-COUMARIC ACID IN FRUIT PEELS

E. Buffon^{1,2}, N.R. Stradiotto^{1,2}

¹ Institute of Chemistry, São Paulo State University (UNESP), 14800-060, Araraquara, São Paulo, Brazil

² Bioenergy Research Institute, São Paulo State University (UNESP), 14800-060, Araraquara, São Paulo, Brazil

*e-mail: edervaldo.buffon@unesp.br

Introduction

p-Coumaric acid (p-CA) has been the subject of several studies due to its beneficial effects on human health [1]. The pharmacological effects of p-CA include high activity to eliminate free radicals, anti-inflammatory, antimicrobial, antineoplastic and antidiabetic activities, as well as neuroprotective, hepatoprotective and nephroprotective effects [1–3]. In this sense, p-CA has been used to obtain several products, including food, cosmetics, pharmaceuticals and chemicals [2]. Considering the importance of p-CA, the development of simple, sensitive, selective, accurate and low-cost analytical methods for the determination of this phenolic acid in different matrices is essential.

In general, electrochemical sensors are simple, sensitive and low-cost devices. However, the lack of selectivity towards the target molecule is the main disadvantage of these sensors. The development of electrochemical sensors based on molecularly imprinted polymers (MIPs) is an alternative to overcome the lack of selectivity of conventional electrochemical detections [4]. 3-Indolacetic acid (3IAA) is a functional monomer that can be used for the development of MIP-based electrochemical sensors due to its easy polymerization, mechanical stability and ability to interact with several analytes. Apart from MIPs, another trend in the development of electrochemical sensors is the use of disposable electrodes. These devices have some advantages when compared to conventional electrochemical systems, such as miniaturization, low-cost, mass production and absence of memory effect. To increase the sensitivity of disposable electrodes, conductive materials have been added to the surface of these electrodes, such as reduced graphene oxide (rGO) and metallic nanoparticles.

Nickel nanoparticles (NiNPs) are materials that have high electrical conductivity, high area/volume ratio, low-cost production and good stability over a wide range of pH and electrical potential [5,6]. rGO is a graphene-derived material obtained from the reduction of graphene oxide (GO). The electrochemical reduction from GO to rGO can be performed directly on the electrode surface in a simple and quick way [4]. The proposed electrode was applied for the detection and quantification of p-CA in banana and orange peels. These samples were selected because they have several structurally similar phenolic compounds in their compositions; this makes these samples suitable for evaluating the performance of the proposed sensor for sensitive, selective and accurate p-CA detection.

Methods

Initially, the screen-printed electrode (SPE) from DropSens (Oviedo, Spain) was activated in a $0.50 \text{ mol L}^{-1} \text{ H}_2\text{SO}_4$ solution applying a potential range from -0.20 to 1.2 V at 100 mV s^{-1} until the electrode currents present stable values (~ 20 cycles). The activated SPE was washed with ultrapure water and modified with rGO as previously described [7]. Here, $50 \mu\text{L}$ of a solution of $0.10 \text{ mol L}^{-1} \text{ Na}_2\text{SO}_4$ containing $0.50 \text{ mg mL}^{-1} \text{ GO}$ were dripped onto the SPE surface and a potential of -1.4 V was applied until an electrodeposition charge of 1.0 mC is obtained. Then, the SPE/rGO was decorated with NiNPs using a solution of $0.10 \text{ mol L}^{-1} \text{ Na}_2\text{SO}_4$ containing $5.0 \times 10^{-3} \text{ mol L}^{-1} \text{ NiSO}_4 \cdot 7\text{H}_2\text{O}$. NiNPs were electrodeposited on the SPE/rGO surface applying a potential of -1.2 V until an electrodeposition charge of 5.0 mC is obtained.

The preparation of the MIP film on the SPE/rGO-NiNPs surface was carried out by the electropolymerization of 3IAA (monomer) in the presence of p-CA (template molecule). To this end, $50 \mu\text{L}$ of a solution of phosphate buffer (PB, 0.10 mol L^{-1} , pH 8.0) containing $5.0 \times 10^{-3} \text{ mol L}^{-1} \text{ 3IAA}$ and $4.0 \times 10^{-3} \text{ mol L}^{-1} \text{ p-CA}$ were dripped onto the SPE/rGO-NiNPs surface. Electropolymerization was carried out by cyclic voltammetry, where a potential range from 0 to 0.70 V at 50 mV^{-1} was applied during three voltammetric cycles. Then, a solution containing ethanol and acetic acid (9:1, v:v) was dripped onto the electropolymerized surface for 60 s to remove the template molecules from the polymeric structure and, consequently, the formation of the imprinted cavities; these steps led to the SPE/rGO-NiNPs-MIP electrode. For comparison, a non-imprinted sensor was prepared using the same experimental conditions in the absence of p-CA; this non-imprinted device was called SPE/rGO-NiNPs-NIP and used as a control material during molecular recognition experiments.

3. Results

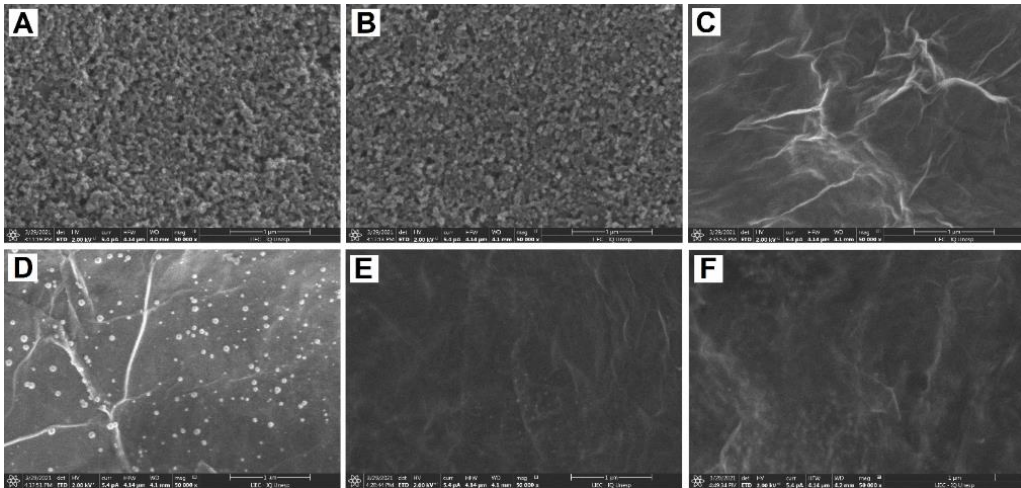


Figure 1. SEM images for: SPE (A) before and (B) after the activation step, (C) SPE/rGO, (D) SPE/rGO-NiNPs, (E) SPE/rGO-NiNPs-MIP and (F) SPE/rGO-NiNPs-NIP.

The modified electrode was characterized by scanning electron microscopy (SEM). Figs. 1A and 1B show the SPE surface before and after the activation step, respectively. Here, one can observe that the activation process did not promote any significant change on the electrode surface. Fig. 1C shows the SPE/rGO surface, where rGO sheets were electrodeposited on the SPE substrate. When compared to SPE, the SPE/rGO surface presented a rougher appearance due to the presence of the rGO sheets. Fig. 1D shows the SPE/rGO-NiNPs surface, where one can observe that the NiNPs were electrodeposited on the rGO sheets without the formation of agglomerates; these nanoparticles were spherical in shape and presented an average diameter of 34 nm. Figs. 1E and 1F show the SPE/rGO-NiNPs-MIP and SPE/rGO-NiNPs-NIP surfaces after electropolymerization, respectively. Here, one notices the presence of a poly(3IAA) film on the SPE/rGO-NiNPs surface; this polymeric film was formed uniformly on the electrode surface and covered all rGO sheets and NiNPs.

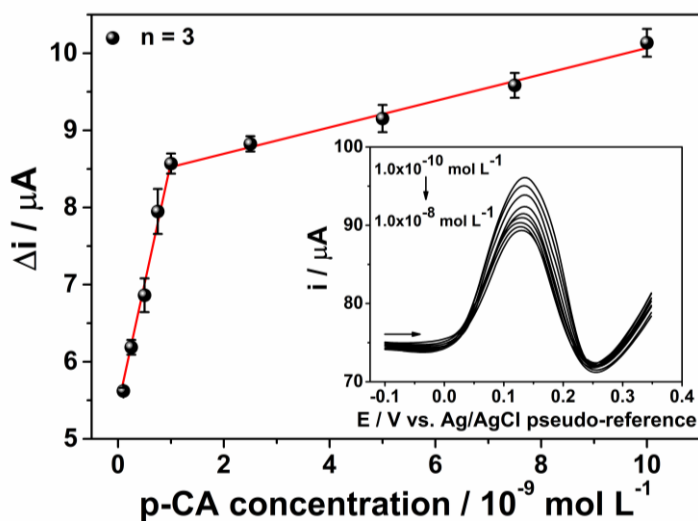


Figure 2. Analytical curve for the SPE/rGO-NiNPs-MIP electrode after the rebinding procedure using different p-CA concentrations. Insert: DPVs obtained after the rebinding procedure using a solution of 0.50 mol L^{-1} KCl containing $5.0 \times 10^{-3} \text{ mol L}^{-1}$ $\text{K}_3[\text{Fe}(\text{CN})_6]$ as an electrochemical probe.

Under optimized conditions, the analytical performance of the SPE/rGO-NiNPs-MIP electrode for p-CA recognition was evaluated through an indirect approach by differential pulse voltammetry using $5.0 \times 10^{-3} \text{ mol L}^{-1}$ $\text{K}_3[\text{Fe}(\text{CN})_6]$ in 0.50 mol L^{-1} KCl solution as a redox probe. The proposed electrode presented two linear ranges: 1.0×10^{-10} to $1.0 \times 10^{-9} \text{ mol L}^{-1}$ and 1.0×10^{-9} to $1.0 \times 10^{-8} \text{ mol L}^{-1}$ (see Fig. 2). The figures of merit, such as limits of detection (LOD) and quantification (LOQ) were calculated from the first linear range (1.0×10^{-10} to $1.0 \times 10^{-9} \text{ mol L}^{-1}$). The values obtained were: $\text{LOD} = 8.1 \times 10^{-11} \text{ mol L}^{-1}$ and $\text{LOQ} = 2.7 \times 10^{-10} \text{ mol L}^{-1}$; these values indicate that the SPE/rGO-NiNPs-MIP electrode has a good sensitivity for p-CA detection. The SPE/rGO-NiNPs-MIP electrode also presented higher sensitivity for p-CA detection when compared to the molecules of gallic acid (GA), caffeic acid (CA), ferulic acid (FA), ascorbic acid (AA) and quercetin (QT). In this study, the SPE/rGO-NiNPs-MIP electrode exhibited a degree of sensitivity for p-CA detection of nearly 4.5, 5.1, 5.2, 9.2 and 26.9 times higher than GA, CA, FA, AA and QT, respectively. Furthermore, this device exhibited excellent intra-day and inter-day repeatability as well as remarkable stability.

To evaluate the applicability of the developed method, the SPE/rGO-NiNPs-MIP electrode was applied for the determination of p-CA in orange and banana peels. The extraction of p-CA from orange peels carried out for 40 min at 30 °C in 80% (v:v) methanol solution, while the extraction from banana peels was conducted in 95% (v:v) ethanol solution for 60 min at 30 °C. The extracts obtained from the banana and orange peels were filtered and diluted 10,000 and 15,000 times in PB (0.10 mol L⁻¹, pH 6.5), respectively. The determination of p-CA in these extracts was performed by the standard addition method. The results obtained were validated by recovery tests. By taking into account the dilution factors, the p-CA concentration found in the banana and orange peel samples were 4.6×10⁻⁶ and 5.6×10⁻⁶ mol L⁻¹ (n = 3), respectively. The mean recovery values ranged from 96 to 102% (RSDs ≤ 4.8%). These results show that the SPE/rGO-NiNPs-MIP sensor has a good analytical performance for p-CA determination in fruit peels.

Conclusions

This work reports the development of a disposable molecularly imprinted electrochemical sensor through the electropolymerization of 3IAA on the of SPE/rGO-NiNPs surface. The results showed that rGO and NiNPs increased the sensitivity of the sensor for the selective detection of p-CA. Under optimal conditions, the SPE/rGO-NiNPs-MIP sensor exhibited low limits of detection and quantification, apart from good selectivity, repeatability, stability and accuracy. This sensor was applied for the determination of p-CA in banana and orange peel samples using small volumes of solutions and samples, which is interesting from the point of view of green chemistry and environmental chemistry. The results obtained showed that the SPE/rGO-NiNPs-MIP electrode can be successfully applied for the determination of p-CA in fruit peels.

References

- [1] P.S. Ferreira, et al., *Crit. Rev. Anal. Chem.* 49 (2019) 21–31.
- [2] R. Long, et al., *Talanta* 196 (2019) 579–584.
- [3] L.M. Ferreira, et. al., *Can. J. Chem.* 95 (2017) 113–119.
- [4] C. Zhang, et al., *Sens. Actuators B: Chem.* 284 (2019) 13–22.
- [5] F.W. Campbell, R.G. Compton, *Anal. Bioanal. Chem.* 396 (2010) 241–259.
- [6] M.A. Beluomini, et al., *Microchim. Acta.* 185 (2018) 170.
- [7] E. Buffon, N.R. Stradiotto, *Microchem. J.* 167 (2021) 106339.

Acknowledgments

The authors would like to thank São Paulo Research Foundation (FAPESP; grants #2017/22401-8, #2019/13818-8 and #2020/16521-3) for the financial support granted during the course of this research

NOVOS MATERIAIS | NUEVOS MATERIALES | NEW MATERIALS

O13 |

LASER-INDUCED GRAPHENE ON POLYIMIDE AND PAPER SUBSTRATES FOR LOW-COST AND FLEXIBLE ELECTROCHEMICAL BIOSENSORS

Nuno F. Santos¹, Bohdan Kulyk¹, Sónia O. Pereira¹, Alexandre F. Carvalho¹,
António J. Fernandes¹, Florinda Costa¹

¹ *i3N & Physics Department, University of Aveiro, Aveiro, Portugal*

* *Nfsantos@ua.pt*

Introduction

Laser-induced graphene (LIG) is a 3D, foamy rGO-like electrically conductive material obtained by laser irradiation of carbon-containing substrates, which are pyrolyzed by the high energy density of an incident laser beam. Since the first report on its controlled production back in 2014, it is becoming increasingly evident that this easy and cost-effective synthesis approach is of great value for many graphene-based devices and applications, circumventing many limitations of other graphene production methods. Electrically conductive patterns made of high surface area graphene foams can be promptly defined on insulating and flexible substrates by selective laser scribing (Figure 1) in an inexpensive, controllable, scalable and competitive manner.

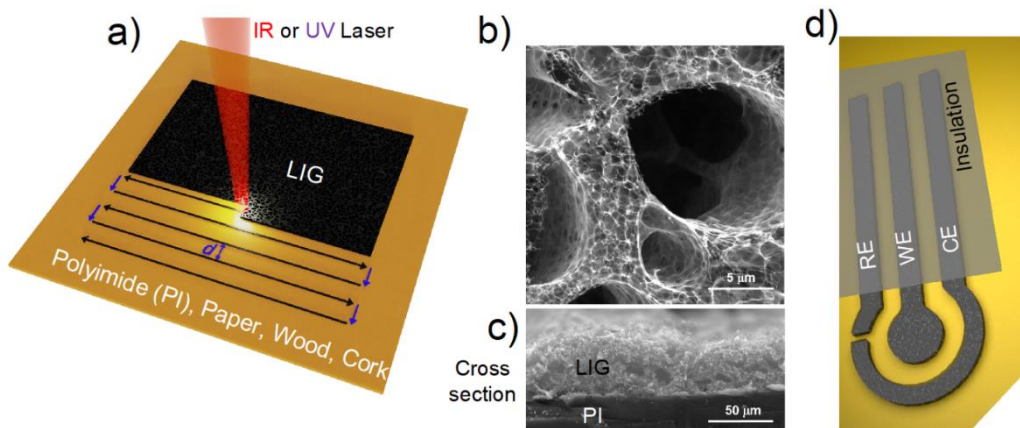


Figure 1: (a) Simplified schematics of direct laser writing of graphene on several possible substrates, (b) and (c) longitudinal and cross section SEM images of PI (Polyimide)-LIG, and (d) schematics of a typical LIG three-electrode electrochemical cell (RE- reference electrode, WE – working electrode and CE – counter electrode).

In particular, LIG presents favourable physico-chemical characteristics for application in flexible electrochemical biosensing, such as stability, high surface area and good electrical conductivity (c.a. 10 to 30 $\Omega\cdot\text{sq}^{-1}$ depending on the substrate material). This translates into fast electron transfer kinetics, up to 1.46×10^{-2} $\text{cm}\cdot\text{s}^{-1}$ as determined for PI-LIG employing $[\text{Ru}(\text{NH}_3)_6]^{2+/3+}$ redox probe [1]. It is also adequate for lab-on-skin devices and other situations where mechanical flexibility is a requirement.

Methods

The graphene selective laser scribing procedure consisted in the irradiation and carbonization of commercially available polyimide sheets, more specifically Kapton^(R), or cellulose filter paper, from Whatman^(R). For paper-LIG synthesis, cellulose filter paper was sprayed with a fire retardant and left to dry in air prior to laser irradiation. A continuous CO₂ laser (10.6 μm) equipped with a computer driven gantry holding a focusing lens or a diode-pumped Nd:YVO₄ pulsed UV laser (355 nm) equipped with a galvanometric head comprising a *f-theta* lens were employed. The scribing of graphene electrodes is accomplished through linear spaced passages of the laser beam at a given speed (usually 25 to 250 $\text{mm}\cdot\text{s}^{-1}$) and at an appropriate line separation *d* (see **Figure 1a**) so that both continuity and structural integrity of the overall film are attained. All LIG electrode types were subjected to detailed morphostructural analysis via scanning electron microscopy, Raman spectroscopy and X-ray photoelectron spectroscopy.

All electrochemical measurements were performed using a Versastat3 electrochemical station (Princeton Applied Research) in three-electrode cell configuration at low area-volume ratio conditions, e.g. 25 mm^2 working electrode area in 50 mL electrolyte solution.

Results

A summary of our research in LIG-based electrochemical sensors scribed in polyimide and paper will be presented, showing efficient detection and quantification of clinically-relevant biomarkers such as dopamine (Figure 2a), glucose (Figure 2b) and uric acid (Figure 2c) [1-3].

Indeed, LIG-based biosensors on PI substrates (PI-LIG) can efficiently and selectively quantify clinically relevant concentrations of dopamine (DA), down to 100 nM, in mixtures with ascorbic acid and uric acid interferents both present at physiologically relevant concentrations (100 μM) (Figure 2a). Moreover, it enables extreme sensitivities of 93 $\mu\text{A } \mu\text{M}^{-1} \text{cm}^{-2}$ at low DA concentrations,

among the highest ever recorded employing non-enzymatic voltammetric approach, comparing favourably to highly sensitive graphene-CNTs-Au NPs composites ($9.2 \mu\text{A } \mu\text{M}^{-1} \text{cm}^{-2}$ [4]) and graphene microelectrodes ($22.1 \mu\text{A } \mu\text{M}^{-1} \text{cm}^{-2}$ [5]), among many others [1,6,7].

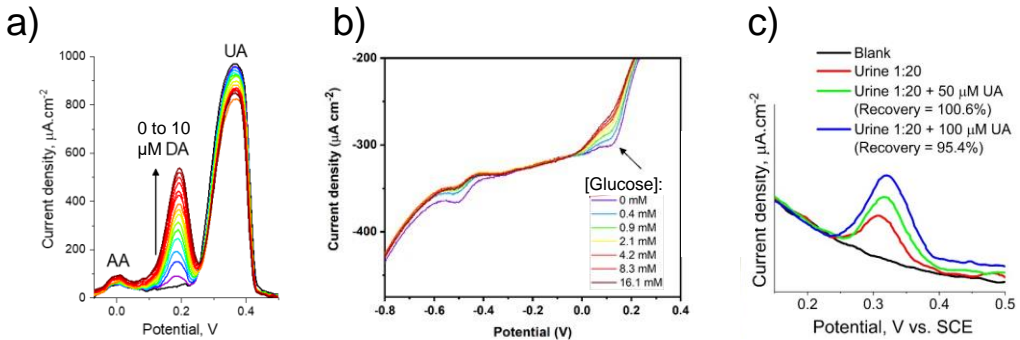


Figure 2: (a) Differential pulse voltammetry (DPV) measurements of dopamine (DA) in ascorbic acid (AA) and uric acid (UA) -containing PBS electrolyte employing PI-LIG transducers. (b) Cathodic branch of cyclic voltammetry (CV) measurements in glucose containing PBS electrolyte employing GOx-functionalized PI-LIG. (c) DPV measurements in dilute human urine samples employing non-enzymatic Paper-LIG sensing unit, yielding UA recoveries close to 100% for spiked samples.

Moreover, glucose oxidase (GOx) adsorbed on PI-LIG transducer surface via simple dropcast method allow for glucose determination in a wide range of concentrations via a cathodic peak at c.a. 0.15 V vs. Ag/AgCl (1 M KCl) (Figure 2b). While the mechanism of detection is not yet fully understood, the occurrence of GOx-LIG direct electron transfer or the formation of a quinone derivative, which mediates electron transfer from GOx to LIG, are strong hypothesis [2].

On the other hand, paper-LIG non-enzymatic biosensors were able to detect and quantify uric acid following a linear response ($R^2 = 0.999$) from 10 to 250 μM with a limit of detection of 3.97 μM , a sensitivity of $0.363 \mu\text{A cm}^{-2} \cdot \mu\text{M}^{-1}$ and adequate selectivity in both synthetic urine formulations and ascorbic acid (AA)-containing electrolytes. Determination of urinary UA content in real samples yielded recoveries of spiked samples of close to 100% at satisfactory reproducibility and stability (Figure 2c) [3].

Conclusions

These results point to the adequateness of these cheap, lightweight, flexible and disposable LIG electrodes to be employed in biosensing devices for point-of-care approaches, a key aspect towards an effective and affordable personalized medicine paradigm envisaged for the near future. Moreover, paper-LIG further adds the advantage of eco-friendliness, a key aspect regarding disposability. Whilst low limits of detection and sensitivities have been demonstrated, more work is still necessary in order to further expand the applicability of LIG regarding other analytes/biomarkers and fully comprehend the fundamental mechanisms beyond the analytical response. Importantly, the scrutiny of the sensing performance in terms of stability and repeatability in complex physiological fluids is still relatively scarce, yet necessary to definitely implement these outstanding transducer materials as valid alternatives in real-world point-of-care scenarios.

References

- [1] N. F. Santos, S. et. al., "IR and UV Laser-induced Graphene: application as dopamine electrochemical sensors". *Advanced Materials and Technologies* 6 6 (2021): 2100007.
- [2] S. O. Pereira, N. F. Santos, A. F. Carvalho, A. J. S. Fernandes, F. M. Costa, "Electrochemical Response of Glucose Oxidase Adsorbed on Laser-Induced Graphene". *Nanomaterials* 11 (2021): 1893.
- [3] B. Kulyk, S. O. Pereira, A. J. S. Fernandes, E. Fortunato, F. M. Costa, N. F. Santos, "Laser-induced graphene from paper for non-enzymatic uric acid electrochemical sensing in urine" (Unpublished).
- [4] Ramakrishnan, S. et al. One-step synthesis of Pt-decorated graphene-carbon nanotubes for the electrochemical sensing of dopamine, uric acid and ascorbic acid. *Anal. Methods* 7, 779–786 (2015).
- [5] Ding, X. et al. A novel nitrogen-doped graphene fiber microelectrode with ultrahigh sensitivity for the detection of dopamine. *Electrochem. commun.* 72, 122–125 (2016).
- [6] Jackowska, K. and Krysinski, P., "New trends in the electrochemical sensing of dopamine". *Anal. Bioanal. Chem.* 405, 3753 (2013).
- [7] Tukimin, N., et al., Y, "Review—Electrochemical Detection of Uric Acid, Dopamine and Ascorbic Acid". *J. Electrochem. Soc.* 165, B258–B267 (2018).

O14 |

UV PHOTODETECTOR BASED ON REDUCED GRAPHENE OXIDE AND n-TYPE Si HETEROJUNCTION

J.L. Pérez Gordillo¹, A. Meléndez¹, J.J. Santiago-Aviles², N.J. Pinto¹, I. Ramos¹

¹*Department of Physics and Electronics, University of Puerto Rico at Humacao, Humacao, Puerto Rico, 00791*

²*Department of Electrical and Systems Engineering, University of Pennsylvania, Philadelphia, PA 19104*

**e-mail: idalia.ramos@upr.edu*

Introduction

The electrical, mechanical, thermal, and optical properties of reduced graphene oxide (rGO) make it an attractive material for the fabrication of photodetectors and other optoelectronic devices. In comparison with graphene, rGO can be prepared using inexpensive materials and simpler fabrication methods with high yields [1]. The properties of this material can be tuned with the precursor solution, synthesis, and reduction processes. A key to the production of high quality rGO is the reduction of oxygen [2]. The sheet resistance of rGO films decreases as the reduction temperature increases. This is attributed to an increase in the number of delocalized π bonds for sp^2 carbons by the reduction. The lower resistance should facilitate the separation and transportation of photo-carriers [3].

In this research, rGO was synthesized by the thermal decomposition of sucrose and reduced by thermal annealing under a nitrogen atmosphere [4]. A heterojunction diode was fabricated by depositing a rGO film on a cleaved n-type Silicon/Silicon Oxide (Si/SiO₂) substrate. We studied the response of the heterojunction to UV irradiation at room temperature. We will discuss the preparation and characterization of rGO, the heterojunction fabrication, and analysis of UV photoconduction.

Methods

rGO

Graphene oxide (GO) was prepared by hydrothermal carbonization of a 0.1 M solution of sucrose (sugar) in H₂O at 200°C. The GO was reduced by thermal annealing at 600°C for 2 h in a nitrogen atmosphere. The resultant rGO flakes were characterized using Scanning Electron Microscopy (SEM), Energy Dispersive Spectroscopy (EDS), profilometry, and UV-Vis spectroscopy. A schematic of the preparation process is depicted in Fig. 1.

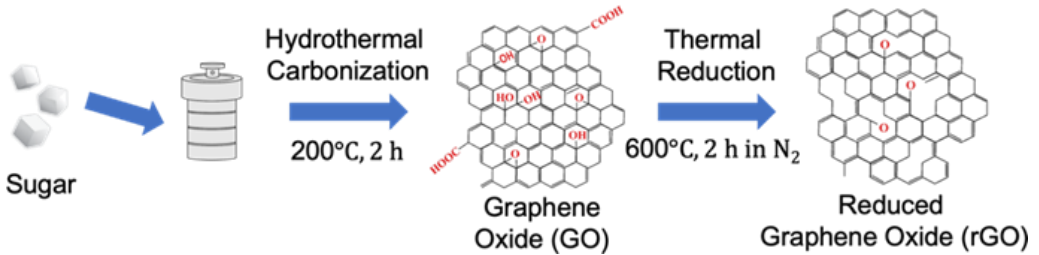


Fig.1. Schematic of rGO preparation process: GO is produced by hydrothermal carbonization of sucrose (sugar) and reduced to rGO by sintering under nitrogen.

Device

The rGO/n-Si diode was fabricated by using a commercially available n-doped Si wafer with a 200 nm oxide layer, with pre-patterned gold electrodes over the oxide surface. A Si/SiO₂ substrate was cleaved through the electrodes. The exposed cleaved surface had the edge of the gold electrode separated from the doped Si by the insulating SiO₂ layer. We then transferred the rGO film onto the edge of the substrate, bridging the insulating layer. The sample was oven dried in air at 70°C for at least 1 h before performing any measurements. A schematic of the device is shown in the inset of Fig. 3a.

UV-Photoconduction

The current-voltage (I-V) characteristics of the diode were measured in vacuum at room temperature using a Keithley 6517B electrometer by applying voltages from -1 V to +1 V in darkness and after irradiation. A 4 W-UV-lamp (2.46 W/m²) with a 365 nm wavelength, was used to irradiate the rGO-n-Si heterojunction. The measurements were conducted in the reverse bias region with no applied voltage (0 V) and low voltages of -0.1 V and -0.5 V. The times of exposure to UV light ranged from 5 to 20 s.

Results

rGO Characterization

Figure 2(a) shows a typical EDS spectrum and SEM image (inset) for a rGO film. The spectrum reveals 86.6 atomic % of Carbon and 13.4 % of Oxygen. The average thickness of rGO films analyzed with profilometry (results not shown) was 110 nm. The optical bandgap of rGO was estimated from the UV-Vis absorption spectra in Fig. 2(b) (inset). The intercept of the best fit of the Tauc

plot: $(\alpha hv)^2$ versus hv Fig. 2(b) gives a bandgap of $E_g = 2.12 \pm 0.01 \text{ eV}$ [5]. This value is consistent with others reported in literature that range between 1.00 and 3.11 eV [5-6].

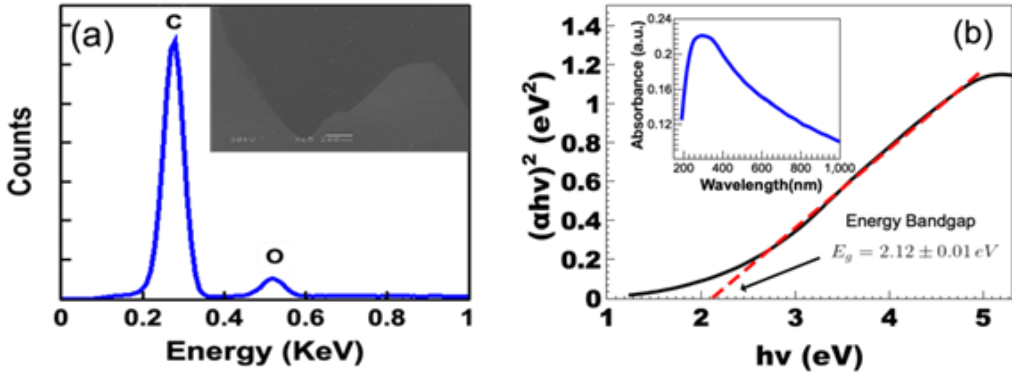


Fig. 2. (a) EDS spectrum and SEM image (inset) of rGO film.(b) Tauc plot with bandgap determination and UV-Vis spectrum (inset).

Heterojunction diode

The I-V plot of the rGO/n-Si diode at room temperature in darkness is shown in Fig. 3(a), with schematic diagrams of the device as insets. The results show the typical exponential behavior of a rectifying diode in forward and reverse bias.

The diode current can be represented $I(T, V) = I_S \left(e^{\frac{qV}{nkT}} - 1 \right)$, where I_S is the saturation current, q is the electron charge, V is the applied voltage, n is the ideality factor, k is the Boltzmann constant, and T is the temperature.

To study the photodetection properties and the rectification behavior of the device under irradiation we analyzed the photocurrent: $I_{ph} = |I_L - I_d|$ and responsivity: $R_p = \frac{I_{ph}}{P_{XA}}$ [7-8]. In these equations, I_L is the current under irradiation and I_d is the current in darkness, P is the power density of the UV lamp, and A is the sample area impacted by light. The device maintains the rectification properties under UV illumination with a 365 nm wavelength. The values of the responsivity are depicted in Fig. 3(b). The high values of R_p suggest the phenomenon of carrier-multiplication or internal gain exist [7]. These results are consistent with others reported in literature for rGO heterojunctions. A heterojunction with other semiconductor material creates a built-in electric field

at the junction that facilitates the separation of charge carriers. Prevention of electron-hole recombination and their effective collection make heterojunction photodetectors highly efficient [8].

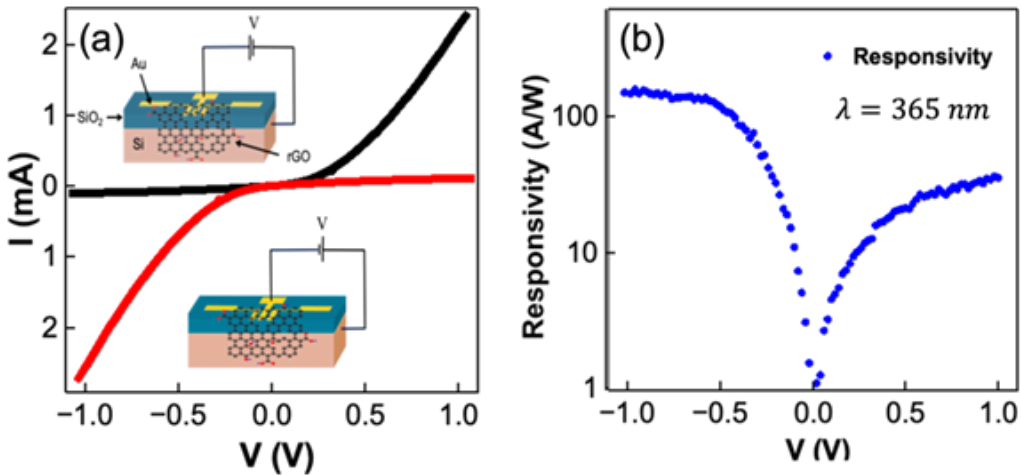


Fig. 3. (a) I-V characteristics of rGO/n-Si heterojunction in forward (black) and reverse (red) bias. The inset shows schematics of the device with electrical connections in forward and reverse bias. (b) Responsivity after irradiation with UV light for 5 s.

Figure 4(a) shows the optical response of the device for ON and OFF switching of the light, with applied voltages of -0.1 V and -0.5 V for time intervals of 5 s. The response and recovery times for -0.1 V and -0.5 V are shown in Fig. 4(b) and 4(c), respectively. The response time (t_{resp}) to UV light is computed as the time needed for the sensor to reach between 10% until 90% of the maximum current. The recovery time (t_{rec}) is the time to go from 90% to 10% of the maximum current. Various consecutive cycles with sharp transitions between the ON and OFF states were measured for our device. The measurements are stable and reversible. The response times are 1.2 s for -0.1 V and 1.4 s for -0.5 V. The recovery times are 1.6 s for -0.1 V and 1.7 s for -0.5 V. The values reported in literature for rGO devices vary considerably and range from microseconds to hundreds of seconds [7-8]. Fig. 4(d) shows the photosensor response to UV light without an external voltage source. The stable and reversible photoresponse suggest the rGO/n-Si heterojunction has the potential to be used in self powered devices.

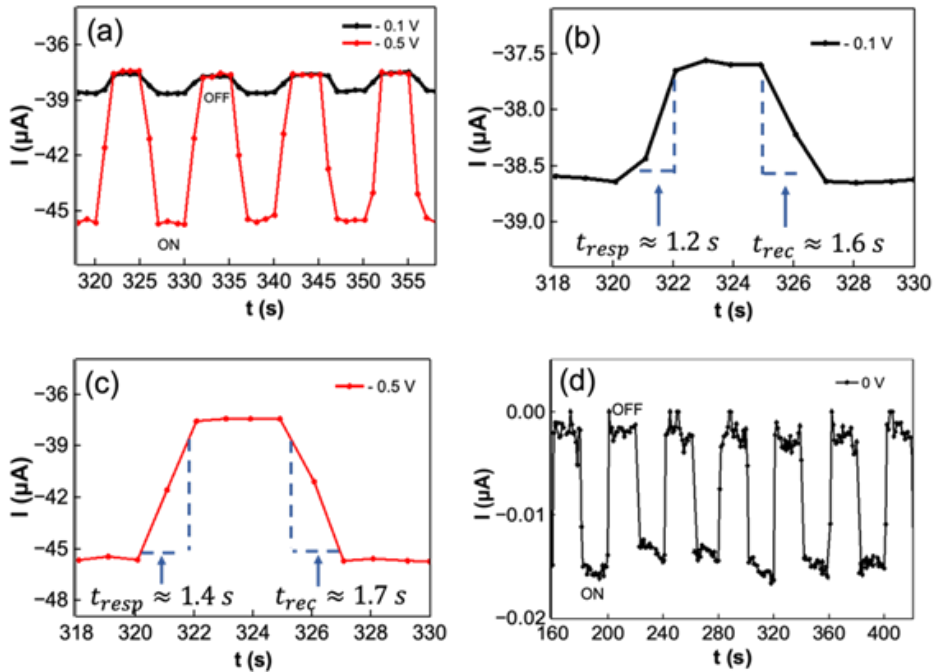


Fig. 4. (a) on-off response to uv light (365 nm) exposure in 5 s intervals, for applied voltages of -0.1 v and -0.5 v. (b) and (c) response and recovery times for a typical on-off cycle, with -0.1 v and -0.5v. (d) on-off response in 20 s intervals with 0 v bias.

Conclusions

High quality and electrically conductive rGO films were synthesized from hydrothermal carbonization of sucrose and thermal annealing. A rGO-nSi heterojunction was fabricated by depositing rGO onto the cleaved edge of a SiO₂/Si substrate. The I-V characterization of the device shows the typical behavior of a rectifying diode in forward and reverse bias. When exposed to UV light of 365 nm, the heterojunction shows good photoconduction properties with applied low voltages of -0.1 V and -0.5 V. The responsivity values of over 100 A/W suggest very good photodetection properties. The optical response of the device for the ON/OFF switching of the UV light, for the applied biases of -0.1 V, and -0.5 V, show stable cycles with response and recovery times between 1 and 2 s. The response to UV irradiation with 0 V is a promising result and show independence from the voltage source. The zero or low voltage photodetection properties, and the simple and inexpensive methods used to produce rGO and fabricate this device; make it attractive for the development of self-powered photoconduction devices.

References.

- [1] Smith, A.T., LaChance, A.M., Zeng, S., Liu, B., Sun, L., Synthesis, properties and applications of graphene oxide/reduced graphene oxide and their nanocomposites, *Nano Mater. Sci.* 1, 31-47 (2019).
- [2] Punckt, C., Muckel, F., Wolff, S., Aksay, I.A., Chavarin, C.A., Bacher, G., Mertin, W. The effect of degree of reduction on the electrical properties of functionalized graphene sheets, *Appl. Phys. Lett.* 102, 023114 (2013).
- [3] Zhu, M., Li, X., Guo, Y., Li, X., Sun, P., Zang, X., Wang, K., Zhong, M., Wu, D., Zhu, H., Vertical junction photodetectors based on reduced graphene oxide/silicon Schottky diodes, *Nanoscale*, 2014,6, 4909-4914 (2014).
- [4] Tang, L., Li, X., Ji, R., Teng, K.S., Tai, G., Ye, J., Wei, C., and Lau, S.P. Bottom-up synthesis of large-scale graphene oxide nanosheets, *J. Mater. Chem.* 22, 5676 (2012).
- [5] Jilani, A., Othman, M.H.D., Ansari, M.O., Kumar, R., Alshahrie, A., Ismail, A.F., Khan, I.U., Sajith, V.K., Barakat, M.A., Facile spectroscopic approach to obtain the optoelectronic properties of few-layered graphene oxide thin films and their role in photocatalyst, *New J. Chem.* 41, 14217-14227 (2017).
- [6] Abid, P.S., Islam, S.S., Mishra, P., Ahmad, S. Reduced graphene oxide (rGO) based wideband optical sensor and the role of Temperature, Defect States and Quantum Efficiency, *Sci. Rep.* 8, 3537 (2018).
- [7] Kumar, G., Prakash, N., Singh, M., Chakravorty, A., Kabiraj, D., Singh, S.P., Prabir, P., Khanna, S.P. Solution-Processed-2D on 3D Heterojunction UV-Visible Photodetector for Low-Light Applications, *ACS Appl. Electron. Mater.* 1, 1489-1497 (2019).
- [8] Li, G., Liu, L., Wu, G. Chen, W., Qin, S., Wang, Y., Zhang, T. Self-Powered UV-Near Infrared Photodetector Based on Reduced Graphene Oxide n-Si Heterojunction, *Small* 12(36), 5019-5026 (2016).

Acknowledgments. This research is sponsored by the PENN-UPR Partnership for Research and Education in Materials (PREM) with funds from the USA National Science Foundation (NSF) Grant DMR-2122102.

O15 |

HOST-GUEST SENSING SYSTEM BASED ON SULFONATOCALIXARENE AND PYRANOFLAVYLIUM DYE FOR BIOGENIC AMINE SENSING DURING FOOD SPOILAGE

Ana Sofia Pires^a, Nuno Basílio^b, Vânia Gomes^a, Nuno Mateus^a, Victor de Freitas^a,
Luís Cruz^{a,*}

^aREQUIMTE/LAQV, Department of Chemistry and Biochemistry, Faculty of Sciences,
University of Porto, Porto, Portugal.

^bLaboratório Associado para a Química Verde (LAQV), REQUIMTE, Departamento de
Química, Faculdade de Ciências e Tecnologia, Universidade Nova de Lisboa,
2829-516 Monte de Caparica, Portugal.

* luis.cruz@fc.up.pt

Introduction

Food quality is a central issue in today's food economics mainly due to the growing demands of consumers. Information availability and environmental concerns are the reasons for the growing scientific research on this field, ultimately leading to an increase in food quality [1]. The rise of health problems due to food spoilage or toxicity has motivated researchers to focus on the development of innovating new methods for controlling food quality, serving the purpose of public health [2]. Biogenic amines are biologically active nitrogen-containing compounds, formed in the normal metabolism of animals, plants and micro-organisms via decarboxylation of the respective amino acid through enzymatic reactions. The presence of these biomolecules in food products is undesirable and their ingestion in significant amounts can cause headaches, respiratory distress, heart palpitations and several allergic disorders [3]. Although biogenic amines are usually quantifiable by chromatographic methods, this kind of analysis is unsuitable for *in situ* sensing or rapid screening [4]. The main goal of this work was the development of a colorimetric host-guest molecular switch based on interactions between a bioinspired 10-methylpyrano-4'-hydroxyflavylium[5] guest dye and the *p*-sulfonatocalix[8]arene macrocyclic host with sensing ability for biogenic amines.

Methods

The interaction between macrocycle and pigment as well as biogenic amine detection was evaluated through UV-Vis spectroscopy. This non-covalent interaction in a host/guest system has shown promising results for applications regarding functional materials or switch systems as covered in multiple scientific papers [6].

Results

The macrocycle-dye system was optimized in terms of molecular ratio and the working pH was taken from the maximum differences between the free pigment (pK_a 6.72) to the one complexed with the macrocycle (pK_a 8.45) (Figure 1).

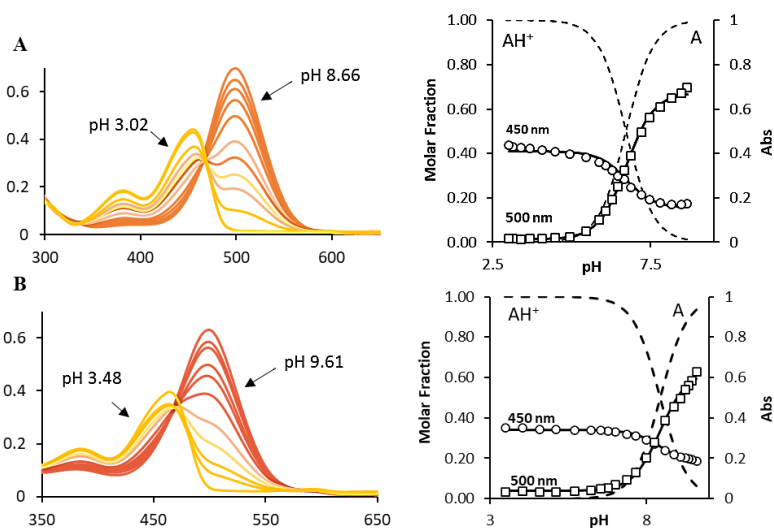


Figure 1- A) Spectral variation as a function of pH of 10-methylpyrano-4'-hydroxyflavylium (Dye, 0.5 mM) and fitting achieved for pK_a = 6.72. B) Spectral variation as a function of pH of Dye-SC8 (0.1:0.5 mM) and fitting achieved for pK_a = 8.15.

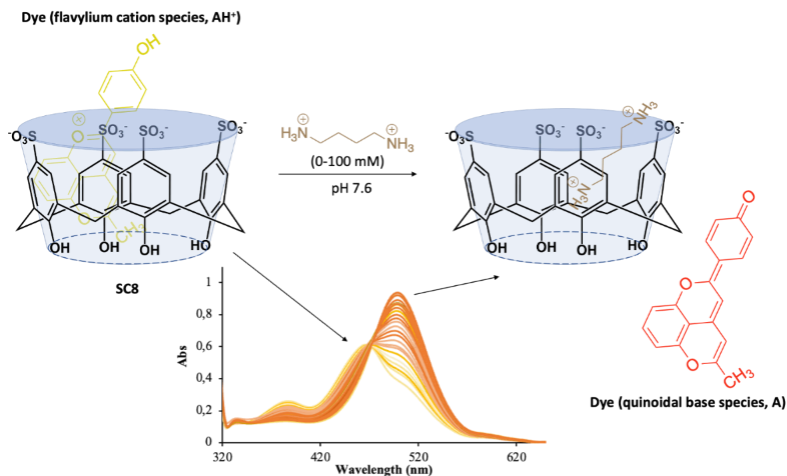


Figure 2: Example of the Dye-SC8 (0.05:0.5 mM) system in the presence of increasing concentrations of putrescine (0-100 mM) at pH 7.6.

Overall, in a phosphate buffer solution (pH 7.6), the complex was able to encapsulate putrescine in solution with concomitant release of the quinoidal base species of dye to the bulk, with spectral variation from yellow to pink-red (Figure 2).

Conclusions

This host-guest system demonstrated great potential for the detection of biogenic amides, one of the main indicators of food spoilage.

References

- [1] Sajdakowska, M.; Gębski, J.; Gutkowska, K.; Żakowska-Biemans, S., Importance of health aspects in Polish consumer choices of dairy products. *Nutrients* **2018**, *10* (8), 1007.
- [2] Bayarri, S.; Carbonell, I.; Barrios, E. X.; Costell, E., Acceptability of yogurt and yogurt-like products: Influence of product information and consumer characteristics and preferences. *Journal of Sensory Studies* **2010**, *25*, 171-189.
- [3] Kaur, N.; Chopra, S.; Singh, G.; Raj, P.; Bhasin, A.; Sahoo, S. K.; Kuwar, A.; Singh, N., Chemosensors for biogenic amines and biothiols. *Journal of Materials Chemistry B* **2018**, *6* (30), 4872-4902.
- [4] Gomes, V.; Pires, A. S.; Mateus, N.; de Freitas, V.; Cruz, L., Pyranoflavylum-cellulose acetate films and the glycerol effect towards the development of pH-freshness smart label for food packaging. *Food Hydrocolloids* **2022**, 107501.
- [5] Gomes, V.; Guimaraes, M.; Goncalves, G.; de Freitas, V.; Cruz, L., Bioinspired synthesis and physical-chemical properties of a new 10-methylpyrano-4'-hydroxyflavylum chloride salt. *Synlett* **2020**, *31* (04), 334-338.
- [6] Romero, M. A.; Mateus, P.; Matos, B.; Acuña, A. n.; García-Río, L.; Arteaga, J. s. F.; Pischel, U.; Basílio, N., Binding of flavylum ions to sulfonatocalix [4] arene and implication in the photorelease of biologically relevant guests in water. *The Journal of Organic Chemistry* **2019**, *84* (17), 10852-10859.

Acknowledgments

This work was supported by the Associate Laboratory for Sustainable Chemistry, Clean Processes and Technologies LAQV. The latter is financed by national funds from UIDB/50006/2020. This work was also supported by the project PTDC/OCE-ETA/31250/2017 funded by FCT and FEDER. Ana Pires acknowledges the research grant from the project PTDC/OCE-ETA/31250/2017. Luís Cruz acknowledges the FCT research contract (DL 57/2016/CP1334/CT0008). Vânia Gomes acknowledges the PhD grant from FCT (SFRH/BD/136556/2018)

O16 |

PHOTOSENSITIVE NANOPOLYMERSOMES AS ELECTROACTIVE SPECIES CARRIERS: TOWARDS THE DEVELOPMENT OF BIOSENSORS

Jennifer Quinchia¹, Andrés F. Cruz-Pacheco¹, Jahir Orozco^{1*}

¹Max Planck Tandem Group in Nanobioengineering, Institute of Chemistry, Faculty of Natural and Exact Sciences, University of Antioquia, Complejo Ruta N, Calle 67 No. 52-20, Medellín 050010, Colombia.

*e-mail: grupotandem.nanobioe@udea.edu.co

Introduction

There is a considerable demand for simple but sensitive and specific detection of biomarkers of different molecular levels, particularly for diagnosing diseases. Biosensors are powerful tools for detecting low levels of targets of biological interest. The determination of biomarkers by using electrochemical biosensors is at the forefront of disease diagnosis research because of the unique features of biosensors, such as high sensitivity, specificity, accurate quantification, rapid response, versatility, and simple operation [1,2]. Furthermore, appropriate amplification strategies are needed to convert the biological recognition events into enhanced electrochemical signals in biosensors with outstanding analytical features [3,4].

Some signal amplification strategies for ultrasensitive determination of biomarkers involve nanomaterials as carriers to enrich signaling species [4,5]. They include silica, carbon, polymers, or other porous nanomaterials. Those based on vesicles are highly attractive due to their ability to encapsulate (bio)molecules or nanoparticles in their aqueous core and their hydrophobic bilayer without covalent binding. Moreover, it allows the (bio)molecules to release, retaining their (bio)activity and stability and providing chemical versatility, with an impact on the enhanced electrochemical (bio)sensing [5]. For example, liposomes (lipidic vesicles) have recently received significant attention as multi-functional carriers in immuno- and geno-assays by translating molecular recognition events into an electrochemical or colorimetric signal. This is due to their ability to encapsulate large amounts of enzymes/redox probes [6,7]. However, compared to their analogous counterparts, polymersomes (polymeric vesicles) have been less studied as multi-functional carriers in biosensors [8] despite their advantageous features, including the high chemical versatility, size-modulation, stimulus-dependent membrane permeability, and surface

modification [9]. In this context, the design of electroactive species nanocarriers based on highly stable electroactive specie-loaded nanopolymersomes with photoresponse as the release mechanism are innovative materials to be further incorporated in highly efficient immunobiosensing formats.

Methods

Two photosensitive amphiphilic copolymers (AZO-PEMA and Biotin-AZO-PEMA) were synthesized by the one-step nucleophilic addition of amine-containing hydrophobic (4-aminoazobenzene, AZO) and hydrophilic (amine-PEG3-Biotin, Biotin) moieties onto a poly(ethylene-alt-maleic anhydride) (PEMA) backbone. The amphiphilic copolymers were self-assembled by nanoprecipitation technique with the in-situ encapsulation of electroactive species of different molecular nature: (i) molecules as methylene blue (MB) and ferrocene (Fc) in the hydrophilic core and hydrophobic bilayer of polymersomes, respectively; (ii) the enzyme horseradish peroxidase (HRP); and (iii) inorganic platinum nanoparticles stabilized with polyvinylpyrrolidone (PVP-PtNPs) in the hydrophilic core (Figure 1). Experimental conditions were optimized to form the loaded polymersomes and disrupt them by ultraviolet (UV) irradiation at 365 nm. The system was fully characterized by Fourier-transform infrared spectroscopy (FTIR), nuclear magnetic resonance (NMR), dynamic light scattering (DLS), electrophoretic light scattering (ELS), transmission electron microscopy (TEM), UV spectrophotometry and electrochemical techniques.

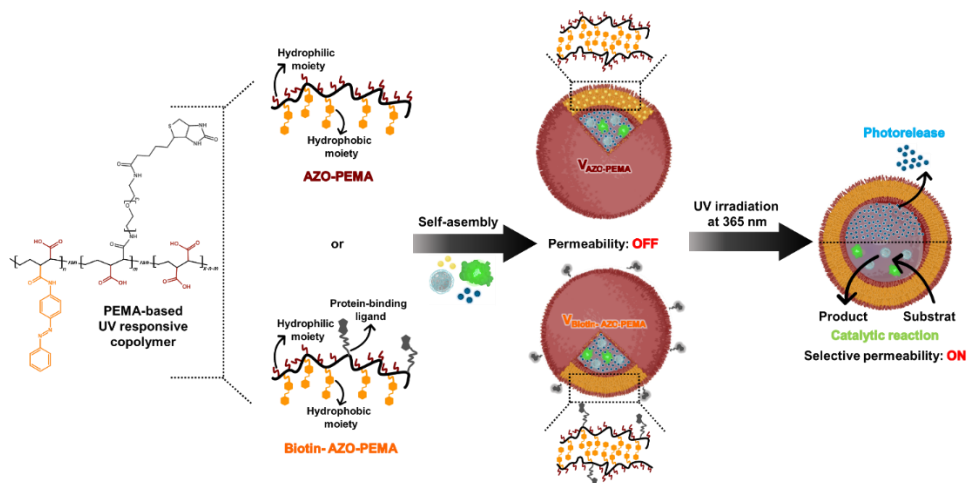


Figure 1. Schematic representation of photosensitive nanopolymersomes as electroactive species carriers. PEMA backbone was substituted with 4-aminoazobenzene (AZO) and amine-PEG3-biotin (biotin). Biotin is denoted as 'm' in the scheme; $m = 0$ for AZO-PEMA. n in the scheme represents the degree of substitution of AZO.

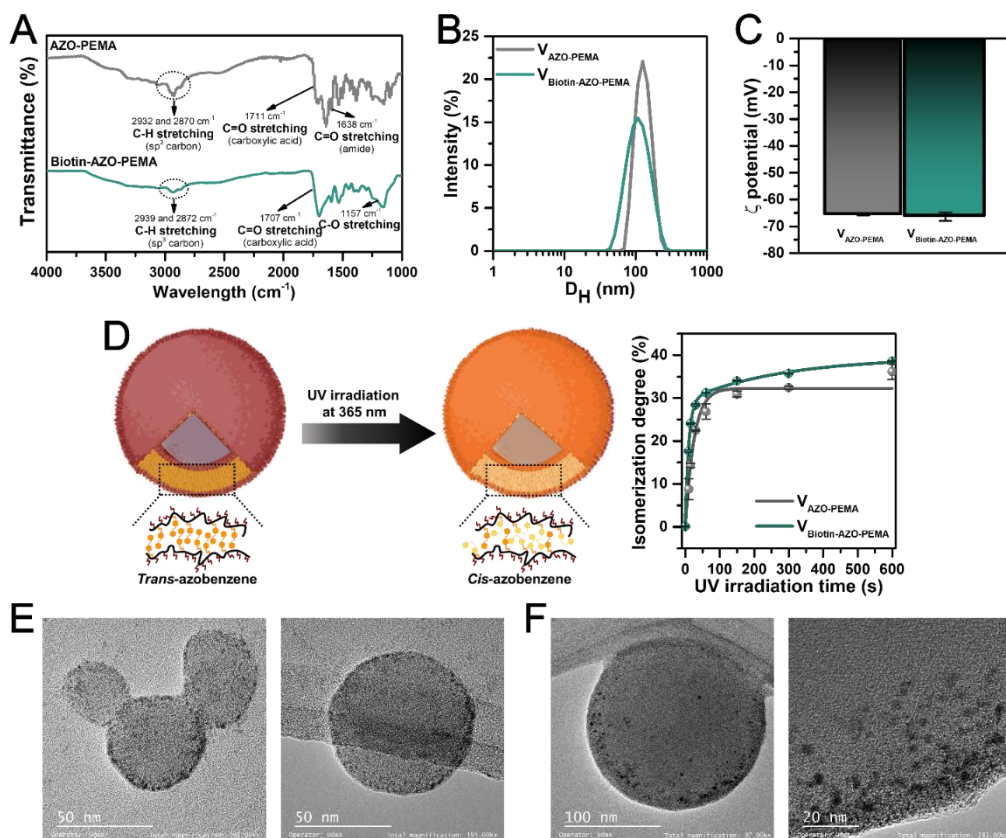


Figure 2. (A) FTIR spectrum of amphiphilic copolymers AZO-PEMA and Biotin-AZO-PEMA. (B) Particle size distribution measured by DLS, (C) surface charge measured by ELS, and (D) isomerization degree for $V_{\text{AZO-PEMA}}$ and $V_{\text{Biotin-AZO-PEMA}}$ in water, pH \sim 4.0. TEM images of $V_{\text{AZO-PEMA}}$ encapsulating (E) ferrocene and (F) PVP-PtNPs.

Results

Two novel photosensitive amphiphilic copolymers were synthesized by a nucleophilic addition reaction that led to residual carboxylic acids as hydrophilic groups, AZO moieties as a photoswitchable chemical compound and hydrophobic groups, and biotin moieties as a protein-binding ligand and hydrophilic groups. The amphiphilic copolymers were self-assembled in nanopolymerosomes with of 125 ± 1 nm and 100 ± 1 nm in size for $V_{\text{AZO-PEMA}}$ and $V_{\text{Biotin-AZO-PEMA}}$, and highly stable polymer due to the low surface charge (\sim 65 mV). Polymerosomes also exhibited high cargo-retention efficiency even for weeks. Furthermore, the polymerosomes'

exposure to UV irradiation at 365 nm produced transitions of the azobenzene molecules from *trans* to *cis* reaching a degree of isomerization of up to 40% in water. However, the partial or total disruption of the polymersomes depending on the irradiation time and the medium. This conformational transition in the bilayer after UV irradiation promoted a selective permeability, in which small molecules such as MB can be released while nanometer-sized cargos such as HRP and PVP-PtNPs remain in the polymersomes' hydrophilic core. However, small substrates can penetrate the polymersomes allowing enzyme/nanozyme-substrate reaction. These mechanisms promoted the maximum release extent of small electroactive species without diminishing the enzymatic and enzymatic-like activity of HRP and PVP-PtNPs under constant UV irradiation, which is very promising for developing biosensors with polymersome-based nanocarriers for signaling enhancement.

Conclusion

Novel photosensitive nanopolymersomes as electroactive species carriers were designed as an innovative material to enhance analytical signals in biosensing. Under optimal conditions, the electroactive species' encapsulation was shown to be a promising amplification strategy to be incorporated into the design of electrochemical biosensors among a large spectrum of possibilities, which work is ongoing.

References

- [1] Quinchia, J.; et al. *Micromachines*. **2020**, 11(4): 411.
- [2] Vásquez, V.; et al. *Analytica Chimica Acta*. **2022**, 1205: 339718.
- [3] Cajigas; S.; et al. *Biosensors: Biosensors With Signal Amplification*. Reference Module in Biomedical Sciences, Elsevier, **2021**.
- [4] Zheng, Y.; et al. *Biosensor and Bioelectronics*. **2021**; 178: 113021.
- [5] Dincer, C.; et al. *Advanced Materials*. **2019**, 31(30): 1806739.
- [6] Tao, Y.; et al. *Theranostics*. **2017**, 7(4): 899.
- [7] Hu, R.; et al. *Scientific reports*. **2020**, 10(1): 1-11.
- [8] Ghorbanizamani, F.; et al. *ACS sensors*. **2021**, 6(8): 2988-2997.
- [9] Rideau, E.; et al. *Chemical society reviews*. **2018**, 47(23): 8572-8610.

Acknowledgments

The work has been funded by MINCIENCIAS, MINEDUCACIÓN, MINCIT and ICETEX through the Program Ecosistema Científico Cod. FP44842-211-2018, project number 58536. J.O thanks support from The University of Antioquia and the Max Planck Society through the cooperation agreement 566-1, 2014. We thank The Ruta N complex for hosting the Max Planck Tandem Groups.

O17 |

NATURAL NANOSTRUCTURED MATERIALS AS TUNEABLE PHOTONIC SENSING PLATFORMS

J.W. Goessling¹, P. Martínez-Pérez², L. Rodriguez-Lorenzo³, B. Espiña³, R. Vilarinho⁴, J. Serôdio¹, M. Lopez-Garcia⁴

¹*Centro de Estudos do Ambiente e do Mar (CESAM), Department of Biology, University of Aveiro, Campus de Santiago, Aveiro 3810-193, Portugal*

²*Nanophotonics Technology Center, Universitat Politècnica de València, Camino de Vera s/n, 46022 Valencia, Spain*

³*Water Quality Research Group, International Iberian Nanotechnology Laboratory, Av. Mestre José Veiga, Braga 4715-330, Portugal*

⁴*Natural and Artificial Photonic Structures and Devices Group, International Iberian Nanotechnology Laboratory, Av. Mestre José Veiga, Braga 4715-330, Portugal*

*jgoessling@ua.pt

Abstract

Nanostructured materials have a wide range of applications. We tested the usability of natural nanostructured materials grown by diatom algae as cost-effective sensing platforms. These highly ordered silicon dioxide structures open bandgaps in the visible and near infrared spectral range, reminiscent of advanced slab photonic crystals. The natural lattice structures are highly conserved and with low defect rates, resulting in highly reproducible measurements of refractive index contrast to analytes. We show the potential of natural photonic structures from diatoms in resolving low concentrations of analytes such as glucose, and will discuss the utilization of silica surface functionalization, *in vivo* doping techniques and biodiversity to tune the spectral properties for a wide range of applications.

Introduction

Diatoms are some of the most abundant microalgae on Earth, contributing to global carbon sequestration and oxygen production by photosynthesis². Their most intrinsic feature is the encasement in a silicon dioxide miniaturized shell named frustule (Fig. 1). Frustules are perforated with minute nanometric features, which are commonly arranged in periodic lattices. Our earlier research confirmed that some diatom silica parts function as slab photonic crystals with bandgap properties in the visible and near infrared spectral range³. The structures are highly reproducible within one species, paving the way for cost-effective and more environmentally friendly photonics⁴. In the current study we tested the quality of the natural photonic structure in sensing of refractive index changes by

immersion with different analytes, such as Glucose. To gain control over the detectable spectral range and the sensitivity of the biotic sensing device we furthermore functionalized the silica with titanium dioxide in order to shift the refractive index of the slab and to enhance refractive index contrast. We will also discuss other methodologies to tune and control the photonic spectral range, including *in vivo doping* and the application of biodiversity.

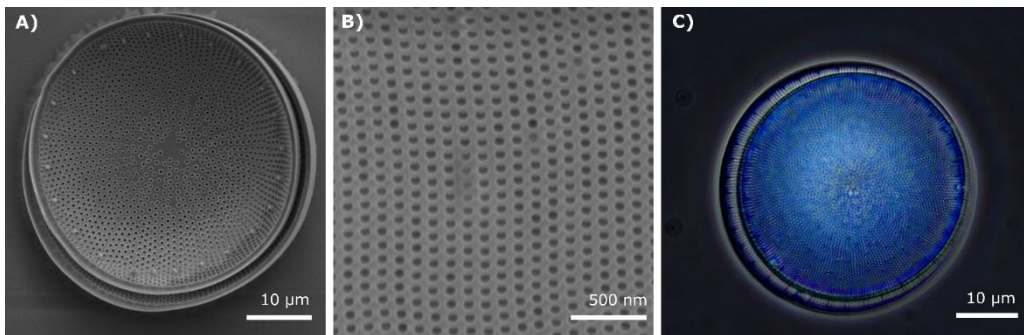


Fig. 1: Nanostructured materials grown by diatoms. A) Overview of a silicon dioxide structure after removing the organic cell component. B) Photonic crystal lattice with nanometric pores. C) Blue structural coloration of the natural system in dark field (published in¹).

Methods

Diatom growth and frustule preparation

The diatom *Coscinodiscus granii* (strain K-1834) was obtained from the Norwegian Culture Collection of Algae (NCC). Organic cell content was removed with sulfuric and hydrochloride acid, prior to oxalic acid treatment, as described in detail elsewhere⁴. The acids were then replaced with distilled water.

Functionalization

The samples containing diatom structures were incubated in polyelectrolyte solutions. The supernatant was discarded, and the pellet was then resuspended in ultrapure water. Finally, polyelectrolyte-coated diatom structures were functionalized with citrate-coated TiO₂ nanoparticles. The samples were then incubated at room temperature and centrifuged. Functionalized structures were stored in MilliQ water. Functionalization was confirmed with Energy-dispersive X-ray spectroscopy, zeta potential and dynamic light scattering.

Microscatterometry

Reflectance of individual structures was measured in a micro-scatterometry setup adapted for this type of measurement³. In principle, white light from a halogen tungsten lamp was focused to ca. 2 µm with high magnification objective lens onto the structure as described elsewhere³. Reflected light was collected in the

back-focal plane with a 1 mm multimode fiber connected to an Ocean Optics spectrometer. The fiber was placed in the center of the reflected beam, thereby collecting angles $\pm 5^\circ$ normal incidence. Reflectance spectra were normalized to measurements in the dark and reflectance spectra from a silver mirror.

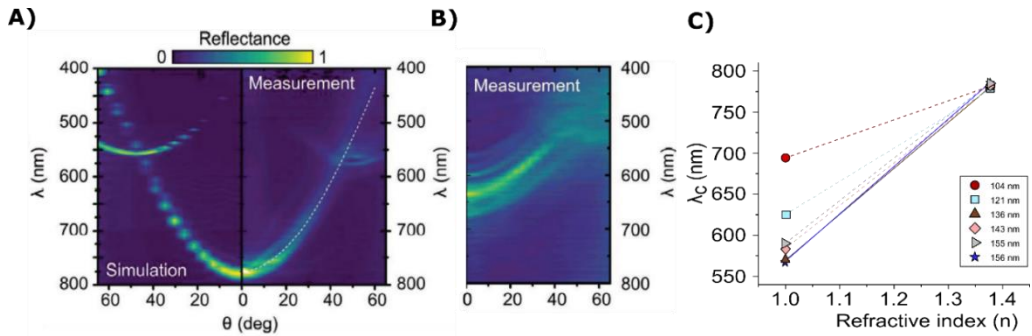


Fig. 2: Photonic bandgap determination in diatom silicon dioxide structures. A) Measured and simulated bandgap dispersion as a function of light incidence in water. B) Bandgap dispersion in air. C) Bandgap detection at normal incidence using different individual structures with various pore diameter. At low refractive index contrast, results are highly reproducible. At large contrast the pore filling volume influences the central spectral reflectance characteristics. A) and B) are reproduced from³. C) reproduced from⁴.

Results

Natural slab structure reproducibility

The structure of the natural photonic slab has two central features with relevance for the photonic system: The period between holes and the pore diameter of the holes. We demonstrated that the period was highly preserved between individuals of the same species, while the pore diameter showed a natural variation. The defect rate, however, as determined as missing pores over the slab surface, was low⁴ (ca. 1% in average; data not shown).

Photonic properties as a function of refractive index environment

The dispersion of the energy bandgap in the tested structure was reproducible at low index contrast, and highly sensitive to the index changes in the surrounding medium. However, we observed a significant influence of the pore diameter on the spectral response, determining the immersion volume of the slab (Fig. 2).

Conclusions

We show that natural silicon dioxide slabs from diatoms work as highly reproducible photonic detection platforms, responding to low refractive index changes. Some structural features – determining the photonic properties such as

pore diameter - can vary between different individual specimen. Using surface-functionalization of the structures, the photonic properties can be spectrally tuned (unpublished data; presented at conference). However, as frustules can also incorporate environmental factors during the growth of the living cell, we propose that the photonic properties can further be tuned by *in vivo* doping techniques. In addition, as more than 100,000 diatom species with various frustule features could exist in nature⁵, one can imagine an equal number of photonic nanomaterials with various periods and pore dimensions, eventually covering the full spectral range for application in photonics.

In fact, Ria de Aveiro is a unique ecosystem harboring a plethora of diatom species. They provide ecosystem services and produce oxygen for roughly 10,000 people of the Aveiro region⁶ – but can they in future also serve as innovation hub for the design and extraction of natural nanostructured dielectric materials?

Acknowledgements

JWG and L.R.-L. are grateful for support through Concurso Estímulo ao Emprego Científico Individual grants (no. 2020.04217.CEECIND and no. 2020.04021.CEECIND, respectively) granted by the Fundação para a Ciência e a Tecnologia (FCT), Portugal. JWG and MLG thank the FCT for support through grant no. PTDCBTA-BTA20612021. PMP thanks the support of the Ministry of Universities and Recovery of Spain and its Transformation and Resilience Plan funding by European Union-Next Generation EU, through the Margarita Salas call from Universitat Politècnica de València (Valencia, Spain).

References

- (1) Núñez-Sánchez, S.; Lopez-Garcia, M. Bio-Based Optical and Photonic Materials: Towards Nature-Based Production Methods for Photonics. *Photoniques* **2021**, No. 110, 36–39.
- (2) Geider, R. J.; Delucia, E. H.; Falkowski, P. G.; Finzi, a C.; Grime, J. P.; Grace, J.; Kana, T. M.; La Roche, J.; Long, S. P.; Osborne, B. a; Platt, T.; Prentice, I. C.; Raven, J. a; Schlesinger, W. H.; Smetacek, V.; Stuart, V.; Sathyendranath, S.; Thomas, R. B.; Vogelmann, T. C.; Williams, P.; Woodward, F. I. Primary Productivity of Planet Earth: Biological Determinants and Physical Constraints in Terrestrial and Aquatic Habitats. *Glob. Chang. Biol.* **2001**, *7* (8), 849–882.
- (3) Goessling, J. W.; Wardley, W. P.; Lopez-Garcia, M. Highly Reproducible, Bio-Based Slab Photonic Crystals Grown by Diatoms. *Adv. Sci.* **2020**, 1903726.
- (4) Goessling, J. W.; Shanti Paul, V.; Santiago González, A. A.; Asworth, M.; Manning, S. R.; Lopez Garcia, M. Biosilica Slab Photonic Crystals as an Alternative to Cleanroom Nanofabrication. *Faraday Discuss.* **2020**.
- (5) Guiry, M. D. How Many Species of Algae Are There? *J. Phycol.* **2012**, *1063* (July), 1057–1063.
- (6) Frankenbach, S.; Ezequiel, J.; Plecha, S.; Goessling, J. W.; Vaz, L.; Kühl, M.; Dias, J. M.; Vaz, N.; Serôdio, J. Synoptic Spatio-Temporal Variability of the Photosynthetic Productivity of Microphytobenthos and Phytoplankton in a Tidal Estuary. *Front. Mar. Sci.* **2020**, *7* (March), 1–22.

O18 |

COLORIMETRIC ASSAYS FOR CARDIOVASCULAR BIOMARKERS DETECTION USING GOLD NANOPARTICLES

M. António^{1*}, T. Lima^{2,3}, R. Ferreira^{4,5}, M. Fardilha², J. Bastos^{2,6}, R. Vitorino^{2,5,7} and A. L. Daniel-da-Silva¹

¹*CICECO-Aveiro Institute of Materials, Department of Chemistry, University of Aveiro, 3810-193 Aveiro, Portugal*

²*iBiMED-Institute of Biomedicine, Department of Medical Sciences, University of Aveiro, 3810-193 Aveiro, Portugal*

³*Cancer Biology and Epigenetics Group, Research Center of Portuguese Oncology Institute of Porto (GEBC CI-IPOP) & Porto Comprehensive Cancer Center (P.CCC), 4200-072 Porto, Portugal*

⁴*QOPNA, Department of Chemistry, University of Aveiro, 3810-193, Aveiro, Portugal*

⁵*LAQV-REQUIMTE, Chemistry Department, University of Aveiro, 3810-193, Aveiro, Portugal*

⁶*Cardiology Department, Hospital Infante D. Pedro, Centro Hospitalar do Baixo Vouga, Aveiro, Portugal*

⁷*UnIC@RISE, Department of Surgery and Physiology, Cardiovascular R&D Center, Faculty of Medicine of the University of Porto, Alameda Professor Hernâni Monteiro, 4200-319 Porto, Portugal*

**maantonio@ua.pt*

Introduction

Several biomarkers have been identified and their levels are associated with various cardiovascular diseases (CVD) or cardiovascular risk outcomes. Two of these CVD biomarkers are the C-reactive protein (CRP) and galectin-3 (Gal-3), which have been associated with the risk of developing CVD [1] and with heart failure [2], respectively. These biomarkers have been detected using various approaches such as ELISA-based assays that offer low limit of detection (LOD) [3,4]. However, these strategies require the use of costly chemicals, are time-consuming, and can be difficult to perform [5]. In addition, most of the assays with low LOD use more than one nanomaterial and expensive equipment to perform the detection assays [6,7]. There is a demand for new strategies that provide low-cost and, high-sensitive detection of CRP and Gal-3 using common laboratory equipment. Gold nanoparticles (AuNPs) are frequently applied to biosensing due to their chemical stability, straightforward surface modification, high molar absorption coefficient and biocompatibility. Also, their distinctive localized surface plasmon resonance (LSPR) band enables the development of colorimetric methods based on plasmonic coupling [8,9]. The strategies described in this research demonstrate the versatility of AuNPs to detect colorimetrically CRP [10] and Gal-3 in biofluids using UV-VIS spectroscopy.

Methods

Synthesis of gold nanoparticles

The synthesis of spherical AuNPs was performed using the Turkevich method, according to António *et al.* [10]. Briefly, a HAuCl₄ aqueous solution (100 mL, 1 mM) was heated until boiling, under reflux and vigorous stirring. Then, 10 mL of 38.8 mM sodium citrate solution was added and after color change the reaction continued for 1 h.

Procedure for detection of CRP using AuNPs

In a typical procedure for the detection of CRP (20 mM Tris-HCl, 0.28 M NaCl, pH = 7.4), the aptamer solution (30 µL, 2 µM, Tris-HCl with EDTA, pH 7.4) was added to the AuNPs colloid (200 µL, 1.82 mM Au) to obtain Apt-AuNPs. Then, the CRP solution (30 µL, CRP concentration (0.889–20.7 mg/L)) was added to Apt-AuNPs suspension. The resulting mixture was stirred (300 rpm) at 37 °C for 5 min. Then, a NaCl aqueous solution (60 µL, 0.2 M) was added, and the colloid was analyzed through UV–VIS spectrophotometry to determine the aggregation ratio (A_{670}/A_{520}) [10].

Synthesis of AuNPs@MUDA@Ab@BSA probes

The synthesized AuNPs were modified with MUDA (11-mercaptoundecanoic acid) in the presence of NaOH [11,12]. After centrifugation, the AuNPs@MUDA were bioconjugated with antibody of galectin-3 (Ab) via carbodiimide coupling. Then, a BSA solution was added to block non-specific interactions [12–14].

Procedure for detection of galectin-3 using AuNPs@MUDA@Ab@BSA

In a typical procedure, 30 µL of galectin-3 concentrations in 0.01M PBS pH 7.4 (0 - 320 µg.L⁻¹) were added to 200 µL of the AuNPs@MUDA@Ab@BSA. The resulting mixture was stirred at 325 rpm for 60 minutes at 25°C and then analyzed through UV-VIS spectroscopy to determine the aggregation ratio (A_{750}/A_{526}), where A_{750} and A_{526} are the absorbance values at 750 nm and 526 nm, respectively.

Results

Detection of CRP

The Apt-AuNPs aggregation could be observed by naked eyes as the concentration of the CRP increased. The observation of absorbance spectra of the Apt-Au NPs revealed the evolution of the salt-induced aggregation after adding CRP at variable concentrations. The aggregation ratio, A_{670}/A_{LSPR} , was in a good linear relationship with the concentration of CRP up to concentrations of 20.7 mg.L⁻¹ (R^2 of 0.9938), with a LOD of 1.23 µg.mL⁻¹ (Figure 1). The aptamer-CRP dissociation constant (kd) was found to be 1.93 nM. The specificity of the system was analyzed using BSA, Apro and Pro. K proteins and L-Glu, Urea and AA

molecules, indicate that the system Apt-AuNPs is selective for CRP detection. The CRP-spiked urine samples (diluted 1:100) were tested and the resulting AR was similar to that in the buffer, suggesting that the molecules present in urine did not interfere markedly in the detection.

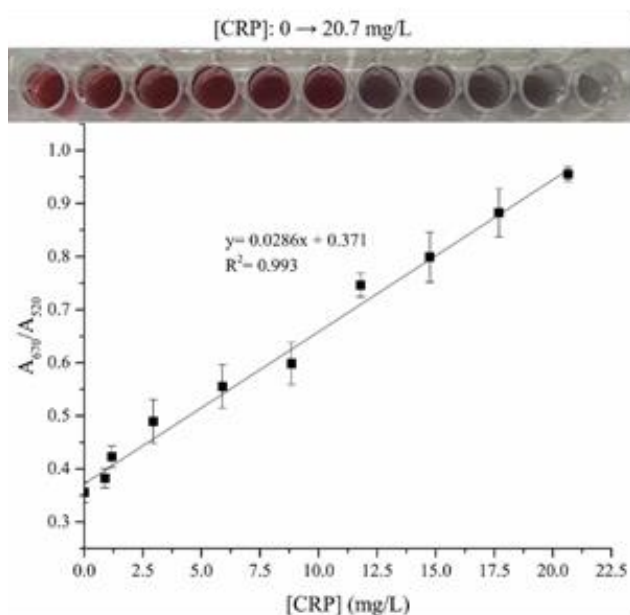


Figure 1: A photo of detection trials (top); Calibration curve of CRP concentrations in buffer (bottom).

Detection of Gal-3

The presence of Gal-3 resulted in partial aggregation of AuNPs@MUDA@Ab@BSA, which could be observed with naked eye at high Gal-3 concentrations. A linear relationship was found between the A_{750}/A_{526} and Gal-3 concentrations ($0-160 \mu\text{g}\cdot\text{L}^{-1}$) was found (Figure 2). This linear relationship was observed in 0.01 PBS pH=7.4, diluted saliva (1:10) and fetal bovine serum (1:100) with a sensing range and LOD of $0 - 200 \mu\text{g}\cdot\text{L}^{-1}$ and, $10.8 - 31.5 \mu\text{g}\cdot\text{L}^{-1}$, respectively. The k_d was estimated to be around $0.214 - 0.483 \text{ nM}$, depending on the complexity of the matrix. The system was found to be selective for BSA, α -amylase, IgG, ascorbic acid, urea and glycine. The stability of AuNPs@MUDA@Ab@BSA was ensured for 10 days. In addition, the system was tested in human plasma samples and compared with Western blot analysis. The Gal-3 concentrations obtained agreed with the Western blot results.

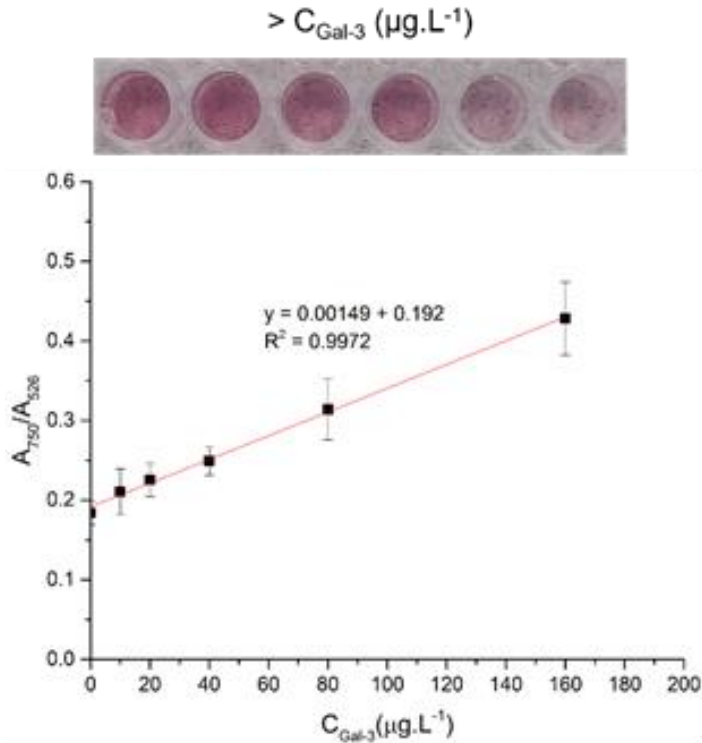


Figure 2: A photo of detection trials (top); Calibration curve of Gal-3 concentrations in buffer (bottom).

Conclusions

The developed colorimetric methods for CRP and Gal-3 detection use a UV–VIS spectrophotometer, which is helpful for budget-limited laboratory and implementation of point-of-care testing. The CRP detection was fast (5 min), with a sensing range (0.889–20.7 mg/L). Preliminary results indicate the application of CRP detection method to diluted urine, however, further studies are need for the analysis of complex samples. The Gal-3 was detected in different matrices 0.01 PBS pH=7.4, diluted saliva and fetal bovine serum with a sensing range and LOD of 0 - 200 $\mu\text{g.L}^{-1}$, 10.8 - 31.5 $\mu\text{g.L}^{-1}$, respectively. The method was tested in human plasma samples and compared with Western blot technique. The applicability of AuNPs@MUDA@Ab@BSA on complex fluids at a large scale needs to be investigated.

References

- [1] P. M. Ridker and N. Cook, *Circulation* **109**, 1955 (2004).
- [2] R. A. De Boer, D. J. A. Lok, T. Jaarsma, P. Van Der Meer, A. A. Voors, H. L. Hillege, and D. J. Van Veldhuisen, *Ann. Med.* **43**, 60 (2011).
- [3] T. F. Scientific, Human Galectin-3 ELISA Kit, 2018.
- [4] Thermo Fisher Scientific, CRP Human ELISA Kit, 2019.
- [5] S. A. Vance and M. G. Sandros, *Sci. Rep.* **4**, 5129 (2014).
- [6] M. Mahyari, S. E. Hooshmand, H. Sepahvand, S. Gholami, A. H. Rezayan, and M. A. Zarei, *Mater. Chem. Phys.* **269**, 124730 (2021).
- [7] Z. Tang, J. He, J. Chen, Y. Niu, Y. Zhao, Y. Zhang, and C. Yu, *Biosens. Bioelectron.* **101**, 253 (2018).
- [8] M. António, R. Vitorino, and A. L. Daniel-da-Silva, *Talanta* **230**, (2021).
- [9] M. António, J. Nogueira, R. Vitorino, and A. L. Daniel-Da-Silva, *Nanomaterials* **8**, 200 (2018).
- [10] M. António, R. Ferreira, R. Vitorino, and A. L. Daniel-da-Silva, *Talanta* **214**, 120868 (2020).
- [11] L. Meng, J. H. Yin, Y. Yuan, and N. Xu, *RSC Adv.* **8**, 9327 (2018).
- [12] J. P. Oliveira, A. R. Prado, W. J. Keijok, P. W. P. Antunes, E. R. Yapuchura, and M. C. C. Guimarães, *Sci. Rep.* **9**, 1 (2019).
- [13] nanoComposix, BioReady 40 Nm Carboxyl Gold Covalent Conjugation Protocol, 2021.
- [14] H. Liu, Y. Cheng, Y. Chen, H. Xiao, Y. Sui, Q. Xie, R. Liu, and X. Yang, *J. Electroanal. Chem.* **861**, (2020).

Acknowledgements

We thank the Fundação para a Ciência e a Tecnologia (FCT), FCT/MEC (PIDDAC), European Union, QREN, FEDER, and COMPETE for the project CICECO-Aveiro Institute of Materials, UIDB/50011/2020 & UIDP/50011/2020 & LA/P/0006/2020, the project iBiMED (UIDB/04501/2020, POCI-01-0145-FEDER-007628), UnIC (UID/IC/00051/2019) and the project LAQV- REQUIMTE (UIDB/50006/2020). M.A. thanks FCT for the PhD grant (SFRH/BD/136881/2018). T. L. thanks FCT for the PhD grant (SFRH/BD/136904/2018). A.L.D.-d.-S. acknowledges FCT for the contract (IF/00405/2014). R.V. thanks the FCT for the Investigator Grant (IF/00286/2015).

P10 |

A FLOW INJECTION SETUP TO DETERMINE OXYTETRACYCLINE WITH A PIEZOELECTRIC QUARTZ CRYSTAL

Marta I. S. Veríssimo^{1*}, Ana S. Sousa, M. Teresa S. R. Gomes^{1*}

¹ CESAM, Department of Chemistry, University of Aveiro, Campus de Santiago, 3810-193 Aveiro, Portugal

*email: mverissimo@ua.pt, mtgomes@ua.pt

Introduction

The use of antibiotics is a common practice, being widely used in human and veterinary medicine. Residues of antibiotics in the environment are becoming ubiquitous due to their widespread use, worsened by the abusive and inappropriate application and by the ineffectiveness of treatments to eliminate antibiotics in Wastewater Treatment Plants.

Antibiotics such as fluoroquinolones and tetracycline are complex molecules which possess several functional groups within the same molecule. They have low volatility, are generally quite soluble in water, and are hydrophilic, having low log K_{ow} [1]. These antibiotics also tend to form complexes with divalent ions, such as Ca^{2+} and Mg^{2+} and to be absorbed in soils and sediments, leading to their persistence in the environment. This is one of the biggest concerns with these two classes of antibiotics. Once released into surface water, they accumulate in soils and sediments, delaying their degradation and prolonging contact with microorganisms, thus favouring the emergence of bacterial resistance.

Oxytetracycline (OTC) or (4S,4aR,5S,5aR,6S,12aS)-4-(dimethylamino)-3,5,6,10,12,12a-hexahydroxy-6-methyl-1,11-dioxo-1,4,4a,5,5a,6,11,12a-octahydrotetracene-2-carboxamide (IUPAC name) is one of the tetracyclines most used. The official method for OTC analysis is the expensive High-Performance Liquid Chromatography (HPLC).

The objective of this work was to develop a low-cost sensor, based on a piezoelectric quartz crystal, for OTC. In the absence of an OTC receptor, we decided to try a molecularly imprinted polymer (MIP) already proposed for the OTC solid-phase extraction [2].

The sensor was characterized by evaluating its reversibility, sensitivity, selectivity, working range, and detection limit. Sensor characteristics were compatible with a time-efficient method for OTC determination.

Methods

Figure 1 shows the Flow Injection Analysis (FIA) system developed for OTC detection and quantification. A pressurized solution (Milli-Q water or HEPES buffer) carried the injected sample towards one of the sensor electrodes.

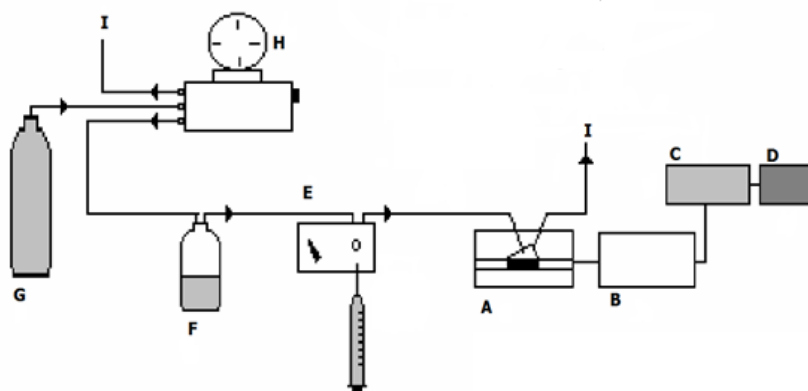


Figure 1 – Experimental setup: A) tefflon cell with the acoustic wave sensor; B) oscillator circuit; C) BNC 2121 connector; D) counter/timer PXI 1031 connector to a PC; E) injection port; F) Milli-Q water or buffer solution; G) nitrogen; H) pressure regulator; I) waste.

The MIP was synthesized according to literature [2]. The OTC pre-polymerisation mixture comprised OTC (1.16 mmol), methacrylic acid (9.28 mmol), the cross-linking ethylene glycol dimethacrylate (46.42 mmol) and the initiator azobisisobutyronitrile (1.02 mmol) dissolved in the porogen dimethylsulfoxide (13.33 ml). The polymer obtained was crushed, ground and wet-sieved, and finally washed, and characterized by FTIR.

The piezoelectric crystal was 9 MHz, polished AT-cut HC-6/U with gold electrodes (Renlux Crystal Ltd). The crystal was coated by drop-coating with a polyvinylchloride/2-nitrophenyl octyl ether membrane, dissolved in tetrahydrofuran, and containing the previously prepared MIP.

The sensor was connected to a home-made oscillator. A Counter/Timer Device PXI 1031 from National Instruments was used to obtain the frequencies of oscillation of the crystal, which were stored at 1s intervals on a PC, with data acquisition software written in LabView.

OTC solutions of known concentration were injected into the FIA injection valve, and as soon as the solution reached the coated quartz crystal, the frequency of oscillation of the coated piezoelectric quartz crystal decreased, and the difference to baseline was computed. The flow of Milli-Q water was able to restore baseline frequency, allowing the system with the sensor to be reused right after.

Results

Figure 2 showed the typical response of the piezoelectric sensor when an OTC standard of 80 ppm prepared in Milli-Q water was injected into the FIA system. From Figure 2, we can observe that response of the sensor was fast (36 s), and the piezoelectric sensor completely recovered in approximately 60 s.

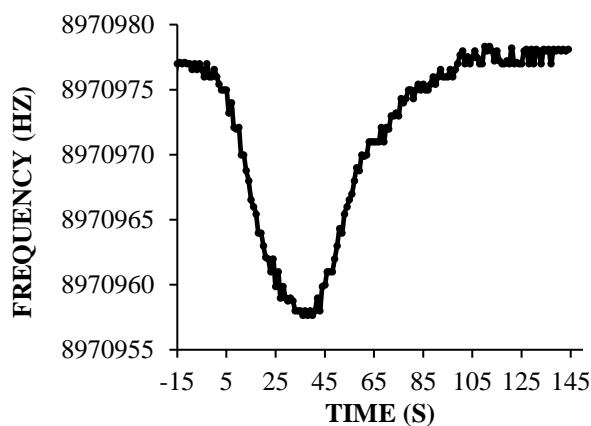


Figure 2 – Frequency decrease (ΔF) of the piezoelectric sensor during the time of analysis (s) caused by the injection of an 80 ppm OTC solution in the FIA system.

OTC is an amphoteric molecule with several polar/ionic groups and multiple environmentally relevant disassociation constant (pKa) values (pKa values of 3.57, 7.49, and 9.44) [3]. Thus, OTC may exist as a cation, a zwitterion, or a net negatively charged ion at environmentally relevant pH conditions. The medium pH is a significant factor in adsorption because it influences the properties of the target compound (OTC). Therefore, control of pH is fundamental to maintain OTC at the same ionic form during experiments. HEPES buffer, with a useful pH range from 6.8 to 8.2 was used to control pH.

Figure 3 shows the response of the piezoelectric sensor to OTC standard solutions, using Milli-Q water or HEPES buffer (pH 7.2). Frequency values represent an average of 4 replicates (error bars are presented in the graphic).

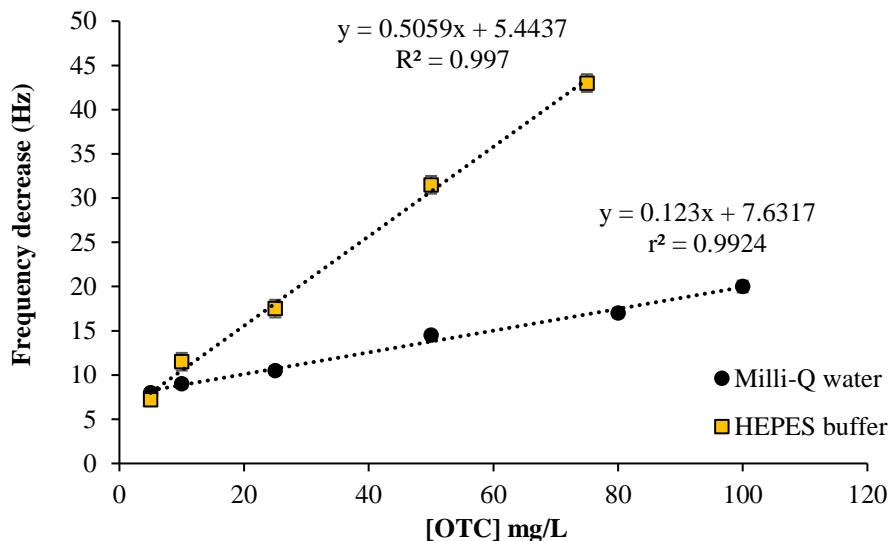


Figure 3 - Response of the piezoelectric sensor to OTC standards prepared with Milli-Q water or HEPES buffer and using Milli-Q water or HEPES buffer as carrier flow, respectively. Each value is the average of 4 replicates (error bars included).

From Figure 3, it is possible to observe that the sensor sensibility increases in HEPES medium, with controlled pH, comparing to the results obtained for Milli-Q water.

Conclusions

This work confirms the possibility of using molecularly imprinted polymers as ionophores for organic ion recognition in piezoelectric transduction.

The developed piezoelectric sensor responds fast and reversibly to OTC either in Milli-Q water as in HEPES buffer, with the mass sensor presenting a LOD of 0.80 mg/L and a LOQ of 2.66 mg/L in HEPES. As far as we know this is the first piezoelectric sensor for OTC in literature.

Results of the selectivity against the most common salts (NaCl, MgCl₂, CaCl₂) and antibiotics (tetracycline, ciprofloxacin, enrofloxacin, oxolinic acid) found in waters will be presented at the Congress.

References

- [1] Harrower J, McNaughtan M, Hunter C, Hough R, Zhang Z, Helwiga K (2021) Chemical Fate and Partitioning Behavior of Antibiotics in the Aquatic Environment—A Review. *Environ Toxicol Chem* 40:3275–3298.
- [2] Caro E, Marcé RM, Cormack PAG, Sherrington DC, Borrull F (2005) Synthesis and application of an oxytetracycline imprinted polymer for the solid-phase extraction of tetracycline antibiotics. *Anal Chim Acta* 552:81-86.
- [3] Peng FJ, Zhou LJ, Ying GG, Liu YS, Zhao JL (2014) Antibacterial activity of the soil-bound antimicrobials oxytetracycline and ofloxacin. *Environ Toxicol Chem* 33:776-783.

Acknowledgements

The authors are grateful to FCT/MCTES for the financial support of CESAM (UIDP/50017/2020 + UIDB/50017/2020 + LA/P/0094/2020) through national funds. M. Veríssimo is funded by national funds (OE), through FCT - Fundação para a Ciência e a Tecnologia, I.P., in the scope of the framework contract foreseen in the numbers 4, 5 and 6 of the article 23, of the Decree-Law 57/2016, of August 29, changed by Law 57/2017, of July 19.

P11 |

SIMULTANEOUS VOLTAMMETRIC DETERMINATION OF ACETAMINOPHEN, ASCORBIC ACID AND URIC ACID BY USE OF INTEGRATED ARRAY OF SENSORS MODIFIED WITH MESOPOROUS CARBON AND METALLIC NANOPARTICLES AND ELECTRONIC TONGUE PRINCIPLES

E. Rodríguez-Franch¹, A. Herrera-Chacon¹, I. Álvarez-Prada², X. Cetó¹, J. García-Antón², X. Sala², M. del Valle^{1*}

¹ *Sensors and Biosensors Group, Department of Chemistry, Universitat Autònoma de Barcelona, Edifici Cn, 08193 Bellaterra, Barcelona, Spain*

² *SelOxCat Research Group, Department of Chemistry, Universitat Autònoma de Barcelona, Edifici Cn, 08193 Bellaterra, Barcelona, Spain*

**email: manel.delvalle@uab.cat*

Introduction

Electrochemical sensors provide a response to the growing demand of fast and cost-effective analytical methods to allow the on-site detection of relevant analytes in sectors such as clinical, food, industrial, environmental and forensic chemistry. However, when attempting the multi-determination of several species in such complex matrixes, overlapping between different peaks appearing at similar potentials may hinder its individual quantification. In order to improve their analytical properties, the incorporation of nanometric materials has emerged as a promising approach over the last years. For this reason, there is great interest in the development and integration of new chemically functionalized nanomaterials that allow the construction of sensitive, stable, robust and increasingly species-selective sensors and biosensors. Unfortunately, few chemical (bio)sensors are available that function optimally without any interference or matrix effect when attempting the simultaneous analysis of several compounds in real samples. To overcome these drawbacks, new strategies, such as electronic tongues (ETs) ^[1,2], have been developed in recent years.

In this context, the present work aims to demonstrate the potential of a sensor array based on metallic nanoparticles as electro catalysts incorporated into mesoporous carbon (MC) as the supporting material for the analysis of a mixture of three compounds of pharmaceutical interest; namely, acetaminophen, ascorbic acid and uric acid. To this end, a new strategy for the modification of the sensors surface based on MC decorated with metal nanoparticles (gold, palladium and copper) was explored, in order to improve their responses and electrochemical performance ^[3,4]. Next, voltammetric responses were processed with data processing strategies (such as principal component analysis and artificial neural

networks) to reduce the complexity of the data and achieve the simultaneous determination of the three compounds.

Methods

Four different systems of metallic nanoparticles (M-NPs) supported on mesoporous carbon (MC), based on palladium, copper and gold, the latter first without additional stabilizer and then using 4-phenylpyridine (PP) as stabilizer, have been prepared ^[5,6].

These M-NPs have been studied by scanning electron microscopy (SEM) and transmission electron microscopy (TEM). From the SEM images, it can be ensured the presence of the nanoparticles on the mesoporous carbon and their homogenous disposition on the electrode surface. From TEM, the M-NPs dimensions were obtained, including particle size and deviation.

The base electrodes, graphite-epoxy composite electrodes, were prepared in the laboratory ^[7]. Once the M-NPs were synthesized, they were added into the surface electrode via ink-dropcasting ^[4]. The ink was obtained through the addition of graphite, the M-NPs and dimethylformamide. Once the surface was modified, the electrodes were cured for overnight into the fridge.

Electrochemical measurements were performed with a PalmSens four-channel multipotentiostat using a combination Ag/AgCl reference and platinum counter electrode. All the parametric conditions were optimized to achieve best response of the electrochemical sensors (scan rate, potential window, step potential, equilibration time, etc.).

Results

M-NPs were successfully synthesized and integrated onto the electrode surface via ink-dropcasting. Then, these M-NPs modified electrodes were characterized by electron microscope techniques showing the presence of metallic compounds onto the surface electrode (as shown in Figure 1).

The material was further characterized with TEM in order to assess the particle size and its deviation (data not shown), giving values of 6.2 ± 2.6 (nm), 39.6 ± 12.7 (nm), 22.5 ± 17.8 (nm) and 6.2 ± 1.6 (nm) for Pd-NPs@MC, Cu-NPs@MC, Au-NPs@MC and AuPP-NPs@MC, respectively. Then, EDXS study were done to determine that the M-NPs were integrated into the sensor to further confirm that the observed particle correspond to the actual metal.

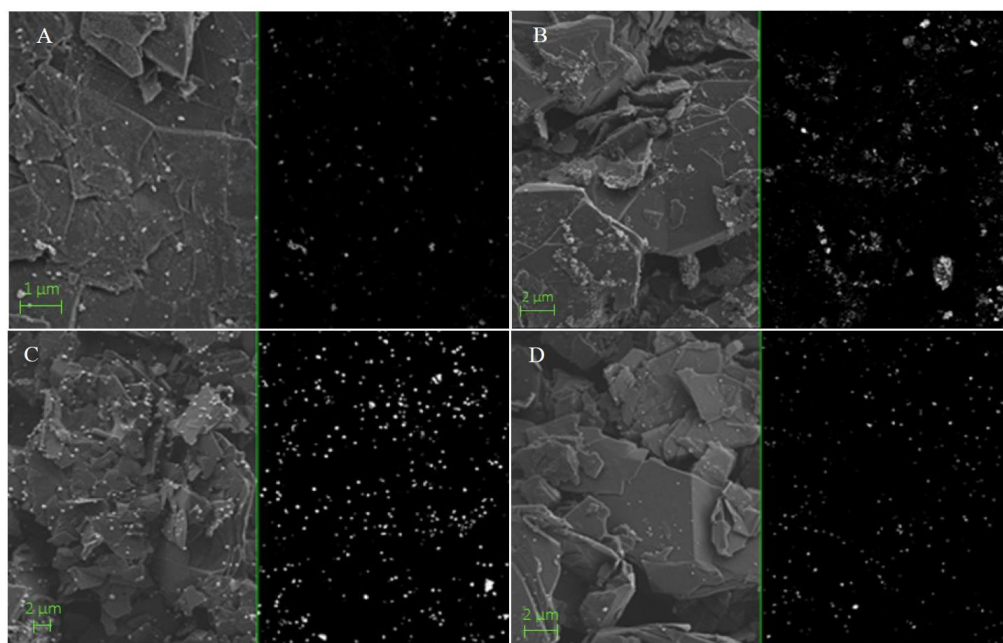


Figure 1. SEM electrode surface image, left, (and its backscattered image, right) for: (A) Pd-NPs@MC, (B) Cu-NPs@MC, (C) Au-NPs@MC and (D) AuPP-NPs@MC.

Multicomponent determination

For calibrating the response of the system, a response model was developed, using a tilted factorial experimental design (3^3) for its building. The model was fed with the compressed voltammograms, using Discrete Wavelet Transform (DWT), whose coefficients were entered in an artificial neural network (ANN) predicting the concentrations of the three electroactive species. The model performance was evaluated with an additional external subset of samples distributed randomly along the experimental domain. In order to assess the performance of the system, comparison lines of obtained vs. expected concentrations of the three evaluated species were calculated, both for training and external test subsets. Table 1 summarizes the comparison lines obtained by linear regression; at the same time, absolute Root Mean Square errors (RMSE) and Normalized Root Mean Square errors were also used to ascertain the goodness of fit of the model. Figure 2 shows the comparison of obtained vs. expected values, where the correct, ideal trend was verified.

Table 1. Results of the regression lines for the comparison between obtained vs. expected values, for the different data sets and the three considered drugs. Intervals calculated at the 95% confidence level.

Compound	Slope	Intercept (μM)	R^2	RMSE (μM)	NRMSE	Total RMSE	Total NRMSE
Training subset (n=27)							
Paracetamol	1.009 ± 0.010	-2.0 ± 1.9	0.9994	2.26	0.00834	1.78	0.00660
Ascorbic	1.006 ± 0.007	-0.9 ± 1.4	0.9997	1.56	0.00583		
Uric acid	0.998 ± 0.007	0.4 ± 1.3	0.9997	1.41	0.00521		
Testing subset (n=12)							
Paracetamol	1.029 ± 0.110	-3.2 ± 21	0.978	11.5	0.0426	10.2	0.0380
Ascorbic	1.048 ± 0.109	-7.6 ± 18	0.979	10.8	0.0404		
Uric acid	1.008 ± 0.075	-3.8 ± 13	0.989	8.01	0.0297		

RMSE: root mean square error; NRMSE: normalized root mean square error

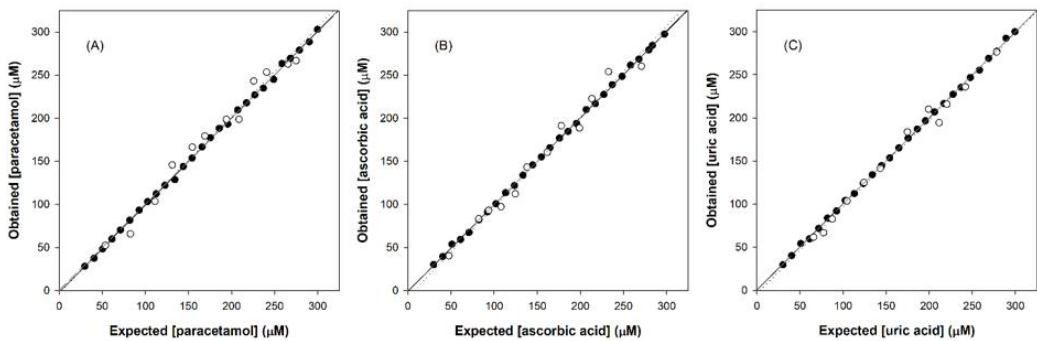


Figure 2. Modeling ability of the optimized DWT-ANN. Comparison graphs of obtained vs. expected results for (A) paracetamol, (B) ascorbic acid and (C) uric acid, for the training (\bullet , solid line) and testing subsets (\circ , dotted line). Dashed line corresponds to ideality ($y = x$).

Conclusions

The present approach presents a voltammetric Electronic Tongue system based on the use of simple modified electrodes based on mesoporous carbon for individual quantification of the different drugs, demonstrating the powerful effect of ANN as an analysis tool for the determination of key compound in clinical industry. Therefore, future work has to focus on the suitability for different applications.

References

- [1] D. Ortiz-Aguayo, M. Bonet-San-Emeterio, M. del Valle, *Sensors*, **2019**, 19, 3286.
- [2] M. Sarma, N. Romero, X. Cetó, M. del Valle, *Sensors*, **2020**, 20(17), 4798.
- [3] J. Creus, S. Drouet, S. Suriñach, P. Lecante, V. Collière, R. Poteau, K. Philippot, J. García-Antón, X. Sala, *ACS Catalysis*, **2018**, 8, 11094–11102.
- [4] A. C. de Sá, A. Cipri, A. González-Calabuig, N. R. Stradiotto, M. del Valle, *Sensors and Actuators B: Chemical*, **2016**, 222, 645-653.
- [5] C. Barrière et al., *Journal of Materials Chemistry*, **2012**, 22, 2279-2285.
- [6] C. Amiens et. al., *New Journal of Chemistry*, **2013**, 37, 3374-3401.
- [7] A. Cipri, M. del Valle, *Nanoscience and Nanotechnology*, **2014**, 14, 6692-6698.

Acknowledgements

The authors acknowledge the support of the Spanish Ministry of Science and Innovation (MCINN) through project PID2019-107102RBC21

P12 |

MODIFICATION OF NATURAL PHOTONIC CRYSTALS BY TAILORING OF THE REFRACTIVE INDEX CONTRAST

R. Vilarinho¹, J. W. Goessling², M. Lopez-Garcia¹

¹*Natural and Artificial Photonic Structures and Devices Group, International Iberian Nanotechnology Laboratory, Av. Mestre José Veiga, Braga 4715-330, Portugal*

²*Centro de Estudos do Ambiente e do Mar (CESAM), Department of Biology, University of Aveiro, Campus de Santiago, Aveiro 3810-193, Portugal*
rafael.vilarinho@inl.int

Abstract

Photonic crystals are dielectric structures with the ability to manipulate light at the nanoscale. Recent research confirmed the existence of natural photonic crystal structures in the exoskeletons of microscopic algae, the diatoms. We used FDTD numerical methods to simulate the optical response of the system when the refractive index contrast of the structure is enhanced by adding suitable materials to the pore structure. The thickness of these materials is also optimized through these simulations. Then, using cleanroom-based thin-film deposition techniques for various materials, we demonstrate that an altered pore structure introduces shifted spectral properties. This study provides an opportunity to implement these biomaterials in future projects involving light-harvesting.

Introduction

Nowadays, due to the miniaturization of components nanoscale technologies are at an all-time high. Light, the most widely available source of energy, can be manipulated at nanoscale with the aid of photonics, including the use of photonic crystals. Photonic crystals are nanoscale structures characterized by periodic patterns, e.g., pore lattices filled with a different refractive index than that of the bulk material. The existence of a periodic dielectric function due to the crystal periodicity, gives rise to the so-called photonic bandgap, a set of wavelengths/energies and crystallographic directions for which propagation within the photonic crystal is forbidden. The existence of a bandgap is of extreme technological interest since it allows to strongly modify light-matter interaction within the crystal by means of morphology rather than material properties. For example, strongly enhanced absorption at the photonic bandgap edges is possible⁵. Interestingly, to modify the photonic properties and position of the bandgap, one can also modify the crystal parameters, such as the pore volume, by introducing materials with different refractive index properties.

Photonic crystals are commonly produced in cleanrooms, with the use of nanofabrication techniques, thus obtaining structures with highly defined parameters and properties. However, in demand of a high reproducibility, the fabrication of photonic structures can become cost-unfriendly, not to mention the difficulty that some techniques require environmentally hazardous methods. An alternative to those conventional techniques for the fabrication of photonic crystals is offered by diatoms, i.e. microalgae which grow structures with photonic crystal-like characteristics named the girdles¹. A girdle is a split ring structure, consisting of a silica slab perforated with holes (Fig.1A). Fig.1B and Fig.1C show a more detailed view of the porosity of this structure. These pores have a rather complex morphology in 3D and are arranged in a periodic pattern characterized by a lattice constant with geometries that can vary between species, including square and hexagonal types².

There are today no protocols for specifically manipulating the girdle lattice constant. We approached this by modification of the pore filling volume via deposition of different materials, in which the effective refractive index of the system will change. The latter is crucial since the spectral width of the bandgap is directly related to the refractive index contrast between the bulk and the pores in certain circumstances; the larger the contrast the wider the spectral width of the bandgap becomes.

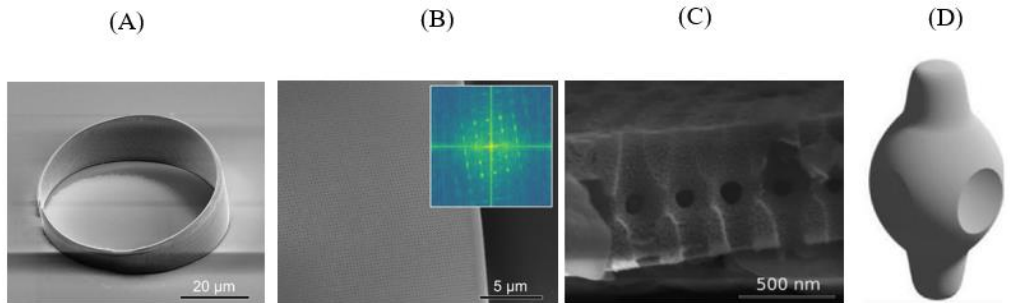


Fig.1: Girdle morphology. (A) Overview of the split-ring like girdle structure. (B) Surface pore lattice and FFT periodicity transform. (C) Cross section view of the internal structure, showing the complexity of the pore system. (D) Schematic of the pore volume fraction filled by the non-silica filling medium.

Methods

FDTD Simulations

To have an idea of how the photonic properties of the girdle slab will change, some simulations are being carried out using the commercial tool Lumerical

FDTD. The aforementioned simulations are being executed for the *Coscinodiscus granii*, whose girdles exhibit a rectangular lattice with a lattice constant of *ca.* 285 nm. The pores are being filled with materials of higher refractive indexes, such as silicon nitride, titania and silicon, with an optimized thickness, in order to measure the reflectance at normal incidence, giving us the position of the bandgap.

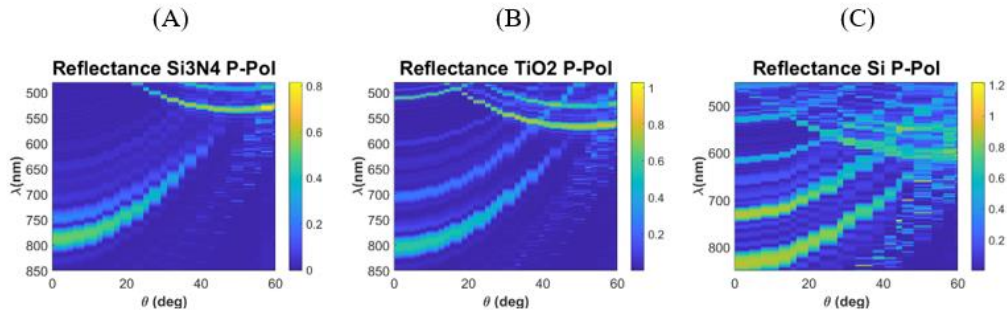


Fig.2: Simulations of the angle dependence of the reflectance of a girdle-like structure with three different materials with a thickness of 30 nm. Pores filled with: (A) silicon nitride, (B) titanium and (C) silicon. FDTD Simulations were based on previous models developed for the natural system².

Optical characterization

For the optical characterization, we aim to measure the reflectance at normal incidence to detect the position of the bandgap, as well as at various angles, to see how the structure behaves and to study the dispersion of the bandgap. These measurements are carried out in a Fourier Image Spectroscopy setup, using a 50 μm optical fiber and a 100x oil immersion lens. For measurements with water as the immersion medium, the girdles are immobilized in glass slab that was previously deposited with poly-lysine.

Results

The effect of the refractive index contrast

Simulations performed in Lumerical FDTD show a strong reflectance peak that is blue-shifted for large angles. The reflectance peak is characteristic of the photonic bandgap and then allows us to monitor its evolution as we introduce new materials in the structure. As can be observed, the bandgap becomes wider as the refractive index of the material deposited increases ($n_{\text{Si}_3\text{N}_4}=2.0458$, $n_{\text{TiO}_2}=2.6142$, $n_{\text{Si}}=3.9766$). Also, when the contrast is increased, a red-shift is observed at all angles, as well as the appearance of secondary gaps at shorter wavelengths and large angles. Simulations shown in Fig.2 assume the immersion medium to be water.

Film thickness optimization

The material that's desired to deposit must have a thickness large enough such that it plays a significant role in the photonic properties. However, too thick material layers would close the pores completely. Our simulation results show that a thickness of 30 nm for the three materials used in this study is a good trade-off between tunability of the optical properties and pore size. For this selection, it was taken into account the amount of localized field within the structure, in which it was maximum for 30 nm.

Conclusions

We conclude that one can in fact tune the photonic properties of girdle bands by depositing higher refractive index materials inside the pores. The material deposition can be realized either in a cleanroom or using *in vivo* doping, exploiting natural incorporation mechanisms during the growth of the diatom exoskeleton. Diatoms are present in all oceans, rivers, and ponds all in high quantities, counting at least 100,000 species. It is nearly possible to measure all their various photonic properties for utilization in specific applications, such as light harvesting for solar cells. But acknowledging that some organisms developed structures with high-quality properties that can be used for photonic applications is a major step for future eco-friendly and cost-effective projects involving biomaterials, serving as an alternative to cleanroom nanofabricated photonic crystals.

References

- [1] Johannes W. Goessling, William P. Wardley, and Martin Lopez-Garcia. "Highly Reproducible, BioBased Slab Photonic Crystals Grown by Diatoms". In: *Advanced Science* 7.10 (2020), p. 1903726.
- [2] Johannes W. Goessling et al. "Biosilica slab photonic crystals as an alternative to cleanroom nanofabrication?" In: *Faraday Discuss.* 223 (0 2020), pp. 261–277.
- [3] Martin Lopez-Garcia et al. "Light-induced dynamic structural color by intracellular 3D photonic crystals in brown algae". In: *Science Advances* 4.4 (2018), eaan8917.
- [4] William P. Wardley, Johannes W. Goessling, and Martin Lopez-Garcia. Plasmonic crystals with highly ordered lattice geometries using continuous metal films on diatom bio-silica as both scaffolds and sources of tuneability. 2021. url: <https://arxiv.org/abs/2108.01602>.
- [5] Mortensen, N. A., & Xiao, S. (2007). Slow-light enhancement of Beer-Lambert-Bouguer absorption. *Applied Physics Letters*, 90(14), 141108.

Acknowledgments

RV, MLG and JWG thank the Fundação para a Ciência e a Tecnologia for support through grant no. PTDCBTA-BTA20612021.

P13 |

SYNTHESIS OF MICROPARTICLES OF $\text{Cu}_2\text{ZnSnS}_4$ BY HYDROTHERMAL METHOD AND ITS APPLICATION AS CONGO RED PHOTOCATALYST

Paula Salazar¹, Rodrigo Henríquez¹, Pablo Zerega¹, Francisco Figueredo¹
¹Laboratorio de Electroquímica, Instituto de Química, Facultad de Ciencias, Pontificia
Universidad Católica de Valparaíso, Av. Universidad 330, Valparaíso, Chile.
*e-mail: paula.salazar@pucv.cl

The textile, food and pharmaceutical industries are expanding daily worldwide, they are located within the most polluting industries due to the fact that wastewater is discharged into watercourses with high concentrations of dyes and traces of drugs. Many of these compounds are stable to light and biodegradation, being considered as emerging organic contaminants [1]. Advanced oxidation processes (AOPs) emerge as an effective alternative for the removal and elimination of this type of contaminants. Heterogeneous photocatalysis has been extensively studied as it is an efficient, low-cost and durable method. As the main photocatalyst, TiO_2 , has been used for the degradation of a large number of dyes and drugs. The disadvantage of TiO_2 is its absorption in the UV region of the solar spectrum [2]. On the other hand, quaternary chalcogenides based on $\text{Cu}_2\text{ZnSnX}_4$ ($X = \text{S}, \text{Se}$) are a possible alternative due to their close band gap (ca. between 0.8 to 1.5 eV depending on the phase considered), low cost, abundance of its constituent elements in the earth's crust and its low toxicity. As a photocatalyst, $\text{Cu}_2\text{ZnSnS}_4$ (CZTS) has shown good results in the treatment of some emerging organic pollutants, but studies are scarce [3].

The objective of this work was to synthesize CZTS by means of a low-cost hydrothermal method and to evaluate it as a potential photo-catalyst in the photo-degradation of Congo Red (CR). The synthesis of microparticles using a mixture of: 2 mmol of CuCl_2 , 1 mmol of ZnCl_2 , 1 mmol of SnCl_2 and 4 mmol of $\text{CH}_4\text{N}_2\text{S}$ in a Teflon reactor at 200°C for 72 h.

Characterization was performed through scanning electron microscopy (SEM), X-ray diffraction (XRD) and UV VIS spectroscopy. For simple photocatalysis, a 0.04 mM CR solution was and 35 mg of microparticles were added and shaken in the dark for 30 min to generate adsorption-desorption equilibrium. Then, the solution was exposed to a 1000 W sunlight simulator and aliquots of 500 μL of solution were taken to monitor photo-degradation using a UV VIS spectrophotometer.

The concentration value of the solution can be obtained through a calibration curve of the CR dye and the degradation of CR by photocatalysis over time could be obtained according to formula (1):

$$\text{Efficiency of degradation (\%)} = \frac{C_0 - C_t}{C_0} \times 100 \quad (1)$$

Where C_0 is the concentration of Congo Red solution before light, C_t is the concentration of CR solution at time t after light.

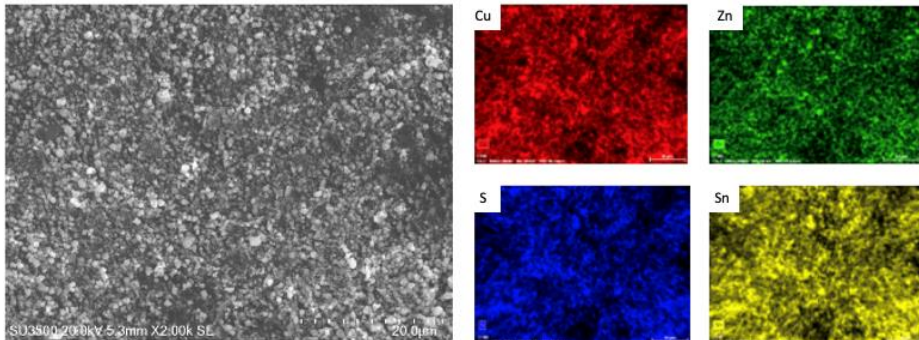


Fig.1 SEM image of CZTS microparticles synthesized using the hydrothermal method at 2.00k, elemental mapping of microparticles.

Figure 1 shows the SEM image of the synthesized CZTS microparticles, compact and uniform microparticles with average diameters of 0.83 μm can be observed. On the other hand, the composition analysis in mapping mode shows that the microparticles obtained present a homogeneous distribution of the 4 constituent elements of the quaternary phase. The structural characterization of the obtained microparticles is shown in Figure 2. In the XRD pattern, the peaks located at 28.35°, 47.23°, 56.00°, 69.17° and 76.30° can be associated to crystallographic planes (112), (220), (312), (400) and (316) according to the pattern from CZTS tetragonal kesterite ICDD 04-015-0223.

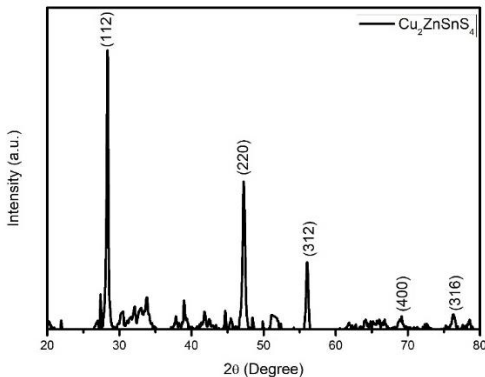


Fig.2 XRD of CZTS microparticles synthesized by hydrothermal method at 200 °C in 72 h in concentration 2:1:1:4.

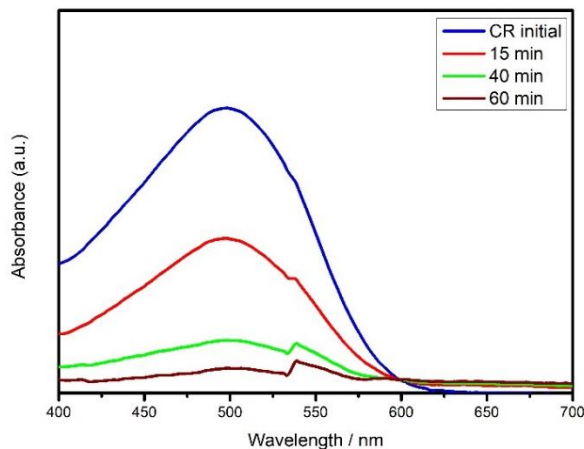


Fig.3 Molecular absorption spectrum obtained in the photo-degradation of CR.

Through the analysis of the UV VIS spectra (see Fig. 3), it has been possible to determine that the photodegradation process has a yield of 90.2% with only 60 minutes of exposure.

In conclusion, the hydrothermal method has proven to be an economic direct synthesis route through which the $\text{Cu}_2\text{ZnSnS}_4$ phase can be obtained with high crystallinity and without the presence of unwanted binary or tertiary phases. This can be employed in the photo-degradation of CR in a highly efficient and fast process. The characteristics confirm that the CZTS phase can be considered in the degradation of emerging organic contaminants. In the future, it will be expected to characterize by determining the band gap (E_g) of the phase, Raman, BET, XPS, Mott-Schottky, EIS and, on the other hand, build the degradation mechanism by identifying intermediates in HPLC -MS.

Reference

- [1] Oturan, M. A., Aaron, J. J., *Critical Reviews in Environmental Science and Technology* 44(23), 2014, pp. 2577-2641.
- [2] Tang, H., Zhang, D., Tang, G., Ji, X., Li, W., Li, C., Yang, X., *Ceramics International* 39(8), 2013, pp. 8633-8640.
- [3] Guo, Y., Wei, J., Liu, Y., Yang, T., Xu, Z., *Nanoscale research letters* 12(1), 2017, pp. 1-7.

Acknowledgments

Dr.(c) P.S. are grateful for the economic support of the SCHOLARSHIP of the Pontificia Universidad Católica de Valparaíso, "PUCV Postgraduate Scholarship Beneficiary 2021".

P14 |

CHARACTERIZATION OF Al_2O_3 AND SiO_2 ULTRA-THIN FILMS DEPOSITED BY ALD FOR MICROFABRICATED RUBIDIUM VAPOR CELLS

F. M. Cunha*, M. F. Silva, J. H. Correia

CMEMS-UMinho – University of Minho, Campus Azurem, 4800-058, Guimarães, Portugal

LABELS – Associate Laboratory, Braga/Guimarães, Portugal

*e-mail: pg47183@uminho.pt

Introduction

Alumina (Al_2O_3) and silicon dioxide (SiO_2) films were characterized for their suitability as a protective coating for microfabricated rubidium vapor cells (magnetic sensors for magnetoencephalography). The resistance enhancement of the vapor cells by implementing an ALD (Atomic Layer Deposition) film is the final goal. Typically, an ALD system presents excellent control over the ultra-thin film's thickness (< 20 nm) and allows complex 3D structures to be covered with a high-aspect-ratio coating [1–3]. Figure 1 represents a rubidium vapor cell with an ALD coating layer.

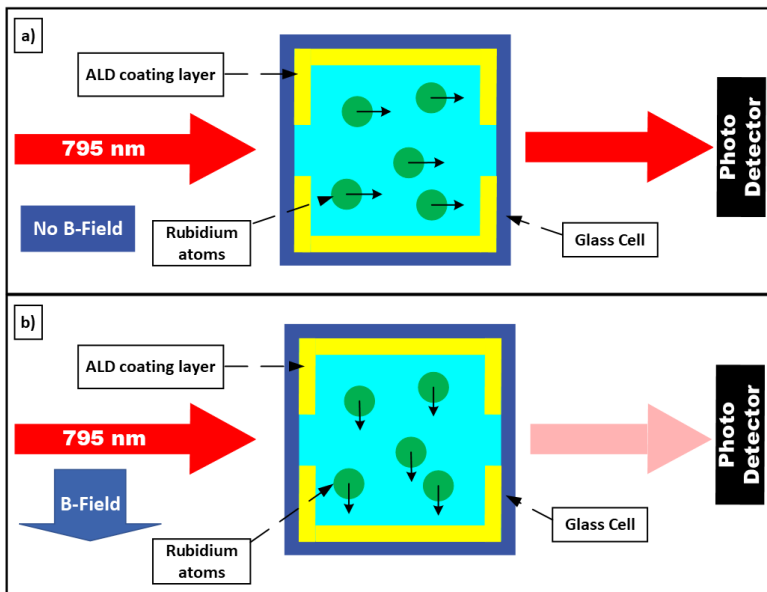


Figure 1. Representation of a microfabricated rubidium vapor cell; (a) Without magnetic field; (b) With a magnetic field.

The ALD system used (from SENTECH Instruments GmbH) has an excellent thickness precision control (at the atomic level) using an *in-situ* ellipsometer in real-time during the deposition of the ultra-thin films. Also, the depositions can be done by Plasma-Enhanced ALD (PEALD) or Thermal ALD (ThALD). This work shows the characterization (optical and using energy dispersive spectroscopy) of Al₂O₃ and SiO₂ ultra-thin films such as the thickness, refractive index, and chemical composition. Also, the ALD recipe parameters are presented with the growth per cycle (GPC) value for each deposition. Moreover, the deposition, of different films, is done without the vacuum breaking in both techniques (PEALD and ThALD). Therefore, the ALD technique can be used to increase the lifetime of microfabricated rubidium vapor cells (in glass/silicon) by an ultra-thin (approximately 10 nm thick) coating layer deposited on the internal cell walls [4,5].

Furthermore, the ALD ultra-thin films present different industrial applications: in semiconductors, automobiles, aeronautics, aerospace, energy, optical devices, displays, high-resolution screens, and solar panels, among others.

Methods

A 10 nm ultra-thin film of Al₂O₃ was deposited by ThALD and 10 nm ultra-thin films of Al₂O₃, and SiO₂ were deposited by PEALD technique at 200 W of electrical power in a silicon (Si) n-type (100) substrate. A warmed-up reactor at 100 °C was controlled and the precursors' lines were heated to 125 °C. The substrate temperature was fixed at 250 °C for Al₂O₃ and SiO₂. The ALD precursors were heated at 60 °C for the SiO₂. The ALD precursors pulverization time varies between 60 - 180 ms with a co-reactant between 60 ms for ThALD and 5 s for PEALD. The ALD purge time varies between 1 s and 5 s. For the deposition of the Al₂O₃, the GPC was 0.72 Å/cycle by ThALD technique and 1.12 Å/cycle by PEALD technique. The deposition of SiO₂ by PEALD technique had a GPC of 1.03 Å/cycle.

Results

Figure 2 shows the refractive index measured by spectroscopic ellipsometer in a range between 400 nm to 900 nm for the Al₂O₃ and SiO₂ ultra-thin films in comparison to the literature references.

Ellipsometry is a well-known technique to obtain the refractive index and the thickness of thin films. Typically, the measurements considered a model with a small 2 nm layer of SiO₂ due to the wafer's contact with the atmosphere. The

PEALD and ThALD Al_2O_3 show an average refractive index of approximately 0.1 below the reference refractive index (Figure 2 black line), the same result is observed with the refractive index of PEALD SiO_2 . Also, the measured thickness by the ellipsometry technique show: 11 nm \pm 0.5 nm thick for the ThALD Al_2O_3 , 10.5 nm \pm 0.5 nm thick for the PEALD Al_2O_3 , and 11 nm \pm 0.5 nm thick for the PEALD SiO_2 .

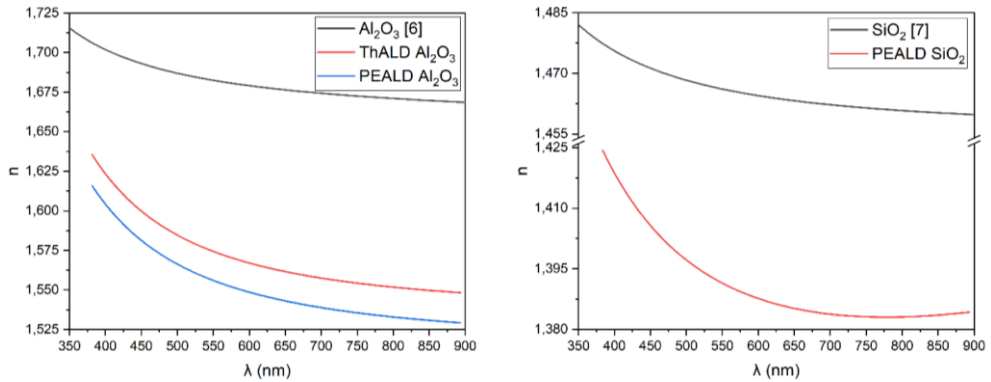


Figure 2: Comparison between the refractive index values measured and the literature[6,7].

Furthermore, Energy Dispersive Spectroscopy (EDS) characterization for identifying and quantifying the elemental composition of the ultra-thin films was performed.

Figure 3 shows the EDS elemental analysis using 5 kV of power. The PEALD Al_2O_3 shows an atomic percentage of 58.65% for Oxygen (O) and 41.35% for Aluminum (Al) with a mass percentage of 45.69% for O and 54.31% for Al. The atomic percentage for ThALD Al_2O_3 shows 59.37% for O and 40.63% for Al with a mass percentage of 46.42% for O and 53.57% for Al.

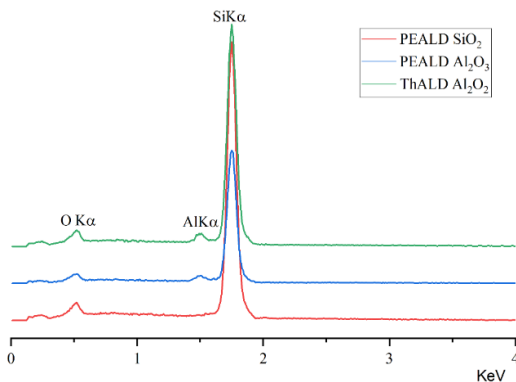


Figure 3: Elementary analysis with EDS of PEALD Al_2O_3 , ThALD Al_2O_3 , and PEALD SiO_2 .

Conclusions

The deposition of ultra-thin films of Al_2O_3 and SiO_2 by ALD was presented. Characterization techniques were used to find the chemical, physical and optical properties of the films. The ellipsometry characterization technique of the deposited materials allows to obtain the refractive index and confirm the ultra-thin film thickness. The ellipsometry technique shows a refractive index below the theoretical values and a thickness upper than what was measured *in-situ* (during the deposition). The EDS chemical characterization show a main peak which represents the substrate Si n-type (100). This peak is so relevant because the deposited ultra-thin films thickness is below 20 nm (ultra-thin film). The Al_2O_3 chemical characterization is very close to the theoretical values for the atomic percentage (60% for O and 40% for Al) and mass percentage (47% for O and 53% for Al). The obtained results are very close to the expected values, but a crystalline analysis using a precise technique such as X-ray photoelectron spectroscopy (XPS) must be done.

Therefore, this work presents the characterization of the Al_2O_3 and SiO_2 ultra-thin films to increase the lifetime of microfabricated rubidium vapor cells (in glass or silicon) for application in magnetoencephalography.

References

- [1] S.M. George, Atomic layer deposition: An overview, *Chem. Rev.* 110 (2010) 111–131.
- [2] M. Kemell, E. Härkönen, V. Pore, M. Ritala, M. Leskelä, Ta_2O_5 and TiO_2 based nanostructures made by atomic layer deposition, *Nanotechnology*. 21 (2010).
- [3] T. Faraz, H.C.M. Knoop, M.A. Verheijen, C.A.A. Van Helvoirt, S. Karwal, A. Sharma, V. Beladiya, A. Szeghalmi, D.M. Hausmann, J. Henri, M. Creatore, W.M.M. Kessels, Tuning Material Properties of Oxides and Nitrides by Substrate Biasing during Plasma-Enhanced Atomic Layer Deposition on Planar and 3D Substrate Topographies, *ACS Appl. Mater. Interfaces*. 10 (2018) 13158–13180.
- [4] S. Karlen, J. Gobet, T. Overstolz, J. Haesler, S. Lecomte, Lifetime assessment of RbN_3 filled MEMS atomic vapor cells with Al_2O_3 coating, *Opt. Express*. 25 (2017) 2187.
- [5] S. Woetzel, F. Talkenberg, T. Scholtes, R. Ijsselsteijn, V. Schultze, H.G. Meyer, Lifetime improvement of micro-fabricated alkali vapor cells by atomic layer deposited wall coatings, *Surf. Coatings Technol.* 221 (2013) 158–162.
- [6] R. Boidin, T. Halenkovič, V. Nazabal, L. Beneš, P. Němec, Pulsed laser deposited alumina thin films, *Ceram. Int.* 42 (2016) 1177–1182.
- [7] L. V. Rodríguez-de Marcos, J.I. Larruquert, J.A. Méndez, J.A. Aznárez, Self-consistent optical constants of SiO_2 and Ta_2O_5 films, *Opt. Mater. Express*. 6 (2016) 3622.

Acknowledgments

This work was supported by: Project MME reference 105399 and FCT with the project MPhotonBiopsy, PTDC/FIS-OTI/1259/2020, Infrastructures Micro&NanoFabs@PT, reference NORTE-01-0145-FEDER-022090, POR Norte, Portugal 2020.

P15 |

STRUCTURAL AND OPTICAL PROPERTIES OF SPRAYED UNDOPED ZnO THIN FILMS SUITABLE FOR RESISTIVE GAS SENSORS

J. A. Rodríguez.

Facultad de Física-IMRE, Universidad de la Habana, San Lázaro y L, 10400, Plaza, Habana, Cuba.

E-mail: jar@fisica.uh.cu

introduction

The coexistence of very high electrical conductivity and optical transparency makes the so called “Transparent Conducting Oxides (TCOs)” unique materials for a wide range of applications. They include [1]: window defrosters, transparent thin films transistors, light emitting diodes, semiconductor lasers, transparent electrodes for flat panel displays and solar cells as well as resistive gas sensors. In particular, this last application is just the subject of intensive investigation in view of the necessity to sense different harmful gases.

Even though different TCOs have been obtained, studied and used so far, increasing attention is devoted to ZnO last years. This is related to its unique properties. In fact, besides its high conductivity and transparency, it is a non-pollutant, biocompatible and direct wide-band gap semiconductor ($E_g \sim 3,3eV$ at 300K), with great mechanical, chemical and thermal stability and high efficiency of radiative recombination (efficient photoluminescence) [2]. This last property allows using ZnO for luminescent down shifting conversion to improve efficiency of photovoltaic devices [3]. Moreover, it can be obtained through simple, low cost and suitable for mass production processes, such as spray pyrolysis [4], just making this material competitive regarding ITO (indium-tin oxide), the classical and most used TCO.

Regarding the development of resistive sensors of various gaseous substances, ZnO is widely used in view of its high surface sensitivity to both, oxidizing and reducing gases. Indeed, the behavior of such devices depends on surface reactions taking place between the gas to be sensed and the sensor material. This fact implies the necessity to increase the area/volume ratio of the active sensor region which may be achieved by using polycrystalline nanostructured (nanocrystalline) materials. From the other hand, nanostructured ZnO layers with good physical properties may be obtained by using spray pyrolysis technique [5-6].

We are engaged in a systematic work aimed to obtain sprayed ZnO thin films with adequate properties for gas sensors and photovoltaic applications. An own experimental spray set-up was developed. Thin films of ZnO, several hundred nm thick and $\sim 1\text{cm} \times 1\text{cm}$, corresponding to different values of the experimental set-up parameters were deposited on corning glass substrates. Some preliminary results, as obtained through Scanning Electron Microscopy, X-Ray diffraction, and optical transmittance and photoluminescence spectra measurements, are described here.

Methods

The experimental set-up for spray pyrolysis is a classical one with some particularities. Indeed, the typical spray nozzle was substituted by an insulin plastic syringe with a very thin stainless-steel needle. The needle tip is placed within the centre of the carrier gas (N_2) stream, thus producing the spray. All solution containers and conductors are glassy or plastic but the needle, to minimize contamination through contact with metallic parts. The solution flow rate was controlled through the height of the liquid column from the spray nozzle to the container, which was fixed at 33cm . A Mariotte configuration was employed to keep constant the pressure of the liquid column and, consequently, the solution flow rate. Substrate temperature was controlled within $\pm 5^\circ\text{C}$ through a thermocouple with the help of a temperature controller.

Table 1. Data for studied samples.

Sample	Sub. Tem. ($^\circ\text{C}$)	Dep. Time (min)
1	300	10
2	300	20
3	300	10
4	360	15
5	360	10
6	360	5

Depositions were achieved by using aqueous 0,1M zinc nitrate solution. Nozzle-substrate distance was fixed at 32cm . Nitrogen flow rate was fixed and controlled by a flowmeter. Six different samples were selected for the present study (see table 1). They correspond to two substrate temperature values, i. e., 300°C and 360°C and different deposition times, ranging from 5min to 20min , being these parameters the most important to determine the final film properties [5]. All deposited films were annealed during four hours on air at 400°C for structure stabilization.

Results

Almost transparent, nanostructured, with good homogeneity to naked eye, good adhesion to the substrate and stable and repetitive properties ZnO layers, were obtained.

Due to the importance of substrate temperature during deposition, a comparative analysis is achieved for samples corresponding to 300°C and 360°C . Figure 1 depicts SEM micrographs with magnification $20,54 K \times$ for sample 2 (left micrograph) and 5 (right micrograph). A fine granular microstructure is observed for both of the samples. However, on average, the dimension of the grain are about 100nm for sample 2 and about 150nm for sample 5 (as determined by $80K \times$ micrographs), thus yielding a more compact material for the first. This fact should be taken into account for gas sensor applications, since the permeability of the sensor material to the sensed gas plays an important role in the device response [5]. In both cases, grains are formed by a few nanocrystallites, as can be appreciated through higher magnification micrographs.

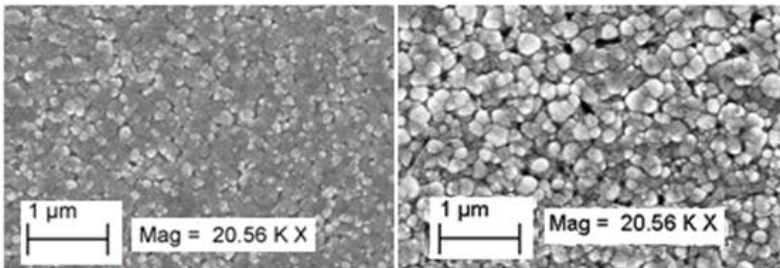


Fig. 1 SEM micrograph for sample 2 (left) and sample 5 (right).

X-Ray diffraction spectra for the same samples (2 and 5) were obtained and compared with patterns corresponding to polycrystalline thin film and monocrystalline volumetric ZnO samples. The good correlation observed allows establishing, in all cases, the typical hexagonal Wurtzite microstructure. A rough calculus through the Debye-Scherrer formula and using these spectra yielded values for nanocrystallite diameters of about $25,9\text{nm}$ and $28,6\text{ nm}$ for samples 2 and 5 respectively, as evaluated through (002) and (101) maxima.

Transmittance spectra for samples 2 and 5 were also obtained. Spectrum for a clean glass substrate was also determined (see figure 2). Having into account the direct character of the optical gap of ZnO, a Tauc's plots was achieved, thus

yielding respective band-gap values of 3,270eV and 3,275eV, in accordance with reported values for this material, obtained through the same technique [7].

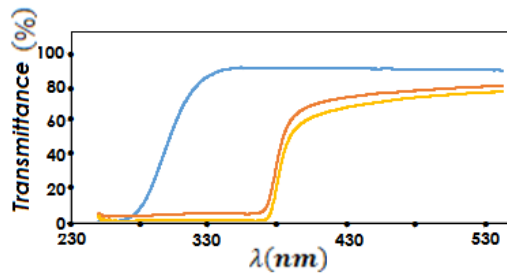


Fig. 2 Transmittance spectra for samples 2 (red), 5 (yellow) and glass substrate (blue).

Finally, figure 3 shows room temperature system corrected photoluminescence spectra, excited by the 325nm line of a 30mW He-Cd laser, for samples 1 and 3, deposited at 300°C and for samples 4 and 6, deposited at 360°C . Interesting features are observed. Firstly, all of the spectra exhibit a sharp maximum at about 380nm (3,26eV), which has unambiguously been ascribed to the fundamental band to band emission (free exciton line). Since undoped samples are considering, the rest of the spectra should represent contributions of transitions between conduction and/or balance bands and intra band-gap energy levels due to different lattice defect such as oxygen or Zn vacancies, interstitial zinc or oxygen and intersite defects [8]. Observe the analogies and differences between behavior of PL spectra for samples deposited at the same and different temperatures. However, in all cases, the phenomenon of down shift conversion is observed, thus indicating the possibility of using the deposited films for photovoltaic applications.

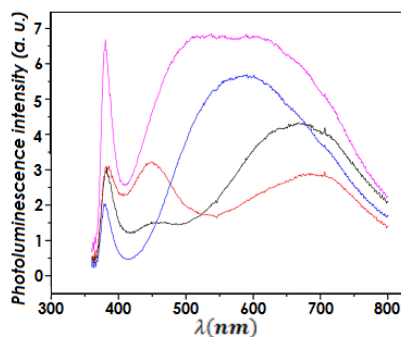


Fig. 3 Photoluminescence spectra for samples 1 (black), 3 (red), 4 (blue) and 6 (pink).

Conclusions

The developed technology based on a spray pyrolysis process allows obtaining nanostructured undoped ZnO thin films with controlled and adequate physical properties for different applications. The possibility of using this approach to develop resistive gas sensors is envisaged. Moreover, the films exhibit efficient photoluminescence in the visible and infrared portion of the spectrum when excited with ultraviolet radiation thus indicating the presence of a down shifting conversion and the possibility to increase the efficiency of photovoltaic devices.

References

- [1]- Transparent conducting oxide films for various applications: a review. Rakesh A. Afre, Nallin Sharma, Maheshwar Sharon and Madhuri Sharon. *Rev. Adv. Mater. Sci.*, 53, (2018) 79-89.
- [2]- Zinc Oxide-From Synthesis to Applications: A Review. Agnieszka Kolodziejczak-Radzimska and Teofil Jesionowski. *Materials*, 7, (2014) 2833-2881.
- [3]- Zinc oxide nanoparticles for improvement of thin film photovoltaic structures' efficiency through down shifting conversion. K. Znajdek et al. *Opto-Electronic Review*, 2,5 (2017) 99-102.
- [4]- A comprehensive review on ultrasonic spray pyrolysis technique: Mechanism, main parameters and applications in condensed matter. Saeed Rahemi Ardecani et al. *Journal of Analytical and Applied Pyrolysis*, 141, (2019) 1-19.
- [5]- Peculiarities of nitrogen dioxide detection with sprayed undoped and indium-doped zinc oxide thin films. R. Ferro, J.A. Rodríguez and P. Bertrand. *Thin Solid Films*, 516, (2008) 2225–2230.
- [6]- Chemical spray pyrolysis deposition of transparent and conducting Fe doped CdO thin films for ethanol sensor. K. Sankarasubramanian, P. Soundarrajan, K. Sethuraman, K. Ramamurthi. *Materials Science in Semiconductor Processing*, 40, (2015) 879–884.
- [7]- Characterization and Studying of ZnO Thin Film deposited by Spray Pyrolysis: Effects of Annealing Temperature. H. Belkhalifa et al. *Optik*, 127, (2016) 2336-2340.
- [8]- Structural and photoluminescence properties of ZnO thin films obtained by a sol-gel process. J. Petersen et al, *Journal of Applied Physics*, 104, (2008) 113539.

Acknowledgements

The author is deeply grateful to the Institute of Microelectronics of Barcelona for the use of the experimental facilities to obtain the photoluminescence spectra and the SEM micrographs. In particular, to Dr. César Fernández for his help in obtaining the latter.

P16 |

SRO/NITRIDE-BASED ELECTROPHOTONICS FOR SENSING APPLICATIONS

A. A. González-Fernández^{1,2*}, J. Hernández-Betanzos², M. Aceves-Mijares², O. Pérez²,
F. Orozco², C. Domínguez-Horna¹

¹ *Instituto de Microelectrónica de Barcelona (IMB-CNM, CSIC), Universitat Autònoma de Barcelona, 08193 Bellaterra, Spain*

² *National Institute for Astrophysics, Optics and Electronics (INAOE), Department of Electronics, P.O. Box 51, Puebla 72000, Mexico.*

**e-mail: research@gonzalez-fernandez.net*

Introduction

The search for integrable Si-based light sources using quantum phenomena has conveyed Light Emitting Capacitors (LECs) using Silicon Rich Si Oxides (SRO). The main advantage of this kind of emitter is its ability to be integrated directly into crystalline Si wafers using processes regularly used for Integrated Circuit (IC) fabrication. However, SRO-based LECs can present disadvantages compared to other external light sources, such as relatively low intensities [1].

Nevertheless, its unique character of self-alignment and auto-coupling to photonic elements, the possibility of distribution along all the area of the chip, and seamless integration in electronics, makes them an outstanding alternative for developing a variety of applications that can take advantage of an integrated light source. The development of photonic Lab-on-a-chip (LOC) is one of the most interesting.

For this to be a reality, it is necessary to adopt a new holistic approach to integrating emitters, photonic elements, photodetectors, and driving electronics, instead of treating photonic and electronic components separately to later couple them. This new point of view can show that the apparent disadvantages of the emitters may be easy to overcome, not relevant at all, and even advantageous in some cases, achieving better results in the pertinent characteristics for specific applications in shorter times.

In this work, we study the possibilities of obtaining electrophotonic systems, including light emitters, passive photonic building blocks, and photodetectors that can be monolithically integrated into the emitters/detectors driving/processing electronics. We depart from the characteristics of SRO-based LECs and explore the behavior and limits that basic passive photonic elements present when transmitting and manipulating the light from them. We also overview traditional and novel photodetectors than can be integrated into emitter-waveguide-

photodetector schemes and the possibilities of using them for sensing applications.

Methods

All systems are designed and fabricated in the framework of CMOS fabrication processes, based on crystalline silicon wafers and its traditional methods for doping, etching, SiO₂ growth or deposition, and Si₃N₄ fabrication using Chemical Vapor Deposition (CVD) techniques. Photonic components are based on the SiN Photonic Integration Platform by IMB-CNM (CSIC). References [2], [3] are examples of publications containing details of the fabrication methods of SRO and SRO-based LECs and emitter-waveguide-detector transceivers. Electrical characterization of devices was done using a custom-made software controlling two Keithley source/meters, models 2450 and 2636, to characterize the emitter and the photodiodes using a probe station in controlled dark conditions. Passive photonic building blocks were simulated using the modules MODE and FDTD of the software Lumerical using the optical parameters of the materials widely available in the literature, which matched experimental results from ellipsometry characterization to pilot films. Simulation of fabrication processes and photodetecting device performances were done using Silvaco-Athena and Silvaco-Athlas software.

Results

Emitters

A variety of methods can be used to obtain LECs, each one with its advantages and disadvantages regarding fabrication, compatibility, and integrability, as well as emission characteristics and turn-on voltages [1], [2]. For sensing applications, Si₃N₄/SRO bi-layer emitters in which the Si enrichment is performed through ionic implantation are particularly interesting. These allow for direct coupling of Si₃N₄ waveguides (WG) in which a significant part of the light is produced in the nitride/SRO interface, directly inside the same photonic passive element. This way, coupling issues are eliminated, and relatively low bias powers are possible, improving integrability to standard IC. This way, instead of only focusing on improving the emission of LECs, a better coupling, guiding, and detecting of the light can be pursued, as the improvement margins for this are greater than those for LEC efficiency optimization. Figure 1 presents some examples of different LEC stack structures and a micrograph of a Si₃N₄/SRO bilayer emitting light.

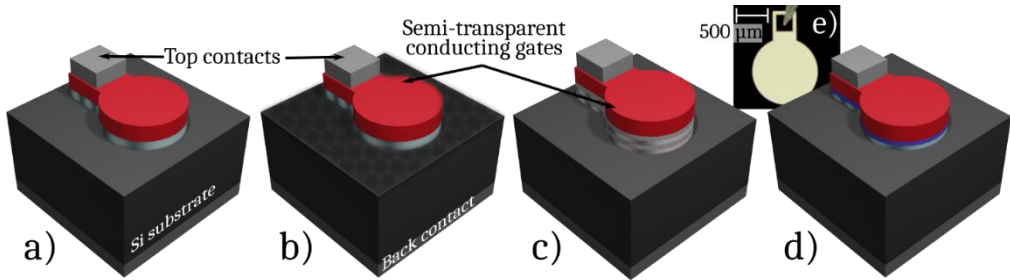


Figure 1. Schematic of the structures for LECs fabricated on Si substrate with transparent conductors as gates and Al contacts on top and reverse to drive the emitters. Active layers are single SRO films on polished (a) and textured (b) surfaces; alternating films of SRO with different concentrations (c); and $\text{Si}_3\text{N}_4/\text{SRO}$ bilayer (d). (e) shows a micrograph of a $\text{Si}_3\text{N}_4/\text{SRO}$ LEC with a polysilicon gate emitting light under electrical stimulation.

Photonic elements

While sensing schemes can be achieved using only straight slab WG, the possibility of integrating other blocks such as bends, tappers, or splitters would expand the freedom for designers and the platform's flexibility. It is necessary to verify the feasibility of such elements in the frame of the available materials, techniques, and emitters. Figure 2 shows the results from wave propagation simulations in Si_3N_4 passive photonic components. The designs can be adjusted to the preferred wavelength based on future applications. Still, it is demonstrated that bends, tappers, splitters, couplers, and others can be achieved with the technology compatible with the previously analyzed LECs.

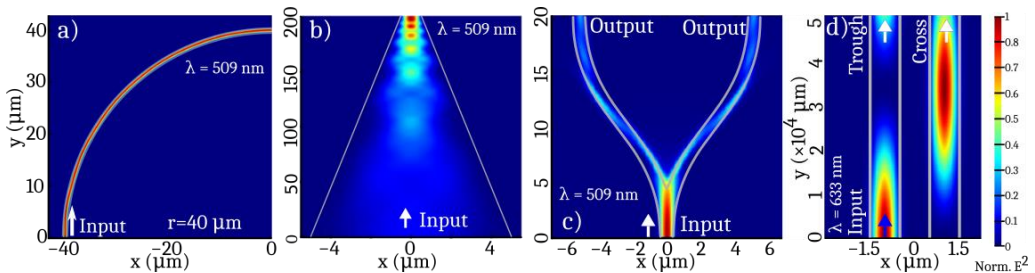


Figure 2. Simulations of electric field propagation in photonic elements with 60 nm thick Si_3N_4 core and SiO_2 cladding for light with $\lambda=509$ nm or $\lambda=633$ nm. (a) Bend, (b) Tapper, (c) Splitter, and (d) Directional coupler. The color scale indicates the value of the normalized square of the electric field E^2 .

Photodetectors and complete transceivers

The emission spectra of the SRO-based LECs are very convenient for direct integration of Si photodetectors, as the range is within an acceptable responsivity. Therefore, a simple p-n junction photodiode can be easily integrated into the

systems by placing it directly under the waveguide core, next to a buried cladding to contain the field until its detection is required. The higher refractive index of Si also plays in favor of light transmission to the detection region. However, the relatively low efficiency of such emitters presents a challenge compared to external ones. Aside from the constant efforts to improve the efficiency of the emitters, an alternative way to tackle this issue is the design of seamlessly integrated photodetectors, and WG optimized for the specific wavelengths of interest. The monolithic nature of electrophotonics allows for novel approaches that take advantage of CMOS-compatible materials and planar technology. Figure 3 shows two possibilities of integrating a photodetector in an emitter-waveguide-photodetector scheme at the wafer level, which completes the full emitter-transmitter-photodetector (transceiver) requirement for the development of photonic sensors. These schemes allow for easy functionalization of transceivers as sensors by creating a cavity that will enable the contact between an analyte and WG. This way, the photodetector will provide electrical signal changes depending on the characteristics of the substance, as the propagation of light will be affected by its optical parameters and hence, the intensity of the detected light. The proof of concept of this approach has been published in [4]. Experimental results on fabricated transceivers using the scheme depicted in figures 3 a) and b) indicate that, when using a core thickness of 430 nm, it is possible to obtain photocurrent signals in the order of nA for LEC driving voltages of 5 V. In addition, theoretical projections of novel photodetectors with gain as the one depicted in figure 3 c) foresee even higher photocurrent values[5]. These results significantly reduce the complexity and footprint of the driving and processing circuitry, guaranteeing the possibility of obtaining a true electrophotonic integrated circuit with all necessary photonic and electronic elements in a single chip.

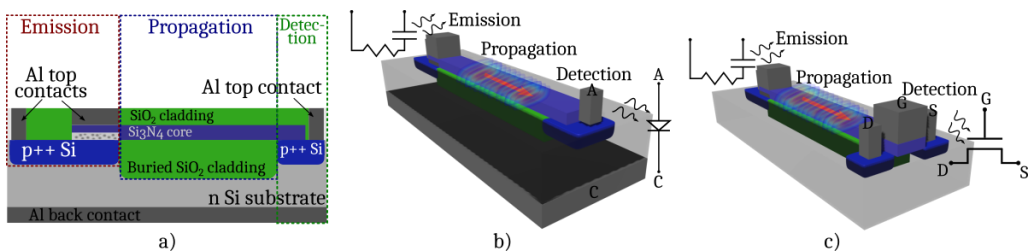


Figure 3. a) Cross-section of a complete emitter-waveguide-photodetector scheme using a p-n junction as photosensing device; b) 3D representation of the same scheme; and c) 3D representation of an emitter-waveguide-photodetector using an integrated "Wavesensor" like the one proposed in [5], which introduces a photosensor inspired in the structure of a MISFET, but using the core of the waveguide as the insulator below the gate.

Conclusions

The evolution of SRO-based light sources has allowed their practical use in integrated photonic systems. As opposed to photonic circuits with external light sources, the presented approach conveys unprecedented flexibility in the distribution of the light sources. The characteristics of the emitted light make it very well suited for laboratory-on-chip applications. The presented simulations show that it is possible to design passive photonic elements that can transmit and manipulate light emitted by the LECs. The specific design for applications can take advantage of the very tight integration to improve the overall performance of the systems significantly, as design from a holistic perspective allows for more efficient use of the photons and electrons for the desired purposes. Redesigns beyond the first proof of concept experimentally showed a significant step forward in reducing the required powers to drive the emitters for detectable photocurrents, allowing for designing integrated driving and processing electronic circuitry to be obtained in the same chip and process. The overall results of the advancements in SRO-nitride-based electrophotonics show that this is one of the most promising ways to achieve an actual CMOS-compatible photonic LOC in a medium-short time.

References

- [1] J. Juvert *et al.*, "DC Electroluminescence Efficiency of Silicon Rich Silicon Oxide Light Emitting Capacitors," *Journal of Lightwave Technology*, vol. 31, no. 17, pp. 2913–2918, Sep. 2013.
- [2] J. Alarcón-Salazar *et al.*, "Comparison of light emitting capacitors with textured and polished silicon substrates towards the understanding of the emission mechanisms," *Journal of Luminescence*, vol. 203, no. June, pp. 646–654, Nov. 2018.
- [3] M. Perálvarez *et al.*, "Si-nanocrystal-based LEDs fabricated by ion implantation and plasma-enhanced chemical vapour deposition.," *Nanotechnology*, vol. 20, no. 40, p. 405201, Oct. 2009.
- [4] A. A. González-Fernández, *et al.*, "Refractive index sensing using a Si-based light source embedded in a fully integrated monolithic transceiver," *AIP Advances*, vol. 9, no. 12, p. 125215, Dec. 2019.
- [5] J. Hernández-Betanzos *et al.*, "Understanding the Light Detection in an Integrated Novel Electrophotonic Wavesensor Photodetector," *Applied Sciences*, vol. 12, no. 3, p. 1264, Jan. 2022.

Acknowledgments

The authors acknowledge the support by CONACyT. The authors recognize the great work by the IMB-CNM (CSIC) cleanroom personnel and its SiN Photonic Integration Platform (<https://www.imb-cnm.csic.es/en/micro-and-nanofabrication-clean-room/silicon-nitride-photonic-integration-platform>).

**DESENHO E TECNOLOGIA DE SENSORES E MEMS | DISEÑO Y TECNOLOGÍA
DE SENSORES Y MEMS | DESIGN AND TECHNOLOGY OF SENSORS AND MEMS**

O19 |

CoNi AND Ni-BASED BARCODES TOXICITY FOR TAGGING AND MAGNETIC MANIPULATION OF HELA CELLS

M. I. Arjona^{1*}, C. González-Manchón², S. Durán¹, M. Duch¹, R. P. del Real³, A. Kadambi¹, J. P. Aguil¹, M. Redondo-Horcajo², L. Pérez-García^{4,5,6}, E. Gómez^{6,7}, T. Suárez² & J. A. Plaza¹

¹*Instituto de Microelectrónica de Barcelona, IMB-CNM (CSIC) Campus UAB, 08193 Cerdanyola, Barcelona, Spain.*

²*Centro de Investigaciones Biológicas Margarita Salas, CIB (CSIC), 28040 Madrid, Spain.*

³*Instituto de Ciencia de Materiales de Madrid, ICMM (CSIC), Cantoblanco, 28049 Madrid, Spain.*

⁴*School of Pharmacy, University of Nottingham, University Park, Nottingham, UK.*

⁵*Departament de Farmacologia, Toxicologia i Química Terapèutica, Universitat de Barcelona, 08028 Barcelona, Spain.*

⁶*Institut de Nanociència I Nanotecnologia (IN2UB), Universitat de Barcelona, 08028 Barcelona, Spain.*

⁷*Departament de Ciència de Materials i Química Física, Universitat de Barcelona, 08028 Barcelona, Spain.*

*e-mail: mariaisabel.arjona@imb-cnm.csic.es

Abstract

Microtechnologies provide new opportunities for chip miniaturization, allowing the study of the microworld. Silicon chips as barcodes, biochemical and mechanical sensors or electrical devices have been internalized into cells without interfering their viability. To progress on the integration of new functionalities, we propose intracellular chips with magnetic capabilities for cell manipulation. Here, we explore two technologies to obtain suspended chips made of cobalt/nickel (CoNi) alloy and nickel (Ni) with magnetic capabilities. We develop a technology based on photolithographic processes in combination with electroplating methods to grow metal layers. The fabricated devices combining coding and magnetic capabilities, were demonstrated for tagging a subpopulation of HeLa cells and their subsequent magnetic separation. We envision the combination of multiple functionalities to sophisticated intracellular chips that improve current techniques for cell magnetic manipulation, sorting or tracking.

Introduction

The identification of objects at the micro- and nanoscale is a challenge, where the progress on semiconductor technologies allows the fabrication of miniaturized chips at the scale of living cells [1]. For instance, researchers have used microbarcodes as labelling tools as they are representations of data attached to the

object of interest for clear identification, avoiding misreading [2], while other techniques based on magnetic approaches have been followed to identify and manipulate systems at the microscale [3,4]. In this sense, the combination of functional features, as identification and magnetic capabilities, support the development of innovative devices capable to identify a subpopulation of cells coupled with their manipulation by external magnetic fields.

In this work, we present a technological development of an initial top-down photolithographic microfabrication technology encompassing the batch fabrication of millions of reproducible devices at the microscale. We demonstrate the bottom-up integration of magnetic materials with a specific electroplating process. Co and Ni metals and their alloys can be electroplated, a technique compatible with microelectronic fabrication techniques. Co shows a higher magnetic saturation than Ni, which implies higher magnetic forces. However, pure Co was discarded due to its reported cell toxicity [5,6]. Despite the presence of Co, CoNi devices were tested as the alloy might not impact on cell viability. Therefore, we center our technological development on the electroplating of Ni and CoNi alloy.

Specific tools with multifunctional proficiencies are requested to explore cells behaviour. We take a step forward and present a proof of concept of magnetic intracellular chips for tagging and manipulating subpopulations of living cells. In particular, we study HeLa cells viability upon magnetic barcode uptake and investigate the magnetic separation and isolation of a subpopulation of HeLa cells with internalized magnetic intracellular chips as barcodes from the rest of the cell culture, and study their viability after the magnetic separation [7].

Results & Methods

Our previously designed polysilicon barcodes used for cell labelling were fabricated using a photomask with positive patterns of the codes to transfer the design via photolithography directly onto the substrate [8]. However, for the electrodeposition of the metal layers, in this work, it was necessary to first obtain an inverted barcode photoresist mould where CoNi alloy and Ni will be subsequently grown to fill the voids of this mould. The fabrication of the magnetic barcodes started with a 100 mm p-type silicon wafer as substrate (Fig. 1a), where a 1 μm -thick silicon oxide (SiO_2) layer was later deposited as a sacrificial layer (Fig. 1b). An initial 50 nm-thick Titanium (Ti) layer and a second 50 nm-thick Ni layer were evaporated as seed layers to allow the further deposition of the Ni or the CoNi alloy (Fig. 1c and 1d, respectively). Then, a 0.9 μm -thick photoresist

coat (Fujifilm OiR 620-09) was spun and patterned by photolithography to obtain an engraved pattern of the devices on the wafer (Fig.1e,f). After that, we proceed to the metal layer deposition (CoNi or Ni) by customized electroplating processes to reach the required thickness of $\sim 1 \mu\text{m}$ and, lastly, the photoresist was stripped with acetone, and the sample was later rinsed with isopropyl alcohol and deionized water for 1 minute (Fig.1g).

A two-step process was developed to release the chips: first, the samples were exposed to a thermal shock of 20 minutes at $200 \text{ }^\circ\text{C}$ and their subsequent rapid cooling to $21 \text{ }^\circ\text{C}$ (Fig.1h), and a second highly effective peel-off method, previously developed to release Suspended Planar-Array (SPA) chips[9,10] where a drop of an aqueous mounting medium (Fluoromount, Sigma-Aldrich) was placed directly on top of the chips, left to solidify at room temperature (RT) (Fig.1i), and the subsequent manual force to peel the solidified membrane encircling the chips (Fig.1j). Finally, the chips were collected in Eppendorf tubes by centrifugation after dissolving the water-soluble membrane (Fig.1k).

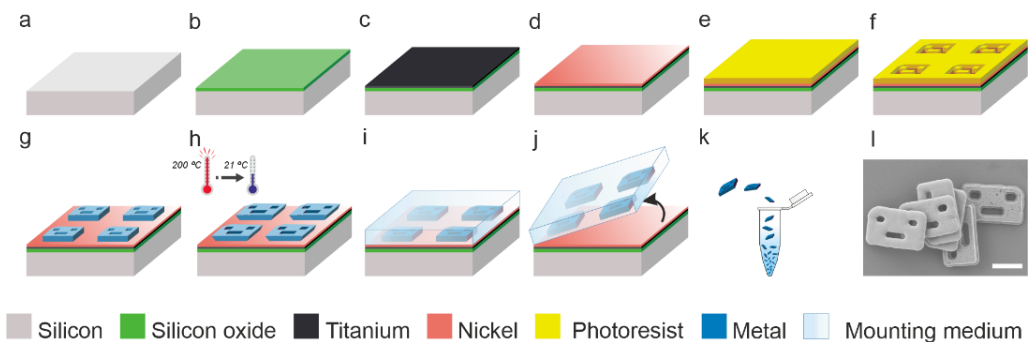


Figure 1. Description of the fabrication process and the released magnetic barcodes. Scale bar: $5 \mu\text{m}$

The intended uses of the suspended CoNi and Ni barcodes (Fig.11) encompass living cell tagging and cell manipulation, hence, cell toxicity studies were done with both materials. HeLa cells were grown and co-cultured with the barcodes following a protocol to facilitate cell-device contact as well as microscopic analysis. Simultaneously, we investigated whether the material could affect cell viability by culturing HeLa cells over CoNi and Ni substrates. Hence, we fabricated a platform ($0.5 \text{ mm} \times 1.5 \text{ mm}$ of lateral dimension) with two distinct neighbouring layers consisting in the bare Ni and CoNi alloy in a single piece of wafer. Moreover, a second platform with an Au coating was developed to

encapsulate the CoNi and Ni layers, thus cells seeded over the platform will be limited to be in contact with the biocompatible Au coating.

A visual exploration under an optical microscope was enough to certify the negative effects of the CoNi devices on cells. These barcodes, even not being internalized, resulted toxic to the cells, with general cell death after the first day in co-culture. HeLa cells seeded on the coated platforms (both, CoNi and CoNi Au-coated) showed markedly reduced viability after 48 h of incubation, compared to those grown on the Ni side of the platforms, where cell growth and attachment were intact. These results show that the CoNi alloy affects HeLa cells viability while Ni devices do not seem to alter their normal functions. To further assess HeLa cell viability, we used a fluorescence vital dye labelling, and observed that barcode-bearing HeLa cells appeared viable and identical to neighbouring cells.

After demonstrating their biological compatibility, the Ni barcodes were demonstrated to label HeLa cells showing that the cell underwent division cycles comparable to those of the surrounding control cells [7]. Additionally, a simple proof of concept of magnetic cell manipulation was performed by placing a magnet at the bottom of the well containing HeLa cells co-cultured with Ni barcodes. After a 15 s exposure, most of the cells without a device could be transferred to another well while the cells with internalized Ni barcodes remained in the bottom trapped by the magnetic field gradient. After that, we checked cell viability up to 4 days after the magnetic separation, and both, barcode-bearing and non-bearing HeLa cells, were perfectly healthy.

Conclusions

In this work, we present the technological development to integrate magnetic manipulation capabilities into intracellular barcode chips. Initially, the fabrication technology of CoNi alloy was successfully achieved, nevertheless, CoNi devices were later found to be toxic for living HeLa cells. These results were simultaneously confirmed with the experiments carried out on the dual-layer platform system, both without and with Au coating, concluding that CoNi is a non-suitable alloy for living cell applications. Conversely, Ni barcodes were fabricated and tested in HeLa cells, that apparently preserved their functionality and ability to proliferate with the internalized devices. Consequently, it was demonstrated that Ni barcodes allows the separation of HeLa cells with internalized Ni barcodes, with the consequent enrichment of this cell population. Adequate cell growth up to 4 days after the magnet exposure results in healthy cultures suitable for further experiments. A wide range of chips covering several

applications has been previously demonstrated: as polysilicon barcodes for cell tracking[8], as mechanical sensors for intracellular mechanics[11-13], as biochemical sensors with the use of SPA chips[9,10], and even as radio-frequency identification and transceiver systems for tracking and monitoring living cells[14]. This study provides the development and demonstration of magnetic intracellular chips for cell manipulation, coupled with the capacity of tagging subpopulation of cells. These initial results will open the possibility of using magnetic intracellular chips in cell biology applications. We envision the integration of magnetic manipulation into multifunctional chips as a key element in field of intracellular devices.

References

- [1] J. Zimmerman, R. Parameswaran & B. Tian, *Biomater. Sci.* 2(5) (2014): 619–626
- [2] P.J. Sweeney. *RFID for Dummies*. John Wiley & Sons, 2010
- [3] G. Zhang, et al. *Journal of Nanoparticle Research* 11.2 (2009): 441-448
- [4] A. Fornara, et al. *Nano letters* 8.10 (2008): 3423-3428
- [5] E. Sabbioni, *Nanotoxicology* 8.1 (2014): 88-99
- [6] S. Chattopadhyay, et al. *Chemico-biological interactions* 226 (2015): 58-71
- [7] M. I. Arjona, et al. *Scientific Reports* 11(1) (2021): 1-9
- [8] E. Fernandez-Rosas, *Small* 5.21 (2009): 2433-2439
- [9] N. Torras, et al. *Advanced Materials* 28.7 (2016): 1449-1454
- [10] J.P. Aguil, et al. *Advanced Functional Materials* 27(13) (2017): 1605912
- [11] R. Gómez-Martínez, et al. *Nature Nanotechnology* 8(7) (2013): 517
- [12] M. Duch, et al. *Nature Materials* 19.10 (2020): 1114-1123
- [13] M. I. Arjona, et al. *Advanced Materials* (2022): 2109581
- [14] X. Hu, et al. *Physical Review Applied* 8.1 (2017): 014031

Acknowledgments

This study was financed by the Spanish Government through project MINAHE6 (TEC2017-85059-C3), MINAHE7 (PID2020-115663GB-C3), and FEDER funding. M.I.A. thanks the MCIU for the predoctoral Grant (BES-2015-075932) and the University of Granada for the guidance and support within the doctoral program. A.K. thanks Sastras University for the international mobility grant. The authors also thank the Clean Room of IMB-CNM (CSIC) for fabrication of the chips, and the Confocal Laser and In Vivo Multidimensional Microscopy Service at CIB (CSIC) for great support.

O20 |

PHOTONIC PLANAR TAPER WAVEGUIDE

P. Lourenço^{*a,b}, A. Fantoni^{a,b}, J. Costa^{a,b}, M. Fernandes^{a,b}, M. Vieira^{a,b}
^a*DEETC-ISEL-Instituto Politécnico de Lisboa, 1949-014 Lisboa, Portugal*
^b*CTS-UNINOVA, Caparica, Portugal*
^{*}*e-mail: pj.lourenco@campus.fct.unl.pt*

Introduction

In photonic integrated circuits it is often necessary a structure to compensate for the cross-section mismatch between waveguides of different dimensions. One of the most representative instances of such a constraint is the vertical outcoupling of light, often used between an optical fibre and a photonic integrated chip. The Electromagnetic (EM) beam of energy diffracted by a resonant waveguide grating propagates in free space and towards a single mode optical fibre, where it couples with its fundamental mode.

This grating structure must be wide enough to assure efficient coupling with the beam of energy of the optical fibre. Typical core widths are approximately 10 μm and 5 μm for single mode optical fibres operating in the near infrared and visible wavelengths, respectively. Thus, these grating structures must be wider to couple the fundamental mode of the resonant waveguide grating with the diffracted EM energy beam, which is coupling to the lowest order mode of the optical fibre.

Furthermore, the optical interconnects linking operational structures in the photonic integrated circuit are usually single mode waveguides, 400 to 500 nm wide. Thus, a spot-size conversion is necessary between the single mode waveguide and the resonant waveguide grating mode profiles. Often, a taper waveguide performs the lateral expansion of the propagating mode and provides mode profile matching between narrow and wider waveguides. Once the lateral expansion of the mode profile occurs efficiently (no losses), we get adiabatic transfer of energy between the different cross-section waveguides, and the only mode propagating in the wider structure is the fundamental one.

Back in 1977, Burns et al. (Burns, Milton, and Lee 1977) have presented the general derivation of equations to guide the design of adiabatic waveguide tapers while minimizing their length. The derived main rule of adiabatic taper design is governed by the following equation:

$$\theta < \frac{\lambda_0}{2Wn_{eff}} \quad (1)$$

here, θ is the local half angle at a given z point along the taper, λ_0 is the free space wavelength, W is the width of the taper at a given z location and n_{eff} is the modal index of the propagating mode in the taper. Moreover, the half slope of a linear taper (or a linear section of a taper) is given by:

$$\tan\left(\frac{\alpha}{2}\right) = \frac{W_{high} - W_{low}}{2L} \quad (2)$$

where, α is the sum of left and right sidewall angles (assuming a symmetric taper), W_{high} and W_{low} are the waveguides wider and narrower widths, respectively, and L is the length of the taper waveguide.

Previous work (Burns et al. 1977) reported an adiabatic parabolic taper waveguide (reduced to three linear segments to facilitate fabrication) connecting 30 μm and 4 μm wide waveguides, only through a taper over 2 mm long. Nonetheless, parabolic tapers are not the only solutions for adiabatic coupling. There are other configurations also capable of highly efficient transfer of EM energy between different cross-section waveguides. Namely, one may find reports in the literature of adiabatic exponential, gaussian and linear taper waveguides. Nevertheless, they all require long tapered waveguides and shallow slopes of the sidewalls.

More recently, research has been developed on a different taper configuration – the denominated non-adiabatic tapers. Examples of such configurations have been reported by Spühler (Spuhler et al. 1998) and Luyssaert (Luyssaert et al. 2005) which, by exploiting the developments in genetic algorithms, have announced highly efficient and compact non-adiabatic taper waveguides. Also, Zhang (Zhang et al. 2017) and Liu (Liu et al. 2018) used a similar strategy to design their compact tapers. The former exploited the effective medium theory to design a row of inclusions of a different refractive index material, to converge the EM beam through a linear taper and into a focal point, and the latter, by placing identical inclusions along the sides and in the core of the taper waveguide, obtained a staircase-like taper with perturbations of the core refractive index at locations calculated by an evolutionary algorithm.

Finally, Huang (Huang and Ho 2005) has exploited the Graded Index (GRIN) concept by designing a structure that consisted of several layers of alternating materials with different thicknesses, creating a material with a parabolic refractive

index profile along the height of the structure. Our proposed line of action considers a similar approach, only creating a specific refractive index profile through the width of the structure instead of along its thickness.

This work bases its approach on the GRIN concept to design an inverted taper waveguide, at the operating wavelength of 1550 nm. The engineered structure consists of a planar metamaterial waveguide, which is able to expand laterally the propagating mode's profile from 450 nm to 14.27 μm (typical width of the resonant waveguide grating), within an 11.1 μm long structure. Follows the evaluation of the coupling efficiency of a typical linear inverted taper as a function of the structure length, thus establishing a reference for comparison with the results obtained by the proposed planar metamaterial waveguide.

Methods

The development of the presented structures has been accomplished through RSoft (RSoft n.d.), a photonic device tools platform for the design, simulation, analysis and optimization of arbitrary optical structures. In this work, we have used the software packages implementing the beam propagation method (BeamPROP n.d.) and the finite differences time domain algorithm (FullWAVE n.d.), for the simulation and performance analysis of the designed structures. The beam propagation method has been employed to evaluate the propagation in longer structures and where reflections are of no significance (inverted taper and wider section waveguide), and the finite differences time domain algorithm was utilized to analyse the propagation/reflection through/at complex structures (planar metamaterial taper waveguide) and interfaces between materials.

In our simulations, we have considered an identical Silicon-on-Insulator (SOI) platform for both the linear inverted taper and the planar metamaterial waveguides. This platform consists of, from bottom to top, a semi-infinite layer of Silicon (Si), a Silicon Dioxide (SiO_2) layer 2 μm thick and where the 250 nm high Hydrogenated Amorphous Silicon (a-Si:H) taper waveguides are designed as deposited halfway upwards the SiO_2 height, and a semi-infinite layer of air. Figure presents a 3D representation and a Z plane cut of the refractive index of both structures.

The linear inverted taper waveguide has been evaluated regarding its coupling efficiency for a range of representative structure lengths, namely 150 μm , 200 μm , 250 μm and 300 μm , as the first set of iterations, and 400 μm , 550 μm , 700 μm , 850 μm and 1000 μm , for the second set. The coupling efficiency has been

determined by launching the fundamental Transverse Electric (TE) mode of the narrower cross-section (250 nm x 450 nm) and monitor the overlap integral as it couples to the fundamental mode of the wider cross-section (250 nm x 14.27 μm). Simultaneously, we monitor the total power propagating in the inverted taper waveguide. Figure depicts (on the left) the lateral field expansion as propagation evolves throughout the structure for the 850 μm long inverted taper waveguide and the coupling efficiency results obtained for the first and second sets of iterations.

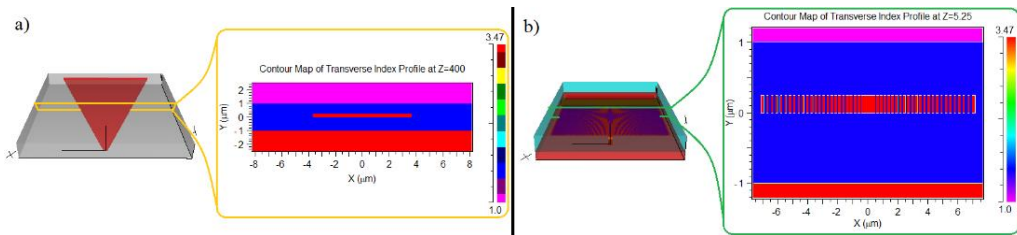


Figure 1 - a) 3D representation and cut plane at Z=400 μm of the linear taper; b) 3D representation and cut plane at Z=5.25 μm of the planar metamaterial waveguide.

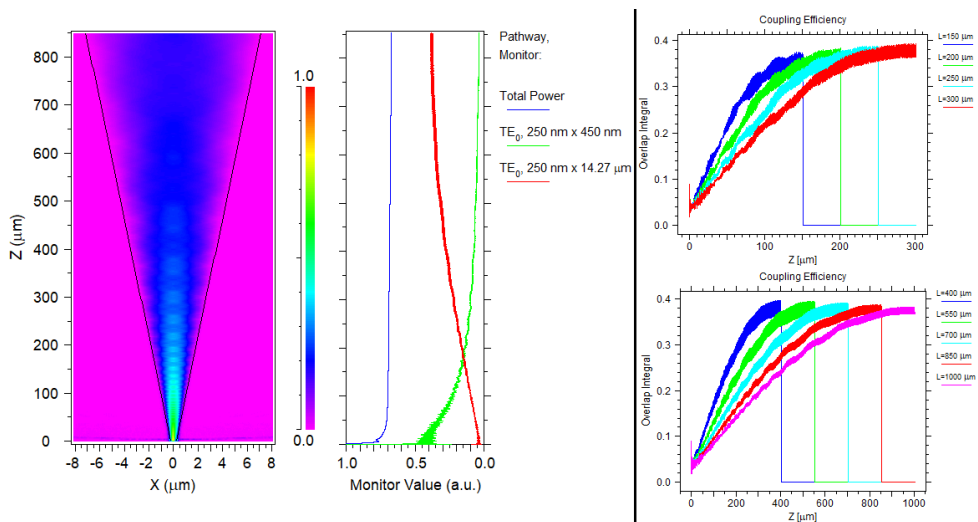


Figure 2- (left): fields propagation along the 850 μm instance of the linear taper waveguide; graph shows the coupling/decoupling evolution of the fields with the fundamental mode of the wider/narrower cross-section. (right): coupling efficiency obtained for the iterated lengths of the inverted taper waveguide.

We evaluated the performance of the planar taper waveguide by launching the fundamental mode at the input waveguide (cross-section 250 nm x 450 nm), while monitoring the mode’s propagation throughout the structure and assessing the coupling efficiency through the overlap integral to the fundamental mode of the wider cross-section waveguide (250 nm x 14.27 μm). Figure 3 shows the fields propagation along the structure and the obtained coupling efficiency.

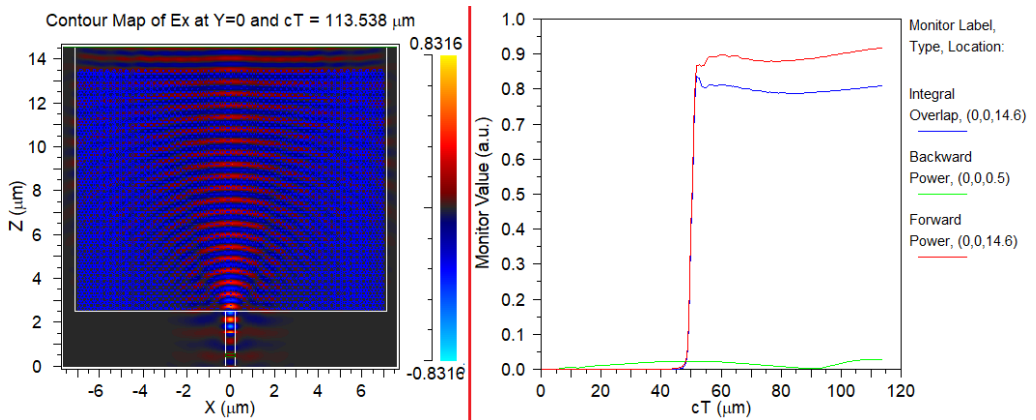


Figure 3 - (left): propagation of the fields throughout the structure; (right): integral overlap over the TE₀ mode of the wider cross-section waveguide at the end of propagation.

Results

The coupling efficiency data of the linear inverted taper waveguide was curve approximated through a moving least squares fit, for interpretation purposes. Figure 4 shows the graphs obtained for all iterated instances of the structure and the best result is the 550 μm long taper, with a coupling efficiency of -1.19 dB. The other iterations have presented the following results: [150 μm <> -1.51 dB]; [200 μm <> -1.39 dB]; [250 μm <> -1.28 dB]; [300 μm <> -1.22 dB]; [400 μm <> -1.21 dB]; [550 μm <> -1.19 dB]; [700 μm <> -1.21 dB]; [850 μm <> -1.23 dB]; [1000 μm <> -1.27 dB].

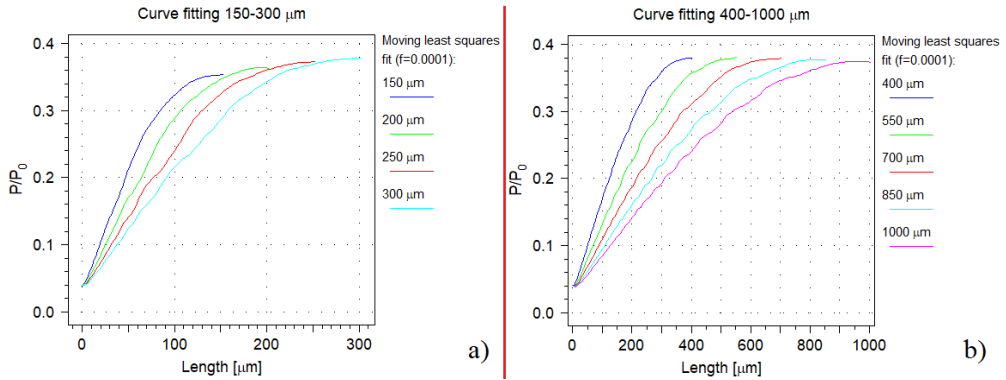


Figure 4 - Moving least squares fit; a) iterated lengths 150-300 μm ; b) iterated lengths 400-1000 μm .

Regarding the planar taper waveguide, the results obtained for the propagated fields and the fundamental mode of the wider cross-section revealed a coupling efficiency of -0.92 dB. Nevertheless, these fields were propagated through a waveguide 100 μm long and compared with the propagation of the fundamental mode under the same conditions, the former revealing a lower coupling efficiency of 0.55 dB when compared to the latter, as depicted in Figure 5.

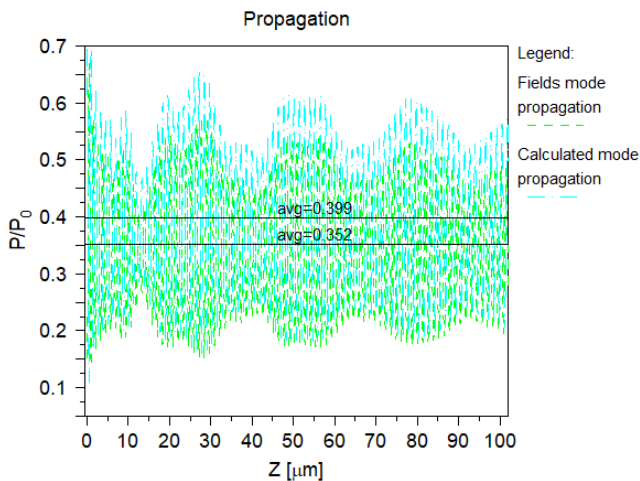


Figure 5 - Propagation of the fields obtained at the planar taper waveguide and the fundamental mode of the wider waveguide.

Conclusions

In this work we propose an alternative approach for the lateral expansion of a propagating fundamental mode. By using a planar taper waveguide consisting of a metamaterial structure, we were able to expand laterally the TE_0 mode from 450 nm to 14.27 μm in a waveguide 11.1 μm long, resulting in an integral overlap penalty of 0.55 dB, when assuming as reference the calculated TE_0 mode and, as arbitrary propagation length, a 100 μm a-Si:H waveguide embedded in SiO_2 .

Considering the obtained results for both, the best case scenario of length iterations ranging 150 μm to 1000 μm , the 400 μm long taper has achieved a coupling efficiency of -1.20 dB, and the 11.1 μm long planar taper waveguide has shown -1.53 dB for the same metric. Moreover, and analysing the results obtained at the other length iterations, we realize that the planar taper waveguide presents lower coupling efficiency than all the other instances, although not significant.

Given the differences in magnitude for the coupling efficiencies obtained in our proposed planar taper waveguide, we have concluded that our metamaterial based structure performs just as well as a linear inverted taper and may present itself as an alternative replacement for the latter structure. Moreover, the reported coupling efficiency resulted of lateral expansion (from 450 nm to 14.27 μm) of the mode profile in a metamaterial planar waveguide 11.1 μm long, while a typical linear inverted taper waveguide requires several hundreds of micrometres.

References

- BeamPROP. n.d. "BeamPROP - Synopsys." Retrieved March 4, 2020 (<https://www.synopsys.com/photonic-solutions/rsoft-photonic-device-tools/passive-device-beamprop.html>).
- Burns, W. K., A. F. Milton, and A. B. Lee. 1977. "Optical Waveguide Parabolic Coupling Horns." *Applied Physics Letters* 30(1):28–30.
- FullWAVE. n.d. "FullWAVE - Synopsys." Retrieved December 29, 2019 (<https://www.synopsys.com/photonic-solutions/rsoft-photonic-device-tools/passive-device-fullwave.html>).
- Huang, Yingyan, and Seng-Tiong Ho. 2005. "Superhigh Numerical Aperture ($NA \gg 15$) Micro Gradient-Index Lens Based on a Dual-Material Approach." *Optics Letters* 30(11):1291.
- Liu, Yingjie, Wenzhao Sun, Hucheng Xie, Nan Zhang, Ke Xu, Yong Yao, Shumin Xiao, and Qinghai Song. 2018. "Adiabatic and Ultracompact Waveguide Tapers Based on Digital Metamaterials." *IEEE Journal of Selected Topics in Quantum Electronics* 25(3).

Luyssaert, Bert, Peter Bienstman, Peter Vandersteegen, Pieter Dumon, and Roel Baets. 2005. "Efficient Nonadiabatic Planar Waveguide Tapers." *Journal of Lightwave Technology* 23(8):2462–68.

RSoft. n.d. "Synopsis RSoft Solutions." Retrieved July 10, 2021 (<https://www.synopsys.com/optical-solutions/rsoft.html>).

Spuhler, M. M., B. J. Offrein, G. L. Bona, Roland Germann, Ilana Massarek, and Daniel Erni. 1998. "A Very Short Planar Silica Spot-Size Converter Using a Nonperiodic Segmented Waveguide." *Journal of Lightwave Technology* 16(9):1680–85.

Zhang, Jingjing, Junbo Yang, He Xin, Jie Huang, Dingbo Chen, and Zhang Zhaojian. 2017. "Ultrashort and Efficient Adiabatic Waveguide Taper Based on Thin Flat Focusing Lenses." *Optics Express* 25(17):19894.

Acknowledgements

This research has been supported by EU funds through the FEDER European Regional Development Fund and by Portuguese national funds by FCT – Fundação para a Ciência e a Tecnologia through grant SFRH/BD/144833/2019, and by projects IPL/2021/MuMIAS-2D/ISEL and IPL/2021/wavesensor_ISEL.

P17 |

SISTEMA ELECTRÓNICO PARA MEDICIÓN DE CALIDAD DE SUSTANCIAS: DISEÑO E IMPLEMENTACIÓN

D. Palacio Abril¹, S. Sierra Alarcón¹, J. J. García¹, F. Segura-Quijano¹

¹Universidad de los Andes, Bogotá, Colombia
da.palacio@uniandes.edu.co

INTRODUCCION

Hoy en día existen cantidad de estudios y laboratorios que trabajan analizando el impacto de químicos y sustancias en las contacto con las personas. Aun así, se tienen circunstancias en donde se necesita tener medidas in situ que indiquen la presencia de algún componente nocivo para el ser humano. Este es el caso de las bebidas alcohólicas; que hacen parte de los productos de mayor consumo en el mundo con un 35% del total de la población según reporta el Ministerio de Salud de Colombia [1] y que adicionalmente a esto se tiene que a nivel país, una de cada cinco botellas de licor viene adulterada según *Euromonitor Internacional* [2]. Otro caso competente es la contaminación del agua con partículas que van desde pesticidas hasta mercurio según ORARBO [3]. Este proyecto se centra en el diseño y desarrollo electrónico de un sistema de detección de sustancias contaminadas haciendo uso de un microcontrolador de bajo consumo y sensor NFC. Se plantea el aprovechamiento de la energía transferida por un dispositivo NFC que permita la alimentación del sistema y la extracción de los datos de este empleando el concepto de *Energy Harvesting*. En términos de medición y caracterización de sustancias se empleará el concepto de *huellas digitales* asociando la capacitancia de un sensor cerámico al entrar en contacto con el líquido en análisis.

METODOLOÍA

Como se mencionó en la descripción, el sensado y caracterización de las sustancias se realizará mediante el uso de capacitores cerámicos, los cuales al entrar en contacto con diferentes sustancias dan como respuesta un cambio de capacitancia. Dichos sensores varían sus medidas en el orden de los 1 a los 200 picofaradios por lo que el método de medición debe que ir de acuerdo con la escala. La curva de calibración se realiza con capacitores cerámicos medidos en un *LCR meter* (medidor de capacitancias, resistencias e inductancias) de referencia *SR715*, el cual tiene un error del 0.2% y una tasa de muestreo de hasta

20 mediciones por segundo [4]. Para la calibración se emplea parte del método de medición, en el cual, Se relaciona la medida de capacitancia en el *LCR meter* con la lectura del *ADC (Analog to Digital Converter)*. El microcontrolador usado tiene una resolución de 12 bits para variaciones de voltaje entre 0 y 3.3 voltios, esto quiere decir que en el sistema dará como resultado un valor entre 0 y 4095, donde 0 representa el límite inferior y 4095 se asociará a la lectura del voltaje máximo; 3.3 voltios. Es menester mencionar que tanto para calibración o medición se hace un promedio de 44 tomas de datos para aumentar la precisión del método. A continuación, se muestra el diagrama de bloques del proceso de calibración del sistema para lectura de capacitores entre el rango estimado.

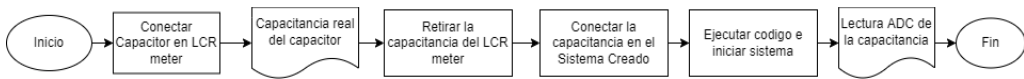


Figura 1. Diagrama de bloques calibración del sistema.

Para este proyecto se emplea un sensor NFC de referencia *ST25DV16* [5] incorporado en un módulo *Extended Click* de *MakroE* [6] y la tarjeta de desarrollo *STM32F103C6* [7], a la cual se le cambió el núcleo por uno de bajo consumo con referencia *STM32L151C6* [8]. La comunicación entre estos dos componentes se hace mediante el protocolo *I2C* dado que el módulo *NFC* tiene una memoria programable *EEPROM* en la cual se almacenan los datos que se quieren enviar a través de la lectura de radiofrecuencia y se modifican registros de configuración que habilitan o inhabilitan funcionalidades. Para lo que le compete a este proyecto se requiere realizar dos tareas; registrar información por medio de *I2C* que pueda ser leída por un dispositivo externo por medio de radiofrecuencia *NFC* y habilitar la funcionalidad de *Energy Harvesting* mediante la modificación de registros para aprovechar dicha energía.

RESULTADOS

Para la calibración del dispositivo se obtienen 2 curvas que siguen una tendencia exponencial que corresponden a los dos tipos de rangos de medición, el primero corresponde a la medida entre 1 pF y 10pF y el segundo entre 10pF en adelante. En la siguiente figura se muestran dichas curvas de calibración realizada para el prototipo en desarrollo con conexiones de capacitor entre los pines A12 y B12.

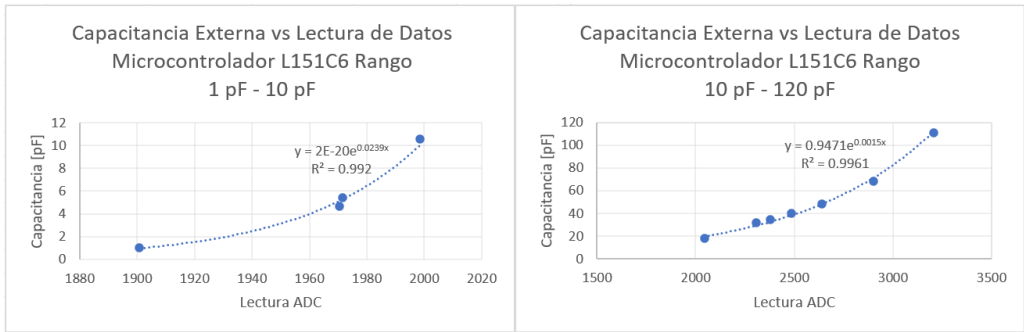


Figura 2. Curvas de calibración sistema de medición de capacitâncias.

Utilizando las ecuaciones que siguen las tendencias de la curva se realizan pruebas otras capacitancias con el mismo LCR se realizan mediciones y se comparan con el método implementado en el prototipo propio obteniendo errores promedio de 5%. Adicionalmente, se obtienen desviaciones estándar promedio de 0.014; valor con el que se asegura precisión en la medición. En la *Figura 3*. Se evidencia la curva que relaciona el valor teórico de las capacitancias con el obtenido en el sistema el cual presenta un coeficiente de correlación cercano al uno, lo que implica que el sistema es funcional para los rangos requeridos.

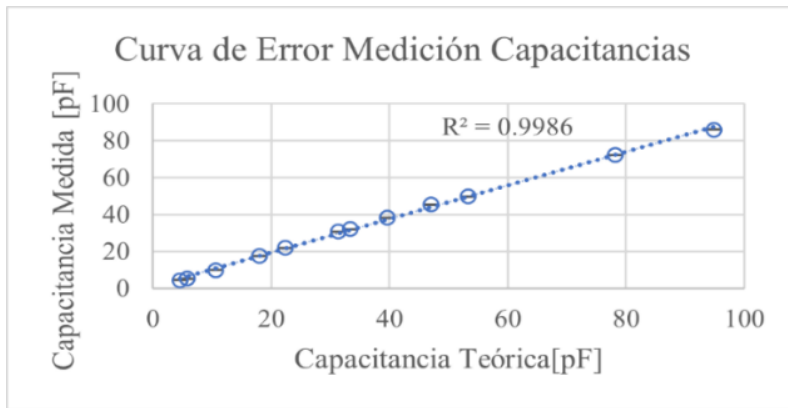


Figura 3. Curva de error de medición de capacitância.

Finalmente se hacen pruebas de alimentación energética para mirar si con la energía entregada por el NFC se podía alimentar toda la cadena de medición. Por lo que se conecta el pin de cosecha de energía del modulo NFC a la alimentación del microcontrolador de bajo consumo. Se realizan pruebas haciendo mediciones

de diferentes capacitancias usando únicamente la alimentación del protocolo NFC y se tiene éxito en las mismas. Para dichas pruebas se coloca el celular en modo de tarjetas NFC de iPhone hasta que el led incorporado de la tarjeta de desarrollo comience a parpadear, en ese momento la medición se habrá realizado y por medio del aplicativo móvil *NFC Tool* [9] se obtiene la medida de este. Como se desea producir un prototipo compacto se realiza un diseño PCB del sistema que incorpore todas las funciones y tenga un tamaño menor. En la siguiente figura se presentan el prototipo funcional junto con el diseño PCB realizado:

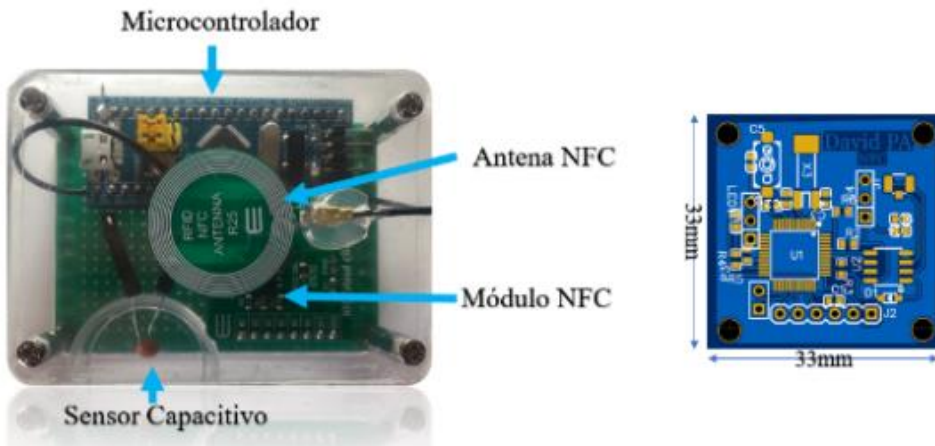


Figura 4. A la izquierda el diagrama de partes del prototipo y a la derecha el diseño pcb con medidas

CONCLUSIONES

El método de medicina realizado presenta alta precisión y exactitud para los rangos en los que se encuentran los sensores capacitivos, lo que hace posible la caracterización de compuestos líquidos con variables electrónicas para determinación de posibles contaminantes en sustancias.

Dada la presencia de los dispositivos móviles en la cotidianidad, se pueden realizar dispositivos electrónicos que aprovechen componentes de estos para así generar menor impacto ambiental ligado al menor uso de recursos, como pantallas y baterías.

REFERENCIAS

- [1] Ministerio de Salud y Protección Social, «Estrategia Nacional de Repuesta Frente al Consumo de Alcohol en Colombia,» [En línea].
- [2] La República, «Una quinta parte de las bebidas alcohólicas en el territorio nacional se ve afectada por la ilegalidad,» [En línea].
- [3] El Observatorio Regional Ambiental y de Desarrollo Sostenible del Rio Bogotá, «Causas y consecuencias de la contaminación del agua en Colombia,» 2021. [En línea]. Available: <http://www.orarbo.gov.co>.
- [4] Stanford Research Systems, «LRC Meters,» [En línea]. Available: <https://www.thinksrs.com/products/sr715720.html>.
- [5] STMicroelectronics, «ST25DV-I2C series Dynamic NFC Tags,» [En línea]. Available: <https://www.st.com/en/nfc/st25dv-i2c-series-dynamic-nfc-tags.html>.
- [6] MikroElektronika, «NFC Extend Click,» [En línea]. Available: <https://www.mikroe.com/nfc-extend-click>.
- [7] STMicroelectronics, «STM32F103C6 Mainstream Performance line,» [En línea]. Available: <https://www.st.com/en/microcontrollers-microprocessors/stm32f103c6.html>.
- [8] STMicroelectronics, «STM32L151C6 Ultra-low-power Arm Cortex-M3 MCU,» [En línea]. Available: <https://www.st.com/en/microcontrollers-microprocessors/stm32l151c6.html>.
- [9] wak dev, «NFC TOOLS - IOs,» [En línea]. Available: <https://www.wakdev.com/en/apps/nfc-tools-ios.html>.

P18 |

PROJETO DE ENCAPSULAMENTO DE SENSORES INERCIAIS USANDO TECNOLOGIA LTCC

Hector Rodriguez A., Seabra, A C.

Escola Politécnica Universidade de São Paulo

Instituto de Pesquisas Tecnológicas, Processo nº 2019/17658-5, Fundação de Amparo à

Pesquisa do Estado de São Paulo

e-mail: armandohrb@usp.com

Introduction

LTCC (Low Temperature Cofired Ceramics) technology has a vast variety of applications due its adaptability to the different necessities that may arise during the development of an electronic device especially MEMS(Micro-electromechanical systems)[1] devices for the different purposes or situations in which we may want to use or apply them instead of more common PCB(Placed Circuit Board) board; taking into account the amount and frequency of data that is intended to be gathered or monitored and the conditions to which the electronic sensor will be submitted and LTCC based substrate could be ideal. Our project consists in the encapsulation of an accelerometer chip in a LTCC to measure acceleration for various exterior applications. For our project purposes, wireless connection is a must when gathering the accelerometer readings[2], so a viability, functionality and efficiency comparison and characterization in regards to the use of the same wireless chip and antenna on a normal FR-4 PCB board and LTCC board is due to take place.

Methods

For our research the main method is the building of two identical boards one in common PCB substrate and another on LTCC so that we can compare and gather faithful data to analyze, first step is the selection of the main components that are to be used.

For the accelerometer, an ADXL313 chip was selected due to availability and Ultralow power that scales automatically with data rate and Low noise performance.

For the wireless adapter we selected the nRF52832 64 MHz Cortex-M4 with FPU with 512/256 KB Flash, 64/32 KB RAM 2.4 GHz Transceiver 2 Mbps, 1 Mbps Bluetooth Low Energy.

The antenna selected was an RF ANT 2.4GHZ CHIP 2450AT07A0100T due to availability in our labs.

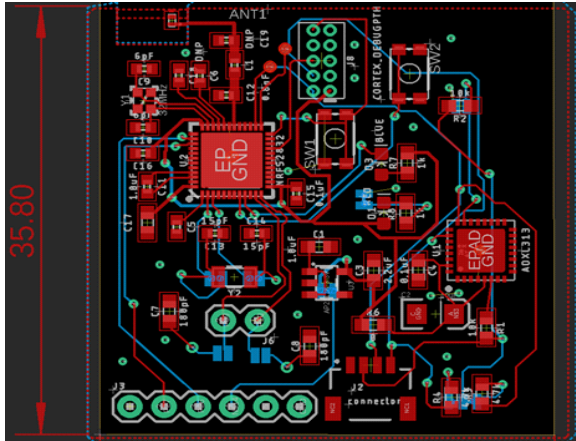


Fig1. Projected board in a PCB software.

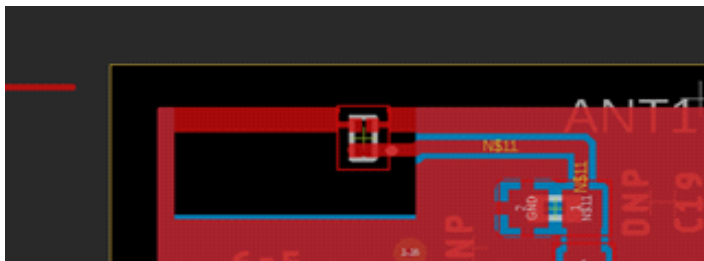


Fig2. Placing of the antenna on the corner of the board.

The same structure and placing are going to be used in both types of board (LTCC and PCB) [Fig1]; when placing the antenna on the board, it was necessary to calculate the dimensions of the antenna connection paths and resize the projected paths and selecting a corner of the board [Fig2]. The different materials used for substrates have different permittivity dielectric constant, in the case of FR-4 the constant is ~ 4.6 , and in the LTCC (Dupont Microcircuit Materials, 951 Green Tape) ~ 8.7 , making the calculations for the types of substrates we obtained the dimensions of widths necessary to obtain the desired impedance of 50Ω for the antenna to work optimally.[2]

For a constant of $4.6 W=0.3\text{mm}$ (FR-4).

For a constant of $\sim 8.7 W=0.2\text{mm}$ (LTCC).

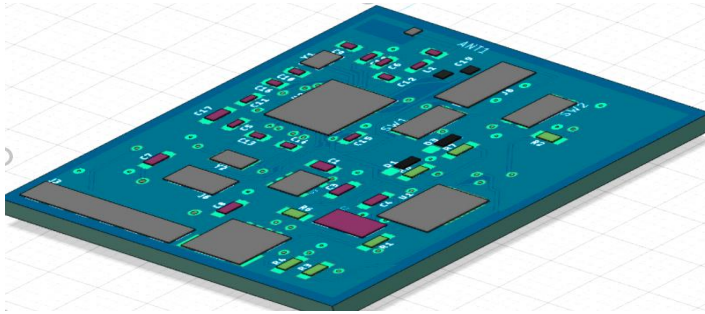


Fig3. 3D projection of the LTCC board

In the construction process of the LTCC board, 8 layers of 250 μm LTCC without sintering are due to be used. Once sintered, each has an approximate dimension of 214 μm , a reduction of 15% in the Z axis. Once stacked, the final height of the device is 1.72 mm.[3]

Results

The research work is at the stage of finalizing the PCB board construction and tuning, the LTCC board construction is yet in construction stage so still needs to be finished to run the tests and comparisons. The construction of the device separate devices allows to have an insight of the difficulty process of construction of both types of boards allows checking the functionality and responses of the accelerometer with the antenna and to create a working pattern of the components on the substrates, these results will be used as a comparative experience when comparing the efficiency of the accelerometer in the LTCC, and at the time of comparison of the wireless communication profile.

The high dielectric constant permittivity of the LTCC material has allowed greater freedom when choosing the solution for the wireless connection for this device.

Mechanical characteristics of the LTCC substrate have facilitated the positioning of components in the package, resulting in a strong and compact package, with a low level of complexity.

As we have the possibility of 3D construction, there is more freedom when designing the layout of the components and the connection paths because there is no contact between connection paths of different circuit elements because they are not in the same layer.

The next step in the fabrication of the device is, if necessary, further decoupling the external source to include additional filter components, with the expectation that the later inclusion of components for this will not affect the total size of the devices in this first version.

Applications

Our Institutions propose to approach the topic of Digital Transformation through two research axes - Advanced Manufacturing and Smart and Sustainable Cities - which are in line with the mission to develop and apply technological solutions to increase the competitiveness of companies and promote the quality of life of the population. In this context, the idea of using inertial sensors arose, using an accelerometer that can be basically applied in three directions: In surveillance and prevention of landslides, water leaks and control of dams, and the IPT forestry group that is instrumenting trees to control collisions and fall of trees in the cities.

Conclusions

At this stage of the work the differences in material substrates implied in distinct design approaches, as the LTCC has different properties and the equipment used for the construction are not always the same as the regular PCB boards. When looking at the two devices the possibility of building 3D structures in the LTCC substrate is an excellent characteristic that ensures better efficiency when utilizing the available space, further comparative tests need to be carried with the completed prototypes for further data gathering.

References

- [1] P. Overview and M. Properties, “Low Temperature Co-fired Ceramic (LTCC) Design Guidelines for RF 3D Package Module Design”.
- [2] U. Ullah *et al.*, “Antenna in LTCC Technologies: A Review and the Current State of the Art,” *IEEE Antennas and Propagation Magazine*, vol. 57, no. 2, pp. 241–260, 2015.
- [3] W. B. Lim, Y. S. Cho, Y. J. Seo, and J. G. Park, “Shrinkage behavior of LTCC hetero-laminates,” *J Eur Ceram Soc*, vol. 29, no. 4, pp. 711–716, 2009.

Acknowledgments

I’m extremely grateful to the Fundação de Amparo à Pesquisa do Estado de São Paulo (FAPESP) and to the IPT that financed the research that that gave rise to this scientific article. I’d like to express my deepest thanks to my advisor Antonio Carlos Seabra for his support and patience, and to my supervisor Mario Ricardo Gongora Rubio for his support and assistance at all times.

P19 |

MEMS-BASED FABRICATION OF AN ATOMIC VAPOR CELL FOR BRAIN MAGNETIC FIELD MEASUREMENT

H. M. Pereira*, J. N. Vieira, E. M. F. Vieira, J. A. Rodrigues, M. J. Maciel*,
J. H. Correia

¹ *CMEMS-UMinho, University of Minho, Guimarães, Portugal*

² *LABELS - Associate Laboratory, Braga, Guimarães, Portugal*

**e-mail: hugo.pereira@dei.uminho.pt, mmaciel@dei.uminho.pt*

Introduction

MEMS-based atomic vapor cells have a wide range of applications, as they can be miniaturized for chip-scale atomic clocks, atomic gyroscopes and atomic magnetometers. Current available techniques for imaging and registering the human brain activity are based on superconducting quantum interference devices (SQUIDs) that require the use of liquid helium at 4 K to reach the desired levels of sensitivity. With high maintenance and high production costs, SQUIDs also impose a restriction in the type of exams that can be performed as the patients must maintain their head in a fixed position due to the large volume of these equipment [1,2]. Thus, advancements in this field of work towards portable and low-cost magnetoencephalography devices are necessary, and, in recent years, optically pumped atomic magnetometers (OPMs) have been showing promising steps in that direction. OPMs are composed by three main components: a resonant light source at the transition of the alkali atoms, a transparent vapor cell filled with the desired alkali metal, and a photodiode to monitor the intensity of the light transmitted through the vapor cell. Reductions on the transmittance of light intensity indicate an increase of the external magnetic field strength [3,4].

In this work, we will focus on the principal component of the OPM: the alkali metal vapor cell; more precisely in the anodic bonding technique for the fabrication of an atomic vapor cell filled with rubidium (Rb), obtained through rubidium azide (RbN_3) UV decomposition.

Methods

The fabrication procedure of the described atomic vapor cell comprises four main steps: (i) creation of a hollow cavity cell in a silicon wafer through micromachining techniques (such as dry or wet etching), (ii) bonding at ambient atmosphere of a transparent glass on one side of the wafer, (iii) insertion of the desired RbN_3 aqueous solution in the formed cavity and (iv) final bonding of the top side glass wafer in vacuum, in order to hermetically seal the vapor inside the

cell, as represented in Figure 1. The process of bonding both glass wafers onto the silicon wafer allows for a very strong electrostatic sealing and is referred to as anodic bonding. This is possible for these two materials as they have similar coefficients of thermal expansion, and it can be achieved by heating up the wafer stack to temperatures ranging from 200 °C up to 500 °C and by applying a voltage differential between the two different wafers of 200 V to 1000 V [5,6]. Under the effects of high temperature, the Na_2O present in the glass dissociates into Na^+ and O^{2-} , and the glass becomes conductive. Alongside this, a high voltage is applied between both materials, with the cathode electrode connected to the glass wafer and the anode electrode to the silicon wafer, creating a cation depletion layer that allows for the formation of a Si-O-Si covalent bond at the interface between the wafers, thus bonding the wafer stack, as detailed in Figure 1. As this bonding process is a result of strong electrostatic forces that intimate and attract both substrates together, these are expected to be bonded indefinitely [5].

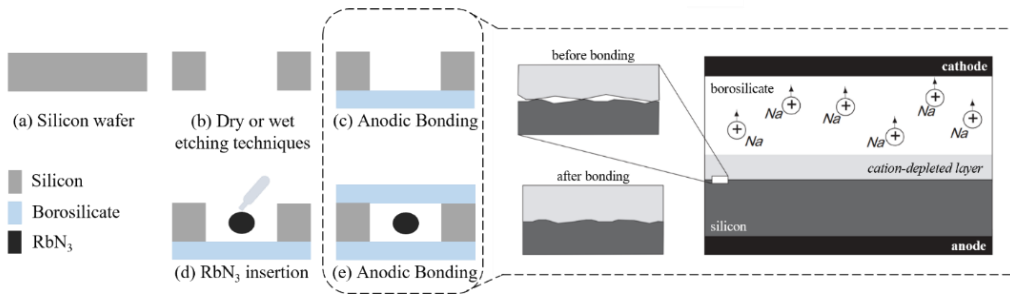


Figure 1 - Fabrication steps of a RbN₃ filled MEMS-based atomic vapor cell with the anodic bonding process represented in more detail (adapted from [5]).

This sealing process is often described as being very robust, and therefore proper preparation and cleaning of the silicon and glass wafers is required, and is often not detailed in literature. Double-side polished (DSP) silicon wafers must be used, and it has been reported that SiO₂ formation at the contact interface cannot be too thick, otherwise intimate contact is not achieved [5,7]. Therefore, our preparation starts with the submerging of the silicon wafer in a Silox Vapox III solution for roughly 15 min. Silox Vapox III is a strong oxide etchant with a high etch rate ($\approx 600 \text{ \AA}/\text{min}$ for thermal oxides). Afterwards, the wafer is rinsed with deionized water and isopropyl alcohol to remove etchant excesses, dried with compressed nitrogen, and submerged in acetone to undergo an ultrasonic bath at 40 °C for 20 min. Finally, the wafer is removed from the ultrasonic bath and is once again

rinsed with deionized water and isopropyl alcohol, and dried with compressed nitrogen. As for the glass wafers, they simply undergo ultrasonic bath in acetone at 40 °C for 20 min, and are afterwards rinsed with deionized water and isopropyl alcohol and further dried with compressed nitrogen.

In order to optimize the anodic bonding process, we manually diced DSP silicon wafers into small substrates with a diamond-tipped pen and utilized DSP 20x20 mm borosilicate wafers. The process is performed in a custom-made vacuum chamber (minimum pressure of 10^{-6} mbar), equipped with an electrical resistance and electrical contacts connected to the exterior. We applied a temperature of roughly 270 °C to the wafer stack and a voltage of 1000 V, during approximately 10 minutes. Coupled to the voltage feeding circuit, we connected an amperemeter, that allows to evaluate the current flowing through the wafer stack and consequently monitor the bonding process.

Results

Several anodic bonding tests have been performed for different temperature and voltage values in clean room conditions. It is expected that higher temperatures result in a better and faster bonding at the interface between the wafers, however our custom-made chamber imposes a limitation of 300 °C. Nevertheless, as we are utilizing RbN_3 to form the desired Rb vapor inside the cell, the temperature limitation is not problematic considering that RbN_3 has been reported to thermally decompose above 355 °C [8]. Therefore, we applied a temperature of 270 °C and we observed that a voltage of 1000 V was yielding the most satisfactory bonding results.

By observing the electrical current flowing through the wafer stack, it is possible to assess how the bonding process is evolving and it can provide an indication of when it is finalized [5]. As reported in literature, after the desired temperature is achieved, on the moment of applying the high voltage differential across the wafer stack, a peak in current is achieved followed by a fast exponential decay, which should gradually reach close to zero [5]. Figure 2 (a) shows a current-time graph for 270 °C and 1000 V, where a peak current value of roughly 235 μA is registered at the early stages of the bonding process. Successive experiments have shown that a bonding time of 10 min in our conditions, not only causes the current to decay to very low values, as expected, but also appears to be necessary to obtain a good quality anodic bonding. Additionally, the bonding quality can be observed macroscopically. Figure 2 (b) presents one of the anodic bonding experiments, where it is possible to see a large darker region that indicates a proper bonding, with a few lighter one-off regions where bonding was not well performed. With a

microscopic view of those lighter spots, it is possible to conclude that a minimal number of residues caused by improper cleaning or small ambient residues could reduce the intimate contact between the wafers. Additionally, some lighter regions can be related to small cracks and fractures that may occur in glass during the anodic bonding process that propagate through the glass-silicon interface [6]. None of these issues should, however, invalidate the performed anodic bonding, as long as most of the area is properly bonded, the alkali metal vapor is not expected to dissipate through the wafer stack.

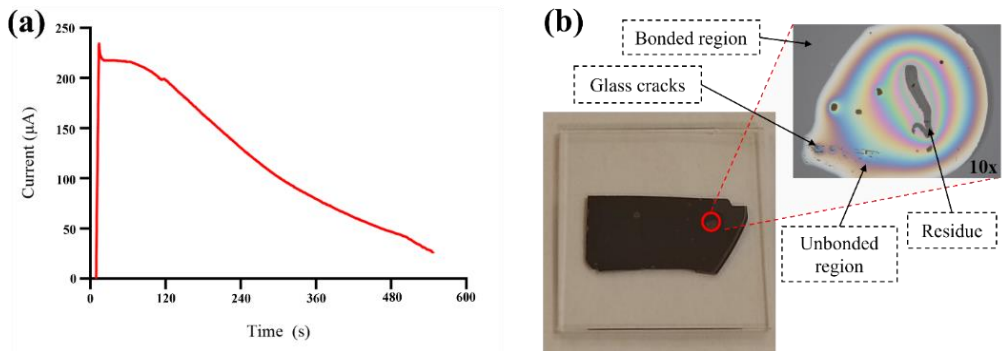


Figure 2 - (a) Current-time graph registered by the amperemeter while performing anodic bonding, (b) macroscopic and microscopic view of an anodic bonding experiment, where the presence of a small residue and the appearance of spontaneous glass cracks caused the highlighted region not to be bonded.

Conclusions

We present a detailed way to successfully perform the anodic bonding technique, a crucial step in the fabrication of MEMS-based atomic vapor cells. With the conditions optimized for our custom-made anodic bonding chamber, our focus lies on creating an atomic vapor cell filled with RbN_3 . This proves to be an advantageous method of filling alkali vapor cells since the UV decomposition reaction after sealing the cell originates N_2 , an ideal buffer gas for atomic magnetometers, avoiding the need to backfill the vacuum chamber with a desired buffer gas pressure. Moreover, with access to an atomic layer deposition equipment, we wish to explore glass wall coatings to improve the lifetime of these cells through depositing oxides such as Al_2O_3 , TiO_2 , SiO_2 and even nitrides like Si_3N_4 , and to fabricate an easy to mass-produce, low-cost, chip-scale atomic

magnetometer with a long lifetime to pave the way for a new generation of magnetoencephalography scans.

References

1. T. M. Tierney, N. Holmes, S. Mellor, J. D. López, G. Roberts, R. M. Hill, E. Boto, J. Leggett, V. Shah, M. J. Brookes, R. Bowtell, and G. R. Barnes, *Neuroimage* **199**, 598 (2019).
2. T. H. Sander, J. Preusser, R. Mhaskar, J. Kitching, L. Trahms, and S. Knappe, *Biomedical Optics Express* **3**, 981 (2012).
3. E. Boto, N. Holmes, J. Leggett, G. Roberts, V. Shah, S. S. Meyer, L. D. Muñoz, K. J. Mullinger, T. M. Tierney, S. Bestmann, G. R. Barnes, R. Bowtell, and M. J. Brookes, *Nature* **2018** 555:7698 **555**, 657 (2018).
4. V. K. Shah and R. T. Wakai, *Phys. Med. Biol.* **58**, 8153 (2013).
5. P. Ramm, J. J. Lu, and M. M. v. Taklo, *Handbook of Wafer Bonding* (Wiley, 2012).
6. J. Wei, Z. P. Wang, H. Xie, and Ng Fern Lan, in *4th Electronics Packaging Technology Conference, 2002*. (IEEE, n.d.), pp. 85–90.
7. T. M. H. Lee, D. H. Y. Lee, C. Y. N. Liaw, A. I. K. Lao, and I.-M. Hsing, *Detailed Characterization of Anodic Bonding Process between Glass and Thin-Film Coated Silicon Substrates* (2000).
8. T. Overstolz, J. Haesler, G. Bergonzi, A. Pezous, P.-A. Clerc, S. Ischer, J. Kaufmann, and M. Despont, in *2014 IEEE 27th International Conference on Micro Electro Mechanical Systems (MEMS)* (IEEE, 2014), pp. 552–555.

Acknowledgments

This work is supported by: Project MME reference 105399; CMEMS-UMinho Strategic Project UIDB/04436/2020 and UIDP/04436/2020; and Infrastructures Micro&NanoFabs@PT, NORTE-01-0145-FEDER-022090, Portugal 2020.

H. M. Pereira thanks FCT for the Ph.D. grant 2021.06647.BD.

P20 |

MEMS RUBIDIUM VAPOR CELL FOR OPTICALLY PUMPED MAGNETOMETERS

J. N. Vieira*, H. M. Pereira, E. M. F. Vieira*, J. A. Rodrigues, M. J. Maciel,
J. H. Correia

¹ CMEMS - UMinho, University of Minho, 4800-058, Guimarães, Portugal

² LABBELS - Associate Laboratory, Braga, Guimarães, Portugal

*e-mail: a83520@alunos.uminho.pt; d8408@dei.uminho.pt

Introduction

Magnetoencephalography (MEG) is the technique that allows direct imaging of the human brain electrophysiology, through the measurement of the magnetic fields generated by the neuronal currents in the brain scalp [1,2]. MEG technology uses superconducting quantum interference devices (SQUIDs), which require a cryogenic cooling system, and, consequently, thermal isolation. The main disadvantage of the SQUIDs is the loss of the neuromagnetic field detection, as the distance between magnetic source and sensor increases. In very recent years, there has been a scientific effort in the development of alternatives to SQUIDs, eliminating the need for cryogenic cooling equipment [3,4]. Optically pumped magnetometers (OPM) based on vapor cells of alkali-metals have emerged as a promising alternative to SQUIDs [5]. The main benefit of OPMs compared to SQUIDs is the precision of measurement in very low magnetic fields, without the requirement of complex cryogenic equipment, which reduces the volume of the MEG system and the maintenance costs [1–3,6,7]. The vapor cells allow for precise measurement of the magnetic fields using optical spectroscopy: the spin of the atoms forms a collective moment that changes in the presence of an external magnetic field, resulting in the variation of the transmittance of the vapor cell containing the atoms of the alkali-metal [3]. One significant advantage of OPMs is the microfabrication possibility [3,8], which is addressed in this work. The two most used and commercially available alkali-metals vapor cells (cesium and rubidium) were firstly compared. As a result of this comparison, a miniaturized cell fabrication based on the generation of alkali-metal vapor inside a sealed MEMS structure is proposed.

Methods

In OPMs, the increase of the external magnetic field is translated into a decrease of the light transmitted by the pump beam through the alkali-metal vapor cell.

This phenomenon is more prominent if the direction of the magnetic field is perpendicular to the light beam emitted. To compare the most used alkali-metal vapor cells for low magnetic field applications, a convenient optical-magnetic setup was created. Two commercially available alkali-metal vapor cells, from Thorlabs, were acquired for this purpose: rubidium-87 (^{87}Rb) isotope [9] and cesium (Cs) [10]. According to the results of this study, a complete design of the vapor cell miniaturization is here addressed. The fabrication process is based on the conventional glass-silicon-glass sandwich structure. Three main chemical reactions are currently used for the production of Rb/Cs considering the MEMS cells application, and are summarized in **Table I**.

Table I: Summary of the main chemical reactions used for alkali-metals production. X is Rb or Cs.

Chemical reaction	Temperature	Observations	Ref.
$\text{BaN}_6 + \text{XCl} \rightarrow \text{BaCl} + 3\text{N}_2 + \text{X}$	200 °C	Reversible reaction could be occurred which limits the sensitivity of the magnetometer.	[8]
$2\text{XN}_3 \rightarrow 2\text{X} + 3\text{N}_2$	450 °C	Azide decomposition through UV light.	[11]
$2\text{XCl} + \text{Ca} \rightarrow 2\text{X} + \text{CaCl}_2$	720 °C	Deformation of glass windows due to high temperature reaction. Granular Ca forms limits dispensing in MEMS cells.	[12]

Considering the proposed reactions, the alkali-metal azide decomposition is the most promising method for our proposed MEMS cells. It presents itself as a cost-effective solution, without the need for complex technological equipment, and the UV activation simplifies the decomposition process. Moreover, the photodecomposition method is advantageous in the sense that the azide product form is more stable at room temperature than the metal form of the material.

Results

Figure 1 represents the transmittance of the commercially available ^{87}Rb and Cs vapor cells for D1 transitions, 795 nm and 895 nm, respectively. The results obtained follow a biphasic exponential decay, characterized by being the sum of two decay processes happening at the same time: an initial fast decay for weak magnetic fields and a slow decay for stronger magnetic fields. Therefore, these results show a higher sensitivity for Rb vapor cells, as a more significant drop in the light transmittance is observed as a function of the magnetic field increase. According to this analysis, the Rb alkali-metal vapor cell is more suitable to be incorporated in OPMs.

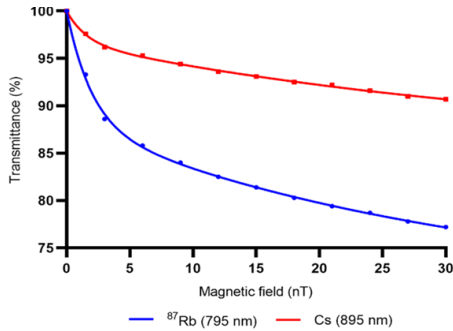


Figure 1 - Transmittance of light (%) as a function of magnetic field (nT), for the D1 transition of ^{87}Rb and Cs vapor cells, respectively.

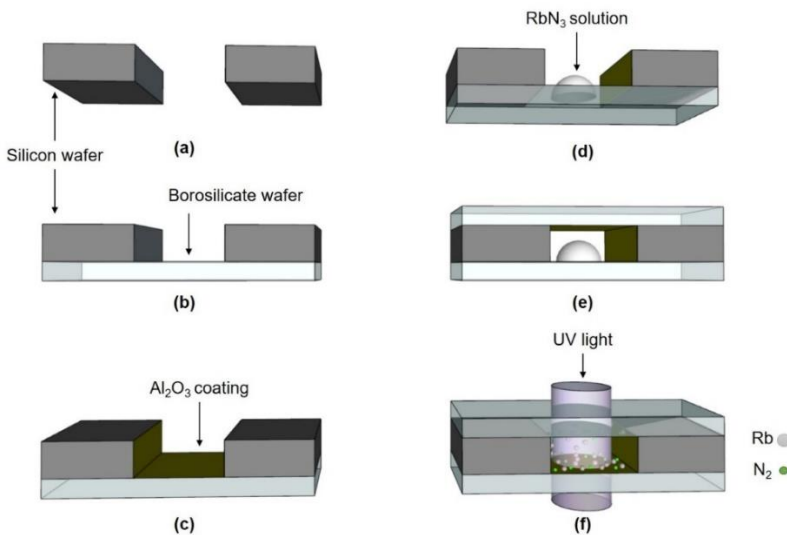


Figure 2 - (a-f) Process steps for obtaining the millimeter-level Rb vapor cell through decomposition of the alkali-metal azide by UV photolysis (not to scale).

One of the methods of MEMS cell fabrication includes the alkali compound decomposition induced by exposing encapsulated cells to UV radiation (see **Table I**). As a result, Rb and N_2 are obtained inside the cell. The steps of the proposed cell fabrication are shown in **Figure 2**, which include the preparation of silicon and borosilicate wafers; deep reactive ion etching (DRIE) of a silicon wafer, to obtain a millimeter-level cavity (Figure 2 (a)); anodic bonding between the first glass wafer and the bottom of the Si wafer (Figure 2 (b)); coating of all the cell walls with a Al_2O_3 thin layer to improve the vapor cell lifetime (Figure 2 (c)); micro-dispensing of the rubidium azide (RbN_3) aqueous solution into the millimeter-level cavity and dried at ambient atmosphere (Figure 2 (d)) and second anodic bonding of the top glass wafer, that will be performed at low temperature,

in order not to thermally decompose the alkali-metal azide compound ($< 300\text{ }^{\circ}\text{C}$), under controlled Ar atmosphere (Figure 2 (e)). In the last step, the metallic Rb and N_2 buffer gas will be created through UV irradiation of the RbN_3 aqueous solution, following the decomposition reaction: $2\text{RbN}_3 \rightarrow 2\text{Rb} + 3\text{N}_2$ - Figure 2 (f). For this purpose, a low-pressure lamp emitting at UV (peak wavelength of 254 nm) will be used. Long exposure is necessary to get a high yield decomposition of RbN_3 .

Conclusions

The transmittance results show that the ^{87}Rb alkali-metal vapor cell is more suitable to be incorporated in OPMs over the Cs cell. The fabrication of a millimeter-level alkali-metal vapor cells by using borosilicate and silicon wafers, through microfabrication technology is here proposed. This approach opens the perspective for massive production of OPMs and, therefore will contribute to the new generation of MEG based on OPMs, that will have high impact in diagnoses of some neurological diseases affecting the worldwide population, such as epilepsy and dementia.

References

1. T. H. Sander, J. Preusser, R. Mhaskar, J. Kitching, L. Trahms, and S. Knappe, *Biomed. Opt. Express* **3**, 981 (2012).
2. E. Boto, N. Holmes, J. Leggett, G. Roberts, V. Shah, S. S. Meyer, L. D. Muñoz, K. J. Mullinger, T. M. Tierney, S. Bestmann, G. R. Barnes, R. Bowtell, and M. J. Brookes, *Nature* **555**, 657 (2018).
3. C. Johnson, P. D. D. Schwindt, and M. Weisend, *Appl. Phys. Lett.* **97**, (2010).
4. M. Xie, J. F. Schneiderman, M. L. Chukharkin, A. Kalabukhov, B. Riaz, D. Lundqvist, S. Whitmarsh, M. Hamalainen, V. Jousmaki, R. Oostenveld, and D. Winkler, *IEEE Trans. Biomed. Eng.* **64**, 1270 (2017).
5. T. M. Tierney, N. Holmes, S. Mellor, J. D. López, G. Roberts, R. M. Hill, E. Boto, J. Leggett, V. Shah, M. J. Brookes, R. Bowtell, and G. R. Barnes, *Neuroimage* **199**, 598 (2019).
6. V. K. Shah and R. T. Wakai, *Phys. Med. Biol.* **58**, 8153 (2013).
7. V. Shah, S. Knappe, P. D. D. Schwindt, and J. Kitching, *Nat. Photonics* **1**, 649 (2007).
8. L.-A. Liew, S. Knappe, J. Moreland, H. Robinson, L. Hollberg, and J. Kitching, *Appl. Phys. Lett.* **84**, 2694 (2004).
9. Thorlabs - Rb, (2012).
10. Thorlabs - Cs, (2012).
11. L.-A. Liew, J. Moreland, and V. Gerginov, *Appl. Phys. Lett.* **90**, 114106 (2007).
12. W. Wei, J. Shang, W. Kuai, S. Qin, T. Wang, and J. Chen, in *2012 13th Int. Conf. Electron. Packag. Technol. High Density Packag.* (IEEE, 2012), pp. 1639–1641.

Acknowledgments

This work is supported by: Project MME reference 105399; CMEMS-UMinho Strategic Project UIDB/04436/2020 and UIDP/04436/2020; and Infrastructures Micro&NanoFabs@PT, NORTE-01-0145-FEDER-022090, Portugal 2020.

H. M. Pereira thanks FCT for the Ph.D. grant 2021.06647.BD.

P21 |

MEMS-BASED WAVEGUIDE SiO₂ FABRICATED BY RIE PROCESS FOR OPTICAL SENSING

V. H. Rodrigues*, J. R. Freitas, M. F. Silva, J. H. Correia

CMEMS-UMinho – University of Minho, Campus Azurem – 4800-058, Guimarães – Portugal

LABELS – Associate Laboratory, Braga/Guimarães, Portugal

*e-mail: a85402@alunos.uminho.pt

Introduction

The Reactive Ion Etching (RIE) is an etching technology used in microfabrication. RIE is a type of dry etching and uses chemically reactive plasma to remove material deposited on wafers (e.g. silicon dioxide (SiO₂) or silicon nitride (SiN)). The plasma is generated under low pressure (vacuum) by an electromagnetic field. High-energy ions from the plasma attack the material and react with it, volatilizing material from the unmasked areas to create the desired pattern. MEMS (Microelectromechanical systems) fabrication of SiO₂ planar waveguide for single-mode propagation are a solution in terms of reproducibility, surface roughness control and precise fabrication for application in optical devices.

The proposed planar waveguide design for single-mode propagation is illustrated in Figure 1. The waveguide is composed by a SiO₂ layer (high-refractive index) deposited (by sputtering) on a borosilicate glass substrate (BR33) with approximately 80% of SiO₂ in its chemical composition (low-refractive index – 1.47). The high-refractive index of the SiO₂ layer can be tuned by controlling the deposition parameters of the deposition process. Typically, the main materials for waveguides are SiO₂ and SiN and the RIE masking layer is aluminum-based (Al).

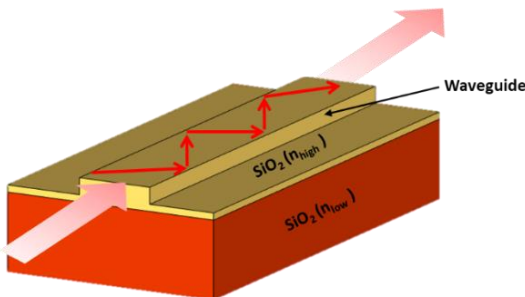


Figure 1 - Example of a MEMS-based SiO₂ planar waveguide.

The waveguide was fabricated by photolithography using shadow masks based in photosensitive polymers (photoresist) which are patterned by ultraviolet light exposed in a Direct Write Lithography (DWL) equipment [1,2]. This approach avoids the use of a physical shadow mask.

A RIE system from *Samco Inc* model RIE-1C was used to etch the SiO₂ layer after the mask patterning. The plasma is created by oxygen (O₂) and the etching gas is tetrafluoromethane (CF₄). The plasma releases fluoride (F) ions and radicals which react with the SiO₂ layer. Also, nitrogen (N₂) is used as a purge gas to keep the vacuum pump working and to stabilize the reaction chamber. This work shows the RIE parameters, identifying the etch rates, aspect ratio of the SiO₂ layer. Also, a photolithographic process for the Al patterning is presented and compared to the performance with the photoresist mask. Therefore, MEMS-based waveguides SiO₂ is a reliable microfabrication process for optical devices [3,4].

Methods

Figure 2 shows the representation of the MEMS-based waveguides SiO₂ fabrication steps (SiO₂ and Al layers deposition, photolithography and the RIE process result) used.

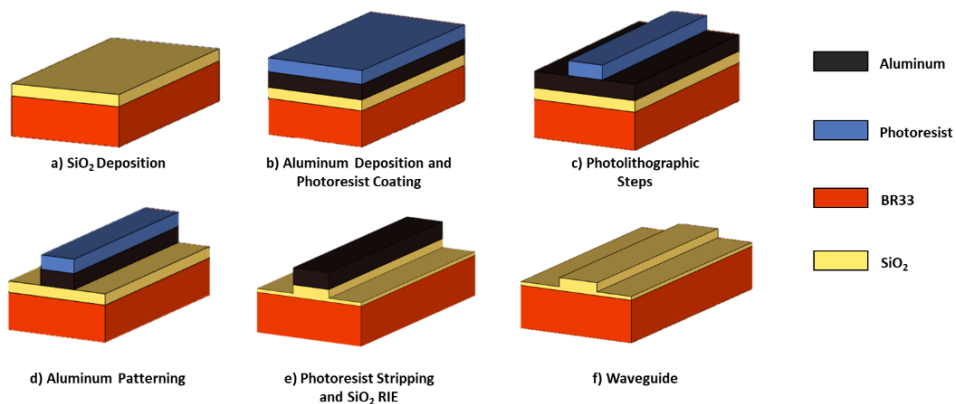


Figure 2 - Representation of MEMS-based waveguides SiO₂ fabrication steps; a) SiO₂ deposition, b) Al layer deposition, c) Photolithography, d) Aluminum patterning, e) RIE of SiO₂ Layer, f) Waveguide result.

The BR33 substrate was previously cleaned on an ultrasonic bath and dried by N₂ spray. A SiO₂ 200 nm thick (with a refractive index higher than the BR33 substrate refractive index) was deposited by means of RF magnetron sputter deposition from a SiO₂ target in argon (Ar)/N₂ plasma represented in Figure 2 (a). The sputtering chamber was evacuated to at least 4.7×10^{-6} mbar by means of a turbo molecular pump. The sputtering parameters were: Ar gas flow of 15 sccm, RF power of 150 W, and substrate temperature of 60 °C. The next step represented in Figure 2 (b) shows a 300 nm thick Al RIE masking layer deposited by electron beam technique (e-beam). The e-beam parameters were: vacuum pressure at

5.3×10^{-6} mbar, filament voltage of 7 KV with current fixed at 100 mA and substrate temperature of 22 °C. Figure 2 (c) shows the RIE masking layer patterned by photolithography using 3 mL of positive AZ 4562 photoresist and exposed by the DWL equipment from *Heidelberg* Model μ MLA. The exposed photoresist was removed by AZ 351B developer with 1:4 dilution on deionized water. Figure 2 (d) shows the patterning of the Al masking layer removed by 50 mL phosphoric acid (H_3PO_4) wet etching bath during 10 minutes at room temperature. Figure 2 (e) shows the stripping of the unexposed AZ 4562 in a stirred puddle with 150 mL of AZ 100 remover for around 8 minutes and the RIE process to the SiO_2 layer. The Figure 2 (f) shows the removal of the remaining Al with H_3PO_4 wet etching bath and the waveguide result. The RIE process was done by constantly adjusting the equipment parameters to study the influence on depth and wall smoothness for waveguide production. The BR33 (with 80% of SiO_2) etch rate study was performed by adjusting the RIE radio frequency (RF) power in a range between 50 W to 200 W with a step of 50 W. The influence of the O_2 plasma gas flow was also studied by varying it by 0, 20 and 40 mL/min with a fixed CF_4 etching gas flow of 40 mL/min. Furthermore, the RIE masking layer design was also studied to understand the etching gas penetration in depth influence. The depth evaluation was performed by the profilometer model Dektak 150 from *Veeco*. This equipment uses a 12.5 μ m diameter stylus to scan the substrate surface. All the measurements were done at a 500 μ m by 500 μ m square.

Results

Figure 3 shows the etch rates results for BR33 (with 80% of SiO_2) etching with different RF power and different O_2 gas flow. The CF_4 etching gas flow was fixed to 40 mL/min.

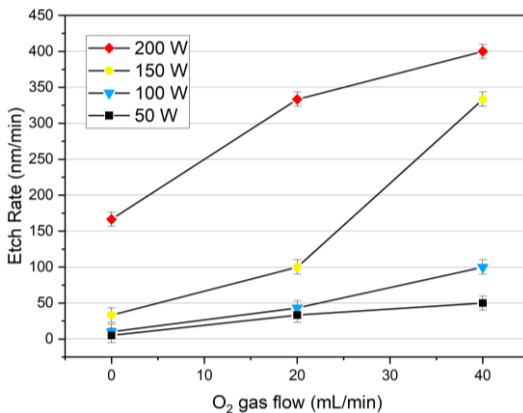


Figure 3 – BR33 (with 80% of SiO_2) etch rate results for different O_2 flows and RF Power with fixed CF_4 gas flow (40 mL/min).

The higher etch rate (400 nm/min) was obtained at the maximum RF power (200 W) and the O₂ flow of 40 mL/min. Also, for the RF power of 200 W and O₂ flow at 20 mL/ the difference is only 66 mL/min comparing to the maximum. Moreover, with the same O₂ flow (20 mL/min) the etch rate difference between the RF power of 150 W to 200 W is higher (230 nm/min). Besides, the etch rate, at RF power lower than 150 W and with O₂ gas flow at 40 nm/min is very low (100 nm/min). These results prove that influence of the O₂ gas flow is lower at lower RF power. Furthermore, the Al RIE masking layer proved to be reliable for high-powered plasmas.

Conclusions

The use of RIE to fabricate the MEMS-based waveguide SiO₂ allows the wall and surface roughness precise control, high aspect ratio and reproducibility. The Al RIE masking and SiO₂ layer adhesion to the BR33 substrate were good and reproducible with the selected deposition techniques. Also, the photolithographic process for patterning the Al using H₃PO₄ is reliable even for dimensions smaller than 500 μm. The Al layer used as a mask is better than photoresist mask for high-power RIE system and long-etching time. The etch rate is very influenced by the O₂ gas flow and RF power. With O₂ flow of 20 mL/min the etch rate difference between the RF power of 150 W to 200 W is higher (230 nm/min). However, with RF power lower than 150 W and O₂ gas flow at 40 nm/min the results are very low (100 nm/min). Moreover, this work proves that for larger shapes (> 500 μm) the etch rate was higher by allowing better RIE gas penetration. Finally, the future work consists in developing different waveguide patterns.

References

- [1] S.A. Campbell, *Fabrication engineering at the micro and nanoscale*, Oxford University Press, 2008.
- [2] D.T. Martin-Abood, *Characterization of Reactive Ion Etch Chemistries Using Direct Write Lithography Write Lithography*, n.d.
- [3] C. Jung, I. Hong, M. Lee, J. Lee, J.H. Lee, D.I.D. Cho, Design of MEMS-based SiO₂ Waveguides on Quartz Substrate for Evanescent Field-based Saturable Absorbers, 9th Int. Conf. Inf. Commun. Technol. Converg. ICT Converg. Powered by Smart Intell. ICTC 2018. (2018) 725–728.
- [4] W.T. Li, D.A.P. Bulla, J. Love, B. Luther-Davies, C. Charles, R. Boswell, Deep dry-etch of silica in a helicon plasma etcher for optical waveguide fabrication, *J. Vac. Sci. Technol. A Vacuum, Surfaces, Film.* 23 (2005) 146–150.

Acknowledgments

This work was supported by: project MME reference 105399 and FCT with the project MPhotonBiopsy, PTDC/FIS-OTI/1259/2020, Infrastructures Micro&NanoFabs@PT, reference NORTE-01-0145-FEDER-022090, POR Norte, Portugal 2020.

P22 |

RUBIDIUM VAPOR CELLS FABRICATED BY ADDITIVE MANUFACTURING

J. M. Borlido*, J. A. Rodrigues*, H. M. Pereira, B. Esteves, M. J. Maciel,
E. M. F. Vieira, J. H. Correia

CMEMS – UMinho, University of Minho, 4800-058, Guimarães, Portugal

LABELS – Associate Laboratory, Braga/Guimarães, Portugal

**e-mail: a84371@alunos.uminho.pt, jrodrigues@dei.uminho.pt*

Abstract

The vapor cell is the basic working unit of magnetoencephalography (MEG) device based on optical pumping atomic magnetometers (OPMs). Additive manufacturing emerges as a simpler and cheaper way of producing these devices when compared to traditional MEMS techniques. In this work, vapor cells were fabricated in clear resin and coated with sodium silicate (Na_2SiO_3). Transmittance measurements show that the resin and coating allow vapor cell operability at a wavelength of 795 nm. Sodium silicate coating can be used to promote cell airtightness with low loss in transmittance.

Introduction

The MEG exam is a technology that allows the mapping of brain electrophysiology by recording magnetic fields derived from the flow of neuronal electrical currents [1]. In this technology, the main sensing system is based on superconducting quantum interference devices (SQUIDs). These bulky devices (which require cryogenic cooling) are expensive and costly to maintain. OPMs have more recently emerged as magnetic sensing alternatives that are comparable in sensitivity to SQUIDs [2]. The main advantages of these devices are their ability to be miniaturized and the possibility to place the sensors at distances very close to the patient's scalp, increasing the spatial resolution and sensitivity of the sensors to the brain magnetic fields. Besides, it is possible to integrate these sensors into a flexible cap, adaptable to each patient, allowing the movement of the patient's head [3]. The simple setup of an OPM contains three crucial elements: a light source, a high-pressure vapor, and a detection system. Normally, a glass cell containing the alkali metal vapor (rubidium, potassium, or cesium) under high pressure is used [4]. A 795 nm circularly polarized laser beam is used to spin-polarize the atoms of the vapor and a photodiode is used to detect the intensity of the laser light through the cell. At zero magnetic field, the spin

magnetic moments align with the laser beam and the transmission of the laser light to the photodiode is maximum. Magnetic field perpendicular to the laser beam causes Larmor precession, decreasing light transmission (detected by the photodiode). So, the light detected by the photodetector is a magnetic field indicator [2, 5]. Figure 1 shows the schematic illustration of the working principle of the OPM sensor.

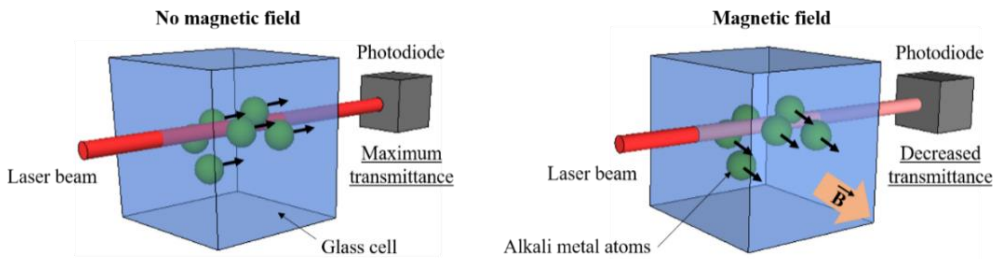


Figure 1. Working principle of the OPM sensor. At zero magnetic field (left) the light transmittance is maximum and in the presence of the magnetic field (right) the light transmittance is reduced.

Currently, these devices are fabricated using micro-fabricated (MEMS) techniques. These techniques are widely explored in the literature and generally use expensive equipment and material, only allowing the fabrication of single vapor cells. In this work we explore the use of additive manufacturing techniques for the fabrication of rubidium vapor cells, aiming to solve several problems related to the fabrication of vapor cells via MEMS techniques, such as the sealing of glass and silicon wafers by anodic bonding, and the high complexity and costs of the fabrication process.

Methods

The additive manufacturing processes used in the development of rubidium vapor cells were fused deposition modeling (FDM) and digital light processing (DLP). In the FDM process, a polymer filament is melted in a pressurized heated printing nozzle and deposited on the printing bed or in previously deposited layers. The fused layers quickly cool and solidify, forming a final piece with the desired shape. DLP uses UV-curable liquid resins. UV radiation is projected through a 2D screen, allowing the simultaneous polymerization of an entire layer. This process is repeated continuously for all layers by moving the printing table along the ZZ axis.

The cells were designed with cubic geometry, dimensions of 10 mm x10 mm x 10 mm, and a wall thickness of 0.41 mm. The vapor cell body was fabricated in clear resin (for transparency) using an Anycubic Photon Mono 4K printer and the cell-matrix support was fabricated in thermoplastic polyurethane (TPU) (for elastic properties) using an Ultimaker S3. The cell body printing process resulted in two parts: a hollow cube without the top face and a face of 10 mm x 10 mm x 0.41 mm. The outer cell walls were coated with sodium silicate in aqueous solution. When drying, this material has the ability to leave a thin and transparent layer that waterproofs the surfaces and reduces the porosity of the materials. It was used to improve the airtightness of the cells [6]. Then, the cells were attached to the TPU structure by UV resin curing. After pipetting the rubidium azide aqueous solution inside the hollow cube, the top face will be attached to the cell by UV resin curing. This sealing process must be done under vacuum. Lastly, the rubidium vapor is produced by the azide photochemical decomposition (UV irradiation at 254 nm). Figure 2 shows the fabrication process of a rubidium vapor cell matrix by additive manufacturing techniques.

In order to study the optical properties of the resin cell walls, some walls samples were taken to a spectrophotometer to measure the transmittance of the material, as the beam passes through one or two faces of the cell.

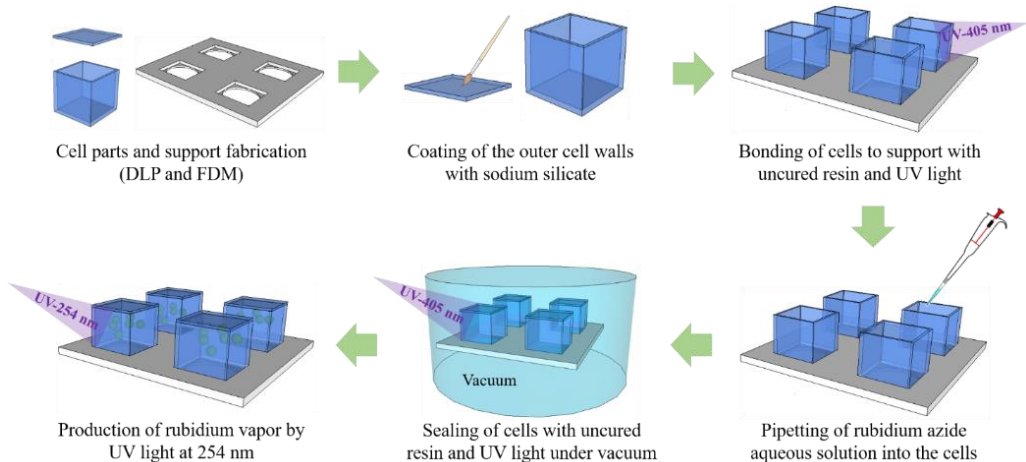


Figure 2. Fabrication process of a rubidium vapor cell-matrix by additive manufacturing.

Results

Figure 3 shows the cells and support structure fabricated by additive manufacturing.

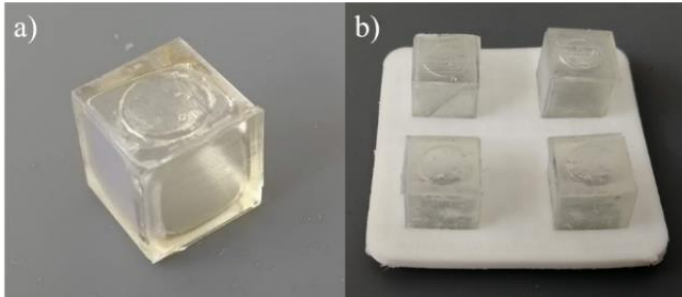


Figure 3. Structures fabricated by additive manufacturing: a) resin cell; b) resin cells on TPU support.

Figure 4 shows the graph of light transmittance through one or two resin cell walls with and without Na_2SiO_3 coating.

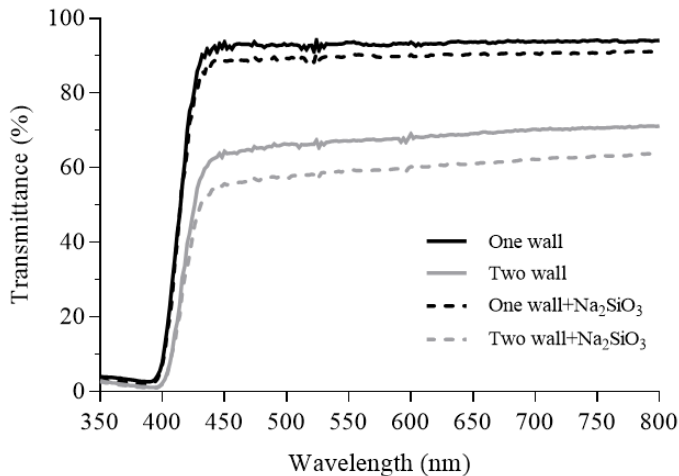


Figure 4. Light transmittance through one or two resin cell walls with and without sodium silicate coating.

At 795 nm (rubidium resonant wavelength), the light transmittance through one and two uncoated resin walls was 93.9 % and 71 %, respectively. On the other hand, the light transmittance through one and two Na_2SiO_3 coated resin walls are 91 % and 63.7 %, respectively.

Conclusions

This work demonstrated that it is possible to use additive manufacturing technology in the fabrication of rubidium vapor cells for MEG. The resin used in the fabrication of the cells body guarantees adequate transmittance for the operability of the sensor and the TPU material has good elastic properties for supporting the cells close to the patient's scalp. The sodium silicate coating used to improve the airtightness of the cells resulted in a decrease in light transmittance. New coatings can be done in the future, e.g. acrylic or alumina, to improve cell transmittance and sealing.

References

- [1] M. Xie, J. F. Schneiderman, M. L. Chukharkin, A. Kalabukhov, B. Riaz, D. Lundqvist, S. Whitmarsh, M. Hämäläinen, V. Jousmäki, R. Oostenveld, and D. Winkler, "Benchmarking for on-scalp MEG sensors", *IEEE Transactions on Biomedical Engineering*, 64(6):1270-1276, 2017.
- [2] E. Boto, N. Holmes, J. Leggett, G. Roberts, V. Shah, S. S. Meyer, L. D. Muñoz, K. J. Mullinger, T. M. Tierney, S. Bestmann, G. R. Barnes, R. Bowtell and M. J. Brookes, "Moving magnetoencephalography towards real-world applications with a wearable system", *Nature*, 555:657–661, 2018.
- [3] V. K. Shah and R. T. Wakai, "A Compact, High Performance Atomic Magnetometer for Biomedical Applications", *Physics in Medicine and Biology*, 58(22):8153–8161, 2013.
- [4] T. M. Tierney, N. Holmes, S. Mellor, J. D. López, G. Roberts, R. M. Hill, E. Boto, J. Leggett, V. Shah, M. J. Brookes, R. Bowtell and G. R. Barnes, "Optically pumped magnetometers: From quantum origins to multi-channel magnetoencephalography", *NeuroImage*, 199:598-608, 2019.
- [5] W. Happer, "Optical Pumping", *Reviews of Modern Physics*, 44(3):169-249, 1972.
- [6] X. Yang, W. Zhu and Q. Yang, "The viscosity properties of sodium silicate solutions", *Journal of Solution Chemistry*, 37:73–83, 2008.

Acknowledgements

This work is supported by: Project MME reference 105399; CMEMS-UMinho Strategic Project UIDB/04436/2020 and UIDP/04436/2020; Infrastructures Micro&NanoFabs@PT, NORTE-01-0145-FEDER-022090, Portugal 2020. H. M. Pereira thanks FCT for the PhD grant 2021.06647.BD.

CONDICIONAMENTO DE SINAL E INSTRUMENTAÇÃO |
ACONDICIONAMIENTO DE SEÑAL Y INSTRUMENTACIÓN | SIGNAL
CONDITIONING AND INSTRUMENTATION

O21 |

INEXPENSIVE CORN STARCH BASED SUPERCAPACITOR FOR SIGNAL CONDITIONING AND DETECTION

F. Yuan¹, C. Kertzer Saul^{1,2}, J.J. Santiago-Aviles¹

¹ *University of Pennsylvania, Electrical and Systems Engineering Dept. Philadelphia, PA, 19104*

² *present address: Universidade Federal de Parana, Curitiba, Parana, Brasil.*

**e-mail: cyro.saul@gmail.com*

Introduction

With the popularization of IoT (Internet of Things) a substantial demand for low voltage, inexpensive, non-polluting, and safe energy storage devices is expected. Powering the IoT is a non-trivial challenge where carbon-based EDLCs with aqueous electrolytes might represent good alternative (inexpensive and reliable), if a convenient process to produce high surface area inexpensive carbon (activated carbon) electrodes is utilized. There are fundamentally two types of supercapacitors, the electrical double layer capacitor (EDLCs), and the redox or pseudo-capacitor (fundamentally a small electrochemical battery). The EDLC super-cap¹ works by generating and accumulating pure electrostatic charges at the electrodes interface. Note that the EDLC performance as a capacitor is a strong function of the electrodes surface area accessible to the electrolyte ions. Therefore, porous (activated) carbons are among the best materials for electrode manufacturing, not only because of it is a good electrical conductor with high specific surface area, adequate porosity, and chemical stability, but it can be easily obtained from sustainable, natural, abundant and low-cost resources. As all capacitors, the supercapacitor consists of two electrodes, the anode and cathode, both immersed in a conducting liquid or electrolyte². In this report we present results on the fabrication of a simple and inexpensive supercapacitor constructed with starch-based carbon sponge electrodes.

Methods

Hydrothermal carbonization (HTC) is a quick and convenient route for the transformation of polysaccharides into carbon. It is low temperature/high pressure method, with a considerable high yield.³ The exothermic carbonization reaction reduces the energy budget during the process, simultaneously increasing its capability of adsorption. Adsorption is directly related to the material specific surface area (SSA) and pore structure. To enhance the SSA the physico-chemical process of “activation” is often utilized. The “activation” processes usually

involve high temperatures (from 700 °C. to 1100 °C) and the use of oxidizing gases (O₂, CO₂)/vapor assisting the thermal treatment. The evolution of the pore structure is driven by the reaction between the gas utilized for the activation and the carbon atoms synthesis of the electrodes materials involves the hydrothermal carbonization of starch (one of various techniques for crystallizing substances from high-temperature aqueous solutions at high vapor pressures), followed by activation (fundamentally the generation of a high specific surface area) of the carbonized starch product using KOH (a strongly alkaline exothermic solute). This process, schematized in figure 1, leads to carbon nano/microspheres which are highly dispersed in size as shown in figure 2.

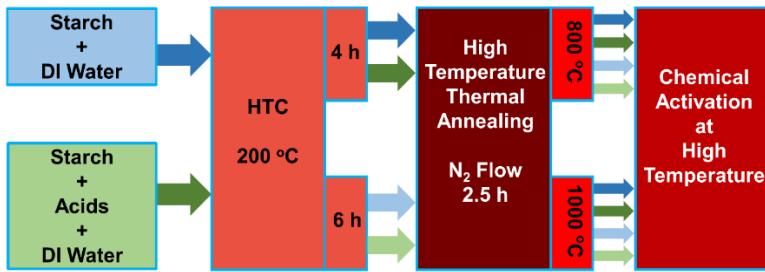


Figure 1 - Schematic of the standard activation process.

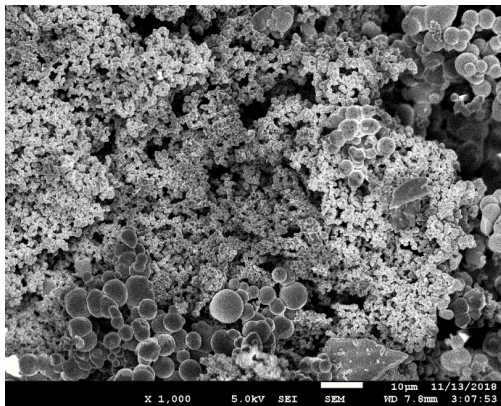


Figure 2 – Highly dispersed nano/microspheres of carbon using Starch + H₂SO₄ – HTC 6h – and thermal annealing at 800 °C.

In this work we developed a shorter and less energy consuming process. We tested both inorganic and organic acids and the thermal annealing (1 h) was performed directly with high ratios of KOH (KOH:HTC Carbon / 4:1 for example) to induce activation along with the annealing, as shown in figure 3. In this figure HSAM stands for High Surface Area Material.

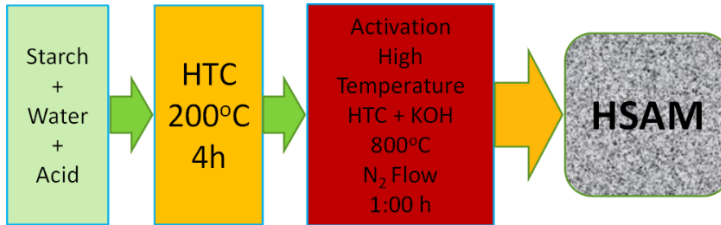


Figure 3 – Schematic of the developed process that reduced the number of steps and the energy consumption.

The result of this process was the synthesis of a sponge like carbon which presented higher surface area than the nano/microspheres, as illustrated in the figure below.

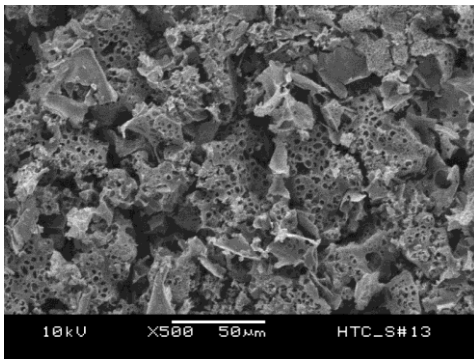


Figure 4 – Sponge like carbon obtained using Starch + Acetic Acid (HTC 4h) followed by annealing with KOH:Carbon (4:1).

The electrochemical characterization of the EDLC electrode was performed using an in-lab developed sample holder. A 3 electrodes conventional cell (activated carbon working electrode, a SS counter, and Ag/AgCl reference electrode). The potentiostat software was developed in the lab using LabView software in conjunction with a Keythley 2450 Source Meter Unit (SMU). The cyclovoltammetry (CV) curves obtained were fitted using Excel software to determine the 1 HSAM electrode EDLC parameters, considering a simple circuit consisting of an ideal capacitor in series with a resistor and in parallel with a second one. This circuit is powered by a scanning voltage source with a constant rate $\phi = (V/s)$. The series resistor is seen as a lump parameter (ESR) and the parallel resistor depict all losses (physical and chemical) in the system.

The fittings were always performed on the second cycle to eliminate the first cycle transients.

Results

Figure 5 presents both the CV experimental data (blue squares) as well as the fitting (red line) for an electrode HSAM obtained using Starch + Phosphoric Acid (4h HTC) followed by an annealing with KOH: Carbon (6:1) at 800 °C/1 h. The CV curve was obtained at in a 1M NaSO₄ aqueous solution using a rate of 0.01 V/s. The electrode has 1 cm² of area.

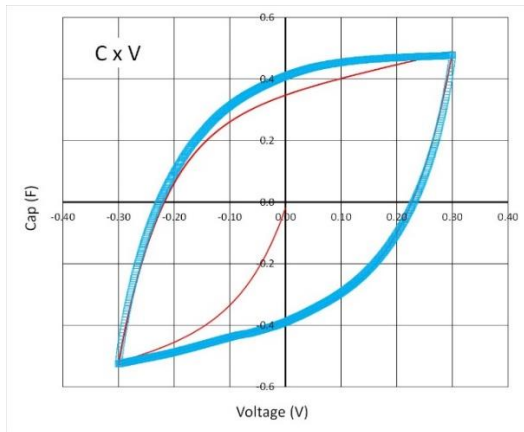


Figure 5 – CV curve and fitting of an HSAM electrode obtained using Starch + Phosphoric Acid (4h HTC) followed by an annealing with KOH: Carbon (6:1) at 800 °C/1h.

The electrode material characterization revealed that the use of KOH during the activation process resulted in carbon sponges possessing large specific surface area and capacitances in the range up to 150 F/g.

Conclusions

A simplified method of preparing activated carbon with a well-developed porous structure and substantial specific capacitance was obtained via an HTC process including KOH activation. By the addition of acids during the HTC process the processing time was considerably reduced while the reaction yield was increased. Using KOH for the activation resulted in highly porous carbon spheres with substantial specific surface area.

References

- [1] Ho J., Jow T.R., Boggs S. **IEEE** (elect. Ins. Mat) 26-1,20 (2010).
- [2] Conway, B.E. *Electrochemical Supercapacitors*, Kluwer Academic /Plenum Publishers, N.Y. (1999)
- [3] Smith A.M., Whittaker C., Shield I, and Ross A.B. **Fuel** 546 (2018).

Acknowledgments

The authors would like to acknowledge the collaboration of the Physics Department of the Federal University of Parana, In Curitiba, Brazil, for their generosity in serving one of the co-authors (CKS) with a Sabbatical leave of absence during the 2018-2019 academic year.

P23 |

FEATURE EXTRACTION ACCELERATION BY THE PREDICTION OF THE STEADY STATE RESPONSE FOR SOLID STATE GAS SENSORS

S. Muñoz-Aguirre*, D. Silva-Apango, G. Beltrán-Pérez, J. Castillo-Mixcóatl

¹ *Facultad de Ciencias Físico Matemáticas, Benemérita Universidad Autónoma de Puebla, Av. San Claudio y 18 Sur, Col. San Manuel, CU, CP 72570, Puebla, México*

**e-mail: smunoz@fcfm.buap.mx*

Abstract

Feature extraction acceleration is important for different purposes, for instance, in research and industry it is necessary to accelerate the recognition of volatile organic compounds as this would save time for important decisions. In the present work a study about steady-state sensor response prediction using the transient response for metal-oxide sensors was performed. Two characteristics of the output response were extracted: an analysis of the slopes obtained when starting the gas stimulus using the finite difference method together with the non-linear regression fitting to know the time constant of the sensor and the maximum value obtained from a digital low pass filter. As a result, we obtained predictions very close to the measured value, with an error of less than $\pm 5\%$, in a time approximated to 8.4 % of the one necessary to reach the steady state.

Introduction

Acceleration of feature extraction for gas sensors is essential for the detection of gases that can be very dangerous to human health, such as inhaling inert gases or any other poisonous gas that can cause suffocation and death [1,2]. Metal oxide gas sensor arrays have been used due to their wide availability in the market and their simplicity of use, in addition to their rapid response compared to other sensors [3]. For this reason, they have been widely used in food product quality testing, breath analysis for disease detection, environmental monitoring on gas leak detection platforms [4,5]. The sensor response can be divided in the transient response and the steady-state response, the former being the change that is induced when a stimulus is presented to the sensor and the latter being when the output response remains constant. The sensor response of gas sensors has a behavior as the form of a first order system. Therefore, when a gas stimulus is applied to these sensors, through a data analysis obtained at the stimulus beginning, we can be able to predict the steady state response [3]. In the present work, we propose that if the sensor time constant is known, it will only be

necessary to multiply it by the slope at the starting of the transient response, so it can be said that it is a simple method to apply and can be implemented on a personal computer or even in a microcontroller that records the responses.

Methods

In the present work, the TGS2620 (Figaro Inc) gas sensor was used. It is a metal oxide semiconductor gas sensor, which is composed of a sensing element made with aluminium oxide (Al_2O_3). The sensor can detect several volatile organic compounds, specifically ethanol. The use of an integrated heater calibrated by the manufacturer allows a higher sensitivity to ethanol over other compounds. A simple circuit like a voltage divider can measure the variation in the sensor conductivity as an output signal related to gas concentration (Figure 1). The transient response is the behavior of a system to any variation from an equilibrium (initial value) to another steady state (final value). It is related to any event that affects the balance of the system, in this case a gas step stimulus.

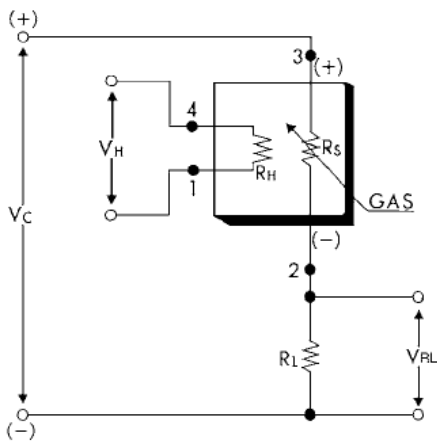


Figure 1. Circuit to measure the sensor response

The output signal in voltage $V(t)$ obtained from the sensor is given by the Equation 1, which is the mathematical description of a first-order system response

$$V(t) = V_0 (1 - e^{-t/\tau}), \tag{1}$$

where V_0 is the static sensitivity, which is the value where the output signal remains constant over time, also known as the steady state. The time constant of the system is given by τ and determines the time in which we can consider that the steady state is reached, for practical measurements this happens in a time equal to 5τ .

We can obtain an interesting deduction if we derive Equation 1 with respect to time and evaluate it at a time equal to zero, in this way we obtain Equation 2

$$V_0 = \tau \left. \frac{dV(t)}{dt} \right|_{t=0}. \quad (2)$$

This equation tells us that by knowing the sensor time constant τ and the slope of the sensor response function at time $t = 0$, it is possible to know the steady state response. However, for real applications, it would be necessary to measure the first portion of the sensor response to determine a value that can be used as an approximation of the derivative of the response in $t = 0$. Therefore, an approximation of Equation 2 must be used, expressed as Equation 3, where m is the slope calculated from discrete points measured from the sensor response. In this way, from the beginning of the transient response, we can predict the steady state of the sensor

$$V_0 = \tau m \quad (3)$$

The responses were measured with a dynamic system that applied a gas step stimulus of an ethanol sample at different concentrations determined by the air flow (300 ml/min, 400 ml/min, and 500 ml/min). This was to investigate the dependency of the obtained results with that parameter.

Results

In figure 2a, the sensor responses as measured in a dynamic system are shown. The magnitudes change with the flow rate, since it determines the concentration of the sample, in this case ethanol. In Figure 2b, it is shown a zoom of the first points of the response. A clear delay in the response starting, which is not evident in figure 2a can be observed. Different slope calculations were performed taking 3 experimental points, looking for the value that most approximates the ideal initial slope value ($t=0$) determined by the ideal response (Equation 1), whose curve is shown in a blue line. It was found that the slope determined at around 1.7 s was the best approximation. Therefore, it was used to perform the prediction of the steady state response. Additionally, an average value of $\tau = 4.01$ of the constant time was determined from Equation 1 and used to determine the experimental steady state sensor response in $5\tau = 20.2$ s. Therefore, we used such value to perform the predictions.

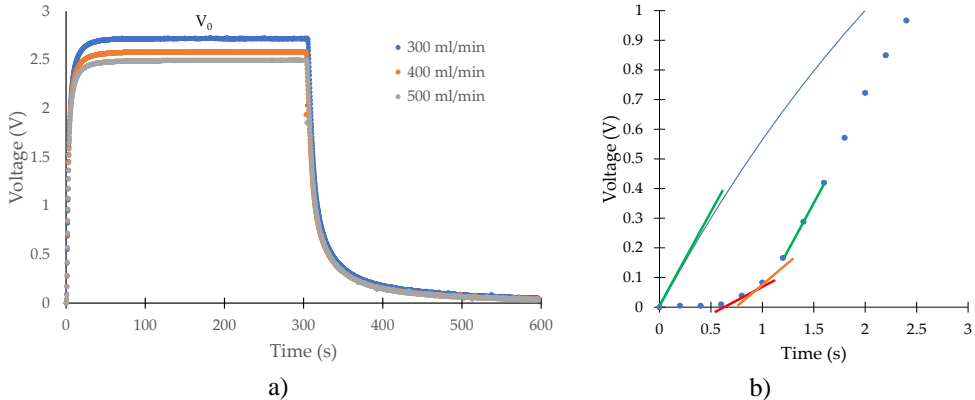


Figure 2. a) An example of sensor responses measured for ethanol at different flow rates, b) a zoom of the first points of the sensor response, where shows the slope used for the steady state prediction.

Figure 3 shows the result of the predictions. The plot shows the ratio between the predicted value for different slopes to that of the experimental steady state measured at 20.2 s. We can observe that the values close to 1.7 s (enclosed in the red circle) are inside an error of $\pm 5\%$. Therefore, we can say that it was possible to perform the predictions with a quite small deviation. Moreover, the enclosed points are not the only that perform the prediction, also there are other points that are located inside the 5% error. However, these values appear lately in time (around 2.5 s). From these results, if we consider that the steady state is reached at 20.2 s and we performed the prediction in 1.7 s, we can say that an acceleration of more than 18 s was achieved, i.e., in around 8.4 % of the time that it takes to reach the steady state.

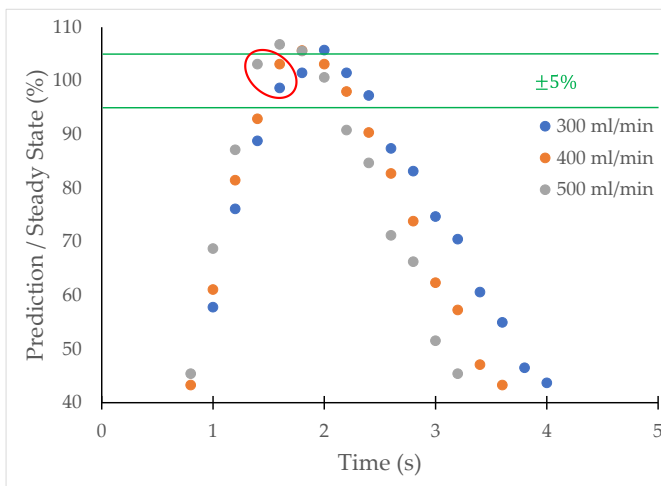


Figure 3. The plot shows the ratio between the predicted value calculated at 1.7 s in function of different slope calculations to the steady state response measured at 20.2 s.

Conclusions

The acceleration of feature extraction was studied in the present work. A TGS 2620 gas sensor was used and its response to ethanol was measured. The slope in the experimental response that best fits to the derivative of the ideal response curve was calculated and used to perform a prediction of the steady state response at 20.2 s (5τ). It was found that the slope at 1.7 s was the most adequate value. The prediction was successfully performed inside an error of $\pm 5\%$. From the prediction, an acceleration of 18 seconds was achieved, that can be useful to perform feature extraction. This method can be used for other kind of sensors.

References

- [1] EIGA Hazards of Inert Gases and Oxygen Depletion. Eur. Industrial Gases Assoc. DiMaio, V.J.M.; DiMaio, [2] D. Forensic Pathology; 2nd ed.; CRC Press: Boca Raton: FL, USA, 2001.
- [3] Osorio-Arrieta, D.; Muñoz-Mata, J.; Beltrán-Pérez, G.; Castillo-Mixcóatl, J.; Mendoza-Barrera, C.; Altuzar-Aguilar, V.; Muñoz-Aguirre, S. Reduction of the Measurement Time by the Prediction of the Steady-State Response for Quartz Crystal Microbalance Gas Sensors. *Sensors* 2018, 18, 2475.
- [4] Jia, W.; Liang, G.; Tian, H.; Sun, J.; Wan, C. Electronic nose-based technique for rapid detection and recognition of moldy apples. *Sensors (Switzerland)* 2019, 19, 1–11.
- [5] Marzorati, D.; Mainardi, L.; Sedda, G.; Gasparri, R.; Spaggiari, L.; Cerveri, P. A Metal Oxide Gas Sensors Array for Lung Cancer Diagnosis Through Exhaled Breath Analysis. *Proc. Annu. Int. Conf. IEEE Eng. Med. Biol. Soc. EMBS 2019*, 1584–1587.

Acknowledgments

CONACYT Project CB-2016-01, grant number 286647

P24 |

INTEGRACIÓN DE REDES NEURONALES CON SISTEMAS ANALÍTICOS INTEGRADOS PARA LA CUANTIFICACIÓN DE METALES PESADOS EN SOLUCIÓN ACUOSA

V. E. Manqueros Aviles¹, H. Coto Fuentes¹, F. Valdés Perezgasga²,
K. V. Guevara Amatón², J. Alonso-Chamarro³, P. Couceiro³

¹*Instituto Tecnológico Superior de Lerdo, Av. Tecnológico 1555, CP35150, Lerdo, Durango, México*

²*Instituto Tecnológico de la Laguna, Blvd. Revolución s/n, CP27000 Torreón, Coahuila, México*

³*Departamento de Química, Universidad Autónoma de Barcelona, Bellaterra, Barcelona, España*

*e-mail: vema6791@gmail.com

Introducción

Desde el 2016 a la fecha se encuentra en operación un sistema analítico para la cuantificación de cobre en las aguas vertidas de la mina Milpillias, propiedad del grupo Met – Mex Peñoles en Sonora, México, con el objetivo de monitorear los niveles del metal y tomar las medidas necesarias en caso de encontrarse fuera de norma. Dicho sistema fue desarrollado en el marco de un convenio de colaboración entre la empresa antes mencionada y las instituciones: Instituto Tecnológico de la Laguna y la Universidad Autónoma de Barcelona. El sistema de medición actual realiza lecturas de cobre en soluciones acuosas una vez cada hora, a partir de una curva de calibración que elabora al principio de la jornada, con cuatro concentraciones obtenidas de un patrón de cobre. Para las mediciones, el sistema utiliza principios de absorción en el espectro visible, usando un LED verde como fuente de luz (505 nm). Las concentraciones se obtienen por triplicado, y se ha observado la generación de burbujas como uno de los principales inconvenientes durante las mediciones, aspecto inherente a sistemas microfluídicos. Dichas burbujas afectan las mediciones, y actualmente provocan que se desestimen una o varias de las tomas de muestras. Si bien no es considerable la cantidad de reactivos que se desechan durante el fallo provocado por las burbujas, la pérdida de mediciones sí podría acarrear problemas.

El presente trabajo propone el uso de redes neuronales como opción para la cuantificación de metales pesados actualmente cobre, y a corto plazo cobalto en solución acuosa, aún en presencia de burbujas. A partir del entrenamiento y aprendizaje, el sistema detectará la aparición de burbujas durante las mediciones, siendo capaz de tomar o no en cuenta dicha medición según sea el caso, representando una gran ventaja respecto al sistema anterior.

Métodos

El sistema está compuesto por una microfluídica elaborada a partir de polímeros transparentes, donde una serie de canales permite la mezcla de los reactivos (soluciones NRS, buffer y la solución a medir o el patrón) y el cambio de coloración. En cierta parte del recorrido de dichos canales existe un área más grande “ventana”, donde se encuentra la fuente de luz (LED verde de 505 nm de longitud de onda) y un fotodiodo como sensor. En la Figura 1 se pueden apreciar los elementos que conforman el sistema analítico en forma esquemática. Además, se muestran las mediciones durante la calibración y toma de muestra del sistema.

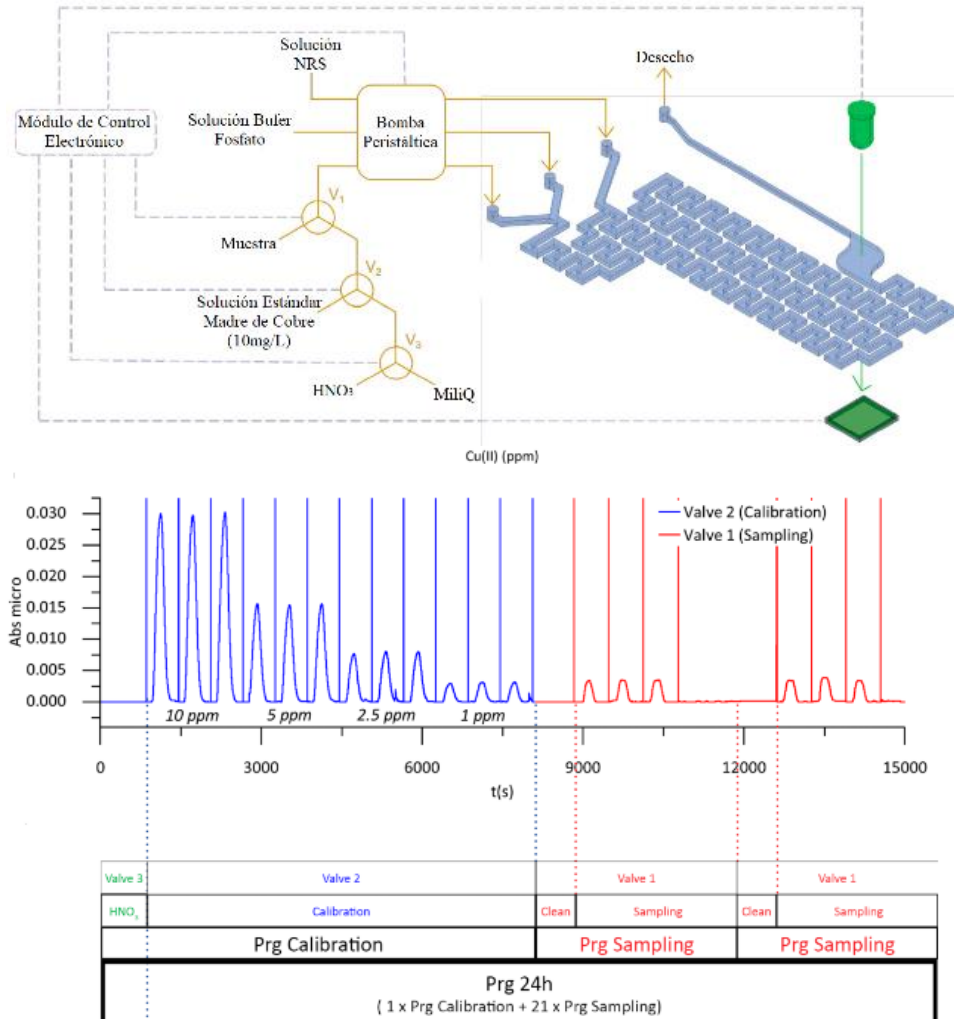


Figura 1. Esquema del sistema y tiempos de Calibración y muestreo.

El acondicionamiento y adquisición de la señal es manejada por un microcontrolador PSoC 5, el cual contiene internamente los elementos analógicos necesarios para realizar el tratamiento de la señal proveniente del fotodiodo. El microcontrolador también se encarga de controlar la intensidad de iluminación del LED, manejar los tiempos de conmutación de las válvulas, así como la velocidad de operación de la bomba.

Para el desarrollo del algoritmo de medición se dividió el trabajo en dos etapas. La primera, consistió en elaborar una red neuronal artificial y entrenarla haciendo uso de librerías de TensorFlow y NumPy en el ambiente de Python 3.9. Para el entrenamiento y cálculo de los pesos, se utilizó una computadora personal y series temporales para la extracción de información de mediciones de concentración de cobre obtenidas en el sistema actual. Durante esta primera etapa se probaron dos redes neuronales: la primera con tres entradas una capa oculta de cuatro neuronas y una salida; la segunda con tres entradas, dos capas ocultas, cada una con cuatro neuronas, y una salida. Las magnitudes obtenidas después del entrenamiento se pusieron a prueba en una red neuronal artificial implementada en la plataforma DUE de Arduino, con la intención de corroborar que la red podía distinguir concentraciones. En la segunda etapa se desarrolló todo el algoritmo de las redes neuronales en microcontroladores de alta gama, con la finalidad de poder medir concentraciones en sistemas analíticos sin la intervención de computadoras personales u otras herramientas de software. El algoritmo que se implementó es el de retropropagación (*backpropagation*), el que debió programarse en los diferentes ambientes de programación según el microcontrolador. Las librerías fueron desarrolladas desde cero, sin la utilización de librerías de terceros, como las que existen en desarrollos de software de uso libre para microcontroladores o sistemas embebidos.

En la solución propuesta, el entrenamiento se realiza en el mismo sistema embebido o microcontrolador, desarrollando el algoritmo de *backpropagation*, las funciones de activación de la red, la generación de números aleatorios, la estimación del error y la propagación hacia delante o inferencia. Para el entrenamiento de la red fueron necesarias varias mediciones con diferentes características, pero con similitudes al sistema actual en funcionamiento: como lo son triplicado de la medición para concentraciones de 10, 5, 2.5 y 1 ppm, así como burbujas en diferentes partes de la curva de medición. Con las mediciones obtenidas se procedió a extraer diferentes características de series temporales como: el valor eficaz (RMS) el valor absoluto (MAV) y la longitud de forma de onda (WL), estos tres valores serán las entradas de la red neuronal artificial

(RNA). En la Figura 2 se muestran los resultados de las pruebas realizadas para concentraciones de 10 ppm y 5 ppm.

Resultados

En los resultados de la experimentación fue evidente la importancia del número de capas ocultas, y en menor medida, el número de épocas del entrenamiento de la red neuronal, lo que sí es relevante para el desempeño de una red entrenada en el microcontrolador. Otro aspecto importante es que, las extremadamente bajas frecuencias de las señales propias del sistema analítico actual, permiten al sistema de medición con inteligencia artificial realizar ajustes de sus parámetros, considerándose una ventaja. En las imágenes mostradas en la Figura 2 se aprecian los resultados de la propagación hacia delante de la red neuronal y la estructura usada. Se puede apreciar que en el entrenamiento a mayores épocas y más capas ocultas en la estructura de la red, la función de pérdida disminuye haciendo el error más pequeño, lo cual resulta en que la red puede detectar con mejor asertividad las concentraciones para la que es entrenada.

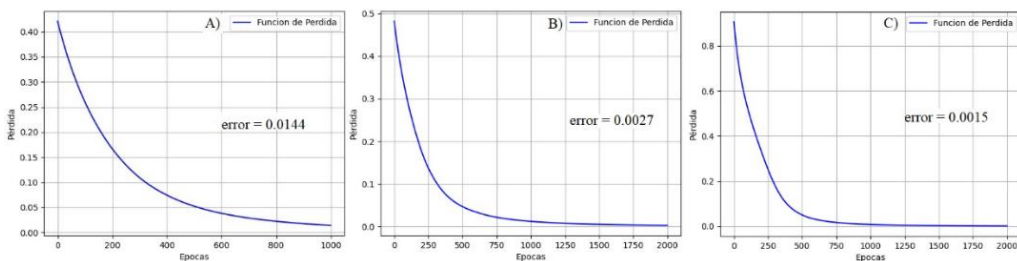


Figura 2. Función de pérdida de diferentes entrenamientos de la red neuronal.

La Tabla 1 muestra los resultados obtenidos durante el entrenamiento de una red neuronal de prueba, con un factor de aprendizaje (*ratio learning*) de 0.05, una capa oculta de 4 neuronas y una de salida, utilizando los microcontroladores: ESP32, PSoC6, Portenta H7 y Raspberry Pico. Para el experimento se limitó el entrenamiento a 1000 épocas, la unidad de tiempo utilizada en la tabla son los segundos.

Tabla 1. Resultados de entrenamiento en microcontroladores

Microcontrolador	Épocas	Tiempo[s]	Error
<i>ESP 32</i>	1000	1031	0.000168
<i>Raspberry Pi Pico</i>	1000	717	0.000189
<i>PSoC 6</i>	1000	57	0.000262
<i>Portenta H7</i>	1000	66	0.000121

Conclusiones

Hasta el momento los resultados obtenidos son alentadores, dado que la red ha funcionado correctamente en la cuantificación de concentraciones dentro del rango que fue entrenada, pero aún falta una mejor evaluación de su desempeño ante factores como las burbujas, cobrando gran importancia el entrenamiento de ésta bajo condiciones que presenten dichos eventos no deseados. En el caso de los microcontroladores, se puede apreciar que los tiempos más aceptables pertenecen a los microcontroladores PSoC 6 y el sistema Portenta H7. Aunque faltan pruebas con diferentes configuraciones en cuanto a la relación de aprendizaje, épocas, arquitecturas de redes neuronales e incluso otras ramas de la inteligencia artificial.

Referencias

- [1] Arief, Z., Sulistijono, I. A., & Ardiansyah, R. A. (2015, September). Comparison of five time series EMG features extractions using Myo Armband. In 2015 international electronics symposium (IES) (pp. 11-14). IEEE.
- [2] Dokic, K., Radisic, B., & Cobovic, M. (2020, March). MicroPython or Arduino C for ESP32-Efficiency for Neural Network Edge Devices. In International Symposium on Intelligent Computing Systems (pp. 33-43). Springer, Cham.
- [3] Guevara Amatón, K. V., Couceiro, P., Coto Fuentes, H., Calvo-Lopez, A., SándeZ, N., Moreno Casillas, H. A., . & Alonso-Chamarro, J. (2019). Microanalyser prototype for on-line monitoring of copper (II) ion in mining industrial processes. *Sensors*, 19(15), 3382.
- [4] LeCun, Y. A., Bottou, L., Orr, G. B., & Müller, K. R. (2012). Efficient backprop. In *Neural networks: Tricks of the trade* (pp. 9-48). Springer, Berlin, Heidelberg. Agradecimientos

Agradecimientos

Este proyecto recibió un financiamiento parcial de la compañía Met-Mex Peñoles. Uno de los autores (V. E. Manqueros Aviles) recibe una beca doctoral del Consejo Nacional de Ciencia y Tecnología de México.

MULTI-PHOTON MICROSCOPY SETUP FOR INTEGRATION IN COLONOSCOPES: AN OVERVIEW

R. B. Freitas ^{1,2,*}, M. J. Maciel ^{1,2}, S. Pimenta ^{1,2,*}, M. S. Belsley ³, J. H. Correia ^{1,2}

¹ *CMEMS – UMinho, University of Minho, 4800-058, Guimarães, Portugal*

² *LABELS – Associate Laboratory, Braga, Guimarães, Portugal*

³ *Center of Physics, University of Minho, 4710-057, Braga, Portugal*

**e-mail: ruben.freitas@dei.uminho.pt; sara.pimenta@dei.uminho.pt*

Introduction

Multi-photon microscopy (MPM) is considered one of the breakthrough inventions. This technique is based on the intracellular endogenous fluorescent signal, such as the two-photon excited fluorescence and second-harmonic generation (SHG) [1–3]. MPM provides optical sectioning from deep specimens with high scattering properties, restricting fluorophore excitation to the focal plane [4]. This type of microscopy can provide real-time information about cellular morphology and perform three-dimensional tomography on fresh tissues, being an excellent replacement for traditional laborious histopathology. MPM could be very sensitive in the diagnosis of colorectal cancer during conventional colonoscopy [1–3,5]. Among the endogenous fluorophores that can be imaged by MPM, nicotinamide-adenine dinucleotide (NADH) and flavine-adenine dinucleotide (FAD) are the most relevant. The fluorescent signal of these fluorophores can be acquired for cancer monitoring, because changes in the metabolism of glucose occur in cancerous cells, even before morphological changes appear in the tissues [6,7]. On the other hand, the SHG collagen signals can also be used to study tumor-induced changes in matrix organization [5].

The commercial MPM equipment is bulky and inadequate for miniaturization applications [1–3]. This work aims to integrate MPM in conventional colonoscopes (Figure 1), by developing a microfabricated MPM setup. The MPM prototype will be used complementarily to colonoscopy and will provide the *in-vivo* optical biopsy of colorectal tissues, being capable to detect human colon cancer in its early stage. Some studies related to the development of miniaturized probes with MPM technology have already been carried out. However, all of them focus only on the scanning system (probe) miniaturization, no study achieved the direct integration of the probe in a conventional colonoscope, and the probes are exclusively tested in ex-vivo tissues or animals. Thus, more studies are needed to successfully implement this technology in colonoscopy. This abstract presents an

overview of the MPM setup and some experiments already performed towards the final prototype implementation.

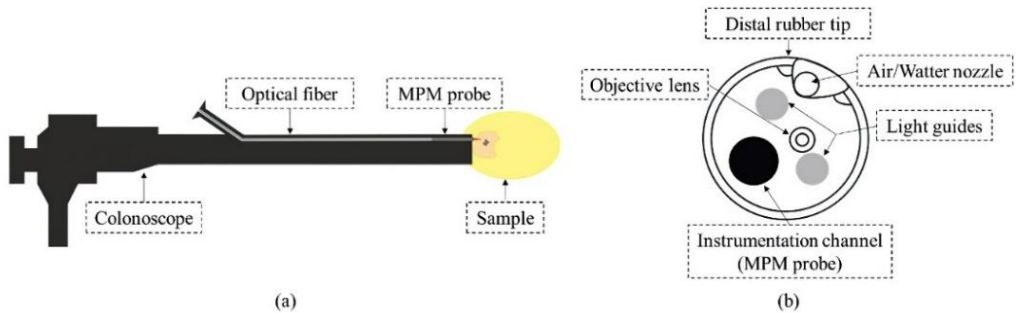


Figure 1. Colonoscope with a MPM probe: (a) side view; (b) front view.

Methods

This work will focus on the development of an MPM prototype based on the schematic presented in Figure 2. This setup includes the assembling of optical components, a microfabricated MPM probe (piezoelectric tube-based with GRIN lens assembly) for integration in the instrumentation channel of a commercial colonoscope, and optical filters for the MPM detection system.

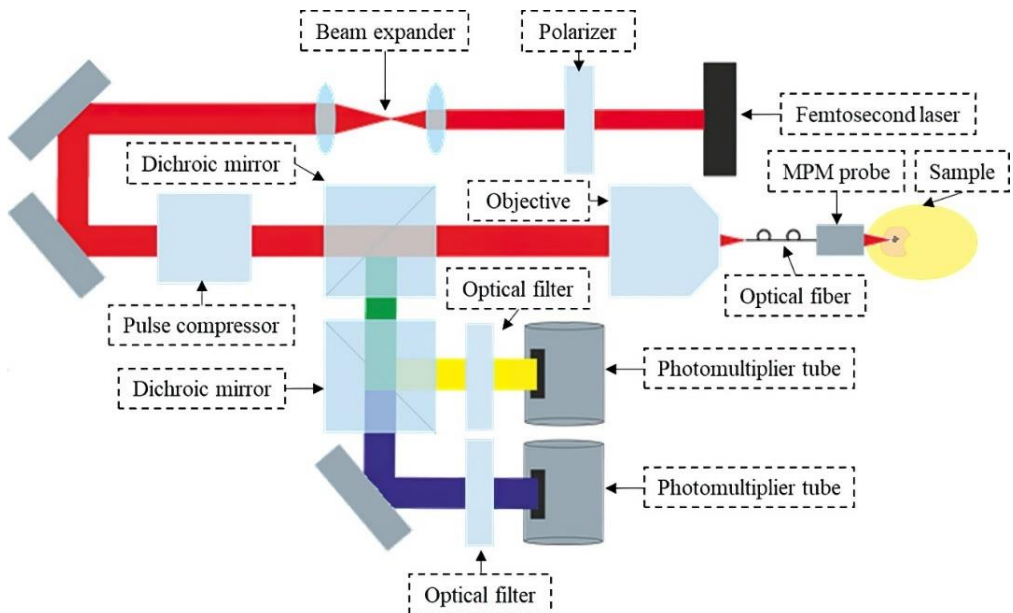


Figure 2. Schematic of the MPM prototype.

The microfabricated MPM probe should have a diameter smaller than the instrumental channel of conventional colonoscopes (3.8 mm). The piezoelectric tube to scan the tissue will be fabricated using conventional MEMS technologies for the deposition of the piezoelectric material (zirconate titanate), such as physical vapor deposition (PVD) and atomic layer deposition (ALD). The fabrication of GRIN lenses will be performed using photolithography, thermal reflow, and PDMS (polydimethylsiloxane) demolding. The optical filters will be implemented with a multilayer of dielectric thin-films (SiO_2 as the low-refractive index material and TiO_2 as the high-refractive index material). Before microfabrication using a PVD technique (RF-sputtering), the optical filters must be designed and simulated at a software tool (TFCalc 3.5). The optical filters will be used to ensure that only the signals emitted by the fluorophores will be acquired by the MPM detection system. Since NADH presents an emission wavelength peak at 460 nm, and FAD at 525 nm, at least two optical filters centered at those wavelengths should be designed and fabricated [6,7].

Experimental results

Ultrashort-pulse compressor: as presented in Figure 2, an important component of the MPM setup is an MPM laser ultrashort-pulse compressor. This component is useful for tissue imaging since allows the maintenance of ultra-short pulses, despite the optical path. The laser time compression improves the number of photons that reach the focal point at a given time, increasing the intensity of the generated signals. The compressor schematic based on the work developed by Akturk *et al.* in 2006 [8] is presented in Figure 3 (a). For this experiment, the prism-corner cube separation has varied a total of 15 cm in intervals of 1 cm using a rail. The output pulse full-width at half maximum (FWHM) was measured using an autocorrelator (APE Mini). The obtained values are presented in Figure 3 (b).

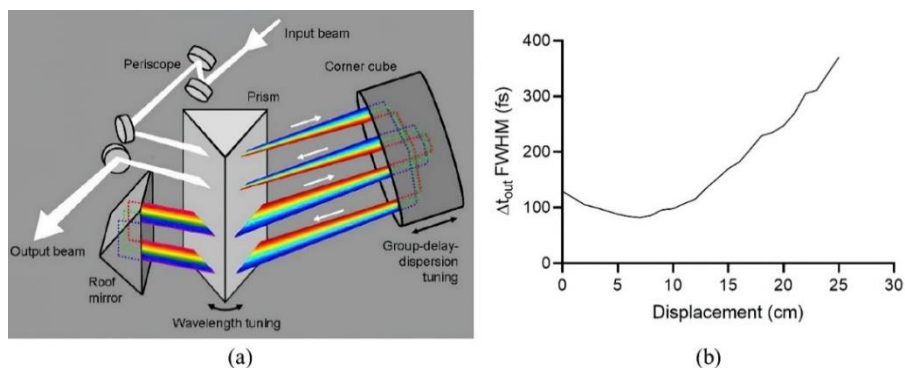


Figure 3. Ultrashort-pulse compressor: (a) schematic [8]; (b) variation of the output pulse FWHM with the prism-corner cube separation.

Optical filters: the optical filters simulation requires the use of the materials (SiO_2 and TiO_2) refractive indices. This task is crucial to obtain the thickness of each thin-film, which will form the narrow and high transmission filter at the wavelength of interest. Those refractive indices can be variable according to deposition method and microfabrication conditions. Thus, individual thin-films of SiO_2 (89.87 nm thick) and TiO_2 (91.36 nm thick) were deposited by RF-sputtering and characterized with profilometry (Veeco Dektak 150) and ellipsometry (J. A. Woollam alpha-SE). All the obtained results for the refractive indices are presented in Figure 4, where is also presented the theoretical refractive indices stated in the literature for comparison.

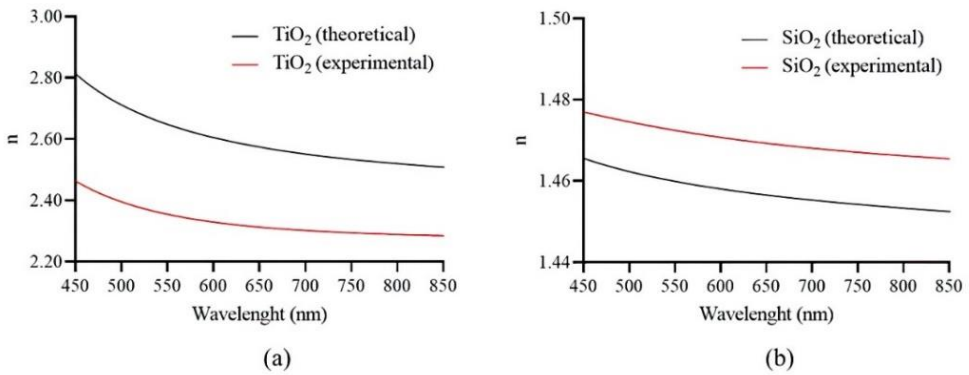


Figure 4. Theoretical and experimental refraction indices: (a) SiO_2 ; (b) TiO_2 .

Conclusions

This abstract presents some experimental work towards the implementation of a MPM setup for integration in conventional colonoscopes. Experiments with an ultrashort-pulse compressor for a MPM laser proved that the duration of the pulse varies with the prism-corner cube distance, and so the ultrashort-pulse compressor is working correctly. Regarding the optical filters, thin-films were deposited by RF-sputtering and characterized by ellipsometry. The results show that the deposited materials present refractive indices similar to the theoretical values, stated in the literature.

References

1. K. He, L. Zhao, Y. Chen, X. Huang, Y. Ding, H. Hua, L. Liu, X. Wang, M. Wang, Y. Zhang, and Z. Fan, *J. Gastroenterol. Hepatol.* **34**, 2144 (2019).
2. C. J. R. Sheppard, *J. Biomed. Opt.* **25**, (2020).
3. F. Helmchen and W. Denk, *Nat. Methods* **2**, 932 (2005).
4. M. Rubart, *Circ. Res.* **95**, 1154 (2004).
5. R. K. P. Benninger, M. Hao, and D. W. Piston, in *Rev. Physiol. Biochem. Pharmacol.* (Springer Berlin Heidelberg, Berlin, Heidelberg, 2008), pp. 71–92.
6. R. K. P. Benninger and D. W. Piston, *Curr. Protoc. Cell Biol.* **59**, (2013).
7. J. R. Lakowicz, *Principles of Fluorescence Spectroscopy*, 3rd ed. (Springer US, Boston, MA, 2006).
8. S. Akturk, X. Gu, M. Kimmel, and R. Trebino, *Opt. Express* **14**, 10101 (2006).

Acknowledgments

This work was supported by FCT with the project MPhotonBiopsy, PTDC/FIS-OTI/1259/2020. R. B. Freitas thanks to FCT for the Ph.D. grant 2021.06966.BD.

P26 |

SIMULACIÓN DE LA INSTRUMENTACIÓN ELECTRÓNICA ASOCIADA AL ISFET MEDIANTE EL CIRCUITO INTEGRADO CD-4007

H. Rodríguez¹, A. Castellanos¹, E. Valdés¹, C. Domínguez-Horna²

¹ Centro de Investigaciones en Microelectrónica de Cuba,

² Instituto de Microelectrónica de Barcelona

*e-mail: humbertorg@cime.cujae.edu.cu

Introducción

El ISFET (transistor de efecto de campo sensible a iones) es un transductor electroquímico de estado sólido desarrollado con la tecnología microelectrónica de fabricación de circuitos integrados [1]. El ISFET se puede definir como un MOSFET (transistor de efecto de campo semiconductor de óxido de silicio) donde la capa metálica de la puerta se sustituye por una membrana sensible a los iones, un electrolito y un electrodo de referencia [2]. Si utilizamos como membrana sensible nitruro de silicio (Si₃N₄), óxido de tántalo (Ta₂O₅) u óxido de aluminio (Al₂O₃), este sensor permite determinar la concentración de iones H⁺ (pH) del electrolito. Por lo tanto, el ISFET es un transistor de efecto de campo cuyo voltaje de umbral (V_{th}) es proporcional a un estímulo químico.

En este trabajo proponemos la utilización del circuito integrado CD4007 como ISFET en el programa de simulación LTspice, con el objetivo de estudiar y validar los circuitos acondicionadores de señal diseñados o por diseñar para este tipo de sensor. La temática relacionada con la modelación del ISFET y su uso en programas de simulación ya ha sido tratada. Se destacan los trabajos de Martinoia y Massobrio [3, 4 y 5] relacionados con la obtención de modelos del ISFET para los programas de simulación tipo SPICE. También encontramos contribuciones a la modelación de este tipo de sensor para herramientas TCAD (Technology Computer-Aided Design) [6 y 7]. Samah et. al [8] presentan un macromodelo del ISFET para LTspice. Viton-Zorrilla and Lezama [9] presenta una plataforma software para la simulación del ISFET con herramientas de código abierto. Sinha et. al [10, 11 y 12] desarrollan macromodelos SPICE para ISFETs con puerta de nitruro de silicio y de óxido de aluminio, y en un caso utilizan datos experimentales y técnicas de Machine Learning en dispositivos FPGA para aplicaciones industriales IoT del ISFET en medición de pH. A pesar del trabajo realizado en la modelación del ISFET y su utilización en programas de simulación, consideramos pertinente con esta contribución, proponer una herramienta software para el estudio y validación de los circuitos acondicionadores de señal

del ISFET. Se ha identificado un dispositivo electrónico (CD4007) que puede ser utilizado con una herramienta software para validar, por medio de la simulación, el correcto funcionamiento de nuevas propuestas de circuitos acondicionadores de señal para ISFETs.

Métodos

El CD4007 [13] es un circuito integrado que presenta 6 transistores MOSFET de canal inducido: 3 canal N y 3 canal P. En cuatro de los transistores, el terminal de sustrato (bulk) es independiente al terminal de fuente (source). Lo anterior permite variar el voltaje umbral (V_{th}) del transistor MOS variando el potencial entre sustrato y fuente. Como herramienta software de simulación utilizaremos el LTSpice [14] a la cual se le ha añadido el modelo del CD4007 [15].

La figura 1 muestra el esquemático utilizado para simular un transistor MOS canal N del CD4007 utilizando LTSpice. Se aprecia que el terminal de fuente (s) ha sido colocado a tierra (gnd) y se ha conectado una fuente de voltaje de DC en cada uno de los tres otros terminales (drenaje (d), puerta (g) y sustrato (b)).

Utilizando la directiva `.dc`, colocada en la parte inferior del esquemático, se configura para realizar un análisis de DC, el cual consiste en cinco ciclos de variaciones (barridos) del V_{gs} desde 0V hasta 5 V con incremento de 1 mV. Cada barrido en el V_{gs} se realiza para cinco potenciales de DC diferentes de V_{bs} con valores de 0V, -1V, -2V, -3V y -4V.

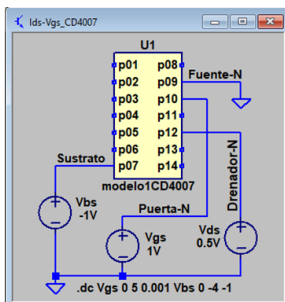


Fig. 1 Esquemático para simular la CD4007 con LTSpice

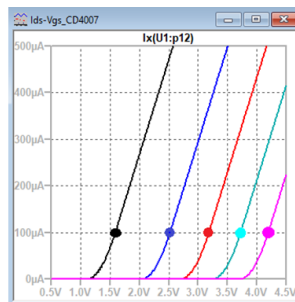


Fig. 2 Curvas I_{ds} vs. V_{gs} para $V_{ds}=0.5V$ y V_{bs} de 0V, -1V, -2V, -3V y -4V

Tabla 1. Puntos de operación del transistor MOS canal N del CD4007 para V_{ds} e I_{ds} constantes (0.5V y 100 μA) y los cinco valores de V_{bs}

V_{ds}	I_{ds}	V_{bs}	V_{gs}
0.5 V	0.1 mA	0 V	1.595 V
0.5 V	0.1 mA	-1 V	2.527 V
0.5 V	0.1 mA	-2 V	3.187 V
0.5 V	0.1 mA	-3 V	3.728 V
0.5 V	0.1 mA	-4 V	4.198 V

Nota: Terminales del MOS N utilizado
terminal 9: Fuente (Source – s)
terminal 10: Puerta (Gate – g)
terminal 12: Drenador (Drain- d)
terminal 7: Sustrato (Bulk – b)

La figura 2 muestra el visor de forma de onda de LTSpice con las curvas I_{ds} vs. V_{gs} obtenidas para los cinco valores distintos en V_{bs} . Se puede apreciar cómo la variación del V_{bs} en el transistor MOS ha ocasionado una variación en el voltaje umbral (V_{th}) del dispositivo. Este comportamiento permite que el MOS pueda

sustituir al ISFET en el circuito acondicionador de señal del sensor. La tabla 1 muestra para el transistor MOS, los valores de los cinco puntos de operación destacados en la figura 2, lo cuales se caracterizan por un V_{ds} constante de 0.5V y una I_{ds} constante de 100 μA .

La figura 3 muestra el primer circuito acondicionador de señal (CAS) para ISFET que utilizaremos para demostrar que si se varía el V_{bs} del MOSFET, este transistor se puede comportar como el ISFET. Este acondicionador de señal [16] es una variante de seguidor de fuente y drenador. Se caracteriza por polarizar al ISFET con V_{ds} constante de 0.5 V e I_{ds} constante de 100 μA . La respuesta eléctrica al estímulo químico se obtiene en el voltaje entre fuente y puerta (V_{sg} o $-V_{gs}$). En el esquema ubicado a la derecha en la figura 3, el ISFET ha sido sustituido por el MOSFET y la fuente de voltaje de directa V_{bs} . Las variaciones de voltaje en V_{bs} serán equivalentes a la variación del pH de la solución donde se encuentra el ISFET ya que las variaciones de V_{bs} provocan una variación del V_{th} del transistor MOS.

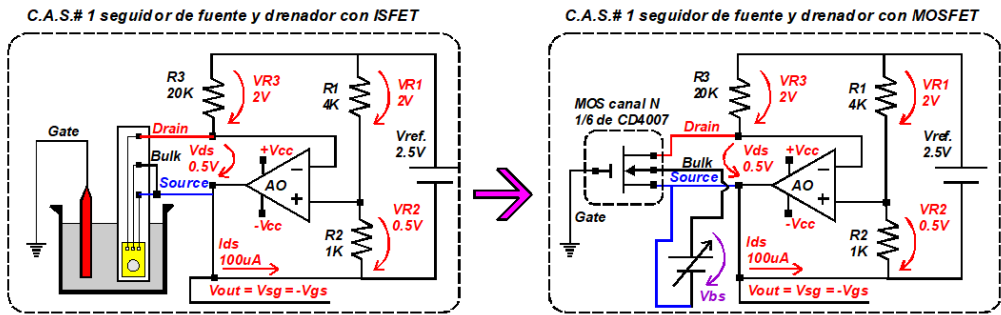


Fig 3. Circuito acondicionador de señal # 1 para ISFET: con ISFET (izquierda) y con MOSFET canal N (derecha).

La figura 4 muestra el segundo circuito acondicionador de señal para ISFET que utilizaremos para validar la hipótesis que se presenta en este trabajo. Este acondicionador de señal [17] es otra variante de seguidor de fuente y drenador con un principio de funcionamiento similar al acondicionador de señal presentado en la figura 3.

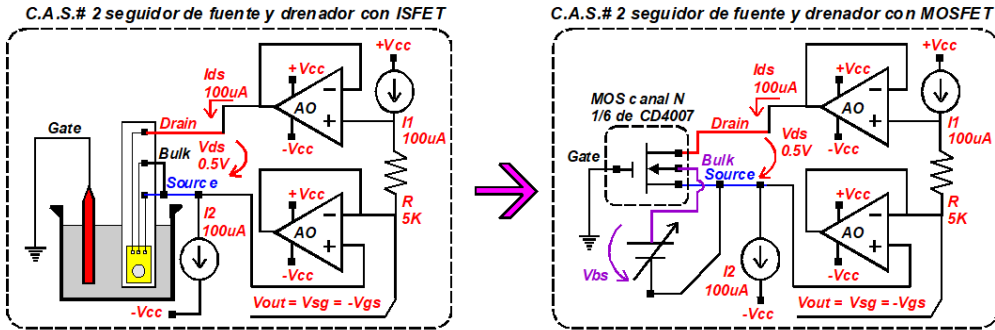


Fig 4. Circuito acondicionador de señal # 2 para ISFET: con ISFET (izquierda) y con MOSFET canal N (derecha).

Resultados

Las figuras 5 y 6 muestran los resultados de la simulación con LTspice de los dos circuitos acondicionadores de señal analizados donde el ISFET fue sustituido por el transistor MOS canal N del circuito integrado CD4007.

En ambas figuras a la izquierda se muestra el esquemático simulado y a la derecha, los resultados en el visor de forma de onda. En ambos circuitos se realizó un análisis de DC variando el V_{bs} de -4 V a 0 V con incrementos de 1 mV. Se puede observar como en ambos casos se mantiene un V_{ds} constante de 0.5 V (gráficos ubicados al centro) y una I_{ds} constante de 100 μA (gráficos ubicados en la parte inferior). Los gráficos ubicados en la parte superior de cada visor de forma de onda se corresponden con $-V_{gs}$ (voltaje de salida del CAS) y se puede apreciar cómo, en ambos casos, varía linealmente a medida que aumenta el V_{bs} (eje horizontal del visor). Esto se debe a la variación del V_{th} del MOSFET con la variación de V_{bs} .

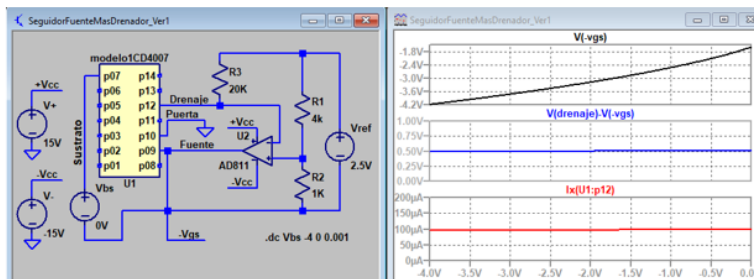


Fig. 5 Resultados de la simulación con LTspice del CAS # 1.

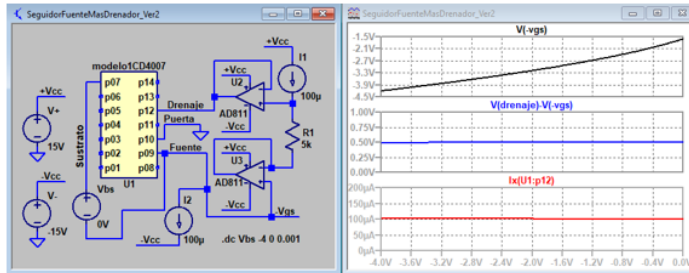


Fig. 6 Resultados de la simulación con LTspice del CAS # 2.

La tabla 2 representa los valores del voltaje de salida (-Vgs) de los dos CAS para cinco valores del Vbs (0V, -1V, -2V, -3V y -4V). Se debe destacar que -Vgs es el inverso del potencial Vgs del transistor MOS que sustituye al ISFET. Si comparamos estos valores con los de la tabla 1, podemos notar una gran correspondencia, dado que en todos los casos el MOS ha estado polarizado con Vds constante de 0.5V y en la tabla 1 los valores de Vgs se corresponden para una Ids constante de 100 uA. La última fila de la tabla 2 refleja la diferencia entre el valor de Vgs del MOS en cada CAS y el Vgs obtenido en la tabla 1 para los cinco valores de Vbs seleccionados.

Tabla 2. Valores del -Vgs de cada CAS para diferentes valores de Vbs y diferencia del Vgs respecto a tabla 1 para cada Vbs.

	Circuito acondicionador de señal # 1					Circuito acondicionador de señal # 2				
Vbs	0 V	-1 V	-2 V	-3 V	-4 V	0 V	-1 V	-2 V	-3 V	-4 V
-Vgs	-1.594 V	-2.522 V	-3.179 V	-3.718 V	-4.187 V	-1.593 V	-2.527 V	-3.189 V	-3.732 V	-4.203 V
dVgs	1 mV	5 mV	8 mV	10 mV	11 mV	2 mV	0 mV	2 mV	4 mV	5 mV

Conclusiones

En este trabajo se ha demostrado utilizando el software LTspice, que la variación del voltaje de salida (-Vgs) en los dos CAS analizados obedece a una variación del parámetro voltaje umbral (Vth) del transistor provocada por la variación del Vbs. Por tanto, se ha identificado un dispositivo electrónico (CD4007) que puede ser utilizado con una herramienta software para validar, por medio de la simulación, el correcto funcionamiento de nuevas propuestas de circuitos acondicionadores de señal para ISFETs.

Referencias

- [1] P. Bergveld, Development of an Ion-Sensitive Solid-State Device for Neurophysiological measurements, IEEE Transactions on Bio-Medical Engineering, Volume BME-17, Number 1, January, 1970, pp. 70-71.
- [2] P. Bergveld and A. Sibbald, Analytical and Biomedical applications of Ion-Selective Field Effect Transistors, Elsevier, 1988.
- [3] M. Grattarola, G. Massobrio and S. Martinoia, Modeling H⁺-Sensitive FET's with SPICE, IEEE TRANSACTIONS ON ELECTRON DEVICES. Vol. 39. No.4. April 1992.
- [4] S. Martinoia and G. Massobrio, A behavioral macromodel of the ISFET in SPICE, Sensors and Actuators B 62, 2000, pp.182–189.
- [5] S. Martinoia, G. Massobrio and L. Lorenzelli, Modeling ISFET microsensor and ISFET-based microsystems: a review, Sensors and Actuators B 105, 2005, pp.14–27.
- [6] A. Bandiziol, P. Palestri, F. Pittino, D. Esseni and L. Selmi, A TCAD-Based Methodology to Model the Site-Binding Charge at ISFET/Electrolyte Interfaces, IEEE TRANSACTIONS ON ELECTRON DEVICES, 2015.
- [7] E. Mohammadi and N. Manavizadeh, An Accurate TCAD-Based Model for ISFET Simulation, IEEE TRANSACTIONS ON ELECTRON DEVICES, 2018.
- [8] N. L. M. A. Samah K. Y. Lee and R. Jarmin, H⁺-ion-sensitive FET macromodel in LTSPICE IV, J Comput Electron 15:1407–1415, 2016.
- [9] L. Viton-Zorrilla and J. Lezama, A software platform for ISFET simulation based on open source tools to fit model parameters, 978-1-7281-3646-2/19, IEEE, 2019.
- [10] S. Sinha, , N. Sahu, R. Bhardwaj, A. Mehta, H. Ahuja, S. Srivastava, A. Elhence and V. Chamola, Machine Learning on FPGA for Robust Si₃N₄-gate ISFET pH Sensor in Industrial IoT Applications, IEEE Transactions on Industry Applications, Sept. 2021
- [11] S. Sinha, , N. Sahu, R. Bhardwaj, H. Ahuja, R. Sharma, R. Mukhiya and C. Shekhar, Modeling and simulation of temporal an temperature drift for the development of an accurate ISFET SPICE macromodel, Journal of Computational Electronics 19:367–386, 2020.
- [12] S. Sinha, T. Pal, P. Sharma, D. Kharbanda, P. K. Khanna, A. Tanwar, R. Sharma and R. Mukhiya, Fabrication, Characterization, and Modeling of an Aluminum Oxide-Gate Ion-Sensitive Field-Efect Transistor-Based pH Sensor, Journal of Electronic Materials 50:7085–7097, 2021
- [13] <https://www.ti.com/lit/gpn/cd4007ub-mil>, “Hojas de especificaciones del circuito integrado CD4007”, 15/abril/2022.
- [14] <https://www.analog.com/en/design-center/design-tools-and-calculators/ltspice-simulator.html>, Sitio web del software LTSpice.
- [15] https://eva.fing.edu.uy/pluginfile.php/216104/mod_page/content/11/4007.mod, Sitio web con modelo spice para el CD4007.
- [16] P. Bergveld, Thirty years of ISFETOLOGY: What happened in the past 30 years and what may happen in the next 30 years, Sensors and Actuators, B 88 (2003), pp. 1–20.
- [17] C. Jimenez, A. Bratov, N. Abramova and A. Baldi, ISFET Based Sensors: Fundamentals and Applications, Encyclopedia of Sensors, Volume X: Pages (1–46), ISBN: 1-58883-056-X.

Agradecimientos

Los autores agradecen el financiamiento brindado por el Consejo Superior de Investigaciones Científicas (CSIC) de España, para la realización de este trabajo a través del Proyecto Intramural Especial (PIE) “Instrumentación avanzada para sensores de estado sólido” (ref. No. 201950E045)

MICROSSISTEMAS ANALÍTICOS INTEGRADOS E LAB-ON-A-CHIP | MICROSSISTEMAS ANALÍTICOS INTEGRADOS Y LAB-ON-A-CHIP | ANALYTICAL INTEGRATED MICROSYSTEMS AND LAB-ON-A-CHIP

O22 |

MICROREACTORS IN PROTEIN PEGYLATION: TOWARDS HIGHER YIELDS AND SPECIFICITY

João H. P. M. Santos^{1,2}, Aline F. Oliveira², Marta L. M. Bejarano², Ariel P. Lima², Mileyde Araújo¹, Adalberto Pessoa Jr¹, Carlota O. Rangel-Yagui¹, Mario R. Gongora-Rubio^{2*}

¹*Department of Biochemical and Pharmaceutical Technology, University of São Paulo, São Paulo 05508-000, Brazil*

²*Bionanomanufacturing Center, Institute for Technological Research (IPT), São Paulo 05508-901, Brazil*

**e-mail: gongoram@ipt.br*

Introduction

Therapeutic biological products based on proteins are of increasing interest in the biopharmaceutical field [1]. This class of drugs is characterized by its high specificity, offering the possibility to treat complex diseases once considered untreatable. Nonetheless, protein drugs are usually associated with low solubility profiles, short shelf-lives, short circulating half-lives and susceptibility to cleavage by proteolytic enzymes. To date, several techniques have been implemented to increase solubility, improve molecular stabilization and enhance protein pharmacokinetics [2-3]. Most of these techniques focus on the bioconjugation of proteins with polymers, such as PEGylation, generating improved drugs, *i.e.* biobetters, which are superior when compared to the original biological [3]. Among the large array of bioconjugation techniques, PEGylation is the most auspicious alternative. This strategy is FDA and EMA approved and it has been used to develop several protein drugs currently on the market [3]. Through careful selection of the reaction chemistry, one or more polyethylene glycol (PEG) molecules can be attached to the proteins, producing PEG–protein conjugated species with one or more grafted polymeric chains. PEGylation of therapeutic proteins is commonly carried using *N*-hydroxylsuccinimide (NHS) functionalized mono-methoxy PEG (mPEG-NHS). NHS esters of the PEG react with *N*-terminal amine groups of the protein at pH 7.0-8.5 to form stable amide bonds (**Figure 1 A**). In PEGylation reaction, parallel reactions between the PEG reactive groups and the protein functional amino acids may occur (*e.g.* alkylation reaction with protein nucleophiles like lysines), resulting in a heterogeneity of various PEGylated protein forms and unmodified protein. In addition, hydrolysis of the reactive PEG is also a major drawback (**Figure 1 B**). The addition of excess amounts of reactive PEG associated with long reaction times are some of the strategies used to minimize the drawbacks of hydrolysis reactions, such as low

yields. However, the high price of the reactive PEG makes its use in excess costly and alternatives must be explored to turn the PEGylation process economically viable. Other challenges that need to be addressed in PEGylation are the development of (i) site-specific PEGylation reactions to avoid the heterogeneity of PEGylated conjugates and (ii) reactions with enhanced yields and shortened times.

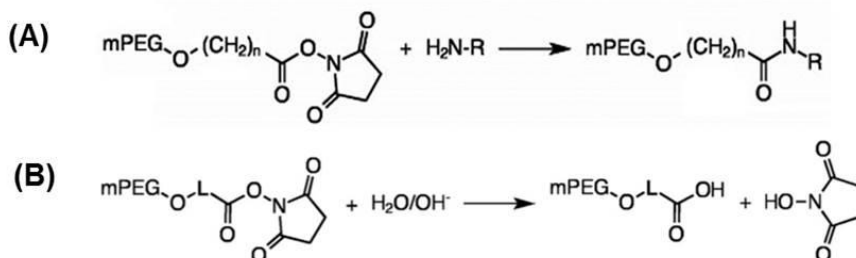


Figure 1. PEGylation reaction of primary amines in proteins, forming an amide linkage, using mPEG-NHS. (A) Hydrolysis reaction of mPEG-NHS (L - spacer group) (B).

In order to overcome those challenges, a new approach to PEGylation using micro-reactors is herein studied. Microfluidic-based systems are widely used for high throughput screening of chemical and biochemical synthesis since parallelization as well as internal and external integrations can be easily implemented for control, detection, and analysis [4]. Micro-reactors and integrated microsystems are used to eliminate some of the major limitations of conventional batch-reactors such as extended time reactions, high consumption of costly reagents, reduced specificity and reproducibility due to poor control on reaction and quenching. Moreover, reaction optimization is straightforward as different sets of reaction conditions can be studied in a short period, expediting the establishment of ideal reaction conditions. One of the novel materials used in microfluidics is LTCC (Low Temperature Co-fired Ceramics) [5], The main advantages of this material are chemical inactivity, chemical resistance, good thermal conductivity, high temperature stability. Moreover, LTCC tapes can easily be cut into the desired geometry to accomplish the mechanical function and tune the desired reaction.

Methods

PEGylation reaction: batch and microfluidic scale

The PEGylation reaction was performed using mPEG-NHS of different molecular weights (MW): 5, 10, 20 and 40 kDa for two model proteins: lysozyme and L-asparaginase. The reactive PEG used promotes an acylation reaction of the amino groups of amino acids with the ester groups of the reactive PEG, resulting in stable amide bonds (**Figure 1A**). The reaction was performed in batch and microfluidics (**Figure 2**) using the following conditions: 100 mM phosphate buffer ($\text{KH}_2\text{PO}_4/\text{K}_2\text{HPO}_4$) at pH 7.5, using a molar excess of reactive PEG of 1:15 and 1:25 for lysozyme and L-asparaginase respectively, at $T = 25 \pm 1$ °C. For batch process, the reaction time was 30 minutes, under stirring at 400 rpm. The PEGylation reaction was optimized in terms of yields and specificity by microfluidics (**Figure 2B**). This technique was used to increase the mass transfer between the solutes and, consequently, the reaction speed.

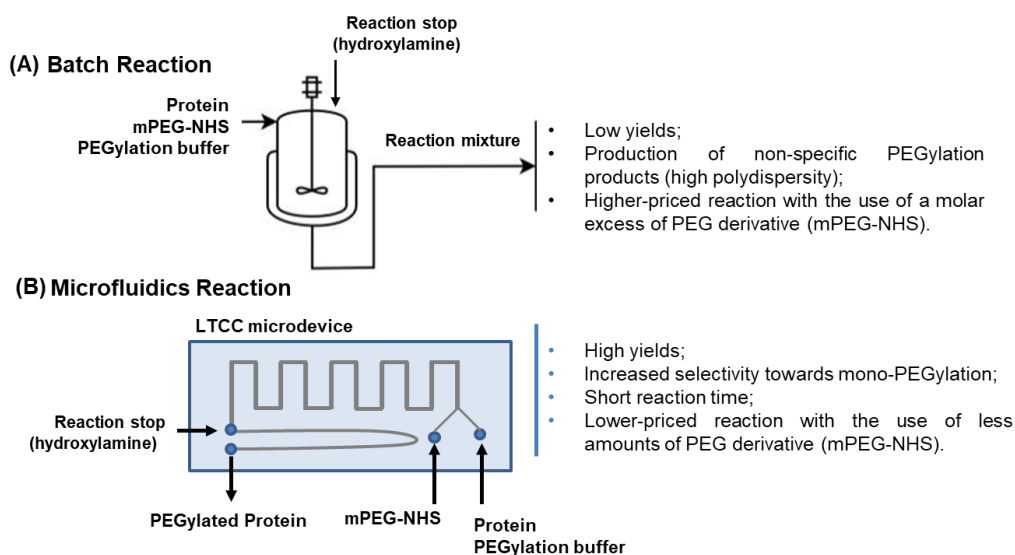


Figure 2. Schematic diagrams for batch protein PEGylation (**A**) and LTCC-based microreactor protein PEGylation (**B**).

In this work, PEGylation reactions were conducted in a microreactor (micromixer) with crossing-channels geometries (**Figure 3**). This type of channel configuration is appropriate for the Reynolds number values handled in LTCC-based microreactor protein PEGylation ($0,5 \leq \text{Re} \leq 20,8$). The microreactors were

manufactured using the LTCC technique, with cross sections of $260 \mu\text{m} \times 260 \mu\text{m}$. The PEGylation reactions were carried out at room temperature by injecting a reactive PEG solution in buffer through one of the microreactor inlets and protein solution through the other inlet, using HPLC pumps. The influence of volumetric flow and residence time distribution (RTD) in the microreactor on the reaction yield and specificity were investigated.

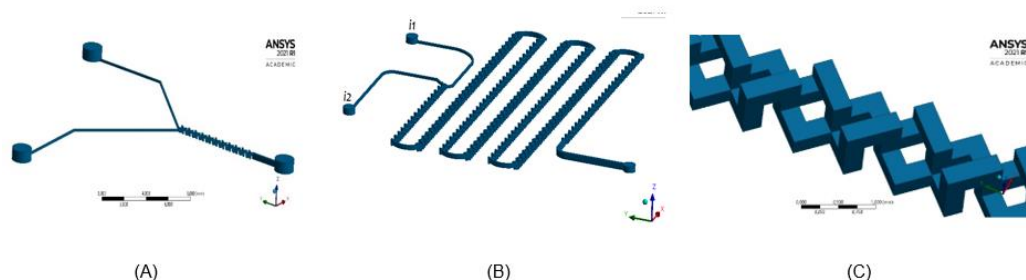


Figure 3. Evaluated LTCC-based microreactor for the protein PEGylation (A e B) and crossing-channels side-view (C).

In order to observe the behavior of the fluids in the tested microdevices, computational simulations are being carried out, applying the Computational Dynamic Fluid (CFD) technique. The flow structure in the micromixers was studied with the CFD code ANSYS Fluent 2021 R1. LTCC-based Microreactors/micromixers performance was evaluated from the results of the CFD study by calculating the mixing (M) and performance (PI) indexes.

$$M = 1 - \sqrt{\frac{\sigma^2}{\sigma_{\text{máx.}}^2}}; \quad \text{PI} = \frac{M}{\Delta P}$$

Results

The batch reactions resulted in yields ranging from $20\% \pm 4\%$ to $52\% \pm 3\%$ for lysozyme and $15\% \pm 2\%$ and $59\% \pm 6\%$ for L-asparaginase. For higher MW PEGs (*i.e.* 20 and 40 kDa), the PEGylation yield greatly reduced due to steric impediment. In terms of reaction specificity, the maximum monoPEGylation yield was obtained for lower MW mPEG-NHS, 5 kDa ($42.3\% \pm 2.1\%$ and 37.07%

$\pm 2.35\%$ for lysozyme and L-asparaginase, respectively). For 40 kDa mPEG-NHS only mono-PEGylation protein was formed but in lower yields.

The microfluidics-based reactions occurred for inlet flow rates of 40.0, 20.0, 10.0, and 6.7 $\mu\text{l}\cdot\text{min}^{-1}$ corresponding to lower reaction times compared to batch reactions (less than 15 min). The yield and specificity of the bioconjugation was greatly improved for both model proteins.

CFD results showed that the crossing-channel micromixer promotes efficiently mixing ($M\approx 1$) of the reactant solutions in the microchannels by splitting and recombination of the fluidic currents, inducing chaotic advection in the microchannels by multilayer lamination, with low values of total pressure drop ($10^{-2} \leq \Delta P \leq 10^{-3}$ bar).

The microchannels with a hydraulic diameter (D_h) of 260 μm gave the highest performance index (PI) values, for all the flow rates evaluated, showing that the crossing-channel micromixer geometry with these dimensions is the best option to promote mixing in the adopted Reynolds number range ($0.5 \leq Re \leq 20.8$), under the conditions studied in the protein PEGylation reaction.

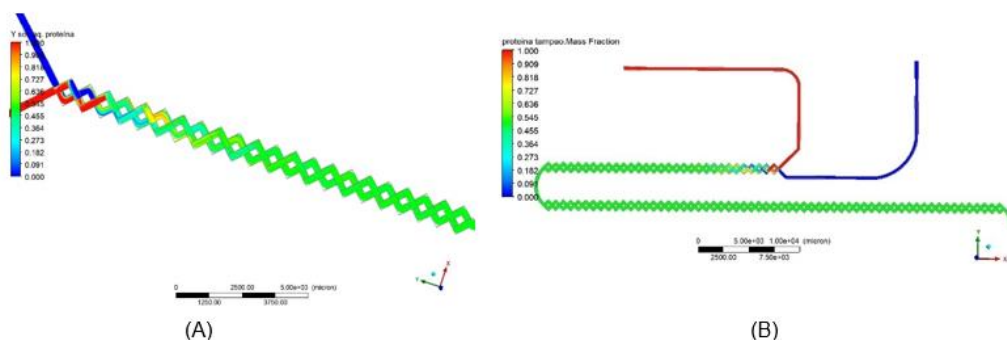


Figure 4. Streamlines colored by protein mass fraction. CFD results of LTCC-based Crossing-channels microreactor with 22 (A) e 382 (B) sections.

The adjustment of the microreactor volume, increasing the number of sections from 22 (Figure 4A) to 382 (Figure 4B), allowed longer residence times of the reagents inside the microreactor and more contact between the reactive PEG and the protein molecules, favoring the increase of the reaction yield with residence times up to 8 min.

Conclusions

Continuous flow microreactors offer precise control on the residence time, *i.e.*, give narrow residence time distribution (RTD), which makes them highly suitable for rapid and residence time sensitive reactions. Through microfluidics, the PEGylation reaction yield increased significantly, alongside with the selectivity of mono-PEGylation. The integration of the PEGylation reaction and monoPEGylated purification in microreactors with 3D surfaces effects to promote the mixture is worth investigating in the future.

References

- [1] Carter, P. H., Berndt, *et al.* *Nat. Rev. Drug Discov.* 15, 673–674 (2016)
- [2] Veronese, F. M. *Biomaterials* 22, 405–417 (2001)
- [3] Ginn, C., *et al.* *Future Med. Chem.* 6, 1829–46 (2014)
- [4] Madadkar, P., *et al.* *Biomicrofluidics* 12, 044114 (2018)
- [5] Gomez, H. C., Cardoso, R. M., Schianti, J. de N., de Oliveira, A. M., & Gongora-Rubio, M. R. (2018). *Micromachines*, 9(6). <https://doi.org/10.3390/mi9060285>

Acknowledgments

The authors are grateful for the financial support of the São Paulo Research Foundation-FAPESP (grants # 2018/25994-2, 2016/22065-5 and 2013/08617-7), the National Council for scientific and Technological Development-CNPq, the Coordination of Improvement of Higher Level Personnel CAPES (Project # 001), and IPT (Institute for Technological Research) for the J.H.P.M. Santos visiting researcher contract.

The authors would also like to express their gratitude to the FAPESP-PDIP projects (Process 2017 / 50343-2) and FINEP CTInfra (Agreement 01.18.0082.00) for the financial support for the acquisition of hardware and licenses of the ANSYS-CFD software, used in the computational simulations.

O23 |

FUNCTIONALIZATION OF A FULLY INTEGRATED ELECTROPHOTONIC SILICON CIRCUIT FOR SENSING BIOMOLECULES

O. Pérez-Díaz¹, A. A. González-Fernández^{1,2}, C. Domínguez-Horna¹,
J. M. Pedraza-Chávez¹ and M. Aceves-Mijares^{1*}

¹ National Institute for Astrophysics, Optics and Electronics (INAOE), Department of Electronics, P.O. Box 51, Puebla 72000, Mexico.

² Instituto de Microelectrónica de Barcelona (IMB-CNM, CSIC), Universitat Autònoma de Barcelona, 08193 Bellaterra, Spain.

*e-mail: maceves@ieee.org

Introduction

The development of the LAB-ON-A-CHIP (LoC) has produced a high social impact since it can be used for applications such as environmental sensing [1, 2] or medical diagnostics [3, 4, 5]. However, up to now, most of the research efforts require an external light source [6, 7] presenting alignment problems and making the systems incompatible with CMOS technology. The development of silicon-based photonic components, including light sources [8], using CMOS technology has allows the possibility to exploit the advantages of Si microelectronics coupled to optics. In the past, we have presented a fully integrated silicon-based electrophotonic circuit fabricated using CMOS technology. The device consists of a silicon based light emitting capacitor (LEC), a waveguide with silicon nitride core and silicon dioxide cladding, and a silicon photodiode, all monolithically integrated in a silicon substrate [9]. When the LEC is activated, the produced light is directly injected into the waveguide, and part of the electromagnetic field (the so called evanescent field) propagates through the cladding. To make the system a sensor, a cavity for an analyte can be created etching the upper cladding. The interaction between the substance and the evanescent field results in changes of light intensities reaching the photodiode, which in turn depend on the characteristics of the analyte. The ability to sense liquids with different refractive index using this scheme has already been proven in [10]. Considering such background, this idea has the potential to be extended to sense specific biomolecules trough the functionalization of the waveguide for their attachment, which will result in modifications to the transmission of the light if the target biomolecules are present in the analyte. In the present work, a method for the functionalization of the nitride waveguide core device is proposed. After the process, the device was tested using Biotin, concluding that the system and the

functionalization method are suited for their future application in more complex LoC systems.

Methods

To functionalize the silicon nitride waveguide surface, (3-Aminopropyl) triethoxysilane (APTES $\geq 98\%$) and Glutaraldehyde (GTA = 25 %) were used [11]. The methodology consisted in the immersion of the sample in a 2% APTES solution in ethanol, volume proportion 1:49, for 3 hrs. Then, the chip was rinsed in ethanol and cured at 110°C for 10 min. For the GTA deposition, the chip was immersed in a 2% GTA solution in phosphate buffered saline (PBS), volume proportion 4:46, for 2 hrs, after this time the chip was rinsed with PBS and dried with N₂. It is worth of notice that APTES and GTA were deposited under N₂ atmosphere at room temperature.

For the biomolecule sensing, Biotin at 4mM was deposited on the functionalized silicon nitride waveguide surface for 2 hrs at room temperature, after that, the chip was rinsed with PBS [12]. The chip was characterized by optical microscopy and atomic force microscopy (AFM). The photodiode's response was measured when the waveguide was functionalized and when the Biotin was deposited.

Results

Figure 1a presents the chip after the functionalization process. The red circle corresponds to the zone where the APTES-GTA was deposited.

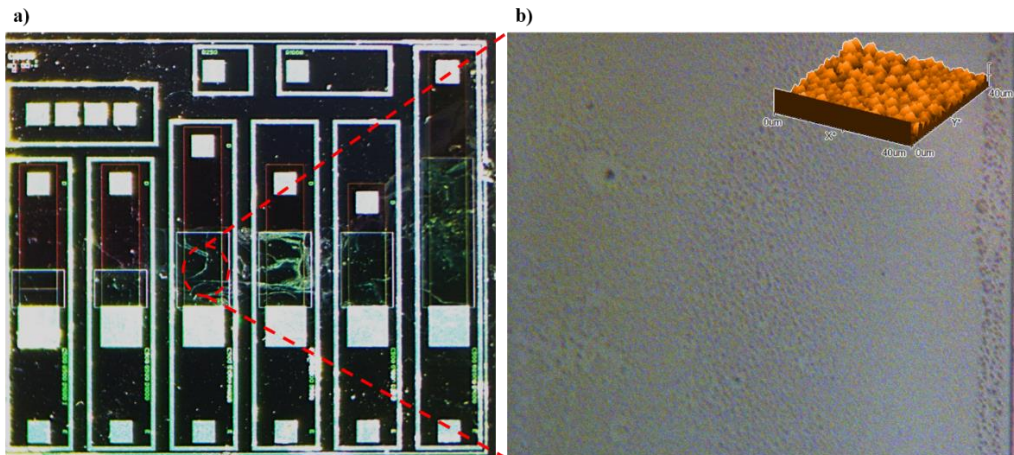


Figure 1. a) Chip after the functionalization process and b) zoom view of the waveguide surface cover with APTES-GTA, Insert: AFM image of the APTES-GTA.

Figure 1b shows a zoom to the waveguide surface. It can be seen that the surface is fully covered with particles. This can be better observed in the Figure's insert, where an AFM image is presented. These results agree with the ones reported in [13]. This methodology was applied in several chips obtaining the same result, demonstrating the reproducibility of the process.

Figure 2a shows the photocurrent detected by the photodiode when the LEC is on and the device is functionalized, but no Biotin has been captured. As expected, the photocurrent depends on the applied voltage in the photodiode (V_{pn}) and the LEC voltage. Figure 2b) presents the photocurrent after the Biotin deposition. There is a significant photocurrent increase. The values are five times higher as compared to the just functionalized chip. This can be associated to the interaction between the evanescent field and the Biotin. The AFM tests (insert image) confirm such effect, as they show the change of the functionalized surface due to the Biotin presence. Several Biotin test were performed, obtaining similar behavior in all cases. These results indicate that the electrophotonic circuit developed by our group is capable of detecting the presence of biomolecules if the waveguide cores are adequately processed.

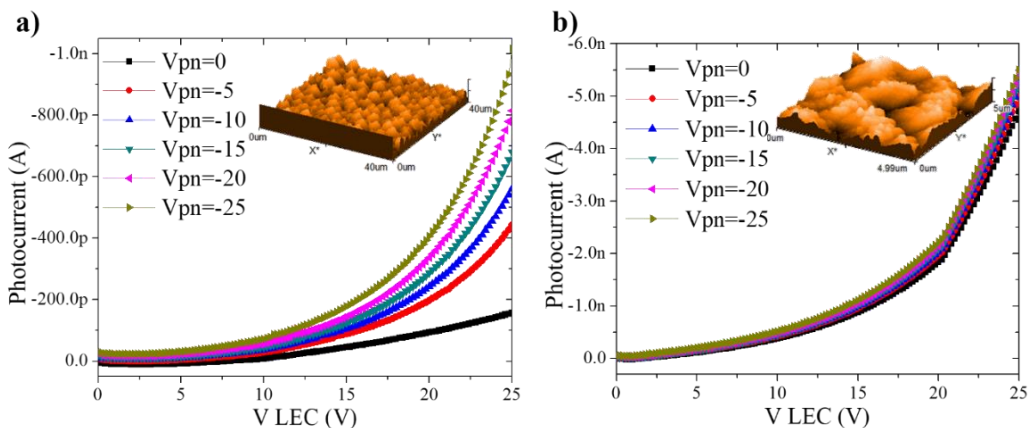


Figure 2. a) Measured photocurrent when the waveguide is functionalized, the insert shows the surface with the APTES-GTA and b) measured photocurrent when the Biotin is on the waveguide.

Conclusion

A methodology to functionalize the surface of a silicon nitride waveguide was presented, numerous experiments showed that the methodology is reproducible. The electrophotonic circuit showed an increment in photocurrent that can be

associated to the interaction of the evanescent field with the Biotin molecules. Several chips were tested obtaining similar results, confirming the electrophotonic circuit is capable of sensing biomolecules. The advantage of our system is its full integration in silicon, that is the light source is included in the chip, and its compatibility with CMOS technology.

References

- [1] Y. Shi, H. L. Liu, X. Q. Zhu, J. M. Zhu, Y. F. Zuo, Y. Yang, F. H. Jiang, C. J. Sun, W. H. Zhao and X. T. Hand, *Lab Chip*, vol. 18, pp. 2994-3002, 2018.
- [2] M. Alidoust, M. Baharfar, M. Manouchehri, Y. Yamini, M. Tajik and S. Seidi, *Trends in Analytical Chemistry*, vol. 143, p. 116352, 2021.
- [3] P. V. Lode, *Clinical Biochemistry*, vol. 38, p. 591 – 606, 2005.
- [4] S. Su, M. Monsur Ali, C. D. M. Filipe, Y. Li and R. Pelton, *Biomacromolecules*, vol. 9, p. 935-941, 2008.
- [5] J. V. Jokerst, J. W. Jacobson, B. D. Bhagwandin, P. N. Floriano, N. Christodoulides and J. T. McDevitt, *Anal. Chem.*, vol. 82, p. 1571-1579, 2010.
- [6] J. J. Colás, A. Parkin, K. E. Dunn, M. G. Scullion, T. F. Krauss and S. D. Johnson, *Nat. Commun.*, vol. 7, p. 12769, 2016.
- [7] Q. Xiong, C. Y. Lim, J. Ren, J. Zhou, K. Pu, M. B. Chan-Park, H. Mao, Y. L. Lam and H. Duan, *Nat. Commun.*, vol. 9, p. 1743, 2018.
- [8] J. Alarcón-Salazar, L. Palacios-Huerta, A. A. González-Fernández, A. Morales-Sánchez and M. Aceves-Mijares, London, Intechopen, 2018, pp. 9-26.
- [9] A. A. Gonzalez-Fernandez, J. Juvert, M. Aceves-Mijares and C. Dominguez, *IEEE Photonics Journal*, vol. 8, pp. 1-13, 2016.
- [10] A. A. González-González-Fernández, W. W. Hernández-Montero, J. Hernández-Betanzos, C. Domínguez and M. Aceves-Mijares, *AIP Advances*, vol. 9, p. 125215, 2019.
- [11] J. Diao, D. Ren, J. R. Engstrom and K. H. Lee, *Anal. Biochem.*, vol. 343, pp. 322-328, 2005.
- [12] S. N. Aisyiyah Jenie, Z. Du, S. J. P. McInnes, P. Ung, B. Graham, S. E. Plush and N. H. Voelcker, *J. Mater. Chem. B*, vol. 2, p. 7694-7703, 2014.
- [13] T. D. To, A. T. Nguyen, K. N. T. Phan, A. T. T. Truong, T. C. D. Doan and C. M. Dang, *Adv. Nat. Sci.: Nanosci. Nanotechnol.*, vol. 6, p. 045006, 2015.

Acknowledgments

The authors want to thank to Conacyt for the financial support to develop the present work and to Dr. Rubén Ramos García and Dra. Teresita Spezia Mazzocco for facilitating the Biotin, Dr. Mario Moreno for allow the use of the microelectronic lab during the pandemic. We also appreciate the help of Leticia Tecuapetla for the AFM images.

P27 |

MICROANALIZADORES AUTOMÁTICOS MODULARES PARA LA MONITORIZACIÓN DE METALES PESADOS EN PROCESOS HIDROMETALURGICOS

Pedro Couceiro ¹, Karla Victoria Guevara Amatón ², Hesner Coto Fuentes ², V. E. Manqueros Aviles ², Francisco Valdés Perezgasga ² and Julián Alonso-Chamarro ¹ *

¹Grupo de Sensores y Biosensores, Departamento de Química, Universidad Autónoma de Barcelona

²Instituto Tecnológico de la Laguna, México, Cuauhtémoc y Revolución s/n, 27000 Torreón Coahuila, México

*e-mail: Julian.Alonso@uab.es

Introducción

El control de los procesos de producción industrial, y en concreto los relacionados con la hidrometalurgia, requiere de sistemas analíticos capaces de suministrar información que permitan seguir su evolución en función del tiempo. Dicha información ayuda a optimizar los procesos e implementar medidas correctoras en tiempo real si así fuera necesario. Para simplificar la obtención de dicha información y minimizar su coste, el presente trabajo tiene como objetivo el desarrollo de microanalizadores químicos de bajo coste de fabricación, operación y mantenimiento capaces de monitorizar, de forma automática, autónoma y continua, diferentes procesos industriales relacionados con la minería y la metalurgia.

La utilización de una estrategia de integración modular de elementos da versatilidad al proceso de construcción del microanalizador y permite modificar con sencillez su configuración para adaptarla a las singularidades de los diferentes procesos industriales que se deseen monitorizar.

Las tecnologías de microfabricación multicapa elegidas abren la posibilidad obtener prototipos de forma simple y rápida, a bajo coste. Permite además introducir con facilidad modificaciones en el diseño de las plataformas de microfluídica, estructura base de los microanalizadores, para adaptarlas a cada proceso y aplicación concreta. Adicionalmente, el diseño de los microanalizadores y sus actuadores asociados (válvulas, bombas, etc.) hacen posible, vía la electrónica de control y el software desarrollado, reconfigurar automáticamente los parámetros operacionales del microanalizador. De este modo dichos parámetros pueden adaptarse, sin modificación de hardware, a las necesidades de la metodología analítica que se pretende implementar en cada situación.

Como primera aproximación experimental a la propuesta conceptual se ha desarrollado un microanalizador automático de Cu(II) para monitorizar este elemento en diferentes procesos hidrometalúrgicos. La configuración inicial del microanalizador se diseñó para monitorizar el impacto ambiental de procesos de lixiviación acida [1] (MFIACu V1). Posteriormente, el microanalizador se reconfiguro para adaptarlo a la monitorización de cobre y otros metales, en diferentes etapas del proceso de refinación hidrometalúrgica en una fundidora de Zinc.

Métodos

Los microanalizadores están integrados por siete módulos independientes. Todos los reactivos empleados en este trabajo fueron de grado analítico. El Na_2HPO_4 , NaH_2PO_4 , HNO_3 y la disolución stock de cobre para ICP se adquirieron de Sigma-Aldrich. La sal disódica del ácido 3-hidroxi-4-nitroso-2,7-naftalenodisulfónico (NRS) se adquirió de Fluka. Las soluciones de trabajo de Cu (II) (10 mg/l), tampón de fosfato (pH ajustado a 6,6), reactivo NRS y HNO_3 (0,1 M) se prepararon en agua MilliQ y se desgasificaron antes de su uso. El módulo de microfluídica se construyó utilizando copolímero de olefina cíclica (COC) (TOPAS). El módulo de detección óptica miniaturizado estaba compuesto por un lector óptico compacto fabricado en polimetilmetacrilato (PMMA) (Ferplast), con alojamiento integrado para un LED de 505 nm (Roithner Lasertechnik B5B-433-B505), y un fotodiodo (Hamamatsu S1337-66BR). El módulo de fluídico se ensambló utilizando microválvulas solenoides de tres vías (NResearch 161T031), una bomba peristáltica (Gilson Minipuls 3), tubos de tygon (d.i 1.2 mm) y PTFE (d.i. 0,8 mm, Tecnyfluor). El módulo de control electrónico se construyó sobre una placa de circuito impreso diseñada internamente y construida en otro lugar (Shenzhen JLC Electronics Ltd.). El módulo de control electrónico es un chip PSoC 5 CY8C5868AXI-LP035 (Cypress Semiconductor). El módulo software ha sido desarrollado utilizando el lenguaje de programación C. Los módulos del microanalizador se ensamblaron en un gabinete inalámbrico industrial (Banner BWA-EF14128).

Resultados

Como se puede ver en la Fig.1, podemos encontrar un amplio rango de concentraciones de metales a lo largo del proceso de refinación hidrometalúrgica de Zn. A partir del prototipo MFIACu V1 que con un camino óptico de 1 mm, esta optimizado para monitorización de Cu(II) en el rango de 0.5-10 mg/L, se tendrán que proceder a modificaciones que permitan obtener microanalizadores que operativamente cubran todo el rango de concentraciones de cobre requerido.

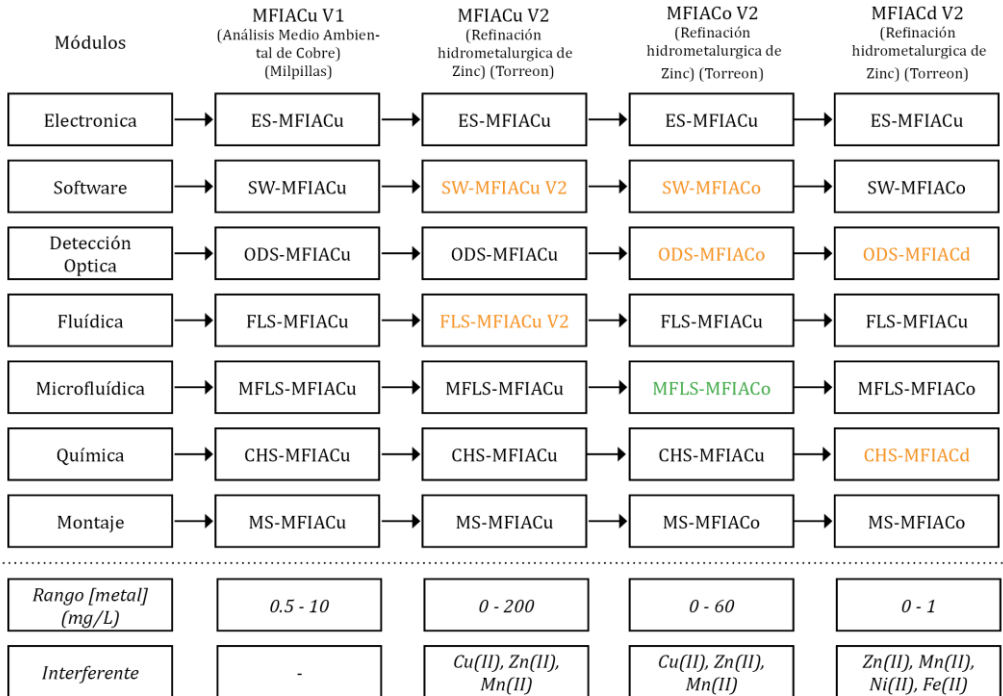


Fig. 1 Descripción esquemática de los módulos de microanalizador para Cu(II) (MFIACu), Co(II) (MFIACo) y Cd(II) (MFIACd), en función de su aplicación. En negro, módulos que no necesitan adaptación; en naranja, módulos que necesitan adaptación y en verde los que exigen un rediseño completo.

Para cubrir el rango alto de concentraciones (10-200 mg/L) de este metal podemos diluir automáticamente la muestra utilizando las microválvulas solenoide del Módulo Fluídico. Rediseñando el Módulo Software que controla las microválvulas podemos adaptar la operativa del microanalizador al nuevo rango. Para el rango de concentraciones bajas (0-1 mg/L), se han construido Módulos Microfluídicos específicos con mayor camino óptico lo que permite aumentar la sensibilidad del microanalizador. Teniendo en cuenta la composición de las muestras en estas etapas del proceso, también se han diseñado módulos microfluídicos que incorporan microcolumnas de intercambio iónico para eliminar las interferencias de Zn(II) y Mn(II) que se encuentran a alta concentración en la muestra (15 g/L y 4 g/L, respectivamente). Para la determinación de Cu(II) y Co(II) se usa el mismo reactivo colorimétrico (NRS). La diferenciación entre ambos metales se consigue utilizando diferentes

longitudes de onda de trabajo para monitorizar cada uno de ellos. Para la determinación de Cd(II), el módulo químico se ha rediseñado teniendo en cuenta las características específicas del reactivo colorimétrico seleccionado (Cadion). Los datos experimentales obtenidos con el MFIACu V1, optimizado para la monitorización medioambiental de Cu(II) y el MFIACu V2, optimizado para la monitorización de Cu(II) de la etapa de descubrido del proceso de refinación hidrometalúrgica de Zn, se muestran en la Fig. 2 como ejemplo de la potencialidad de los Microanalizadores modulares. Las modificaciones del Módulo Software del MFIACu V2 ha permitido introducir una dilución de muestra, necesaria para que la concentración de esta se ajuste al rango de trabajo del Microanalizador. Además, modificaciones en la programación del Módulo Software permiten definir el procedimiento de calibración utilizado. En el caso del MFIACu V1 se ha utilizado la interpolación sobre recta de calibración y para el MFIACu V2, debido a la mayor complejidad de la matriz de la muestra, se ha implementado el método de adición estándar.

Conclusiones

El diseño y fabricación de microanalizadores utilizando una estrategia de integración modular de elementos permiten una fácil adecuación operacional de los dispositivos a los condicionantes de cada etapa del proceso y/o aplicación en estudio. Dada la singularidad, tanto de los procesos a monitorizar como de la composición de las muestras implicadas, las tecnologías de fabricación elegidas permiten un prototipado rápido a bajo coste de pequeñas series de instrumentos versátiles, automáticos, autónomos y de reducido tamaño y consumo de reactivos y energía.

Referencias

- [1] doi:10.3390/s19153382
- [2] doi: 10.1016/S0003-2670(98)00658-8

Agradecimientos

Los autores agradecen el soporte financiero de Metalúrgica Met-Mex Peñoles S.A. de C.V. y del Ministerio de Ciencia e Innovación a través proyecto PID2020-117216RB-100

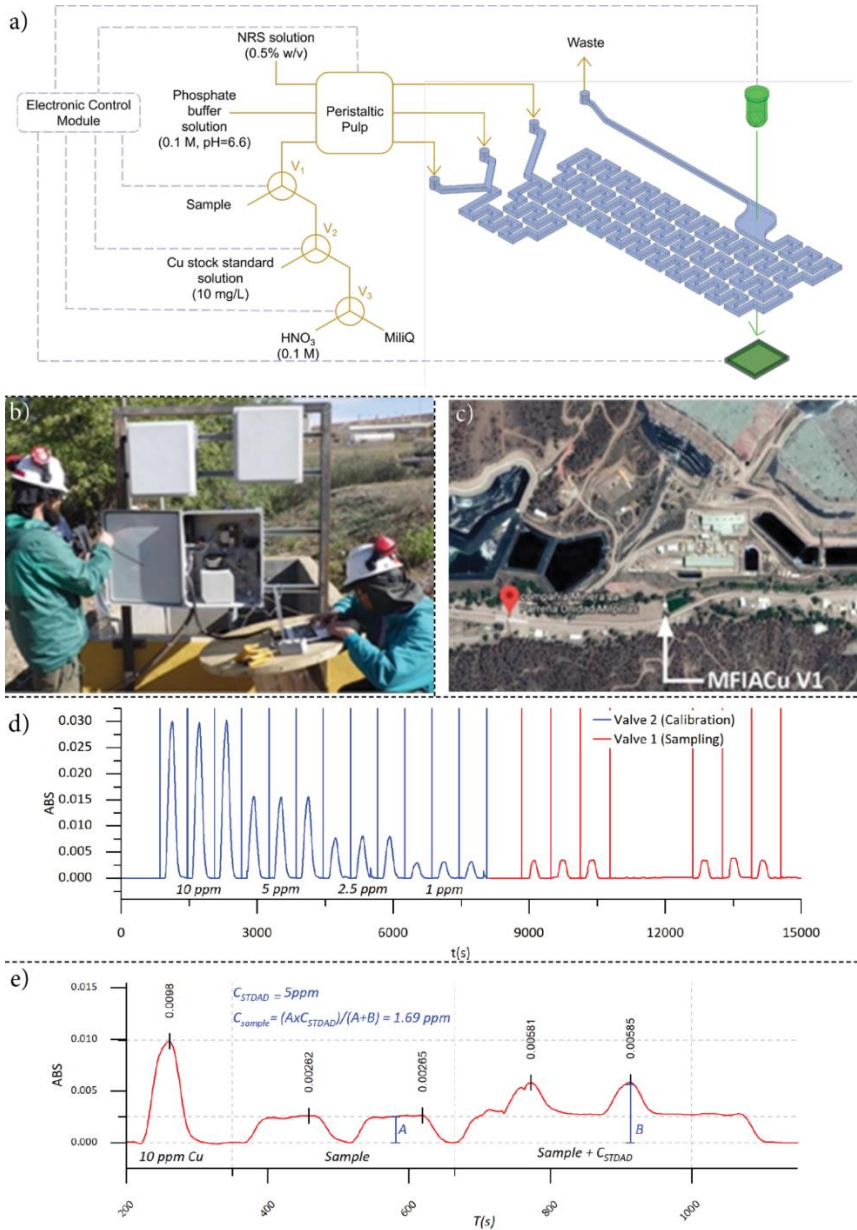


Fig 2 a) Representación esquemática del microanalizador. b) Fotografía del MFIACu V1 instalado en campo. c) Ubicación de equipo en la explotación minera. d) Registro de la cuantificación de Cu (II), con recta de calibración utilizando el MFIACu V1 optimizado para análisis medioambiental, e) Registro de cuantificación de Cu(II), utilizando el método de adición estándar [2], utilizando el MFIACu V2 en una muestra de la etapa de descobrizado del proceso de refinación hidrometalúrgica de Zn.

P28 |

OPTIMIZACIÓN DEL SISTEMA ANALÍTICO INTEGRADO PARA EL MONITOREO DE IÓN COBRE EN EFLUENTES DE UNA MINA

K. V. Guevara Amató¹, F. Valdés P. ¹, H. Coto F², J. Alonso-Chamarro³, P. Couceiro.³

¹ TecNM/Instituto Tecnológico de la Laguna, Blvr. Revolución s/n, CP27000 Torreón, Coahuila, México

²TecNM/Instituto Tecnológico Superior de Lerdo, Av. Tecnológico 1555, CP35150, Lerdo, Durango, México

³Grupo de Sensores y Biosensores, Departamento de Química, Universidad Autónoma de Barcelona, Bellaterra, Barcelona, España

kvguevara@correo.itlalaguna.edu.mx

Introducción

El establecimiento de metodologías analíticas para la determinación de Cu (II) en soluciones acuosas en procesos industriales y ambientales es un tema muy importante debido a la toxicidad del metal y a su constante presencia en el medioambiente. Las técnicas por excelencia para la determinación rutinaria de concentraciones de Cu (II), están basadas en Absorción Atómica o Espectrometría de Masa inducido con plasma (ICP). Sin embargo, la utilización de estas técnicas está restringido a laboratorios centralizados por su alto costo y limitada portabilidad. Una alternativa es la utilización de microanalizadores de flujo continuo que incorporan sistemas de detección colorimétrica. Estos microanalizadores permiten el monitoreo de parámetros medioambientales en tiempo real, de forma automática y autónoma [1],[2].

Para monitorizar la concentración de Cu (II) presente en el agua de descarga de la mina La Parreña, propiedad del grupo Met – Mex Peñoles, vertida al arroyo Milpillas en Sonora, México, se desarrolló e instaló un microanalizador de flujo continuo de Cu (II) (MFIACu) que opera a bajo costo de mantenimiento. El MFIACu tiene como finalidad asegurar que el efluente cumpla con los niveles establecidos de Cu (II) por la Legislación Ambiental Mexicana [3].

La primera versión del MFIACu (MFIACuV1) se instaló en la mina La Parreña en el año 2018. Debido a la lejana ubicación de la mina y el clima de inseguridad en la zona, las asesorías y las revisiones presenciales se complican, por lo que la optimización del microanalizador en funcionamiento se realizan de manera gradual. En este trabajo se presentan optimizaciones del MFIACuV1, realizadas a forma de solucionar problemas encontrados in-situ, aumentar la robustez y autonomía del microanalizador.

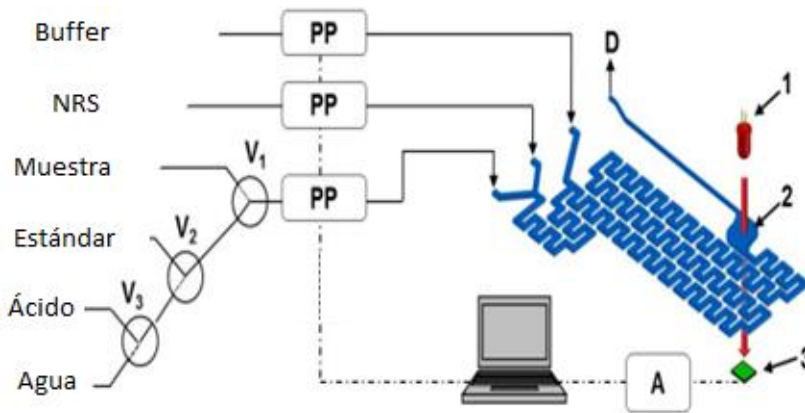


Figura 1. Diagrama esquemático del MFIACu. PP: bomba peristáltica; V: válvulas de 3 vías; A: Microanalizador; D: desecho; ----conexiones eléctricas; conexiones fluídicas; 1: LED 505 nm; 2 Cámara de detección; 3: Fotodetector

Metodología

El microanalizador de flujo continuo de Cu (II) (MFIACu) está constituido por siete módulos independientes. En el módulo de química, todos los reactivos empleados en este trabajo fueron de grado analítico. El fosfato de di sodio (Na_2HPO_4), fosfato monosódico (NaH_2PO_4), ácido nítrico (HNO_3) y la disolución stock de cobre para ICP se adquirieron de Sigma-Aldrich. La sal disódica del ácido 3-hidroxi-4-nitroso-2,7-naftalenodisulfónico (NRS) se adquirió de Fluka. Las soluciones de trabajo de Cu (II) (10 mg/l), solución amortiguadora de fosfatos (pH ajustado a 6.6), reactivo NRS y HNO_3 (0.1 M) se prepararon en agua MilliQ y se desgasificaron antes de su uso. El módulo de microfluídica se construyó utilizando copolímero de olefina cíclica (COC) (TOPAS) [4]. El módulo de detección óptica miniaturizado estaba compuesto por un lector óptico compacto fabricado en polimetilmetacrilato (PMMA) (Ferplast), con alojamiento integrado para un LED de 505 nm (Roithner Lasertechnik B5B-433-B505), y un fotodiodo (Hamamatsu S1337-66BR). El módulo de fluídico se ensambló utilizando microválvulas solenoides de tres vías (NResearch 161T031), una bomba peristáltica (Gilson Minipuls 3), tubos de tygon (d.i 1.2 mm) y PTFE (d.i. 0,8 mm, Tecnyflour). El módulo de control electrónico es sistema modular construido sobre una placa de circuito impreso diseñada internamente y construida en otro lugar (Shenzhen JLC Electronics Ltd.), este módulo tiene integrado un microcontrolador PSoC CY8C5868AXI-LP035 (Cypress Semiconductor). El módulo del software fue desarrollado utilizando el lenguaje de programación C.

Los módulos del microanalizador se ensamblaron en un gabinete inalámbrico industrial (Banner BWA-EF14128).

Resultados

Con las modificaciones introducidas se pretende mejorar el funcionamiento del MFIACu y aumentar su autonomía. Para lograrlo se realizaron algunos ajustes, entre los que destacan el cambio en la fluídica, el procedimiento de preparación de los reactivos, y cambio en el sistema de comunicación entre el microanalizador y el centro de comunicación de la mina. En la Tabla 1 se presenta el resumen de las modificaciones implementadas.

Tabla 1. Resumen de las modificaciones implementadas en el MFIACu.

Modulo	Variable	MFIACuV1	MFIACuV2
Electrónica	Tarjeta		
	Comunicación	Tiempo, ABS.	Tiempo, $V_{\text{Fotodiodo}}$, ABS, [Cu (II)], Temperatura.
Química	Biocida	x	2-Cloroacetamida
Fluídica	Inyección de la muestra (s)	160	160
	Limpieza de muestra (s)	440	250
	Tiempo de análisis de muestra (s)	600	410
	Autonomía (1 galón de cada reactivo)	8	10

A partir de la experimentación desarrollada con la primera versión de la tarjeta de control electrónico, se procedió al rediseño de esta, con el objetivo fundamental de ampliar las prestaciones del sistema y el número de recursos del microcontrolador PSoC. La tarjeta principal rediseñada incluye una fuente de tensión 0 – 5 V opto acoplada, adicionada para el control de dispositivos como la bomba peristáltica y válvulas.

Para la comunicación de los datos del MFIACu con el centro de comunicación de la mina se utiliza transmisión vía radio. Inicialmente, se disponía de un radio de 2 canales, que permitía la monitorización en tiempo real del proceso analítico, por

registro del Tiempo y ABS. Sin embargo, la comunicación de la concentración de Cu (II) al centro de comunicación de la mina se hacía después del procesamiento de la señal obtenida. La sustitución de un radio de 2 por uno de 4 canales permitió aumentar el número de variables transmitidas, eliminado así el procesamiento de la señal y permitiendo al centro de comunicación de la mina obtener la concentración de Cu (II), de forma continua, en tiempo real.

En el MFIACuV1, se utilizaron filtros inline, con poro de 5 μm , para eliminar problemas relacionado con el crecimiento de biomasa en el interior de los sistemas fluidicos. Sin embargo, estos filtros presentan un volumen muerto significativo comparado con el volumen total del MFIACu, originando un aumento del volumen de reactivo necesario para cada análisis. Para eliminar la utilización de filtros inline, se introdujo un biocida en la preparación del reactivo colorimétrico (NRS) y de la solución amortiguadora en el MFIACuV2. La consecuente optimización de los parámetros hidrodinámicos del MFIACu ha permitido aumentar de 8 a 10 días la autonomía del microanalizador.

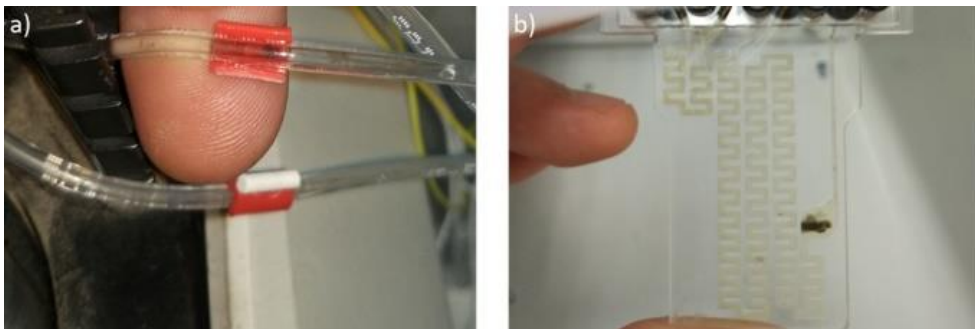


Figura 2. Creciente de biomasa en los sistemas fluidicos del MFIACu.

Conclusiones

De las metodologías analizadas para la determinación del Cu (II), se logró establecer una adaptación para realizarla de forma continua, directamente de un efluente de mina de cobre, esta adaptación de la muestra, se lleva a cabo por la mezcla de los reactivos, solución amortiguadora de fosfatos 0.1 M, reactivo colorimétrico NRS 1.06 mM, obteniendo un pH neutro que permite realizar lecturas espectrofotométricas a una longitud a 505 nm.

El problema relacionado con el crecimiento de biomasa, se resolvió adicionando biocida, 2-cloroacetamida en la preparación la solución amortiguadora y el reactivo colorimétrico NRS, con esto se remplazaron los filtros en los canales de los reactivos, el uso del biocida permitió reducir los tiempos de limpieza y de

inyección total, respectivamente, permitiendo aumentar la autonomía del MFIA_{Cu} de 8 para 10 días.

Fue posible aumentar la infraestructura de comunicación en la Mina La Parreña, utilizando las potencialidades de procesamiento de señal del microanalizador, actualmente se transmiten 4 señales: Absorbancia, Concentración de Cu(II), Temperatura ambiente y Tensión, contra los dos únicos datos registrados (Tiempo vs ABS), el rediseño de la tarjeta principal permitió el desarrollo una secuencia de programación que se repiten cada 24 horas, obteniendo una calibración diaria del sistema y la determinación de la concentración de Cu(II) en muestras reales en promedio por hora, por lo que actualmente es utilizado con un mayor potencial.

Referencias

- [1] A. Manz, N. Graber, and H. M. Widmer, "Miniaturized total chemical analysis systems: A novel concept for chemical sensing," *Sensors Actuators B Chem.*, vol. 1, no. 1–6, pp. 244–248, Jan. 1990.
- [2] M. Sequeira, "Towards autonomous environmental monitoring systems," *Talanta*, vol. 56, no. 2, pp. 355–363, 2002.
- [3] Semarnat, "Nom-001-Ecol-1996," 2016.
- [4] O. Ymbern, N. Sáñez, A. Calvo-López, M. Puyol, and J. Alonso-Chamarro, "Gas diffusion as a new fluidic unit operation for centrifugal microfluidic platforms," *Lab Chip*, vol. 14, no. 5, p. 1014, 2014.

P29 |

DEVELOPMENT OF A MICROSWITCH MADE IN LTCC-PDMS TECHNOLOGY APPLICABLE TO MICRO TOTAL ANALYSIS SYSTEMS

T. S. Rosa¹, A. C. Seabra¹

¹ Polytechnic School, University of São Paulo, Sao Paulo 05508010, Brazil

*e-mail: ticianerosa@usp.br

Introduction

Since microfluidic devices perform several processes for distinct applications, it is crucial that the design of each component bears in mind the overall performance after the system integration. As an example, specific flow rate ranges considering chemical analyzers for distinct applications are normally restricted to measurement conditions [1], which can be attained by projecting microchannel size. Despite the comprehensiveness and acceptance of micro total analysis systems (μ TAS) and lab-on-a-chip (LOC) devices, no standard microfluidic basic components are found in literature [2,3], as it is the case of transistors for integrated circuit industry. Besides the fact that glass, polymers and silicon are the materials commonly used for conventional microfabrication technologies in order to have a full microanalyzer on a chip, Low Temperature Co-Fired Ceramic (LTCC) can be used to develop miniaturized and chemical compatible devices with fast prototyping methodology [4]. In this paper, a microswitch is proposed, designed applying analytical methods, and fabricated employing LTCC-PDMS technology.

Physical design and implementation of an LTCC on-off microswitch device is demonstrated. One model was used to describe microchannel fluidic behavior, especially those with rectangular cross-section, routinely used in microfluidic devices. Another model to describe PDMS microbridge deformation was applied, allowing to estimate the elastic stiffness of several manufactured membranes. From this approach, the microswitch design was conducted regarding the simulation results associated with both models, aiming miniaturization. Applying LTCC-PDMS fabrication methodology, the fluidic devices were manufactured as established by theoretical design and an experimental setup was proposed in order to evaluate system performance.

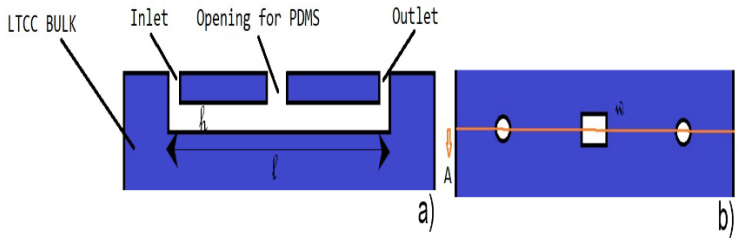


Fig. 1 (a) Top view of the proposed LTCC microfluidic switch module and (b) its respective cross-section. Channel dimensions l , h e w are indicated on the figure.

Methods

In order to develop a functional microvalve, it is necessary to integrate an actuation system to a microfluidic switch. Though in literature several actuation methods were implemented for systems developed in micrometric scale, meeting specific application requirements is a challenge, since each method has its limitations. Besides that, the mechanical structure responsible to perform system actuation have significant influence on microswitch performance, and the theoretical analysis applied in this work will assist the design of the whole device. Figure 1 presents a scheme of LTCC microswitch structure, showing its two fluidic ports and the fluidic opening that gives place for PDMS membrane actuation. The microswitch was designed to work as a pressure-driven microsystem, where fluidic flow can be restricted by the actuation of a membrane plunger placed inside the microchannel, amid inlet and outlet ports. The fluidic model is used in order to assure that required flow rates can be achieved with the membrane in open state, and the mechanical model is used to analyze the fluidic force required to deflect the membrane in order to close fluid flow. Thereunto, microchannel hydraulic resistance is applied theoretically considering circular and rectangular cross-sectional shapes and the elastic behavior associated with flexible microbridges is assumed to be device actuation checkpoint. LTCC device manufacturing was accomplished considering the optimized dimensions for its channels and the integrated PDMS microbridge size. The microfluidic model is described by the solution of the Navier-Stokes's equation considering microchannels subjected to pressure-driven water flows. PDMS microbridge modeling is summarized to find out its elastic constant k , relating force to the respective displacement as demonstrated on the following equation:

$$k = \frac{F_z}{u_z}$$

It is necessary to design each ceramic tape pattern for implementation in an LTCC substrate, individually on each layer. Consequently, the designer must anticipate the geometric shapes of each layer of ceramic tape, in a way that by stacking all sheets following a proper order, the desired microfluidic device is achieved. In this work, all patterns and geometries were designed using Autodesk's AutoCAD 2007 graphics software. Considering ceramic shrinkage after the sintering process (Dupont Microcircuit Materials, 951 Green Tape, Product Description) project dimensions were enlarged by 12.7% with respect to x and y directions and 15% in z direction, ensuring that the constructed devices are within acceptable dimensions for assembly. The machined LTCC sheets were stacked by isostatic lamination. The sintering of the green tapes was carried out in an electric furnace.

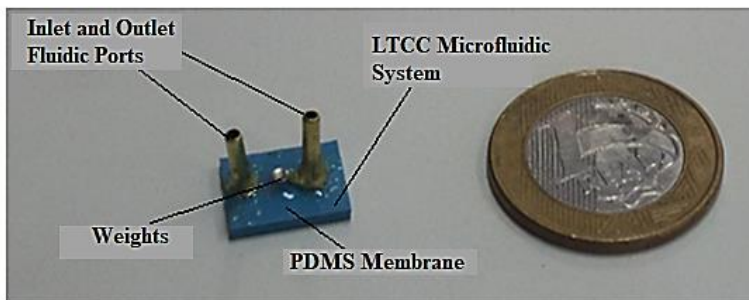


Fig. 2 LTCC-PDMS microswitch device built in this work next to 1 BRL coin for scale.

Results

The experiments with the fabricated devices were carried out to evaluate microchannel fluidic resistance and microswitch performance (Fig. 3). Fluidic resistance tests included a fluid reservoir, a graduated test tube, a chronometer, the LTCC microchannel built on a microswitch device and circular silicone pipes (1 mm-diameter) to connect the elements. The experiment measured the water flow rate through silicone pipe or LTCC channels as a function of hydrostatic pressure. All experiments were performed at room temperature using deionized water as working fluid. Flow rate measurements were performed via volumetric observation obtained in a specific clock.

Figure 3 demonstrates that for a hydrostatic pressure of 220 Pa, a flow rate up to 20 mL/min can be achieved through the circular silicone tube. According to Bartels micropump manual used in this experiment, a pressure of about 1 kPa is produced when the flow is 0.1 mL/min, suggesting that silicone tubes do not restrict fluid flow, and thus, the micropump will set the operational system flow rate. Additionally, from figure 4, both rectangular channels (added to silicone tubes) require less than 0.1 kPa in order to provide up to 0.2 mL/min, indicating that micropump exerts more resistance to fluid transport than the designed rectangular channels 1 (1 cm-length; 216 μm -high; 100 μm -width) and 2(1 cm-length; 216 μm -high; 300 μm -width). Therefore, the micropump will induce water flow rate over the whole system, and both channels (1 and 2) will work properly for any micropump configuration.

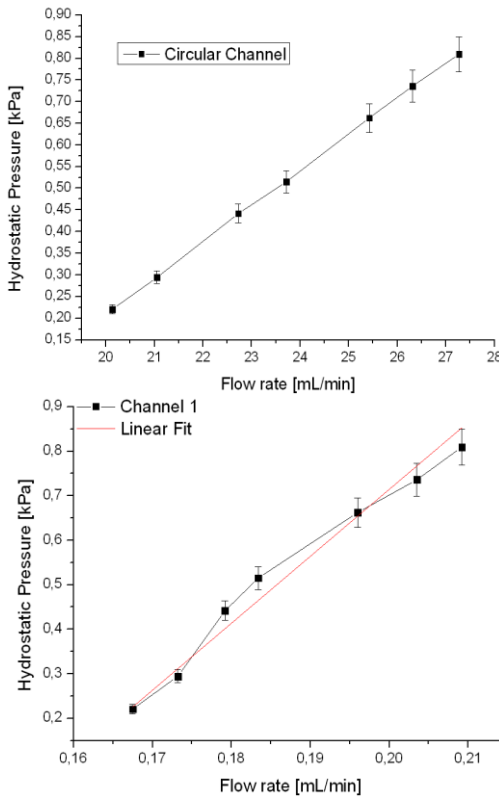


Fig. 3 Deionized water flow rate through circular channels (13 cm length, 1 mm inner diameter) against applied hydrostatic pressure.

Fig. 4 Deionized water flow rate through rectangular channels 1 and 2, as function of applied hydrostatic pressure.

Conclusions

This paper introduces the design and fabrication of a microswitch for LTCC microsystem. The microswitch was designed using a model that predicts rectangular and circular channels static response, associated with real characteristics of micro total analysis systems. Regarding microswitch experimental investigations, results demonstrated that a weight of 120 g deflects the PDMS microbridge, reducing the flow rate from 0.42 mL/min to 50 μ L/min. This result demonstrates that microvalve stroke for microfluidic system integration and automation can be achieved applying actuation principles such as electromagnetic or electric methods. However, it is necessary to keep in mind that an improvement in fabrication and integration of PDMS membrane to LTCC chip must be performed in order to design a functional electric or electromagnetic microvalve.

References

- [1] da Rocha ZM, Martinez-Cisneros CS, Seabra AC, Valdés F, Gongora-Rubio MR, Alonso-Chamarro, J (2012) Compact and autonomous multiwavelength microanalyzer for in-line and in situ colorimetric determinations. *Lab Chip* 12:109-117.
- [2] Oh KW; Ahn CH (2006) A review of microvalves. *J Micromech Microeng* 16:R13.
- [3] Laser DJ, Santiago JG (2004) A review of micropumps. *J Micromech Microeng* 14:R35.
- [4] Gongora-Rubio MR, Espinoza-Vallejos P, Sola-Laguna L, Santiago-Aviles JJ (2001) Overview of low temperature co-fired ceramics tape technology for meso-system technology (MsST). *Sens Actuators A Phys* 89:222-241.

P30 |

INTEGRAÇÃO E AUTOMATIZAÇÃO DO FUNCIONAMENTO E DO PROCESSO DE AQUISIÇÃO DE DADOS LEITURA DE UM SISTEMA DE SENSORES NUMA BANCADA DE CALIBRAÇÃO DE MEDIDORES DE VAZÃO DE LÍQUIDOS

Idrissa Deme^{1,2}, M.H. Farias², A.V. Alvarenga²

¹Instituto Nacional de Metrologia Qualidade e Tecnologia (Inmetro), Avenida. Nossa Senhora das Graças, 50 - Vila Operária - Duque de Caxias - CEP: 25250-020, Rio de Janeiro - Brasil

²Universidade do Estado do Rio de Janeiro (UERJ), Rua São Francisco Xavier, 524 –

CEP:20550-013, Maracanã, Rio de Janeiro - Brasil

idrissdeme@yahoo.fr

INTRODUÇÃO

O presente trabalho tem como objetivo principal apresentar o processo de controle e aquisição de dados de um conjunto de sensores empregados na calibração de medidores de vazão de líquidos na Divisão de Metrologia em Dinâmica de Fluidos (Dinam) do Instituto Nacional em Metrologia Qualidade e Tecnologia (Inmetro). Este sistema de calibração de medidores de vazão de líquidos que é baseado no método gravimétrico era, inicialmente, totalmente operado manualmente. A operação manual era fonte de problemas em termo de tempo, número de operadores, erros sistemático, controle dos atuadores e dificuldades de melhorar a exatidão da medição. O processo de controle e aquisição de dados foi feito através da especificação e dimensionamento dos instrumentos de medição e atuadores e da integração das diferentes partes do sistema usados nas medições, assim como da automatização no registro e transferência dos dados de alguns instrumentos e no controle de outros usando o software LabVIEW® (Laboratory Virtual Instrument Engineering Workbench). Uma avaliação do funcionamento do Sistema automatizado em relação ao manual foi realizada por meio da calibração de um medidor mássico que já havia sido calibrado na bancada com controle manual. Os resultados do teste foram compatíveis com os resultados das calibrações anteriores e, inclusive uma diminuição nos valores das incertezas de medição foi constatada como uma das principais vantagens da automatização junto com uma redução no tempo de medição. Esses testes foram realizados por um só operador, enquanto o sistema manual necessitava de pelo menos dois ou três operadores. Isso permitiu estabelecer no Inmetro uma metodologia confiável com rastreabilidade ao Sistema Internacional de Unidades (SI), que contribuirá para garantir a qualidade e a confiabilidade das medições, com menores incertezas dos resultados e menos necessidade da intervenção humana na aquisição e tratamento de dados.

METODOLOGIA

Foram realizados testes experimentais em paralelo à pesquisa bibliográfica no intuito de proporcionar ao sistema um processo de funcionamento automatizado. Assim, o acionamento e desligamento das bombas, a aquisição e registros dos dados das balanças como os do meio ambiente e os cálculos dos parâmetros necessários à calibração foram automatizados. Um programa desenvolvido em Labview para integrar e sincronizar todo o processo. O programa desenvolvido neste ambiente conta com uma interface de usuário que corresponde às diferentes fases do processo de calibração incluindo a transferência dos dados para planilha de tratamento de dados. Para avaliar o funcionamento do sistema automatizado foram feitas um total de cinco (5) séries de medições com um medidor mássico tipo Coriolis previamente calibrado manualmente. Cada série corresponde à faixa de vazão de 20 kg/min, 60 kg/min, 80 kg/min, 100 kg/min e 120 kg/min. Para cada faixa foram realizadas seis (6) medições dando um total de trinta (30) medições. Uma avaliação da incerteza de medição foi feita seguindo o método do ISO GUM, para os dois estados do sistema e os parâmetros principais comparados posteriormente. A figura 1 abaixo mostra o funcionamento do sistema.

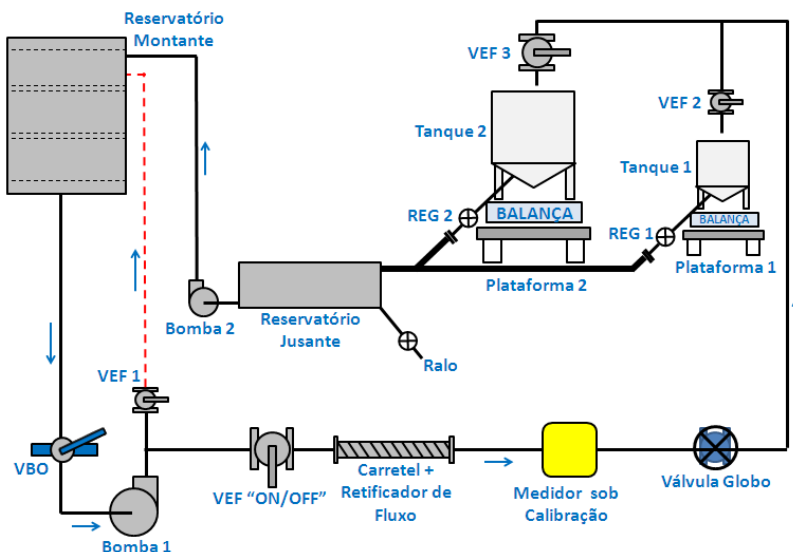


Figura 1: Funcionamento da bancada de calibração da Dinam/Inmetro. (VEF: Válvula Esférica; VBO: Válvula Borboleta; REG: Registro)

RESULTADOS

O acionamento e desligamento das bombas, a aquisição e registros do dados das balanças como os do meio ambiente (temperatura, pressão e humidade do ar) e o cálculos dos parâmetro necessários á calibração foram automatizados. A tabela1 abaixo mostra os equipamentos e sensores que foram alvo da automatização assim como o procedimento de registro associado.

Tabela 2: Modo de operação e equipamentos usados na automatização dos atuadores e sensores

Foco da automatização/controle	Modo de operação	Material usado
Registro das temperaturas de entrada e saída do medidor e do ambiente	Automatizado/com possibilidade de usar manualmente	Termopares + módulo NI 9211
Controle da bomba 1 para controle da vazão a montante	Automatizado/com possibilidade de usar manualmente	Inversor cfw09 + módulo NI 9263
Acionamento da bomba 2 para reabastecimento do reservatório	Automatizado/com possibilidade de usar manualmente	Relês acopladores + módulo NI 9274.
Aquisição de dados do medidor	Automatizado/ com possibilidade de usar manualmente	Câmera digital + Cabo USB NI
Aquisição dos dados medidos pelas balanças	Automatizado/ com possibilidade de usar manualmente	Balança de 300 kg e 35 kg com saídas RS-232 + Cabo RS-232 NI.
Aquisição e tratamento de dados com o Labview	Automatizado/com possibilidade de fazer manualmente	Computador (planilha) + programa integrado.

A integração do sistema com destaque das diferentes etapas da calibração foi realizado em um único programa usando o software Labview® e a figura2 apresenta um fluxograma resumindo os passos automatizados controlados por este programa.

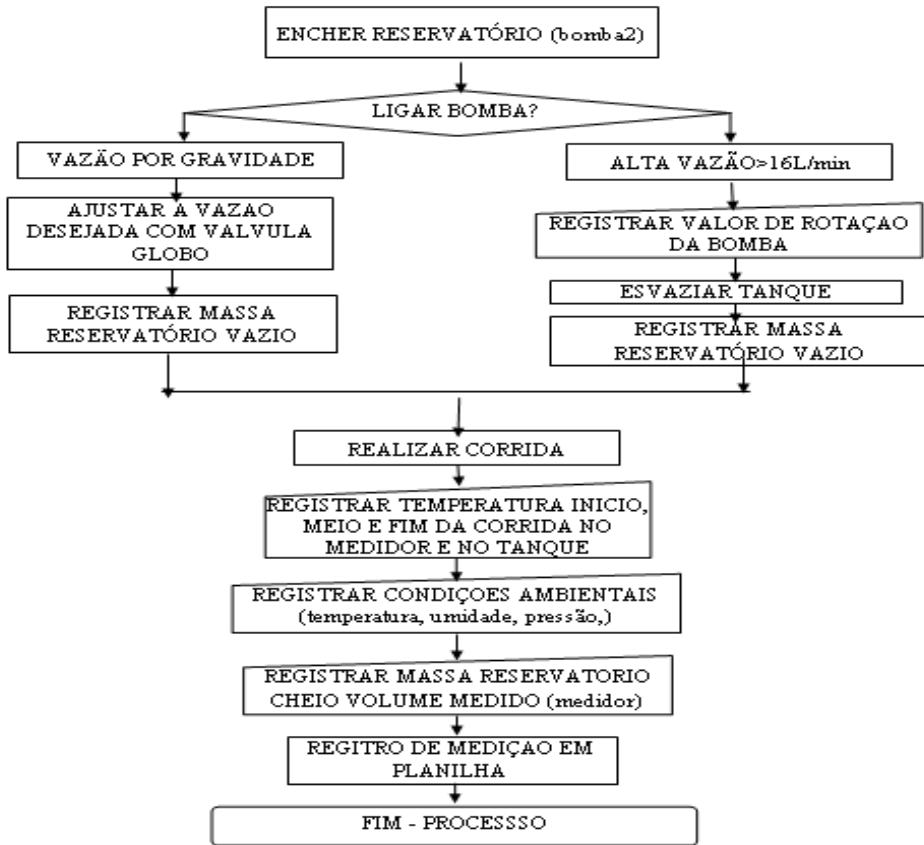


Figura 2: Fluxograma do programa de controle e aquisição de dados integrado.

O processo de controle e integração dos sensores não suprimiu a possibilidade de operação manual de nenhum equipamento. Portanto, a bancada pode continuar funcionando de forma manual ou automatizada, permitindo comparações diretas entre aspectos específicos dos dois procedimentos. Na tabela 2 a comparação da incerteza de medição relacionada ao fator de medição F_m entre o sistema manual e automatizado e mostrou a consistência do sistema automatizado que possibilitou além da redução do número de operadores (de 3 para 1) e do tempo de calibração, a avaliação e melhor controle dos parâmetros que mais influenciam na calibração que são: a repetitividade, o volume totalizado pelo medidor de vazão e a massa totalizada na balança.

Tabela 3: Comparação dos valores de incerteza relativa entre a calibração manual e a automatizada.

Faixa de vazão (kg/min)	20	60	80	100	120
Incerteza do Fm do sistema Manual (%)	0,17	0,038	0,023	0,023	0,035
Incerteza do Fm do sistema automatizado (%)	0,15	0,030	0,021	0,017	0,017

CONCLUSÕES

A automatização do sistema além de ter possibilitado a redução da incerteza de medição no processo de calibração foi positivo para outros aspectos. São eles: a redução do número de operadores e minimização do erro sistemático, a otimização do processo de aquisição e tratamento de dados com planilhas de cálculos prontas, bastando endereçar onde registrar os dados e obter os resultados no final da medição e a Facilidade de realizar mais corridas melhorando a repetitividade e possibilidade de analisar de forma específica o impacto de algumas variáveis de processo que não podem ser monitoradas de modo contínuo na operação manual. A automatização do sistema abre o caminho para várias possibilidades de estudos visando alguns aspectos específicos da bancada como, o estudo do efeito do controle da vazão pela bomba, a determinação mais precisa da massa evaporada de água nas balanças, ou ainda o refinamento de dados relacionados à temperatura do líquido no medidor.

References

- [1] JCGM, Avaliação de dados de Medição - Guia para a expressão de incerteza de medição (ISO-GUM). 1ª edição brasileira. ed. Rio de Janeiro: Instituto Nacional de Metrologia, Qualidade e Tecnologia (INMETRO), 2012.
- [2] Rainer, E.; Karlheinz, B.; Hans-Joachim B. Design and realization of the high precision weighing systems as the gravimetric references in PTB's national water flow standard, Measurement. Science. Technology. Nº 23, 2012.
- [3] SEJONG, C. et al. Development of water flow standard system for calibrating water flow meters up to 2000 m³/h in KRISS. International Flow Measurement Conference (fomeko). Sydney, Australia: FLOMEKO. 2016.

Acknowledgments

Instituto Nacional de Metrologia Qualidade e Tecnologia (INMETRO) – Brasil, Programa Nacional de Apoio ao Desenvolvimento da Metrologia, Qualidade e Tecnologia (Pronametro) - Brasil

SENSORES INTELIGENTES E REDES SEM FIOS | SENSORES
INTELIGENTES Y REDES INALÁMBRICAS | SMART SENSORS AND WIRELESS
NETWORKS |

O24 |

ARCHITECTURE OF A BI-DIRECTIONAL VLC SYSTEM FOR NAVIGATION AND MESSAGE TRANSMISSION

P. Louro^{1,2}, M. Vieira^{1,2,3}, M. A. Vieira²

¹*Electronics Telecommunications and Computer Dept. ISEL/IPL, R. Conselheiro Emídio Navarro, 1, 1949-014 Lisboa, Portugal*

²*CTS-UNINOVA, Quinta da Torre, Monte da Caparica, 2829-516, Caparica, Portugal*

³*DEE-FCT-UNL, Quinta da Torre, Monte da Caparica, 2829-516, Caparica, Portugal*
**e-mail: plouro@deetc.isel.ipl.pt*

Introduction

Light emitting diodes (LEDs) are the basis for Visible Light Communication (VLC) technology due to their ability to simultaneously provide low energy consumption light and enable the possibility of wireless communication [1,2]. These features empowered VLC as an effective communication technology due to the ubiquity of the illumination spots, especially in indoor applications. VLC is being considered as an additional method for future fifth generation (5G) wireless communications also due to its wide bandwidth and immunity to electromagnetic interference. In indoor navigation it is also a promising application, where GPS signals are inefficient, and visible light can enable the accurate determination of position and provide guidance services.

Methods

In this work we propose links based on VLC for Infrastructure-To-Vehicle (I2V), Vehicle-To-Infrastructure (V2I) and Vehicle-To-Vehicle (V2V) able to provide indoors, bi-directional communication for robot navigation in automated warehouses. The link I2V provides indoor localization information [3,4] inside the warehouse enabling navigation services. Information about the availability of the goods on the racks under their coverage area is also transmitted to the mobile robots. The links V2I and V2V provide cooperation services to enhance system performance.

Figure 1 displays the communication channels established between the lamps and the mobile robots, for I2V, V2I and V2V communication.

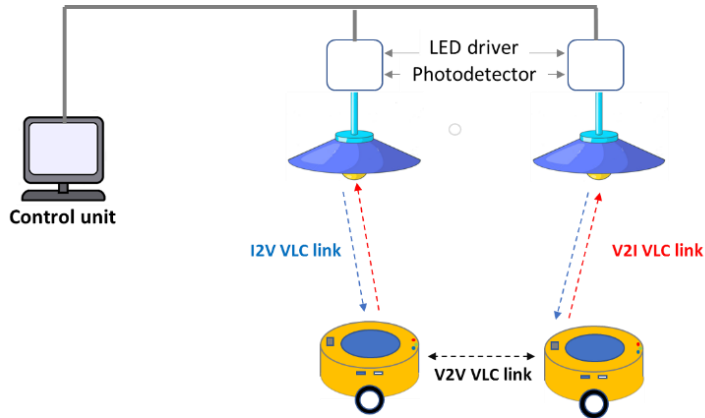


Figure 1 - Smart communication system with V2I, I2V and V2V channels.

The system uses four transmission optical channels supplied by the modulation of white tri-chromatic LEDs that establish an optical bi-directional communication link between static infra-structures and mobile devices.

The transmitter proposed in this VLC system uses ceiling lamps based on commercial white LEDs. with red, green and blue emitters (w-RGB LEDs). Each ceiling lamp is composed by four white LEDs framed at the corners of a square (Figure 2).

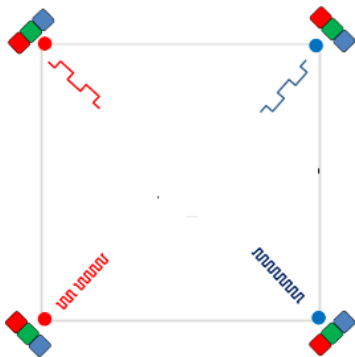


Figure 2 – Configuration of the VLC emitter with 4 RGB white LEDs.

The luminous intensity of each emitter is regulated by the driving current for white perception by the human eye and the divergence angle is around 120°.

On each corner only one chip of each white LED is modulated for data transmission carrying useful information. The other emitters of the LED are only supplied with DC to maintain white color illumination. Red (R; 626 nm), Green (G; 530 nm), Blue (B; 470 nm) and violet (V; 390 nm) LEDs, are used [5].

In the receiver unit, the system uses as photodetector, a multilayered pin-pin heterostructure based on a-SiC:H. The device is manufactured on a glass substrate and inserted between two transparent electrical contacts. Due to the use of different absorbing materials in each pin heterostructure, the absorption profile is dependent on the light wavelength, which provides different levels of sensitivity within the visible spectrum. This sensitivity can be tuned under appropriate optical or electric bias.

The photodetector used for the transduction of the optical signal is a monolithic heterojunction composed by two pin structures built on a glass substrate and sandwiched between two transparent electrical contacts (Figure 3). The intrinsic absorbers of the device are based on a-Si:H and a-SiC:H, which provide high sensitivity in the visible range. Both intrinsic layers were designed to detect separately short and long visible wavelengths. The front intrinsic layer is narrow (200 nm) and exhibits a higher bandgap material (2.1 eV, a-SiC:H). The back intrinsic layer is thicker (1000 nm) and has a lower bandgap semiconductor (1.8 eV, a-Si:H). This design confers high absorption of the blue light (shorter wavelengths) and high transparency of the red wavelength to the front absorber (pin 1) and high absorption of longer wavelengths (red light) to the back absorber (pin 2).

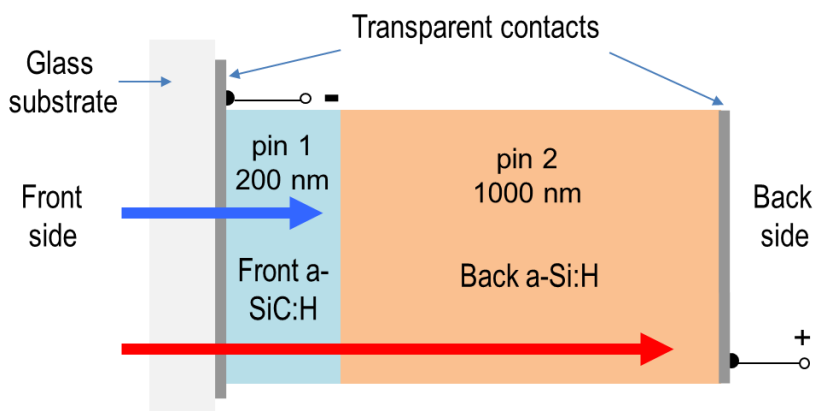


Figure 3 - Configuration of the photodetector at the receiver module.

In the proposed system, the frame modulation of each channel is designed with different word codes. Each of these blocks of bits addresses different functionalities in the message, namely, synchronization, identification of the channel/navigation cell and transmission of the message. The optical excitation induced by the modulation of the emitters in the LEDs generates an output signal dependent on the wavelength and frequency of the modulated channels, which is related to the device position and to the transmitted message. The design of the code words concerns the coding modulation for up and down link communication, considering the need for stable, non- flickering illumination during data transmission. Run length limiting line codes are used in downlink communication (static illumination infrastructure to mobile device) to balance the distribution of symbols. The on-off modulation technique is used to carry digital information into LED light signals. The decoding algorithm ensures error correction using parity bits to check signal integrity. Statistical analysis of the error rate is used to assess the navigation accuracy and the integrity of the decoded message.

Results

In Figure 4 it is displayed the photocurrent signal acquired along the forward path at positions under the coverage of RR'BB' and R'BB' together with the calibration curve (I2V link).

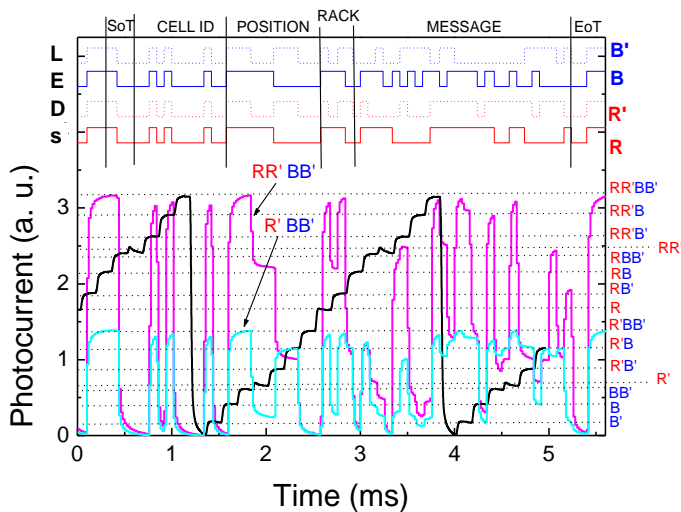


Figure 4 - Photocurrent signal acquired along the forward path at positions under the coverage of RR'BB' and R'BB'. In superposition it is displayed the calibration grid. At the top it is displayed the input optical signals (R, R', B and B').

In the I2V link, the communication is established from the mobile robot to the infrastructure. In this link a single monochromatic can be used, and the optical signal contains only a single channel. Consequently, the correspondent transduced electrical is not a multiplexed signal, and the decoding procedure, although also based on a calibration data, is much more simpler.

Conclusions

Bi-directional communication using VLC in both downlink and uplink channels has been addressed in a robot navigation system. The proposed indoors application deals with infrastructure to vehicle (I2V), vehicle to infrastructure (V2I) and vehicle to vehicle (V2V) communication in a warehouse. The vehicle is a robot, that moves autonomously inside the warehouse carrying goods from the carts to the packaging station. The transmitted data is encoded in a 64 bits word, defined using specific data frames in communication channel. Codification of the optical signals ensured synchronization between frames. The code word of each channel was designed to ensure synchronization between frames, to transmit information of the transmitter identification and of spatial location. Flickering effects were addressed by proper control of the amount of transitions to zero. The experimental evaluation in small range indoor conditions (up to 5 m) also demonstrated that the decoding solution can provide robust communications. The Bit Error Rate of the system using OOK and direct bit decoding through the calibration data presents higher errors for low intensity channels, which can be mitigated using parity check bits for error decoding.

References

- [1] Căilean, A.M.; Dimian, M. Current Challenges for Visible Light Communications Usage in Vehicle Applications: A Survey. *IEEE Communications Surveys & Tutorials* 2017, 19, 4, pp. 2681-2703.
- [2] Chowdhury, M. Z.; Hossan, M. T.; Islam, A.; Jang, Y. M. A Comparative Survey of Optical Wireless Technologies: Architectures and Applications. *IEEE Access* 2018, 6, 9819-9840.
- [3] Louro, P., Silva, V., Vieira, M.A., Vieira, M., "Viability of the use of an a-SiC:H multilayer device in a domestic VLC application", *Phys. Status Solidi C* 11, No. 11–12, 1703–1706 (2014).
- [4] P. Louro, M. Vieira, M. A. Vieira, "Geolocalization and navigation by visible light communication to address automated logistics control," *Opt. Eng.* 61(1), 016104 (2022).
- [5] P. Louro, M. Vieira, M. A. Vieira, "Indoors Geolocation Based on Visible Light Communication", *Sensors & Transducers*, Vol. 245, Issue 6, October 2020, pp. 57-64.

ACKNOWLEDGEMENTS

This work was sponsored by FCT – Fundação para a Ciência e a Tecnologia, within the Research Unit CTS – Center of Technology and systems, reference UIDB/00066/2020.

O25 |

INTELLIGENT SPLIT INTERSECTIONS USING COOPERATIVE VEHICLE VISIBILITY COMMUNICATION

M. A. Vieira^{1,2}, M. Vieira^{1,2,3}, P. Louro^{1,2}, P. Vieira^{1,4}

¹*Electronics Telecommunication and Computer Dept. ISEL, R. Conselheiro Emídio Navarro, 1959-007 Lisboa, Portugal*

²*CTS-UNINOVA, Quinta da Torre, Monte da Caparica, 2829-516, Caparica, Portugal.*

³*DEE-FCT-UNL, Quinta da Torre, Monte da Caparica, 2829-516, Caparica, Portugal.*

⁴*Instituto de Telecomunicações, Instituto Superior Técnico, 1049-001, Lisboa, Portugal*

**e-mail: mv@isel.ipl.pt*

Abstract

We propose a Visible Light Communication system based on Vehicle-to-Vehicle, Vehicle-to-Infrastructure and Infrastructure-to-Vehicle communications able to safely manage vehicles crossing through an intersection leveraging Edge of Things facilities. By using the streetlamps, street lights and traffic signaling to broadcast information, the connected vehicles interact with one another and with the infrastructure. Using joint transmission, mobile optical receivers collect data, calculate their location for positioning and, concomitantly, read the transmitted data from each transmitter. In parallel with this, an intersection manager coordinates traffic flow and interacts with the vehicles via Driver Agents embedded in them. A communication scenario is established and a “mesh/cellular” hybrid network configuration proposed. Data is encoded, modulated and converted into light signals emitted by the transmitters. As receivers and decoders, optical sensors with light filtering properties, are used. Bidirectional communication between the infrastructure and the vehicles is tested. To command the passage of vehicles crossing the intersection safely queue/request/response mechanisms and temporal/space relative pose concepts are used. Results show that the short-range mesh network ensures a secure communication from street lamp controllers to the edge computer through the neighbor traffic light controller with active cellular connection and enables peer-to-peer communication, to exchange information between Vehicular Visible Light Communication (V-VLC) ready connected cars.

Introduction

Vehicles can connect to others, or to the infrastructure, providing an Internet connection. In this area, VLC have a great potential for applications due to their relatively simple design for basic functioning, efficiency, and large geographical

distribution. VLC is an emerging technology that enables data communication by modulating information on the intensity of the light emitted by LEDs. In the case of vehicular communications, the use of VLC is made easier because all vehicles, street lights, and traffic lights are equipped with LEDs, using them for illumination. In this way communication in both directions (uplink and downlink) can be carried out without any restriction or inconvenience to pedestrians in the vicinity. So, vehicular networking applications can take advantage of the LED-equipped lighting modules and transportation infrastructure to realize V-VLC. Here, the communication and geolocalization is performed using the street lamps, the traffic signaling and the head and tail lamps, enabling the dual use of exterior automotive and infrastructure lighting for both illumination and communication purposes [1]. The proposed V-VLC system is composed of several transmitters, the street lights and the traffic signals, which transmit map information and traffic messages required to the moving vehicles. A Vehicle-to-Everything (V2X) traffic scenario is established and bidirectional communication between the infrastructure and the vehicles is tested, using the VLC request/response concept. Every vehicle is equipped with a receiver module for receiving the mapped information generated from the street lamps. The receiver modules include a photodetector based on a tandem a-SiC:H/a-Si:H pin/pin light controlled filter [2,3] that multiplex the different optical channels, perform different filtering processes (amplification, switching, and wavelength conversion) and decode the encoded signals, recovering the transmitted information. The goal is a cooperative system that supports guidance services and uses an edge/fog based architecture. Here, the streetlights and traffic lights, through VLC, report its geographical positions and specific information to the drivers since its infrastructure can also be reused to embed the edge/fog nodes in them. Cooperative localization is realized in a distributed way with the incorporation of the indirect V2V relative pose estimation method.

V-VLC vehicular communication

The system is composed by two modules: the transmitter and the receiver located at the infrastructures and at the driving cars. The block diagram and the transmitter and receiver relative positions of the V-VLC system are presented in Figure 1. Both communication modules (transmitter and receiver) are software defined, where modulation/ demodulation can be programmed. On the transmission side, a modulation and conversion from digital to analog data is done. The visible light emitted by the LEDs passes through the transmission medium and is then received by the MUX device. Line of Sight (LoS) is mandatory. White light tetra-chromatic sources are used providing a different data channel for each chip. Data is encoded,

modulated and converted into light signals emitted by the transmitters. Modulation and digital-to-analog conversion of the information bits is done using signal processing techniques. The signal is propagating through the optical channel and a VLC receiver, at the reception end of the communication link, is responsible to extract the data from the modulated light beam. On the receiving side, this is first done by a silicon carbide (SiC) pinpin MUX device that acts as an active filter for the visible region of the light spectrum [4, 5]. After receiving the signal, it is in turn filtered, amplified, and converted back to digital format for demodulation. The system controller consists of a set of programmable modules.

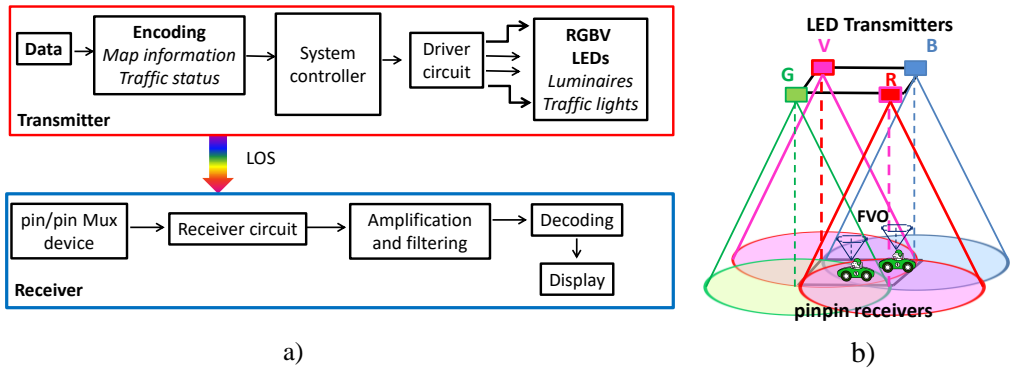


Figure 1. a) Block diagram: transmitters and receiver modules. b) 3D Relative position of the transmitter and receiver units .

Lighting plans for a four-legged and a split the intersection are shown in Figure 2. The emitters are located at the nodes along the roadside. Thus, each LED sends a I2V message that includes the synchronism, its physical ID and the traffic information. When a probe vehicle enters the streetlight’s capture range, the receiver replies to the light signal, and assigns a unique ID and the traffic message [6].

The typical single intersection (is attached to sixteen roads, eight incoming from and eight outgoing to North, West, South, and East neighbor crossroads’ roads. The split intersection starts with only one main street that connects two crossroads (Intersection1-Intersection 2). Four traffic flows were considered in both. In the four-legged intersection one is coming from West (W) with three

vehicles (*a,c,d*) approaching the crossroad, Vehicle *a* with straight movement and Vehicle *c* and Vehicle *d* with left turn only. In the second flow, Vehicle *b* from East (E), approaches the intersection with left turn only. In the third flow, Vehicle *e*, oncoming from South (S), has a right-turn approach. Finally, in the fourth flow, Vehicle *f*, coming from North, goes straight.

a)

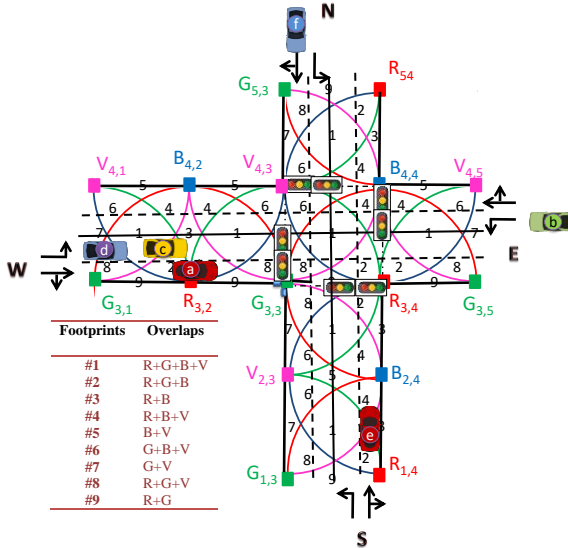
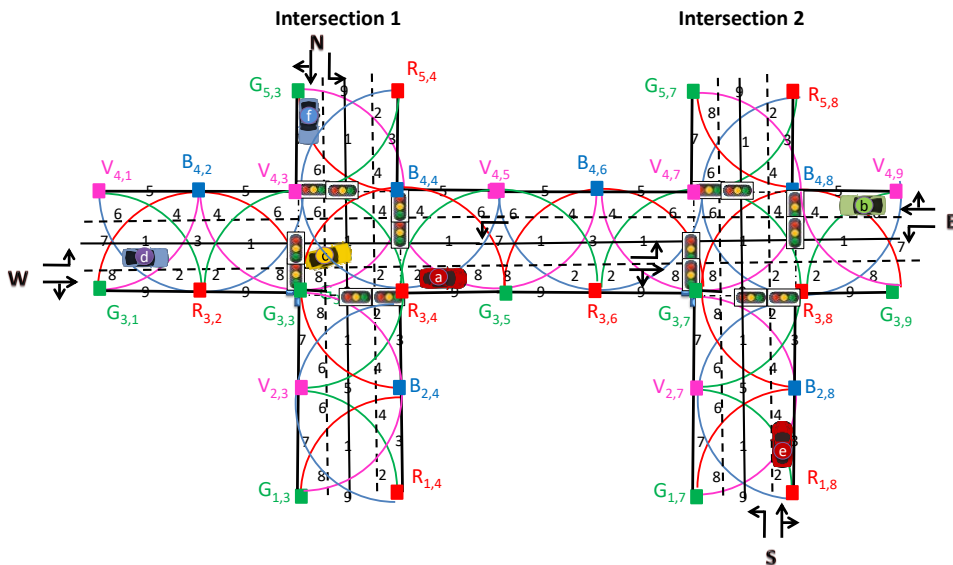


Figure 2. V2X optical infrastructure and generated joint footprints in a crossroad (LED array=RGBV color spots). a) Standard intersection. b) Split intersection.

b)



In Figure 3 it is displayed the normalized MUX signals and the decoded messages assigned to the IM and received by Vehicles *a*, *b* (Figure 3a) and *c* (Figure 3b) at different response times. On the top the transmitted channels packets [R, G, B, V] are decoded. In the right side, the received channels for each vehicle are identified by its 4-digit binary codes and associated positions in the unit cell.

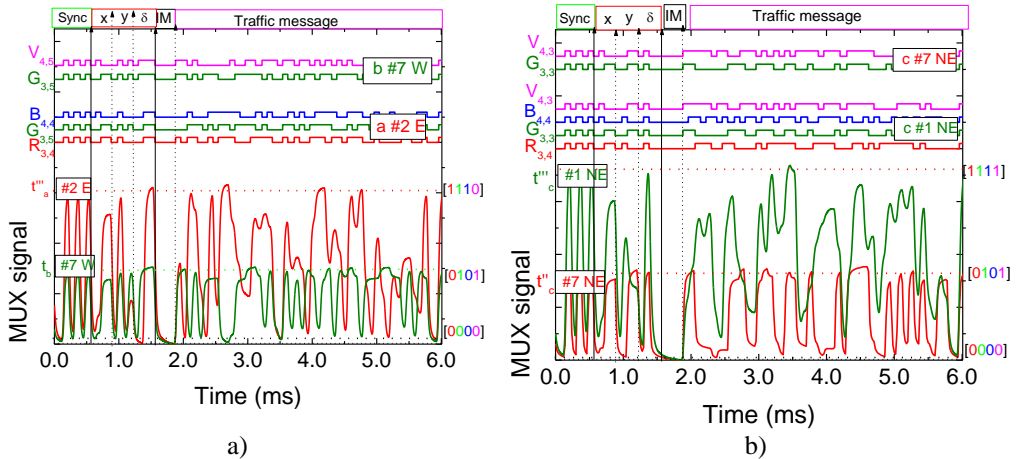


Figure 3 Normalized MUX signal responses and the assigned decoded messages acquired by vehicles *a*, *b* and *c* at different response times. On the top the transmitted channels packets [R, G, B, V] are decoded. a) Vehicle *a*, pose #2E, and vehicle *b*, pose #7W). b) Vehicle *c*, poses #7NE, #1NE.

Results show that, as the receiver moves between generated point regions, the received information pattern changes.

Vehicle *a*, driving the right lane goes straight to E. Then, this vehicle enters the crossroad through #8 (t'_a) and leaves it in the exit #2 at t''_a , as displayed in the figure, keeping always the same direction (E). Vehicle *b* after crossing Intersection 2, approaches the Intersection 1, asked permission to cross it (t_b) and receives authorization when the vehicle *a* left the intersection (t''_a). In Figure 3b, signal responses and the assigned decoded messages from vehicle *c* inside the intersection are displayed at t'_c and t''_c . Data shows that vehicle *c*, driving in the in the left lane, receives order to enter the intersection in # 7, turning left (NE) and keeps moving in this direction across position #1 toward the North exit. In both intersections, before the request of vehicle *d* to cross Intersection 1, the IM is aware through the request made by its leader *c* that a follower is approaching (*d*). Three actions must be taken to promote smooth movement avoiding

congestions and delays: changing the synchronism of intersection 2, delaying the passage of vehicles *b* and finally, allowing the joint passage of vehicles *b* and *d* at Intersection 1 in the same traffic phase.

Conclusions

This paper explores the concept of queue/request/response for the management of split intersections using V-VLC ready connected cars. To command the passage of vehicles crossing the intersection queue/request/response mechanisms and temporal/space relative pose concepts were used. A communication scenario is established and a “mesh/cellular” hybrid network configuration proposed. As a proof of concept a phasing of traffic flows is suggested. Results show that the vehicles’ arrival is controlled and scheduled to cross the intersections in order to minimize traffic delay. Through Vehicle to Everything (V2X) communication, the travel time that influences traffic channeling in different routes can be calculated, allowing in real-time the acquisition of data about vehicle speed, spacing, queues, and traffic jams.

References

- [1] Caputo, S. Mucchi, L., Cataliotti, F., Seminara, M., Nawaz, T., and Catani, J. “Measurement-based VLC channel characterization for I2V communications in a real urban scenario,” *Veh. Commun.*, vol. 28, Apr. 2021, Art. no. 100305.
- [2] Vieira, M. A., Louro, P., Vieira, M., Fantoni, A., and Steiger-Garçon, A., “Light-activated amplification in Si-C tandem devices: A capacitive active filter model,” *IEEE sensor journal*, 12 (6), 1755-1762 (2012).
- [3] Vieira, M. A., Vieira, M., Vieira, P., Louro, P., “Optical signal processing for a smart vehicle lighting system using a-SiCH technology,” *Proc. SPIE 10231, Optical Sensors 2017*, 102311L (2017);
- [4] Vieira, M. A., Vieira, M., Silva, V., Louro, P., Costa, J., “Optical signal processing for data error detection and correction using a-SiCH technology,” *Phys. Status Solidi C* 12 (12), 1393–1400 (2015).
- [5] Vieira, M. A., Vieira, M., Louro, P., Vieira, P., "Bi-directional communication between infrastructures and vehicles through visible light," *Proc. SPIE 11207, Fourth International Conference on Applications of Optics and Photonics*, 112070C (3 October 2019).
- [6] Vieira, M. A., Vieira, M., Louro, P., Vieira, P., "Bi-directional communication between infrastructures and vehicles through visible light," *Proc. SPIE 11207, Fourth International Conference on Applications of Optics and Photonics*, 112070C (3 October 2019).

O26 |

A VISIBLE LIGHT COMMUNICATION SYSTEM TO SUPPORT INDOOR GUIDANCE

M. Vieira^{1,2,3}, M. A. Vieira^{1,2}, P. Louro^{1,2}, P. Vieira^{1,4}

¹*Electronics Telecommunication and Computer Dept. ISEL, R. Conselheiro Emídio Navarro, 1959-007 Lisboa, Portugal*

²*CTS-UNINOVA, Quinta da Torre, Monte da Caparica, 2829-516, Caparica, Portugal.*

³*DEE-FCT-UNL, Quinta da Torre, Monte da Caparica, 2829-516, Caparica, Portugal.*

⁴*Instituto de Telecomunicações, Instituto Superior Técnico, 1049-001, Lisboa, Portugal*

**e-mail: mv@isel.ipl.pt*

Abstract

To support people's wayfinding activities we propose a Visible Light Communication (VLC) cooperative system that supports guidance services and uses an edge/fog based architecture for wayfinding services. A mesh cellular hybrid structure is proposed. The dynamic navigation system is composed of several transmitters (ceiling luminaries) which send the map information and path messages required to wayfinding. The luminaires are equipped with one of two types of nodes: a "mesh" controller that connects with other nodes in its vicinity and can forward messages to other devices in the mesh, effectively acting like routers nodes in the network and a "mesh/cellular" hybrid controller, that is also equipped with a modem providing IP base connectivity to the central manager services. These nodes acts as border-router and can be used for edge computing. Mobile optical receivers, using joint transmission, collect the data at high frame rates, extracts their location to perform positioning and, concomitantly, the transmitted data from each transmitter. Each luminaire, through VLC, reports its geographic position and specific information to the users, making it available for whatever use. Bidirectional communication is implemented and the best route to navigate through venue calculated. The results show that the system makes possible not only the self-localization, but also to infer the travel direction and to interact with information received optimizing the route towards a static or dynamic destination.

Introduction

Nowadays, wireless networks have seen a demand for increased data rate requirements. For a realistic coverage with the data rate requirements, a large bandwidth is needed which remains a limiting factor when compared with the RF

communication technologies [1]. Moreover, recent advancements in VLC wireless communication have generated a growing interest in indoor navigation due to their ability to enable a wide range of applications and services, taking advantage of the more interference free VLC channel, when compared with the usual RF. Visible Light Communication (VLC) makes use of the higher frequencies in the visual band and extends the capabilities of data transmission using general light sources [1]. VLC transmits data by high-speed switching or flickering at a rate that is not perceivable to the naked eye. It presents advantages when compared with the Wi-Fi, namely the invulnerability to hackers since it does not penetrate through the wall, its high capacity and efficiency. VLC has been regarded as an additional communication technology to fulfill the high data rate demands and as a new affiliate in the beyond fifth-generation (5G) heterogeneous networks. It can be easily used in indoor environments using the existing LED lighting infrastructure with few modifications [2]. The VLC systems use the wavelength range between 380 nm and 780 nm and the LEDs are used as light sources and transmitters. This means that the LEDs are twofold by providing illumination as well as communication. Research has shown that compared to outdoors, people tend to lose orientation a lot easier within complex buildings. Fine-grained indoor localization can be useful, enabling several applications [3]. Indoor positioning systems provide several users at the same time with indoor location data to simplify wayfinding on their mobile device. As these systems are deployed in smart building, visitors will be able to receive step-by-step instructions to their destinations.

This work focuses on the use of VLC as a support for the transmission of information, providing advertising services and specific information to users. Here, the luminaire, through VLC, reports its geographical positions and specific information to the users since its infrastructure can also be reused to embed the fog nodes in them. The system is composed of several transmitters (LEDs luminaries) which send the map information and path messages required to wayfinding. Data is encoded, modulated and converted into light signals emitted by the transmitters. Every mobile terminal is equipped with a receiver module for receiving the mapped information generated from the ceiling light and displays this information in the mobile terminal. The receiver module includes a photodetector based on a tandem a-SiC:H/a-Si:H pin/pin light controlled filter [4,5].

Communication system and cooperative localization

The system is composed by two modules: the transmitter and the receiver. The block diagram and the transmitter and receiver relative positions are presented in Figure 1.

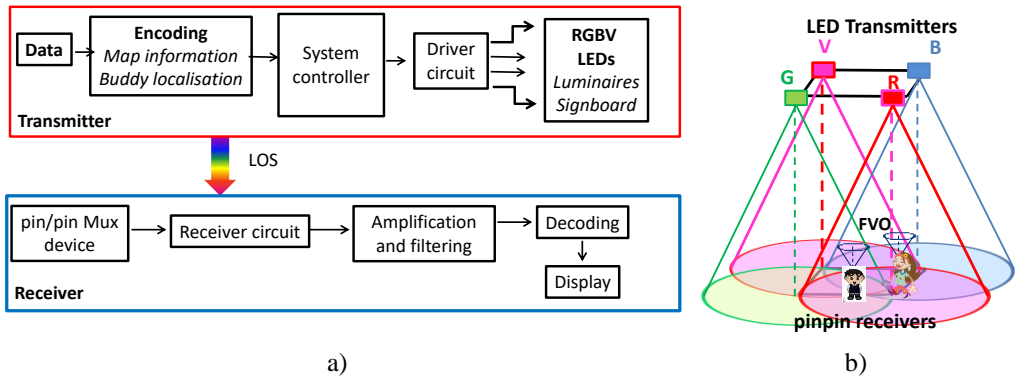
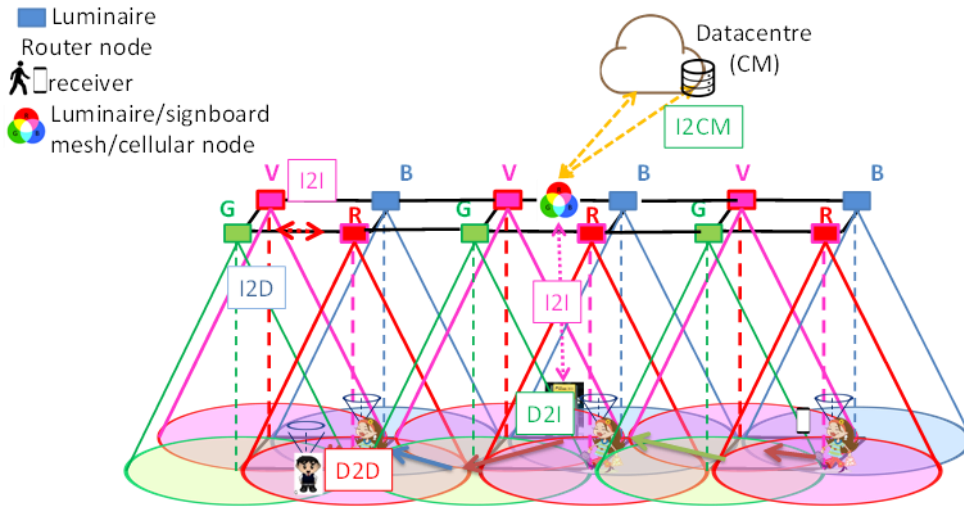


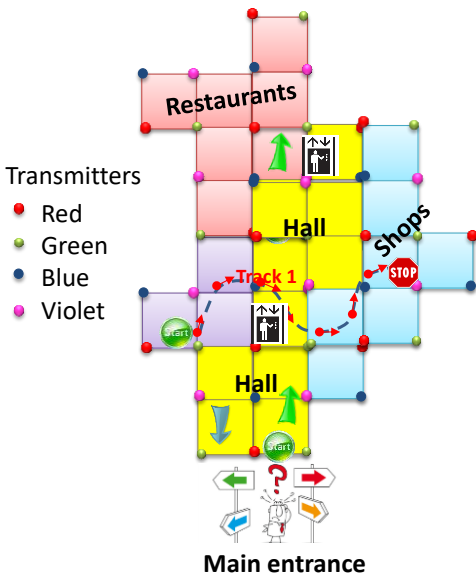
Figure 1. a) Block diagram and transmitters and b) receivers 3D relative positions.

The VLC photosensitive receiver is a double pin/pin photodetector based on a tandem heterostructure, p-i'-n/p-i-n sandwiched between two conductive transparent contacts. An On-Off Keying (OOK) modulation scheme was used to code the information. The obtained voltage is then processed, by using signal conditioning techniques (adaptive bandpass filtering and amplification, triggering and demultiplexing), until the data signal is reconstructed at the data processing unit (digital conversion, decoding and decision) [6,7].

A mesh cellular hybrid structure to create a gateway-less system is proposed in Figure 2a. This architecture consists of VLC-ready access equipment, nodes that provide the computing resources, end devices, and a controller that is in charge of receiving service requests and distributing tasks to fog nodes. This architecture has advantages when compared with other cloud centralized architectures. The proposed scenario is a multi-level building and is illustrated in Figure 2b. A user navigates from outdoor to indoor. It sends a request message to find the right track (D2I) and, in the available time, he adds customized points of interest (wayfinding services). The requested information (I2D) is sent by the emitters at the ceiling to its receiver.



a)



b)

Figure 2. a) Mesh and cellular hybrid architecture. b) Indoor layout and proposed scenario.

Multi-person cooperative localization

Bi-directional communication between VLC emitters and receivers is available through the control manager interconnected with a signboard receiver located at each unit cells. These communications channels constitute the uplink (D2I) and downlink channels (I2D) as exemplified in Figure 3a. Each user (D2I) sends to the local controller a “request” message with the pose, $q_i(t)$, (x,y,z, δ) , that gives his location and orientation, the user code (pin_i) and also adds its needs (code meeting and wayfinding data). For route coordination the CM, using the information of the network’s VLC location capability, sends a personalized “response” message to each client at the requested pose with his wayfinding needs. In Figure 3b, the MUX synchronized signals received by two users that have requested wayfinding services, at different times, are displayed.

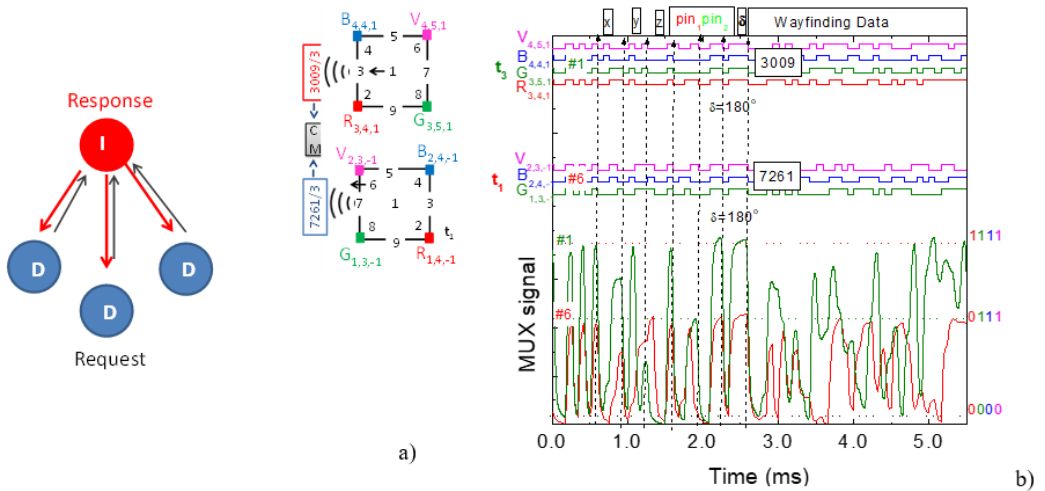


Figure 3 a) Communication channels established between the infrastructure and the users for geolocation and guidance. b) MUX/DEMUX signals assigned requests from two users (“3009” and “7261”) at different poses ($C_{4,4,1}$; #1W and $C_{2,3,1}$; #6 W) and in successive instants (t_1 and t_3).

In Figure 3b, the MUX synchronized signals received by two users are displayed. We have assumed that a user located at $C_{2,3,1}$, arrived first (t_1), auto-identified as (“7261”) and informed the controller of his intention to find a friend for a previously scheduled meeting (code 3). A buddy list is then generated and will include all the users who have the same meeting code. User “3009” arrives later

(t_3), sends the alert notification ($C_{4,4,1}; t_3$) to be triggered when his friend is in his floor vicinity, level 1, identifies himself (“3009”) and uses the same code (code 3), to track the best way to his meeting. After this request (t_3), the buddy finder service uses the location information from both user’ devices to determine the proximity of their owners ($q_{ij}(t)$) and sends a response message with the best route to the meeting.

Conclusions

A cooperative indoor VLC localization and navigation system based on ceiling landmark route instructions is proposed. In a multi-level building scenario, the architecture of the system based on a mesh cellular hybrid structure, and the protocol of communication were defined. Bi-directional communication between the infrastructure and the mobile receiver was analyzed. According to global results, the location of a mobile receiver is found in conjunction with data transmission. When applied to large buildings, the VLC system can assist users in finding the shortest path to their destination, guiding them on their way. VLC's dynamic LED-aided navigation system is designed to give users accurate route guidance and enable navigation and geotracking.

References

- [1] Ozgur, E., Dinc, E., and Akan, O. B., “Communicate to illuminate: State-of-the-art and research challenges for visible light communications,” *Physical Communication* 17 pp. 72–85, (2015).
- [2] O’Brien D. et al. “Indoor visible light communications: challenges and prospects,” *Proc. SPIE* 7091, 709106 (2008).
- [3] Vieira, M., Vieira, M. A., Louro, P., Vieira, P., and A. Fantoni, “Fine-grained indoor localization: optical sensing and detection,” *Proc. SPIE* 10680, Optical Sensing and Detection V, 106800H (9 May 2018).
- [4] Vieira, M. A., Vieira, M., Louro, P., Silva, V., Vieira, P., "Optical signal processing for indoor positioning using a-SiCH technology," *Opt. Eng.* 55 (10), 107105 (2016).
- [5] Vieira, M., Vieira, M.A., Louro, P., Fantoni, A. and Steiger, A.G., “Light-activated amplification in Si-C tandem devices: A capacitive active filter model,” *IEEE sensor journal*, 12, NO. 6, 1755-1762 (2012).
- [6] Vieira, M. A., Vieira, M., Silva, V., Louro, P., Costa, J., “Optical signal processing for data error detection and correction using a-SiCH technology,” *Phys. Status Solidi C* 12 (12), 1393–1400 (2015).
- [7] Vieira, M. A., Vieira, M., Louro, P., Vieira, P., "Bi-directional communication between infrastructures and vehicles through visible light," *Proc. SPIE* 11207, Fourth International Conference on Applications of Optics and Photonics, 112070C (3 October 2019).

P31 |

WIRELESS SENSOR NETWORK SYSTEM FOR LANDSLIDE MONITORING

Alison F. B. Wioppiold¹, Antonio C. Seabra²

^{1, 2} *Escola Politécnica da USP*

Av. Professor Luciano Gualberto, 158

05508-010 - São Paulo, São Paulo, Brazil

fabricio.bilha@usp.br

Abstract

Landslides are frequent problems in several regions of Brazil and the world, leaving thousands of people homeless and even causing deaths. The development of wireless sensor networks (WSNs) is an alternative for monitoring landslide risk areas. However, the system must have a low energy consumption, small size, and a low financial cost for its adoption and implementation by cities. Thus, this work aims to demonstrate, through the synthesis of commercial hardware circuits and the adoption of communication protocols available in the literature, a system concept capable of measuring the soil moisture and movement, operating off the energy grid and with wireless data transmission. Therefore, a systematic review of the literature is carried out to find technological evidence for the design of a prototype, followed by the performance of functional and energy autonomy tests to verify and measure the availability of the system. The results aim for low-energy, low-cost and small size characteristics, so the monitoring can be disseminated and the disasters avoided.

Introduction

The economic and social development, the demographic increase, and the growth of cities have modified several existing natural aspects, increasing the vulnerability and risk to which society is exposed. The occupation of hillsides, for example, makes the dwellings installed on them more exposed to the effects of adverse events, such as heavy rains, since there is a lack of adequate infrastructure for prevention or mitigation [1].

The continuous observation of potentially unstable areas, which may generate risk situations, is a process that is little used but of crucial importance. As a part of the disaster risk management process, systematic observation and measurement techniques can be combined with weather forecasting to strengthen the capacity to face the adverse impacts of natural disasters and the possibility of tragedies

occurring. It allows, for example, civil defense teams to reach risk locations in time to carry out the preventive removal of residents and forward them along safe routes, to previously established shelters or refuges, where they can stay harbored until the situation normalizes [2].

Within this context, the main objective of this work is to demonstrate a concept of a monitoring system capable of measuring ground acceleration movements, operating without the need for external energy (off the grid), and transmitting data without the need for wires. This concept focuses on a reduced area, an affordable cost for Brazilian municipalities, and energy efficiency, which are the main contributions of the research. In addition, it is intended to achieve the following specific objectives: (1) provide different messages about terrain conditions (risk levels); and (2) keep the system available for as long as possible even under unfavorable environmental conditions.

Materials and Methods

To satisfy all these objectives the method defined to meet the study stages is the Design Science Research Methodology (DSRM) [3]. This method consists of six procedural steps that aim to ensure the rigor and relevance of the research. Are they, in a nominal sequence: (1) problem identification and motivation, (2) define the objectives for a solution, (3) design and development, (4) demonstration, (5) evaluation, and (6) communication.

In step three of the DSRM method, there is the creation of an artifact that, in the present work, is composed of the node elements of the sensor network. This artifact takes as a starting point positive and negative aspects of previous works, whose monitoring techniques involve data collection on the surface and subsurface and data availability (almost) in real-time. Such nodes have in common four main components, namely: sensing/detection, data processing, data transmission, and energy supply [4]. With this in mind, the present work foresees the incorporation of two sensors for the conversion of physical phenomena into electrical signals for the design and development stage of the project. The first one is used to measure the node acceleration, an inertial measurement unit (IMU) based on microelectromechanical systems (Micro-Electro-Mechanical Systems – MEMS). This kind of sensor is relevant because most commercial options can switch the operation between passive and active modes. The capacity to switch to a passive mode and reduce power consumption when no activities are observed for a preset period can considerably optimize energy consumption [5]. Once it is possible to notice a terrain increase acceleration during and after the occurrence of more intense precipitations [6], at least a second sensor will be added to aid in

the detection of landslides by measuring the moisture content in the soil. The level considered alarming will depend, above all, on the type of soil and the slope of the terrain. Furthermore, the processing unit's main task is to control the sensors and execute communication protocols and basic signal processing algorithms on the data collected from the sensors. The communication unit, which is an integral part of the processing module, transmits the processed information to a server using GPRS communication service to transmit data. In addition, for devices to work for months or, ideally, years, without battery replacement, an intelligent power system is required, so an Energy Harvesting system is also integrated. It is very suitable for the target application due to the concept of wireless sensor networks with solar energy capture (Solar Energy Harvesting WSN - SEH-WSN) [7].

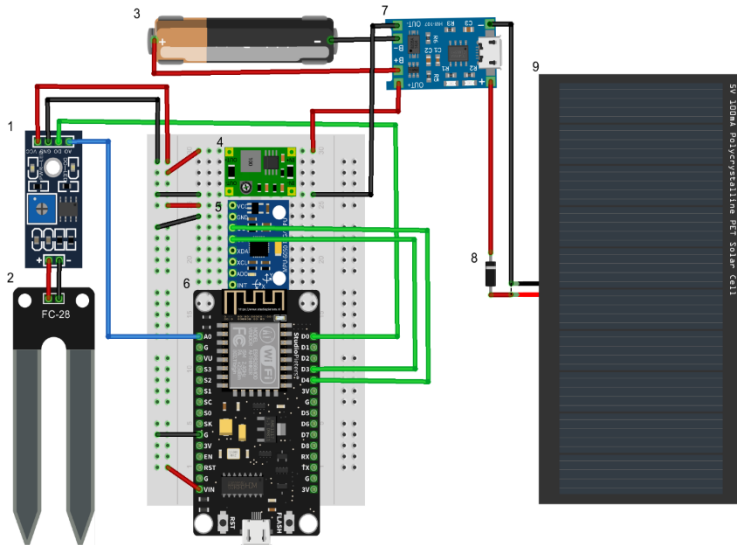


Figure 1 - Architecture of the preliminary sensing device.

Figure 1 shows the hardware components used in the prototype. Items 1 and 2 are responsible for sensing soil moisture and indicate values that must be compared to saturation parameters according to soil characteristics at the installation site (MAX485 RS485 transceiver and S-Soil MTEC-02A). Item number 5 is the IMU, which combines a 3-axis gyroscope, a 3-axis accelerometer, and a digital motion processor (MPU-6050). The number 6 is an inexpensive System-on-a-Chip (SoC) called ESP32 (T-Call V1.4 ESP32 wireless module SIM Card SIM800L). It

contains crucial elements for data processing and also transmission. The other items make up the SEH, converting solar energy into electrical energy and directing this to the lithium battery charger module and thus to the system as a whole (respectively in ascending order: 18650 battery lithium-ion battery, MT3608 step up power apply booster, TP4056 1A lithium battery charging module, 1N5819 diode, solar cell 5V 230mA 100.8x82.5).

Results

Both the hardware and software implementation of the devices must be optimized for cost, size, and power consumption. The proposed cost of each sensor element in the network is still fully accessible to small cities, with a value of fewer than 300 dollars per node.

For field applications, reduced power consumption is essential. Even without the support of the Energy Harvesting system, the equipment must have an efficient consumption to be able to work for long periods without running out of energy. At the moment, the system still has non-optimized energy consumption during the monitoring. Furthermore, tests are being conducted to check the need for sensor replications (two or more moisture sensors), and how the soil permeability index requires higher sampling frequency and, consequently, more data transmission. Refining the readings and improving the amount and frequency of information exchange during communication is essential to an effective energy scaling to the SEH.

Finally, the small size is a requirement that also involves the issue of cost, considering the large-scale implementation with logistical feasibility and even aspects of energy consumption. While the scale is not as energy-intensive as communication itself, it is equally relevant at the local level. The small dimensions of the node are currently one of the strongest points of the solution compared to other related works.

Conclusions

This work exposed the current development of a wireless sensor network for landslide monitoring. In this phase of architectural design and development, it is important to be aware of failures that may occur in field devices. As a result, aspects related to energy shortages and data transmission failure between nodes are being analyzed. It is necessary to give adequate attention during the conception and, later, in the validation of the network to fulfill the established objectives and still have the best possible levels of reliability and availability.

References

- [1] Capacitação em gestão de riscos / Centro Universitário de Estudos e Pesquisas sobre Desastres. 2 ed. Porto Alegre: Universidade Federal do Rio Grande do Sul, 2016.
- [2] Caracterização e tipologia de assentamentos precários: estudos de caso brasileiros / editores: Maria da Piedade Morais, Cleandro Krause, Vicente Correia Lima Neto. Brasília: Ipea, 2016.
- [3] Peffers, Ken & Tuunanen, Tuure & Rothenberger, Marcus & Chatterjee, S. A design science research methodology for information systems research. *Journal of Management Information Systems*, 2007, 24, pp. 45-77.
- [4] Jasmin, C. S. & Mathew, A. P. Power efficient comparator architecture for wireless sensor nodes. *International Conference on Emerging Technological Trends (ICETT)*, 2016, pp. 1-5.
- [5] Giri, P., Ng, K., & Phillips, W. Wireless Sensor Network System for Landslide Monitoring and Warning. *IEEE Transactions on Instrumentation and Measurement*, 2019, 68, pp. 1210-1220.
- [6] LEÃO, J. C. & SOUZA, P. H. D. Sistema inteligente de monitoramento de deslizamento de solos. *Revista Gestão e Sustentabilidade Ambiental*, 2018, 7, pp. 508-524.
- [7] Sharma, H. & Haque, A. & Jaffery, Z.A. Modeling and Optimisation of a Solar Energy Harvesting System for Wireless Sensor Network Nodes. *J. Sens. Actuator Netw*, 2018, 7, pp. 123-141.

SENSORES DE ONDAS ACÚSTICAS | SENSORES DE ONDAS ACÚSTICAS |
ACOUSTIC WAVE SENSORS

P32 |

AUTOMATION OF THE DROP-CASTING DEPOSITION METHOD FOR POLYMERIC SENSING FILMS OVER A QUARTZ CRYSTAL MICROBALANCE

A.I. Bravo-Sánchez¹, G. Beltrán-Pérez¹, J. Castillo-Mixcóatl¹, V. M. Altuzar-Aguilar¹ and S. Muñoz-Aguirre.^a

¹*Facultad de Ciencias Físico-Matemáticas, Benemérita Universidad Autónoma de Puebla, Av. San Claudio y 18 Sur, Col. San Manuel, CU. C.P. 72570, Puebla, México*

**e-mail: smunoz@fcfm.buap.mx*

Abstract

The creation of a sensor array with different films for the discrimination of volatile organic compounds (VOCs) with similar chemical structure, such as the alcohol family, is necessary mainly because of two factors: the first one is that the responses obtained when measuring these compounds are very similar, so that a way to distinguish the behavior would be very useful. The second factor is that these compounds, in high concentrations, can cause serious injury to humans. For the fabrication of gas sensors, the drop-casting method is very useful due to its simplicity, however, its main disadvantage is the low repeatability in the deposition of sensing films, therefore in this work we present the implementation of an automated drop-casting system. This system is essential to have a better control in the fabrication of sensors, since they need a very similar sensing film thickness and must be manufactured in the same way. As a result, an improvement in the sensor manufacturing process has been obtained, which is quantifiable, since for the manual drop-casting deposition method an average efficiency of 20 % was obtained, while for the automated system it was up to 80 %, for the case of an apiezon L polymeric film.

Introduction

An electronic nose consists of an array of electrochemical sensors with partial selectivity and an appropriate pattern recognition system, capable of recognizing simple or complex odors [1]. An important part of the electronic nose is the sensors array, which transforms a chemical input into an electrical signal, producing for each odor a unique response pattern, which is called the olfactory fingerprint [2]. Pattern recognition techniques are applied to this response to discriminate or classify the type of odor being analyzed [3]. There are several types of gas sensors that can compose the sensors array [4], in our case, quartz crystal microbalance (QCM) will be used, which are piezoelectric devices capable

of detecting small mass variations, they generate an output signal of frequency changes due to the mass loading effect [5].

For the sensors fabrication a sensing film is deposited over the QCM for the detection of a volatile organic compound (VOC), which is carried out by the process of adsorption, where atoms, molecules of gases or liquids are trapped or retained on a surface [6]; and absorption, which is the retention of a substance by the molecules of another, either in liquid or gaseous phase [7]. The sensitivity of these sensors is quite high, for instance, a 30 MHz QCM has a sensitivity of $1 \mu\text{g}/\text{cm}^2$. The gas detection is given by an amount of odorant molecules on the surface of the sensing film deposited over the QCM electrode, a fact that is manifested as a change in the resonant frequency of the sensor [8]. One of the main problems in the manual drop-casting deposition method for polymeric sensing films is the low reproducibility, therefore the automation is essential to have a better control in the sensors fabrication. In this work, the results of the automation are presented, showing an improvement in the sensing film deposition process.

Methods

A pipette (2-20 μL , BrandTech Scientific Inc.) was modified to be implemented in the automated deposition system; it was adjusted to deposit 2 μL drops. The support for the modified pipette was designed to achieve a mechanism that could allow to push the pipette plunger to a desired point and return to the starting position. For this, a linear actuator (Modified servo linear actuator, Disalvo, N.) [8] was used as a basis and a modification was performed to hold the pipette and avoid displacements. The linear actuator system works with a metal gear servomotor (MG995, Tower Pro Pte Ltd.) [9], which moves a toothed rail with limited movement in one direction (one degree freedom).

A circular base where the QCM crystal and the solution to be used could be placed, was modeled with the 3D Builder program (Microsoft) and printed in a 3D printer. Another linear actuator was fixed to this base to achieve a movement in one direction, this helped to simplify the movement of the crystal and the solution, achieving a better precision in the movement routine. A wooden base was fabricated to allow the automated pipette mounting together with the linear actuator that moves the QCM and the solution to be deposited (Figure 4a). This improved the repeatability in the deposition process of the sensing film solution over the QCM electrodes. Finally, an interface was developed in computer program to control the deposition system (Figure 4c).

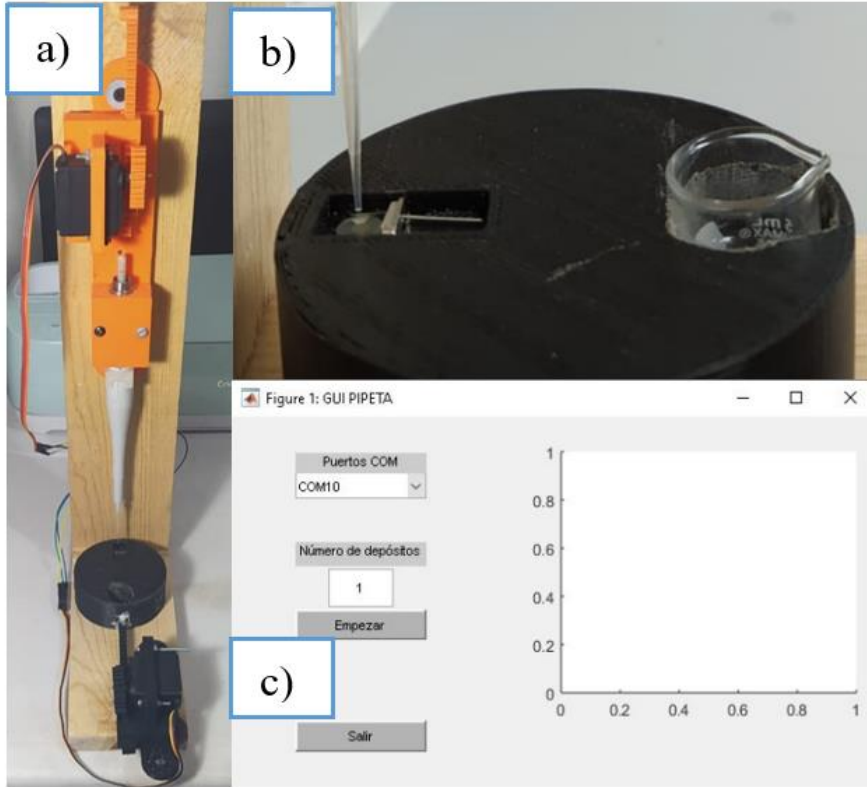


Figure 1. Automated deposition system.

A set of 8 crystals were deposited with ethyl cellulose and 17 crystals were deposited with apiezon L. Both are polymeric materials frequently used as sensing films in QCM gas sensors. The sensing film thickness (Δd) is estimated using Equation (1), where f_0 is the fundamental resonance frequency of the crystal, ρ_q is the density, μ_q is the shear modulus of the quartz material, ρ_f is the sensing film polymer density and Δf is the change in the fundamental resonance frequency of the crystal before and after the deposition.

(1)

$$\Delta d = -\frac{\sqrt{\rho_q \mu_q}}{2} \frac{\Delta f}{f_0^2 \rho_f}$$

Results

An analysis of the sensing film thickness was performed using the Gaussian distribution, the results are shown in Figure 2. This allows to locate the real thickness values (orange points) compared with the values given by the normal distribution (blue line). For ethyl cellulose, it can be seen in Figure 2a, that the values distributed around an average value of $0.126 \mu\text{m}$, with a deviation of $0.03 \mu\text{m}$, and there are 3 values out of the $\pm 1\sigma$ limits, which means that the sensors are out of the established range. However, more data are necessary to know how many sensors are still useful outside this σ criterion, since sensors above 1σ are still useful, while those below -1σ are not, due to their very low sensing film thickness. Similarly, for the apiezon L sensing film (Figure 2b), an average of $0.141 \mu\text{m}$ was obtained and it can be observed that there are 3 values out of the limits of $\pm 1\sigma$, which is equivalent to an 18% error in the thickness expected by the deposition system. From the 2 sets of sensing films deposition, a repeatability in desired thicknesses was observed, since for Ethyl cellulose a dispersion of 20% ($0.03 \mu\text{m}$) was found, while for Apiezon L such value was 14% ($0.02 \mu\text{m}$).

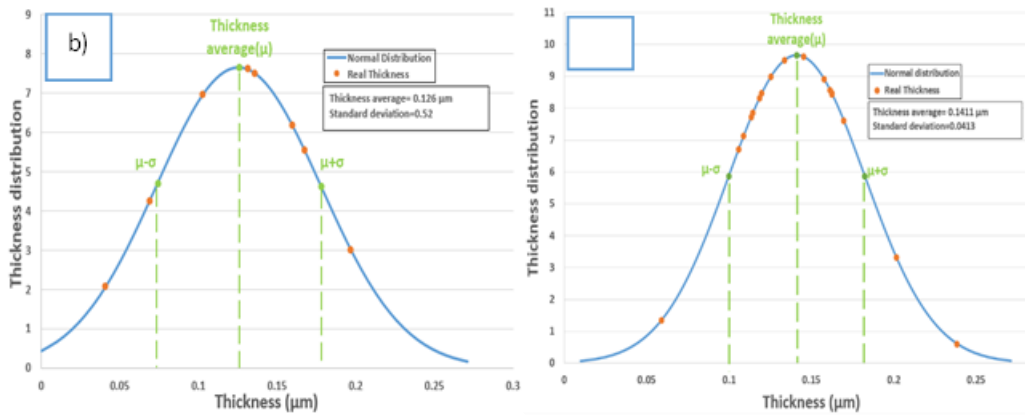


Figure 2. Gaussian distribution plots of thicknesses compared to the real thicknesses obtained.

A comparison with the manual drop-casting method was performed. For this case, an efficiency of the obtained sensing film thickness was as low as 20%, while for the automated drop-casting method, an efficiency of 82% was obtained for the case of apiezon L and 72% for ethyl cellulose.

Conclusions

The automation of the drop-casting deposition method has been successfully studied and developed, the characterization of the deposition method was performed with 2 polymers as sensing films, ethyl cellulose and apiezon L, for both films 2 μL were deposited per side of the QCM. For the ethyl cellulose film there was a variation between obtained thicknesses of 20% (0.03 μm) and for the apiezon L film there was a variation of 14% (0.02 μm). Similarly, with this automation, the percentage of efficiency in the gas sensor manufacturing process has increased, since the manual drop-casting method had a 20% efficiency and an improvement of up to 82% (apiezon L) has been achieved in obtaining functional gas sensors.

References

- [1] Gardner, J. W., Bartlett, P. N. *Electronic Noses: Principles and Applications*. Oxford University Press 1-5. Oxford USA, 1999.
- [2] Nagle, H. T., Gutierrez-Osuna, R., and Schiffman, S. S. (1998). The how and why of electronic noses. *IEEE spectrum*, 35(9), 22-31.
- [3] Muñoz-Aguirre, S., Yoshino, A., Nakamoto, T., Moriizumi, T. Odor approximation of fruit flavors using a QCM odor sensing system. *Sensors and Actuators B-chemical*, 123(2007), 1101-1106.
- [4] Liu, X., Cheng, S., Liu, H., Hu, S., Zhang, D., Ning, H. A Survey on Gas Sensing Technology. *Sensors*, 12(7) (2012), 9635–9665. «
- [5] Rodríguez-Torres, M., Altuzar, V., Mendoza-Barrera, C., Beltrán-Pérez, G., Castillo-Mixcóatl, J., & Muñoz-Aguirre, S. (2020). Discrimination Improvement of a Gas Sensors' Array Using High-Frequency Quartz Crystal Microbalance Coated with Polymeric Films. *Sensors*, 20(23), 6972.
- [6] Glossary – BrownfieldStsc. (n. d.). <https://Brownfieldstsc.Org/>. Retrieved on April 22, 2022, from: <https://brownfieldstsc.org/glossary?q=1>
- [7] Ucha, F. (2009). Absorción. Definición ABC. Retrieved on August 10, 2018, from: <https://www.definicionabc.com/general/absorcion.php>
- [8] DiSalvo, N. (2018). Modified servo linear actuator. MakerBot's Thingiverse. Retrieved April 24, 2022, from <https://www.thingiverse.com/thing:2765586>
- [9] MG995 – Tower Pro. (2014). Tower Pro Pte Ltd. Retrieved April 24, 2022, from: <https://www.towerpro.com.tw/product/mg995/>

Acknowledgments

CONACYT Project CB-2016-01, grant number 286647

P33 |

DEVELOPMENT OF A RELATIVE HUMIDITY PID CONTROL FOR THE CHARACTERIZATION OF GAS SENSORS BASED ON QUARTZ RESONATORS

O. Sosa-Ramos*, G. Beltrán-Pérez, J. Castillo-Mixcóatl, V. M. Altuzar-Aguilar,
S. Muñoz-Aguirre

Facultad de Ciencias Físico- Matemáticas, Benemérita Universidad Autónoma de Puebla, Av. San Claudio y 18 sur, Col. San Manuel, Ciudad Universitaria, Puebla, Pue C.P. 72570, México.

**e-mail: smunoz@fcfm.buap.mx*

Abstract

Gas sensors are a crucial part of systems called electronic noses. One type of sensor frequently used is the one based on quartz crystal microbalance (QCM). However, relative humidity (RH) is a parameter that affects the response of these sensors. To study this phenomenon, in the present work a PID (Proportional, Integral and Derivative) RH control system was developed. The system generates desired RH values in a range of 10% to 90%. The control minimizes the absolute error to a value of $\pm 1.5\%$. A gas sensor with an ethyl-cellulose sensing film was constructed using the drop-casting method. A dynamic system was used to obtain the measurements of the sensor responses to RH, in order to investigate its contribution to the response. The measurement and data acquisition system was automated by graphic interfaces in the computer and the use of microcontrollers. In the present work, the results of the RH- PID control system are shown, as well as the characterization of the QCM sensor response, as a function of humidity. It was found that such response increases linearly.

Introduction

The gas sensors used are based on quartz crystal microbalance (QCM) [1], that work under the piezoelectric effect. The electrodes on the quartz surface produce a surface wave when a potential is applied between them and in turn react with oscillations of certain frequencies [2]. The advantages of working with this type of sensors are the high responses when exposed to gas molecules, as well as their low cost. However, they also have responses to different parameters such as humidity, therefore it is necessary to perform a characterization considering all these factors. The operation principle of the sensors is that when the gas molecules are absorbed to the sensing film, they causes a shift in the QCM resonance frequency (ΔF), which is measured by a frequency meter [3-4].

Methods

The sensing film solution was prepared by mixing ethyl-cellulose with chloroform, where the concentration vary depending on the thickness required. The sensing films were deposited by the drop-casting method, that consists of using a graduated micropipette whit a 2 μ l solution, and it was deposited on both faces of the QCM.

The equation that relates the mass changes with frequency changes is the Sauerbray equation. (Equation 1)

$$\Delta f = \frac{-kf_0^2 \Delta m}{A} \quad (1)$$

where Δf is the change in the crystal oscillation frequency, f_0 is the fundamental oscillation frequency of the QCM, Δm is the mass change, k is a constant related to quartz characteristics and A is the area of the QCM electrode.

A PID controller is a simultaneous feedback control mechanism widely used in industrial control systems, it uses the error parameter, which is defined as the difference between the desired value and the actual value of the system to be controlled. Equation (2) represents the control signal [5-6].

$$u(t) = kpE(t) + ki \int E(t) dt + kd \frac{dE(t)}{dt} \quad (2)$$

where kp , ki , kd correspond to the specific gain parameters of the control system. The programming of the control mechanism was carried out with a microcontroller (PIC 18F4550, Microchip Inc.), and by means of the pulse width modulation (PWM) technique, the necessary energy was supplied to a commercial humidifier (Miniso) that generates water vapor at the rate necessary for the system to reach the desired humidity value.

For the characterization of the sensors in the dynamic sensor response measurement system, beside of the humidity controller, a chamber that generates vapors of volatile organic compounds at controlled concentrations was used. The sensor that measures the real-time response of temperature and RH is the DHT22 (Aosong Electronics Co.,Ltd), which has a sensitivity of 0.1% and an accuracy of $\pm 2\%$. In addition, there is a valve system to generate a gas step stimulus, which was applied to the sensor at a controlled temperature. Finally, the system uses an oscillator and a frequency meter that provides 5 data per second and a computer

where the data were stored for later analysis. The experimental setup is shown in Fig. 1 [3].

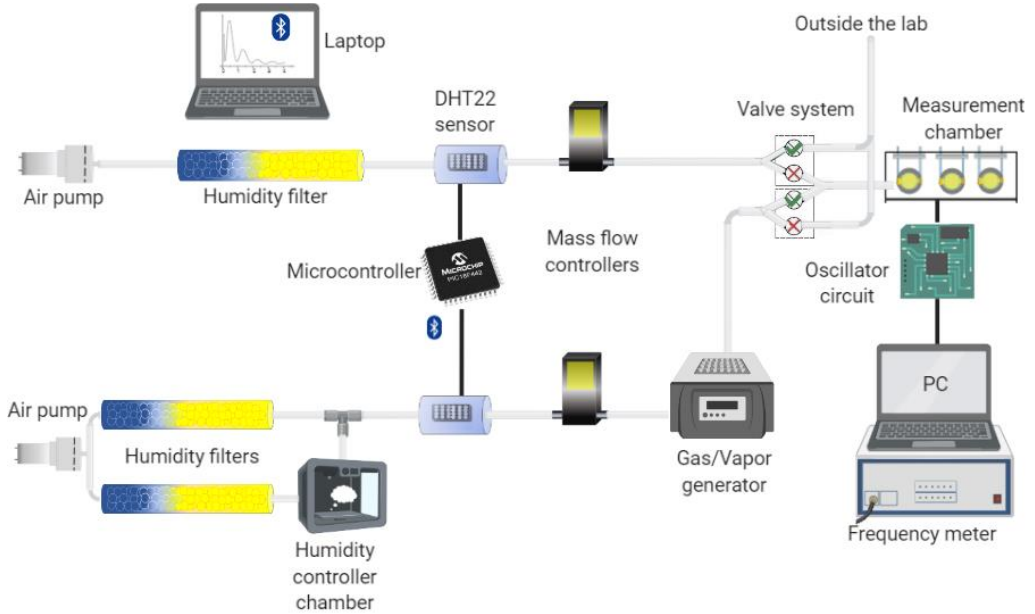


Fig. 1 Experimental Setup.

Results

The response of the RH control system is shown in Fig. 2a, it is observed that the control range goes from 10% to 90% RH, moreover in values lower or equal to the ambient humidity it was observed that the stability of the control is better, while for higher values it was observed that there are fluctuations in the desired humidity value. Averaging these values in the desired RH steps, an absolute error $\approx 1.5\%$ was achieved.

The Fig. 2b shows the response of the QCM sensor with an ethyl-cellulose film to humidity changes in the range of 20% to 80% RH, which is where the highest stability was reached for the measurements. The baseline frequency from which the sensor started was at 10% RH at 25°C. It can be noted that the response increases as the humidity increases, several measurements were made and after performing fitting methods, it was found that the sensor response increases linearly in function of RH changes, as is observed in the inset of the Fig. 2b.

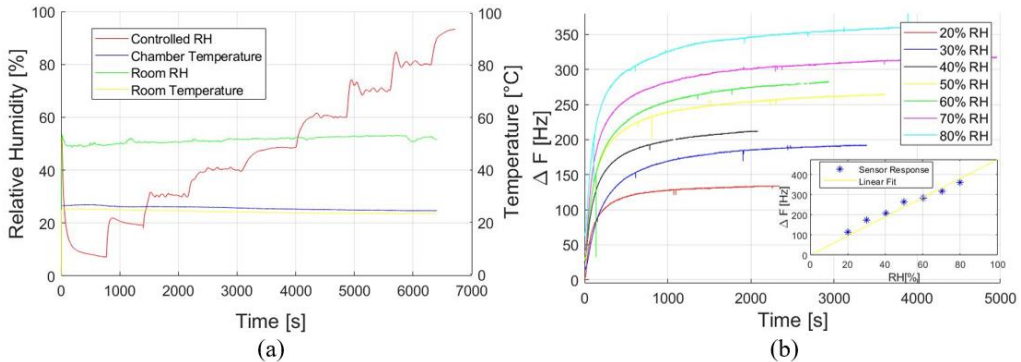


Fig. 2 (a) Relative humidity control results (10%-90%). (b) Sensor responses to different RH values.

Conclusions

The RH control system works for the purposes of performing characterization of different QCM sensors with different films sensitive to different compounds such as some VOCs. The sensing films deposited by drop-casting method are functional and show high effectiveness in detecting different compounds. Experimental results show that the response of the sensor with ethyl cellulose film increases linearly as the humidity increases, it is necessary to perform measurements with other sensing films.

References

- [1] Gardner, J. W. and Bartlett, P. N. *Electronic Noses, Principles and Applications*. Oxford Science Publication, 1999.
- [2] Rodríguez-Torres, M.; Altuzar, V.; Mendoza-Barrera, C.; Beltrán-Pérez, G.; Castillo-Mixcóatl, J.; Muñoz-Aguirre, S. Discrimination Improvement of a Gas Sensors' Array Using High-Frequency Quartz Crystal Microbalance Coated with Polymeric Films. *Sensors* 2020, 20, 6972.
- [3] Osorio-Arrieta, D. L., Muñoz-Mata, J. L., Beltrán-Pérez, G., Castillo-Mixcóatl, J., Mendoza-Barrera, C. O., Altuzar-Aguilar, V., Muñoz-Aguirre, S. Reduction of the Measurement Time by the Prediction of the Steady-State Response for Quartz Crystal Microbalance Gas Sensors. *Sensors*, 18(8) (2018) 2475.
- [4] Muñoz-Aguirre, S., López-Casique, A., Alcántara-Iniesta, S., Castillo-Mixcóatl, J., Beltrán-Pérez, G., y Muñoz-Aguirre, N. High-resolution gas/odor sensors using high-frequency quartz crystal microbalance. *Sensors and Materials*, 26(3) (2014) 131-136.
- [5] Ogata, K. (1998). *Ingeniería De Control Moderna* (3a. Ed.). Madrid: Prentice Hall Hispanoamericana.
- [6] FRANKLIN, G.F.; POWELL, J.D., Emami-Naeini, A., *Digital Control of Dynamical Systems*, 3rd Ed (1998). Ellis-Kagle Press, Half Moon Bay, CA ISBN 978-0-9791226-1-3.

Acknowledgments

CONACYT Project CB-2016-01, grant number 286647

P34 |

RESPONSE MEASUREMENT ACCELERATION OF QCM-BASED GAS SENSORS USING THE TRANSIENT RESPONSE

M.A. Moreno-Acosta¹, G. Beltrán-Pérez², J. Castillo-Mixcóatl², S. Muñoz-Aguirre^a

¹ *Facultad de Ciencias Físico-Matemáticas, Benemérita Universidad Autónoma de Puebla, Av. San Claudio y 18 Sur, Col. San Manuel, CU. C.P. 72570, Puebla, México.*

e-mail: smunoz@fcfm.buap.mx

Introduction

The reduction of the measurement time of any electronic device for gas detection is essential, since certain gases or substances become harmful to human health so that reducing the measurement time will allow us to develop faster and more efficient systems for the detection, recognition and classification of gases. Therefore, there is the need to develop a device that emulates the process of identification of aromas which is known as electronic nose [1-2]. A fundamental part of electronic noses is the gas sensors array used for detection, in this case specifically gas sensors based on quartz crystal microbalance (QCM) were used. Their principle of operation is based on the adsorption of gas molecules on the sensing film, which generates a decrease in the resonance frequency [3]. The sensor response measurement time is currently a major problem for gas detection as these sensors have a relatively slow response, on the order of tens of minutes. Therefore, reducing the response time of gas sensors is important since it allows the development of faster and more efficient gas detection and classification systems. In this work we propose to reduce the measurement time of these gas sensors by the prediction of the steady state response from the transient one using a successive fitting approach [4-5] to a bi-exponential model.

Methods

Four QCM-based sensors (AT cut, 12 MHz) coated with an ethyl cellulose sensing film with different thicknesses were used for the present study. A dynamic system was used to measure the sensor response to ethanol for different concentrations in the range of 721 to 1737 ppm. The measured responses were used to perform an analysis using the method described in the next section.

Method of successive fittings

The study of the transient response of gas sensors based on QCM consists of obtaining the information through the rise and recovery of the response curve. The sensor response model is described by a bi-exponential model (equation (1)),

which is the sum of two exponentials with different time constants.

$$y = C - (k_1 e^{-\frac{t}{\tau_1}} + k_2 e^{-\frac{t}{\tau_2}}) \quad (1)$$

where C is the parameter associated to the steady state response, k_1 and k_2 are constants indicating the amplitude of the exponentials, τ_1 and τ_2 are time constants. Once the experimental response is obtained, the data are processed and the transient response is analyzed, the first experimental points are taken, fitting point by point (successive fittings) to the bi-exponential model equation (1) of the sensor response until a prediction of the steady state response value is obtained without having to reach such state. For this, a computer program implementing two nonlinear least squares regression methods, the Gauss-Newton method and the Levenberg-Marquardt method, were used.

The implemented algorithm starts loading the response data (y,t) where y is the frequency shift value in hertz and t is the time in seconds. First of all an initial estimation of the parameters C , k_1 , k_2 , τ_1 and τ_2 is needed as well as the first partial derivatives of the objective function (bi-exponential model) for each of the parameters. Then the technique to be performed is chosen either the Gauss-Newton or the Levenberg-Marquardt one. As convergence criteria it was proposed to obtain a correlation coefficient between the data and the curve fitting larger than 0.8 or to reach a maximum number of 20 iterations. The fitting process is performed for the first data point and the program tests if the criteria are reached at each iteration. If the correlation criteria is reached, it is assumed that the algorithm converged, else, the algorithm waits for the 20 iterations to finish the fitting process, even though in this case a good fitting could not be attained. After that, the obtained parameter values are stored and the next data is acquired to start a new fitting process, now with $n + 1$ data. The successive fitting processes are repeated until a stable value of C parameter is obtained. At the end, the data are displayed, and the experimental response is plotted against the fitting obtained with the new values.

Results

Four sensors were fabricated with different thicknesses of an ethyl cellulose sensing film which were exposed to different ethanol concentrations in a dynamic system, in total 16 experimental responses were obtained (Figure 1a). The time evolution of the C parameter was analyzed since this parameter is associated with the steady state response, at the beginning the fitting was not good enough to describe the sensor curve as observed for both Gauss-Newton (Figure 1b) and

Levenberg-Marquardt (Figure 1c) methods. Before 15 seconds the values have high fluctuations, however, after 15 seconds they quickly stabilize and reach a stable value implying that it is possible to predict the steady state value from an analysis of the transient response. In (Figure 1d) the comparison of the value calculated from the method at 15 seconds and the measured response value at the end of the steady state determined from the experimental data for both methods is shown. A linear fitting was performed, obtaining a slope value of approximately 1 with a correlation coefficient of 0.9999. This indicates that at the second 15 it is possible to know in advance what will be the final steady state response value without the need to wait to have the complete experimental response, i.e. a prediction of the steady state response was achieved. With the prediction a reduction in the measurement time of the sensors of about 90% was achieved.

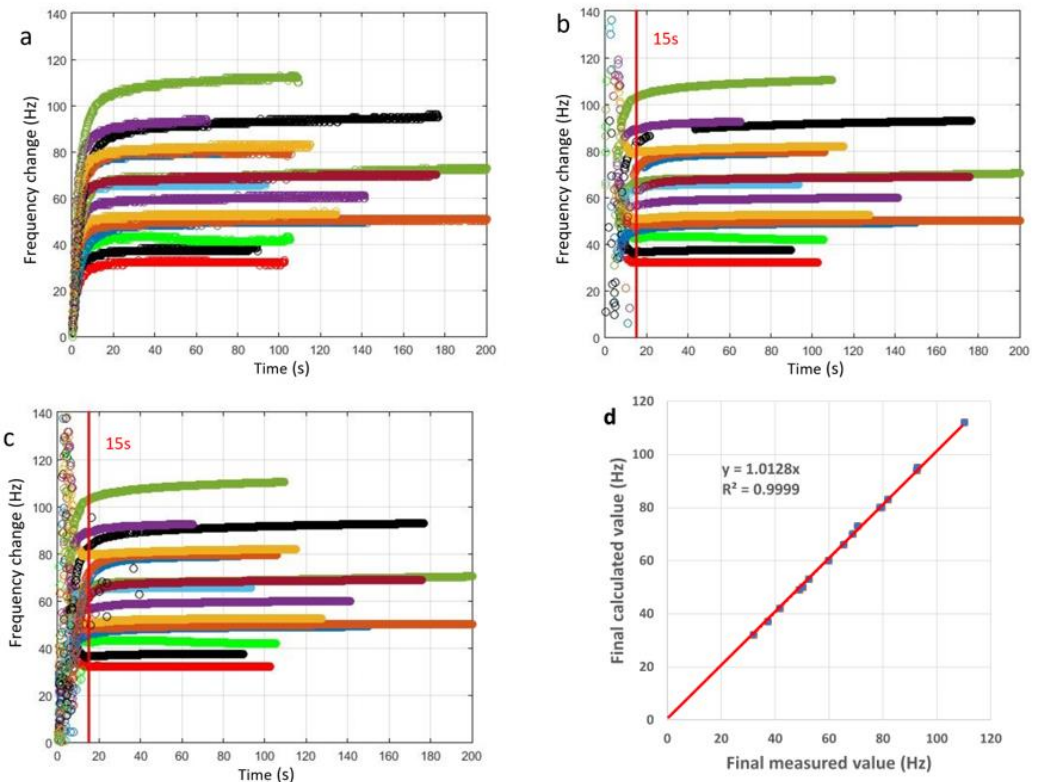


Figure 1. Results obtained. a) Response of the 4 sensors obtained experimentally for different ethanol concentrations. b) Evolution of parameter C of the 4 sensors and trend in 15s, using the Gauss-Newton method. c) Evolution of parameter C of the 4 sensors and trend in 15s, using the Levenberg-Marquardt method. d) Comparison between the value measured experimentally and that obtained by the fitting at 15s.

Conclusions.

In this work, the analysis of the transient response of 12 MHz QCM based gas sensor, was performed in order to predict the steady-state response from the transient one and to reduce the response measurement time. A computer program was implemented using two nonlinear least squares regression methods, the Gauss-Newton and Levenberg-Marquardt method for the analysis of the sensor responses. The parameter corresponding to the magnitude of the steady state response (C parameter) stabilized quickly after 15 seconds with correlation values higher than 0.99. The prediction of the response using the method of successive fittings allows obtaining a final response value in an average of 10% of the time it takes to reach the steady state response.

References.

- [1] I. Moreno, R. Caballero, R. Galán, F. Matía, A. Jiménez. La Nariz Electrónica: Estado del Arte. *Revista Iberoamericana de Automática e Informática Industrial*, 6 (2009) 76-91.
- [2] H. Troy Nagle, S. S. Schiffman, R. Gutierrez-Osuna. The How and Why of Electronic Noses. *IEEE Spectrum*, 9 (1998) 22-34.
- [3] M. Rodríguez-Torres, V. Altuzar, C. Mendoza-Barrera, G. Beltrán-Pérez, J. Castillo-Mixcóatl, S. Muñoz-Aguirre. Discrimination Improvement of a Gas Sensors' Array Using High-Frequency Quartz Crystal Microbalance Coated with Polymeric Films. *Sensors*, 6972 (2020).
- [4] S. Muñoz-Aguirre, T. Nakamoto, and T. Moriizumi, Study of transient response of QCM odor/gas sensors coated with calixarene LB films, *Trans. IEE Jpn.* 119-E (1999) 430-435.
- [5] D.L. Osorio-Arrieta, J.L. Muñoz-Mata, G. Beltrán-Pérez, J. Castillo-Mixcóatl, C. Mendoza-Barrera, V. Altuzar, S. Muñoz-Aguirre. Reduction of the measurement time by the prediction of the steady-state response for quartz crystal microbalance gas sensors, *Sensors*, 2475 (2018).

Acknowledgment.

CONACYT Project CB-2016-01, grant number 286647.

APLICAÇÕES AO MEIO AMBIENTE E AGRICULTURA. POUPANÇA DE ENERGIA | APLICACIONES AL MEDIO AMBIENTE Y A LA AGRICULTURA. AHORRO DE ENERGÍA | APPLICATIONS TO THE ENVIRONMENT AND AGRICULTURE. ENERGY SAVING

O27 |

PLASTIC-OPTICAL-FIBER-BASED SOLAR TRACKER DEVELOPMENT APPLIED FOR AMBIENCES ILLUMINATION

Alexandre Silva Allil^{1*}, Vinicius Ferreira Neves¹, Yan Guilherme Cirto¹, Luiza Costa Pacheco¹, Maria Eduarda Alves Esteves², Regina Célia da Silva Barros Allil¹ and Marcelo Martins Werneck¹

¹ *Photonics and Instrumentation Laboratory, Electrical Engineering Program, Alberto Luiz Coimbra Institute for Graduate Studies and Research in Engineering, Universidade Federal do Rio de Janeiro (PEE/COPPE/UFRJ)*

² *Postgraduate in Computational Biology and Systems (PGBCS), Oswaldo Cruz Institute (IOC/Fiocruz)*

**e-mail: allil@poli.ufrj.br*

Introduction

Considering a large territorial extension and privileged location on the globe, Brazil becomes one of the most privileged countries in the solar incidence in the world. Despite this potential, we still have to invest a lot to be able to effectively take advantage of it. Brazil has in its energy matrix only 1.27% of solar energy, which should be increased because some projects are being implemented in the area, mainly in the Northeast [1]. We currently have about 7439 projects in operation, and for the next few years another 200 are under construction or increasing our capacity by another 20GW and another 391 foreseen for its activities started. As a result, solar energy ceased to contribute only 1.27% to 17.7% of the energy generated in Brazil when all these saved projects ended [2]. Solar energy has attracted attention because it is free, nonpolluting and abundant worldwide. This not only demonstrates its capacity, but the future for humanity, and consequently Brazil, is on its way. As a result, several universities and companies have invested in new technologies for the reuse of solar energy not only through solar panels. These technologies include the solar tracker, which today is used in large power plants to keep the panel perpendicular to the Sun and also in technologies that use fiber optics, mirrors and lenses to track the Sun and guide light into indoor ambiences at low costs of electricity. If we take into consideration that in times of great competition, a company that invests in these technologies may have substantially lower energy costs making its products cheaper and more competitive in the market, we are thus ensuring cheaper products for the population as well as generating electricity employment and profit [3].

This project aims to develop a method that reuses sunlight for confined environments and can be used to efficiently position solar panels, optimize biofuel

production, among others. The Solar Tracker, as its name suggests, is able to predict the position of the highest incidence of sunlight in order to optimize the capture of natural light through optical fibers for indoors illumination and reduce energy consumption.

Methods

The first of the project was to build a PI controller for the solar tracker coupled to a DC motor. With this idea, the block diagram of the project would initially be presented as Figure 1.

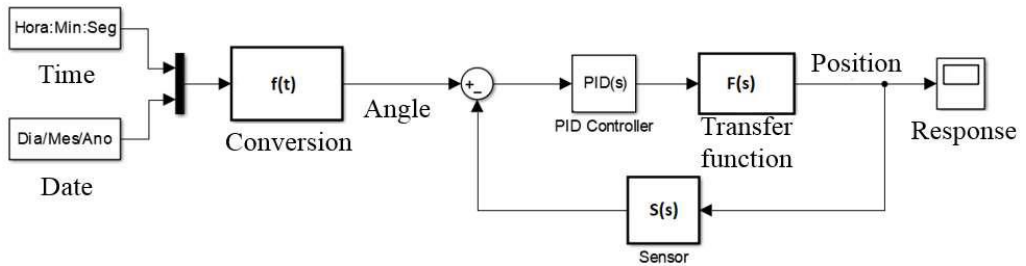


Figure 1 - Proposed block diagram.

This would be the ideal world, where from plant data you can measure the impulse response and use the output signal to perform PID calibration. However, unfortunately, a problem was responsible for not guaranteeing a greater simplicity of the system, causing it to not have the desired balance. This problem causes the engine to be stopped in one position to spin a little further at an indefinite displacement but within the clearance size. Since the desired position is never reached, this also causes the PI control to readjust the position causing unwanted system swings. As a result, the system oscillates indefinitely, moving at unstable equilibrium points [4].

In order to measure the tracker position throughout the day an electronic instrumentation was applied on the system. Two sensors (accelerometer and gyroscope) were employed.

As it can be seen in Figure 2, the Tracker is made up of several parts where the prototype was made to be lightweight and suffer little from weathering.

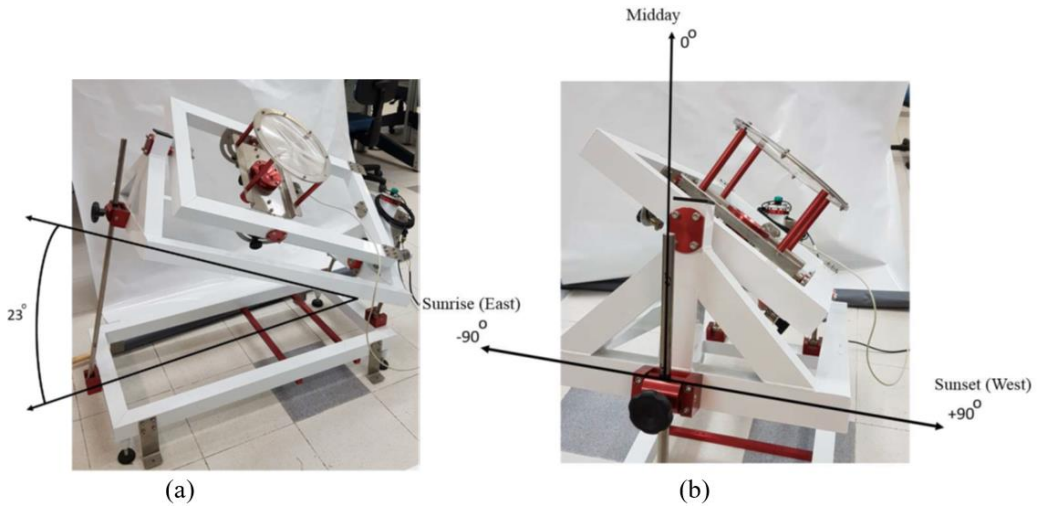
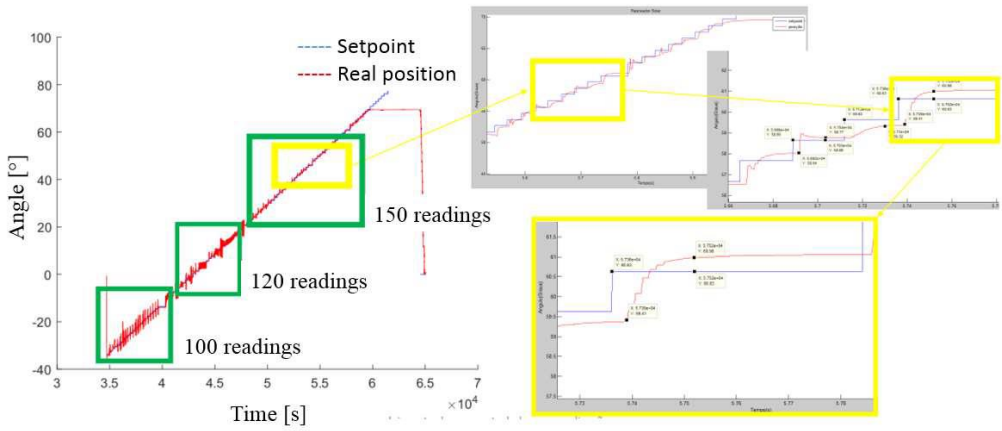


Figure 2 – (a) Angulation with respect to latitude. (b) presents the tracking angles described by the prototype during the day.

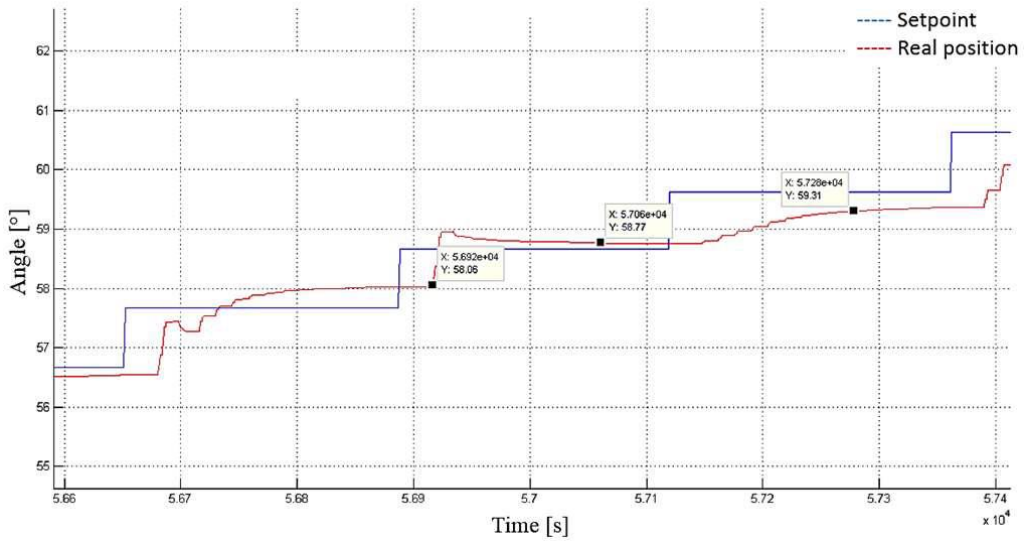
The angle of 23° is due to the current position on the globe and should be calibrated to the latitude of the globe where the equipment will be installed. The tracker is also made up with a 30-centimeter Fresnel lens; With it, the Sun's rays converge to a focal point that has an infrared filter and prevents damage due to energy from infrared radiation in the optical fiber bundle.

Results

The Figure 3 presents the data measured over a day of tracking. One can see from point 60x104 the tracker signal returns to zero while the reference keeps moving forward, because at very high angles it is already night and the amount of sunlight no longer becomes expressive. Therefore, for safety, we choose to send the tracker to the starting point in order to start a new cycle the next day, again.



(a)



(b)

Figure 3 (a) The plant behaves appropriately to the project needs (150 readings). (b) Solar tracker response (a small zoom from Figure 3 (a)).

Conclusion

This letter presented the development of a solar tracker. The control system consisted of Microcontrollers (Esp-32 and arduino) to manage all project components, which are stored by means of a Real Time Clock (RTC) and local geographic information such as latitude, longitude and fixed time to calculate the best angular position. The project has as its main challenge the control of the DC motor, which effectively performs precise angular displacements and self-adjust the best solar position periodically during the day. The system presents three degrees of freedom. The DC motor held responsible for tracking the Sun controls the declination angle; the azimuth angle and the latitude angle are manually adjusted. As long as the system keeps at the same position around the globe, the latitude obviously does not change.

The amount of collected power during a sunny day is approximately 1kW/m^2 . This power ratio provides a huge illumination at the end of our optical fibers bundle. Our system provides an illumination around 600 lux, which attends the Brazilian standards (ABNT NBR 5413) of illumination for indoor ambiances.

We developed a library to calculate the sunrise and sunset time, for each day of the year. With this information, we can calculate the duration of the day. Additionally, we know that the Earth turns 360 degrees over 24 hours around the Sun, which gives the correct velocity that our DC motor must attend from the sunrise time till the sunset time.

References

- [1] SOLAR, P. “Quanto custa a energia solar fotovoltaica”, jan. 2019.
- [2] RODRIGUES, I. V. “Sistema de monitoramento remoto de um rastreador solar”,
- [3] DORF, R. C., BISHOP, R. H. Sistema de Controle Moderno. 8 ed. Rio de Janeiro, LTC Editora, 2001.
- [4] NARENDRA, KUMPATI S. ANNASWAMY, A. M. Stable Adaptive Systems-dover Publication. 1 ed. Minnesota, Englewood Cliffs, 2012.

Acknowledgments

Special acknowledgment to FAPERJ (Fundação de Amparo à Pesquisa do Estado do Rio de Janeiro) which has been sponsoring the project since its beginning with scholarships and technical supports.

O28 |

AVEIRO STEAM CITY PROJECT: A GOOD PRACTICE WITH URBAN AIR QUALITY SENSORS NETWORK

D. Graça^a, J. Reis^a, V. Rodrigues^a, M. Rebelo^a, A. Monteiro^a, A. Miranda^a, M. Lopes^a,
C. Borrego^a

^a *CESAM & Department of Environment and Planning, University of Aveiro, 3810-193 Aveiro, Portugal*

**e-mail: dfgraca@ua.pt*

Introduction

Air pollution is the single largest environmental health risk in Europe leading to the loss of healthy years of life and premature deaths. According to the World Health Organization (WHO), in 2019, 91% of the world's population lived in places where WHO air quality guidelines were not met [1], [2].

Urban air pollution is currently a critical problem, causing numerous negative impacts on human health. Monitoring the concentration of air pollutants is an important task in managing urban air quality. In large urban areas of developed countries, there are public and even private monitoring networks that monitor air quality to verify compliance with legislation, to support scientific research and provide air quality information to citizens [3].

Rapid technological development today allows the production of sensors and electronic components with smaller dimensions and is less expensive than reference equipment. These factors allow the easy incorporation of these sensors in small monitoring stations that require little energy to operate and can be installed in greater numbers and locations and thus increase spatial coverage, allowing a mapping with a higher spatial resolution of air quality in urban areas, validation of atmospheric dispersion models, providing valuable datasets to apply data fusion and data assimilation techniques, and evaluation of population exposure. There are also disadvantages in the use of these sensors, including the fact that they are less accurate than reference methods despite responding well to adequate humidity, temperature and atmospheric pressure conditions [3], [4].

This study aims to analyze air quality (time and spatial distribution) in the city of Aveiro (Portugal) using data from a sensor network installed under the Aveiro STEAM City project funded by the European Union through the Urban Innovative Actions program. This project aims to study the impact of transport

management and urban planning on air and noise quality in the city of Aveiro, providing information to citizens in real-time, through an online digital platform.

Methods

Under the Aveiro STEAM City project, 9 air quality and noise monitoring stations, complemented by two meteorological stations, were installed at various strategic points at variable heights in buildings of the urban network of the city of Aveiro (figure 2), affected by different types of pollutant emission sources such as traffic congestion areas and residential areas.

The air quality monitoring stations are composed of sensors of PM10, PM2.5, NO₂, O₃, CO, the main air pollutants, and additionally CO₂, which will not be studied because it doesn't have relevance in outdoor air quality. Before being installed in monitoring locations, the gas sensors are calibrated with reference gases. In addition, all sensors were subjected to outdoor ambient air conditions and compared with measurements from reference instruments placed outside at a short distance, in order to validate the performance of the sensors. In addition, the signal from the sensors can be adjusted by wire, when a drift occurs. To stabilize sensor measurement conditions, air quality monitoring stations also have air conditioning systems and air pumped with a regular flow of air through an inlet.

Data communication and transmission are performed through transmission systems that use Ethernet and LoRaWAN technology in a modular way and support other possible communication modules for WiFi, 3G/4G or other technologies.

In this study, the analyzed data comprise the period from June 1, 2020, to March 31, 2021. A process of data calibration and validation was applied, considering the problems at the monitoring stations and the data collection efficiency requirements of Directive 2008/50/EC.

Results

Figure 1 shows daily, weekly and seasonal variations of PM10 and PM2.5 and it is possible to verify that the concentrations of the stations follow similar patterns. The concentrations of PM10, PM2.5 and CO are significantly higher at night, mainly in winter, which may be due to residential combustion (e.g., wood burning for residential heating). The station located at "Museu Arte Nova" stands out for having two peaks of high concentration of these pollutants in summer during the period between 11am and 7pm. These are most likely due to specific cooking patterns (e.g., grill) in the restaurants located a few meters from this station. Over

the weekend the concentrations of these pollutants tend to increase in winter (which may be linked with the fact that more people spend their time at home making use of residential combustion) and a tendency to decrease in the summer. For NO₂, two periods with higher concentrations during the day are visible, at 8 am and 6 pm, coincident with the commuting periods (higher road traffic levels). In addition, all the stations register lower concentrations during weekends. O₃ concentrations present very similar patterns in all the stations with the maximum concentrations being measured in the period of higher solar radiation levels.

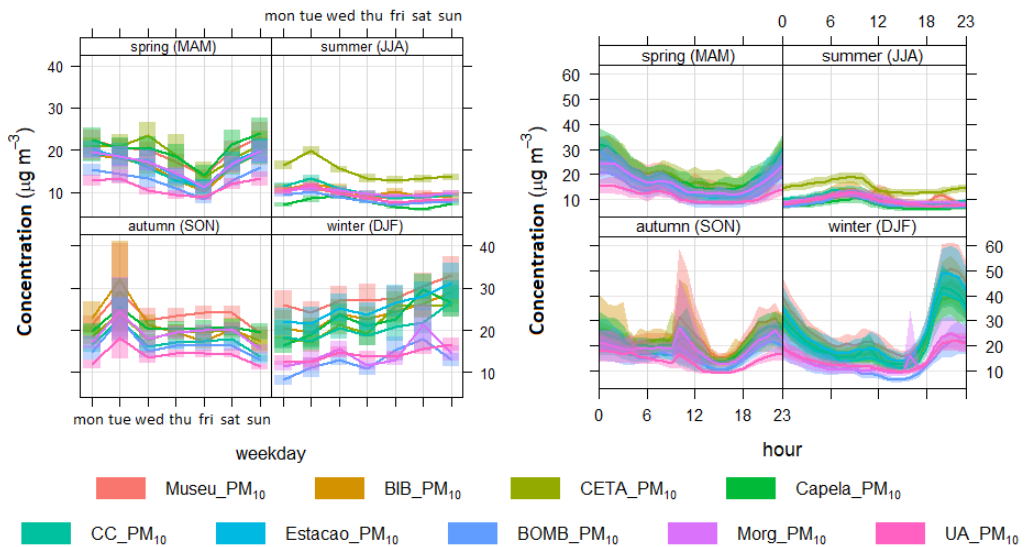


Figure 1. Weekly (left) and hourly (right) variation of PM10 for all monitoring stations for each season.

Figure 2 shows the air quality indexes calculated for each monitoring station. The air quality in Aveiro is generally good (dark green) during most of the analysed period. However, there are periods when air quality is classified as “medium” and in a few periods where it is classified as “weak” and “bad” quality. For instance, for the monitoring station located at Biblioteca Municipal the calculated air quality index shows 28% of very good, 47% of good, 14% of medium, 7% of weak, 2% of bad and 2% with no data air quality. The "weak" and "bad" air quality ratings are mainly due to high particle concentrations (PM10 and PM2.5) arising

from the two episodes of pollution, the Albergaria-a-Velha wildfire in September and residential combustion in winter.

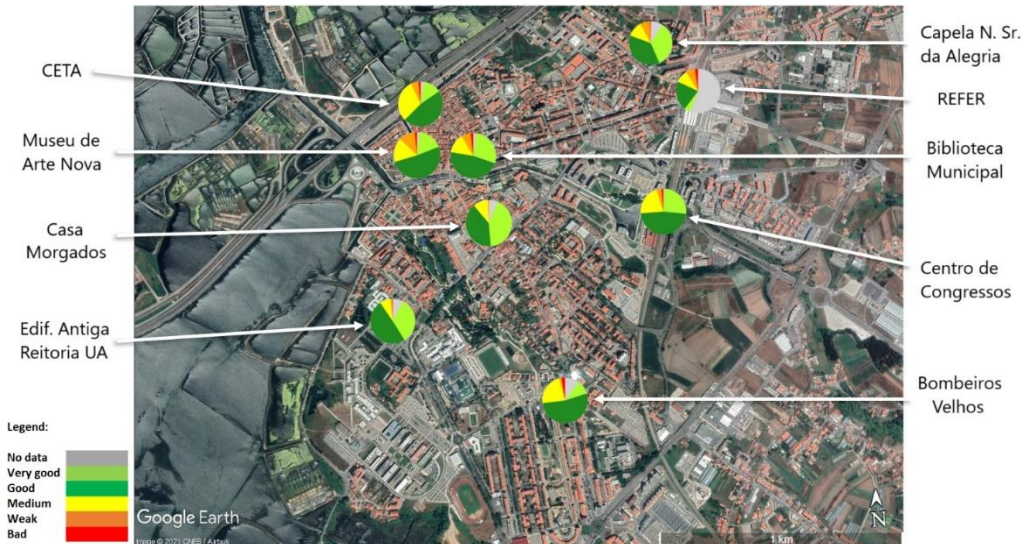


Figure 2. Distribution of frequencies of the air quality indexes each day for the overall period between June 2020 and March 2021 in every STEAM City station in the city of Aveiro.

Conclusions

The sensors network installed within the city of Aveiro allows the evaluation of the air quality in the city, which is globally good, but pollution episodes – associated to specific meteorological conditions, city events or residential practices - may occur. Due to the good number of stations and its spatial distribution, it was possible to identify which areas of the city were most affected by the identified pollution episodes and explore the local associated emission sources. This network provides policy makers and citizens with important information during critical pollution events, enabling them to act accordingly and alert the population to the risk of exposure. The analysis of long data series is an important support for the definition of measures to improve air quality and overall well-being.

References

- [1] WHO, “Ambient (outdoor) air pollution,” 2021. [https://www.who.int/en/news-room/fact-sheets/detail/ambient-\(outdoor\)-air-quality-and-health](https://www.who.int/en/news-room/fact-sheets/detail/ambient-(outdoor)-air-quality-and-health).
- [2] EEA, “Europe’s air quality status 2022,” 2022. <https://www.eea.europa.eu/publications/status-of-air-quality-in-Europe-2022/europes-air-quality-status-2022> (accessed Apr. 01, 2022).
- [3] S. Munir, M. Mayfield, D. Coca, and S. A. Jubb, “Structuring an integrated air quality monitoring network in large urban areas – Discussing the purpose, criteria and deployment strategy,” *Atmos. Environ.* X, vol. 2, no. March, p. 100027, Apr. 2019.
- [4] F. Karagulian, M. Gerboles, M. Barbieri, A. Kotsev, F. Lagler, and A. Borowiak, Review of sensors for air quality monitoring. 2019.

Acknowledgments

A special thanks is given to give to European Union Regional Development Fund within the framework of the European Urban Innovative Actions program and to FCT/MCTES for the financial support to CESAM (UIDP/50017/2020+UIDB/50017/2020+LA/P/0094/2020), through national funds.

O29 |

INTERCOMPARISON BETWEEN AIR QUALITY MICROSENSORS AND CONVENTIONAL MONITORING DATA

J. Reis^a, D. Lopes^a, K. Karatzas^b, M. Lopes^a

^a*CESAM & Department of Environment and Planning, University of Aveiro, 3810-193 Aveiro, Portugal*

^b*Environmental Informatics Research Group, School of Mechanical Engineering, Faculty of Engineering, Aristotle University of Thessaloniki, Greece*

**e-mail: johnnydreis@ua.pt*

Introduction

The health protection of the population and its quality of life are some of the major challenges to be addressed by the scientific and technical community, along with the social, environmental and territorial sustainability goals. Furthermore, the growing awareness of society and environmental deterioration conditions associated with high air pollution levels led the scientific community to rethink its atmospheric monitoring policies [1].

Air quality monitoring networks with high spatial coverage would allow a better understanding of the air pollution levels, the atmospheric emission sources (e.g. industries and road transport) and the dynamics of atmospheric pollutants (e.g. daily patterns and dispersion), and help the decision-makers on the definition of atmospheric improvement measures. Thus, it is eminent to find more economical and flexible alternatives, with economized maintenance requirements and energy. These requirements can be obtained with small low-cost microsensors and by using alternative techniques, rather than conventional ones. Air quality microsensors are a recent technology with a huge potential for use applicability as has been shown by several studies worldwide [2]. However, doubtful data quality and lack of regulations in this market - microsensors or low-cost monitoring systems - can be identified.

The main purpose of this work is to evaluate the performance of air quality and meteorological low-cost microsensors through comparison with data from a conventional atmospheric monitoring station.

Methods

To achieve the proposed objective a low-cost monitoring station built with air pollutants and meteorological microsensors were installed next to a conventional air quality monitoring station from the national monitoring network. The selected

location is a school in the highly industrialized municipality of Estarreja. This region is an important industrialized urban area having the third major chemical complex in Portugal.

The installed microsensors include air pollutants and meteorological measuring equipment at a feasible cost (significantly lower than traditional solutions), equipped with real-time data processing and communication systems so that air quality measurements can be taken based on current data. Table 1 shows the features (i.e., measured parameter, sensor model, type of technology and accuracy) of the sensors (by pollutant) used in this work.

Table 1. Main features of the sensors.

Table 1. Main features of the sensors.

Parameter	Model	Technology	Range	Accuracy
PM10	Gassensor	Laser scattering	0 – 500 $\mu\text{g}\cdot\text{m}^{-3}$	25% at 50 $\mu\text{g}\cdot\text{m}^{-3}$
O ₃	Alphasense - AH	Electrochemical sensor	5 – 500 $\mu\text{g}\cdot\text{m}^{-3}$	$\pm 25 \mu\text{g}\cdot\text{m}^{-3}$
NO ₂	Alphasense - B42F	Electrochemical sensor	5 – 500 $\mu\text{g}\cdot\text{m}^{-3}$	$\pm 25 \mu\text{g}\cdot\text{m}^{-3}$

After being tested and calibrated (laboratory and field-based calibration procedure comparing the microsensor results with the data from the reference equipment), the microsensor was installed in a secondary school in Estarreja, where the reference equipment from the Portuguese air quality monitoring network is installed, 1 km from the industrial chemical complex.

The conventional air quality monitoring station is composed by an optical particle sensor (for particles with an aerodynamic equivalent diameter less than or equal to 10 μm); and electrochemical sensors of ozone (O₃) and nitrogen dioxide (NO₂). The microsensors were lodged in a temperature-proof and controlled environment. The ambient air was measured, from June-November 2018 (6 months period), simultaneously using microsensors and a standard reference equipment to collect data for intercomparison and validation. This allows to verify the accuracy of the measurements obtained by the microsensors and whether they can be used as indicative measurements as defined in the European Air Quality Framework Directive [4]. During the study period (from 1st June to November the 30th 2018), data was collected and analyzed, using relevant statistical parameters taking into account the meteorological conditions registered, to evaluate the microsensors performance.

Results

Figure 1 shows the comparison between monthly averages (upper panel) and the daily median air pollution levels cycle (bottom panel), using a microsensor and reference method, from June–November 2018, for PM₁₀, NO₂ and O₃.

The microsensors tend to overestimate (negative mean bias) the air pollution levels for the analyzed pollutants. The highest errors were registered for PM₁₀ in October, while for NO₂ (-96%; 5.0 µg.m⁻³) and O₃ (63%; 57 µg.m⁻³) the lower performance was recorded in November. For the O₃, the microsensor error increased with the decrease of the air pollution levels measured by the reference method, while for the remaining pollutants (PM₁₀ and NO₂) there is no clear trend in the registered microsensor errors.

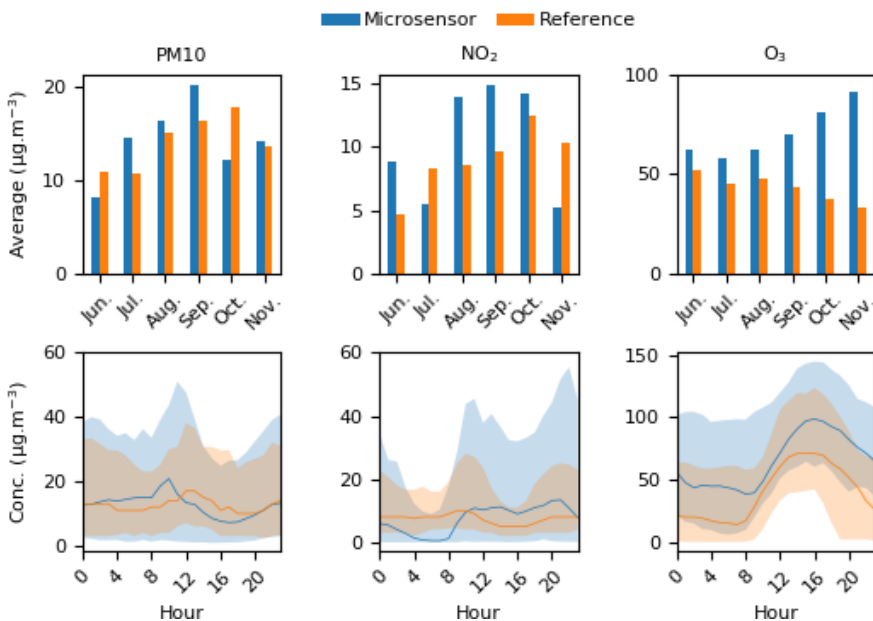


Figure 1. Monthly concentrations (upper panel) and the daily median air pollution levels cycle (bottom panel), from June–November 2018, for PM₁₀, NO₂ and O₃. The shaded areas in the bottom panel represent the 95% confidence interval.

For the O₃, the microsensor was capable of reproducing the daily variation measured at the reference station (the correlation coefficient was 0.92), with an increase in concentrations in the early morning (8 am), continuing until about 4

pm due to the rise of the solar radiation intensity. After, the O₃ levels gradually decreased and reached a minimum level at around 9 am. For the remaining pollutants, the microsensors recorded poor performance in reproducing the daily air pollution levels cycle, with a correlation coefficient of 0.26 and -0.34 for PM10 and NO₂, respectively.

Conclusions

The main goal of this work was to evaluate the microsensors accuracy when measuring PM10, NO₂ and O₃ levels, in an industrial region. The measurements were performed between June 2018 and November 2018 (a 6 months period), and the results were compared to a reference equipment installed nearby. The microsensors recorded a reasonable performance in reproducing the monthly and daily air pollution patterns measured at the reference air quality monitoring station. However, complementary studies, considering a longer measurement time period and machine-learning algorithms, are required to contribute to their calibration and further development.

References

- [1] WHO (World Health Organization), 2013. Health Risks of Air Pollution in Europe e HRAPIE Project: Recommendations for Concentration Response Functions for Cost-benefit Analysis of Particulate Matter, Ozone and Nitrogen Dioxide. Report of WHO Regional Office for Europe, Copenhagen, 60 pages.
- [2] Borrego, C., Costa, A.M., Ginja, J., Amorim, M., Coutinho, M., et al. 2016. Assessment of air quality microsensors versus reference methods: The EuNetAir joint exercise. *Atmos. Environ.* 147, 246–263.
- [4] EU, Directive (EU) 2016/2284 of the European Parliament and of the Council of 14 December 2016 on the reduction of national emissions of certain atmospheric pollutants, amending Directive 2003/35/EC and repealing Directive 2001/81/EC, 2016.

Acknowledgements

A special thanks are given to give to OHMI - Observatoire Homes-Millieus – Estarreja for the financial support and to FCT/MCTES for the financial support to CESAM (UIDP/50017/2020+UIDB/50017/2020+LA/P/0094/2020), through national funds.

O30 |

SISTEMA PARA EL MONITOREO DE LA CALIDAD DEL AIRE EN LA ZONA METROPOLITANA DE LA LAGUNA

H. Coto Fuentes¹, F. Valdés Perezgasga², D. Michel Medrano²

¹*Instituto Tecnológico Superior de Lerdo, Av. Tecnológico 1555, CP35150, Lerdo, Durango, México*

²*Instituto Tecnológico de la Laguna, Blvd. Revolución s/n, CP27000 Torreón, Coahuila, México*
**e-mail: hesnercf@gmail.com*

Introducción

En la actualidad pocas zonas urbanas de México cuentan con sistemas de monitoreo efectivos que comuniquen a la población la manera de conducir sus vidas ante eventos de contaminación. La mayoría de los sistemas de medición de la calidad del aire (SMCAs) que existen, se encuentran dispersas en 30 de las 32 entidades federativas (Quintana Roo y Baja California Sur no tienen), y son de tipo estacionaria, por lo que a pesar de encontrarse integradas al Sistema Nacional de Información de la Calidad del Aire (SINAICA), la información que se obtiene de ellas es insuficiente, o no muestra una perspectiva más dinámica y abarcadora de la situación de los contaminantes en el aire (Villaseñor, 2016) (Zuk, 2007).

El monitoreo de la calidad del aire es el resultado del diseño e instalación de redes de estaciones, los procedimientos de muestreo y el análisis de los contaminantes atmosféricos. Entre los contaminantes atmosféricos más importantes se encuentran: SO₂, CO, PST, PM10, ozono y óxidos de nitrógeno (NO_x). A este grupo de elementos se les conoce como contaminantes criterio, para los cuales existen normas de calidad del aire con el objetivo de proteger la salud humana, así como el bienestar de los ecosistemas.

En el marco antes descrito, la existencia de estaciones móviles portátiles de bajo costo, con características de conectividad a la nube, geolocalización, diseñadas pensando en la ciencia ciudadana, sin dudas aumentarían el volumen de información a procesar, y con ello, la calidad de los estudios de alcance y las medidas que de ellos se originen, con el objetivo fundamental de incidir en mejorar la calidad del aire en las ciudades.

Métodos

El desarrollo de la industria electrónica ha permitido una reducción del tamaño de los equipos electrónicos, aumentando su robustez y fiabilidad. Los sensores de gas, partículas suspendidas totales, entre otras, no son la excepción, por lo que en

la actualidad es posible la implementación de estaciones de medición de calidad del aire considerablemente más pequeñas e igual de confiables que las hasta ahora utilizadas (típicamente se instalan dentro de furgonetas o vehículos de tamaño medio). Las comunicaciones son otro factor que inciden positivamente en la obtención de redes de estaciones más pobladas. El acceso a internet se ha facilitado y el concepto de Internet de las Cosas es también aplicable a los equipos de medición de la calidad del aire (Telefónica, 2011).

Para el desarrollo del Sistema de monitoreo de la calidad del aire en la Zona Metropolitana de la Laguna, México, se han definido tres etapas: Implementación de las estaciones portátiles de calidad del aire (KNARIO: nombre registrado de las estaciones en el Instituto Mexicano de la Propiedad Industrial), Integración de las estaciones a una plataforma en la nube que permita almacenar, analizar y mostrar los resultados de las mediciones, Implementación de procedimientos de calibración que garanticen la fiabilidad de las mediciones realizadas por las estaciones.

La primera etapa del Sistema se llevó a cabo durante el año 2021, evaluando distintas opciones de *hardware*, haciendo hincapié en la portabilidad, conectividad, la geolocalización y capacidades de incrementar las prestaciones con cambios mínimos (utilización de sistemas programables en un chip). Entre las tecnologías evaluadas para el control de las estaciones se encuentran: M5Stack (5F, *Tangwei Stock Commercial Building, Bao'an District, Shenzhen, China*), en particular sus variantes con microcontrolador ESP32 orientadas a la operación con Azure y AWS), y los microcontroladores PSoC (*Programmable System on Chip*) (Infineon, Munich, Alemania). Destacables por sus capacidades de acondicionamiento analógico y digital, debido a sus arreglos programables internos, permitiendo la reconfiguración total de las funcionalidades del componente según las necesidades.

En la segunda etapa se desarrolló un portal WEB de acceso universal para la consulta ciudadana de la calidad del aire en la región. En paralelo se realizaron actividades de la tercera etapa, desarrollando los procedimientos para la correcta calibración de las estaciones, así como la planificación de las rutas de monitoreo y las primeras tomas de muestras con todo el sistema funcional.

Resultados

La Tabla 1 muestra un resumen de las características del módulo de medición seleccionado y funcional en las estaciones KNARIO, con el que se puede medir

todos los contaminantes criterio de la norma oficial mexicana, a excepción del dióxido de azufre. El módulo ZPHS01B es fabricado por la compañía Winsen Electronics Technology (Jinsuo Road 299, *National High-Tech Zone*, Zhengzhou, China), líder en soluciones para la medición de gases.

Tabla1. Resumen de características técnicas del módulo de sensores ZPHS01B.

Modelo		ZPHS01B
PM2.5	Rango	0~1000 $\mu\text{g}/\text{m}^3$
	Rango de tamaño de partículas	0.3-10 μm (PM1.0, PM2.5, PM10)
CO	Rango	0~5000 ppm
	Precisión	$\pm(50\text{ppm}+5\%$ de las lecturas)
O ₃	Rango	0~10 ppm
	Resolución	0.01 ppm
NO ₂	Rango	0.1~10 ppm
	Resolución	0.05ppm

Para la gestión de los recursos de la estación se optó por el módulo Core2 compatible con AWS de M5Stack. La capacidad modular de la plataforma facilitó la integración de la electrónica necesaria para localizar la toma de muestras, así como la conexión a internet utilizando la red de telefonía celular, disponible en toda el área metropolitana de la Laguna. Cuenta además con una pequeña pantalla donde se implementó una interfaz básica a través de la cual constatar el correcto funcionamiento de las estaciones. Para la recopilación de los datos se utiliza una etiqueta de geolocalización con la hora, latitud y longitud de las variables muestreadas, las que son enviadas a la nube siguiendo el protocolo MQTT y almacenadas en una base de datos.

En la Tabla 2 se muestran los módulos y la función que desempeñan en las estaciones KNARIO:

Tabla2.

Módulo	Función
M5 Core2 para AWS	Control de todo el sistema, interfaz hombre – estación.
COM.X NB-IoT (SIM7020G)	Módulo de comunicación sobre GSM. Conexión con la nube, transmisión de datos y notificaciones.
COM.GPS module (NEO-M8N) con antena	Obtención de las variables relacionadas con las etiquetas de geolocalización.
ZPHS01B	Obtención de los valores de los contaminantes criterio de calidad del aire.

Conclusiones

Las estaciones KNARIO en funcionamiento demostraron la viabilidad de los distintos módulos seleccionados, logrando la medición de cinco contaminantes criterio de los 6 normados en México, además de la correspondiente conexión con la nube para el almacenamiento y posterior publicación de las mediciones. El bajo costo de las estaciones, en comparación con las utilizadas hasta el momento por las entidades gubernamentales, junto a su portabilidad y movilidad, permitirá un aumento considerable de la densidad de estaciones, y con ello, del volumen de datos recopilados.

Las dos familias de microcontroladores evaluadas demostraron ser excelentes candidatos para el control de las estaciones, permitiendo grados de acondicionamiento, procesamiento y conectividad acordes a las nuevas tecnologías. El manejo de la energía fue otro punto a favor, garantizando un uso eficiente de las baterías y con ello la portabilidad que se propone.

Actualmente los trabajos continúan en la creación de procedimientos que permitan una calibración rápida y sencilla de las estaciones, así como en la planificación de las principales rutas a mapear en la zona metropolitana de la Laguna, de manera que la información recabada pueda ser utilizada como herramienta para la toma de decisiones por parte de los distintos niveles de gobierno, en cuanto a la contaminación de la calidad del aire.

Referencias

Telefónica, F. (2011). Smart Cities: un primer paso hacia la Internet de las Cosas (Vol. 16). Fundación Telefónica.

Villaseñor, S. Z. H. (2016). “Estudios ambientales de las emisiones vehiculares, producción de ladrillo, exposición personal a contaminantes, monitoreo de la calidad del aire, hidrocarburos y partículas, en la ciudad Victoria de Durango, Durango, 63.

Zuk, M. (2007). Tercer almanaque de datos y tendencias de la calidad del aire en nueve ciudades mexicanas. Instituto Nacional de Ecología.

Agradecimientos

Este proyecto fue financiado parcialmente por el Tecnológico Nacional de México y la Secretaría de Medio Ambiente de Coahuila de Zaragoza. Uno de los autores (D. Michel Medrano) recibió una beca del Consejo Nacional de Ciencia y Tecnología de México.

P35 |

EVALUATION OF IN-SOIL NUTRIENT PROBES IN DIFFERENT TYPES OF SOILS

E. Arasa-Puig¹, J. Cuerva Salas², R. Álvarez Garrido², J. Alonso-Chamarro^{1*}

¹ *Group of Sensors and Biosensors, Universitat Autònoma de Barcelona, 08193, Bellaterra, Spain*

² *VerdeSmart Co S.L, Alcalde Mora Claros 1, 24001, Huelva, Spain*

**e-mail: julian.alonso@uab.es*

Introduction

Nutrients availability by plants are regulated by the interaction of the physical, chemical, and biological properties of soil. To comprehend these processes and how they are influenced by environmental conditions would enable the optimization of nutrient availability and, therefore, the plant productivity.

Nutrient uptakes take place by physical contact between mineral soil surface and plant roots, which absorb nutrients from soil solution. Nutrient concentration in soils decrease after plants uptake. Consequently, many chemical and biological reactions occur to replace these nutrients to soil solution. The ability of the soil to recover nutrient's concentration in the soil solution is known as buffer capacity (BC). It is pH dependant and is regulated by the minerals that can be dissolved from the soil to stand the soil solution, microbial reactions and, mainly, by the ion exchange capacity of the soil or the organic materials used as agricultural substrates.

Ion exchange is a reversible process by which a cation or anion adsorbed on the surface is exchanged with another cation or anion in the soil solution. Cation exchange (CEC) is generally considered to be more important than anion exchange capacity (AEC) in most agricultural soils. The origin of the surface charge is fundamental to understand nutrient availability and retention in soil. Furthermore, also the capacity of soil to retain water and therefore nutrients would have an impact on BC. [1]

In conclusion, to estimate the real availability of nutrients in the soil it is necessary to know the compounds remaining in solution and the buffer capacity of the soil. There is a wide variety of lysimeters (suction probes), which are used to determine the concentration of nutrients in soil solution, but they are not capable of giving information about BC. In this sense, this work presents a biparametric probe of nitrate and potassium (called Nutrisens) [2] that can be inserted directly in the

soil, thus procuring continuous and real-time information on the trend of concentration of both ions in the soil solution and the soil BC simultaneously.

Results obtained in laboratory tests with the Nutrisens probe show its behaviour in soils with different BC. Finally, measurements obtained in real field conditions, in soils with different BC, where the same fertirrigation procedure were applied, will be presented.

Experimental

To carry out laboratory experiments, different kind of agricultural substrates characterized for different degrees of BC were introduced into a glass beaker perforated at the bottom. Inside the glass container, a Nutrisens probe together with suction probes (Rizhosphere, Netherlands) were installed. Then, nutrient solution or water were added, and suction of soil solution was performed. The Nutrisens probe uses ion-selective electrodes as a detection system. The nitrate sensor signal has been inverted to display trends more intuitively. Lectures were carried out using a portable ion-selective potentiometer powered by a computer (SDIAN6, TMI, Spain).

To improve the crop management in agricultural exploitations, precision agriculture has developed sensor platforms (including dataloggers) that allow the monitoring of different parameters of interest related to the crop in real time. Wireless transmission of the acquired information is used. To perform the experimental study in real farm conditions, Nutrisens and suction probes were installed in two different areas of the same crop field. The soil composition in each location is different being one mainly illite clay and the other montmorillonite clay.

Results and discussion

The behaviour of different kind of soils (sandy, perlite, coconut fibre) characterized for different surface charges were studied. To exemplify and understand how the system works, results obtained in a sandy soil (SiO_4^-) with moderate CEC, an extremely low AEC and a high-water filtration rate are presented. This soil presents a moderate BC towards cations and very low BC towards anions.

Figure 1A and B show the evolution of the Nutrisens probe signal, and the values obtained by the suction probe, when fertilizer solutions with the same concentration of nutrients were added sequentially. In the case of the nitrate ion, as the sand has a reduced BC (low), the addition of a solution with a constant

concentration of this ion generated a slightly increase in the signal supplied by the Nutrisens probe. This increment was due to the fertilizer solution remaining between the sand particles. Successive additions of the same solution did not increase the Nutrisens probe signal. The nitrate concentration measured in solution, obtained with the suction probe, was practically identical to that of the original fertilizer solution, indicating its low capacity to retain this ion (red line). However, the potassium soil probe signal increased with the successive addition of fertilizer solution. In the suction probe solution, the values obtained differed from the original concentration of the fertilizer solution since potassium was adsorbed on the negatively charged particles of the sand (red line). This difference decreased when consecutive washings with the fertilizer solution were carried out. The number of free negative charges present in the sandy soil was reduced by the previously fixed potassium.

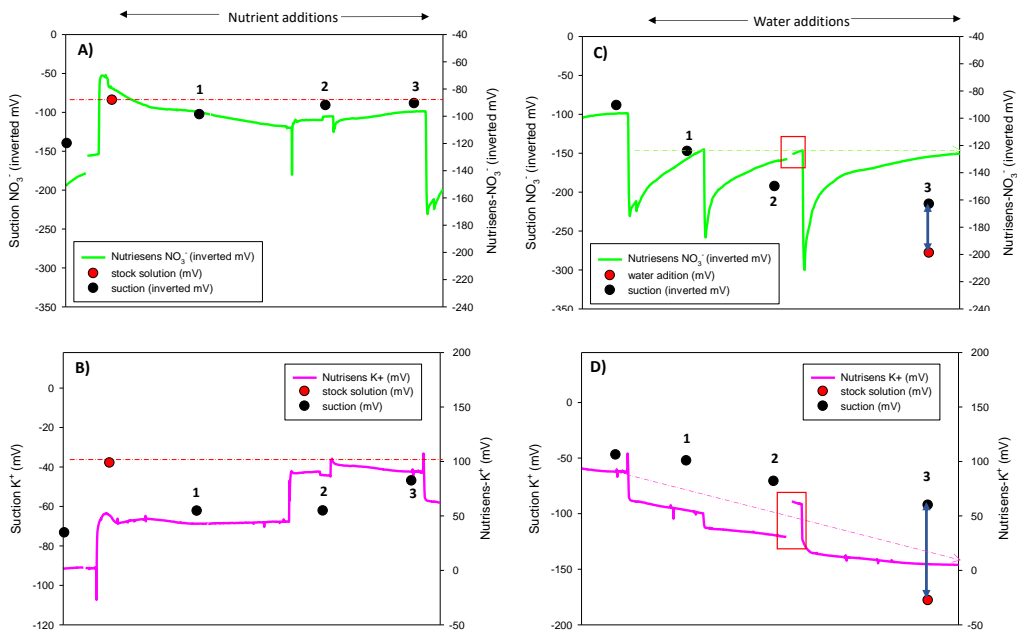


Figure 1. Nutrisens signal evolution (green: nitrate, pink: potassium) and suction data when nutrients (A, B) or water (C, D) were added in a dark sandy soil.

Figure 1C and D show successive washings with water of the sandy soil. In the case of nitrate, the final Nutrisens signal remained stable after each addition of water. The concentration of the solution obtained with the suction probe decreased gradually with each addition. The final concentration level was slightly higher

than that corresponding to water but lower than that read by the Nutrisens probe (blue arrow). This indicates a certain capacity to retain nitrate, although scarce. In contrast, in the case of potassium, the Nutrisens signal gradually decreased during washing, as did the concentration in the suction probe solution. On the third wash, what was suctioned had a concentration much higher than that of the washing water (blue arrow), thus indicating a greater initial capacity to fix potassium that is subsequently released. The box in red in fig. 1C and D correspond to a drying period. In the case of potassium (1D), an increase in the Nutrisens signal was observed due to pre-concentration of potassium. On the other hand, in the case of nitrate (1C), since there was hardly any nitrate left in the soil solution and it could not be released from its structure, the increase in the Nutrisens signal was practically imperceptible.

Figure 2 shows several examples of the Nutrisens response (potassium A, B and C, nitrate D and E) in different types of soil where the grey box corresponds to the difference between the minimum and maximum potential recorded by the probe.

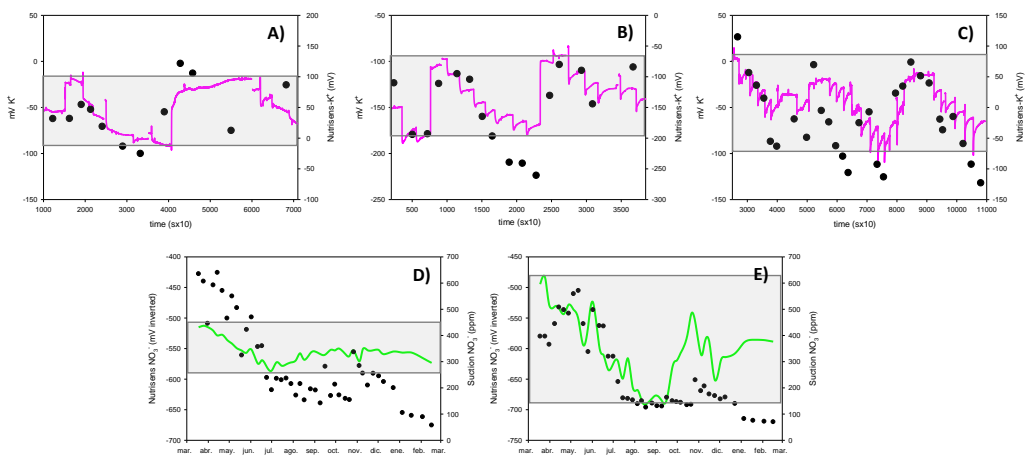


Figure 2. Nutrisens signal evolution (pink: potassium; green: nitrate) and suction data (black dots) in soils with different BC (grey square). Laboratory test: A) dark sandy soil, B) perlite, C) fiber coconut. Real field data: D) Illite clay; E) Montmorillonite clay.

Figure 2A corresponds to a dark-coloured sandy soil (CEC 10-20 mEq/100g) [3], 2B to perlite (CEC 25-35 mEq/100g) and 2C to coconut fibre (CEC 39-60 mEq/100g) [4]. As can be seen, for potassium, the higher the CEC of the soil, the greater the range of potential variation (grey box). And the same was observed in

figure 2D and E for nitrate, which corresponds to a real example of probes installed in the same field and crop, where the same fertilization treatments were applied. The soil of D corresponds to an illite and E to a montmorillonite, being AEC higher in the later for its small particle size. Some of the discrepancies observed between suction variation trends and Nutrisens are due to the fact that the latter depends on soil moisture (nutrient pre-concentration/dilution).

Conclusions

The possibility of obtaining a signal that depends both on the concentration of nutrients in the soil solution and on its physicochemical characteristics, such as BC, as provided by Nutrisens, is of great importance since it gives information on the real availability of nutrients in a soil and its accumulation(reserves). Knowing this factor, together with the climate forecast data, would allow an application of fertilizers on demand. An excess dosage, which would end up leaching towards water tables, thus contaminating the aquifers, would be avoided. Similarly, nutrient deficiencies could also be detected in real time and corrective measures applied to optimize production.

References

- [1] Havlin, J.L.; Tisdale, S.L.; Nelson, W.L.; Beaton, J.D. (2017). Soil fertility and fertilizers: an introduction to nutrient management. Pearson. ISBN-978-93-325-7034-4
- [2] PCT/ES2016/070853, Continuous monitoring probe in real time of chemical parameters of interest directly in soils and system for continuous monitoring and in real time of said chemical parameters of interest.
- [3] Raviv, M; Heinrich Lieth, J. (2008). Soilles culture: theory and practice. Elsevier. ISBN 978-0-444-52975-6
- [4] Archipova, L. (2007). Ecology of tree roots in substrates of The Hague. Alterra-rapport 1590. ISSN 1566-7197

Acknowledgments

Authors are grateful to the Spanish Ministerio de Economía, Industria y Competitividad and Ministerio de Ciencia e Innovación and FEDER through the project PID2020-117216RB-100 for its financial support. We also aknowledge the contribution of Consejería de Empresa, Industria y Portavocía de la Región del Múrcia through the Project Agricultura Sostenible con Vertido Cero de Nitrato en Mar Menor.

INDUCTIVE SALINITY SENSOR

Maria Barroso¹, J.L. Rocha¹, C.L. Faria¹, P.A. Gomes³, L.M. Gonçalves^{1,2}

¹ *CMEMS-UMinho, University of Minho, Campus de Azurém, Guimarães, Portugal*

² *LABELS –Associate Laboratory, Braga/Guimarães, Portugal*

³ *CBMA-Molecular and Environmental Biology Centre, University of Minho, Braga, Portugal*

**e-mail: mariabarroso731@gmail.com*

Introduction

Salinity is defined as the weight in grams of dissolved salts in one kilogram of seawater. The measurement of salinity is important in oceanography because salinity have effect on the sea life and water quality. Unusual conductivity and salinity are indicative of pollution [1], regardless anthropogenic or natural sources. Aquatic species adapt to specific salinity levels. If this level is altered, it can result in the death of them, because there are changes in the oxygen concentrations (higher salinity, lower dissolved oxygen concentration). Therefore, some species have adapted to live in estuaries, where salinity is constantly changing. Salinity determinations are usually made indirectly, measuring electrical conductivity, which depends on salinity and temperature [1]. The goal of this work is the development of a low cost, high autonomy inductive salinity sensor to integrate into a sensor network for water column measurement from estuaries to deep ocean applications [2,3].

Methods

To measure the conductivity of liquids, we can use one of two methods: inductive or contact (with two or four electrodes). Two-electrode conductivity sensors consist of two electrodes spaced at a constant length apart. A four-electrode conductivity cell introduces two more electrodes to the sensor, compared to the previous one. The four-electrodes measurement is used instead of the simplest two-electrodes to avoid interference of electrodes aging in long term deployments [1].

The inductive method uses an electric field, instead of electrodes, to apply current in the water sample to measured. Despite a slightly higher cost, there advantages of using an inductive sensor can be enumerated [4]: biofouling-proof, improved accuracy, low maintenance and are more cost-effective over time.

According to Striggow & Dankert [5], the inductive conductivity sensor is based on a transformer that, depending on the salt concentration in the water, measures

the conductivity. Inductive sensors can be manufactured in two ways: by using only one transformer or using two transformers. In the first case, and the simplest way, is to use one transformer, whose secondary coil is formed by the circulating liquid, which in this case is sea water. Although this configuration is quite simple, it has not been applied to oceanographic conductivity sensors. The double transformer, as the name implies, uses two transformers, where water circulates in both the secondary coil of the first transformer and the primary coil of the second transformer. It is important to arrange the two transformers in such a way that the only coupling between them is only the seawater.

The inductive sensor, using two transformers, consists of two toroid-shaped coils embedded next to each other. According to Wood et al, [6] these coils form current transformers. The sensor is designed so that part of the liquid medium forms a closed current path that passes through both coils, as shown in the figure 1. The first winding N_1 produces a magnetic field in the water, causing a current to flow in the water (water implements the secondary winding N_2 of transformer T_1) which in turn is proportional to the conductance. This current (that is also the primary winding N_3 of second transformer T_2) causes a magnetic field in the secondary winding (N_4) of second transformer, where the voltage (or current) in the second winding is measured.

The sensor is immersed in liquid, in this case seawater. Looking at the picture, the transmitting toroid or coil has an inductance L_1 , and the receiving toroid has an inductance L_3 . Applying an AC voltage or sinusoidal current to the transmitting coil induces a magnetic current I_2 , an inductive voltage V_2 in the seawater and a resistance R . R represents the resistance of water, calculated from conductivity. The receiving coil receives the magnetic flux from the seawater cycle and gives an inductive voltage V_3 [4].

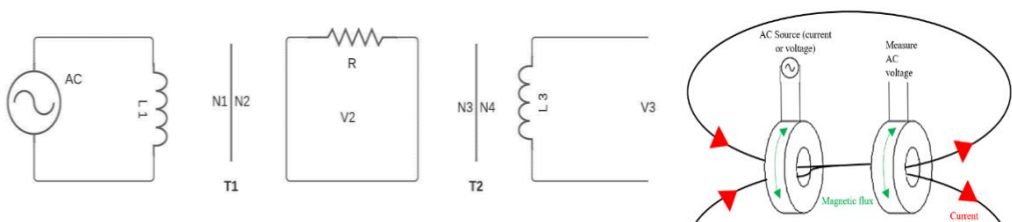


Figure 1- Schematic (left) and diagram (right) to explain the operation of a toroidal inductive salinity sensor.

Results

For this work, toroid-shaped coils were chosen. This selection was made since toroids are more efficient in producing inductances. That is, for the same inductance, toroids require fewer turns and a smaller size than solenoids. Toroids also present less flux loss, there is only magnetic field inside the toroid. Regarding the core, ferrite was chosen, as the eddy currents in the core are zero. In addition, the magnetization of the material can easily change direction, reducing energy losses due to hysteresis, thus increasing the inductance compared to the other cores.

Several coil dimensions were used, with different number of turns with isolated copper wire, as presented in table 1. Two coils were used to implement a salinity sensor, as described before. Sensors A, B, C and D use two equal coils. Sensor E and F uses different sized coils.

Table 1- Dimensions of coils.

Toroids						
					A+C	A+D
Internal Diameter (mm)	19.73	7.5	10.7	12.16	19.73	19.73
External Diameter (mm)	33.25	17.4	18.1	24.35	10.7	12.16
					33.25	33.25
Thickness (mm)	11.05	8.6	5.4	11.05	18.1	24.35
					11.05	11.05
Number of Turns	50	25	25	50	5.4	11.05
					100	100
Copper Wire Diameter (mm)	0.46	0.35	0.35	0.38	25	50
					0.46	0.46
Reference	MP7548MDGC	MP1506L4AS	MP1603L4AS	MP1710MDGC	-----	-----

Several water samples were prepared in laboratory, weighing deionized water and marine salt, with salinity from 1 PSU to 50 PSU. Fabricated sensors were tested with sinusoidal excitation voltage (amplitude in the range 50 mV to 1.5 V) and in frequencies ranging from 50 kHz to 400 kHz. Voltage was measured in the receiver coil. For each coil, tested in single frequency with a single water sample, output voltage was always proportional to input voltage. However, for higher input voltages, higher output voltages were obtained, and a consequent higher signal-to-noise ratio, due to constant noise voltage. For these reason, following tests were performed always with an amplitude voltage of 1 V.

Figure 2 presents the output voltage (y-axis), as function of applied frequency (x-axis) for several different salinity values of water (different line colors). The

results in figure 2 show that a resonant frequency exists (not achieved in graphs from models A, B, C) where salinity influences the output voltage. Bellow or above this resonant frequency, salinity influence is less notorious. Model D, E and F resonant frequency is respectively 200 kHz, 130 kHz and 120 kHz, approximately. In model F, more frequencies were analyzed between 100 kHz and 150 kHz, and is also patented that resonant frequency slightly shifts to higher frequency with salinity increase. Moreover, output voltage depends on salinity, with measurements at resonant frequency.

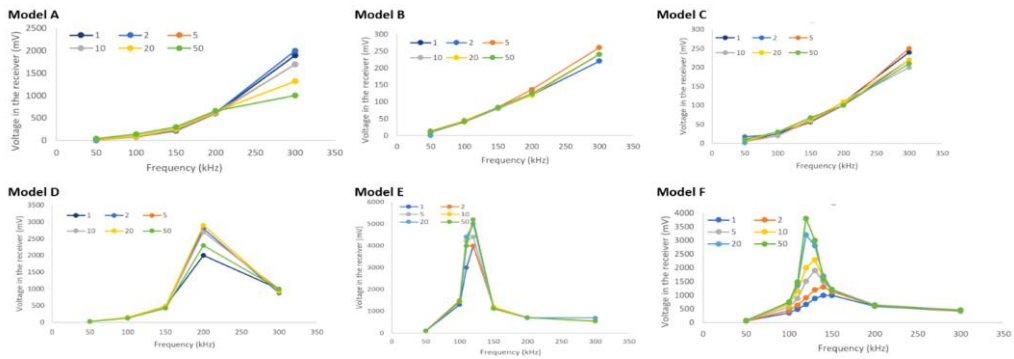


Figure 2 – Output voltage function of excitation frequency, for different salinity values, in each sensor model.

Figure 3 presents the output voltage of model F, function of salinity, with excitation voltage 1V, at a few frequencies around resonance (110 kHz to 140 kHz). It was found sinusoidal excitation at 1V, frequency in this range these sensor is able to discriminate different water salinity, from 1 PSU to 50 PSU. In a logarithmic scale of salinity, the relation is almost linear, enhancing the capability to implement a large scale sensor, measuring from fresh water to high salinity brines.

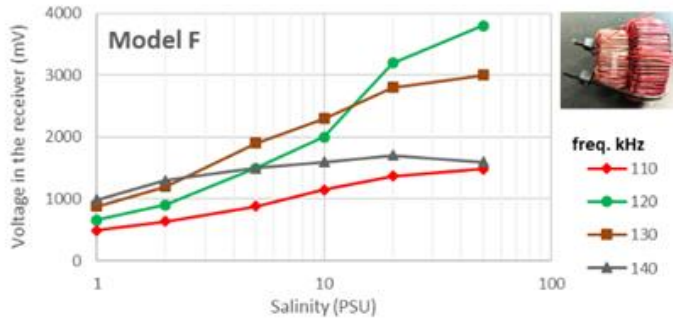


Figure 3 - Output voltage dependence with salinity in model f, for a few excitation frequencies near resonance.

Conclusions

In this work, six coil configurations for measuring water conductivity were analyzed. These models combine toroids with and without the same diameter of ferrous nucleus. As results show, some of the models in which the configuration has the same diameter and the same number of turns, it is not possible to discriminate samples with low or high salt content, with excitation frequency below 300 kHz. For this, it was necessary to create two new models, where a combination between coils was used. In these it is possible to discriminate the different salinity solutions, from 1 PSU to 50 PSU. Future work will create an autonomous sensor, integrated into a sensor network, for estuary and deep-sea applications.

References

- [1] JL Rocha, T Matos, MS Martins, SF Lopes, PA Gomes, R Henriques. Cost Effective CTD for Long Term Deployments in Water Columns. OCEANS 2021: San Diego–Porto, 1-7 2021.
- [2] CL Faria, MS Martins, T Matos, R Lima, JM Miranda, LM Gonçalves. Underwater Energy Harvesting to Extend Operation Time of Submersible Sensors, *Sensors* 22 (4), 1341 2022.
- [3] CM Penso, JL Rocha, MS Martins, PJ Sousa, VC Pinto, G Minas. PtOEP–PDMS-Based Optical Oxygen Sensor, *Sensors* 21 (16), 5645.
- [4] Sheng, W. U., Hui, L., Liang, J.-J., Yu, T., Deng, Y., Li, H.-Z., & Ning, L. (2015). Investigation of the Performance of an Inductive Seawater Conductivity Sensor.
- [5] Striggow, K., & Dankert, R. (1985). Communications The Exact Theory of Inductive Conductivity Sensors for Oceanographic Application.
- [6] Wood, R. T., Bannazadeh, A., Nguyen, N. Q., & Bushnell, L. G. (2010). A salinity sensor for long-term data collection in estuary studies. MTS/IEEE Seattle, OCEANS 2010.

Acknowledgments

This work was funded by Programa Operacional Regional do Norte (NORTE2020), Project Atlantida, NORTE-01-0145-FEDER-000040 and by FCT national funds, PTDC/EAM-OCE/6797/2020.

APLICAÇÕES À BIOMEDICINA E À SAÚDE | APLICACIONES A LA BIOMEDICINA Y A LA SALUD | APPLICATIONS TO BIOMEDICINE AND HEALTH

BIOSENSING STRATEGIES FOR EXOSOMES

M. Bernuz^{1,2}, A. Pallares-Rusiñol^{1,2}, R. Rossi^{1,2}, C. Fernández-Senac^{1,2}, M. Martí²,
M.I. Pividori^{1,2*}

¹ *Institute of Biotechnology and Biomedicine, Universitat Autònoma de Barcelona, Bellaterra, Spain*

² *Grup de Sensors i Biosensors, Departament de Química, Universitat Autònoma de Barcelona, Bellaterra, Spain*

**e-mail: Isabel.Pividori@uab.cat*

Introduction

There is a growing demand for biomarkers that can help detect diseases at an early stage, as well as for follow-up of patients and therapeutic strategies. Exosomes are the next big step to reach this goal. Exosomes are membrane encapsulated biological nanometric particles of endocytic origin, which are released by all types of cells. The characterization of exosomes is exceptionally challenging with current technologies. Exosomes are between 30–200 nm in diameter, a size that makes them out of the sensitivity range to most cell-oriented sorting or analysis platforms, as is the case of the classical flow cytometers [1]. Conventional procedures for exosome detection usually require relatively large sample volumes and involve a preliminary purification [2] and preconcentration step by ultracentrifugation to prevent interferences in the sample. Nanoparticle tracking analysis (NTA), followed by the specific detection, including LC-MS/MS, Western Blot, RT-PCR, or flow cytometry are usually performed [3]. The whole procedure is thus time consuming, requiring skilled personnel as well as laboratory facilities and benchtop instrumentation. Therefore, there is a growing need for novel methods to accurately characterize and specifically determine the concentration of exosomes in complex biological fluids. Since the early reports on magnetic separation technology [4], magnetic particles (MPs) have been used as a powerful and versatile preconcentration tool in a variety of analytical and biotechnology applications and in emerging technologies including microfluidic devices and biosensors [5-8]. In this paper addresses the study of an electrochemical immunosensor with magnetic actuation in different formats, for the characterization and quantification of exosomes derived from three breast cancer cell lines (MCF7, MDA-MB-231 and SKBR3).

Methods

The exosomes were first characterized by Transmission Electron Microscopy and nanoparticle tracking analysis. Further characterization in terms of the specific

receptors on the surface of the exosomes was performed with confocal microscopy, flow cytometry and magnetic immunoassay in different formats (as depicted in Figure 1). For the electrochemical biosensing, the exosomes were preconcentrated from cell-culture supernatant (and eventually in human serum) on magnetic particles modified with antibodies against the general tetraspanins CD9, CD63 and CD81, as well as specific receptors of cancer (CD24, CD44, CD54, CD326 and CD340), as depicted in Figure 1, panel B. All the materials and methods were previously described in detail [5-8].

Results

Cryo-TEM micrographs on exosomes derived from breast cancer cell lines are shown in Figure 2. The micrographs revealed the typical exosome consisting of well-shape exosome vesicles with closed circular lipid bilayers comprising packed membrane proteins with a 110 nm diameter.

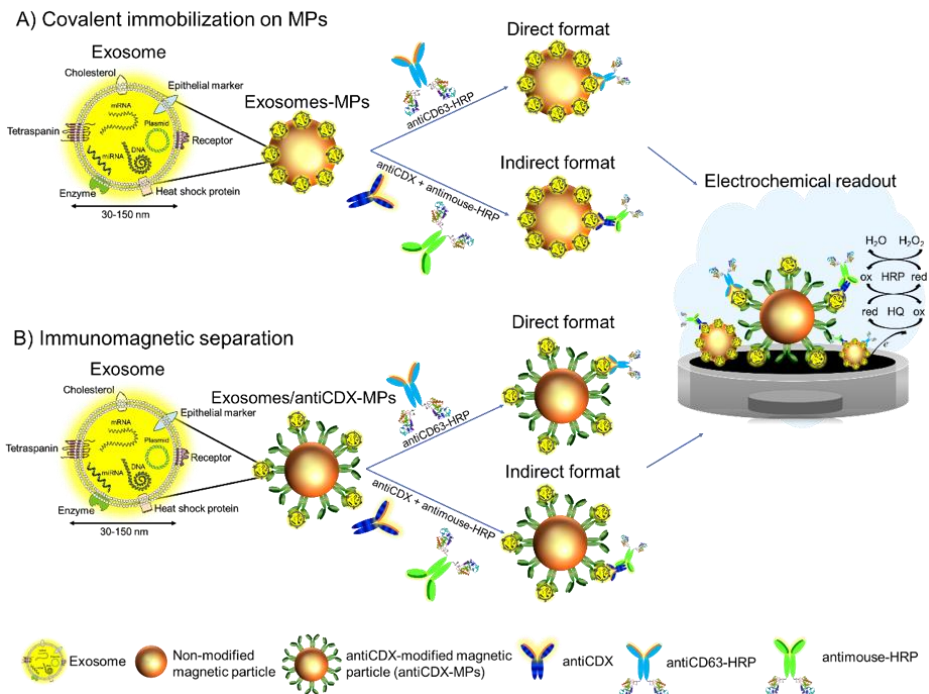


Figure 1. Different formats for the isolation of exosomes on magnetic particles, followed by electrochemical biosensing

Further characterization in terms of the specific receptors on the surface of the exosomes was performed with confocal microscopy (Figure 3), flow cytometry

and magnetic immunoassay in different formats (as depicted in Figure 1 and Figure 4). The electrochemical immunosensor can reach a limit of detection of 10^5 exosomes μL^{-1} directly in human serum, when performing the immunomagnetic separation with antiCD81 modified magnetic particles and the labeling based on CD24 and CD340 as cancer-related biomarker, avoiding the interference from free receptors in the serum matrix [7]. Furthermore, the electrochemical immunosensor shows reliable results for the differentiation of healthy donors and breast cancer individuals based on specific epithelial biomarkers.

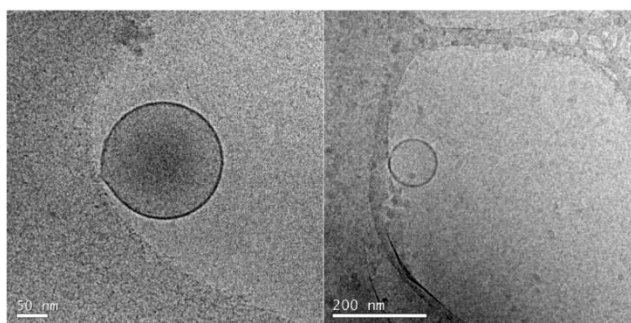


Figure 2. Cryo-TEM images of the exosomes-derived from human serum. These exosomes were applied onto formvar-carbon EM grids, maintained at $-182\text{ }^\circ\text{C}$ with 200-kV acceleration voltage during the whole process. The images were obtained by the authors from the Service of Microscopy, Universitat Autònoma de Barcelona.

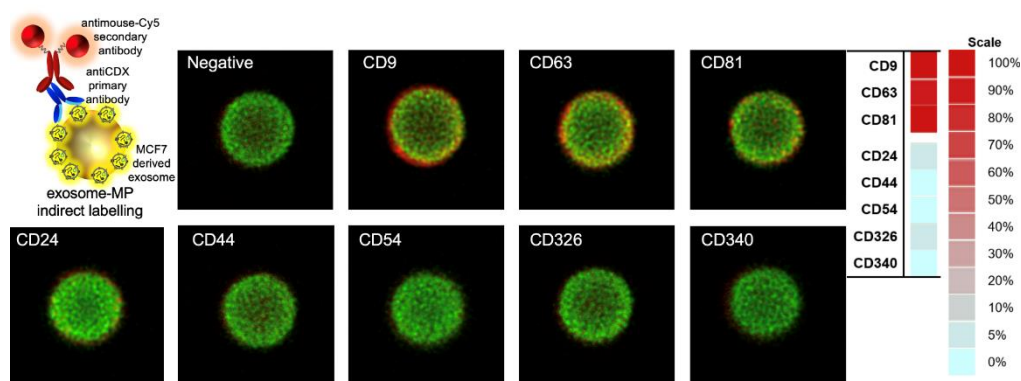


Figure 3. Confocal microscopic characterization of MPs covalently modified with MCF7 breast cancer derived exosomes, followed by indirect labeling with mouse antiCDX (being CDX either CD9, CD24, CD44, CD54, CD63, CD81, CD326 and CD340 biomarkers) and antimouse-Cy5. The scale indicates the percentage of positive entities.

Another approach involves a biosensor combining the immunomagnetic separation and the electrochemical biosensing based on the intrinsic ALP activity of the exosomes [5,6]. This approach explores for the first time two different types of biomarkers on exosomes, in a unique biosensing device combining two different biorecognition reaction: immunological and enzymatic, as shown in Figure 5. Besides, the intrinsic activity of alkaline phosphatase (ALP) in exosomes as a potential biomarker of carcinogenesis as well as osseous metastatic invasion was also explored.

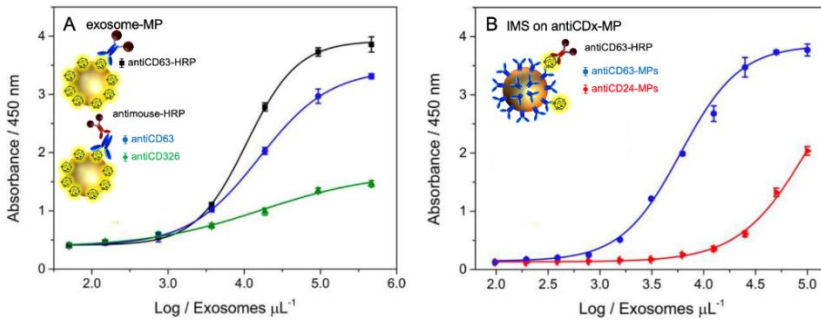


Figure 4. Magneto-actuated immunoassay for detection of MCF7 exosomes ranging from 0 to 4.5×10^5 exosomes μL^{-1} . (A) covalently immobilization of the exosomes on MPs (exosomes-MPs), followed by indirect labeling with (●) antiCD63 and (▲) antiCD326, and by direct labeling with (■) antiCD63- HRP antibody. (B) IMS of the exosomes on (▶) antiC24-MPs and (●) antiCD63-MPs, followed by direct labeling with antiCD63-HRP antibody. In all cases, the concentration of MPs was fixed in 1×10^6 MPs. The error bars show the standard deviation for $n = 3$. Adapted from Ref [8].

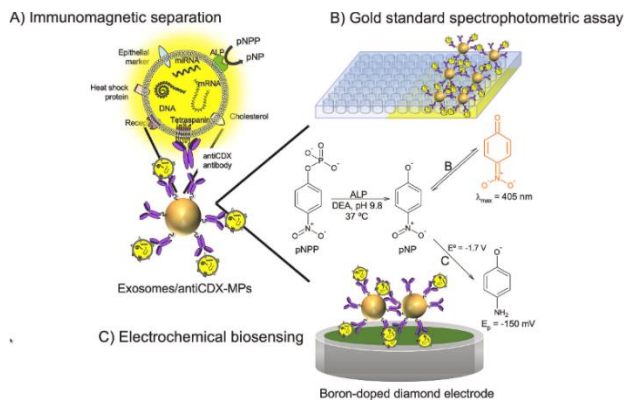


Figure 5. Different approaches for the detection of alkaline phosphatase (ALP) activity in osteoblast-derived exosomes by optical readout and electrochemical biosensor.

Conclusions

It is demonstrated that the electrochemical biosensor improves the analytical performance of the gold standard colorimetric assay for the detection of ALP activity in exosomes, providing a limit of detection of 4.39 mU L^{-1} , equivalent to 10^5 exosomes μL^{-1} . Furthermore, this approach is used to detect and quantify exosomes derived from serum samples of breast cancer patients. The electrochemical biosensor shows reliable results for the differentiation of healthy donors and breast cancer individuals based on the immunomagnetic separation using specific epithelial biomarkers CD326 (EpCAM) combined with the intrinsic ALP activity electrochemical readout.

References

- [1] Johnstone RM, Adam M, Hammond JR, Orr L, Turbide C (1987). *J. Boil. Chem.* 262: 9412–9420.
- [2] Patel GK, Khan MA, Zubair H, Srivastava SK, Khushman M, Singh S, Singh AP (2019). *Sci. Rep.* 9: 5335.
- [3] Théry C, Amigorena S, Raposo G, Clayton A (2016) *Curr. Protoc. Cell Biol.* 30: 3–22.
- [4] Rembaum A, Yen R, Kempner D, Ugelstad J (1982) *J. Immunol. Methods* 52:341–351.
- [5] Moura SL, Pallarès-Rusiñol A, Sappia L, Martí M, Pividori MI (2022) The activity of alkaline phosphatase in breast cancer exosomes simplifies the biosensing design. *Biosensors and Bioelectronics* 198: 113826.
- [6] Sanchez MA, Felice B, Sappia LD, Moura SL, Martí M, Pividori. MI (2020) Osteoblastic exosomes. A non-destructive quantitative approach of alkaline phosphatase to assess osteoconductive nanomaterials. *Materials Science and Engineering: C* 115, 110931.
- [7] Moura SL, Martín CG, Martí M, Pividori MI (2022) Electrochemical immunosensing of nanovesicles as biomarkers for breast cancer. *Biosensors and Bioelectronics* 150, 111882.
- [8] Moura SL, Martín CG, Martí M, Pividori MI (2020) Multiplex detection and characterization of breast cancer exosomes by magneto-actuated immunoassay. *Talanta* 211:120657.

O32 |

SIMULTANEOUS QUANTITATIVE ANALYSIS OF SEVERAL ELECTROLYTES IN SWEAT SAMPLES USING A FLOW SYSTEM AND POTENTIOMETRIC DEVICES

M. Rovira¹, A. Roldán¹, C. Lafaye², M. Saubade², C. Fernández-Sánchez¹,
C. Jimenez-Jorquera*¹

¹ *Instituto de Microelectrónica de Barcelona (IMB-CNM), CSIC, Bellaterra, Spain*

² *Médecine du sport et de l'exercice, Centre hospitalier universitaire Vaudois (CHUV),
Lausanne, Switzerland*

* *e-mail: cecilia.jimenez@csic.es*

Introduction

During the practice of exercise, the thermoregulatory action leads to sweating and the consequent loss of water, electrolytes and other biomarkers. The monitoring of these biomarkers would enable personalized diagnosis and would help to prevent pathologies related to dehydration [1]. Although sweat is an easily accessible biofluid, small volume samples are collected for its analysis. For this reason, sweat samples must be analyzed with systems able to perform low volumes. In that context, several attempts have been reported in the last decade to achieve compact, affordable, and wearable platforms for healthcare and sport activities real-time monitoring [2]. However, the accurate quantification of biomarkers in sweat remains still a challenge. This abstract reports the design of a flow assembly and validation of ion-selective field-effect transistors (ISFETs) for the detection and quantification of ions in sweat samples. Microfabricated ISFETs are robust and allow integration with various interfacing electronic readouts being CMOS-compatible. Sodium, potassium and pH ISFETs were used in this work.

Results demonstrate that this type of sensors can be used for the continuous and accurate monitoring of ions in sweat during the performance of physical activities.

Methods

A flow assembly was designed to perform the measurements under flow conditions. This was fabricated with poly(methyl methacrylate) (PMMA) using a CO₂-laser system (Epilog Mini 24, Epilog Laser, United States). This assembly was formed by 110 mm x 60 mm PMMA layers of different width. A 500 µm width channel was defined. The different layers were attached with PSA and O-rings were used to avoid fluid leakage. An image of the assembled structure is

showed in Figure 1. External tubing and a peristaltic pump were used for driving the solutions into the flow cell. The PMMA cell contained a reference electrode and the ISFETs selective to the different analytes.

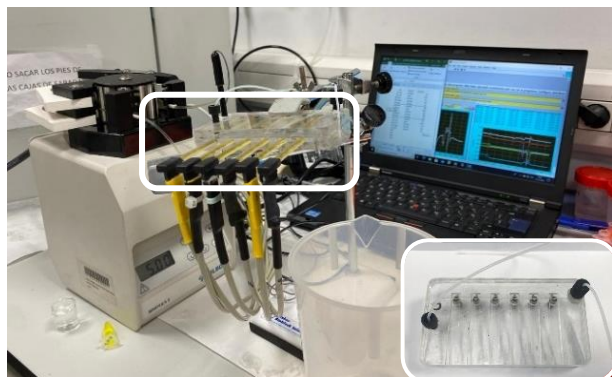


Figure 1. Set-up for in flow measurements using three ISFET sensors (pH, Na and K) and a commercial reference electrode.

ISFET chips were fabricated on silicon substrates at the Institute of Microelectronics of Barcelona according to standard photolithographic techniques. They had a Si_3N_4 gate and were wire-bonded on standard printed-circuit boards (PCB). They were modified with polymeric membranes to be selective to pH, Na^+ and K^+ . A Dri-Ref Reference Electrode of 5 mm diameter (World Precision Instruments, Sarasota, Florida, USA) was used.

The potentiometric measurements were performed with a portable homemade multi-ISFET meter system fabricated at the IMB-CNM. Briefly, this system (21 cm \times 10 cm \times 3 cm) enables the real-time simultaneous measurement of six ISFETs by including the power supply unit, the digital part and the analogue part in the same device. The ISFET measurement was carried out by applying 100 μA and 0.5 V between the drain and the source, and recording the ISFET gate potential (in mV). The resulting output voltages are related to the analyte concentrations in solution following the Nernst equation. The visualization of the results and their treatment was carried out with a laptop connected by USB to the multi-ISFET meter by employing a virtual instrument programmed with LabView 2013 (National Instruments, Austin, USA).

Artificial sweat solution was used as matrix for ISFETs calibrations and characterization tests. It was prepared following the composition described in [3].

Five sweat samples were collected in Lausanne's University Hospital (*Centre Hospitalier Universitaire Vaudois*) in Switzerland. Volunteers performed high

intensity exercise and sweat from different positions of their body was collected. These samples were analyzed by ionic HPLC, and using potentiometric devices such our ISFETs and Laquatwin ion selective commercial devices.

A protocol for ions determination in sweat samples in the flow system was established. Between samples, water and air were driven into the cell to clean the system and to avoid dilution of the sample. Following this procedure, each sample analysis lasted only few minutes.

Results

At first, it was studied the best flow rate of the system considering the time for stabilization of the signal and the sensitivity achieved. The best flow rate was 0.5 mL/min.

The accuracy of the system was first evaluated with five synthetic sweat samples with different concentrations of the analytes of interest. Sensors were calibrated before and after the *ad hoc* samples. A difference in behavior was observed for sensors with selective membranes (Na and K ISFETs) and without (pH ISFET). While pH ISFETs gave an error below 5% and presented equal calibration curves before and after, Na and K ISFETs results showed the lack of membrane conditioning, which resulted in concentration differences of 17% in average and 4 mV/decade in average between slopes. By comparing both calibrations we could also conclude that there was a good reversibility of the signal.

As described in Methods section, five sweat samples were analyzed with the three different techniques: ISFETs in flow system, Laquatwin devices and ionic HPLC (only for Na⁺ and K⁺). The last was the standard method used to validate the results obtained in our set up.

The concentrations of the electrolytes are shown in Figure 2. When comparing ISFETs results for the five sweat samples to HPLC ones, an average relative error of 18% was obtained for both Na and K ISFETs. However, regarding that samples 1 and 2 correspond to samples collected at the same moment from the right and left sides of the chest, respectively, similar concentrations of Na⁺ and K⁺ would be expected. Due to its deviation from the trend, some systematic error could have occurred during the analysis of sample 2 in ionic HPLC. Therefore, HPLC concentration values for sample 2 were excluded from the data analysis, obtaining average relative errors of 16,7% for Na⁺ and 12,5% for K⁺ determination with ISFETs. For commercial Laquatwin sensors, measurements showed average

relative errors of 3.1% and 9.3% compared to HPLC for Na^+ and K^+ ions, respectively.

On the other hand, pH ISFET measurements were only compared to Laquatwin results, and the relative error was 2.4% in average.

These results demonstrated that there is an important matrix effect on the selective polymeric membranes of ISFETs when measuring real sweat samples.

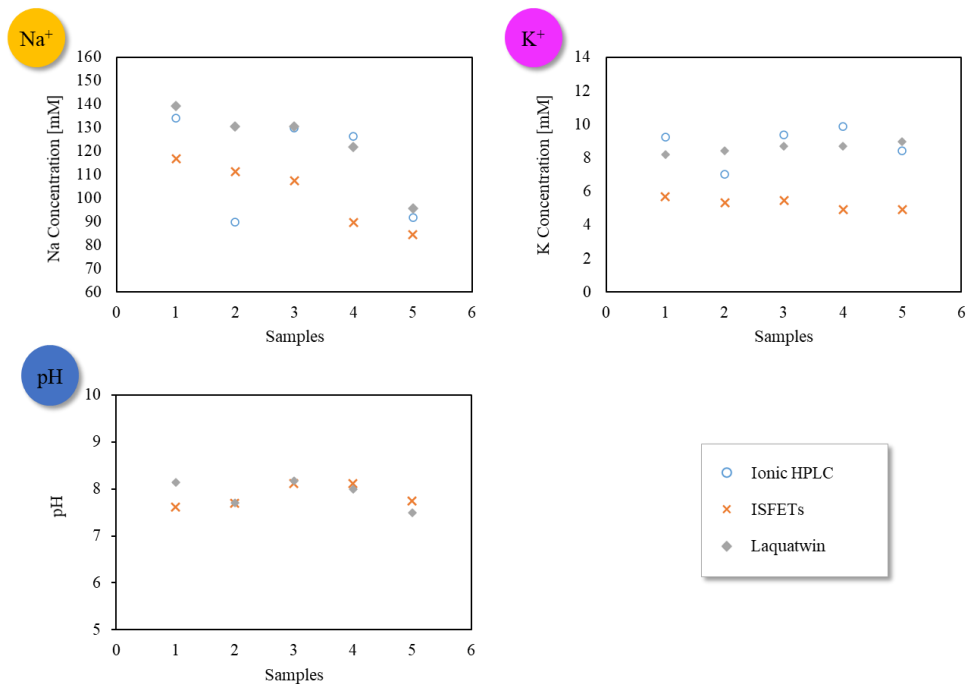


Figure 2. Results of five sweat samples' analysis with the three methods.

Conclusions

The flow system designed to analyze the three electrolytes on the sweat samples has been characterized and validated with standardized techniques. This allows to measure low volumes of samples with a high sampling rate.

The analysis of five sweat samples with pH, Na and K ISFETs has demonstrated that pH values are comparable to a commercial device while Na^+ and K^+ data has an important dispersion in comparison with Laquatwin devices and ionic HPLC due to the effects of the sample matrix to the membrane of ISFETs. Next studies

will be addressed to the characterization of polymeric membranes behavior in this matrix over time and correcting the ISFETs response.

References

- [1] R. A. Neal, H. C. Massey, M. J. Tipton, J. S. Young, J. Corbett, *Front. Physiol.* 2016, 7, 564.
- [2] Ghaffari, R., Rogers, J. A., Ray, T. R., *Sens. Actuators B Chem.* 2021, 332, 129447.
- [3] C.J. Harvey, Ryan F. LeBouf, Aleksandr B. Stefaniak, *Toxicol. in Vitro* 2010, 24, 1790–1796.

Acknowledgements

This work is performed in the frame of the WeCare project (SNSF, Sinergia program CRSIIS_177255/1) and used the Spanish ICTS Network MICRONANOFABS supported by the Spanish Ministry of Science and Innovation.

O33 |

IMPEDIMETRIC AND CAPACITIVE BIOSENSING OF β -1,4-GALACTOSYLTRANSFERASE-V COLON CANCER BIOMARKER

D. Echeverri, J. Orozco*

Max Planck Tandem Group in Nanobioengineering, Institute of Chemistry, Faculty of Natural and Exact Sciences, University of Antioquia. Complejo Ruta N, Calle 67 N°52-20, Medellín, 050010, Colombia

*e-mail: grupotandem.nanobioe@udea.edu.co.

Introduction

β -1,4-Galactosyltransferase-V glycoprotein (β -1,4-GalT-V) is an enzyme with glycosyltransferase activity that synthesizes lactosylceramide and glycosylates high-branched N-glycans. There is evidence that colorectal cancer (CRC) tumor cells overexpress this glycoprotein concerning normal cells and release it into the body fluids. Hence, this suggests that the β -1,4-GalT-V glycoprotein could be used as a biomarker in CRC diagnosis/prognosis [1]. Conventional methods (such as ELISA and liquid chromatography-based methods) enable the determination of the β -1,4-GalT-V glycoprotein accurately but have some limitations, including the use of sophisticated and centralized laboratory equipment and laborious experimental procedures, and skilled personnel. Furthermore, glycosyltransferases are at low levels in the human serum of healthy individuals concerning patients diagnosed with cancer. Thereby, there is a challenge for early cancer diagnostic at the point of care based on the detection of β -1,4-GalT-V glycoprotein.

Electrochemical biosensors allow overcoming the challenge of β -1,4-GalT-V glycoprotein detection. These biosensors enable the affordable and accurate detection of the analyte at low concentrations, with high specificity, in simple formats, and with rapid response. Among electrochemical biosensors, the label-free impedimetric and capacitive architectures are promising for diagnosis at the point of care. In addition, label-free electrochemical biosensors are ultrasensitive, highly specific, reagent-less (concerning labeled-based approaches), and amenable to miniaturization. All these attributes make electrochemical biosensors good candidates for point-of-care molecular diagnostic devices.

As a proof of concept, we developed impedimetric and capacitive architectures to detect the colon cancer biomarker β -1,4-GalT-V. Both biosensors use an anti- β -1,4-GalT-V antibody immobilized onto the electrode surface, which recognizes the analyte by biochemical affinity. We monitored the biorecognition molecular

event by electrochemical impedance spectroscopy (EIS) and electrochemical capacitance spectroscopy (ECS). The resultant biosensors were highly specific for the β -1,4-GalT-V glycoprotein, detecting and quantifying it in human raw serum samples, thus holding considerable potential for determining this cancer biomarker and other proteomic cancer-related biomarkers.

Methods

We fabricated both biosensors following four main steps: 1) electrode activation, 2) surface modification and characterization, 3) antibody immobilization and blocking of the unspecific binding sites, and 4) detection of the biorecognition molecular event by EIS and ECS. We used screen-printed gold and carbon electrodes (SPAuEs and SPCEs) in the impedimetric and capacitive biosensors. First, we activated both electrodes by cyclic voltammetry in acidic conditions and modified the surface of the working electrodes. For example, we modified the SPAuE surface with a mixed self-assembled monolayer (SAM) of mercaptohexanol/mercaptoundecanoic acid for the EIS-based biosensor; and the SPCEs with a nanocomposite of gold nanorods (AuNRs) and Prussian blue (PrB) as the redox compound for the ECS-based biosensor. Next, we immobilized the antibody on the SPAuE/SAM covalently by EDC/NHS chemistry and the SPCE/AuNRs/PrB by adsorption. When we completed the antibody immobilization, we blocked both electrodes' unspecific binding sites with ethanolamine (ETA) in the SPAuE/SAM and bovine serum albumin (BSA) in the SPCE/AuNRs/PrB. Once we assembled the biosensors, we made them interact with β -1,4-GalT-V glycoprotein to capture it onto the electrode surface by a biochemical affinity reaction, thereby producing changes in the electronic properties at the electrode/solution interface correlated with changes in the glycoprotein concentration.

We characterized each fabrication step by electrochemical techniques with $[\text{Fe}(\text{CN})_6]^{4-/3-}$ as a redox probe in solution to characterize the impedimetric biosensor. In contrast, we did not use a redox probe in the solution to characterize the capacitive biosensor but instead used phosphate buffer (PB) as a supporting electrolyte. Next, we characterized the biosensing interfaces by CV and conducted the EIS analysis to obtain the impedance spectra in each architecture. Then, from Nyquist diagrams, we obtained the charge transfer resistance (R_{ct}) fitting the experimental spectra to an electrical equivalent circuit and used it as the transduction signal for the impedimetric biosensor [2]. Similarly, we conducted the EIS in PB for the capacitive biosensor and converted impedance spectra into capacitance, obtaining the redox capacitance C_r , using the inverse of redox

capacitance ($1/C_r$) as the transduction signal [3]. Finally, we evaluated the biosensors' response to different β -1,4-GalT-V glycoprotein concentrations and constructed a calibration curve to determine the analytical performance.

Results

Figures 1-2 show the electrochemical performance characterization of the biosensors at each fabrication step. The electrical interfacial changes suggested a successful biosensor assembly and glycoprotein capture onto the electrode surface. In addition, we determined the analytical parameters from results obtained in the calibration curves (see Figures 1D and 2D). We observed an enhancement in the analytical performance detecting the glycoprotein by capacitance as a transduction signal.

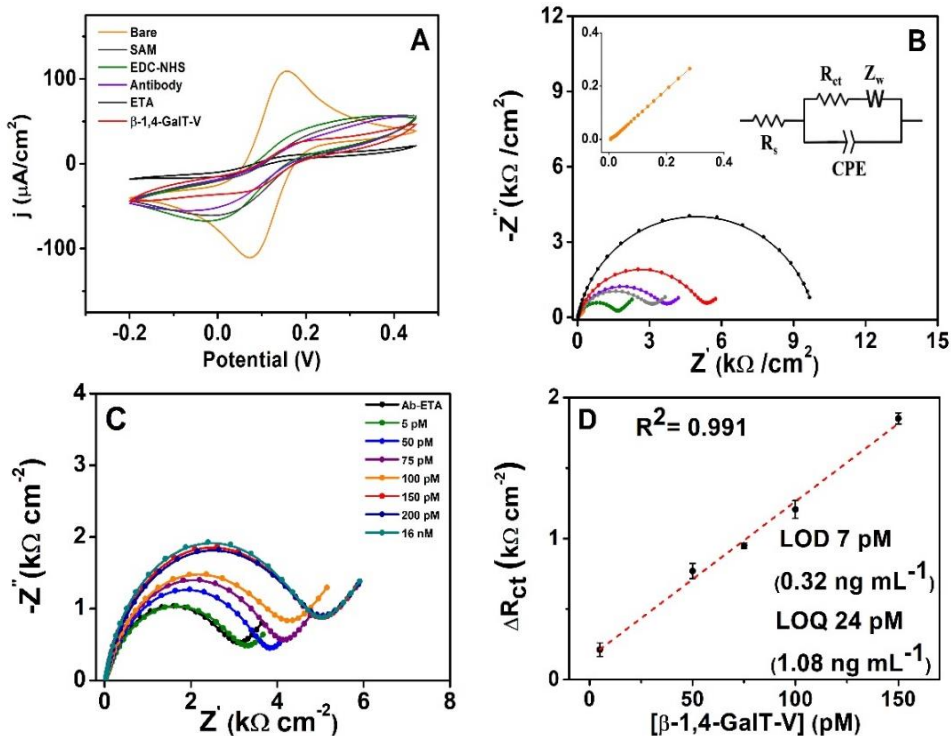


Figure 1. Electrochemical characterization of the impedimetric architecture (A) Cyclic voltammograms and (B) Nyquist plot for each biosensor's assembly step (the bare electrode and the electrical equivalent circuit are in the inset). (C) Nyquist plot at different glycoprotein concentrations. (D) Linear calibration curve. EIS parameters: frequency range 100 kHz to 0.1 Hz, amplitude 10 mV. The redox probe was 5 mM $[\text{Fe}(\text{CN})_6]^{4-/3-}$ / PBS 10 mM, pH 7.4.

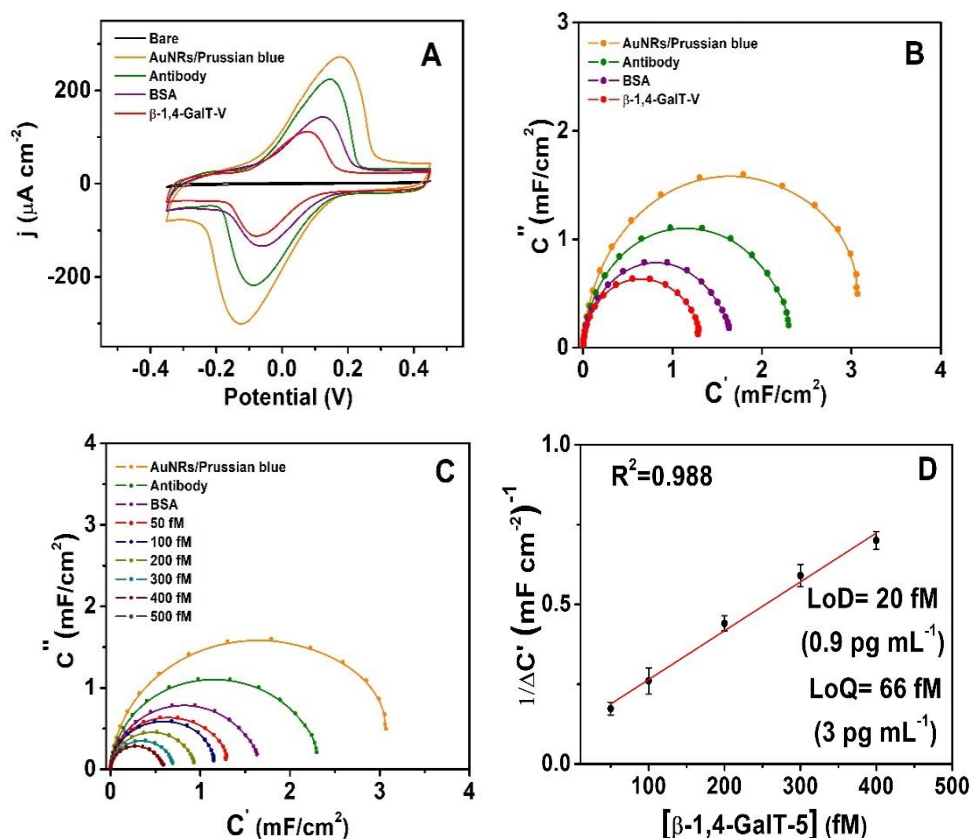


Figure 2. Electrochemical characterization of the capacitive architecture (A) Cyclic voltammograms and (B) Nyquist capacitive plot for each biosensor's assembly step. (C) Nyquist capacitive plot at different glycoprotein concentrations. (D) Linear calibration curve. EIS parameters: frequency range 100 kHz to 0.1 Hz, amplitude 10 mV. The supporting electrolyte was phosphate buffer (PB) 10 mM, pH 7.4.

Conclusions

We successfully developed two architectures of label-free electrochemical biosensors. These devices can detect the β -1,4-GalT-V glycoprotein at concentrations of clinical relevance. We compared the impedimetric and capacitive architectures and determined that the capacitive biosensor is highly sensitive and enhances the analytical performance for the detection of β -1,4-GalT-

V glycoprotein concerning the impedimetric device achieving a β -1,4-GalT-V glycoprotein detection at femtomolar concentrations. This biosensor detects the biomarker in human serum at levels of clinical relevance, hence could use for real applications at the point of care.

References

- [1] S.B. Chatterjee, J. Hou, V.V. Ratnam Bandaru, M.K. Pezhouh, A.A. Syed Rifat Mannan, R. Sharma, Lactosylceramide synthase β -1,4-GalT-V: A novel target for the diagnosis and therapy of human colorectal cancer, *Biochemical and Biophysical Research Communications*. (2019) 380–386.
- [2] D. Echeverri, J. Orozco, β -1,4-Galactosyltransferase-V colorectal cancer biomarker immunosensor with label-free electrochemical detection, *Talanta*. 243 (2022) 123337.
- [3] P.R. Bueno, G. Mizzon, J.J. Davis, Capacitance spectroscopy: A versatile approach to resolving the redox density of states and kinetics in redox-active self-assembled monolayers, *Journal of Physical Chemistry B*. 116 (2012) 8822–8829.

Acknowledgments

The work has been funded by MINCIENCIAS, MINEDUCACION, MINCIT, and ICETEX through the Program Ecosistema Científico Cod. FP44842-211-2018, project number 58536. J. O thanks support from The University of Antioquia and the Max Planck Society through the cooperation agreement 566–1, 2014. Finally, we thank The Ruta N complex and EPM for hosting the Max Planck Tandem Groups.

O34 |

DISPOSABLE BIOMEDICAL DEVICES FOR AT-HOME MONITORING OF DIFFERENT METABOLIC DISEASES

B. Rebollo-Calderon, E. Alberto Serrano, J. Martínez Roldán, A. Calvo-López,
M. Puyol and J. Alonso-Chamarro

¹ *Group of Sensors and biosensors, Autonomous University of Barcelona, SPAIN*

**e-mail: beatriz.rebollo@uab.cat*

Introduction

Inherited Metabolic Diseases (IMD) are rare diseases which cause the disruption of different metabolic processes by the mutation of one of their enzymes, leading to the accumulation in blood of different metabolites depending on the specific enzyme and metabolic pathway affected. Some IMD such as urea cycle disorders and organic acidemias, phenylketonuria (PKU) and uremia entail the accumulation in blood of different nitrogenous compounds, in this case ammonium (NH_4^+), phenylalanine (Phe) and urea, respectively¹⁻³. The accumulation of these compounds is a medical emergency that, if left untreated, can lead to severe irreversible brain damage, coma and even death. Nevertheless, there are no commercial devices available for at-home determination of these previously mentioned metabolites in blood. The regular monitoring of these diseases can only be carried out at reference hospitals every 15-30 days or when patients present symptoms.

To overcome this obstacle, we propose a disposable, low cost and robust device for the fast detection of biomarkers in capillary blood that is easy to use by the patients themselves and would allow them to manage their disease at home.

It consists of a potentiometric Cyclic-Olefin-Copolymer (COC) platform that contains two solid-state ion selective electrodes (ISE) for NH_4^+ , one acting as a reference and the other as a working electrode, and includes a polyvinylidene fluoride (PVDF) gas diffusion membrane to avoid the potential interfering effect of other cations present in the sample. There are two main characteristics of the analytical platform worth highlighting: the first one is the self-calibration prior to performing the analytical measurement, and the second is its versatility, so it can be tailored to the indirect measurement of a vast range of metabolites by the incorporation of an enzyme that converts the target analyte into NH_4^+ .

Methods

The proposed analytical device (*Fig. 1A and B*) has been fabricated following a process described elsewhere⁴. In the case of the determination of NH_4^+ (*Fig. 1C*), we use NaOH as a donor solution to convert the NH_4^+ into volatile NH_3 , which can cross the gas diffusion membrane, and on the other side, it is converted back to NH_4^+ in the presence of a buffer at neutral pH, acting as an acceptor solution. In the case of the determination of other nitrogenous compounds (*Fig. 1D*), we incorporate an enzyme, which converts the analyte into NH_3 .

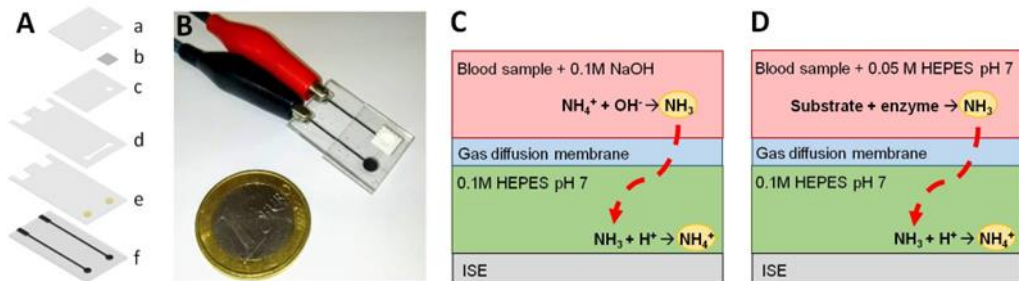


Figure 1: A) CAD design where a) is the layer where sample is deposited; b) a PVDF membrane; c); d) a layer with saline bridge; e) a layer with PVC NH_4^+ membranes; f) a layer with ISE conductive supports. B) Real image of the microdevice. C and D) Schematic representation of the determination process for NH_4^+ (C) and other nitrogenous analytes (D).

Results

The structural, chemical and kinetic variables for the determination of three analytes of interest were evaluated and the summary of this optimization can be seen in *Tab. 1*.

Table 1: Summary of the optimum values of the chemical and kinetic variables for NH_4^+ , urea and phenylalanine determination.

Variable	NH_4^+	Urea	Phe
Ionophore %	2%	2%	1%
ISE diameter	1.8mm	1.8mm	3.3mm
Sample volume	3 μl	3 μl	4,5 μl
[Donor solution]	NaOH 0.1M	HEPES 0.1M pH 7	HEPES 0.1M pH 9
[Acceptor solution]	HEPES 0.1M pH 7	HEPES 0.1M pH 7	HEPES 0.1M pH 7
Time of analysis	4 min	10 min	7 min (6 min agitation)
Enzyme	-	Urease	Phenylalanine dehydrogenase
[Enzyme]	-	25U/ml	100U/ml
Co-enzyme	-	None	NAD ⁺
[Co-enzyme]	-	-	3.3mM

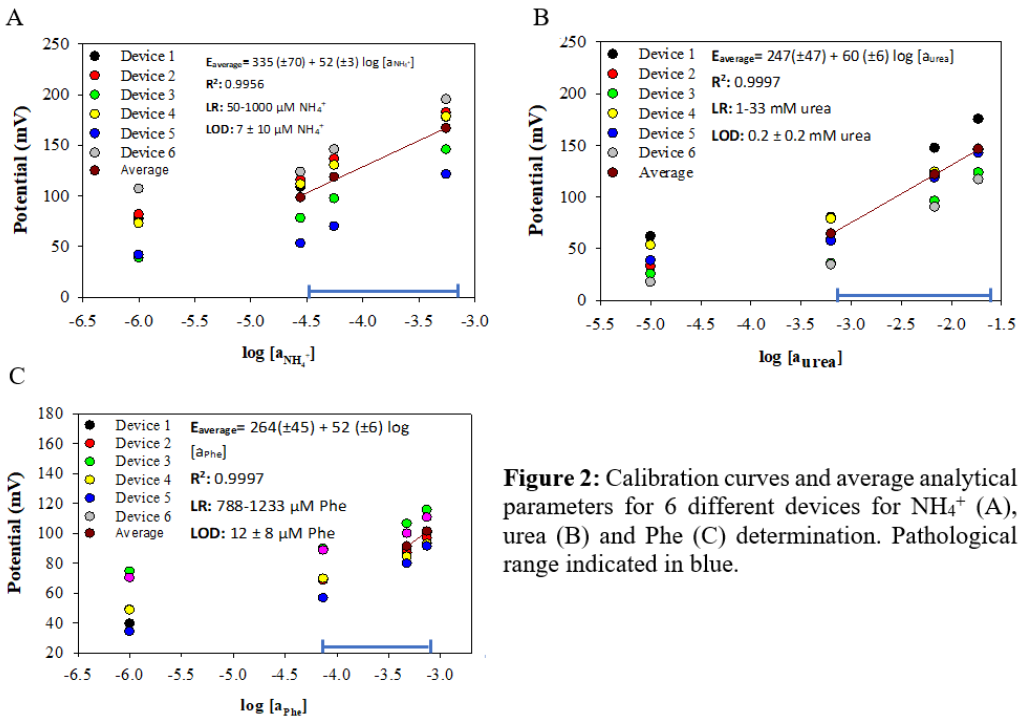


Figure 2: Calibration curves and average analytical parameters for 6 different devices for NH_4^+ (A), urea (B) and Phe (C) determination. Pathological range indicated in blue.

With these optimized conditions, different calibrations were performed in order to obtain the analytical features of the analytical devices for NH_4^+ (Fig. 2 A), urea (Fig. 2 B) and Phe (Fig. 2 C). In the case of the determination of NH_4^+ and urea, the linear ranges obtained cover the whole range of pathological concentrations of these metabolites in blood. In the case of Phe determination, the activity of the phenylalanine dehydrogenase was not enough to obtain satisfactory analytical characteristics in acceptable analysis time, even though agitation through vibration was included during the analysis. To obtain a wider linear range to cover the whole pathological concentration of Phe in blood we would need either a very long time of analysis (over 20 minutes) or a higher enzyme activity.

Conclusions

The potential of the proposed biomedical potentiometric platform as a monitoring device for diseases that cause hyperammonemia, and its versatility to be applied to the measurement of other analytes by the incorporation of an enzyme, have been demonstrated.

Future work will focus on the validation of the present platform for NH_4^+ and urea determination by the analysis of real blood samples. This will be done in collaboration with the Sant Joan de Déu Hospital (Barcelona) that will provide samples and carry out parallel measurements with the reference method, and with the Biomedical Instrumentation Group at the Polytechnic University of Catalunya that will design and manufacture miniaturized electronics for signal acquisition and a pairing mobile phone APP for data visualization.

Regarding the determination of Phe, future work will be aimed at increasing the activity of phenylalanine dehydrogenase, through new synthetic paths, to achieve analytical characteristics suitable to the determination of physiopathological Phe concentrations in blood.

References

- [1] Häberle, J. Clinical and biochemical aspects of primary and secondary hyperammonemic disorders. *Arch. Biochem. Biophys.* **536**, 101–108 (2013).
- [2] Cleary, M.A and Skeath, R. Phenylketonuria. *Pediatrics and child health* **29:3**, 111-115 (2019)
- [4] Vanholder, R., Gryp, T. and Glorieux, G. Urea and chronic kidney disease: the comeback of the century? (in ureaemia research). *Nephrol Dial Transplant* **33:4**, 4-12 (2018)
- [3] Calvo-López, A., Ymbern, O., Puyol, M., Casalta, J. M. & Alonso-Chamarro, J. Potentiometric analytical microsystem based on the integration of a gas-diffusion step for on-line ammonium determination in water recycling processes in manned space missions. *Anal. Chim. Acta* **874**, 26–32 (2015).

Acknowledgments

Authors are grateful for the financial support to the Spanish Ministerio de Economía, Industria y Competitividad and Ministerio de Ciencia e Innovación through the projects CTQ2017-85011-R, PDC2021-121558-100 and PID2020-117216RB-100, to Catalan government through the project 2017SGR 220, to Instituto de Salud Carlos III through the project DTS18/00104 and to the Fundación PKU.

O35 |

SURFACE MODIFICATION OF GALLIUM NANOPARTICLES AND THEIR INTERACTION WITH HUMAN SERUM ALBUMIN

N. V. Falcón-Cruz¹, A. Meléndez², I. Ramos², and R. Oyola¹

¹*Department of Chemistry, University of Puerto Rico-Humacao, Call Box 860, Humacao PR 00792*

²*Department of Physics & Electronics, University of Puerto Rico-Humacao, Call Box 860, Humacao PR 00792*

**e-mail: rolando.oyola@upr.edu*

Introduction

Metal nanomaterials, such as gallium nanoparticles, have been found to be considerably valuable in generating new pathways as transducing materials in biosensors and diagnostic approaches.[1] For instance, gallium nitride (GaN) nanoparticles have been proposed as antibacterial, and show biocompatibility and chemical stability.[2] Gallium oxide hydroxide (GaO(OH)) nanoparticles have been used in diagnostic and therapeutic approaches, like cancer treatments.[3] Also, surface conjugation of these materials with the appropriate compounds, like β -cyclodextrin, provides selectivity, facilitates drug delivery, and increases solubility.[3] Recently, we showed that the lag phase of A β 40 aggregation kinetics is significantly retarded by GaN NPs in a concentration dependent manner, implying the activity of GaN NPs in interfering with the formation of the crucial nucleus during A β 40 aggregation.[4] Also, the results showed that GaN NPs can reduce the amyloid fibril elongation rate during the aggregation kinetics. It was speculated that the high polarization characteristics of GaN NPs may provoke a strong interaction between the particles and A β 40 peptide and in this way decrease self-association of the peptide monomers to form amyloids. A better understanding of the interaction of GaNPs with biological components, like proteins, is an important consideration for the improvement of these nanomaterials. Thus, sensing molecular forces that control binding and structural conformations are relevant to develop new nanomaterials.

Human serum albumin (HSA) is the most abundant plasma protein in mammals that serves as ligand carrier and is a model widely used in biophysical and biochemical studies. [5-6] HSA possesses one tryptophan (Trp214) residue in the hydrophobic cavity of Sudlow's site I (subdomain IIA, warfarin binding site), which can be used as a probe for conformational and ligand interactions. HSA has another major binding site, Sudlow's site II (subdomain IIIA, indole/benzodiazepine site). Therefore, it is relevant to probe the interaction of

nanoparticles with HSA to use GaNP as sensors in biological fluids. In the present work, we synthesize and characterize gallium oxide nanoparticles conjugated with β -cyclodextrin (GaOCD) and hydroxyl (GaO(OH)) and probe its interaction with HSA by fluorescence spectroscopy. Our results show that HSA tertiary structure is not affected by GaO(OH) or GaOCD nanoparticles.

Methods

β -Cyclodextrins (β CD), Gallium (III) Nitrate Hydrate [$\text{Ga}(\text{NO}_3)_3 \cdot x\text{H}_2\text{O}$], ammonia solution (2.0 M in ethanol), Na_2HPO_4 , NaH_2PO_4 , and HSA (fatty acids free) were purchased from Sigma-Aldrich (St. Louis, USA). All aqueous solutions contain 20 mM sodium phosphate buffer (PBS) pH = 7.40 and were prepared using nanopure deionized water. The concentration of HSA was determined using molar absorption coefficient of $35,700 \text{ M}^{-1}\text{cm}^{-1}$ (at 280 nm). Gallium oxide nanoparticles (GaO(OH)) were synthesized as reported by Ganguly et al.[3] Briefly, a 1:4 ammonia water solution was added drop by drop to 10 mL of 2.00 mM gallium (III) nitrate hydrate until pH was maintained at 7.0-7.5 where a white precipitate was observed. Conjugation of gallium oxide nanoparticles with β CD (GaOCD) was achieved adding 2.8 mL of 0.5 mM β CD to 10 mL of gallium (III) nitrate hydrate. After well mixed, ammonia water was added drop by drop until pH was maintained at 7.0-7.5 and white precipitate was observed. For both synthesized NPs, solutions were centrifuged at 1200 rpm for 30 min, a minimum of three times, removing the supernatant and washing with deionized water each time. Precipitate was dried in vacuum oven at 60 °C for two days. NPs were then stored under vacuum for future use. NP aqueous dispersions were prepared, dissolving a weighted amount in deionized water and sonicating for 60 minutes. Scanning electron microscopy (SEM) images were obtained at the PREM Materials Characterization Laboratory at University of Puerto Rico-Humacao. Measurements were done on dried samples of GaO(OH) and GaOCD. The solid was dispersed on sampler tape and images taken at different magnifications. For fluorescence emission spectra, an Agilent Cary Eclipse spectrofluorometer with temperature control ($\pm 1 \text{ }^\circ\text{C}$) was used, exciting at 290 nm and scanning between 300 – 500 nm range at scan speed of 120 nm/min. Samples were measured in a 1 cm^2 quartz cell. Measurements for $1.0 \text{ }\mu\text{M}$ HSA solutions were made with excitation and emission slits at 10 nm and the photomultiplier high voltage (PMT) set to 600 V. A stirrer was used consistently through the duration of the experiments. The UV-Vis absorption spectra were obtained on an Agilent 8453 spectrophotometer (Agilent, USA) in a 1.0 cm^2 path length cell. The spectra were measured with their appropriate backgrounds. Solutions containing $1.00 \text{ }\mu\text{M}$ HSA with varying concentrations of GaOCD up to $76 \text{ }\mu\text{g/mL}$ were prepared in a total

volume of 1.5 mL and left stirring for 10 min. Fluorescence spectra were taken at temperature intervals of 5 °C in the range of 20 – 40 °C. Quenching constants were determined using the Stern-Volmer equation: $F_0/F = K_{SV}[Q] + 1$ where F_0 and F are the fluorescence emission intensity of HSA at 340 nm in the absence and presence of the quencher (GaOCD), $[Q]$ is the quencher concentration, and K_{SV} is the Stern-Volmer quenching constant. Corresponding backgrounds were subtracted for each NP concentration. Thermal denaturation of HSA was determined using a 1.00 μ M HSA with 0.0, 20, 40, and 76 μ g/mL GaNP in a total volume of 1.5 mL. The HSA emission spectra were taken at 5 °C intervals in the range of 20 – 100 °C, allowing 8 minutes for equilibration before measurement. The results were the average of three independent measurements. Thermodynamic parameters were obtained based on two-state system.

Results

Morphological Characterization

Dried NPs samples have been characterized using SEM images as well as Energy Dispersive X-ray Spectroscopy (EDS) to determine the morphology and atomic composition of synthesized NPs. **Figure 1a-d** shows SEM image of GaO(OH) and GaOCD. Width and length measurements shows that GaO(OH) NPs are larger than GaOCD (~0.7 μ m vs. 0.4 μ m). Chemical composition of both synthesized NPs was determined by EDS analysis. The mass percent distribution of carbon, oxygen, and gallium in GaO(OH) is 0.00, 14.83, and 85.17, respectively. Capping of GaO(OH) with β CD was validated by the increase in mass % of carbon in the EDS signal: C = 3.44, O = 20.30, and Ga = 76.26 %, respectively.

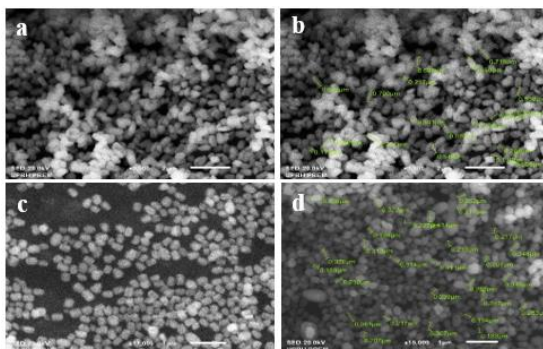


Figure 1. SEM imaging of nanoparticle samples. (a) Low magnification (x9,500) image of GaO(OH) showing rod-like morphology. (b) Length and width measurements indicating GaO(OH) NPs are no larger than 0.7 μ m. (c) High magnification (x17,000) image of GaOCD as nanodisk-like structures with (d) (x15,000) length and width measurements, indicating most are

smaller than 0.4 μm .

Fluorescence Quenching of HSA in the Presence of GaOCD

Quenching of HSA was probed using Trp214 emission in the presence of a variety of GaOCD concentrations for determination of binding constants between 20 - 40°C. **Figure 2** shows that increasing concentration of GaOCD quenches Trp emission, an indication of protein interaction with NP. The Stern Volmer plots' slopes decrease with temperature from 6.1×10^3 to 4.4×10^3 ($\mu\text{g}/\text{mL}^{-1}$), indicative of static quenching mechanisms. [4,6] Fluorescence quenching experiments resulted in low K_{SV} values (10^3 ($\mu\text{g}/\text{mL}^{-1}$)) relative to gold nanoparticles ($>10^8$ M^{-1}). van't Hoff analysis of the quenching data for determination of thermodynamic parameters of binding suggest the presence of electrostatic forces governing HSA and GaOCD interactions.

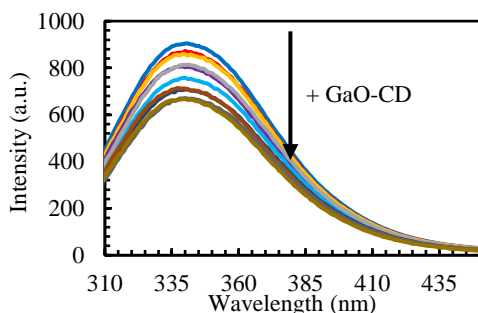


Figure 2. Fluorescence emission spectra of HSA with different concentrations of GaOCD, taken at 20 °C. Increasing concentration of NP causes decrease in emission.

Thermal Denaturation of HAS

Figure 3 shows representative melting curves for the normalized integrated intensity change for HSA as a function of temperature (20 – 100 °C) in the presence of 0 and 76 $\mu\text{g}/\text{mL}$ GaOCD. For determination of T_m values and thermodynamic parameters for thermal denaturation, data was fitted to two-state system.

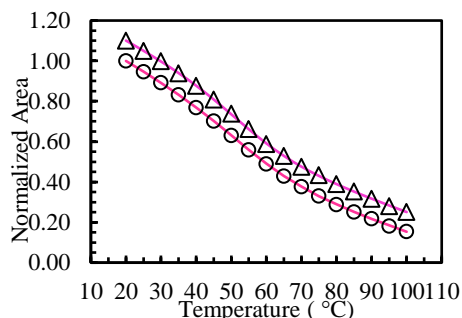


Figure 3. Representative melting curve of HSA (Δ) and in the presence of 76 $\mu\text{g}/\text{mL}$ GaOCD (\circ). Solid lines represent the best fit to two-state equilibrium system. The HSA curve is offset by 0.10 in the Y-axis for presentation purposes.

Melting curves and their corresponding T_m values obtained in the presence of different concentrations of GaOCD are similar. T_m obtained for HSA is in agreement with literature, where two melting point temperatures of 56 (T_{m1}) and

62 (T_{m2}) °C have been reported. [7-9]. These two T_m values have been attributed to sequential denaturation of domain II and domain I, respectively. The presence of GaOCD (up to 76 µg/mL) results in similar T_m , within experimental error, relative to HSA, suggesting that GaOCD does not affect the tertiary structure of the protein in great extent.

Conclusions

This project had the aim of synthesizing and characterizing GaOCD and GaO(OH) and study its interaction with HSA through fluorescence spectroscopy. The preliminary results indicate that the interaction between the GaOCD nanoparticles (up to 76 µg/mL) and HSA is weaker than for gold nanoparticles. Additionally, tertiary structure of HSA is not affected by presence of GaOCD. More studies are required to better understand the interaction of gallium nanoparticles with biomolecules. Proteins and peptides with different physicochemical properties should provide more information about the relative forces governing the NPs and biomolecules interactions.

References

- [1] Li, X.; Liu, X. Group III nitride nanomaterials for biosensing. *Nanoscale* **2017**, *9*, 7320-7341.
- [2] Bain, L. E.; Hoffmann, M. P.; Bryan, I.; Collazo, R.; Ivanisevic, A. Adsorption and adhesion of common serum proteins to nanotextured gallium nitride. *J. Name.*, **2013**, *00*, 1-3.
- [3] Ganguly, B. N.; Verma, V.; Chatterjee, D.; Satpati, B.; Debnath, S.; Saha, P. Study of Gallium Oxide Nanoparticles Conjugated with β -Cyclodextrin: An Application to Combat Cancer. *ACS Appl. Mater. Interfaces*, **2016**, *8*, 17127– 17137.
- [4] Torres, K.M., Delgado, A.S., Serrano, E.R., Falcón-Cruz, N.V., Meléndez, A., Ramos, I., Du, D., and Oyola, R. Gallium nanoparticles as novel inhibitors of A β 40 aggregation. *Mater. Adv.*, **2021**, *2*, 5471-5478.
- [5] Flora, K.; Brennan, J. D.; Baker, G. A.; Doody, M. A.; Bright, F. V. Unfolding of Acrylodan-Labeled Human Serum Albumin Probed by Steady-State and Time-Resolved Fluorescence Methods. *Biophys. J.* **1998**, *75*, 1084–1096.
- [6] Li, Q.; Yang, W. Y.; Qu, L. L.; Qi, H. Y.; Huang, Y.; Zhang, Z. Interaction of Warfarin with Human Serum Albumin and Effect of Ferulic Acid on the Binding. *Journal of Spectroscopy*, **2014**, Article ID 834501, 7 pages.
- [7] Picó, G. A. Thermodynamic Features of the Thermal Unfolding of Human Serum Albumin. *Int. J. Biol. Macromol.* **1997**, *20*, 63–73.
- [8] Farruggia, B.; Picó, G. A. Thermodynamic features of the chemical and thermal denaturations of human serum albumin. *Int. J. Bio. Macromol.* **1999**, *26*, 317-323.
- [9] Das, N. K.; Ghosh, N.; Kale, A. P.; Mondal, R.; Anand, U.; Ghosh, S.; Tiwari, V. K.; Kapur, M.; Mukherjee, S. Temperature Induced Morphological Transitions from Native to Unfolded Aggregated States of Human Serum Albumin. *J. Phys. Chem. B*, **2014**, *118*, 7267–7276.

Acknowledgments

We gratefully acknowledge financial support from the NSF-DMR-2122102.

DETECTION OF DEFECTS ON DISPLAYS BASED ON MICROSCOPIC AND OPTICAL COHERENCE TOMOGRAPHY EXAMINATION

H. M. Pereira ^{1,2,*}, R. B. Freitas ^{1,2,*}, B. Esteves ^{1,2}, C. P. Santos ^{1,2}, Pedro Carvalho ³,
Paulo Compadrinho³, Carlos Rodrigues ³, M. J. Maciel ^{1,2}, E. J. Nunes-Pereira ⁴,
C. A. Silva ^{1,2}, J. H. Correia ^{1,2}

¹ CMEMS – UMinho, University of Minho, Campus Azurem, 4800-058, Guimarães, Portugal

² LABBELS – Associate Laboratory, Braga/Guimarães, Portugal

³ ITEC – Iberiana Technical, Braga, Portugal

⁴ Center of Physics of Minho and Porto Universities (CF-UM-UP), University of Minho, Braga,
Portugal

*e-mail: hugo.pereira@dei.uminho.pt; ruben.freitas@dei.uminho.pt

Introduction

The use of displays in control car panels, smartphones, notebooks and LCD TVs has increased in the last decade. The large-scale manufacturing of new products emphasizes the need for fault detection at an early stage in the assembly process to detect the presence of scratches and particles. Therefore, fast, reliable and efficient displays inspection equipment is essential in order to reduce production-line stoppages, increase productivity and ensure the product reliability.

The fact that these defects may range from a few to hundreds of micrometers poses high demands on the measurement technology to ensure the quality of the product. Also, the metrology techniques should be non-destructive and non-contact, and have automated image processing and analysis capability. Current inspection techniques use machine vision based on a charge-couple device camera [1]. These techniques provide a top view of the display panel surface, which allows quantifying the surface extension of the defect. However, it is not able to provide information on the depth of a scratch or the effect on the structure of the surface caused by particles. Other types of techniques are available for metrology, such as X-rays, computed tomography and ultrasonic imaging, but they do not provide depth resolution at the required scale [2], [3].

In this work, we evaluate the use of: an inspection microscope Nikon Eclipse L200N combined with the microphotography camera Nikon DS-Fi3 and a commercial Optical Coherence Tomography (OCT) system, Telesto II-1325LR from Thorlabs, for analysis of the presence of scratches and particles on the surface of display panels. OCT is a non-invasive and non-destructive modality

that may be used for imaging microstructures at the micrometer scale. This work was performed in the scope of an industrial research project with ITEC company. ITEC company is specialized in the development of automatic inspection equipment for manufacturing quality control.

Methods

OCT is a well-established imaging technology for high-resolution, cross-sectional imaging of biological tissues. Imaging processing and light attenuation coefficient estimation allows to further improve the OCT diagnostic capability.

The operating mechanism of OCT bears resemblance to ultrasound imaging, with the difference that light is used instead of acoustic waves. Near-infrared (NIR) light is the most commonly used. The optical configuration of OCT is based on low-coherence interferometry (LCI), which measures the time delay and the intensity of backscattered light by interference with light traveling along a reference path. The most common configuration of LCI for OCT technology is based on the Michelson interferometer shown schematically in Figure 1. The light beam from a source is split into two parts in a beam splitter; with one part directed to a reference mirror and another to the sample being analyzed. Depending on the properties of the sample, the light can be reflected, refracted, dispersed and absorbed. The light backscattered from the sample interferes with the light reflected from the reference mirror at the beam splitter and the resulting intensity is detected with an optical detector system at the interferometer output. The mathematical description of the operating mechanism of OCT is extensively described in literature [4].

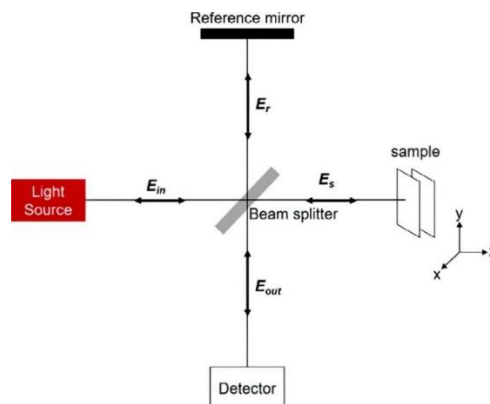


Figure 1 – Michelson interferometer, LCI configuration for OCT technology. E_{in} , E_{out} , E_r and E_s , correspond to the optical fields in the input, output, reference and sample arms, respectively.

Results

The results of the inspection microscope Nikon Eclipse L200N combined with the microphotography camera Nikon DS-Fi3 are excellent to detect defects higher than $5\ \mu\text{m}$ in dimension. However, this technique only allows for a surface level inspection and does not provide a depth-resolved view of the defects. By use of this microscope, as shown in Figure 2 (a) and 2 (b), it was proven possible to detect surface level scratches in LCD screens of roughly $9.5\ \mu\text{m}$ and $6\ \mu\text{m}$ wide in dimension, respectively.

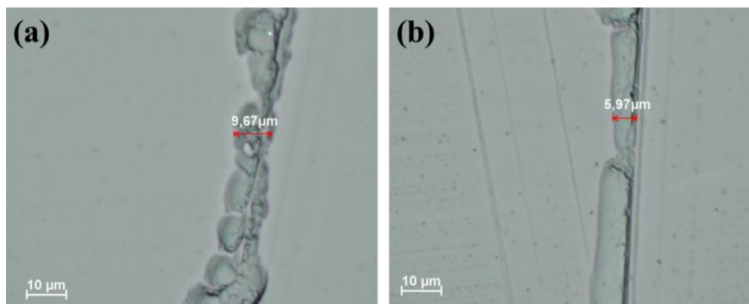


Figure 2 – LCD screens scratches inspection via Nikon Eclipse L200N microscope, where it is possible to detect defects of roughly, (a) $9.5\ \mu\text{m}$ and (b) $6\ \mu\text{m}$ wide.

The commercial OCT system, Telesto II-1325LR from Thorlabs, mounted in a spectral domain (SD) configuration is presented in Figure 3. The OCT system uses a super-luminescent diode (SLD) centered at $1325\ \text{nm}$ and presents a theoretical axial resolution of $12\ \mu\text{m}/9\ \mu\text{m}$ and an imaging depth of $7.0\ \text{mm}/5.3\ \text{mm}$ (air/water). Lateral resolution of the OCT system is decoupled from the axial resolution: while the axial resolution is controlled by the spectral bandwidth of SLD, the lateral resolution is controlled by optics.

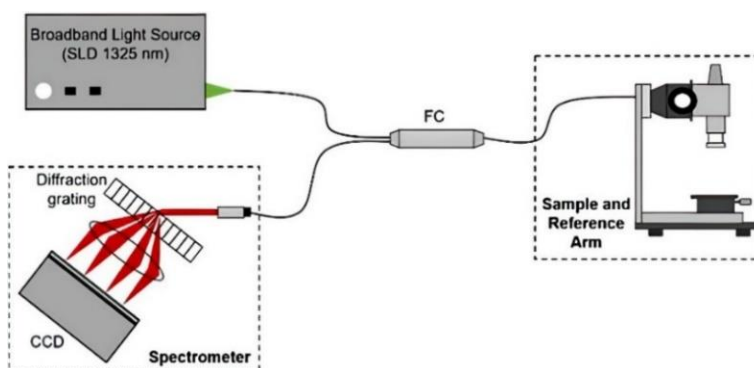


Figure 3 – Schematic of the SD-OCT system Telesto II-1325 LR, from Thorlabs. Reproduced with permission from [5] Thorlabs, Inc.

The imaging probe of Telesto II contains a Michelson-type interferometer, two galvanometric scanning mirrors and a telecentric scanning objective (OCT-LK4 optical kit from Thorlabs, which provides a lateral resolution of 20 μm). The spectrometer specifications fixed a pixel size vertical resolution of 6.91 μm well established in a depth of approximately 0.5 mm, nevertheless this parameter is limited by the optical source and the optical properties of the sample and has been shown to be capable to estimate up to 2 mm in depth [6].

Conclusions

Both methods (the inspection microscope Nikon Eclipse L200N combined with microphotography camera Nikon DS-Fi3 and the commercial OCT system, Telesto II-1325LR from Thorlabs) have shown to be excellent tools for analysis of the presence of scratches and particles on the surface of display panels. However, in order to properly analyze these defects in depth, the use of imaging processing and light attenuation coefficient estimation allows to further improve the OCT diagnostic capability. The OCT light attenuation coefficient estimation eliminates the subjective analysis provided by the direct visualization of the OCT images.

References

- [1] J. H. Kim, S. Ahn, J. W. Jeon, and J. E. Byun, "A high-speed high-resolution vision system for the inspection of TFT LCD," *IEEE Int. Symp. Ind. Electron.*, vol. 1, pp. 101–105, 2001
- [2] L. F. Gladden, "Process Tomography: Principles, Techniques and Applications," *Meas. Sci. Technol.*, vol. 8, no. 4, Apr. 1997.
- [3] L. Salvo *et al.*, "X-ray micro-tomography an attractive characterisation technique in materials science," *Nucl. Instruments Methods Phys. Res. Sect. B Beam Interact. with Mater. Atoms*, vol. 200, pp. 273–286, Jan. 2003.
- [4] M. Maciel, C. Rosa, R. Wolffenbuttel, and J. Correia, "Optical Coherence Tomography within a single microsystem," *J Phys D Appl Phys*, 2018.
- [5] Thorlabs 2021 Telesto® series SD-OCT systems OCT Tutor.
- [6] M. J. Maciel, H. M. Pereira, S. Pimenta, A. Miranda, E. J. Nunes-Pereira, and J. H. Correia, "Differentiation between normal and tumor mammary glands with depth-resolved attenuation coefficient from optical coherence tomography," *Biomed. Phys. Eng. Express*, vol. 8, no. 1, p. 015007, Jan. 2022.

Acknowledgments

This work was supported by project MME and project "ITEC Smart Automation I4.0", FEDER with the reference NORTE-01-0247-FEDER-045073, POR Norte, Portugal 2020.

Cu₂O/CuO COMPOSITE SYNTHESIS BY THERMAL TREATMENT OF Cu₂O THIN FILMS AND ITS APPLICATION AS A NON-ENZYMATIC GLUCOSE SENSOR

F. Figueredo¹, P. Grez¹, R. Schrebler¹, P. Salazar¹, C. Heyser²

¹ *Laboratorio de Electroquímica, Instituto de Química, Facultad de Ciencias, Pontificia Universidad Católica de Valparaíso, Av. Universidad 330, Valparaíso, Chile.*

² *Universidad Autónoma de Chile, Facultad de Ingeniería, Instituto de Ciencias Químicas Aplicadas, Núcleo de Astroquímica & Astrofísica, Av. Alemania 01090, Temuco, Chile.*

**e-mail: franciscofigueredo88@gmail.com*

Introduction

Diabetes mellitus, known as diabetes, is a disease caused by the pancreas, where it generates insulin deficiency, resistance to it or both. It currently affects about 350 million people and according to projections by the World Health Organization (WHO) and the International Diabetes Federation (IDF) it is expected to reach 700 million people with this disease in 2040 [1]. One way to control the disease is to measure glucose levels in physiological fluids where electrochemical sensors generate results in a simple, fast, sensitive and reliable way.

Currently, the majority of glucose sensors are based on the use of enzymes, such as glucose oxidase (Gox) and glucose dehydrogenase (GDH). However, these have low stability against changes in temperature, pH of the medium, etc. Due to this, a growing interest in non-enzymatic electrochemical devices has been generated. Mainly formed from metal oxides, such as Co₃O₄, NiO, ZnO and Cu_xO (2,3). In addition, in the search to improve the electrocatalytic properties of the sensors, the incorporation of composites has been studied, these structures generate redox pairs between the oxidation states in order to obtain structures of greater sensitivity. Based on the above, the present study seeks to carry out a systematic analysis of the detection and quantification of glucose, using a Cu₂O/CuO composite sensor, in the form of thin films.

Methods

First, Cu₂O films on FTO substrate were synthesized by means of a potential pulse at -0.565 using a solution composed of 0.1 M CH₃COONa and 0.02 M (CH₃COO)₂Cu, at pH 5.79 in an inert atmosphere. The Cu₂O/CuO composite was then formed by thermal oxidation of the Cu₂O film in air at 300 and 350°C for 90

minutes with a temperature ramp of 1°C/min. The structures were characterized through scanning electron microscopy (SEM) with X-ray energy dispersive spectroscopy (EDX) and X-ray diffraction (XRD) detector. The tests with glucose were carried out using a conventional cell with three electrodes and 0.1 M NaOH as electrolytic solution, the techniques used were linear scanning voltammetry (LSV) for the comparison curve and obtaining more information about the glucose oxidation process. and chronoamperometry (CA) to determine the calibration curve (sensitivity, LOD, LOQ and response time) and selectivity against different electroactive interferences in physiological fluids such as ascorbic acid, uric acid, dopamine acid and sucrose.

Results

The synthesis of the composites was carried out by thermal oxidation of Cu₂O thin films at 300°C and 350°C with a temperature ramp of 1°C/min. Figure 1A shows the frontal image of the composite, while figure 1B shows its pyramidal morphology with scales making a surface with greater roughness. Also, the presence of the characteristic peaks of both Cu₂O and CuO was confirmed by XRD.

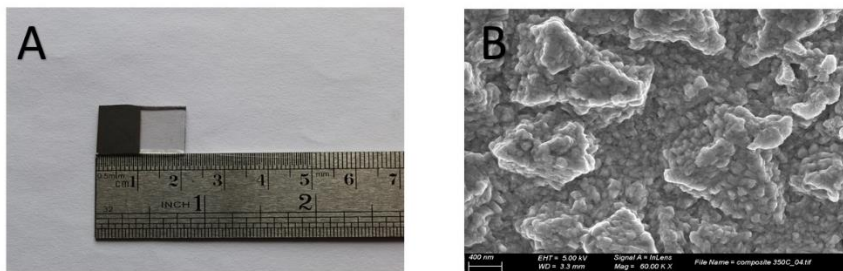


Figure 1 A) Front view of the composite heat treated at 350°C; B) SEM image of the composite at 350°C.

For the tests with glucose, the activity of the composites was compared with the Cu₂O thin film, figure 2A, showing that the thermal treatment at 300 and 350°C generates an increase in the current density of the glucose oxidation peak of 40 and 55%, respectively. Finding the best results with the thermal oxidation at 350°C, from which its most relevant results will be shown.

The different figures of merit of the sensor were then determined from the calibration curve: such as sensitivity ($\mu\text{A}\cdot\text{mM}^{-1}\cdot\text{cm}^{-2}$), LOD (2.32 μM), LOQ (7.21 μM), linear range (0-15 mM) and response time of 4 seconds measured at a

concentration of 1 mM and with 98.9% of the response achieved initially. In addition, was obtained more information about glucose oxidation, being an irreversible process and diffusion-controlled.

Another important point of determining the selectivity of the $\text{Cu}_2\text{O}/\text{CuO}$ electrode against electroactive species, which are present in physiological fluids such as urine or blood. For this, the chronoamperometric response was performed with common interferences such as ascorbic acid (AA), uric acid (UA), dopamine acid (DA) and sucrose (SA), which generally coexist with glucose. The amperometric response, figure 2B, was carried out by polarizing the system at 0.20 V, then G, AA, UA, DA, SA and again G in 0.1M NaOH were added successively. Initially, the amount necessary to reach a concentration of 0.2 mM of each of these species in the electrolyte solution was added to the solution. For each addition, the solution was stirred for 30 s, after which it was stopped and waited until a constant current value was reached. In this context, before the first addition of G, a constant current value was reached at 140 s. Similarly in later additions, after stirring, the system was allowed to stabilize for a period of 240 s. Finally, glucose was added again until reaching a concentration of 2.0 mM. These concentrations were used because literature reports indicate that the concentration of the interferences present in physiological fluids is approximately 10% that recorded by glucose. In relation to the response, it is possible to appreciate that the different interferences show lower current density values in relation to the first addition of glucose, all of them concentrations of 0.2 mM, also in relation to its shape, they all present the same trend, after that it is possible to appreciate a notorious growth of the current peak due to the addition of a higher concentration of glucose. From the figure, it is possible to establish that the proposed $\text{Cu}_2\text{O}/\text{CuO}$ electrode has a very low response to the interferences studied and only responds to glucose additions.

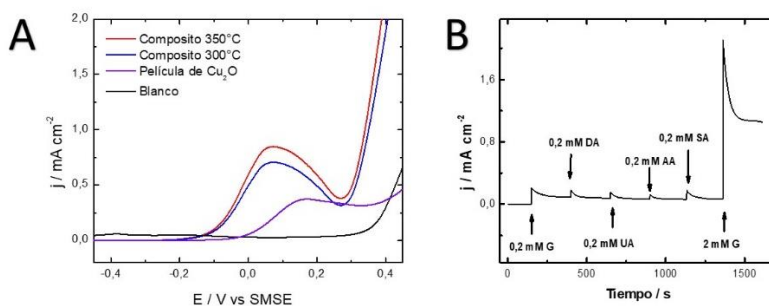


Figure 2. A) Comparison of the electrocatalytic activity response of the Cu_2O film and composite at different temperatures against the glucose oxidation reaction; B) Amperometric response of the different electroactive interferences present in physiological fluids.

Finally, electrode stability was estimated by measuring its current responses to 1.0 mM glucose by linear scanning voltammetry, after the sensor had been stored for 1, 7, 15, 30, 60, and 90 days. In this, it is observed that even after being stored for long periods of time, for example, 60 and 90 days, the current response retains 92.75% and 87.13% of the response generated initially, respectively. Which reveals good long-time stability for the electrode when stored at room temperature.

Conclusions

The conclusions of this work show that it was possible to generate both composites at 300 and 350°C by thermal oxidation, which was corroborated by SEM and XRD.

The tests carried out with glucose showed that the composites at 300°C and 350 registered a 40 and 55% increase in the current density of the glucose oxidation peak when compared to the Cu₂O film, respectively. The study demonstrates that the compound detects glucose in a linear range from 0.1 to 10 mM with a correlation coefficient of 0,99385 and and keeps the 92.58% of its original current response after 60 days.

Finally, it was determined that the proposed electrode shows only response to the presence of glucose and not to other interfering species (eg. ascorbic acid, uric acid, dopamine acid and sacarose), confirming the selectivity of Cu₂O/CuO composite for glucose.

So, the electrode proposed in this study, is a good candidate for to be used as a non-enzymatic amperometric glucose sensor due to the good merit figures.

References

- [1] Atlas de la Diabetes, *IDF* **2019**, 9th ed, 1-180.
- [2] C. Heyser, R. Schrebler, P. Grez, *Journal of Electroanalytical Chemistry* **2019**, 832, 189–195.
- [3] L. Wenbin, C. Guochun, Z. Xingming, D. Yuxiang, Q. Yang, *Sensors & Actuators: B. Chemical* **2020**, 321, 128485

Acknowledgments

The authors, especially PhD.(C) Francisco Figueredo are grateful the financial support of ANID, Beca Doctorado Nacional N°21202131 also to the Pontificia Universidad Católica de Valparaíso, Beneficiario Beca Postgrado 2019 and the Dr. Paula Grez to DI-PUCV with the project N°125.789.

GALLIUM NANOPARTICLES INTERACTION WITH IAPP: CAN GaNPS INHIBITS OLIGOMERIZATION?

N.V. Falcón-Cruz¹, A. S. Delgado², K. M. Torres², A. Meléndez³, I. Ramos³, D. Du⁴,
and R. Oyola¹

¹*Department of Chemistry, University of Puerto Rico-Humacao, Call Box 860,
Humacao PR 00792*

²*Department of Biology, University of Puerto Rico-Humacao, Call Box 860,
Humacao PR 00792*

³*Department of Physics & Electronics, University of Puerto Rico-Humacao, Call Box 860,
Humacao PR 00792*

⁴*Department of Chemistry & Biochemistry, Florida Atlantic University, Boca Raton, FL USA
e-mail: rolando.oyola@upr.edu

Introduction

The deposition of amyloid in the islets of Langerhans in the pancreas is a characteristic pathological feature of Type-2 diabetes. [1-2] These amyloids are composed of islet amyloid, a 37-residue peptide hormone named islet amyloid polypeptide (IAPP) or amylin. IAPP amyloidosis contributes to the β -cell failure in type 2 diabetes and islet transplant failure.[3-4] Several strategies have been attempted to design potential aggregation inhibitors for stabilizing the proteins in native soluble conformations or destabilizing the altered amyloidogenic conformer via intervening protein–protein interactions.[5] Family III nitrides, particularly gallium, aluminum, and indium nitrides, have gained considerable interest for use as transducing materials in biosensors. Specifically, gallium nitride (GaN) is a semiconductor material with wurtzite crystal structure that has a wide (3.4 eV) band gap and is widely used in ultraviolet–blue light emitting diodes, photodetectors and lasers. In addition, GaN demonstrates good biocompatibility and aqueous stability in conditions relevant to biological applications.[6] While GaN has emerged as a promising candidate for biointerfacing, [7] the potential use of GaN as an inhibitor of aggregation of A β 40 has been reported by our research group.[6] Since previous studies have shown that GaN can interact with various cellular components, it is possible that GaN NPs are able to interact with IAPP and in consequence affect the aggregation behavior. In this study, we investigate the effect of GaN NPs and two other derivatives on the aggregation of IAPP in vitro using a combination of biophysical approaches.

Methods

The trifluoroacetic acid free IAPP peptide was obtained from LifeTein LLC Company (NJ, USA) with >95% purity and used as received. All other reagents were from Sigma-Aldrich (USA).

GaNPs Synthesis and surface modification

GaNPs synthesis have been reported previously.[6] Further GaNP surface modification was based on a previous report.[8] Briefly, GaNPs were treated with 50% aqueous solution containing H₂SO₄: H₂O₂ (ratio 3:1) at constant temperature (62 °C) for 1.5 hours. The hydroxylated product (GaOH NP) was washed with nanopure water, centrifugated (5,000 rpm/10-15min) and dried under a flow of nitrogen. The carboxylic acid derivative (GaCOOH NP) was synthesized by mixing ≈ 1 mg of the GaOH NP with 5.0 mL of aqueous 1 mM dodecanodioic acid. The suspension was kept at ~60 °C for 2 hours then washed with water, centrifugated, and dried under a flow of nitrogen.

X-Ray diffraction (XRD) measurements

The phase structures of the nanoparticle samples were identified using X-ray diffraction techniques with a Bruker D2 Phaser with Cu Ka radiation (wavelength of the radiation, $\lambda = 1.54 \text{ \AA}$) operating at 30 kV and 10 mA.

Oligomerization Kinetics

The fluorescence kinetics were measured using a Fluoroskan Ascent microplate reader (Thermo-Nicolet, USA), using the ThT fluorescence emission using filters (bandpass of 15 nm) with an excitation of 435 and emission at 485 nm, respectively. The emission was measured through the bottom of the 96-well plate every five minutes with five seconds of gentle shaking (60 rpm) before readings at 37 °C. GaNPs stock solutions were prepared by dissolving 0.10 mg/mL in nanopure water and sonicated for 30-40 minutes. IAPP (~1.22 mM) was prepared gravimetrically in DMSO. A typical kinetic run consists of 20 mM Tris/HCl buffer, 20 μ M ThT, 12.8 μ M IAPP, and GaNPs between 0.00 to 0.09 mg/mL with a 300 μ L total volume where the DMSO concentration never exceeds 5% v/v.

Scanning electron microscopy (SEM)

SEM images were obtained at the PREM Materials Characterization Laboratory at University of Puerto Rico-Humacao (JEOL JSM-IT-100 with an Energy Dispersive Spectrometer operating at 25 or 30 kV) or at the LRSM Institute at the University of Pennsylvania (FEI Quanta 600 ESEM operating at 15 kV).

Results

GaNPs Morphology

The morphological properties of GaN NPs were reported previously.[6] The GaN NP sizes determined using the Scherrer formula and the (110) peak at 58.2 degrees range from 6 to 12 nm and the structure correlates to hexagonal wurtzite. The energy-dispersive spectrum reveals that the elemental composition of the GaN NPs is 88.53, 10.01, and 1.46 w/w% for gallium, nitrogen, and oxygen, respectively. GaOH shows XRD peaks at 7.4, 9.4, 20.8, 30.5 and 37.0 2θ . In addition, the intensities of the XRD peaks between 30 and 40 for GaN and GaOH are different, an indication of the surface modification by hydroxyl groups and probably a change in crystal structure. Further surface GaOH oxidation using dodecanodioic acid results in GaCOOH. The XRD peak between 25 and 37 2θ for GaCOOH is broader than for both, GaN and GaOH. However, the basic pattern between GaOH and GaCOOH is similar indicating similar spatial atom arrangement. The broadening effect are explained in terms of larger number of interactions between the nearby hydrophobic chains in agreement to Chen et al.[9]

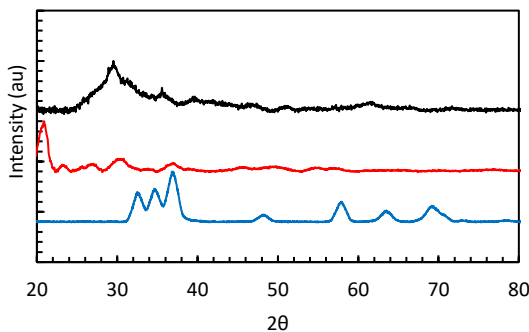


Figure 1: XRD patterns for the GaN (blue), GaNOH (red), and GaCOOH (black) NPs. The plots are shown with linear offset for clarity purposes

Oligomerization kinetics. Kinetics using ThT as a probe

Figure 2A-C shows the time dependent ThT fluorescence intensity changes during IAPP amyloid aggregates formation starting from its monomeric state in Tris/HCl buffer, pH 7.4 in the absence or presence of GaN NPs. All kinetics exhibit a typical sigmoidal shape, characteristic of a nucleation polymerization mechanism, which consists of a lag phase associated with nucleation, a fast growth phase related to the propagation of fibrils, and a final stationary phase related to the aggregated state. Interestingly, the GaNPs surface plays a vital role on the lag phase. GaN and GaOH increases t_{lag} by 3 and 19% relative to IAPP, respectively. However, GaCOOH NPs speed up the t_{lag} by 26%. This speed-up suggests that the long dodecanoic hydrophobic chain in GaCOOH NP provide a

nucleation site that accelerates amyloid formation. A second test to confirm amyloid formation is the use of ANS, a fluorescence probe. However, IAPP oligomers, present during lag phase, do not bind ANS and thus, it only probes the growth and saturation phases.[10] Figure 2D shows the ANS fluorescence after fibril formation under different GaN concentrations. The emission is lower when GaN NP is present. These results agree with the ThT kinetics.

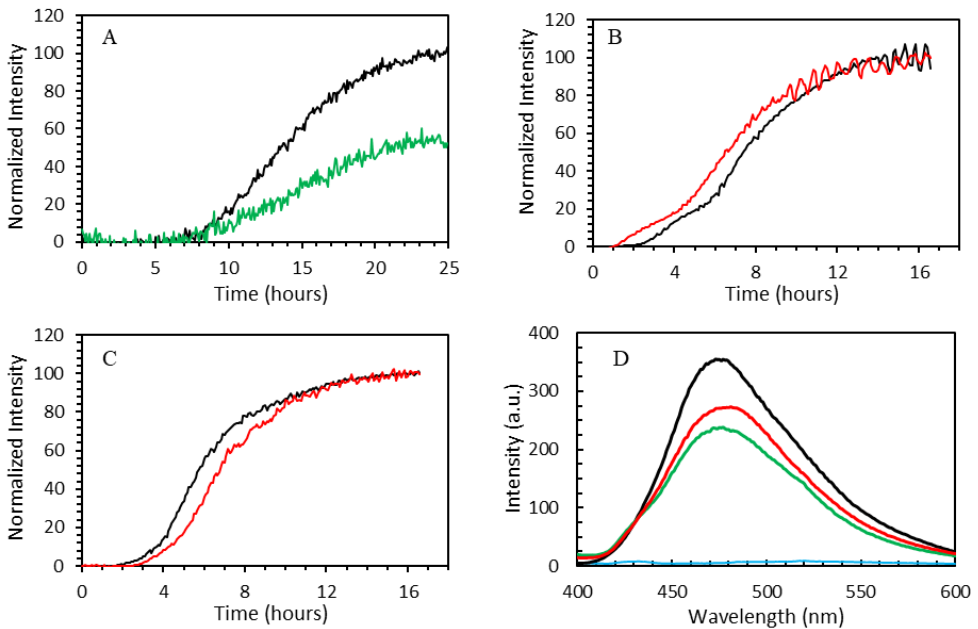


Figure 2: Aggregation kinetics of IAPP (13 μM) in the presence of 87 μg/mL of A) GaN, B) GaCOOH, and C) GaOH, respectively followed by ThT fluorescence. D) ANS fluorescence emission spectra in the presence of IAPP (13 μM) after 96 hours incubation with: 0.00 (black), 50 (red), 92 μg/mL (green) of GaN, and blank (blue).

Conclusions

In summary, we studied the effect of GaN, GaOH, and GaCOOH NPs on IAPP amyloid fibril formation using ThT and ANS fluorescence. Our results show that the presence of GaN and GaOH NPs delays the lag time of IAPP aggregation, indicating its inhibiting activity on crucial oligomeric nucleus formation of the peptide. Also, the results show that GaCOOH NPs can speed up the amyloid fibril lag time of the aggregation kinetics probably due to the presence of a long hydrophobic chain that acts as a nucleation site. Altogether, the GaNPs surface

plays a key role during IAPP aggregation kinetics. Future studies on modification of the surface characteristics of gallium nanoparticles to enhance solubility, selectivity, and sensing may lead to the discovery of new NP inhibitors or sensors for amyloidosis with high biocompatibility and inhibition efficiency.

References

- [1] Cao, P.; Marek, P.; Noor, H.; Patsalo, V.; Tu, L.-H.; Wang, H.; Abedini, A.; Raleigh, D. P., Islet amyloid: From fundamental biophysics to mechanisms of cytotoxicity. *FEBS Letters*, **2013**, 587 (8), 1106-1118.
- [2] Akter, R.; Cao, P.; Noor, H.; Ridgway, Z.; Tu, L.-H.; Wang, H.; Wong, A. G.; Zhang, X.; Abedini, A.; Schmidt, A. M.; Raleigh, D. P., Islet Amyloid Polypeptide: Structure, Function, and Pathophysiology. *Journal of Diabetes Research*, **2016**, 2798269.
- [3] Abedini, A.; Schmidt, A. M., Mechanisms of islet amyloidosis toxicity in type 2 diabetes. *FEBS Letters* **2013**, 587 (8), 1119-1127.
- [4] Nguyen, P.H., Ramamoorthy, A., Sahoo, B.R., Zheng, J., Faller, P., Straub, J.E., Dominguez, L., Shea, J.E., Dokholyan, N.V., De Simone, A., Ma, B., Nussinov, R., Najafi, S., Ngo, S.T., Loquet, A., Chiricotto, M., Ganguly, P., McCarty, J., Li, M.S., Hall, C., Wang, Y., Miller, Y., Melchionna, S., Habenstein, B., Timr, S., Chen, J., Hnath, B., Strodel, B., Kayed, K., Lesné, S., Wei, G., Sterpone, F., Doig, A.J., and Derreumaux, P., Amyloid Oligomers: A Joint Experimental/Computational Perspective on Alzheimer's Disease, Parkinson's Disease, Type II Diabetes, and Amyotrophic Lateral Sclerosis, *Chem. Rev.*, **2021**, 121, 2545–2647.
- [5] Wang, C., Yang, A., Li, X., Li, D., Zhang, M., Du, H., Li, C., Guo, Y., Mao, X., Dong, M., Besenbacher, F., Yang, Y., and Wang, C., *Nanoscale*, **2012**, 4, 1895–1909.
- [6] Torres, K.M., Delgado, A.S., Serrano, E.R., Falcón-Cruz, N.V., Meléndez, A., Ramos, I., Du, D., and Oyola, R. Gallium nanoparticles as novel inhibitors of Aβ40 aggregation. *Mater. Adv.*, 2021,2, 5471-5478.
- [7] Bain, L. E., Hoffmann, M. P., Bryan, I., Collazo, R., and Ivanisevic, A., Adsorption and adhesion of common serum proteins to nanotextured gallium nitride. *Nanoscale*, **2015**, 7, 2360–2365.
- [8] Sahoo, P.; Murthy, P. S.; Dhara, S.; Venugopalan, V. P.; Das, A.; Tyagi, A. K., Probing the cellular damage in bacteria induced by GaN nanoparticles using confocal laser Raman spectroscopy. *Journal of Nanoparticle Research*, **2013**, 15 (8), 1841.
- [9] Chen, Y.; Jyoti, N.; Kim, J., Strong deep-UV and visible luminescence from GaN nanoparticles. *Applied Physics A* **2011**, 102 (3), 517-519.
- [10] Abedini, A., Plesner, A., Cao, P., Ridgway, Z., Zhang, J., Tu, L.-H., Middleton, C.T., Chao, B., Sartori, D.J., Meng, F., Wang, H., Wong, A.G., Zanni, M.T., Verchere, C.-B., Raleigh, D.P., Schmidt, A.M. *eLife* **2016**, 5:e12977.

Acknowledgments

This work was funded by NSF-DMR-2122102 program.

ÍNDICE DE AUTORES | ÍNDICE DE AUTORES | |AUTHORS' INDEX |

Aceves-Mijares, M.....	190, 270
Agusil, J.P.....	196
Allil, A.S.....	82, 334
Allil, R.C.S.B.....	82, 96, 334
Alonso-Chamarro, J.....	74, 112, 247, 274, 279, 353, 379
Altuzar-Aguilar, V.M.....	320, 325
Alvarenga, A.V.....	289
Álvarez, R.....	353
Álvarez-Prada, I.....	169
António, M.....	159
Arasa-Puig, E.....	74, 353
Araújo, M.....	264
Arjona, M.I.....	196
Barroso, M.....	358
Barros-Timmons, A.....	43
Basílio, N.....	148
Bastos, A.C.....	48, 58
Bastos, J.....	159
Bejarano, M.L.M.....	264
Belsley, M.S.....	252
Beltrán-Pérez, G.....	91, 242, 320, 325, 329
Bernuz, M.....	364
Borlido, J.M.....	231
Borrego, C.....	339
Bravo-Sánchez, A.I.....	320
Brett, C.M.A.....	21
Brito, A.R.....	82
Buffon, E.....	132
Cadarso, A.....	38
Calvo-López, A.....	379
Carneiro, C.F.....	107
Carvalho, A.F.....	138
Carvalho, P.....	388
Castellanos, A.....	257
Castillo, J.....	34
Castillo-Mixcóatl, J.....	91, 242, 320, 325, 329
Castro, R.C.....	122
Cetó, X.....	169

Cirto, Y.G.	334
Compadrinho, P.	388
Correia, B.P.	86
Correia, J.H.	17, 181, 218, 223, 227, 231, 252, 388
Costa, F.	138
Costa, J.	201
Costa, L.C.	43
Coto, H.	247, 274, 279, 348
Couceiro, P.	112, 247, 274, 279
Cruz, L.	118, 148
Cruz, M.T.	86
Cruz-Pacheco, A.F.	31, 151
Cuerva, J.	353
Cunha, F.M.	181
Daniel-da-Silva, A.L.	159
Dante, A.D.	96
del Real, R.P.	196
del Toro, N.V.	34
del Valle, M.	169
Delgado, A.S.	396
Deme, I.	289
Díaz, A.M.	38
Domínguez-Horna, C.	38, 190, 257, 270
Du, D.	396
Duch, M.	196
Durán, S.	196
Echeverri, D.	374
Edmonds, T.	25
Espiña, B.	155
Esteves, B.	231, 388
Esteves, M.E.A.	82, 334
Evtuguin, D.V.	43
Figueredo.	392
Falcón-Cruz, N.V.	383, 396
Fantoni, A.	201
Fardilha, M.	159
Faria, C.L.	358
Farias, M.H.	289
Fernandes, A.J.	138
Fernandes, M.	201
Fernández-Sánchez, C.	369
Fernández-Senac, C.	364

Ferreira, M.G.S.	48, 58
Ferreira, R.	159
Figueredo, F.	178
Freitas, J.R.	227
Freitas, P.P.	65
Freitas, R.B.	252, 388
Freitas, V.	118, 148
Gabriel, G.	70
Garate, O.F.	70
Garces, I.	112
García, J.J.	209
García-Antón, J.	169
Gaudin, V.	127
Giménez-Gómez, P.	38
Goessling, J.W.	155, 174
Gomes, M.T.S.R.	164
Gomes, P.A.	358
Gomes, V.	118, 148
Gómez, E.	196
Gonçalves, L.M.	102, 107, 358
Gongora-Rubio, M.R.	264
González-Fernández, A.A.	190, 270
González-Manchón, C.	196
Graça, G.	339
Grez, P.	392
Guevara, K.V.	247, 274, 279
Hassad, F.Z.	127
Hédou, C.	127
Henríquez, R.	178
Hernández-Betanzos, J.	190
Herrera-Chacon, A.	169
Heyser, C.	392
Izquierdo, D.	112
Jimenez-Jorquera, C.	38, 369
Jr, A.P.	264
Kadambi.	196
Karatzas, K.	344
Karavai, O.V.	48, 58
Kulyk, B.	138
Lafaye, C.	369
Lima, A.P.	264
Lima, T.	159

Lopes, D.	344
Lopes, M.	339, 344
Lopez, J.D.	82, 96
Lopez-Garcia, M.	155, 174
Lourenço, P.	201
Louro, P.	296, 301, 307
Maciel, C.	53
Maciel, M.J.	218, 223, 231, 252, 388
Magalhães, J.M.C.S.	53
Magina, S.	43
Manqueros, V.E.	247, 274
Martí, M.	364
Martínez, J.	379
Martinez-Cisneros, C.	112
Martínez-Pérez, P.	155
Mass, M.I.	70
Mateus, N.	118, 148
Medrano, D.M.	348
Meléndez, A.	34, 142, 383, 396
Miranda, A.	339
Monteiro, A.	339
Moreira, F.T.C.	86
Moreno-Acosta, M.A.	329
Muñoz-Aguirre, S.	91, 242, 320, 325, 329
Muñoz-Berbel, X.	38
Naranjo, J.	112
Neves, V.F.	334
Nunes-Pereira, E.J.	388
Oliveira, A.F.	264
Orozco, F.	190
Orozco, J.	31, 151, 374
Oyola, R.	34, 383, 396
Pacheco, L.C.	334
Paiva, C.M.	102
Palacio, D.	209
Pallares-Rusiñol, A.	364
Páscoa, R.N.M.J.	122
Pedraza-Chávez, J.M.	270
Penso, C.M.	102, 107
Pereira, A.C.	86
Pereira, H.M.	218, 223, 231, 388
Pereira, S.O.	138

Pérez Gordillo, J.L:	142
Pérez, O.....	190
Pérez-Díaz, O.....	270
Pérez-García, L.....	196
Pimenta, S.....	252
Pinto, N.J.....	142
Pires, A.S.....	118, 148
Pividori, M.I.....	364
Plaza, J.A.....	196
Puyol, M.....	112, 379
Quinchia, J.....	31, 151
Ramón, E.....	70
Ramos, I.....	34, 142, 383, 396
Rangel-Yagui, C.O.....	264
Rebelo, M.....	339
Rebollo-Calderon, B.....	379
Redondo-Horcajo, M.....	196
Reis, J.....	339, 344
Reyes, M.C.....	48
Ribeiro, C.R.....	102
Ribeiro, D.S.M.....	122
Rivera-Claudio, M.....	34
Rocha, J.L.....	358
Rodrigues, C.....	388
Rodrigues, J.A.....	218, 223, 231
Rodrigues, V.....	339
Rodrigues, V.H.....	227
Rodriguez, A.H.....	214
Rodríguez, H.....	257
Rodríguez, J.A.....	185
Rodríguez-Franch, E.....	169
Rodríguez-Garciapiña, J.L:	91
Rodriguez-Lorenzo, L.....	155
Roldán, A.....	369
Rosa, T.S.....	284
Rossi, R.....	364
Rovira, M.....	38, 369
Rudnitskaya, A.....	43
Sala, X.....	169
Salazar, P.....	178, 392
Sales, M.G.....	86
Santiago-Aviles, J.J.....	142, 238

Santos, C.P.	388
Santos, D.R.	65
Santos, J.H.P.M.	264
Santos, J.L.M.	122
Santos, N.F.	138
Saraiva, M.L.M.F.S.	122
Saubade, M.	369
Saul, C.K.	238
Schrebler, R.	392
Seabra, A.C.	214, 284, 313
Segura-Quijano, F.	209
Serôdio, J.	155
Serrano, E.A.	379
Sierra, S.	209
Silva, A.S.	82
Silva, C.A.	388
Silva, M.F.	181, 227
Silva, M.L.	82
Silva, N.F.D.	53
Silva, P.H.	96
Silva-Apango, D.	242
Soreto, S.	43
Sosa-Ramos, O.	325
Soumet, C.	127
Sousa, A.S.	164
Sousa, M.P.	86
Stradiotto, N.R.	132
Suárez, T.	196
Teixeira, P.	53
Torres, K.M.	396
Valdés, E.	257
Valdés, F.	247, 274, 279, 348
Veiga, L.S.	70
Verdon, E.	127
Veríssimo, M.I.S.	164
Vieira, E.M.F.	218, 223, 231
Vieira, J.N.	218, 223
Vieira, M.	201, 296, 301, 307
Vieira, M.A.	296, 301, 307
Vieira, P.	301, 307
Vilarinho, R.	155, 174
Vitorino, R.	159

Werneck, M.M.....	82, 96, 334
Wioppiold, A.F.B.....	313
Ybarra, G.O.....	70
Yuan, F.....	238
Zerega, P.....	178
Zheludkevich, M.L.....	58